

THE WINDOWLESS GASEOUS TRITIUM SOURCE OF THE KATRIN EXPERIMENT

CHARACTERISATION OF GAS DYNAMICAL AND PLASMA PROPERTIES

Zur Erlangung des akademischen Grades eines
DOKTORS DER NATURWISSENSCHAFTEN
von der Fakultät für Physik
des Karlsruher Instituts für Technologie
genehmigte
DISSERTATION
von
Dipl. Phys. Laura Kuckert
geb. Neumann
aus Berlin

Erstgutachter: Prof. Dr. G. Drexlin
Institut für Experimentelle Kernphysik, KIT
Zweitgutachter: Prof. Dr. Ch. Weinheimer
Westfälische Wilhelms-Universität Münster

Tag der mündlichen Prüfung: 28. Oktober 2016

Declaration of authorship

I declare that I have developed and written the enclosed thesis completely by myself, and have not used sources or means without declaration in the text.

Erklärung der Selbständigkeit

Ich versichere wahrheitsgemäß, die Arbeit selbstständig angefertigt, alle benutzten Hilfsmittel vollständig und genau angegeben und alles kenntlich gemacht zu haben, was aus Arbeiten anderer unverändert oder mit Abänderungen entnommen wurde.

Karlsruhe, 10.10.2016

.....
(Laura Kuckert)

Zusammenfassung

Sie sind die zweithäufigsten Teilchen im Universum, haben einen essentiellen Anteil an dessen Strukturbildung und tragen Informationen aus dem Inneren astrophysikalischer Objekte, denn sie erreichen die Erde fast unbeeinflusst von Wechselwirkungen. Diese besonderen Eigenschaften machen Neutrinos bedeutsam für viele Bereiche der Elementarteilchen- und Astroteilchenphysik, die Kosmologie eingeschlossen. Die Tatsache, dass sie eine von Null verschiedene Ruhemasse besitzen, konnte in verschiedenen Oszillationsexperimenten nachgewiesen werden. Dieser Fakt ist gleichbedeutend mit Physik jenseits des Standardmodells, denn in ihm bleiben Neutrinos masselos. Mögliche Erweiterungen schließen Phänomene wie CP-Verletzung im Leptonsektor, Leptonenzahlverletzung sowie die Existenz rechtshändiger, steriler Neutrinos ein. Im besonderen Fokus steht der Mechanismus, welcher die auffallend kleinen Neutrinomassen generiert, da er möglicherweise mit einer neuen Energieskala verknüpft ist.

Die Kenntnis der absoluten Neutrinomassenskala hierbei unabdingbar um genauere Modelle zu ermöglichen. Trotz langjähriger experimenteller Bemühungen blieb die Frage nach der absoluten Neutrinomasse allerdings bis heute ungeklärt.

Zurzeit werden verschiedene experimentelle Ansätze verfolgt mit dem Ziel, die absolute Neutrinomassenskala zu bestimmen. Der vielversprechendste ist dabei die hochauflösende Spektroskopie des β -Zerfalls des Tritiums, der eine modellunabhängige Bestimmung der Elektronantineutrinomasse erlaubt. Unter Verwendung dieser Methode strebt das Karlsruher Tritium Neutrino Experiment KATRIN als Vorreiter einer neuen Generation von Neutrinomassenexperimenten an, die Sub-Elektronvolt-Massenskala mit einer Sensitivität von 200 meV (90% C.L.) zu erreichen. Der Aufbau des KATRIN Experimentes befindet sich im Tritium Labor Karlsruhe (TLK) auf dem Gelände des Campus Nord des Karlsruher Instituts für Technologie (KIT). Die Verbindung einer Tritiumquelle hoher Luminosität mit einem Spektrometer auf Basis des MAC-E Filterprinzips, welches eine exzellente Energieauflösung ermöglicht, erlaubt es zu dieser bisher unerreichten Sensitivität zu gelangen. Die Inbetriebnahme des kompletten Aufbaus beginnt während der Fertigstellung dieser Dissertation. Die ersten Messungen in denen Tritium in der Quelle zirkuliert wird sind für 2017 geplant.

Zusätzlich zu den experimentellen Herausforderungen, bezüglich des Betriebs eines Systems der Größe von KATRIN unter Ultrahochvakuumbedingungen und einer erforderlichen Stabilisierung der Betriebsparameter auf dem Niveau von wenigen Tausendstel und darunter, müssen alle systematischen Effekte, welche die Form des Elektronspektrums beeinflussen überprüft werden und verstanden sein. Die genaue Kenntnis der Quellcharak-

teristika sowie der physikalischen Prozesse innerhalb der Quelle ist daher von höchster Bedeutung.

In der Rahmen der vorliegenden Arbeit, wurden umfassende Plasma- und Gasdynamikmodelle erstellt und wichtige Quellparameter dieser Prozesse charakterisiert. Die Resultate der zugrunde liegenden Simulationen wurden in die Berechnung der Quellspektren mit einbezogen. Auf diese Weise konnte der Einfluss der verschiedenen untersuchten Effekte sowie deren Modellunsicherheiten auf die Neutrinomassenmessung mit KATRIN quantifiziert werden.

Gasdynamische Eigenschaften der Quelle

Eine der Hauptsystematiken des KATRIN Experiments entsteht durch die Unsicherheit in der Beschreibung der Streuung der β -Zerfallselektronen an Gasmolekülen in der Quelle. Diese Streuprozesse beeinflussen die Form des β -Zerfallsspektrums. Um sie auf verlässliche Weise beschreiben zu können, muss das Produkt aus Säulendichte und totalem inelastischen Streuquerschnitt auf 0.2% genau bekannt sein.

Um in der Lage zu sein, die Säulendichte genau zu berechnen, muss das bisherige Gasmodell, welches lediglich aus dem 10 m langen WGTS-Quellrohr bestand, um Gasflussberechnungen in den Pumpkammern und Strahlrohrelementen der DPS1 erweitert werden, da ein nichtverschwindender Teil des Gases in diesen Komponenten zu finden ist. Die oben erwähnten Komponenten wurden, aufgrund der Komplexität der Berechnung von verdünnten Gasflüssen sowie den großen Unterschieden bezüglich ihrer Geometrie und Gasflusscharakteristiken, in separaten Modellen simuliert. Um diese Rechnungen zu einem Gasmodell der kompletten Quellsektion kombinieren zu können, musste das bereits existierende Strahlrohrgasmmodell grundlegend erneuert werden.

Es wurde gezeigt, dass sich etwa 1% der gesamten Säulendichte in den Komponenten der DPS1, und damit nicht im zentralen 10 m Quellrohr der WGTS, ansammeln. Um die 0.2% Säulendichtegenauigkeit zu erreichen müssen also die Komponenten der DPS1 im Quellmodell, wenn auch mit geringerer Anforderung an die Genauigkeit, berücksichtigt werden. Für den Gasflussreduktionsfaktor in der DPS1 ergab sich ein Wert von 400, die Gasdichte hingegen wird von der Injektion bis zum Beginn der DPS2 um einen Faktor 2000 reduziert.

Es wurde gezeigt, dass die Genauigkeit der Säulendichteberechnung auf Basis des Gasmodells im Wesentlichen von der Unsicherheit der Flussmodellierung innerhalb des zentralen 10 m Quellrohres abhängt. Um zu einer verlässlichen Abschätzung der modellbezogenen Unsicherheit zu gelangen, wurde, auf einem anderen Lösungsansatz beruhend, eine weitere Gasdynamiksimulation dieser Komponente durchgeführt. Es zeigte sich, dass beide Simulationen in der Dichtevertteilung um bis zu 15% voneinander abweichen, ihre Säulendichten jedoch innerhalb von 1% übereinstimmen. Unter weiterer Berücksichtigung der Unsicherheit der Transportparameter, sowie der Eingabewerte für Einlass- und Auslassdruck, liegt die Gesamtunsicherheit der Säulendichteberechnung damit weit über der benötigten Genauigkeit von 0.2%. Das bedeutet, eine experimentelle Bestimmung des Produktes aus Säulendichte und Streuquerschnitt ist zusätzlich zur theoretischen Modellierung unumgänglich.

Diesbezüglich wurde gezeigt, dass es mit dieser Absolutmessung möglich ist, die geforderte Genauigkeit von 0.2% zu erreichen. Das Messergebnis kann weiterhin genutzt werden, um die Anforderungen an die Kenntnis des totalen inelastischen Streuquerschnitts zu lockern – die bisherige Genauigkeit des Literaturwertes liegt bei nur 2%.

Zwischen den Absolutmessungen mit der Elektronenkanone kann es zu Fluktuationen der Säulendichte aufgrund von Schwankungen der Quellparameter kommen. Mehrere Aktivitätsmonitore werden während der KATRIN Messungen genutzt werden um zu überprüfen, ob die Fluktuationen innerhalb des 0.2% Niveaus liegen.

Im Rahmen dieser Doktorarbeit wurde gezeigt, dass das Quellgasmodell genutzt werden kann, um die angesprochenen Schwankungen in der Berechnung des β -Zerfallsspektrums der Quelle zu berücksichtigen. Ungeachtet der relativ großen Unsicherheit der Berechnung des Absolutwertes der Säulendichte kann das Modell benutzt werden, um Säulendichteänderungen aufgrund von Variationen der Betriebsparameter im Prozentbereich präzise zu bestimmen. Um zu überprüfen, inwiefern das Gasmodell für diesen Zweck eingesetzt werden kann, wurden in umfangreichen Fehleranalysen alle Modellierungs- und Eingabeparameter betreffenden Unsicherheiten mit einbezogen. Hierbei ergab sich, die angestrebte 0.1% Stabilität der Quellbetriebsparameter vorausgesetzt, eine Verbesserung der Säulendichtepräzision von den ursprünglich angesetzten 0.2% zu 0.03%. Diese Präzision erlaubt es, die Anforderungen an die Absolutbestimmung des Produktes aus Säulendichte und Streuquerschnitt mit der Elektronenkanone von einer relativen Genauigkeit von 0.14% auf 0.19% aufzuweiten.

Neben den Untersuchungen den integrierten Wert (Säulendichte) betreffend, wurde in dieser Doktorarbeit der Einfluss der Gasdichteverteilung in der Quelle analysiert. Eine genaue Beschreibung der Gasdichteverteilung in der Quelle ist die Basis um die räumlichen Verteilungen der verschiedenen Quellvariablen (Temperatur, Magnetfeld, Geschwindigkeit und elektrisches Potential) in den Berechnungen des Quellspektrums berücksichtigen zu können. Um die erforderliche Genauigkeit der Dichteverteilung abzuschätzen wurden mehrere Geschwindigkeits- und Dichtemodelle in Ensemblesimulationen verglichen. Hierbei wurde gezeigt, dass ein großer Einfluss der korrekten Beschreibung der Geschwindigkeitsverteilung zuzuordnen ist. Im Vergleich der beiden Strahlrohrdichtemodelle ergab sich eine nichtverschwindende systematische Neutrinomassenverschiebung von $(-7.5 \pm 2.4) \cdot 10^{-4} \text{ eV}^2$, was die Notwendigkeit der Verwendung von passenden Dichte- und Geschwindigkeitsmodellen unterstreicht.

Die Absolutmessung mit der Elektronenkanone erlaubt grundsätzlich lediglich eine Bestimmung des Produkts aus Säulendichte und Streuquerschnitt. Daher wurde überprüft, ob eine Säulendichte- und Streuquerschnittsgenauigkeit von 2% ausreichend ist, solange dennoch das Produkt mit einer Unsicherheit kleiner 0.2% bekannt ist. Es wurde gezeigt, dass diese Frage eng mit den oben erwähnten Inhomogenitäten verknüpft ist – im Falle einer ideal homogenen Quelle können die einzelnen Parameter im Produkt nicht unterschieden werden. Indem ein realistischeres Quellmodell zugrunde gelegt wurde konnte gezeigt werden, dass die Unsicherheiten der einzelnen Parameter die Neutrinomassenanalyse beeinflussen können, allerdings nur, falls diese Unsicherheiten größer als etwa 5% sind. Der Einfluss einer Unsicherheit von 2% ergab einen verschwindend geringen Beitrag.

In einer kombinierten Analyse wurden alle erwähnten Unsicherheiten in Bezug auf die Beschreibung der Quellgasdynamik mit einem Quellmodell verknüpft, welches realistische Verteilungen von Temperatur, Magnetfeld und elektrischem Potential enthält. Hierbei ergab sich eine systematische Neutrinomassenverschiebung von $(3.06 \pm 0.24) \cdot 10^{-3} \text{ eV}^2$. Obwohl diese Verschiebung beinahe doppelt so groß ist wie der angestrebte Designwert im Gesamtbudget der KATRIN Systematik, kann die Unsicherheit, welche mit der Beschreibung der Quellgasdynamik verbunden ist, als verstanden angesehen werden – in den verknüpften Untersuchungen wurden mehrere zusätzliche Unsicherheiten mit einbezogen, die bei der Abschätzung des oben genannten Fehlerbeitrages nicht berücksichtigt wurden.

Um die Vorhersagen des entwickelten Gasmodells zu testen, wurden verschiedene Testmessungen vorgeschlagen, die im Rahmen der KATRIN Inbetriebnahmemessungen durchgeführt werden.

Plasmaphänomene in der Quelle

Durch die Emission der Elektronen im β -Zerfall des Tritiums und den damit verbundenen Sekundärionisationsprozessen bildet sich in der Quelle ein kaltes Niedrigdruckplasma. Die elektrischen Felder, die sich innerhalb des Plasmas bilden, bestimmen die Potentialverteilung in der WGTS. Diese Verteilung muss gut bekannt sein, da sie die Startenergie der Elektronen des β -Zerfalls festlegt.

Im Verlauf dieser Doktorarbeit wurde ein umfassendes Plasmamodell erstellt. Beginnend bei einem eindimensionalen Elektronendiffusionsansatz, wurde es hin zu einer zweidimensionalen, axialsymmetrischen drei-Teilchen Fluidplasmabeschreibung entwickelt, in der innere Raumladungsfelder sowie äußere elektrische Felder berücksichtigt werden. Anders als bei früheren Ansätzen zeigten sich bei diesem Modell keine numerischen Instabilitäten. Es konnte nachgewiesen werden, dass die Lösungen auch im Falle der Veränderung verschiedener Plasmaparameter stabil sind.

Das Quellplasma ist in radialer Richtung durch die Oberfläche der Stahlwand begrenzt. In longitudinaler Richtung wird es durch die Goldoberfläche der Rear Wall abgeschlossen. Diese wurde ursprünglich konstruiert, um als elektrisch leitende, senkrecht von den Magnetfeldlinien durchsetzte Oberfläche die von den darin gebundenen Plasmateilchen getroffen wird, das Plasmapotential entlang des Flussschlauches zu bestimmen. Welche Rolle dabei die Austrittsarbeitsdifferenz von ungefähr 1 eV zwischen Stahl- und Goldoberfläche spielt war unbekannt.

Aufgrund der Ausdehnung des neugeschaffenen Plasmamodell in radialer Richtung wurde es im Rahmen der vorliegenden Arbeit möglich, die Auswirkungen jener Oberflächenpotentialdifferenz zu untersuchen. So konnte gezeigt werden, dass ein Unterschied von 1 eV zwischen Stahl- und Goldoberfläche eine große Plasmapotentialinhomogenität von etwa 250 meV entlang der Strahlrohrachse nach sich zieht. Selbst eine Randpotentialdifferenz von 100 mV führt schon zu einer Potentialinhomogenität von 25 meV. Dieser Wert ist bereits doppelt so groß, wie das im KATRIN Design-Report veranschlagte Limit für Quellpotentialdifferenzen.

Anders als erwartet, führen große Potentialdifferenzen der das Plasma begrenzenden Oberflächen zur Bildung von negativen Raumladungen im Plasma – abhängig vom Vorzeichen der Differenz ist entweder der Ausfluss der Elektronen durch ein negatives elektrisches Feld blockiert (die Ionen können die Quelle weiterhin verlassen). Im anderen Fall sättigt der Elektronenfluss, während der Ionenfluss aufgrund der größeren Oberfläche des Strahlrohrs noch weiter ansteigen kann (nur die Ionen können die Stahlwände des Strahlrohrs erreichen, da die transversale Bewegung der Elektronen aufgrund ihrer geringeren Masse stärker durch das Magnetfeld eingeschränkt ist).

Die optimale Konfiguration des Randpotentials, verbunden mit einer maximalen Homogenität des Plasmapotentials, ergibt sich, falls das Rear Wall-Potential leicht negativ ist im Vergleich zum Strahlrohroberflächenpotential (der Unterschied ist im Bereich der Elektronentemperatur, also bei etwa 3.9 mV für 30 K). Falls alle Ränder sich auf dem gleichen Potential befinden, ergibt sich ein ähnliches Resultat. Für diesen Fall wurde die maximale Inhomogenität entlang der Achse des Strahlrohrs zu 6-7 meV bestimmt.

Die Annahme homogener Austrittsarbeiten über die gesamte jeweilige Oberfläche ist unrealistisch. Daher wurde der Einfluss von Potentialdifferenzen unterschiedlicher geometrischer Größe und Stärke entlang der Oberflächen untersucht. Im Bezug auf die Rear Wall sind die materialspezifischen Abweichungen gering (nicht größer als 10 meV). Allerdings können hier durch die Adsorption von Tritium Austrittsarbeitsdifferenzen bis zu 30 mV auftreten. Eine detaillierte Analyse einer Reihe von Rear Wall-Oberflächenpotentialdifferenzen ergab, dass das Rear Wall-Oberflächenpotential, anders als bisher angenommen, sich nicht durch die komplette Länge des Flussschlauches durchsetzt. Die Strukturen sind bereits nach einigen Zentimetern oder sogar schon nach Millimetern ausgewaschen. Das bedeutet, dass

die Inhomogenität des Plasmas sich nicht durch ein ungleiches Potential entlang der Rear Wall beeinflussen lässt. Der absolute Wert des Raumladungspotentials im Plasma hingegen kann sogar von kleinen Rear Wall-Potentialinhomogenitäten stark beeinflusst werden. Die Austrittsarbeit des Strahlrohrmaterials weist deutlich größere Inhomogenitäten auf (bis zu 1 eV). Zusätzlich zu diesen intrinsischen Effekten muss bei 30 K die hohe Wahrscheinlichkeit berücksichtigt werden, dass Tritium an der Stahlwand adsorbiert. Eine Abschätzung der relevanten Adsorptionsprozesse ergab ein ortsabhängiges Adsorptionsprofil, das verknüpft ist mit dem Dichteprofil des Tritiumgases entlang des Strahlrohrs. In entsprechenden Plasmasimulationen zeigte sich allerdings, dass die damit verbundene maximale Austrittsarbeitsspannung von 26 meV kaum in das Plasmavolumen eindringt. Das gleiche gilt für kleinskalige Potentialstrukturen entlang der Strahlrohroberfläche – Differenzen mit Magnituden von -0.1 V to 0.5 V wurden untersucht, zeigten jedoch lediglich einen untergeordneten Effekt auf die Plasmahomogenität.

Es lässt sich schlussfolgern: Differenzen (realistischer Größe), entlang einer Oberfläche haben kaum einen Effekt auf die Messungen mit KATRIN, während Unterschiede zwischen den begrenzenden Oberflächen einen großen Einfluss haben können.

Indem die Rear Wall auf ein bestimmtes Potential gesetzt wird, lassen sich die Oberflächendifferenzen zwischen den beiden begrenzenden Oberflächen ausgleichen. Es wurde gezeigt, dass Messungen mit monoenergetischen Elektronen von ^{83m}Kr , welches mit dem Quellgas zirkuliert wird, Aufschluss über die Oberflächendifferenz geben können, die *a priori* nicht genau bekannt ist. Allerdings finden diese Messungen bei einer erhöhten Strahlrohrtemperatur von etwa 110 K statt. Daher wird erwartet, dass sich das Adsorptionsverhalten von Tritium an den Stahlrohrwänden ändert.

Unterschiedliche Ansätze wurden in dieser Arbeit vorgeschlagen, um die Randpotentiale bei nominalen Tritiumbedingungen zu untersuchen. Die niedrigste Oberflächepotentialdifferenz, die überprüfbar ist, sind 60 eV, was wiederum eine Plasmapotentialinhomogenität von etwa 20 mV bedeutet.

Es wurde gezeigt, dass die Wahrscheinlichkeitsverteilung des Plasmapotentialprofils, welches sich in der Quelle aufbaut, nicht gaussförmig ist, was im Kontrast zu den bisherigen Erwartungen steht. Daher ist der Neutrinosmasseneffekt der simulierten Potentialverteilungen größer als bisher gedacht. Die kleinstmögliche Neutrinosmassenverschiebung ergibt sich, falls sich alle Oberflächen in etwa auf gleichem Potential befinden. In diesem Fall ist die maximale Potentialinhomogenität entlang der Strahlrohrachse etwa 6 mV und der Neutrinosmasseneffekt liegt bei $(-5.8 \pm 2.8) \cdot 10^{-4} \text{ eV}^2$.

Dieser equipotentielle Fall ist wahrscheinlich nicht einstellbar. Eine eher konservative Abschätzung ergibt sich, wenn von einer realistisch erreichbaren Oberflächepotentialdifferenz von 110 meV ausgegangen wird. Für diesen Fall wurde eine systematische Neutrinosmassenverschiebung von $(-1.5 \pm 0.25) \cdot 10^{-3} \text{ eV}^2$ berechnet. Diese kann als repräsentativer Wert für die systematische Neutrinosmassenunsicherheit aufgrund von Plasmaprozessen in der Quelle angesehen werden.

Die Validierung der Vorhersagen der geschaffenen Modelle in Testmessungen während der momentan beginnenden Inbetriebnahmephase von KATRIN bildet den letzten Schritt für das qualitative und quantitative Verständnis der in dieser Arbeit beschriebenen Plasma- und gasdynamischen Prozesse in der Quelle.

Introduction and Objective

Being the second most abundant particles in the universe, and even the most abundant massive ones, neutrinos are of highest interest in the fields of particle physics and astroparticle physics including cosmology. They play a key role in the structure formation in the universe and are messenger particles from astrophysical objects since, different from light, they reach the earth almost undisturbed by interactions. In the Standard Model of particle physics neutrinos stay massless. On the other hand, they were beyond any doubt shown to be massive in a large number of neutrino oscillation experiments, which implies that neutrinos open the door to physics beyond the Standard Model. Related extensions and new concepts can give rise to phenomena like CP-violation in the lepton sector, lepton number violation or postulate the existence of sterile right handed neutrinos. Special interest lies in the mechanism that generates the strikingly small neutrino masses which might even be connected to a new energy scale.

To further develop these models, the knowledge of the absolute neutrino mass scale is indispensable. The determination of this mass scale is still an open issue although already since many years large efforts have been made in order to address this question experimentally.

A variety of different experimental approaches are being pursued in this quest. The most promising method, giving model independent access to the mass of the electron antineutrino, is high precision β -decay spectroscopy of tritium. Pursuing this approach, the next generation neutrino mass experiment KATRIN (Karlsruhe Tritium Neutrino experiment), installed at the Tritium Laboratory Karlsruhe (TLK) at the Campus North side of the Karlsruhe Institute of Technology (KIT), aims to enter the sub-electronvolt neutrino mass scale with a sensitivity of 200 meV (90% C.L.). This unprecedented sensitivity will be reached by combining a high luminosity tritium source with a spectrometer of MAC-E filter type featuring an excellent energy resolution. Starting commissioning measurements of the full system at the time of writing of this thesis, first measurements with tritium cycled in the source are scheduled for 2017.

In addition to the challenging experimental aspects related to the operation of such a large system under ultra high vacuum conditions with a required stability of operation parameters at the per mill level and below, all systematic effects influencing the shape of the electron spectrum need to be understood and under control. A proper understanding of the characteristics of the tritium source as well as an identification and quantification of all source-related processes modifying the measured spectrum of electrons is of utmost importance. Here large efforts have already been made which have led to a detailed source

model that allows to accurately calculate the β -decay spectra that will be measured with KATRIN.

Still, some important information to complete the source model description is missing which is related to the description of properties of the gas flow and to the understanding of processes in the low-density tritium plasma.

To provide this crucial information, the two main objectives of the thesis at hand are:

1. Completion of the picture of gas flow related processes in the source. This includes the simulation of gas dynamics in the components of the first stage of the differential pumping section, and the investigation of its applicability in the neutrino mass analysis with KATRIN.
2. Conception of a detailed plasma model of the source, including the transport of differently charged particles (diffusive and according to the formed electric fields), creation and annihilation processes as well as interactions with boundary surfaces and potentials.

One of the key parameters of the whole experiment, the column density of molecular gaseous tritium, is related to the gas density distribution in the source section. The experimental determination of its absolute value as well as the modelling of its evolution in between these measurements need to be analysed in detail and the related uncertainties have to be investigated thoroughly.

The cold tritium plasma that forms in the source determines the distribution of the electric potential in this component which needs to be as homogeneous as possible since it sets the starting potential energy of the electrons that are created in the plasma. Once the realistic plasma model is set-up, it needs to be used to investigate the potential distribution that forms within and how it is influenced by source parameters and boundary conditions.

The predictions and results obtained with both models are used to quantify the systematic effect of the calculated distributions of source variables and related uncertainties on the neutrino mass measurement with KATRIN.

Outline

This thesis starts with an introduction into the main aspects of neutrino physics in chapter 1, with a particular emphasis on massive neutrinos. The implications of non-zero neutrino masses are discussed and possible mass generation mechanisms are introduced. An insight to different approaches to the experimental determination of the absolute neutrino mass scale is given, focussing on the kinematic approach adopted by single β -decay experiments.

In the subsequent chapter 2 the KATRIN experiment is described, presenting its measurement principle and data analysis procedure. Its main components are reviewed, giving a more detailed description of the tritium source as the main part of this thesis is related to the characterisation of physical processes in the source.

Chapter 3 summarises the simulation of heat transfer processes in the pump ports of the source. The resulting temperature distributions provide important information required for the gas dynamic simulations in these domains that are presented in chapter 4. Here the modelling of gas flow in the different domains of the source sections is characterised and the combination of the single components into a comprehensive gas model is described. Different test measurements are proposed for experimental verification of this model. The key parameter column density is introduced and a detailed investigation of its absolute and relative modelling and measurement uncertainties and their particular impact on the neutrino mass analysis is performed.

Chapter 5 focuses on the description of the formation of the cold tritium plasma in the source. An extensive three-particle plasma model is built including charged particle creation and annihilation processes, surface interactions as well as the complicated interplay

between particle transport and interactions with the electric fields present in the plasma. Measurements with monoenergetic electrons of ^{83m}Kr that can give experimental access to the potential distribution are described. Emphasis is put on the impact of different combinations of boundary surface potentials on the potential distribution that forms in the plasma. The importance of achieving a configuration that sets the plasma facing surfaces on equipotential is underlined. The corresponding systematic effect on the neutrino mass determination is investigated thoroughly.

The final chapter 6 summarises the results obtained in the course of this thesis work.

Contents

Zusammenfassung	v
Introduction and Objective	xi
1. Neutrino physics and current neutrino mass limits	1
1.1. The neutrino – a brief historical overview	2
1.2. Neutrinos in the Standard Model of particle physics	3
1.3. Neutrino oscillations	4
1.3.1. Solving the solar neutrino problem	4
1.3.2. Theoretical description of neutrino oscillations	6
1.3.3. Current experimental oscillation parameter values	9
1.3.4. Matter effects	13
1.4. Neutrinoless double beta decay	16
1.4.1. Two neutrino double beta decay	16
1.4.2. Neutrinoless double beta decay	16
1.5. Neutrino masses – generation and experimental determination	19
1.5.1. Neutrino mass generation	19
1.5.2. Experimental neutrino mass determination	21
2. Neutrino mass measurement with the KATRIN Experiment	29
2.1. Measurement principle	30
2.1.1. MAC-E filter principle	30
2.1.2. Transmission and response function	35
2.2. Neutrino mass sensitivity	36
2.3. Main components	39
2.3.1. Source and transport section	39
2.3.2. Rear section	47
2.3.3. Spectrometer and detector section	50
2.3.4. Monitoring devices for the source and transport section	52
2.4. Simulation and analysis software	55
2.4.1. The particle tracking software Kassiopeia	55
2.4.2. Source and Spectrum Calculation software SSC	55
2.4.3. Spectrum fitting software KaFit	60
3. Temperature distribution in the first Differential Pumping Section DPS1	67
3.1. The modes of heat transfer	69
3.2. Cooling concept of the DPS1 pump ports	70
3.3. Simulation of heat transfer processes in the DPS1	72
3.3.1. Heat transport in the neon and helium cooling tubes	72
3.3.2. Calculation of heat transport in the first pump port	76
3.3.3. Modelling of demonstrator measurement	82
3.3.4. Calculation of heat transport in the second pump port	85

3.4. Conclusion	87
4. Characterization of gas dynamics in the Source and Transport Section	89
4.1. Column density as a key parameter	90
4.2. Simulation of gas dynamics in the Source and Transport Section	94
4.2.1. Theoretical framework	94
4.2.2. Input parameters for intermolecular and gas surface interaction	100
4.2.3. The gas model framework of the KATRIN source	101
4.2.4. Modelling of end effects in the WGTS beam tube	105
4.2.5. Gas dynamics in the WGTS beam tube – a comparative calculation	106
4.2.6. Modelling of gas flow in the DPS1	110
4.2.7. Modelling of pump failure in the DPS1	117
4.2.8. The gas model of KATRIN in SSC – current status	118
4.3. Uncertainties of the gas model	120
4.3.1. Model dependent uncertainties	120
4.3.2. Uncertainty related to input parameters	122
4.4. Modelling of column density changes	124
4.4.1. Limits for modelling of column density variation	128
4.5. Experimental determination of the column density	133
4.5.1. Absolute measurements	133
4.5.2. Monitoring measurements	134
4.6. Verifying the gas model – possible test measurements	135
4.7. Gas dynamics and systematic uncertainty of the neutrino mass measurement	137
4.7.1. Neutrino mass uncertainty related to $\Delta(\rho d \cdot \sigma)$	138
4.7.2. Column density versus scattering cross section	138
4.7.3. Effect of density model	139
4.7.4. Combined gas dynamical uncertainty	142
4.8. Summary	143
5. Investigation of Plasma Phenomena in the WGTS	145
5.1. Theoretical considerations	148
5.1.1. Potential, work function and plasma sheath	148
5.1.2. Charged particle transport and fluid approach	153
5.2. General remarks on the WGTS plasma conditions	159
5.3. Modelling of the WGTS plasma	165
5.3.1. Previous WGTS plasma models	166
5.3.2. Development of a realistic two-dimensional WGTS plasma model . .	167
5.3.3. Influence of plasma conditions and parameters on the WGTS potential	190
5.3.4. Impact of boundary bias and work function on WGTS potential .	205
5.3.5. Effect of electron emission at rear wall	223
5.4. Experimental access to WGTS plasma potential	228
5.4.1. The ^{83m}Kr mode of the Windowless Gaseous Tritium Source . . .	229
5.4.2. Experimental optimisation of rear wall bias voltage	231
5.5. Implications of plasma potential for neutrino mass uncertainty	236
5.5.1. Gaussian potential fluctuations in the WGTS	237
5.5.2. Potential distribution from plasma simulation	239
5.6. Summary	243
6. Conclusions and Outlook	249
Appendix	255
A. Calculation of flow in the cooling tubes	255
B. Calculation of bellow heat transfer coefficients	255

C. Technical data MAG W 2800	258
D. Simulation of characteristic time scale for pressure changes	259
E. Modelling of pump port pressure changes	259
F. Modelling of tritium adsorption at the WGTS tube walls	262

Bibliography	269
---------------------	------------

List of Figures

1.1. Signal from the Poltergeist experiment	3
1.2. Model of solar neutrino spectrum	5
1.3. Neutrino mass differences	8
1.4. Survival probability neutrino oscillation	9
1.5. Survival probability, θ_{13}	13
1.6. Oscillation amplitude in matter	15
1.7. Matter effect ν_e survival probability	15
1.8. Mass parabolas β -decay	17
1.9. Feynman diagrams illustrating $0\nu\beta\beta$ -decay	18
1.10. Cartoon spectrum of $0\nu\beta\beta$ -decay	19
2.1. Integrated and differential KATRIN spectra	31
2.2. Integrated spectra for different neutrino masses	32
2.3. MAC-E filter principle	33
2.4. KATRIN transmission and response function	37
2.5. Katrin beam line	39
2.6. WGTS cryostat	41
2.7. Arrival of the WGTS cryostat	42
2.8. WGTS beam tube cooling principle	43
2.9. KATRIN transmission and response function	46
2.10. CPS CAD model and photograph	47
2.11. Scheme of inner loop	48
2.12. Rear section scheme and experimental set-up	49
2.13. CAD drawing BIXS system	54
2.14. Scheme forward beam monitor	54
2.15. Principle of voxelisation	57
2.16. Schema of SSC spectrum calculation	61
2.17. Toy measurements and analytical spectra	63
2.18. Exemplary outcome of an ensemble test	65
3.1. Cooling schema DPS1 pump ports	71
3.2. Temperature distribution from N_2 and He coolant simulation	75
3.3. Geometry model of first pump port DPS1	76
3.4. 3D temperature distribution 1st pump port DPS1	78
3.5. Longitudinal and azimuthal beam tube end temperature ($T_{\text{TMP}} = 333\text{ K}$)	79
3.6. Longitudinal and azimuthal WGTS beam tube end temperature ($T_{\text{TMP}} = 363\text{ K}$)	79
3.7. Longitudinal and azimuthal WGTS beam tube end temperature ($T_{\text{TMP}} = 393\text{ K}$)	80
3.8. Temperature and irradiated heat power along the WGTS bellow	81
3.9. Temperature distribution demonstrator simulation	83
3.10. Temperature distribution WGTS beam tube end demonstrator simulation	84

3.11. Temperature distribution second pump port DPS1-F	86
3.12. Schema of rear wall and UV-lamp model	87
3.13. Temperature distribution 2nd pump port DPS1-R	87
4.1. Rate dependence on column density	93
4.2. Schema composite STS gas model	94
4.3. KATRIN range of rarefaction	96
4.4. Scheme of angular coefficient method	97
4.5. Pseudo-three dimensional density distributions	104
4.6. Injection chamber geometry	105
4.7. Pressure distribution from end effect calculation, inlet	106
4.8. WGTS pressure distribution with and without end effects	107
4.9. Schema COMSOL beam tube model.	108
4.10. 2D Density and velocity WGTS comparative gas model	109
4.11. Density distribution comparative beam tube model	109
4.12. Longitudinal WGTS beam tube velocity distribution	110
4.13. Pumping probability TMP over temperature	111
4.14. Gas temperature at TMP	112
4.15. Simplified model 1st pump port DPS1	113
4.16. Density distribution in the first DPS1 pump port	115
4.17. 3D density second pump port DPS1	116
4.18. Composite density distribution up to DPS2	117
4.19. Density in 1st pump port DPS1 for assumed shut-down of TMPs	119
4.20. Contributions of single domains to uncertainty of total column density	122
4.21. Column density uncertainty from accommodation coefficient and viscosity	123
4.22. Dependence WGTS throughput and column density on inlet pressure	127
4.23. Dependence column density on temperature and pump port pressure	129
4.24. Uncertainty in calculation of column density changes	131
4.25. Uncertainty calculation of column density due to exit pressure variation at the pump	132
4.26. Density and velocity triangular model	141
4.27. Density and velocity COMSOL model	141
5.1. Plasma density and temperatures	147
5.2. Visualisation of Debye-length	149
5.3. Energies metal surface	150
5.4. Potential and density distribution in plasma sheaths	152
5.5. Sheath potentials and density distributions at emissive wall	153
5.6. Scheme of WGTS plasma	158
5.7. Electron energy distribution	161
5.8. Work function dependence on surface coverage	164
5.9. Plasma distributions from previous plasma model	168
5.10. Electron drift-diffusion density distribution for $U_{\text{rear}} = 0 \text{ V}$, $U_{\text{wall}} = 0 \text{ V}$	170
5.11. Sketch of plasma particle sources and sinks	171
5.12. T_2 density and velocity profiles for 1D plasma	173
5.13. Densities for 1D Discharge Plasma, w./ w.o.recombination	174
5.14. Current densities and potential for 1D Discharge Plasma without convection	175
5.15. Distribution of neutral background gas	176
5.16. 2D potential distribution, planar three-particle drift-diffusion model, grounded	180
5.17. Density distribution 2D three-particle drift-diffusion model, grounded	181
5.18. Potential distribution 2D three-particle drift-diffusion model, $U_{\text{rear}} = 0 \text{ V}$, $U_{\text{wall}} = 1 \text{ V}$	183

5.19. Density distributions 2D three-particle drift-diffusion model $U_{\text{rear}} = 0 \text{ V}$, $U_{\text{wall}} = 1 \text{ V}$	184
5.20. Potential distributions 2D three-particle drift-diffusion model, $U_{\text{rear}} = 1 \text{ V}$, $U_{\text{wall}} = 0 \text{ V}$	185
5.21. Density distribution 2D three-particle drift-diffusion model $U_{\text{rear}} = 1 \text{ V}$, $U_{\text{wall}} = 0 \text{ V}$	186
5.22. Potential distribution 2D three-particle drift-diffusion model, $U_{\text{rear}} = 0.1 \text{ V}$, $U_{\text{wall}} = 0 \text{ V}$	187
5.23. Plasma density distribution axisymmetric plasma model, grounded boundaries	188
5.24. Transversal ion current densities axisymmetric model for grounded boundaries	188
5.25. Plasma potential distribution axisymmetric plasma model, grounded bound- aries	189
5.26. Ion outflow, density distribution, cylindrical plasma $\Delta = 0.1 \text{ V}$	190
5.27. Transversal Electric field for planar and cylinder-symmetric model with $\Delta =$ 0.1 V	191
5.28. Plasma potential distribution axisymmetric plasma model, $\Delta = 0.1 \text{ V}$	192
5.29. Background gas profiles $0.5\rho d_0$	193
5.30. Plasma profiles for reduced column density	193
5.31. 2D plasma potential for reduced column density	194
5.32. Energy dependence two-dimensional fluid model	195
5.33. Density and potential dependence on recombination rate	197
5.34. Density and potential distribution for	199
5.35. T_2 gas model for $L_{\text{WGTS}} = 12 \text{ m}$	200
5.36. Electron density distribution $L_{\text{WGTS}} = 12 \text{ m}$	201
5.37. Potential distribution $L_{\text{WGTS}} = 12 \text{ m}$, $\Delta = 0 \text{ V}$	202
5.38. Potential distribution for $L_{\text{WGTS}} = 12 \text{ m}$, $\Delta = 0.1 \text{ V}$	203
5.39. Potential, ion flux for reduced magnetic field	204
5.40. Plasma potential for different Δ values	207
5.41. Plasma potential divided rear wall voltage 0.05 V and 0 V	209
5.42. Plasma potential divided rear wall voltage 0.05 V and 0 V	210
5.43. Plasma 2D potential divided rear wall voltage 0.05 V and 0 V	210
5.44. Plasma 2D potential divided rear wall voltage -0.05 V and 0 V	211
5.45. Radial ion current bisected rear wall	212
5.46. 2D plasma potential for 5 mm rear wall patches	213
5.47. Radial distributions of plasma potential for 5 mm rear wall patches	214
5.48. Potential distributions for one rear wall patch	216
5.49. Flux density distributions for one rear wall patch	217
5.50. Bias influence on patch potential profile	218
5.51. Tube wall adsorption induced surface potential profile	219
5.52. 1D potential distributions for tube wall adsorption	220
5.53. 2D potential distributions for tube wall adsorption	221
5.54. 2D potential distributions for tube wall surface inhomogeneity	222
5.55. One-dimensional potential distributions for 5 cm rear wall inhomogeneity with different work function shift magnitudes ΔU_{wall}	223
5.56. Potential distributions for electron emitting rear wall, $E_e = 2 \text{ meV}$	225
5.57. Emission induced shift in space charge potential for different electron tem- peratures	227
5.58. Potential distribution for 83 mKr operation	230
5.59. Mean potential and standard deviation for different gas temperatures	232
5.60. Measurement time for optimisation of U_{rear} , rate stability 1×10^{-4}	235
5.61. $U(z)$ for non-optimised rear wall voltage	236
5.62. Δm_ν^2 for Gaussian potential fluctuations in the WGTS	239

5.63. Scattering probability weighted potential	240
5.64. Plasma profile for neutrino mass sensitivity analysis with $\Delta = 60 \text{ mV}$	242
5.65. Δm_ν^2 for linear plasma profile in the WGTS	244
5.66. Probability distribution and ratio of integrated spectrum with linear potential profiles and with zero potential	245
A.1. Geometry gas flow simulation coolants	256
A.2. Velocity distributions of nitrogen and helium coolant	256
B.3. Bellow geometry	256
C.4. Technical data MAG W 2800	258
D.5. Time scale for spreading of inlet pressure disturbance	259
E.6. 2D model 1st pump port DPS1	260
E.7. Uncertainty of pump port pressure calculation	261
F.8. Energies of adsorption	262
F.9. T_2 coverage along WGTS tube, 30 K	266
F.10. Coverage along WGTS tube 110 K	267

List of Tables

1.1. Neutrino oscillation parameters from global analysis	13
2.1. Reference parameters for spectrum calculation	58
3.1. Input material parameter temperature simulation	73
3.2. Temperatures from nitrogen coolant simulation	74
3.3. Temperatures from helium coolant simulation	75
3.4. Modelling of demonstrator	84
4.1. Reduction factors and densities for WGTS and DPS1 components	118
4.2. Column density variation due to not working TMP	137
4.3. Neutrino mass shift from column density and cross section uncertainty	139
4.4. Configuration neutrino-mass analysis for full gas dynamics uncertainty	142
5.1. Outgoing 2D planar plasma currents	178
5.2. Impact of plasma conditions	204
5.3. Differences in potential depending on rear wall bias	206
5.4. Plasma potential values for rear wall patches	215
5.5. Plasma potential values for one rear wall patch	215
5.6. Characteristic plasma potential values for electron emitting rear wall	224
B.1. Dat from used bellows	257

1. Neutrino physics and current neutrino mass limits

Contents

1.1. The neutrino – a brief historical overview	2
1.2. Neutrinos in the Standard Model of particle physics	3
1.3. Neutrino oscillations	4
1.3.1. Solving the solar neutrino problem	4
1.3.2. Theoretical description of neutrino oscillations	6
1.3.3. Current experimental oscillation parameter values	9
1.3.4. Matter effects	13
1.4. Neutrinoless double beta decay	16
1.4.1. Two neutrino double beta decay	16
1.4.2. Neutrinoless double beta decay	16
1.5. Neutrino masses – generation and experimental determination	19
1.5.1. Neutrino mass generation	19
1.5.2. Experimental neutrino mass determination	21
1.5.2.1. Neutrino mass from cosmology	21
1.5.2.2. Neutrino mass from neutrinoless double beta decay . .	22
1.5.2.3. Time-of-flight measurements using supernova neutrinos	23
1.5.2.4. Single beta decay experiments	23

Among the constituents of the Standard Model of experimental particle physics neutrinos bear a particular and important role the description of cosmological and astro-particle physics processes. Our knowledge of the properties of the neutrino is still limited and many question remain unresolved, such as its intrinsic nature – is it a Dirac or a Majorana particle – or its absolute mass scale.

This chapter gives a very brief overview to the theoretical concepts used in neutrino physics as well as experimental approaches and results. It starts with a survey of important historic events related to neutrino physics. Afterwards, in section 1.2, it is briefly discussed how the neutrino is embedded in the Standard Model of particle physics. In section 1.3, the concept of neutrino oscillation is introduced and current measurement results are highlighted. Section 1.4 presents a rare processes the potential which possesses the potential to reveal the intrinsic nature of the neutrino – the neutrinoless double beta decay. The

last section 1.5 is dedicated to the mass of the neutrino. It introduces theoretical concepts for the mass generation mechanism as well as experimental approaches that give access to different aspects of neutrino masses. Herein, the physical process the neutrino mass analysis with KATRIN is based on is introduced.

1.1. The neutrino – a brief historical overview

The story of the neutrino is a story full of puzzles and experimental successes in solving many (but not yet all) of them. It started in 1930, when the new particle, initially named ‘neutron’, was proposed by Wolfgang Pauli as a solution to the puzzle of continuous β -decay spectra. In 1914 Chadwick was able to measure the β -decay spectrum of ^{219}Bi . This spectrum was continuous and therefore fundamentally different from the spectra measured before for α and γ decaying nuclei that produce discrete lines. The continuous β -decay spectrum could not be explained by a two particle decay (into the daughter nucleus and the electron) – The recoil energy of the heavy daughter nucleus is tiny, thus almost the full decay energy should be carried away by the electron. A continuous spectrum could only be explained if the law of conservation of energy is violated or if an additional particle was produced in the decay. The latter hypothesis was formulated by Pauli in a famous letter in 1930 [Pau30]. The additional particle was proposed to be a neutral spin- $\frac{1}{2}$ particle with almost vanishing mass.

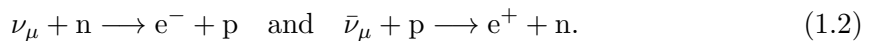
Already in 1933, shortly after Chadwick’s discovery of the neutron [Cha32], Fermi formulated his successful theory of β -decay [Fer34] taking up the idea of the neutrino produced in addition to the electron. The cross section for a neutrino to interact with a nucleus via inverse beta decay was estimated to be $1 \times 10^{-44} \text{ cm}^2$ by Bethe and Peierls [BP34] – Due to the smallness of the cross section they considered the neutrino to be undetectable.

Their prediction held for about twenty years. Still, in 1953 the first neutrino signal was observed by Reines and Cowan. It was confirmed in 1956 [CRH⁺56]. They used nuclear reactors as a strong neutrino source. The detection mechanism was the inverse β -decay



The large background (mainly due to muons) could be suppressed effectively using the delayed coincidence signal of positron annihilation and neutron capture by ^{113}Cd nuclei from cadmium chloride that was dissolved in the water. A characteristic signal is shown in figure 1.1.

A second type of neutrino, the muon neutrino ν_μ , was discovered in 1962 [DGG⁺⁶²] using a neutrino beam produced in the decay of pions and kaons. These neutrinos were concluded to be different from the already known (electron) neutrino type since they were shown not to induce the reactions



A similar principle was used by the DONuT collaboration to detect the tau neutrino. They produced tau neutrinos through the weak decay of D_s mesons. In 2000 the first DONuT results with four detected tau neutrino events were published [KUA⁺⁰¹].

The number of light neutrino flavours¹ was determined by the decay width of the Z^0 boson at the electron-positron collider LEP [DDL⁺⁹⁰]. The hadronic and charged leptonic decay widths were subtracted from the total decay width leaving over the so called *invisible* width Γ_{inv} (particles that cannot be seen by the detectors) – the decay width into neutrinos.

¹with mass m_{ν_α} smaller than half the mass of the Z^0 boson $m_Z/2 \approx 45 \text{ GeV}$

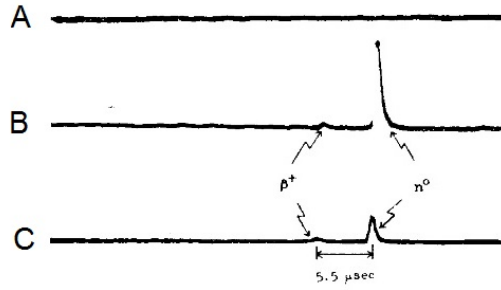


Figure 1.1.: **Exemplary signal from the neutrino experiment of Reines and Cowan.** The three lines A, B and C show the oscilloscope traces related to the three different detectors. A neutrino event, like the one illustrated, shows a delayed coincidence signal in the two first scintillation detectors (B,C) due to positron annihilation and neutron capture, the signal of an inverse beta decay event. A third, separated detector (A) needs to give an anti-coincidence signal to exclude cosmic ray induced events. Figure adapted from [RC56].

Assuming all neutrinos to have the same coupling to the Z^0 boson, the number of neutrino flavours can be calculated as $N_\nu = \Gamma_{\text{inv}}/\Gamma_\nu$, with the decay width of a single neutrino flavour Γ_ν . Using a multi parameter fit of the measured Z^0 resonance for different numbers of light, active neutrino flavours, a number of

$$N_\nu = 2.9840 \pm 0.0083 \quad (1.3)$$

was deduced [EGC⁺06].

1.2. Neutrinos in the Standard Model of particle physics

In the Standard Model of particle physics (SM) the leptonic neutrinos are grouped in three generations together with their charged leptonic partners (e, μ, τ). The same holds for the antineutrinos and their leptonic partners ($\bar{e}, \bar{\mu}, \bar{\tau}$). The leptonic generations are embedded into the electroweak theory by Glashow, Weinberg and Salam [GGM61, Wei67, SW64] around the $SU(2) \times U(1)^2$ gauge symmetry of weak isospin and weak hyper charge by a weak isospin doublet. Neutrinos only take part in weak interactions since they do not carry electric charge or color and hence do not take part in electromagnetic and strong interactions.

To classify weak interactions, it is usefull to introduce the concept of helicity. The helicity operator h can be computed from the momentum vector \vec{p} and the spin vector $\vec{\sigma}$ attributed to the particle

$$h = \frac{\vec{p} \cdot \vec{\sigma}}{|\vec{p}|}. \quad (1.4)$$

The helicity or more concisely the eigenvalue of the helicity operator, can be positive or negative. Different from the Lorentz-invariant *chirality* (intrinsic handedness of a particle), the helicity depends on the frame of the observer³. For massless particles helicity and chirality coincide. The charged current of the weak interaction has been shown to violate parity maximally as it only couples to left-handed particles and right-handed anti particles

²Together with the $SU(3)$ symmetry of strong interaction the $SU(3) \times SU(2) \times U(1)$ gauge group of the SM is formed.

³For massive particles (not travelling at the speed of light) there is always a boosted frame where the helicity flips as the frame overtakes the particle.

(the neutral current violates parity, but not maximally). In 1958 Goldhaber demonstrated in his famous experiment that the helicity of the neutrino is negative [GGS58]. Neutrinos occur as left-handed particles and right-handed antiparticles only. A possible right-handed neutrino is sterile, as it does not take part in weak interactions.

In the Standard Model neutrinos are massless. However, since they oscillate between the different flavour states, see section 1.3, at least two of them need to have mass. Thus, neutrino oscillations belong to physics beyond the Standard Model. Possible mass generation mechanisms are discussed in section 1.5.1.

Since they are uncharged in electromagnetic and strong interactions, neutrinos have the unique possibility to be their own antiparticles – Majorana particles. The Majorana neutrino field is the sum of its left- and right-handed components, ν_R^M and ν_L^M , respectively. Both components are connected by their charge conjugate fields $\nu_j^c = C\nu_j C^{-1}$ with the charge conjugation operator C that connects particle and antiparticle [Bil10]

$$\nu_R^M = (\nu_L^M)^c. \quad (1.5)$$

The nature of the neutrino, i.e., if it is a Dirac or a Majorana particle, is currently unknown. The neutrinoless double beta decay (discussed in section 1.4) offers the possibility to discriminate between both types.

1.3. Neutrino oscillations

During propagation neutrinos change their flavour – for instance an electron type neutrino can turn into a muon or tau type neutrino. This phenomenon is called neutrino flavour oscillation and is caused by the difference between the mass eigenstates, that rule the neutrino propagation, and flavour eigenstates, that take part in the weak neutrino interactions. The neutrino oscillation process violates the flavour lepton number but conserves the total lepton number. Neutrino oscillations imply non-vanishing neutrino masses and can therefore not be explained by the Standard Model. They caused a long standing puzzle with regard to the measured flux of neutrinos originating from the sun. Today, these oscillations are experimentally verified, well described by theory and are used to study neutrino properties.

1.3.1. Solving the solar neutrino problem

In 1970 the pioneering Homestake experiment of R. Davis started to continuously measure the flux of neutrinos produced in the nuclear reactions in the sun over more than twenty years. It was a radiochemical experiment that used the reaction



with an energy threshold of 0.81 MeV to detect (solar) electron neutrinos. Due to the energy threshold, mainly the neutrinos from the decay of ${}^8\text{B}$ (compare figure 1.2) were detected [BDJ76]. After time intervals of about 60 d to 70 d each, the ${}^{37}\text{Ar}$ atoms were extracted. Their amount was measured by observing the ${}^{37}\text{Ar}$ decay. The results were compared to the expectations from the standard solar model (SSM) depicted in figure 1.2 [BSB05].

Throughout its whole running period the Homestake experiment measured a deficit of the detected solar neutrino flux compared to the predicted one [BDJ76, BCDJR85]. After twenty years of measurement, a final counting rate result of

$$2.56 \pm 0.16(\text{stat.}) \pm 0.16(\text{sys.}) \text{ SNU}, \quad (1.7)$$

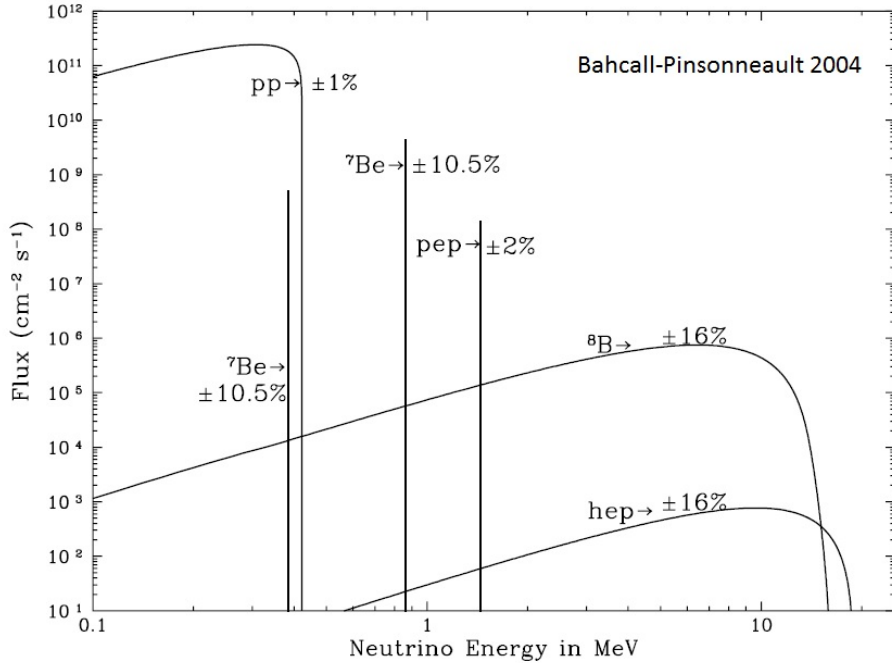


Figure 1.2.: **Energy dependent solar neutrino fluxes predicted from the SSM.**
The fluxes Φ from different neutrino generation mechanisms as well as their uncertainty are included. Figure adapted from [BSB05].

with SNU denoting one solar neutrino unit ($1 \text{ SNU} = 10^{-36}$ captures per target atom per second), was published [CDDJ⁺98]. Only one third of the expected flux, calculated with the SSM, was actually measured. This discrepancy is called the *solar neutrino* problem. The difference between predicted and experimental rates could be due to the following reasons that are either related to experimental uncertainties or to an incomplete theoretical description:

- The neutrino production rate predicted in the SSM is not correct.
- The calculated production rate of ^{37}Ar is not correct (wrong cross section).
- The Homestake experimental result is wrong (undetected experimental uncertainties).
- The neutrino propagation from its origin in the sun to its detection on earth is not understood.

A series of experiments, using different detection methods and a lower energy threshold were used to further study the solar neutrino flux.

The Kamiokande experiment used a detector filled with ultra pure water to be able to perform real-time neutrino flux analysis which is not possible with radiochemical experiments like the Homestake experiment. The solar neutrino flux was measured by observing the Cherenkov light produced by elastically scattered electrons from the neutrino - electron scattering. The measured ^8B neutrino flux was about two times smaller than expected from the solar models [HII⁺91]. Still, Kamiokande was not able to verify the oscillation of solar electron neutrinos due to low statistics.

Kamiokande was also able to detect atmospheric muon neutrinos that were produced in the atmosphere as decay product of hadronic showers. These neutrinos have much larger energies (GeV range) than the solar neutrinos. Thus it was possible to detect them through the charged current reaction (production of a muon in the final state) from neutrino electron scattering and from neutrino nucleon scattering.

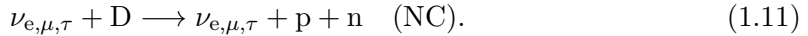
The radiochemical experiments GALLEX, SAGE and GNO used ^{71}Ga to measure the solar electron neutrino flux



This reaction has a low energy threshold (0.23 MeV) which made it possible to observe the large flux of neutrinos from the pp-cycle [Bil10]. The solar neutrino flux measured in these experiments was again lower than the predictions from the SSM and thus confirmed the solar neutrino deficit [HHH⁺99, AVV⁺02, ABB⁺05].

A theoretical explanation for the missing neutrinos was proposed by Pontecorvo in 1958 [Pon58b, Pon58a] even before the experimental evidence was collected. His approach was further elaborated by Maki, Nakagawa and Sakata [MNS62]. Pontecorvo suggested oscillations similar to the $K^0 \rightleftharpoons \bar{K}^0$ oscillations in the neutral kaon system. He proposed the sun to be the ideal object to study these neutrino oscillations [Pon12].

The oscillation explanation to the solar neutrino problem was favoured for a long time [BP77]. However, model independent experimental evidence of solar neutrino oscillations was first produced by the Sudbury Neutrino Observatory (SNO) experiment in 2001. SNO detected the Cherenkov light produced by neutrino reactions in a large tank of heavy water. Electron scattering (ES) as well as neutral and charged current (NC and CC) neutrino reactions were measured:



While all neutrino flavours take part in the NC reactions (breakup of the deuterium nucleus and elastic electron scattering) only electron neutrinos take part in the CC reactions⁴. While the NC reactions are insensitive to the neutrino flavour, the CC reaction is flavour sensitive. Thus, SNO was sensitive to the total neutrino flux (all flavours) as well as to the electron neutrino flux only and could verify the oscillation of solar electron type neutrinos to other flavours – The measured total neutrino flux (all flavours) was in agreement with the predictions from the SSM while the ratio of electron to total neutrino flux was about 1/3 and confirmed the solar electron neutrino deficit measured by prior experiments [AAA⁺01, AAA⁺02].

The importance of the SNO results was recognised through the 2015 Nobel Prize, which was awarded jointly to A. McDonald from the SNO experiment and T. Kajita from the Super-Kamiokande collaboration. While SNO confirmed the oscillation of solar neutrinos and thus solved the solar neutrino problem, Super-Kamiolande was the first experiment that found conclusive evidence for neutrino oscillations using neutrinos produced in the atmosphere by comparing fluxes for different zenith angles (different path lengths, see section 1.3.3).

1.3.2. Theoretical description of neutrino oscillations

The neutrino mass eigenstates $|\nu_i\rangle$ ($i=1,2,3$) and its weak flavour eigenstates $|\nu_\alpha\rangle$ ($\alpha = e, \mu, \tau$) are different. While the weak eigenstates take part in the weak interaction, the mass eigenstates define the propagation and are thus eigenstates of the free Hamiltonian. An analogous concept can be found in the quark sector, where the quark flavours (eigenstates of the strong interaction) mix to form the eigenstates of the weak interaction. The quark mixing, or the transition between eigenstates of strong and weak interaction, is mediated by

⁴In principle ν_μ and ν_τ can also take part in the CC reactions producing a corresponding charged lepton (μ, τ) instead of an electron. However, the energy of solar neutrinos is too low to produce a μ or τ .

the Cabibbo-Kobayashi-Maskawa (CKM) matrix. In the neutrino sector a unitary mixing matrix, called Pontecorvo-Maki-Nakagawa-Sakata (PMNS) matrix U , can be defined that is similar to the CKM matrix in the quark sector. It connects the neutrino mass eigenstates and the eigenstates of the weak interaction:

$$|\nu_\alpha\rangle = \sum_i U_{\alpha i}^* |\nu_i\rangle, \quad |\nu_i\rangle = \sum_\alpha U_{i\alpha} |\nu_\alpha\rangle. \quad (1.12)$$

Assuming three neutrino flavours, and using its unitarity, in the case of Dirac neutrinos the PMNS matrix can be parametrised by four parameters. If the neutrino is of Majorana nature, two complex majorana phases have to be added. In an often used parametrisation there are:

- three angles θ_{12} , θ_{13} and θ_{23} ,
- one Dirac phase δ_D . If it is different from zero, it causes CP violation.
- Two complex Majorana phases δ_{M1} and δ_{M2} . They have non-vanishing values if neutrinos are Majorana particles.

With this parametrisation, the PMNS matrix reads

$$U = \begin{pmatrix} U_{e1} & U_{e2} & U_{e3} \\ U_{\mu 1} & U_{\mu 2} & U_{\mu 3} \\ U_{\tau 1} & U_{\tau 2} & U_{\tau 3} \end{pmatrix} = \begin{pmatrix} 1 & 0 & 0 \\ 0 & c_{23} & s_{23} \\ 0 & -s_{23} & c_{23} \end{pmatrix} \begin{pmatrix} c_{13} & 0 & s_{13}e^{-i\delta_D} \\ 0 & 1 & 0 \\ -s_{13}e^{-i\delta_D} & 0 & c_{13} \end{pmatrix} \cdot \begin{pmatrix} c_{12} & s_{12} & 0 \\ -s_{12} & c_{12} & 0 \\ 0 & 0 & 1 \end{pmatrix} \begin{pmatrix} e^{i\delta_{M1}} & 0 & 0 \\ 0 & e^{i\delta_{M2}} & 0 \\ 0 & 0 & 1 \end{pmatrix}. \quad (1.13)$$

Here s_{ij} and c_{ij} is shorthand for $\sin \theta_{ij}$ and $\cos \theta_{ij}$, respectively. In case of more than three contributing neutrino flavours (sterile neutrinos) one CP phase and one mixing angle need to be added for each extra neutrino [Zub12].

Evolution of flavour eigenstates

From the general solution of the Schrödinger equation it follows that the neutrino state at time t , $|\nu_i(x, t)\rangle$, is related to the initial neutrino state $|\nu_i(x, t=0)\rangle$ in the following way [Bil10]:

$$|\nu_i(x, t)\rangle = e^{-iHt} |\nu_i(x, 0)\rangle \stackrel{H|\nu_i\rangle=E_i|\nu_i\rangle}{=} e^{-iE_it} |\nu_i(x, 0)\rangle. \quad (1.14)$$

For a relativistic approximation $p \approx p_i \gg m_i$ the neutrino energy E_i can be calculated with

$$E_i = \sqrt{p_i^2 + m_i^2} \approx p_i + \frac{m_i^2}{2p_i} \approx E + \frac{m_i^2}{2E}. \quad (1.15)$$

Considering the spatial evolution $|\nu_i(x, 0)\rangle = e^{ip_i x} |\nu_i\rangle$, the initial neutrino flavour state at position $(0, 0)$ evolves to the state at position (x, t) via

$$|\nu(x, t)\rangle = \sum_{i\beta} U_{\alpha i} U_{\beta i}^* e^{ip_i x} e^{-iE_i t} |\nu_\beta\rangle. \quad (1.16)$$

Therefore, the probability to detect a neutrino with flavour β initially produced at $(t=0, x=0)$ as flavour α becomes [Zub12]

$$P(\alpha \rightarrow \beta)(t) = |\langle \nu_\beta | \nu(x, t) \rangle|^2 \quad (1.17)$$

$$= \sum_i |U_{\alpha i} U_{\beta i}^*|^2 + 2\text{Re} \sum_{j < i} U_{\alpha i} U_{\alpha j}^* U_{\beta i}^* U_{\beta j} \exp\left(-\frac{\Delta m_{ij}^2}{2} \frac{L}{E}\right). \quad (1.18)$$

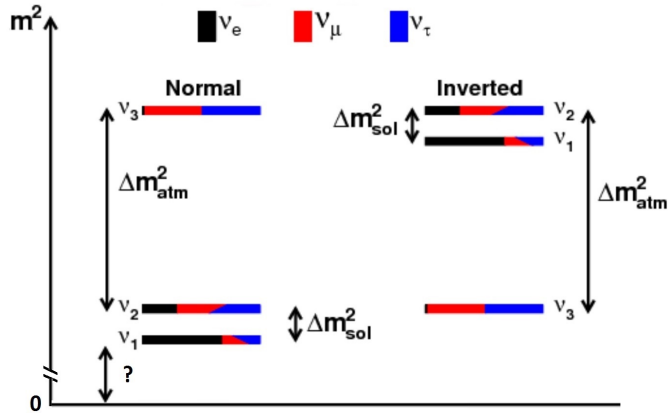


Figure 1.3.: **Neutrino mass squared differences.** The large atmospheric mass difference, $\Delta m_{\text{atm}}^2 \approx \Delta m_{32}^2$ as well as the small solar mass difference $\Delta m_{\text{atm}}^2 \approx \Delta m_{21}^2$ are given. As only the mass squared splittings are measured by oscillation experiments, the ordering of the mass eigenstates (normal or inverted) as well as the absolute scale of the masses is unknown. Figure adapted from [QV15].

Since the first term in equation (1.18) is constant, the oscillation is described by the second term, which depends on the ratio $\frac{L}{E}$ of path length and neutrino energy as well as on the difference of squared masses of the different mass eigenstates $\Delta m_{ij}^2 = m_i^2 - m_j^2$. If neutrinos were massless Δm_{ij}^2 would vanish and no oscillations would occur. Thus, the detection of neutrino oscillations gives evidence for massive neutrinos.

Assuming CP invariance ($U = U^*$), equation (1.18) can be simplified to

$$P(\alpha \rightarrow \beta)(t) = \delta_{\alpha\beta} - 4 \sum_{j < i} U_{\alpha i} U_{\alpha j} U_{\beta i} U_{\beta j} \sin^2 \left(-\frac{\Delta m_{ij}^2}{4} \frac{L}{E} \right). \quad (1.19)$$

Thus, the probability to detect flavour state α , when the neutrino was initially produced in state α (disappearance channel) becomes

$$P(\alpha \rightarrow \alpha) = 1 - \sum_{\alpha \neq \beta} P(\alpha \rightarrow \beta). \quad (1.20)$$

with appearance channels $P(\alpha \rightarrow \beta)(\alpha \neq \beta)$.

Two flavour oscillation

A much simpler description than by equation (1.18) can be given if only oscillations between two neutrino flavours are considered. This is valid since the dominant oscillation pattern is driven by only two flavours while the third flavour only contributes at second (or higher) order corrections as to be seen in figure 1.3. Thus, the mixing is parametrised by one mixing angle θ and one mass square difference Δm^2 by a 2×2 mixing matrix:

$$\begin{pmatrix} \nu_\alpha \\ \nu_\beta \end{pmatrix} = \begin{pmatrix} \cos \theta & \sin \theta \\ -\sin \theta & \cos \theta \end{pmatrix} \begin{pmatrix} \nu_1 \\ \nu_2 \end{pmatrix} \quad (1.21)$$

This means, the transition probability from equation (1.19) simplifies to

$$P(\nu_\alpha \rightarrow \nu_\beta) = \sin^2(2\theta) \cdot \sin^2 \left(\frac{\Delta m^2}{4} \frac{L}{E} \right) = P(\nu_\beta \rightarrow \nu_\alpha), \quad (1.22)$$

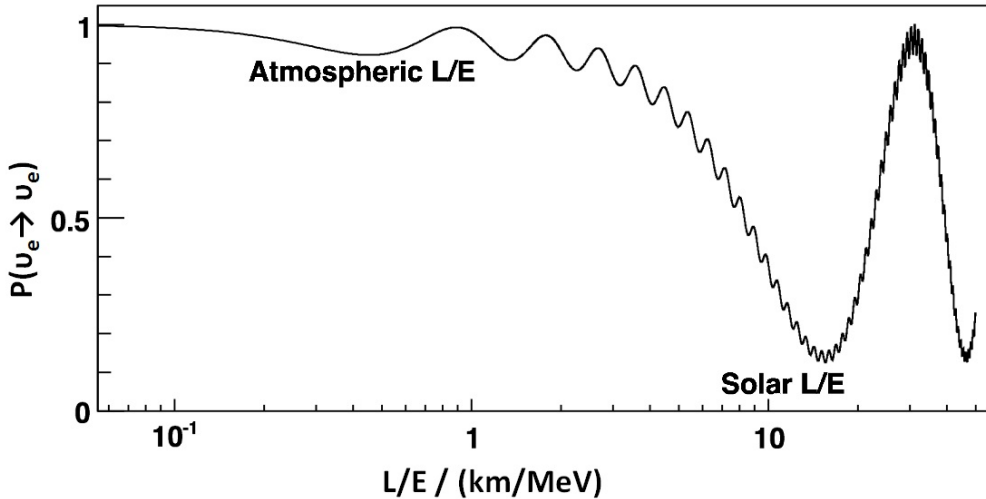


Figure 1.4.: **Survival probability $P(\nu_e \rightarrow \nu_e)$ of an electron neutrino in a three flavour mixing scenario.** The oscillation pattern is given for a three flavour oscillation case, where atmospheric and solar oscillation are superimposed. For small values of L/E the fast atmospheric oscillations with small amplitude ($\Delta m_{32}^2, \theta_{23}$) dominate while for larger values of L/E the slow solar oscillations ($\Delta m_{21}^2, \theta_{12}$) with large amplitude determine the survival probability. Figure adapted from [Par08].

which implies an oscillation length L_0 of

$$L_0 = 4\pi\hbar c \frac{E}{\Delta m^2} \approx 2.48 \frac{E/\text{MeV}}{\Delta m^2/\text{eV}^2} \text{m.} \quad (1.23)$$

The mass square difference of the two involved neutrino mass eigenstates gives the oscillation frequency while the mixing angle θ determines the amplitude. This statement can be adopted to the three flavour case, where two oscillation patterns interfere which is exemplary shown in figure 1.4. Here the survival probability of electron neutrinos is given depending on the value of L/E . The small oscillations with high frequency are determined by the atmospheric oscillation which is ruled by θ_{23} and Δm_{32}^2 . The long range behaviour is determined by the solar oscillation with parameters θ_{12} and Δm_{21}^2 .

1.3.3. Current experimental oscillation parameter values

To be able to determine the mixing angles θ_{12} , θ_{23} and θ_{13} as well as the mass square splittings Δm_{21}^2 , Δm_{32}^2 (Δm_{31}^2) and a possible CP violating phase, neutrinos from a variety of sources need to be analysed. To investigate the individual oscillation parameters, current experiments rely on different neutrino sources, neutrino energies and base lines between source and detector. Independent of the source, two measurement concepts can be distinguished:

- Appearance experiments – detect neutrino flavours that were initially absent in the source. They typically have a relatively low background and a large sensitivity to small mixing angles.
- Disappearance experiments – the survival probability of a particular neutrino flavour is measured. Here the initial flux needs to be known precisely.

The most sensitive position (distance to the source) to observe the oscillation is determined by the mass square splitting and by the energy, or, using equation (1.23), by the oscillation

length L_0 . The oscillation pattern can be observed most sensitively at $L = L_0/2$. For $L \ll L_0$ the oscillations have no time to develop. For $L \gg L_0$ only an average transition probability can be measured, as the neutrino has already been running through several oscillation cycles. Often, L/E can in this case not be measured precisely enough.

The flavour sensitive detection mechanism for neutrinos is the charged-current reaction with nucleus N and its final hadronic state X

$$\nu_{e,\mu,\tau} + N \longrightarrow e, \mu, \tau + X, \quad (1.24)$$

In the following important findings of of current oscillation experiments using various neutrino sources are presented. Here two general source types can be distinguished:

- natural sources, such as the sun, the atmosphere, and supernova explosions (neutrinos from the core of the earth, so-called geo-neutrinos, are not considered here);
- artificial sources, such as reactors and particle accelerators.

Solar neutrinos

Neutrinos produced through fusion reactions in the interior of the sun, at a distance of about 1.5×10^8 km, are of pure electron type. They are generated mainly in the pp-cycle and, to a small amount (1.6%), in the CNO cycle. The energy spectrum of neutrinos produced in different reaction cycles shows monoenergetic lines as well as continuous distributions. The maximal energy of neutrinos originating from the sun is about 15 MeV. The energy distribution and flux of neutrinos produced in the different processes can be calculated with the SSM [BSB05]. The calculated spectrum is depicted in figure 1.2.

Solar neutrino experiments can be grouped in two categories: radiochemical experiments and real-time experiments, depending on the techniques used to measure neutrino fluxes.

Radiochemical experiments

These were the first experiments used to detect solar neutrinos which revealed the problem of the missing solar neutrino flux (see section 1.3.1).

The detection principle of these experiments like Homestake, GALLEX, and SAGE is the neutrino capture by nuclei. The produced unstable daughter nuclei are extracted in certain time intervals and their decay is measured. The existence of these daughter nuclei gives evidence that the neutrino capture reactions had occurred. The abundance of these nuclei provides information on the neutrino flux. The capture reaction sets the energy threshold for the neutrino detection. Compared to the real time experiments, radiochemical methods have significantly lower thresholds of the order of several hundred keV. They have the drawback not to be able to measure time- or energy-resolved. The only temporal information is of the order of the extraction periods.

Real-time experiments

This type of experiments measures time-resolved neutrino fluxes and does provide spectral information too. They use the charged and neutral current reactions for the neutrino scattering off electrons, protons, deuterons or nuclei (see section 1.3.1). The detection principle is based on light that is produced by the scattered particles either by Cherenkov radiation or by scintillation.

Water Cherenkov experiments like SNO, Kamiokande or Super-Kamiokande measure the Cherenkov light produced by fast charged leptons created in the neutrino reactions. Using the Cherenkov cone, these experiments are able to perform particle tracking. Unfortunately, water Cherenkov experiments have a large energy threshold (about 3.5 MeV) and are thus not able to look at the low energy fluxes from pp or ^7Be neutrinos.

Scintillator based experiments use large amounts of organic liquid scintillator. They cannot measure the particle direction but provide good energy resolution and a rather low

energy threshold below 1 MeV [MPS15, Bel16] which makes it possible to detect pep and even pp neutrinos.

As solar neutrinos have relatively low energies, only electron neutrinos can take part in charged current reactions from equation (1.24) – The neutrino energy is too low to produce other leptons than electrons in the final state. Thus, solar neutrino experiments focus on the electron neutrino disappearance channel $P(\nu_e \rightarrow \nu_e)$. They are sensitive to low mass splittings (Δm_{12}^2 and θ_{12}) due to the long baseline from the production in the sun to the detection on earth.

Atmospheric neutrinos

In the atmosphere cosmic rays of high energies (mainly protons and α -particles) interact with atmospheric nuclei. In the decay chain of the produced mesons (mainly pions), muon- and electron-type neutrinos are produced:

$$\pi^+ \rightarrow \mu^+ + \nu_\mu \quad \pi^- \rightarrow \mu^- + \bar{\nu}_\mu \quad (1.25)$$

$$\mu^+ \rightarrow e^+ + \nu_e + \bar{\nu}_\mu \quad \mu^- \rightarrow e^- + \bar{\nu}_e + \nu_\mu. \quad (1.26)$$

Assuming that all muons decay before reaching the earth, the ratio of muon to electron type neutrinos in the atmospheric neutrino flux is about 2. Depending on the neutrino energy this ratio varies considerably as for increasing energy not all muons decay during their path from the atmosphere to the earth due to Lorentz time dilation. The energy of the atmospheric neutrinos is in the GeV range and their baselines vary from 10 km up to the diameter of the earth which makes their oscillation sensitive to mass square differences larger than 10^{-4} eV^2 [Zub12].

The Kamiokande and the IMB experiment detected a discrepancy in the muon to electron neutrino ratio compared to the expectations. Later the upgraded Super-Kamiokande experiment measured a difference between up and down going muon neutrino flux and, more general, a dependence of the number of muon neutrinos on the zenith angle. Using muon neutrino disappearance and electron neutrino appearance they interpreted the missing muon neutrino flux as oscillation to tau neutrinos [FHI⁺98]. Thus, Super-Kamiokande was the first experiment that observed the oscillation of neutrinos beyond a doubt using atmospheric neutrinos.

Today atmospheric neutrinos provide the best value for Δm_{3x}^2 ($x=1,2$) and θ_{23} [Cho16] included in the compilation in table 1.1.

Accelerator neutrinos

Intense neutrino beams can be generated in artificial reactions by shooting an accelerated proton beam at a massive target. This produces pions and kaons that predominately decay into muons and muon neutrinos. Neutrinos stemming from the decay of positively charged mesons and antineutrinos stemming from the decay of negatively charged mesons can be separated by magnetic focussing devices called horns that are sign-selective for the charged mesons. They focus the beam of either positively or negatively charged particles while defocussing the differently charged beam. The charged particles are stopped in a muon shield and only neutrinos are left.

Different from natural sources, the neutrino energy can be tuned. Typical accelerator neutrino energies are in the range from 0.5 GeV to 10 GeV [FHK13]. The produced neutrino flavour is mainly muon-like ($\bar{\nu}_\mu, \nu_\mu$). Electron-type neutrinos ($\nu_e, \bar{\nu}_e$) also contribute a relatively large amount to the neutrino beam. They are created by decaying kaons and in muon decays ($\mu^- \rightarrow e^- + \bar{\nu}_e + \nu_\mu$). The electron content can be tuned by changing

either the proton beam energy or the decay length until the charged particles get stopped [DM08].

Due to the high neutrino energy, large mass squared splittings can be probed (Δm_{32}^2 , $\sin^2(2\theta_{23})$). A typical long baseline experiment (LBL) investigates mass squared differences of about 2.5×10^{-3} eV 2 , similar to atmospheric ones, and has a source-detector distance of several 100 km. Present experiments are even able to reach large neutrino energies of 500 GeV [DM08].

In the 1990s the first accelerator based neutrino experiments were built (KARMEN, LSND, CHORUS and others) to investigate the atmospheric neutrino anomaly (muon neutrino deficit) observed by Kamiokande [HKK⁺88] by confirming the related muon to tau neutrino oscillation $\nu_\mu \rightarrow \nu_\tau$. They were followed by experiments like K2K, MINOS, OPERA and others. Depending on the energy of the neutrino beam, they searched for ν_μ disappearance or for ν_τ appearance [FHK13].

Looking for ν_e appearance at the atmospheric oscillation length, the accelerator neutrino experiments are capable of investigating the mixing angle θ_{13} . Modern long baseline accelerator experiments like T2K and NO ν A also try to set constraints on the CP-phase δ_D , comparing neutrino and antineutrino result. Recent $\bar{\nu}_\mu$ disappearance data for Δm_{32}^2 and θ_{23} from T2K [AAA⁺16] are in agreement with former T2K data from ν_μ disappearance [AAA⁺15] and show no indication for CP-violation or new physics.

A further goal of accelerator based experiments is to answer the question of the neutrino mass hierarchy (see figure 1.3) [AAA⁺15, Pat12], which is to determine the sign of Δm_{32}^2 with the help of the modified oscillation behaviour in matter (MSW effect, see section 1.3.4). This matter oscillation already allowed to determine the sign of Δm_{21}^2 using solar neutrino data.

Reactor neutrinos

Reactors are an intensive terrestrial source of electron antineutrinos. The neutrinos are generated in the reactor core through β decays of the neutron rich nuclear fission products with an average neutrino yield of about 6 per reaction chain and an energy of a few MeV. The produced neutrino flux is proportional to the thermal power of the reactor and drops with the squared distance from the source (reactor core). Because of the relatively low neutrino energy, the charged current reaction (1.24) is only sensitive to electron neutrinos. Thus, reactor neutrino experiments observe the disappearance channel $P(\bar{\nu}_e \rightarrow \bar{\nu}_e)$. In general the inverse beta decay from equation (1.1) with an energy threshold of 1.806 MeV is used as detection reaction. The neutrino energy is derived from the detected positron energy.

The disappearance channel requires a well-known incident neutrino flux. Since the knowledge of the fission processes and the relative contribution of fission products is limited, the calculation of the initial flux has large uncertainties. These can be reduced using a two (or more) detector technology with a near detector, determining the initial neutrino flux, and a far detector measuring the oscillation pattern. This technology is used by the most recent reactor neutrino experiments Daya Bay, RENO, and DoubleChooz.

In the last years large efforts were made to build sensitive, high statistics reactor experiments to measure the mixing angle θ_{13} . A non-vanishing θ_{13} is of special interest since it proofs three flavour mixing. Moreover, in the PMNS matrix it is connected to the CP violating phase δ_D (see equation (1.13)). Up to the measurements of Daya Bay [ABB⁺12, AAB⁺13] and RENO [ACC⁺12], only an upper limit of 0.17 was known for $\sin^2(2\theta_{13})$ [ABB⁺03]. The latest publication of Daya Bay [ABB⁺15] states a best-fit value of

$$\sin^2(2\theta_{13}) = 0.084 \pm 0.005, \quad (1.27)$$

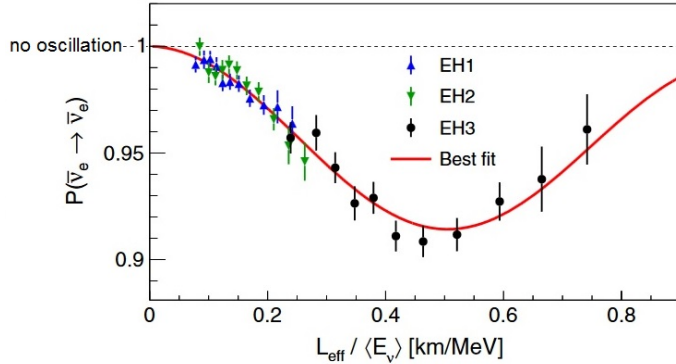


Figure 1.5.: **Electron antineutrino survival probability over effective distance divided by energy from DayaBay measurements.** The data points from the different detectors (EH1, EH2, EH3) are given relative to the no-oscillation scenario. The best-fit value for the oscillation parameters including non-vanishing θ_{13} is given by the solid line. Figure adapted from [ABB⁺15].

which is confirmed by the latest DoubleChooz results [Kan16]. The corresponding survival probability data are shown in figure 1.5 together with the expected survival probability using best fit values. DayaBay also made the most precise measurement on Δm_{32}^2 depending on the mass hierarchy [Y.16]

$$\Delta m_{32}^2(NH) = (2.45 \pm 0.08) \cdot 10^{-3} \text{ eV}^2 \quad (1.28)$$

$$\Delta m_{32}^2(IH) = (-2.55 \pm 0.08) \cdot 10^{-3} \text{ eV}^2, \quad (1.29)$$

$$(1.30)$$

with NH for normal hierarchy and IH for inverted hierarchy. The results of a recent global analysis combining solar, reactor, accelerator and atmospheric neutrino data for a three neutrino mixing scenario from [GGMS16] are given in table 1.1.

Table 1.1.: **Recent neutrino oscillation parameters from global three flavour analysis.** Depending on the sign of Δm_{23}^2 , the mass hierarchy is called normal (NH) or inverted (IH) (see figure 1.3). Both scenarios give slightly different results. Data taken from [GGMS16].

	NH (best-fit value $\pm 1\sigma$)	IH (best-fit value $\pm 1\sigma$)
$\sin^2 \theta_{12}$	$0.304^{+0.013}_{-0.012}$	$0.304^{+0.013}_{-0.012}$
$\theta_{12}/^\circ$	$33.48^{+0.78}_{-0.75}$	$33.48^{+0.78}_{-0.75}$
$\sin^2 \theta_{23}$	$0.452^{+0.052}_{-0.028}$	$0.579^{+0.025}_{-0.037}$
$\theta_{23}/^\circ$	$42.3^{+3.0}_{-1.6}$	$49.5^{+1.5}_{-2.2}$
$\sin^2 \theta_{13}$	$0.0218^{+0.001}_{-0.001}$	$0.0219^{+0.0011}_{-0.001}$
$\theta_{13}/^\circ$	$8.50^{+0.2}_{-0.21}$	$8.51^{+0.2}_{-0.21}$
$\Delta m_{21}^2 / 10^{-5} \text{ eV}^2$	$7.50^{+0.19}_{-0.17}$	$7.50^{+0.19}_{-0.17}$
$\Delta m_{32}^2 / 10^{-3} \text{ eV}^2$	$+2.457^{+0.047}_{-0.047}$	$-2.449^{+0.048}_{-0.047}$

1.3.4. Matter effects

As neutrinos pass through matter, their oscillation probability is modified compared to the vacuum case. This effect was first theoretically explored for neutrino oscillations in

the interior of the sun by Mikheev, Smirnov, and Wolfenstein [MS86, Wol78]. That is why the corresponding effects are often called MSW effects.

In the presence of matter, all neutrino flavours can interact with the nuclei through the neutral current (for energies of solar neutrinos mainly via elastic forward scattering on electrons or nucleons [Wol78]). Only electron neutrinos (with solar neutrino energies smaller than 15 MeV) can interact through the charged current. This results in an effective potential V that applies only to electron neutrinos. This potential is proportional to the electron density of the matter n_e

$$V = \sqrt{n_e G_F}, \quad (1.31)$$

with G_F denoting the Fermi constant. Because of the additional potential the vacuum Hamiltonian H_0 needs to be modified to

$$H = H_0 + V = H_0 + \begin{pmatrix} V & 0 \\ 0 & 0 \end{pmatrix}, \quad (1.32)$$

here written in flavour base. This leads to new mass eigenvalues m_{m1} and m_{m2} with mass eigenstates ν_{m1} and ν_{m2} . The flavour eigenstates can be written introducing a new mixing parameter in matter θ_m [Smi03]:

$$\nu_e = \cos \theta_m \nu_{m1} + \sin \theta_m \nu_{m2} \quad \nu_\mu = \cos \theta_m \nu_{m2} - \sin \theta_m \nu_{m1} \quad (1.33)$$

Here only two-neutrino mixing between electron and muon neutrino is considered. The mixing angle in matter can be calculated with the help of the vacuum oscillation parameters (vacuum oscillation length L_0 , mixing angle θ) [Wol78] as

$$\sin 2\theta_m = \frac{\sin 2\theta}{\sqrt{1 \mp 2 \left(\frac{L_0}{L_R}\right) \cos 2\theta + \left(\frac{L_0}{L_R}\right)^2}}, \quad (1.34)$$

with $L_R = \frac{2\pi}{V} = \frac{\sqrt{2}\pi}{G_F n_e}$. The oscillation length in matter, L_m , can be calculated analogously to the vacuum oscillation length [Wol78, Smi03]

$$L_m = \frac{L_0}{\sqrt{1 \mp 2 \left(\frac{L_0}{L_R}\right) \cos 2\theta + \left(\frac{L_0}{L_R}\right)^2}}. \quad (1.35)$$

The ratio $\frac{L_0}{L_R}$ is proportional to the neutrino energy and the matter electron density. The oscillation amplitude of the transition probability $P(\nu_e \rightarrow \nu_\mu)$ in matter depends (in analogy to the vacuum case in equation (1.22)) on $\sin^2(2\theta_m)$. This term has a resonant character as can be seen from equation (1.34), which means that the oscillation in matter can be significantly enhanced depending on $\frac{L_0}{L_R}$ – even for small mixing in vacuum large oscillations may occur in matter. The vacuum mixing angle determines the width of the resonance as depicted in figure 1.6. Below a critical energy of about 1.9 MeV the oscillation of solar neutrinos is vacuum dominated ($P_{ee} \approx 0.57$); for significantly larger energies, the oscillation is matter dominated ($P_{ee} \approx 0.31$) [Pal15]. So far, ^8B neutrino data from SNO [AAA^{13b}] and KamLAND [AFG¹¹], as well as pp, ^7Be and ^8B solar neutrino data from Borexino [Bel16] confirm predictions from the MSW effect as depicted in figure 1.7. The MSW effect not only occurs in the sun, it also manifests as neutrinos pass through the earth. Using solar neutrinos results in a day / night effect. Earth matter effects can also be observed by long baseline accelerator or reactor experiments.

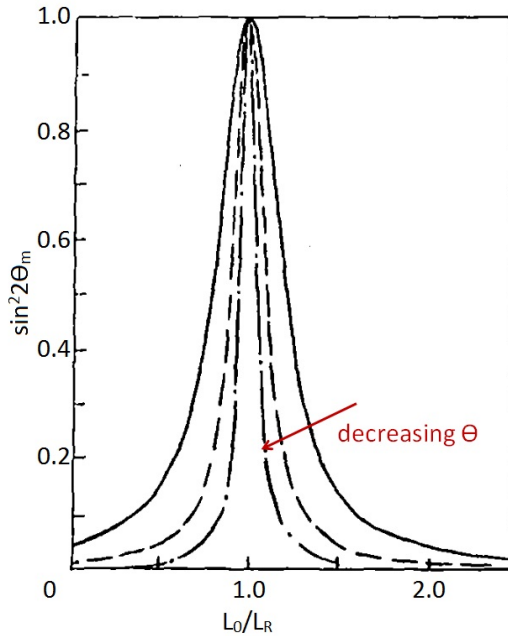


Figure 1.6.: **Resonance of oscillation amplitude in matter.** The matter oscillation amplitude depends on the ratio of vacuum oscillation length and matter refractive length $\frac{L_0}{L_R}$. The ratio is proportional to the matter density and neutrino energy. For $L_R = 2 \cos(\theta) L_0$ the dependence shows a resonance and the amplitude becomes maximal. The width of the resonance decreases with decreasing vacuum mixing angle θ . Figure adapted from [MS86].

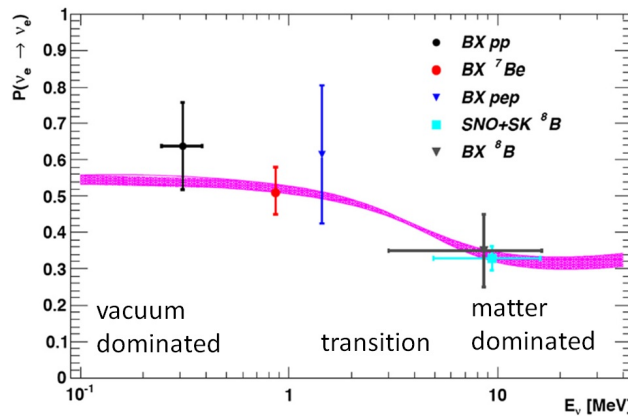


Figure 1.7.: **Solar electron neutrino survival probability over neutrino energy – MSW prediction and experimental data.** The violet band is the MSW prediction including 1σ uncertainty. For low energies the vacuum oscillations dominate, for energies above ≈ 1.9 MeV the matter effects are most important. Borexino, SNO and Super-Kamiokande data are consistent with theoretical predictions. Figure adapted from [Bel16].

1.4. Neutrinoless double beta decay

The neutrinoless double beta ($0\nu\beta\beta$) decay is a process that is able to reveal the intrinsic nature of the neutrino and is thus of highest interest in neutrino physics. Its existence is up to now unclear as even the more probable two neutrino double beta decay is an extremely rare process.

1.4.1. Two neutrino double beta decay

The two neutrino double beta ($2\nu\beta\beta$) decay can be seen as two β -decays occurring simultaneously in one nucleus:

$$(Z, A) \longrightarrow (Z + 2, A) + 2e^- + 2\bar{\nu}_e \quad (2\nu\beta^- \text{ decay}) \quad (1.36)$$

$$(Z, A) \longrightarrow (Z - 2, A) + 2e^+ + 2\nu_e \quad (2\nu\beta^+ \text{ decay}). \quad (1.37)$$

$$(1.38)$$

It is a second-order weak process that is allowed in the Standard Model. Still, it is the rarest known nuclear decay [VR15] and was not observed in the laboratory until 1987 [EHM87]⁵.

Double beta decay can only occur if the mass of the daughter nucleus is smaller than the mass of the mother nucleus (atomic mass A , nuclear charge Z). For $\beta^-\beta^-$ -decay this means:

$$m(Z, A) > m(Z + 2, A). \quad (1.39)$$

On the other hand, in order to be able to observe the process the single β -decay needs to be either energetically forbidden

$$m(Z, A) < m(Z + 1, A), \quad (1.40)$$

or strongly suppressed by selection rules for the nuclear transition between the two states [Zub12]. The mass of a nucleus can be calculated to a good approximation using the Bethe-Weizsäcker formula [Wei35]. It contains a pairing term that considers the spin pairing of protons and neutrons each to spin zero. Nuclei with paired nucleons (even neutron number N and even proton number Z) are more strongly bound and thus have lower masses than the corresponding isobars. This results in two mass parabolas for a given even mass number A , as depicted in figure 1.8. Since the single β -decay is energetically always allowed for the higher mass parabola, $\beta\beta$ -decay can only be observed for the lower parabola, the even-even nuclei, where the single β transitions can be energetically forbidden. Today double beta-decay has been measured for 11 nuclei with large half lives in the range of 10^{19} to 10^{21} years [Rod11].

1.4.2. Neutrinoless double beta decay

Besides the SM allowed double beta decay accompanied by two neutrinos, there is also the SM violating possibility for neutrinoless double beta ($0\nu\beta\beta$)-decay (here given for $\beta^-\beta^-$ -decay)

$$(Z, A) \longrightarrow (Z + 2, A) + 2e^-. \quad (1.41)$$

This decay violates lepton number by 2 and has not been observed so far⁶. The most direct way to introduce neutrinoless double beta decay is via exchange of a light Majorana neutrino, as depicted in figure 1.9a. A neutrino is emitted by one nucleon and absorbed as

⁵Here some earlier hints from geochemical neutrino experiments are not considered.

⁶There was a positive $0\nu\beta\beta$ claim by the Heidelberg-Moscow collaboration for the experiment using ^{76}Ge [KKDHK01]. However recently this claim has been strongly disfavoured by the GERDA experiment [AAA⁺13a, AAB⁺16].

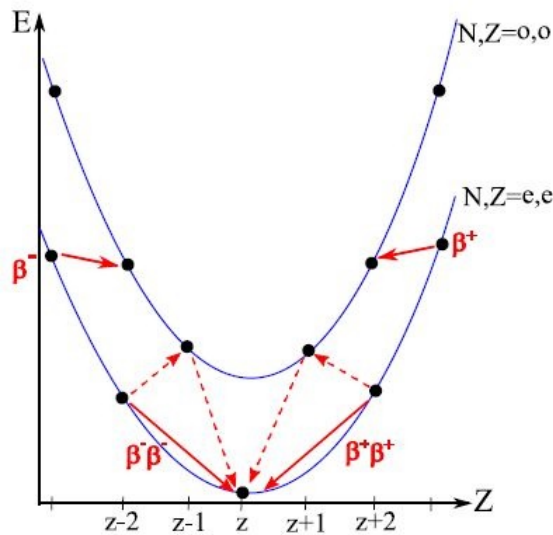


Figure 1.8.: **Mass parabolas for a fixed even mass number.** The binding energy E is given in terms of the proton number Z . Since the binding energy is negative, a larger binding energy means a lower binding and thus a higher nuclear mass. Nuclei with odd neutron and odd proton number (o,o) are bound less strongly than the even even (e,e) nuclei and are thus on the upper mass parabola. Therefore, single β -decays ($\Delta Z = 1$) of an (o,o) to the corresponding (e,e) nucleus is always possible (solid arrows) while single β -decays from o,o nuclei can be energetically forbidden (dashed arrows). In this case, the e,e nuclei can decay via double beta decay ($\Delta Z = 2$), which can be energetically allowed. Figure adapted from [DES].

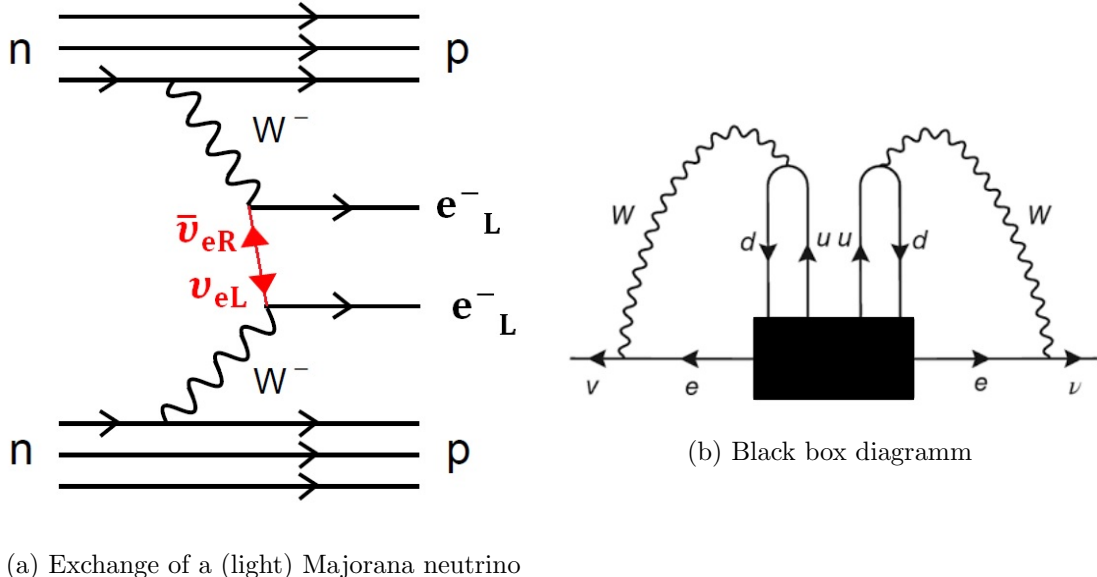


Figure 1.9.: **Feynman diagrams illustrating $0\nu\beta\beta$ -decay.** In (a) the diagram for the exchange of a light Majorana neutrino is shown. A left handed electron neutrino is emitted by one decaying nucleon. It is instantaneously absorbed as a right handed antineutrino by a second nucleon what causes the second β -decay. (b) shows the more general representation of $0\nu\beta\beta$ -decay independent on the particular physical process causing the decay. This model independence is visualised via a black box and known as the Schechter-Valle theorem. Independent on the process triggering the $0\nu\beta\beta$ decay, a Majorana mass term is induced [SV82]. Figure adapted from [VR15].

an antineutrino by another nucleon. The transition from particle to antiparticle requires the neutrino to be of Majorana nature. Furthermore, since the charged current reaction only couples to the left handed neutrinos and the right handed antineutrinos the neutrino helicity needs to change. Since the contribution from right (left) handed (anti-) neutrino fields to the total neutrino field goes with $(\frac{m_\nu}{E})^2$ this is related to a non-zero neutrino mass [Zub12].

There are many other theoretical possibilities for $0\nu\beta\beta$ -decay implying the exchange of hypothetical particles. Still, independent on its actually underlying process, neutrinoless double beta decay proves the neutrino to have a finite Majorana mass. This statement is known as the Schechter-Valle theorem [SV82] and is typically visualised by a black box in the Feynman diagram of $0\nu\beta\beta$ -decay, as shown in figure 1.9b. Via loop processes the interactions can be arranged such that a neutrino-antineutrino coupling as known from the Majorana mass term (see equation 1.46) occurs.

As it provides the unique possibility to test if the neutrino is its own antiparticle (Majorana particle), neutrinoless double beta decay is of large theoretical and experimental interest. The experimental signature of $0\nu\beta\beta$ -decay is a peak in the sum energy spectrum of both emitted electrons at the Q -value of $2\nu\beta\beta$ -decay as depicted exemplarily in figure 1.10. To reach a high $0\nu\beta\beta$ -decay sensitivity one needs a large number of $\beta\beta$ -nuclei, a low $0\nu\beta\beta$ half life $T_{1/2}^{0\nu}$ as well as an ultra low background and high energy resolution in the signal region (Q -value of $2\nu\beta\beta$ -decay). The half life can be computed using [Rod11]:

$$\left(T_{1/2}^{0\nu}\right)^{-1} = G^{0\nu}(Q, Z) |\mathcal{M}^{0\nu}|^2 \frac{\langle m_{\beta\beta} \rangle^2}{m_e^2}. \quad (1.42)$$

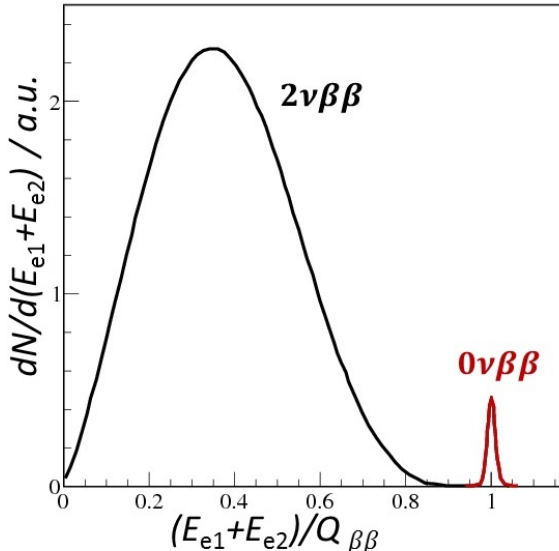


Figure 1.10.: **Cartoon spectrum of $0\nu\beta\beta$ -decay.** The sum spectrum of the two electrons with sum energy $E_{e1} + E_{e2}$ for $2\nu\beta\beta$ -decay is shown (black curve) together with the spectrum of $0\nu\beta\beta$ -decay (red curve). The $0\nu\beta\beta$ -decay produces a peak at the Q -value of $2\nu\beta\beta$ -decay. Amplitudes of the spectra are not to scale. Figure adapted from [WS12].

Here $G^{0\nu}(Q, Z)$ denotes the phase space factor, $\langle m_{\beta\beta} \rangle$ the effective (Majorana) neutrino mass (see equation (1.46)) and $\mathcal{M}^{0\nu}$ the nuclear matrix element of $0\nu\beta\beta$ -decay. The computation of the matrix element is associated with the particular mechanism underlying the decay and is thus strongly model dependent [Bil10, Zub12]. Since only the product of the effective Majorana neutrino mass and the matrix element can be measured, the masses (mass limits) derived from $0\nu\beta\beta$ -experiments are model dependent, too.

A variety of $0\nu\beta\beta$ -candidates is investigated by an even larger number of experiments for example ^{76}Ge (GERDA, Majorana), ^{100}Mo (MOON), ^{136}Xe (KamLAND-Zen, EXO/nEXO, NEXT), ^{130}Te (CUORE, SNO+). Current $0\nu\beta\beta$ -decay half life limits of these isotopes are in the range of 1×10^{24} years to 1×10^{26} years. Current mass limits (see section 1.5.2.2) are on the sub-eV scale [Hen16].

1.5. Neutrino masses – generation and experimental determination

The nature of neutrinos is connected to the process of neutrino mass generation. Both are still an open question as the neutrino stays massless in the Standard Model description. In section 1.5.1 possible mass generation mechanisms for Dirac and Majorana type neutrinos are introduced. There are other possibilities like a Higgs triplet [SV82] or supersymmetry [CEIN00] which are not discussed here. A more detailed discussion on neutrino mass generation can be found in [MAB⁺07].

1.5.1. Neutrino mass generation

In the Standard Model of particle physics, all particles remain massless as a mass term in the Lagrangian \mathcal{L} would break gauge symmetry. A way out is found using the concept of spontaneous symmetry breaking. It is used in the *Higgs mechanism* [Hig64, Kib67] to allow particles to generate mass. Fermion masses are generated by adding a gauge invariant Yukawa term with coupling constant c_e to the Lagrangian which couples the

fermion fields to the Higgs field. In case of a lepton field with left-handed isospin doublet $(\nu_e)_L$ and right-handed singlet e_R the Yukawa Lagrangian gets

$$\mathcal{L}_{\text{Yuk}} = -c_e \left(\bar{e}_R \phi^\dagger \begin{pmatrix} \nu_{eL} \\ e_L \end{pmatrix} + (\bar{\nu}_{eL}, \bar{e}_L) \phi e_R \right). \quad (1.43)$$

For the Higgs field ϕ , one uses the vacuum field $\phi_0 = \begin{pmatrix} 0 \\ v \end{pmatrix}$ with vacuum expectation value v . Thus, an electron mass term $-c_e \frac{v}{\sqrt{2}} \bar{e} e$ is generated with the electron field $e = e_L + e_R$ [DM08]. The neutrino stays massless, since to construct a neutrino mass by this mechanism, a right-handed neutrino singlet would be required.

As shown by several neutrino oscillation experiments, discussed in section 1.3, neutrinos (at least two of them) cannot be massless. But the large difference between charged lepton and neutrino masses of more than five orders of magnitude suggests that the mass generation mechanism may be different.

There are two ways to introduce a non-zero neutrino mass term that are related to the nature of the neutrino (Dirac or a Majorana particle). For the mass generation of Dirac neutrinos three right-handed chiral projections of the neutrino fields $\nu_{\alpha R}$, with $\alpha = (e, \mu, \tau)$, need to be added. These right-handed neutrinos are sterile, which means, they do not couple to the weak interaction and take only part in the generation of masses. Introducing the Dirac mass matrix M^D the mass term has the general form [Bil10]:

$$\mathcal{L}^D = -c_\nu \sum_{\alpha, \alpha'} \bar{\nu}_{\alpha' L} M_{\alpha' \alpha}^D \nu_{\alpha R}. \quad (1.44)$$

The Yukawa coupling c_ν needs to account for the smallness of the neutrino masses. Compared to the electron Yukawa coupling, it has to be more than 2.5×10^5 times smaller (assuming the absolute neutrino mass scale to be below 2 eV).

Due to its electric and strong charge neutrality the neutrino may be its own antiparticle $\nu = \bar{\nu}$ or, in other words, it is its own charge conjugate ν^c with charge conjugation operator C . The right-handed and left-handed components of the majorana neutrino field are connected via $\nu_R = (\nu_L)^c$ and the field can be written

$$\nu = \nu_L + (\nu_L)^c. \quad (1.45)$$

Now a majorana mass term [Maj37] can be constructed that contains only active, left-handed neutrinos [DM08]:

$$\mathcal{L}^M = \frac{m_L}{2} \bar{\nu}_L^c \nu_L. \quad (1.46)$$

The same mass term can be constructed for a right-handed neutrino with mass component m_R . The most general mass term that can be constructed includes all possible two field combinations of $\nu, \bar{\nu}, \nu^c, \bar{\nu}^c$ that produce a Lorentz scalar [Zub12]. Since right-handed neutrinos and left-handed antineutrinos do not take part in charged current weak interactions, they are denoted differently: $\nu_R = N_R$ and $\nu_L^c = N_L^c$. These represent the sterile type neutrinos

$$\mathcal{L}^{D+M} = \frac{1}{2} \left[(\bar{\nu}_L, \bar{N}_L^c) \begin{pmatrix} m_L & m_D \\ m_D & m_R \end{pmatrix} \begin{pmatrix} \nu_R^c \\ N_R \end{pmatrix} + h.c. \right]. \quad (1.47)$$

The mass matrix can be diagonalised to obtain the physical values m_1 and m_2 by introducing two Majorana fields, ϕ_1 and ϕ_2 , such that

$$\mathcal{L} = \frac{1}{2} (m_1 \bar{\phi}_1 + m_2 \phi_2). \quad (1.48)$$

The mass eigenvalues $m_{1,2}$ are [Zub12]:

$$\epsilon_{1,2} \cdot m_{1,2} = \frac{1}{2} \left((m_L + m_R) \pm \sqrt{(m_L - m_R)^2 + 4m_D^2} \right), \quad (1.49)$$

$\epsilon_{1,2}$ is set to $+1$ or -1 to generate only positive masses. The Majorana fields can be calculated by introducing the mixing angle θ given by $\tan 2\theta = \frac{2m_D}{m_R - m_L}$:

$$\phi_1 = \cos \theta (\nu_L + \epsilon_1 \nu_R^c) - \sin \theta (N_L^c + \epsilon_1 N_R) \quad (1.50)$$

$$\phi_2 = \sin \theta (\nu_L + \epsilon_2 \nu_R^c) + \cos \theta (N_L^c + \epsilon_2 N_R). \quad (1.51)$$

Depending on the masses in the mass matrix from equation (1.47) three general cases can be distinguished:

1. Dirac type neutrino : $m_L = m_R = 0$

The fields ϕ_1 and ϕ_2 can be used to construct a Dirac type field which produces a Dirac type mass term in the Lagrangian ($m_D(\bar{\phi}_1 + \bar{\phi}_2)(\phi_1 + \phi_2)$).

2. Majorana type neutrino: $m_D = 0$.

The masses $m_{1,2}$ get the Majorana masses $m_{L,R}$ and the fields $\phi_{1,2}$ get the initial Majorana fields $\nu_L + \nu_R^c$ and $\nu_R + \nu_L^c$

3. Seesaw case: $m_L = 0, m_R \gg m_D$

$m_1 \approx \frac{m_D^2}{m_R}$ and $m_2 \approx m_R$, the fields ϕ_1 and ϕ_2 get representative for a light active neutrino $\phi_1 \approx \nu_L - \nu_R^c$ with small mass m_1 and a heavy sterile neutrino $\phi_2 \approx N_L^c + N_R$ with higher mass $m_2 = m_R$. This mechanism could explain why the active neutrino masses are so light compared to the charged leptons.

1.5.2. Experimental neutrino mass determination

The oscillation measurements described above are only sensitive to the mass squared splittings of the different neutrino mass eigenstates, not to the absolute scale of the masses, which remains unknown to date. There are different experimental approaches to determine the neutrino mass(es) that can be divided into two general categories: direct methods such as single β -decay and time of flight experiments and indirect methods such as mass determination from cosmology data or from neutrinoless double beta decay. Direct methods purely rely on kinematics (energy and momentum conservation). The derived results are thus so-called *model independent*. Indirect methods strongly depend on the model assumptions, i.e. on the cosmological model or the neutrino Majorana nature and the matrix element of $0\nu\beta\beta$ decay. This leads to model dependent uncertainties in the derived neutrino mass results.

Depending on the used method, the observable will be different sums by weight of mass eigenstates.

1.5.2.1. Neutrino mass from cosmology

Neutrinos are, after the photon, the most abundant particles in the universe. Their density is dominated by the *relic neutrinos* stemming from the neutrino decoupling period⁷ in the early universe at a temperature of about 1 MeV [LP14]. Due to the expansion of the universe, the neutrinos got red-shifted to a current temperature of 1.95 K (thermal energy 0.168 meV). Their density is about 112 cm^{-3} for each species [ACC⁺11]. Neutrino temperature and density have not been measured so far due to the low neutrino energy and corresponding extremely low cross sections. The values have been calculated from temperature and density of the cosmic microwave background (CMB) which is closely related to the cosmic neutrino background [LP14].

Due to their large number, neutrinos contribute to the total energy density of the universe even despite their very small mass. Their energy density can be calculated depending on

⁷Decoupling occurred when the neutrino interaction rate with the electromagnetic plasma dropped below the expansion rate of the universe.

the sum of the neutrino masses (for non-relativistic neutrinos) $\sum_i m_{\nu_i}$ and on the Hubble parameter h [Han10]:

$$\Omega_\nu h^2 = \frac{\sum_i m_{\nu_i}}{93.8 \text{ eV}}. \quad (1.52)$$

Assuming the universe to be totally dominated by neutrinos⁸, $\Omega_\nu = \Omega \leq 1$, a most general neutrino mass limit of

$$\sum_i m_{\nu_i} \leq 46 \text{ eV} \quad (1.53)$$

can be derived.

Massive neutrinos are important in the formation of structures in the universe. When they became non-relativistic, their free-streaming length (neutrino horizon) shrank. On scales smaller than this free-streaming length structure formation was washed out [BES80] and the matter power spectrum⁹ is suppressed [LP14]. The free-streaming length as well as the kinetic neutrino energy density strongly depend on the neutrino mass.

Current neutrino mass limits from cosmology are based on several observation channels like small and large scale CMB temperature and polarisation fluctuations and observation of cosmic structures. Neutrino mass limits from cosmology are susceptible to the cosmological model used. Furthermore, they often need to combine different cosmological data sets which causes the limits to be less robust due to tensions between the different data sets [HHW14]. Recent studies using temperature and polarisation data of Planck [AAA¹⁴] derived a neutrino mass limit of [DVGG¹⁶]

$$\sum_i m_{\nu_i} \leq 0.497 \text{ eV} \quad (95\% \text{ C.L.}) \quad (1.54)$$

Extending the data set by further CMB observations and various observations of large scale structures, an even more stringent upper bound of

$$\sum_i m_{\nu_i} \leq 0.12 \text{ eV} - 0.13 \text{ eV} \quad (95\% \text{ C.L.}) \quad (1.55)$$

can be set [DVGG¹⁶].

1.5.2.2. Neutrino mass from neutrinoless double beta decay

The process of neutrinoless double beta decay can be used to derive the neutrino mass. The effective mass related to this currently unobserved decay is the coherent sum of the different mass eigenstates

$$m_{\beta\beta}^2 = \left| \sum_{i=1}^3 U_{ei}^2 m_i \right|^2. \quad (1.56)$$

Due to the Majorana phases entering in equation (1.56) through U_{ei}^2 , the effective mass derived from $0\nu\beta\beta$ -decay can be smaller than the contributing eigenvalues of the mass eigenstates (m_i). The current best limit on the effective neutrino mass from $0\nu\beta\beta$ decay are set by GERDA [AAB¹⁶], EXO [c¹⁴] and KamLAND-Zen [GGH¹³] and are of the order of

$$m_{\beta\beta} < 0.2 - 0.4 \text{ eV}. \quad (1.57)$$

The mass (limit) derived from double beta decay experiments is strongly model dependent due to the actual process that generates the decay and the contributing nuclear matrix elements that have large uncertainties.

⁸In order not to over-close the universe the total energy density Ω should not be larger than one.

⁹amplitude of density fluctuations in the universe as a function of the angular scale (wave number k)

1.5.2.3. Time-of-flight measurements using supernova neutrinos

The time of flight method (TOF) is a kinematic approach and uses the energy-momentum relation $E^2 = p^2 + m^2$. Thus, one is sensitive to the neutrino mass squared like with single β -decay experiments (compare section 1.5.2.4). To be able to detect the effect of tiny neutrino masses in a TOF experiment, the baseline needs to be of the order of 10 kpc^{10} . Thus, a galactic supernova, which is a high luminosity neutrino source, is suitable to investigate the neutrino mass with the TOF method.

In a core-collapse supernova a massive star ($M > 8M_{\odot}$) collapses under its own gravitational pressure when it is no longer able to balance this pressure by an outward thermal pressure created by nuclear fusion. During the collapse of the outer shells, almost the complete gravitational binding energy is released. About 99% of this energy is carried away by neutrinos (and antineutrinos) of different flavours within a time period of roughly 10 s [Zub12]. The neutrinos have average energies of about 10 MeV with energy hierarchy $\langle E_{\nu_e} \rangle < \langle E_{\bar{\nu}_e} \rangle < \langle E_{\nu_{\mu,\tau}} \rangle$ [Sch12].

The duration of flight t_{TOF} depends on the neutrino mass and energy. The TOF difference of two neutrinos with different energies (E_1, E_2) and difference in emission times Δt_0 can be calculated

$$\Delta t_{\text{TOF}} = L \frac{m_{\nu_{\alpha}}^2}{2c} \left(\frac{1}{E_1^2} - \frac{1}{E_2^2} \right) + \Delta t_0, \quad (1.58)$$

with source-detector distance L . The neutrino burst has a considerably long duration of the order several seconds and introduces a relatively large systematic uncertainty since Δt_0 cannot be measured. Thus, the derived mass limit strongly depends on the supernova emission model [Zub12]. The neutrino mass term that occurs in equation (1.58) can be calculated using

$$m_{\nu_{\alpha}}^2 = \sum_{i=1}^3 |U_{\alpha i}^2| m_i^2. \quad (1.59)$$

In this kinetic mass term enters the incoherent sum of the different mass eigenstates.

The famous SN1987A, which was the brightest and closest to earth supernova since 1604, was seen by the neutrino detectors running at that time (Kamiokande, IBM, Baksan). They were able to detect 24 neutrinos originating from this event. A new analysis of the detected results by [LL02] gives a mass limit of

$$m_{\bar{\nu}_e} < 5.7 \text{ eV}. \quad (1.60)$$

1.5.2.4. Single beta decay experiments

Processes that change the atomic number, Z , by one are called β -decays. There are three different modes of nuclear β -decay:

- β^- -decay $\rightarrow Z$ changes by +1, emission of an electron and an electron antineutrino;
- β^+ -decay $\rightarrow Z$ changes by -1, emission of a positron and an electron neutrino;
- Electron capture (EC) $\rightarrow Z$ changes by -1, capture of an electron, emission of an electron neutrino.

Nuclear β^- -decay currently provides the most sensitive direct limit on the mass of the electron antineutrino $m_{\bar{\nu}_e}$ (as defined by equation (1.59)) and, since CPT is conserved, also on the mass of the electron neutrino m_{ν_e} [OW08]. The underlying mechanism of

¹⁰For a supernova in a distance of 10 kpc the arrival time difference on earth will be of the order of seconds for mass difference of about 10 eV [Kra92].

β^- -decay is the transformation of a neutron into a proton under emission of an electron and an electron antineutrino:

$$n \longrightarrow p + e + \bar{\nu}_e, \quad (1.61)$$

On quark level, this means the transition of a down quark into an up quark under emission of a W^- boson that decays into an electron and an electron antineutrino. The energy released in this process is equal to the mass difference of mother and daughter atom. This energy is denoted by the Q -value. Since the mass of the daughter nucleus is large compared to the electron and neutrino masses, the nuclear recoil energy is small. Thus, almost the full amount of released energy is split between the electron and the neutrino.

Kinematics of β -decay

The kinematics of β -decays are described by Fermi's golden rule:

$$\frac{d^2N}{dtdE} = \frac{2\pi}{\hbar} |\langle f | H_{if} | i \rangle|^2 \rho(E). \quad (1.62)$$

Here $\langle f | H_{if} | i \rangle$ denotes the matrix element for the transition of the initial state $|i\rangle$ to the final state $|f\rangle$ and $\rho(E)$ the density of final states. The matrix element can be divided into a leptonic and a nuclear part [OW08]. Considering only allowed transitions, no angular momentum is carried away by the leptons and the leptonic part $|M_{\text{lep}}|^2$ can be calculated using

$$|M_{\text{lep}}|^2 = F(Z + 1, E) \frac{1}{V^2}. \quad (1.63)$$

Here the so-called Fermi function, $F(Z + 1, E)$, needs to be introduced, that accounts for the interaction of the charged lepton (electron) with the Coulomb field of the daughter nucleus. The parameter V is the normalisation volume of the leptonic wave functions. With the help of (1.63) the transition matrix element can be written as [Zub12]

$$|\langle f | H_{if} | f \rangle|^2 \simeq \frac{g^2}{V^2} F(E, Z + 1) |M_{if}|^2, \quad (1.64)$$

where $|M_{if}|$ denotes the nuclear part of the decay matrix element $|\langle f | H_{if} | i \rangle|$ and g the coupling constant of the interaction.

The phase space density can be calculated by multiplying the electron and neutrino density of states, since the nuclear recoil can be neglected. Thus the phase space density gets

$$\rho(E) = \frac{V^2 p_e E p_\nu E_\nu}{4\pi^4 \hbar^6}, \quad (1.65)$$

with total electron and neutrino energies, E and E_ν , and with electron and neutrino momenta, p_e and p_ν . The electron spectrum of β -decay for allowed transitions gets

$$\frac{d^2N}{dtdE} = C \cdot F(E, Z + 1) p_e E \sum_j P_j (E_0 - E_j) \sqrt{(E_0 - E_i)^2 - m_{\nu_e}^2 c^4} \cdot \Theta(E_0 - E - m_{\bar{\nu}_e} c^2), \quad (1.66)$$

with the constant $C = \frac{G_F^2 \cos^2 \theta_C}{2\pi^3} |M_{if}|^2$, where G_F denotes the Fermi coupling constant and θ_C the Cabibbo angle [Zub12]. The decay rate can be seen as a superposition of β -spectra over all electronic excitations of the final states with probability P_j and excitation energy E_j . The Heaviside function Θ ensures the conservation of energy. The endpoint energy E_0 is the decay energy to be split between the two leptons – it equals the Q -value of the decay minus the electronic excitation energy of the particular final state, the recoil energy, and the atomic and molecular binding energies.

Looking at equation (1.66) it is clear that the parameter which can be accessed by single

β -decay experiments is the (anti)neutrino mass squared $m_{\nu_e}^2$ which is the incoherent sum of the three neutrino mass eigenstates m_{ν_i} as introduced in equation (1.59). No Majorana phases α_i occur in equation (1.59), which marks a difference to the coherent sum measured by double β -decay experiments (compare equation (1.56)).

The effects of neutrino mixing are present in the spectrum of β decay, since equation (1.66) is a superposition of β -decay spectra for the different neutrino mass eigenstates m_{ν_i} with endpoint energies $E_e^i = E_0 - m_{\nu_i}$ [AAB⁰⁵]. Still, the mass differences are too small to be observable with current experimental energy resolution and the β -decay rate from equation (1.66) can be described by one effective neutrino mass [FS03].

Tritium experiments

Tritium β -decay experiments to determine the neutrino mass have a long history: Already in 1948 the first measurement of the shape of the tritium spectrum was performed [CAC48]. Therefrom, an upper neutrino mass limit of 1 keV was derived [CAC49].

To date, tritium is, except for ^{187}Re , the only isotope used in direct β^- decay neutrino mass measurements [DHMW13]. The β -decay of tritium



is still used in modern direct neutrino mass experiments like KATRIN [AAB⁰⁵] and Project 8 [MF09]. It is an ideal candidate to be used in direct neutrino mass measurements due to its several advantages:

- **Low endpoint energy** – Tritium β -decay has an endpoint energy of about 18.6 keV [NFB⁰⁶] which is after ^{187}Re the second lowest Q -value of β^- -decay. The region close to the endpoint has the highest sensitivity for the neutrino mass analysis since the neutrino is non-relativistic in this region (as $E_\nu \approx m_\nu$). Thus, a low endpoint energy is preferable in order to have a large neutrino mass impact on the spectrum. A low endpoint energy is also easier to handle experimentally (note that the required retarding potential for the electron spectroscopy is equal to the endpoint energy).
- **Low half life** – A half life of only 12.3 years [LU00] results in a relatively high specific activity.
- **Super-allowed decay** – The nuclear decay of tritium is a super-allowed transition. In such decays, the nuclear matrix element, M_{if} , does not depend on energy and no corrections need to be considered.
- **Low nuclear charge** – The mother and daughter isotopes have low nuclear charges, $Z = 1$ and $Z = 2$, thus the interaction of the emitted electron with the daughter nucleus is low and the corresponding Fermi function, $F(Z = 2, E)$, can be computed precisely [AAB⁰⁵]. Furthermore, inelastic scattering of electrons with the source material is weak.
- **Simple electronic shell configuration** – Due to the simple configuration of the atomic shell structure of the daughter ion $^3\text{He}^+$ the final state spectrum, (P_j, E_j) from (1.66), can be calculated reliably.

In general molecular tritium, T_2 , is used in the neutrino mass experiments. Therefore, the spectrum of rotational and vibrational states of mother and daughter molecules, T_2 and $^3\text{HeT}^+$, in the ground state and even electronic excitations need to be known and included in the calculation. This constitutes a large systematic effect.

Current neutrino mass limits from β -decay

The current best limits on the effective electron (anti)neutrino mass are provided by the experiments in Mainz [KBB⁺05] and Troitsk [ABB⁺11]. Both experiments used a high resolution electrostatic spectrometer based on the principle of Magnetic Adiabatic Collimation combined with an Electrostatic (MAC-E) filter to measure the β -decay spectrum of molecular tritium.

In the Mainz experiment a solid source of T_2 frozen onto a substrate was used. The final result, that is based on data taking in phase II from 1997-2001, sets an effective electron antineutrino mass limit of [KBB⁺05]

$$m_{\bar{\nu}_e} < 2.3 \text{ eV}(95\% \text{C.L.}). \quad (1.68)$$

The Troitsk experiment, that is still running¹¹, uses a gaseous molecular tritium source. The most recent result, published in 2011 [ABB⁺11] sets an upper neutrino mass limit of

$$m_{\bar{\nu}_e} < 2.05 \text{ eV}(95\% \text{C.L.}). \quad (1.69)$$

A combined analysis of both results by the Particle Data Group gives the current best model independent limit on the effective mass of the electron antineutrino which is [G⁺14b]

$$m_{\bar{\nu}_e} < 2.0 \text{ eV}. \quad (1.70)$$

To reach the sub-eV neutrino mass sensitivity, a new generation of β -decay experiments needs to be built. The KATRIN experiment aims to reach a sensitivity of $m_{\bar{\nu}_e} < 200 \text{ meV}$ (90% C.L.) [AAB⁺05] using the (MAC-E) filter principle combined with a gaseous tritium source. To reach this high sensitivity, improvements over the previous experiments in Mainz and Troitsk are required in multiple aspects:

- Higher signal rate – It will be achieved by a large source luminosity.
- Improved energy resolution of about 1 eV.
- Enhanced understanding of source related systematic effects.

At the same time, the background rate needs to be of the order of 10^{-2} counts/s. An overview of KATRIN is given in the following chapter.

An other approach is followed by the Project 8 collaboration [MP15] planning to measure the spectrum of tritium β -decay by detecting the synchrotron radiation of β electrons that are stored in a strong magnetic field (Cyclotron Resonance Emission Spectroscopy – CRES). The electron energy is inferred from the single particle frequency measured by an antenna array. Currently the collaboration has achieved a proof of principle of the CRES technique using a ^{83m}Kr source [ABdV⁺15] and is developing the technique further for use with gaseous tritium.

Rhenium and Holmium experiments

Different from the spectrometer method there is a second approach to measure accurate β -decay spectra with source and detector being identical. Such experiments are based on cryogenic bolometers. The detector is cooled down to cryogenic temperatures of the order of mK. The energy released in the β decay is converted into phonons in the absorber material which causes a small temperature rise ΔT . The temperature rise, measured by a sensitive thermometer, can be related to the energy released in the decay, ΔE :

$$\Delta T = \frac{\Delta E}{C}, \quad (1.71)$$

¹¹It is now focussing on the search of sterile keV neutrinos but won't improve its neutrino mass result further.

with heat capacity C . To get a preferably large temperature rise, the detector scale needs to be small – typical masses are of $\mathcal{O}(\text{mg})$ [WZ13] – and cold, as C typically scales with T^3 .

With calorimeters the total amount of released energy can be measured which is different from the above described spectrometer approach. This means, these experiments do not suffer from the systematic uncertainties in the description of final states and energy loss processes. They measure the entire differential β -beta spectrum and subsequent de-excitations. However, they are affected by pile-up events, which is an other reason, why the detector mass is limited. Thus, large arrays of small detectors need to be built in order to obtain high statistics, since only a small fraction of β -decay events release energies in the region around 1 eV next to the endpoint [DHMW13].

The calorimetric approach is used in experiments measuring the β -decay of Rhenium



and the electron capture of Holmium



These isotopes have very low Q values of 2.492 keV for ^{187}Re [NEB⁺14] and of 2.833 keV for ^{163}Ho [EBB⁺15].

The MIBETA experiment measured an upper limit of the electron antineutrino mass of $m_{\bar{\nu}_e} < 15.6$ eV (90% C.L.) using Rhenium [SAB⁺04].

The electron capture of ^{163}Ho is measured by the ECHO experiment, which aims to reach a sub-eV electron neutrino mass sensitivity in a full-scale experiment¹² [GBD⁺14], by the HOLMES collaboration, that plans to reach a sensitivity of 1 eV [FAB⁺16] and by the NuMECS collaboration [col].

¹²Currently ECHO is working on a mid-scale experiment with a source activity of about 1 kBq. The future full scale experiment will house a ^{163}Ho sources with an activity of about 1 MBq [HBG⁺16].

2. Neutrino mass measurement with the KATRIN Experiment

Contents

2.1. Measurement principle	30
2.1.1. MAC-E filter principle	30
2.1.2. Transmission and response function	35
2.2. Neutrino mass sensitivity	36
2.3. Main components	39
2.3.1. Source and transport section	39
2.3.1.1. Windowless gaseous tritium source (WGTS)	39
2.3.1.2. Differential pumping section (DPS)	45
2.3.1.3. Cryogenic pumping section (CPS)	46
2.3.1.4. Inner loop	46
2.3.2. Rear section	47
2.3.3. Spectrometer and detector section	50
2.3.3.1. Pre-spectrometer	50
2.3.3.2. Main spectrometer	51
2.3.3.3. Monitor spectrometer	52
2.3.3.4. Focal plane detector	52
2.3.4. Monitoring devices for the source and transport section	52
2.4. Simulation and analysis software	55
2.4.1. The particle tracking software Kassiopeia	55
2.4.2. Source and Spectrum Calculation software SSC	55
2.4.2.1. Defining source properties	56
2.4.2.2. Calculation of KATRIN β -electron spectra	57
2.4.3. Spectrum fitting software KaFit	60

The **Karlsruhe Tritium Neutrino** experiment (KATRIN) is a next-generation tritium β -decay experiment constructed to measure the mass of the effective electron antineutrino, $m_{\bar{\nu}_e}$, model independently with an unrivalled sensitivity of 200 meV at 90% C.L. (350 meV at 5σ). KATRIN joins a tritium source of high luminosity and stability with a high-precision energy analysing spectrometer. Along with a low background level and well controlled systematic uncertainties this combination allows to surpass the sensitivity of prior tritium β -decay experiments by one order of magnitude.

The present chapter starts with an introduction to the KATRIN measurement principle. Thereafter, in section 2.2, the statistical and systematic uncertainties and the resulting neutrino mass sensitivity are introduced. In section 2.3 the main components of KATRIN are reviewed with focus on the tritium source that plays an important role in the work at hand. In the last section 2.4 the software utilised to analyse and simulate KATRIN data is introduced. Emphasis is placed on the calculation of source spectra and on the analysis procedure that is used for the investigation of systematic uncertainties and that will finally be used to determine the neutrino mass.

2.1. Measurement principle

KATRIN will use the β decay of molecular tritium to determine the effective electron antineutrino mass in a model independent way (see section 1.5.2.4). The analysis procedure giving access to the neutrino mass is based on a comparison of precisely measured and accurately simulated β -decay electron spectra. The measurement of the electron energy spectrum that carries the information on the neutrino mass will be performed with a MAC-E (Magnetic Adiabatic Collimation combined with an Electrostatic) filter. This principle allows to measure the energy-integrated differential spectrum of electrons stemming from β -decay that is different from the initial differential electron spectrum as given in (1.66). The shape difference of both spectra near the tritium endpoint is illustrated in figure 2.1.

A non-vanishing neutrino mass has an influence on the shape of the differential as well as on the integrated spectrum, especially in the endpoint region of the β -decay, as shown in figure 2.2. The energy region that is most sensitive to the neutrino mass is obtained, by identifying the most pronounced relative difference of (simulated) integrated spectra for a vanishing and a non-zero neutrino mass. The spectra and their relative difference are depicted in figure 2.2. For the calculation of the given spectra a nominal background of 0.01 cps is included since the background rate is crucial for the position of the neutrino mass sensitive energy region. This region is close to the endpoint of the β -decay spectrum (tritium β -decay endpoint about 18.57 keV). Hence, a large amount of measurement time needs to be spent in the endpoint region (standard measurement time distribution shown in figure 2.17).

The modelled spectrum that will be used for neutrino mass analysis needs to account for all processes modifying the energy of the β -decay electrons. Thus, working principle and systematic uncertainties of the tritium source as well as of the spectrometer need to be understood precisely since both components influence the electron spectrum that is measured with KATRIN. In the following section the filtering concept of a MAC-E filter and how its transmission properties affect the spectral distribution of electrons that can pass it are discussed. This information is essential for the spectral modelling of electrons reaching the detector which is further discussed in section 2.4.2.

2.1.1. MAC-E filter principle

A tritium β -decay experiment to determine the neutrino mass needs a high luminosity source, since the information on the neutrino mass is contained mostly in the region around

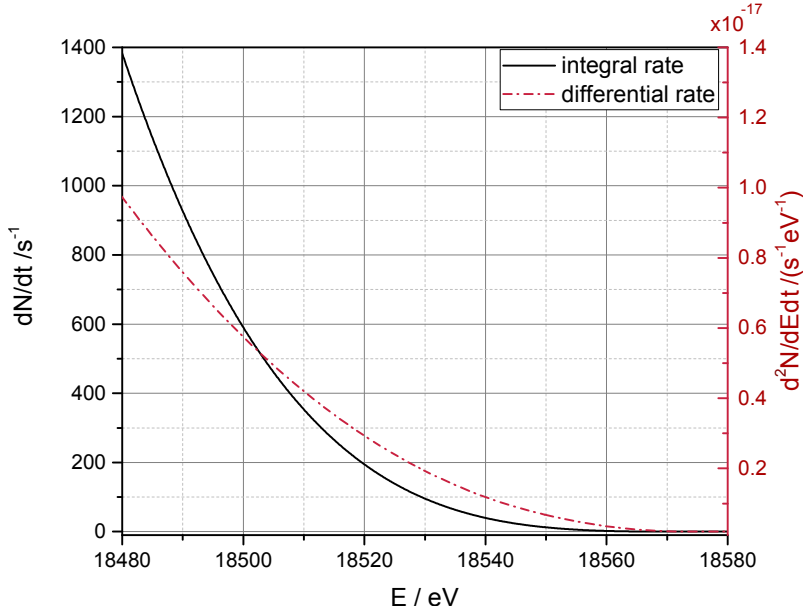


Figure 2.1.: **Differential β -decay spectrum and energy integrated β -decay spectrum measurable with KATRIN.** The integrated spectrum, $\frac{dN}{dt}$, is depicted by the black solid line, the red dashed line marks the differential spectrum $\frac{d^2N}{dtdE}$. The differential spectrum represents the initial spectrum after β -decay and does not contain information on the transmission properties of the experimental set-up. Note the different axis scales and units (left axis – integrated spectrum, right axis – differential spectrum).

the endpoint, where the rate has decayed by about 13 orders of magnitude (see figure 2.1). At the same time, the energy resolution needs to be very good in order to resolve the small distortions from a finite neutrino mass (compared to a vanishing neutrino mass) as shown in figure 2.2. A MAC-E filter, first proposed in [BPT80], combines electrostatic filtering and magnetic adiabatic collimation. It is thus an excellent tool for accurate spectroscopy of electrons emitted by a high luminosity, isotropic source. The method had been optimised to be used in the former neutrino mass tritium β -decay experiments in Mainz and Troitsk [PBB⁺92, Lob85]. In the following, the general principle and characteristic parameters of a MAC-E filter are explained. A visualisation of its working principle is given in figure 2.3.

The kinetic energy of the electrons E_{kin} can be divided in a part that is connected to the cyclotron motion transversal to the magnetic field lines E_{\perp} and a part that belongs to the motion directed along the field lines E_{\parallel} . With θ denoting the angle between electron momentum and magnetic field the kinetic energy reads

$$E_{\text{kin}} = E_{\perp} + E_{\parallel}, \text{ with:} \quad (2.1)$$

$$E_{\perp} = \sin^2 \theta E_{\text{kin}} \quad \text{and} \quad E_{\parallel} = \cos^2 \theta E_{\text{kin}}. \quad (2.2)$$

The magnetic field is assumed to be axisymmetric along the spectrometer axis (z -axis). With an electrostatic filter of such a construction only the longitudinal component E_{\parallel} can be analysed. To reach a high luminosity signal with good energy resolution, the transversal motion needs to be converted into longitudinal motion. Such a transformation can be achieved via the principle of magnetic adiabatic collimation. For the adiabatic motion of an electron along a magnetic field line, the magnetic moment μ is an adiabatic invariant of the motion¹ [BPT80]. It can be calculated from the magnetic field B and from the electron velocity transversal to the magnetic field v_{\perp} : $\mu = \frac{mv_{\perp}^2}{2B}$. In a non-relativistic

¹This can be assumed, if the change in magnetic field during one cyclotron cycle is sufficiently small.

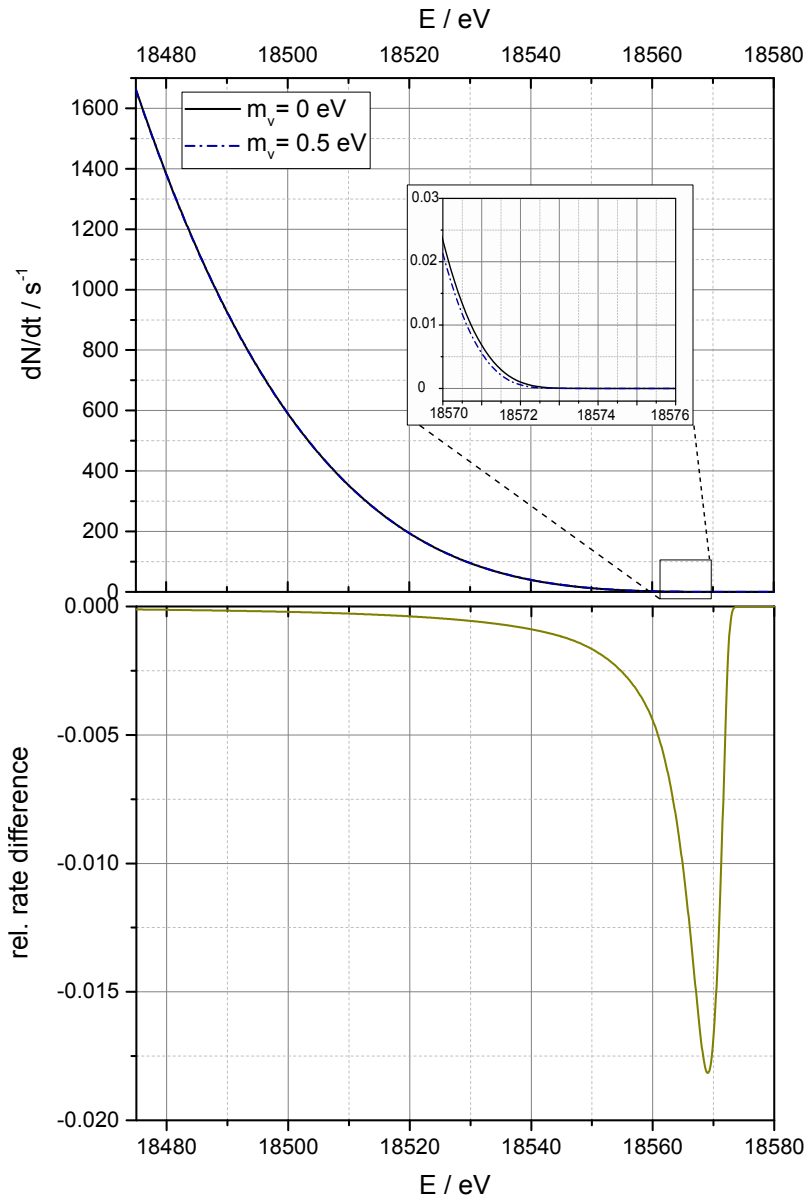


Figure 2.2.: **Integrated β spectra for vanishing and non-zero neutrino mass.** The integrated spectrum for a vanishing neutrino mass is given by the black solid line. The blue dashed line represents a neutrino mass of 0.5 eV. These spectra exhibit a marked difference in the endpoint region, which is thus most sensitive to the neutrino mass measurements (see relative difference plotted in the lower graph). For the calculation of both spectra a constant background rate of 0.01 cps was assumed.

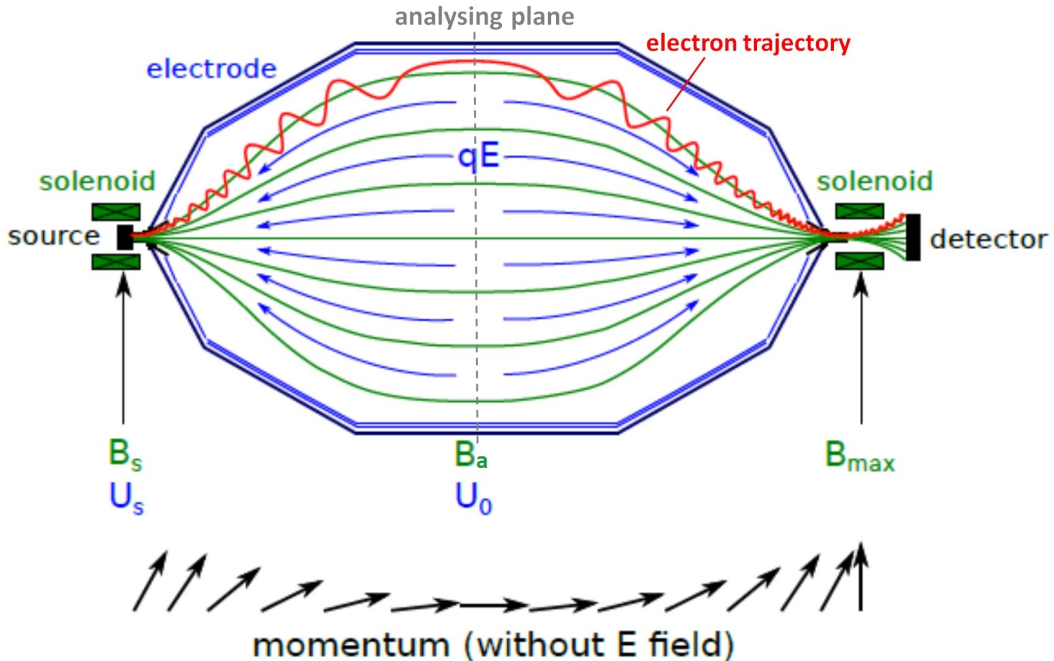


Figure 2.3.: **Principle of a MAC-E filter.** Electrons are produced in the source at a magnetic field B_s and at electric potential U_s (for general considerations assume $U_s = 0$, a non-zero constant source potential can be balanced by a shifted main spectrometer potential U_0 .) The electrons are guided magnetically from the source to the spectrometer and are forced to gyrate (red line) around the magnetic field lines (green lines). Their momentum in transversal direction (and thus their transversal energy) gets transformed into momentum in longitudinal direction while the magnetic field in the spectrometer decreases. When the magnetic field reaches its minimal value, B_a , in the analysing plane, the cyclotron angle θ reaches its minimal value. The electrostatic retarding potential U_0 in the analysing plane reflects electrons with $E_{||} < qU_0$. The momentum of electrons that had enough energy to pass the barrier gets transformed again into transversal momentum by an increasing magnetic field with maximal field strength $B_{\max} > B_s$ next to the detector. Electrons that had been emitted in the source with angles larger than a critical angle get reflected by the magnetic mirror effect. The other electrons reach the detector and get counted. Figure adapted from [Wan13], initially from [AAB⁺05].

approach² kinetic energy and momentum p are related through $E_{\text{kin}} \approx \frac{p^2}{2m}$

$$\mu \approx \frac{E_{\perp}}{B} = \text{const} \quad \rightarrow \quad \frac{E_{\perp 1}}{B_1} = \frac{E_{\perp 2}}{B_2}. \quad (2.3)$$

From the invariance of the magnetic moment it follows that the ratio of transversal energy and magnetic field strength is conserved, too. If the magnetic field strength is reduced by several orders of magnitude, the transversal energy drops accordingly. Due to energy conservation (equation (2.1)), the transversal energy is transformed into energy of longitudinal motion.

To analyse the electron energy with an electrostatic spectrometer, the transversal energy needs to be minimised which can be realised by low magnetic field B_a in the spectrometer³, many orders of magnitude smaller than the magnetic field at the origin of the electron in the source.

The conservation of the magnetic moment leads to another conserved quantity – the magnetic flux Φ_B . The radius r_B of the circular orbit of a particle with electric charge q gyrating around the field lines can be expressed using its velocity component v_{\perp} perpendicular to the magnetic field

$$r_B = \frac{v_{\perp} m}{qB}. \quad (2.4)$$

Using the flux tube cross section A encircled by the cyclotron motion of the electron, the magnetic flux can be calculated

$$\Phi_B = \text{const.} = \int B dA \approx B \pi r_B^2 \stackrel{(2.4)}{\propto} \frac{E_{\perp}}{B}. \quad (2.5)$$

As E_{\perp}/B is an adiabatic invariant of the motion and the same holds for the magnetic flux.

The principle of magnetic collimation works similarly if the magnetic field strength rises again – The energy of longitudinal motion is now transformed into transversal energy according to the increase in magnetic field strength. This gives rise to the so-called *magnetic mirror* effect. If all kinetic energy is transformed into transversal energy, the electron cannot move further along the field line and gets reflected. For a maximal magnetic field B_{max} larger than the magnetic field at the point of electron emission, B_s , the magnetic mirror effect makes it possible to repel electrons with large emission angles θ_s (angle between line of motion and magnetic field line) independent of their total kinetic energy.

The Lorentz force acting on the electron constrains the electron on a gyration path around the magnetic field lines. The path length of the electron through the source⁴ gets extended according to:

$$l_{\text{eff}} = \frac{l_0}{1 + \cos \theta_s}, \quad (2.6)$$

with adapted path length l_{eff} and straight path length l_0 (for $\theta_s = 0$). The larger l_{eff} , the larger the average energy losses mainly due to scattering (cp. section 4.1). As the description of these energy loss processes has relatively large uncertainties, it is beneficial to reduce the path length, or, in other words to limit the starting angle θ_s in the source. For electron emission at the limiting source transmission angle θ_{max} the longitudinal energy gets zero at the position of B_{max} and thus $E_{\perp}(B_{\text{max}}) = E_{\text{kin}}$. For non-relativistic electron motion the transversal energy can be calculated

$$E_{\perp} = \sin^2 \theta E_{\text{kin}}. \quad (2.7)$$

²For electrons with an energy of 18.6 keV the Lorentz factor γ is about 1.04 which allows to treat the motion non-relativistically in first-order approximation.

³The region of minimal magnetic field, B_a in the spectrometer is called the analysing plane.

⁴with a homogeneous magnetic field

Together with equation (2.3) the maximal source transmission angle gets

$$\theta_{\max} = \arcsin \sqrt{\frac{B_s}{B_{\max}}}. \quad (2.8)$$

The energy resolution or, more precisely, filter width ΔE of a MAC-E filter is given by the energy that cannot be analysed, i.e., by the maximal remaining transversal energy in the analysing plane

$$\Delta(E) = E_{\perp}(\theta_{\max}, B_a). \quad (2.9)$$

The remaining energy is maximal for emission under θ_{\max} . Using equation (2.8) and (2.3), the energy resolution for electrons with energy E_{kin} can be calculated

$$\Delta E = \frac{\sin^2 \theta_{\max} E_{\text{kin}}}{B_s} B_a = E_{\text{kin}} \frac{B_a}{B_{\max}}. \quad (2.10)$$

To achieve a possibly high energy resolution the magnetic field in the analysing plane should be as low⁵ as possible while the maximal magnetic field should be preferably high. Still, the higher the maximal magnetic field with respect to the source magnetic field, the more electrons get reflected magnetically. Although this is beneficial in terms of the increased energy loss due to the enhanced path length for larger emission angles, it strongly decreases statistics.

2.1.2. Transmission and response function

The transmission properties of a MAC-E filter for voltage U applied at the spectrometer (retarding energy qU with q denoting the charge of the analysed particle) are summarised by the transmission function $T(E, qU)$. This function only accounts for the properties of the MAC-E filter itself (including the source magnetic field). Source related energy losses (mainly scattering) that change the transmission probability of an electron emitted at initial energy E are included in the so-called *response function* $R(E, qU)$ (its dependence on the axial position z and emission angle θ is neglected here and further discussed in section 4.1).

For zero energy losses in the source, the transmission function defines the integrated rate $\frac{dN}{dt}$ measured at the detector for a given retarding voltage U :

$$\frac{dN}{dt} = \int_{qU}^{E_0} \frac{d^2 N}{dtdE}(E_0, m_{\nu}^2) \cdot T(E, qU) dE, \quad (2.11)$$

with differential β -decay spectrum $\frac{d^2 N}{dtdE}(E_0, m_{\nu}^2)$. To first order the transmission function can be calculated purely analytically. For electrons with surplus energies $E - qU$ less than the energy resolution of the spectrometer the transmission probability depends on the emission angle. Assuming an isotropically emitting source this can be averaged for angles up to θ_{\max}

$$T(E, qU) = \begin{cases} 0 & E - qU < 0 \\ \frac{1 - \sqrt{1 - \frac{E - qU}{E} \frac{B_s}{B_a}}}{1 - \sqrt{1 - \frac{B_s}{B_{\max}}}} & 0 \leq E - qU \leq \Delta E \\ 1 & E - qU > \Delta E. \end{cases} \quad (2.12)$$

This analytical formula describes an optimal MAC-E filter without inhomogeneities. It does not account for realistic spectrometer properties like the actual form of the analysing

⁵The minimal magnitude of the magnetic field strength is limited by the size of the flux tube that increases with decreasing magnetic field strength.

plane⁶ or its retarding voltage distribution. The formula does also not include inhomogeneities in the source magnetic field or energy losses due to synchrotron radiation. These effects had been accurately investigated in [Gro15]. An exemplary analytical transmission function for the MAC-E filter characteristics used in KATRIN is shown in figure 2.4a.

Since electrons lose energy in the source through scattering⁷, their energy distribution gets modified which is not accounted for in equation (2.11). Spectrometer transmission properties as well as source scattering probabilities and energy losses are combined by the response function $R(E, qU)$, which turns equation (2.11) into

$$\frac{dN}{dt} \propto \int_{qU}^{E_0} \frac{d^2N}{dt dE}(E_0, m_\nu^2) \cdot R(E, qU) dE. \quad (2.13)$$

The probability that the electron loses a given amount of energy ϵ when it is scattered inelastically is described by the energy loss function $f(\epsilon)$ which is defined as:

$$f(\epsilon) \propto \frac{1}{\sigma} \frac{d\sigma}{d\epsilon}, \quad (2.14)$$

with total inelastic scattering cross section σ and differential inelastic scattering cross section $\frac{d\sigma}{d\epsilon}$. The response function is obtained by convolving the transmission function with the energy loss function and taking into account multiple scattering with scattering probabilities P_i (P_0 for zero scattering, P_1 for single scattering, ..., see discussion in section 4.1):

$$R(E, qU) = \int_0^E T(E - \epsilon, qU) (P_0\delta(\epsilon) + P_1f(\epsilon) + P_2f \otimes f(\epsilon) + \dots) d\epsilon. \quad (2.15)$$

A response function exemplary for the set-up and standard operation parameters (see table 2.1) of KATRIN is shown in figure 2.4b. The steps and kinks in the curve are due to the contributions from electrons that have scattered multiple times. Their position (difference to the previous kink) is characteristic for the minimal energy loss in inelastic scattering. Further information about the response function of KATRIN and its modelling can be found in [Gro15] and [Zie13].

The response function is essential for a theoretical calculation of the β -decay spectrum and thus indispensable for the neutrino mass analysis.

2.2. Neutrino mass sensitivity

The current most sensitive limit on the effective mass of the electron antineutrino is 2 eV [G⁺14b]. With a discovery potential of 350 meV at 5σ after five years of operation, KATRIN is capable of pushing this limit down by one order of magnitude. In the remaining part of this thesis, talking about the KATRIN neutrino mass measurement, the term ‘effective electron antineutrino mass’, $m_{\bar{\nu}_e}$, will be substituted by ‘neutrino mass’, m_ν . KATRIN’s ability to measure the effect of a non-vanishing neutrino mass is reflected by the sensitivity, S_{m_ν} , with a design value of 200 meV at 90% C.L. for 3 years of data taking (5 calendar years) [AAB⁰⁵]. This leads to a discovery potential of 350 meV at 5σ . The sensitivity is determined by statistical and systematic uncertainties, σ_{sys} and σ_{stat} . They are related to the neutrino mass squared, which is the parameter that can be accessed with KATRIN, see section 1.5.2.4. Aiming for a 90% confidence level the sensitivity becomes:

$$S_{m_\nu} = \sqrt{1.645 \cdot \sqrt{\sigma_{\text{sys}}^2 + \sigma_{\text{stat}}^2}}. \quad (2.16)$$

⁶It is not necessarily a flat plane.

⁷Only about 40% of the β -decay electrons with initial decay energies close to the β -decay end point energy E_0 reach the spectrometer without having scattered.

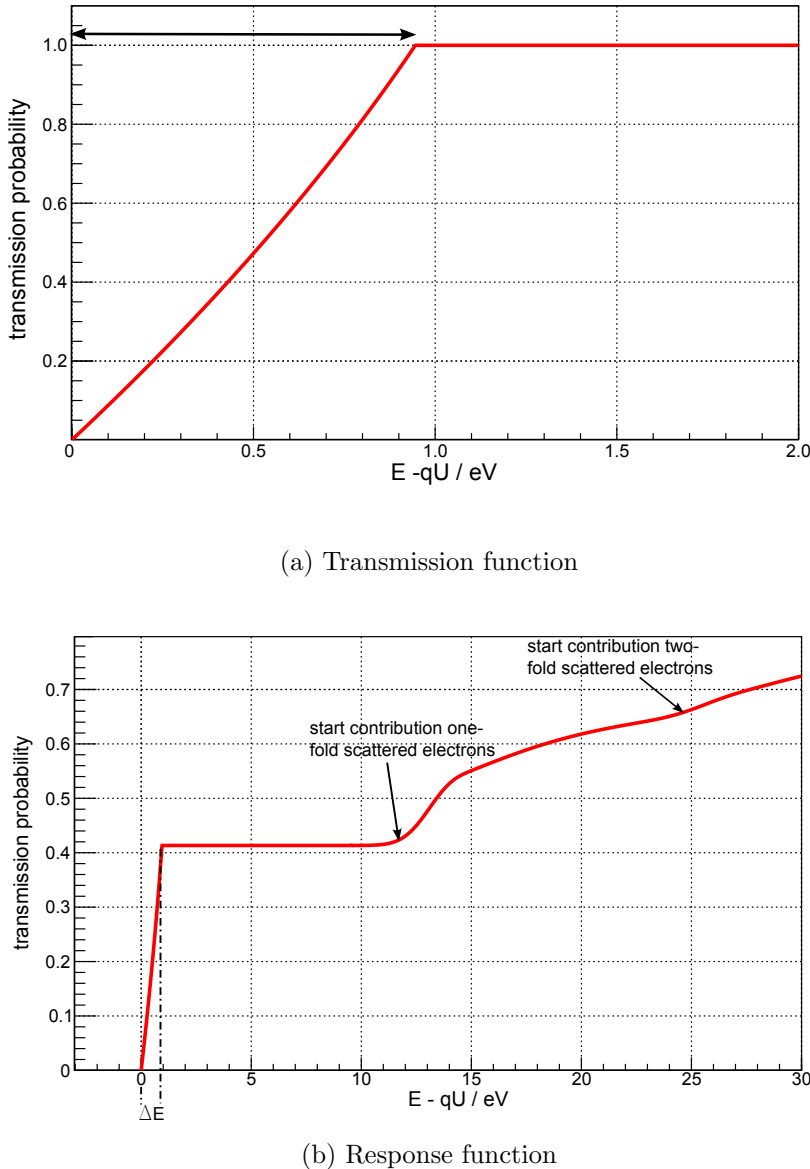


Figure 2.4.: **Transmission and response functions for the KATRIN set-up.** The transmission probabilities that represent in the two graphs the transmission function and the response function are given in terms of the electron surplus energy $E - qU$. The analytical step-like shape of the transmission function is smeared out because of the angular distribution of electron emission in the source and the finite energy resolution of the spectrometer. The width of the transition region (energies with transmission probabilities between 0 and 1) is determined by the energy resolution ΔE . Considering scattering energy losses in the source, the transmission function gets replaced by the response function where the initial transmission function is still visible due to the contribution from unscattered electrons (lowest surplus energies). The kinks in the spectrum are due to the contribution from electrons having scattered multiple times. The minimal energy loss per inelastic scattering is about 12 eV [AAB⁺05]. Thus, the contribution for i -fold ($i=0, 1, 2, \dots$) scattered electrons starts at surplus energies of about i times 12 eV.

Systematic uncertainty

The KATRIN systematic uncertainty budget can be calculated assuming equal contributions from systematic and statistic uncertainties. This means, to reach a sensitivity of 0.2 eV (90% C.L.) the total systematic uncertainty is limited by a value of [AAB⁰⁵]:

$$\sigma_{\text{sys}} \leq 0.017 \text{ eV}^2. \quad (2.17)$$

In [AAB⁰⁵] five major systematics are stated which implies that no individual systematic effect is allowed to cause a neutrino mass squared shift larger than 0.0075 eV². A list of systematic effects can be found in [AAB⁰⁵] and an updated version in [Gro15]. As part of this thesis some of the source related systematic uncertainties are investigated in more detail. In chapter 4 and 5 influences from the gas dynamical source model and its related monitoring parameters as well as from a inhomogeneous source potential distribution will be investigated. Within these analyses the method of ensemble testing, as introduced in section 2.4.3, will be used to calculate the particular systematic uncertainties on the squared neutrino mass, m_ν^2 .

Statistical uncertainty and background contribution

The sensitivity of KATRIN strongly depends on the background level that is reached, since the statistical uncertainty increases with the background rate as discussed in [Kle14]. The KATRIN design sensitivity of 200 meV (90% C.L.) [AAB⁰⁵] was calculated for a background level of 0.01 cps and three effective years of data taking. However, the last commissioning phase of the spectrometer and detector section in 2015 showed a background level that is elevated by a factor of about 50 [Har15, Frä16, Har15, Val16]. In [Har15] detailed information on the contributing background processes can be found. With regard to the actual KATRIN neutrino mass measurement phase, the collaboration is aiming to further reduce the background rate. If this should not be effective, the sensitivity needs to be updated – Using standard KATRIN parameters from [AAB⁰⁵] for the magnetic field strength in the analysing plane ($B_a = 3 \times 10^{-4}$ T), measurement interval ($[E_0 - 30 \text{ eV}, E_0 + 5 \text{ eV}]$) and measurement time distribution, the neutrino mass sensitivity declines to 340 meV (90% C.L.) [Val16]. However, the design values for the magnetic field in the analysing plane, measurement time distribution and scanning analysis interval were optimised for a background rate of 0.01 cps. Thus, updating these parameters for a higher background level offers the potential to improve the neutrino mass sensitivity:

- Modifying the measurement time distribution manly implies to optimise the signal to background ratio for the actual background rate. For a background rate of 0.5 cps this leads to a sensitivity of about 290 meV (90% C.L.) [Kle14].
- Enlarging the analysis interval from 30 eV to 45 eV or 60 eV reduces the statistical uncertainty. It slightly increases the systematic uncertainty related to the description of electron energy loss processes, e.g. inelastic scattering on gas molecules and electronic final states. This needs to be investigated further. Still, the enlarged analysis interval further improves the sensitivity (actual value depends on magnetic field configuration).
- The detected background was shown to be volume dependent [Har15]. This means, decreasing the active volume of the spectrometer by increasing the magnetic field in the analysing plane of the main spectrometer (decrease of flux tube volume) reduces the background level. This option is limited by the energy resolution.

Given the unexpected case the background level cannot be pushed below 0.5 cps [Val16] the KATRIN sensitivity will be:

$$S_{m_\nu} = 240 \text{ meV}, \quad (2.18)$$

if the mentioned mitigation strategies are applied.

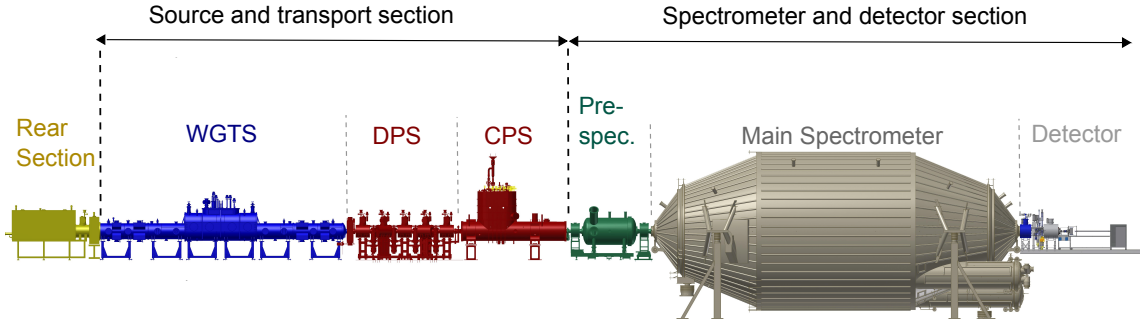


Figure 2.5.: **KATRIN beam line with main components.** The main parts of the rear section are the rear wall and the rear section electron gun. The source and transport section holds the tritium source, WGTS, as well as the differential and cryogenic pumping sections, DPS and CPS. The energy analysis and detection is performed in the spectrometer and detector section which consists of the pre-spectrometer, the main spectrometer and the focal plane detector.

2.3. Main components

The KATRIN beam line can be divided into two general sections:

- Tritium-bearing components – The source and transport section (STS) contains the windowless gaseous tritium source (WGTS), and the differential section and cryogenic pumping section (DPS and CPS) as well as the inner tritium cycle (inner loop). The rear section closes the beam line at the rear side. This part of the KATRIN beam line is in direct contact with tritium and therefore contaminated. Thus, it is housed in the radiation monitored Tritium Laboratory Karlsruhe (TLK).
- Tritium-free components – The spectrometer and detector section (SDS) houses the tandem spectrometer (pre- and main spectrometer) as well as the monitor spectrometer and the detector section. Since it is essentially tritium free, this section is located outside of the monitored TLK area.

An overview drawing of the KATRIN beam line is depicted in figure 2.5. Function and working principle of the main components are summarised in the following subsections.

2.3.1. Source and transport section

The source and transport section needs to produce a large flux of β -decay electrons which is related to a large throughput of gaseous tritium. The decay electrons need to be guided undisturbed to the spectrometer section. This requires a windowless source at large magnetic field. At the same time tritium needs to be prevented from entering into the spectrometer section. The background rate from remaining tritium has to be less than 1×10^{-3} counts/s which is related to a flow rate suppression factor of about 1×10^{14} [AAB⁰⁵]. Consequently, the tritium gas needs to be pumped out efficiently before it can reach the pre-spectrometer. For this purpose, a combination of differential and cryogenic pumps is placed between the source and the spectrometer section.

In the following, the components of the source and transport section will be presented. The WGTS will be discussed in some more detail and its most important characteristics will be introduced.

2.3.1.1. Windowless gaseous tritium source (WGTS)

The WGTS provides the large tritium β -decay activity of about 1.7×10^{11} Bq required for the neutrino mass analysis with KATRIN. It consists of a central 10 m long beam tube

with a diameter of 90 mm made of stainless steel. It is followed by a differential pumping section of 3 m length in front and rear direction each (DPS1-F and DPS1-R).

The central beam tube is cooled to a cryogenic temperature at a set-point between 27 K and 33 K. Due to the large correlation between beam tube temperature and gas density [AAB⁰⁵, Sha03] the beam tube temperature needs to be stabilised and monitored on the per mill level ($\Delta T < 30$ mK) [AAB⁰⁵, Höt12].

To reach the required β -decay activity, a large column density (density integrated over the length of the gas column) of $5 \times 10^{21} \text{ m}^{-2}$ needs to be adjusted in the source. This value is connected to a gas throughput of 1.8 mbar s^{-1} [AAB⁰⁵, Sha03].

Tritium is fed into the WGTS from a temperature stabilised transfer line connected to the inner loop system (see section 2.3.1.4). The stability of the injection WGTS pressure ($\Delta p_{\text{in}}/p_{\text{in}} < 2 \times 10^{-3}$) is achieved using a temperature stabilised, pressure controlled buffer vessel in the gas processing cycle [PSB15]. The actual injection takes place in the middle of the beam tube. It is realised through 415 small holes arranged in 5 rings encircling the beam tube. This configuration minimises the disturbance of gas flow in the injection region [Sha04a, Shr10].

The tritium purity, ϵ_T , and the chemical composition of the tritiated gas⁸ injected into the WGTS are monitored continuously by a Laser Raman System (LARA) which is briefly described in section 2.3.4. To reach a preferably high activity at given column density, the tritium purity should be as high as possible. During standard tritium operation ϵ_T will be larger than 95% [AAB⁰⁵].

The beam tube is surrounded by seven superconducting magnets that produce a strong and homogeneous source magnetic field⁹ of 3.6 T (5.6 T in the beam tube of the DPS1-F) which guarantees equal starting conditions for β -decay electrons originating from different WGTS positions. The magnetic field guides the electrons adiabatically on a cyclotron path to the transport section. For a magnetic flux of $\Phi = 191 \text{ T cm}^2$, which is realised in the KATRIN beam line, the flux tube cross sectional area inside the central WGTS beam tube is, according to equation (2.5), 53 cm^2 .

Strong demands are put on the stability of the WGTS operation parameters (temperature, magnetic field, column density, tritium purity, electrostatic potential) to avoid unrecognised changes and thus modifications of the β -spectrum – usually a stability on the per-mill level is required for these parameters [AAB⁰⁵, BBB¹²]. Unrecognised drifts belong to the source related systematic uncertainties of the neutrino mass analysis. A WGTS overview is depicted in figure 2.6. The construction of the complex WGTS cryostat took several years. In the end it arrived at its final location in the TLK in September 2015. Photographs of the cryostat and its arrival at the TLK are shown in figure 2.7. Since then the mechanical works have been finished and the cryogenic infrastructure has been installed. The testing of 800 sensors and valves has been finished. Currently, the WGTS is cooled down to operation temperature for the first time.

⁸The presence of small admixtures from the other hydrogen isotopologues than T_2 namely DT, HT, DH, D_2 , H_2 is unavoidable.

⁹This only holds for the central 10 m beam tube where the density is highest and where about 98% of the β -decay electrons are produced. In the pump ports the magnetic field drops significantly.

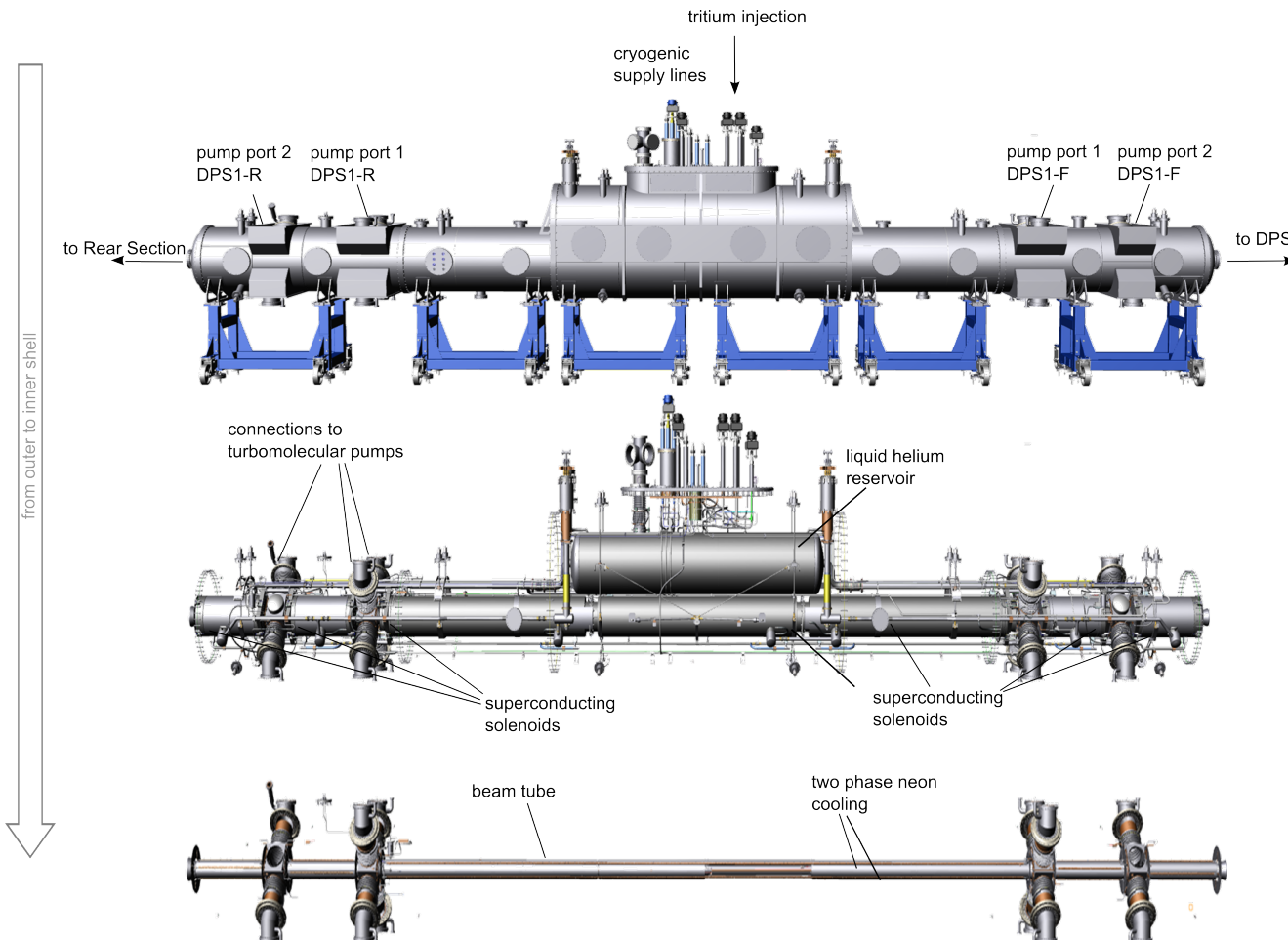


Figure 2.6.: **WGTS cryostat with outermost, intermediate and innermost layer.** The WGTS beam tube consist of a central 10 m long tube between the first pump ports, a tube connecting first and second pump port in the DPS1 and a last part connecting the adjacent components in front and rear direction each. It forms the innermost layer of the WGTS cryostat. Two cooling tubes filled with two-phase neon ($T \approx 30$ K) are lining the beam tube that conducts the tritium gas. Separated by an inner radiation shield, cooled by gaseous helium to about 30 K, the beam tube is surrounded by seven superconducting solenoid modules (cooled by liquid helium to $T \approx 4.5$ K). They provide a homogeneous magnetic field of 3.6 T to 5.6 T inside the beam tubes. An outer radiation shield and an insulation vacuum protect the inner parts from thermal radiation from the room temperature outside. Tritium is injected in the middle of the WGTS beam tube. Four-fold and two-fold pump ports in front and rear direction, equipped with four and two turbomolecular pumps respectively, reduce the tritium flow to the adjacent DPS and rear section.



Figure 2.7.: Arrival of the WGTS cryostat at the tritium laboratory at KIT.

WGTS temperature

The central 10 m beam tube of the WGTS will be held at a cryogenic temperature of 30 K ¹⁰ (technically temperatures between 27 K and 37.5 K are possible). This operation temperature was chosen for the following reasons [AAB⁺⁰⁵]:

1. Due to the cryogenic temperature the thermal movement of tritium molecules is low. As a consequence, the broadening of the electron spectrum caused by the thermal Doppler effect is reduced.
2. The required large column density inside the WGTS can be reached with a reasonable amount of tritium throughput, since the particle current density decreases with increasing temperature (for given throughput) [WAWJ04].
3. The kinetic energy of low energy electrons that form together with the positive ions the plasma inside the source scales with the gas temperature. The higher this energy, the higher the electrostatic potential inside the source due to the production of space charges (see sections 5.1 and 5.3.2.2 for further reading). To achieve a homogeneous potential in the source, the scale of the absolute value of this potential should be close to zero which means the temperature should be preferably low.
4. In [AAB⁺⁰⁵] it was stated that the clustering of tritium molecules, which should be avoided in terms of the description of molecular final state spectra and gas flow, may increase at temperatures below 30 K which gives an lower limit for the operation temperature¹¹.

Even more important than the actual value of the beam tube operation temperature is its temperature stability and homogeneity as discussed above. Therefore, a special cooling system was designed for the WGTS cryostat. It consists of:

- Two tubes of 16 mm diameter filled with two phase (gaseous and liquid) neon are brazed to the beam tube. The particular temperature of coolant and beam tube is

¹⁰This temperature will be used for the *standard* tritium measurements. The WGTS will be operated in a second mode with $^{83\text{m}}\text{Kr}$ gas inside for investigation of the potential distribution inside the WGTS. This requires an increased temperature around 100 K and thus an exchange of the coolant – In the krypton mode argon will be used to cool the beam tube.

¹¹Currently the actual temperature dependence of clustering of tritium molecules is in question. Further investigations are ongoing

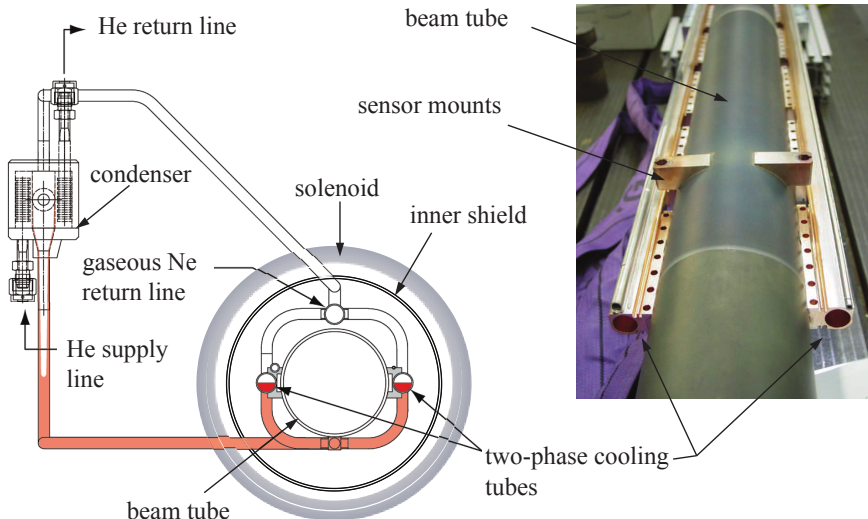


Figure 2.8.: **WGTS beam tube cooling system.** The WGTS beam tube is cooled by two tubes filled with two-phase neon. The temperature in the cooling tube is determined by the saturation pressure of the gaseous neon phase. Gaseous neon gets liquefied again in a condenser, cooled by liquid helium, at the end of the beam tube. Figure adapted from [Höt12].

determined by the saturation pressure of the neon gas. The pressure can be regulated between 1 bar and 10 bar which corresponds to a beam tube temperature stabilised between 27 K and 37.5 K.

- At the end of the 10 m beam tube the gaseous neon flows to a condenser (cooled by liquid helium) and is liquefied again.
- An inner radiation shield insulates the beam tube from the adjacent solenoids as these superconducting magnets are cooled to temperatures of 4.5 K with liquid helium.
- The outer radiation shield and an insulating vacuum below the cryostat vessel protect the innermost part from being heated from the room temperature outside.

An overview of the cooling principle for the WGTS beam tube is depicted in figure 2.8. Detailed information about the cooling concept of the WGTS can be found in [GBB⁺08, Gro09, Höt12, Bod11].

The beam tube temperature stability requirement of 0.1% can be translated to a temperature measurement precision requirement of better than 30 mK¹². The temperature along the beam tube is measured by 24 metallic PT500 sensors. Since the temperature measurement with these sensors is influenced by the strong magnetic fields of the superconducting magnets, they are calibrated in-situ by 24 vapour pressure sensors [GBSS11, Bod11]. The effective working of the WGTS cooling system and the temperature sensor set-up was shown in a test measurement phase from 2010 to 2011 [GBH⁺13, Höt12].

The cooling concept of the DPS1-F and DPS1-R and their pump ports is subject to an order of magnitude less stringent requirements in terms of temperature stability and homogeneity [GBB⁺08]. The working principle of the pump port cooling is overviewed in section 3.2. The temperature distribution along the pump ports of the WGTS and the influence of the large amount of thermal radiation coming from the rotor blades of the turbomolecular pumps [GKRW12] is unknown so far. Still, this distribution is required as essential input for the simulation of gas flow in the WGTS pump ports (see section 4.2.6) that are need to be considered in the calculations to determine their contribution to the

¹²The requirement on the trueness is less stringent ($\Delta T_{\text{abs}} < 0.5 \text{ K}$) [BBB⁺12].

total column density. Therefore, the temperature distributions at the walls of the WGTS pumping sections DPS1-F and DPS1-R were investigated as a part of this thesis. More details and results can be found in the subsequent chapter 3.

WGTS density

The distribution of the gas density in the WGTS cannot be measured directly. Information on its form and amplitude as well as density and flow reduction factors of the WGTS are based on an accurate gas model of the source which was developed in [Höt12]. It will be introduced, refined and expanded in chapter 4 of this thesis.

The column density ρd is a key parameter for the operation of the WGTS and for the modelling of KATRIN spectra. The design value of the column density of $5 \times 10^{21} \text{ m}^{-2}$ is a compromise between high signal rate, low electron energy loss due to scattering, and a reasonably low quantity of tritium. This aspect is discussed in more detail in section 4.1. To get the required column density at an operation temperature of about 30 K, the tritium throughput needs to be about $1.8 \text{ mbar l s}^{-1}$ which leads to a WGTS injection pressure of about $3.4 \times 10^{-3} \text{ mbar}$ (see section 4.2.3 for related calculations of the density distribution). Since column density and source activity (signal amplitude) are strongly correlated, the column density needs to be stable at the per mill level [AAB⁰⁵, Höt12]. However, if the change in column density exceeds this level, but can be modelled with sufficient accuracy, the stability requirement can be relaxed. Thus, it is important to test the ability of the WGTS gas model to simulate column density changes. This is investigated in section 4.5.2.

Since the column density determines the probability for electrons to scatter on gas molecules, it has direct impact on the form of the detected electron spectrum. Thus, the absolute value of the column density realised in the WGTS needs to be known with an accuracy of 0.2%¹³.

The role of the spatial distribution of density inside the WGTS as well as the contributions from the adjacent DPS1-F and DPS1-R sections are still unresolved. This question will be examined in sections 4.2.6 and 4.7.

Electric potential in the WGTS

The electric potential in the WGTS determines the starting potential energy of the electrons produced in the β -decay of tritium in the source. Thus, it has a direct influence on the electron spectrum measured with KATRIN. Inhomogeneities in the potential distribution in the source smear out the β -decay spectrum since electrons originating from different WGTS positions have different starting (potential) energies. An unrecognised drifting of the electric source potential during one measurement run has a similar effect. Thus, high demands are placed on the stability and homogeneity of the WGTS potential. In [AAB⁰⁵] spatial inhomogeneities were estimated to be below 10 meV. This statement is based on a simplified model of the WGTS plasma [NM04] and some general considerations of space charge production in the source [WGT04]. However, the charged particle transport processes, the space charge production, and the electromagnetic fields in the WGTS are coupled and far too complicated to be reliably described by the mentioned model. Furthermore, the influence of a spatial plasma distribution on the electron spectrum needs to be investigated carefully. Previous assumptions of a Gaussian smearing of the electron spectrum are not realistic for the actual WGTS plasma distribution. The whole topic of the WGTS plasma is covered by chapter 5 including the construction of a realistic WGTS plasma model based on simulations, possible measurements to determine particular parameters of the plasma potential distribution, and an investigation of the

¹³To be more precise, the product of column density and total inelastic scattering cross section needs to be known to that accuracy level (see section 4.1).

influence of the electric potential distribution on the neutrino mass analysis.

The three important source characteristics temperature, gas density, and electric potential as outlined above play a key role within the thesis at hand. Investigating their spatial distributions in the WGTS significantly improves the understanding of physical processes determining the shape of the electron spectrum. This allows for a better estimation of source related uncertainties and is the main objective of this thesis.

2.3.1.2. Differential pumping section (DPS)

The DPS is the first component of the pumping section which needs to achieve a total gas flow reduction by a factor of 10^{11} . Thus, together with the WGTS pump ports, a total gas flow reduction of about 10^{14} can be achieved. The DPS alone is designed to reach a flow reduction factor of about 10^5 [AAB⁰⁵]. This value has been confirmed by vacuum simulations [Jan15] and the system is, up to the moment of writing this thesis, being prepared for an experimental verification. The DPS consists of five beam tube elements with a diameter of about 100 mm and with four turbomolecular pumps installed at pump ports that are placed in between the beam tube elements¹⁴. An additional pump port (pump port 0) equipped with two turbomolecular pumps forms the connection to the WGTS.

The DPS has an overall length of 6.5 m. The beam tube elements are arranged in a chicane with an angular bent of 20° in between. This prevents a direct line of sight for the neutral gas particles. Thus they hit the walls and can get pumped away by the turbomolecular pumps. For tritium gas the installed pumps have a pumping speed of about 2400 l s^{-1} [Jan15]. The beam tube is situated in the warm bore of the DPS magnets. These five superconducting magnets produce a strong magnetic field of 5.5 T inside the DPS beam tube elements. It guides the electrons through the chicane without collisions.

Besides the flow reduction and the transport of electrons, the DPS needs to eliminate positive tritium ions. Ions are, like the electrons, guided by the magnetic flux tube and cannot get pumped out like the neutral particles. To prevent tritium ions from entering the spectrometer section, ring electrodes operating at +100 V are installed. These electrode reflect the positive ions. Still, the thermalised ions (ions have gas temperature and thus low energy) cannot get through the WGTS since their motion is blocked by the large opposite streaming gas flow [Glü05, Glü10]. To transport the ions out of the beam tube, three dipole pairs are installed in the DPS beam tube sections. One half cone of each dipole electrode will be operated at negative potential (about -100 V [Win11]). The electric field overlying the magnetic field causes an $E \times B$ drift and shifts the ions further outwards each time they pass the dipole. After several passages, the ions reach the walls, get neutralised and can be pumped out. For a qualitative and quantitative analysis of the ion species present in the DPS, a FT-ICR (Fourier Transform - Ion Cyclotron Resonance)¹⁵ unit is placed at the beginning of the DPS. Further information about ion species and fluxes entering the DPS can be found in chapter 5. Details about WGTS ion production mechanisms are given in [Glü05, Glü10]. The working principle of the ion retention in KATRIN is further discussed in [Win11, Rei09, Kle16].

In the following, the technical status of the DPS is summarised. All DPS components have arrived at KIT. Beam tubes and magnets have been leak tested. The magnets have been cooled down and ramped up to nominal magnetic fields (in stand-alone mode and combined) already in 2015. The DPS at its final position in TLK is depicted in figure 2.9b.

¹⁴Actually the horizontal position of the pumps is below the beam tubes, see figure 2.9a.

¹⁵It was characterised in [UD11].

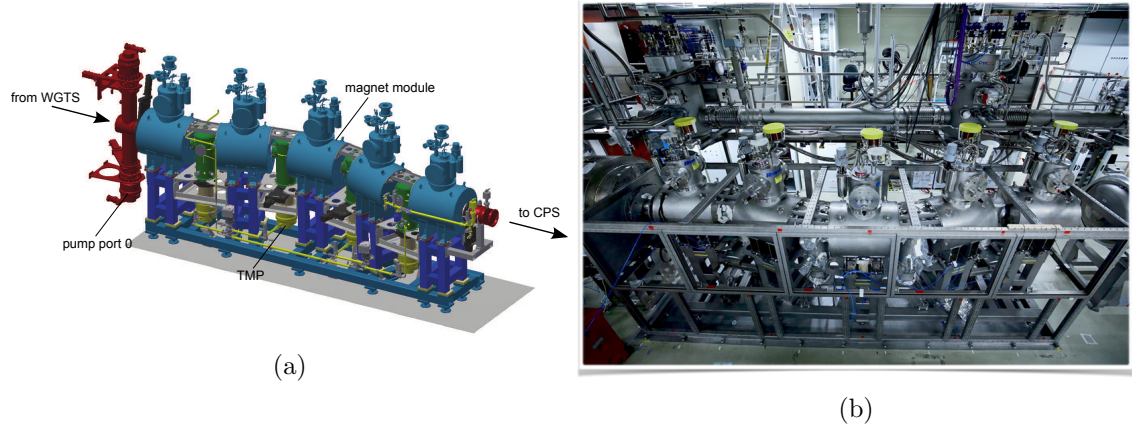


Figure 2.9.: Model of DPS assembly and DPS installed at TLK.

2.3.1.3. Cryogenic pumping section (CPS)

The CPS forms the last tritium retention unit before the beam line reaches the pre-spectrometer which needs to be essentially tritium free. Thus, the CPS needs to achieve a gas flow reduction factor of more than 10^7 [AAB⁰⁵]. The CPS beam tube has a length of about 7 m and a diameter of about 75 mm. The particular beam tube elements are, like in the DPS, arranged in a chicane with an angle of 15° in between the elements. In the centre of the CPS, between the two CPS pump ports (see figure 2.10a) cold argon snow will be frozen on the beam tube surface at a temperature of 3 K. Any neutral gas that hits the argon surface will be adsorbed at the cold layer due to cryosorption with a sticking probability of about 0.7 [Jan15]. The principle of the tritium flow reduction by cryosorption of argon atoms was shown to work in the test experiment TRAP [EBB⁰⁸] and yielded a flow reduction factor of 3×10^7 .

Due to background contribution from adsorbed tritium molecules to the measured β -decay spectrum, the argon layer needs to be regenerated before it has accumulated a tritium activity of 1 Ci which will be reached after about two months [AAB⁰⁵].

Aside from the gas flow retention, the CPS holds calibration and monitoring instruments like the quench-Condensed Krypton Source (CKrS) and the Forward Beam Monitor (FBM). The CKrS will be used to check for retardation potential drifts of the spectrometers using conversion electrons from ^{83m}Kr . The FBM, introduced in section 2.3.4, will be used to monitor the tritium flux and thus the tritium column density. Furthermore, it allows for imaging of the flux tube. With the Faraday cup installed at the detector board, ion fluxes can be measured and the ion suppression system can be tested.

The CPS has arrived at KIT in summer 2015. Meanwhile it is installed in the TLK, a photograph of the CPS at its final position (without installed cryo-infrastructure) in the TLK is depicted in figure 2.10b. Beam tube and magnets have been successively cooled down to working temperature. The magnets have been tested ramping the magnetic field up to 90% of its operational value. First operation with prepared argon frost layer will be in 2017.

2.3.1.4. Inner loop

To guarantee a stabilised tritium gas injection with maximal inlet pressure variations of 10^{-3} , a special gas processing circuit was designed – the inner loop system. It collects the gas that is pumped out in the pump ports of the source and passes the gas through a palladium membrane filter. This separates the non-hydrogen impurities from the hydrogen isotopologues. To achieve tritium purities above 95% continuously, about 1% of the circulated gas is diverted into a tritium recovery and purification system. It is replaced

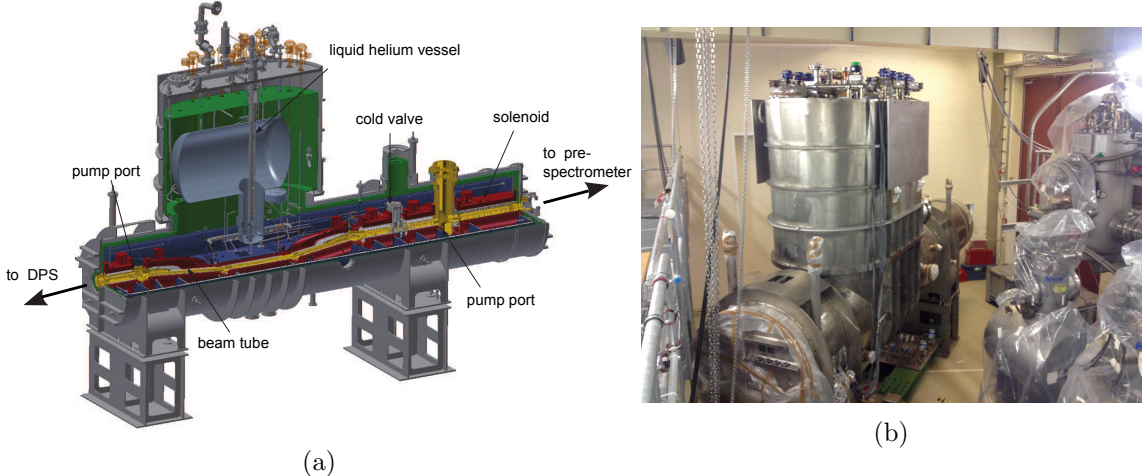


Figure 2.10.: **Model and photograph of CPS assembly installed at TLK.** The argon frost layer will be prepared between the two CPS pump ports. The cold gate valve allow to decouple the CPS from the spectrometer section. The beam tube elements are bend through 15° to prevent direct line of sight. The beam tube is surrounded by superconducting solenoids producing a central magnetic field of 5.7 T. CAD drawing adapted from [Jan15].

by almost pure tritium gas ($\epsilon_T > 98\%$) [AAB⁺05]. The per mill stability of gas injection is realised through a temperature and pressure controlled buffer vessel. The pressure in the buffer vessel will be held on a stable value by a software controlled regulating valve. The temperature in the pressure controlled buffer vessel is about 318 K and stabilised to 0.5 K [PSB15]. This allows to achieve a buffer vessel pressure stability of 0.1 % [Stu10].

The pressure controlled buffer vessel is connected to a temperature stabilised transfer line width a length of 10 m and a large diameter of (25 mm) causing a large conductivity. The gas injection in the WGTS is realised by a capillary with a diameter of 2.1 mm that is over its whole length of 5 m thermally coupled to the WGTS beam tube. This means, it is stabilised at beam tube temperature [PSB15].

A laser Raman (LARA) system is implemented to continuously (within about 100 s) monitor the tritium purity ϵ_T^{16} (see section 2.3.4 for an overview of the LARA system) in-line before the gas is injected in the pressure controlled buffer vessel. All parts of the inner-loop system are implemented in a glove box which acts as a second containment. A more detailed description about the Loop systems in KATRIN can be found in [Stu10]. A simplified flow scheme of the gas processing in the inner loop system is depicted in figure 2.11.

In the commissioning measurements described in [PSB15] the injection pressure stability of the loop system (without WGTS and DPS connection and without LARA system) was tested for various pressures in the injection vessel. The stability requirement of 0.1% was matched for all pressure set points. It even succeeded the requirements by one order of magnitude.

2.3.2. Rear section

The rear section closes the KATRIN beam line at the rear side. It includes a group of calibration and monitoring systems: two X-ray detectors that monitor the source activity using beta-induced X-ray spectroscopy (BIXS, see section 2.3.4) and an angular selective electron gun (e-gun). Moreover it contains a gold-plated surface with an almost uniform

¹⁶The precision of ϵ_T needs to be better than 0.1% since it is directly coupled to the source activity and to the amplitude of the β -decay rate.

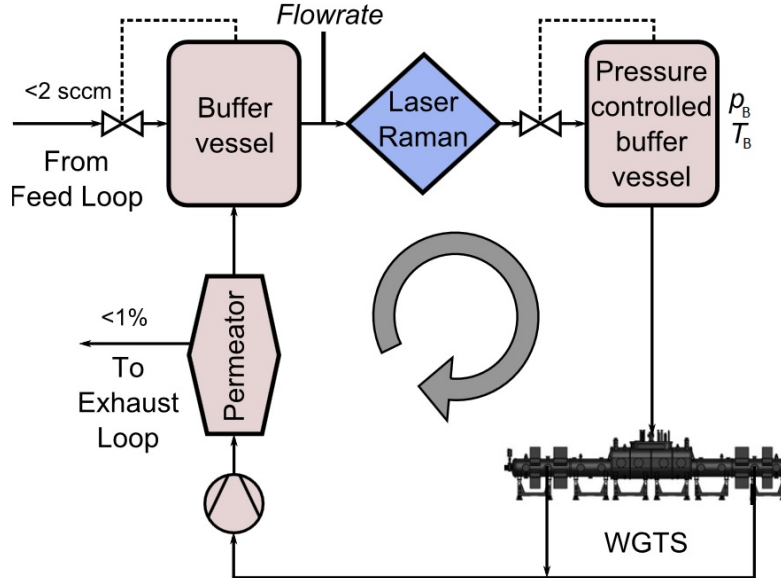


Figure 2.11.: **Flow scheme of inner loop system.** The tritium gas is processed in a closed cycle. After it is pumped out at the WGTS pump ports, it is passed through a permeator filtering out non-hydrogen impurities. A small gas fraction is diverted and replaced by fresh gas with high tritium purity ($\epsilon_T > 98\%$). The isotope composition is analysed in-line by a laser Raman system before the gas is fed into a pressure controlled buffer vessel (with pressure p_B and temperature T_B) that allows for a per mill stability of the WGTS injection pressure. Figure adapted from [BBB¹²].

work function – the rear wall. Scheme and experimental set-up of the rear section are depicted in figure 2.12.

Rear wall

The WGTS contains a low density plasma of secondary electrons and tritium ions (see chapter 5 for a detailed description of the WGTS plasma). The charged plasma particles are confined in the magnetic flux tube of the source and transport section. The rear wall is the single surface in the KATRIN set-up to be hit by this flux tube. Following the arguments given in [AAB⁰⁵], placing a conducting surface into the flux tube in the rear section, the surface potential of this element should determine the electrostatic potential inside the flux tube through the whole length of the source. Aiming for a homogeneous potential with differences not larger than 10 mV sets analogue requirements on the homogeneity and stability of the surface work function. In [Sch16] several candidates of materials and layers have been investigated.

The actual influence of the rear wall work function and its surface potential inhomogeneities on the plasma inside the WGTS is investigated as a main part of this thesis.

The rear wall surface is struck by the β -decay electrons that are transported by the magnetic flux tube. This fact provides a second main function of the rear wall – β -decay electrons that impinge on the rear wall produce X-rays that can be measured by special detectors and be used for source activity monitoring.

If the rear wall surface is irradiated by UV-light, electrons can be emitted through the photo-electric effect. These electrons can be used to reduce the space charge accumulated in the WGTS and thus decrease the absolute value of the potential inside the plasma (see section 5.3.5).

In pre-measurements with inactive gas, these electrons can be used to ionise some of the

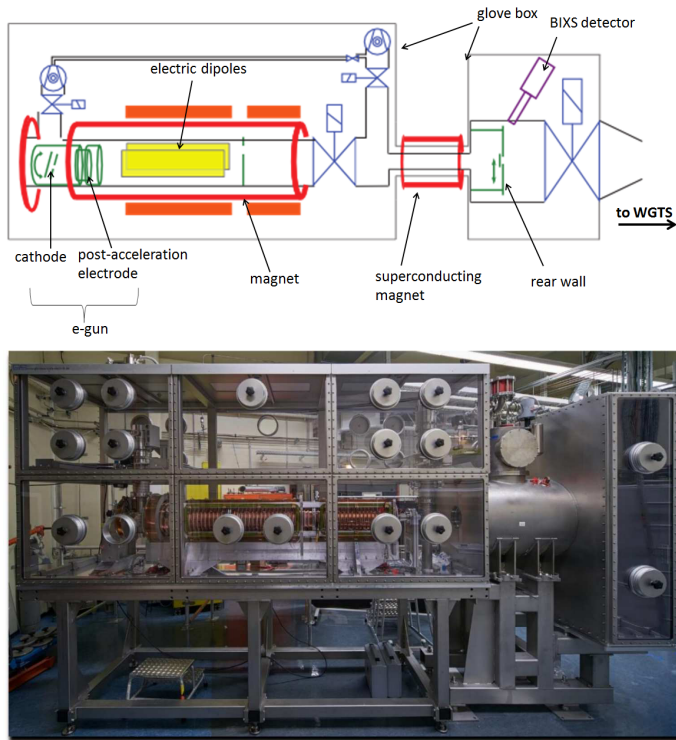


Figure 2.12.: **Rear section scheme and experimental set-up.** The e-gun emits electrons from a cathode irradiated by UV light. The beam angle can be adjusted, tilting the cathode. The produced electron beam gets accelerated to adjustable energies in the range of the β -decay spectrum by post acceleration electrodes. The connected electromagnetic transport system guides them until they reach a small hole in the rear wall. The beam can be shifted using electric dipoles in the transport system. The rear wall hole is closed in operation mode without e-gun. Two X-ray detectors, which monitor the source activity, view the rear wall. Scheme adapted from [Bab14]. The photograph below shows the experimental rear section set-up in the TLK.

gas molecules. This allows to test the ion measurement and ion blocking mechanisms. On the other hand, for an empty WGTS, the electrons emitted from the rear wall can be used to investigate the transmission along the entire KATRIN beam line over the whole cross section of the flux tube.

Rear section e-gun

The rear section electron gun (e-gun) is a source that produces electrons with variable energies through the photo-electric effect. Since its parameters are well known and adjustable, it can be used for precise calibration measurements of the source and transport section as well as of the spectrometer section. The e-gun itself is responsible for the production and acceleration of electrons while the connected electromagnetic transport system guides and shapes the electron beam. The angle of the beam with respect to the magnetic field can be changed by tilting the electron emitting cathode. The beam can also be shifted using a set of dipole electrodes.

The energy spread σ_E depends on the electron rate that needs to be produced by the e-gun [Bab14]. According to [rswg12], it should be smaller than 0.2 eV and the angular beam spread σ_θ should be smaller than 4° for medium intensity and high precision mode.

The electron-gun offers the unique possibility to determine the product of gas column density and scattering cross section which is a key parameter for the modelling of source β -decay spectra (see section 4.1). For this measurement, the e-gun beam is injected into the gas filled and into the emptied WGTS. Comparing the corresponding rates at the detector for both sets, the scattering probability and thus the product of column density and scattering cross section can be determined. In section 4.5.1 the measurement procedure is explained in more detail. A similar procedure will be used to determine the energy loss function.

Detailed information about the rear section design and its requirements can be found in [rswg12] and [Bab14] as well as in [Sch16].

2.3.3. Spectrometer and detector section

In the spectrometer and detector section the energy of the β -decay electrons that come from the source and transport section is analysed. Therefore, a tandem spectrometer set-up consisting of a pre-analysing spectrometer and a high precision main spectrometer is used. A third spectrometer is implemented in a second beam line in order to analyse the small fluctuations of the main spectrometer high voltage precisely. All three components are based on the MAC-E filter principle described in section 2.1.1. At the end of the beam line a segmented detector with high counting efficiency and good energy resolution measures the rate of electrons that have passed the electric potential barriers of the tandem spectrometer.

2.3.3.1. Pre-spectrometer

The pre-spectrometer is built to act as a pre-filtering unit that reduces the β -decay electron flux into the main spectrometer – A low electron rate decreases the probability of rest-gas ionisation and production of secondary electrons. It has a length of about 3.4 m and a diameter of about 1.7 m. Its working principle is based on the MAC-E filter mechanism. A large magnetic field of 4.5 T is created by superconducting solenoids at both ends of the spectrometer. The minimal magnetic field in the centre of the spectrometer vessel is about 15.6 mT. Using equation (2.10) this magnetic field configuration results in an energy resolution ΔE_{pre} of about 70 eV. It is planned to be operated 300 eV below the endpoint of tritium decay, (at a retarding potential U_{pre} of about 18.3 kV). At this voltage set only a fraction of about 1×10^{-7} of all β -decay electrons reaching the

pre-spectrometer would be able to pass [Pra11]. Still, electrons in the analysis interval $E \gtrsim E_0 - 30 \text{ eV}$ have enough energy to overcome the barrier, independent from their emission angle ($E_0 - 30 \text{ eV} > qU_{\text{pre}} + \Delta E_{\text{pre}}$) and the pre-spectrometer can be used without a loss of signal.

The pre-spectrometer is placed in between the main spectrometer and the CPS. Thus, the tritium flow that enters the spectrometer is already reduced by 14 orders of magnitude compared to flow injected in the WGTS. Like the main spectrometer, it needs to be operated at ultra-high vacuum conditions with a remaining pressure of the order of $1 \times 10^{-11} \text{ mbar}$ [AAB⁰⁵]. To reach the vacuum conditions and further reduce the tritium flow in main spectrometer direction, the pre-spectrometer is equipped with non-evaporable-getter (NEG) strips and two TMPs. This reduces the tritium flow to the main spectrometer by two-orders of magnitude [ABB¹⁶].

The pre-spectrometer was used as a test set-up to investigate the main spectrometer vacuum conditions and to study electron transport characteristics and background processes [Mer12, Wan13, Frä10].

2.3.3.2. Main spectrometer

The main spectrometer is a large vessel with ultra high vacuum conditions inside allowing to analyse the electrons stemming from tritium β -decay precisely. For this purpose, a good energy resolution is required which is given by the maximal magnetic field in the beam line and the minimal magnetic field in the analysing plane, since it works as a MAC-E filter. With $B_{\text{max}} = 6 \text{ T}$, which is reached at the pinch magnet at the detector side of the spectrometer, and $B_a = 0.3 \text{ mT}$ in the analysing plane, the energy resolution in the relevant electron energy region around 18.6 keV gets

$$\Delta E = 0.93 \text{ eV} \quad (2.19)$$

(using equation (2.10)) [AAB⁰⁵]. At a source magnetic field of 3.6 T the maximal angle θ_{max} at which electrons produced in the source are not reflected magnetically is, according to equation (2.8),

$$\theta_{\text{max}} \approx 51^\circ. \quad (2.20)$$

To compensate the earth magnetic field and fine shape the magnetic field in the spectrometer, a large volume air coil system surrounds the main spectrometer vessel [GDL¹³]. The whole spectrometer vessel is held on ultra high voltage to apply the retarding potential in the analysing plane. A fine-shaping of the electric potential with an axial symmetric electric field is achieved by a system of double layered wire modules positioned at the inner surface of the spectrometer [Val10]. Since they are held on voltages about 100 V below the vessel voltage, electrons emitted from the vessel wall (produced for example by muons hitting the wall or in radioactive decays) get rejected and cannot reach the flux tube volume.

To be able to transport the magnetic flux tube through the region of lowest magnetic field, the main spectrometer needs to have a large cross section (see equation 2.5) which is reflected by its large central diameter of 10 m. It has a length of about 23 m and a total volume of 1240 m^3 .

Notwithstanding the large tank volume, the background rate needs to be as low as about 0.01 cps in the signal region close to the tritium endpoint energy in order to reach the aimed sensitivity of 0.2 eV [AAB⁰⁵]. This sets high requirements on the vacuum conditions inside the spectrometer tank, since electron collisions with residual gas particles need to be limited. Due to electron energy losses, these collisions modify the detected electron spectrum. Moreover, they create charged particles contributing to the background rate. Thus, the residual gas pressure needs to be lower than about 10^{-11} mbar . The rate of

outgassing of this large inner stainless steel surface area¹⁷ of 690 m^2 is the main challenge in reaching these ultra-high vacuum conditions [ABB¹⁶]. A large pumping speed is thus provided by six TMPs and 3 km of NEG strips [LBDW07, Wol09].

The KATRIN main spectrometer was operated combined with the detector system in different commissioning phases from 2013-2015 to test its transmission properties and vacuum conditions, to analyse background processes and to investigate background reduction methods [Lei14, G14a, Gro15, Har15, ABB¹⁶].

2.3.3.3. Monitor spectrometer

A third spectrometer is installed in a second beam line, which runs parallel to the main KATRIN beam line. This third device was previously used in the Mainz neutrino mass experiment. In the KATRIN set-up it is implemented to monitor the main spectrometer retarding voltage stability on-line. Therefore, both spectrometers are fed by the same high voltage. Observing position and width of the $^{83\text{m}}\text{Kr}$ (K-32) line at 17.8 keV stemming from a ^{83}Rb ion implanted substrate [EBB¹⁴], which is positioned at the spectrometer entrance, main spectrometer voltage drifts on the ppm-level can be detected. The monitor spectrometer was installed and commissioned at KIT between 2010 and 2012. See [Erh16] for detailed information on the monitor spectrometer.

2.3.3.4. Focal plane detector

After the electrons have passed the electrostatic barriers of the spectrometers, they need to be counted. Therefore a PIN (positive intrinsic negative) diode detector is installed downstream the main spectrometer at the front end of the KATRIN beam line. The detector wafer has a diameter of 90 mm and a thickness of 500 μm . It is divided into 12 rings with 12 segments each and four central segments (148 pixel) which are equal in surface area. This allows for spatial resolution of the electron flux and thus to investigate spacial inhomogeneities in the source or spectrometer section.

The pinch magnet, creating the maximal magnetic field, B_{max} , of 6 T, is part of the detector section. The detector waver is placed in the bore of a second superconducting magnet with a magnetic field of 3.6 T.

To achieve a low background to noise level despite low signal rates of about 10^{-2} signal electrons /s, the detector needs to be almost free from intrinsic background ($R_{\text{BG,detector}} \leq 1\text{ mHz}$)[AAB⁰⁵].

At the same time it needs to have a large detection efficiency ($>90\%$) for electrons in the signal region.

The detector is surrounded by a passive shielding made of lead and copper. An active veto against cosmic rays is formed by scintillation panels.

The energy resolution needs to be sufficiently high to allow for discrimination between signal and background electrons. For electron energies around 18.6 keV it is about 2 eV [Sch14].

The detector was commissioned at KIT from 2011 to 2013 [Har12] and operated in combination with the main spectrometer in the commissioning phases between 2013 and 2015 [Sch14, Har16].

2.3.4. Monitoring devices for the source and transport section

Since instabilities of important source operation parameters have a large systematic effect on the KATRIN measurement a set of monitoring devices will be used. Activity monitors are placed at the rear and front end of the source and transport section. The gas composition is analysed as part of the inner loop. The major monitoring systems are listed below.

¹⁷The surface of 592 m^2 from the wire electrodes needs to be considered additionally.

Laser-Raman system

Two different column densities can be assigned to the tritium source: the gas column density ρd_{gas} , and the activity monitored tritium column density, ρd_{T_2} , which determines the amplitude of the β -decay rate. Both quantities are linked via the tritium purity ϵ_{T} . While the gas column density (times inelastic scattering cross section) needs to be known with an uncertainty below 0.2% [AAB⁰⁵, Höt12], the requirement on the active column density can be relaxed by more than one order of magnitude¹⁸ [Höt12, SRS⁺¹³], since the absolute signal amplitude, which is sensitive to the absolute value of ϵ_{T} , is used as free parameter in the neutrino mass analysis (see section 2.4.3). Still, the precision of the active column density needs to be 2×10^{-3} [Höt12] which can be translated to a 0.1% precision requirement on ϵ_{T} [SRS⁺¹³, F⁺¹¹]. This means, a precise non-invasive in-line and near real-time (every 250 s [AAB⁰⁵]) determination of the gas composition and tritium purity needs to be performed within the closed gas circle in the inner loop. Such a measurement can be done using spectroscopy of monochromatic laser light inelastically scattered on molecules (Raman spectroscopy). The wavelength shifts of the scattered light are caused by rotational and vibrational excitations of the molecules. They are characteristic for each molecule species. Thus, it can be used to qualitatively and quantitatively determine the isotopic composition of the analysed sample [Sch13a].

The **LAser RAman** (LARA) system used in KATRIN consists of a measurement cell filled with the tritium gas sample to be analysed. It is placed in the inner loop in front of the pressure controlled buffer vessel. Laser light from a high intensity 5 W SSDP laser [BBB⁺¹²] with a wavelength of 532 nm is scattered in the cell. The scattered light is collected under an angle of 90°. The recorded spectrum is analysed both qualitatively and quantitatively to give the isotopic composition and tritium purity.

The test measurement LOOPINO, performed in 2011, proved that the LARA system is able to match the stability and precision requirements on ϵ_{T} [F⁺¹¹].

Detailed information about the KATRIN LARA set-up can be found in [Sch13a, Rup10, Fis14].

Beta induced X-ray spectroscopy (BIXS) system

A BIXS system is used to monitor the source activity from its position in the rear section. Since almost all β -decay electrons moving towards the focal plane detector get reflected at the retarding potential(s) of the tandem spectrometers, nearly the whole electron flux produced in the source reaches the rear wall. There, the electrons get absorbed and produce X-rays through interactions with matter. These X-rays are measured by two silicon drift detectors that are placed in the rear wall vessel volume and view the rear wall surface from two sides, see figure 2.13. The detectors are separated from the active tritium containing volume by beryllium windows to prevent them from being contaminated with tritium. For pressures below 10 mbar, the measured X-ray count rate depends almost linearly on the β -electron activity [BBB⁺¹²]. The BIXS system provides a high sensitivity within a low measurement time and a low minimal detectable activity [Röl15]. To reach a sensitivity to activity fluctuations of 1×10^{-3} , about 1×10^6 X-rays need to be counted. According to simulations in [Röl15] this requires a measurement duration of 70 s.

The **Tritium Rear wall eXperiment** (TriReX) was built as a proof of principle of the BIXS activity monitoring of gaseous tritium under conditions similar to the WGTS. It proved the feasibility of BIXS to measure 10^{-3} fluctuations in the source activity [Pri13].

¹⁸The ϵ_{T} trueness requirement is set by the description of the molecular final states that are different for the six hydrogen isotopologues.

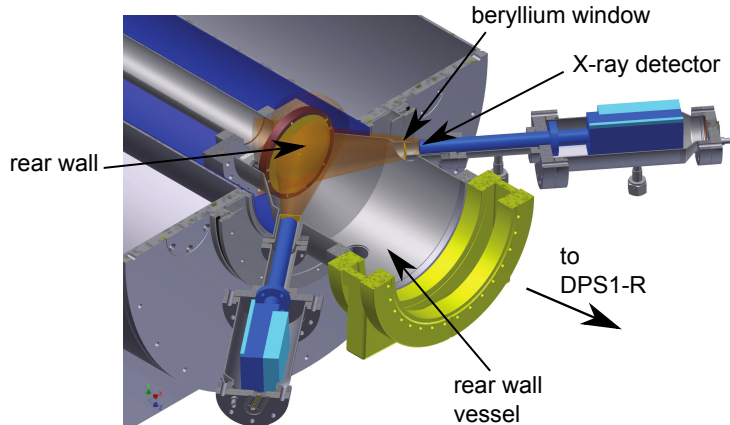


Figure 2.13.: **Components of the BIXS system.** Electrons absorbed at the rear wall produce X-rays that are detected by two silicon drift detectors viewing the rear wall vessel volume through by a beryllium window. Figure adapted from [Röl15].

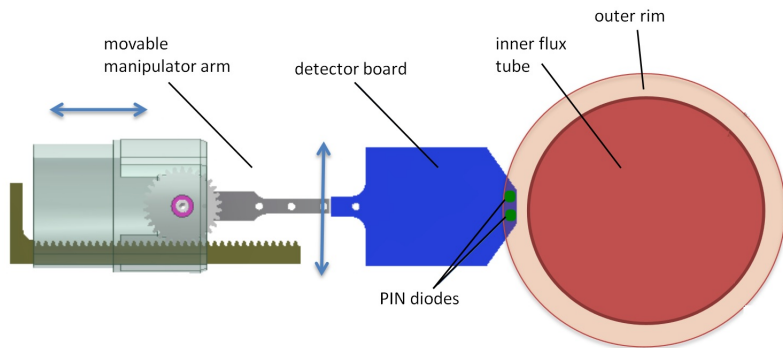


Figure 2.14.: **The forward beam monitor.** The PIN diodes measuring the source activity in the outer rim of the flux tube are mounted on a detector board which can be moved through the cross section of the beam by a manipulator arm. Figure adapted from [Ell16].

Forward beam monitor (FBM)

The FBM will be primarily used to on-line monitor the source activity at the outer rim of the flux tube, thus, without shadowing the β -decay electron signal. This activity monitoring, combined with the tritium purity monitoring, provides important information on column density changes in the source (see section 4.5.2). Besides the activity monitoring mode, which allows to measure the intensity with 0.1% precision in less than 60 s [Ell15, Ell16], it can be used in the so-called scanning mode. Here the FBM is moved through the cross section of the flux tube to measure radial inhomogeneities of the electron flux (mainly related to radial column density inhomogeneities caused by temperature differences, see section 4.2.3). Therefore, PIN-diodes mounted on a detector board will be used [EHH⁺15]. This board is placed on a movable manipulator arm which will be positioned at the end of the CPS, a sketch of the set-up is depicted in figure 2.14. Special requirements need to be fulfilled by the FBM detector: it needs to have a high stability (e.g. small drifts of the amplification factor because of temperature drifts [Ell16]) and a very low dead layer (much smaller than 1000 nm [EHH⁺15]) because of signal electron loss due to backscattering in the dead layer.

Besides the PIN-diodes, a Faraday cup will be placed on the detector board which allows to measure ion fluxes (see [Kle16] for further information).

Monitoring with the rear section e-gun

The electron gun implemented in the rear section will be used to determine the column density in an absolute measurement. In principle, this instrument can also be used for monitoring of column density fluctuations. Different from the other (active) column density monitoring measurements, it is sensitive to changes of the gas column density (active + inactive) with a precision of 0.1%. Therefore, the e-gun beam needs to be shot through the WGTS. The beam electrons need to be measured with two spectrometer retarding voltages. The ratio of the rates detected at the different retarding potentials can be used to observe column density changes [Bab14]. Compared to the two active monitoring methods, the e-gun needs a quite long measurement time of about 5 min and cannot be combined with regular neutrino-mass data taking. The e-gun monitoring measurement is further discussed in section 4.5.2.

2.4. Simulation and analysis software

The software framework KASPER comprises a rich set of KATRIN analysis and simulation packages which are primarily written in C++. They can be linked against each other in order to connect their functionalities. The user interface is based on XML configuration files. An overview of the embedded modules and functionalities can be found in [B⁺11] and [Gro15]. In the following an insight into the particle tracking and simulation software KASSIOPEIA and the statistical analysis tool for sensitivity studies KAFIT is given, and the Source Spectrum Calculation software (SSC) for the calculation of β -decay spectra under KATRIN operation conditions is described.

2.4.1. The particle tracking software Kassiopeia

The software used to investigate the propagation of signal and background particles through the whole 70 m long KATRIN set-up has to satisfy several requirements. It needs to provide accurate field solving and particle tracking algorithms. At the same time it should be extensible, flexible, user friendly and executable in a reasonable amount of computing time. To match all these requirements, a new software called KASSIOPEIA was developed that is tailored to KATRIN purposes. Development began in 2010, afterwards it was improved in the course of several PhD and master theses, among others [Mer12, Käf12, Gro15, Fur15, Cor14].

Within KASSIOPEIA, particles can be tracked through electric and magnetic fields while paying special attention to electron energy loss processes. A tool for the accurate calculation of the electromagnetic fields is given by the KEMFIELD package, see [Cor14] for detailed information. Complicated geometric shapes present in a large number and variety in the set-up are implemented by the KGEOBAG package.

Particle tracks are calculated by solving the equations of motion with the Lorentz equation included. To account for energy losses due to the electron cyclotron motion, a corresponding loss term is implemented. Apart from the tracking through electromagnetic fields, interactions with surfaces and residual gas particles can be considered. Details about KASSIOPEIA are presented in [Gro15] and [Fur15].

2.4.2. Source and Spectrum Calculation software SSC

Since the spectrometer acts as a high pass-filter, the electron spectrum that is recorded by scanning over different retarding voltages is an energy integrated spectrum. Its shape differs from the β -decay electron spectrum at the time of electron emission in the source. Both kinds of spectra can be modelled with SSC. For the computation of integrated β -decay source spectra SSC calculates energy loss or gain processes, like scattering of β -decay

electrons on gas particles and Doppler effects that are related to source variables such as gas particle density, temperature and magnetic fields. With the help of representative models for transmission and response functions (introduced in section 2.1.2), the initial differential spectrum of β -decay is translated into an integrated spectrum, for comparison with the measured one. In connection with the analysis software KAFIT, SSC is intended to be used for the neutrino mass analysis with KATRIN. Meanwhile, it is utilised to investigate source related systematic effects [Höt12, Käf12, Gro15].

The SSC package is based on initial contributions from W. Käfer [Käf12] and M. Hötzels [Höt12] and was further improved by M. Kleesiek [Kle14]. Important additions with regard to the description of gas flow and plasma related source properties have been made within the scope of this thesis.

Since SSC is extensively used in this work to investigate systematic effects related to the description of gas dynamical source properties (in chapter 4) and to model the electrostatic source potential (in chapter 5), the workings of this software package will be described in some more detail below.

2.4.2.1. Defining source properties

SSC is based on the concept of voxelisation, which stands for the subdivision of the source into a user defined number, N_{voxel} , of small volumes. The source can be segmented in three dimensions:

- longitudinal direction (z -axis), the elements are called slices;
- radial direction (r -axis), the elements are called rings;
- azimuthal direction (angle ϕ), the elements are called segments.

Each segmentation contains an user defined number of elements. The three-dimensional representation of a segment is called voxel. The principle is visualised in figure 2.15. Radial and azimuthal segmentation can either be done in equidistant steps or with varying radial and angular width for the different rings and segments in order to retain a similar surface area for each segment¹⁹. The segmentation into concentric rings is generally based on the magnetic field such that the magnetic flux through each ring is constant (see equation (2.5)). The voxelisation represents the transition from a continuous volume to a finite number of elements. The same happens with the continuous fields of the source variables. They become a discrete set:

- Temperature $T(z, r, \phi) \rightarrow T_i$,
- Magnetic field $\vec{B}(z, r, \phi) \rightarrow \vec{B}_i$,
- Tritium purity ϵ (it is assumed to be constant in the source, see chapter 4),
- Gas density $n(z, r, \phi) \rightarrow n_i$,
- Gas velocity $u(z, r, \phi) \rightarrow u_i$,
- Potential $U(z, r, \phi) \rightarrow U_i$.

For fine enough segmentation, meaning a discretisation in z - direction that produces about 500 slices²⁰, it is adequate to define the values of the source variable according to the centre of mass coordinates of each voxel.

The voxels are not only used to set the distribution of source variables: the concept is

¹⁹Thus, with a ring number of twelve (excluding the central bull's eye), and a segment number of twelve, the detector pixels can be mapped to the source.

²⁰This number is related to a column density mismatch between the integrated ($\int_0^z n(z)dz$) and summed variable ($\sum_{i=0}^N n_i$) below 5×10^{-4} . In general, the required segmentation width depends on the scale of inhomogeneities of the source variables and on the investigated effect. For more general purposes, the number of slices can be lower.

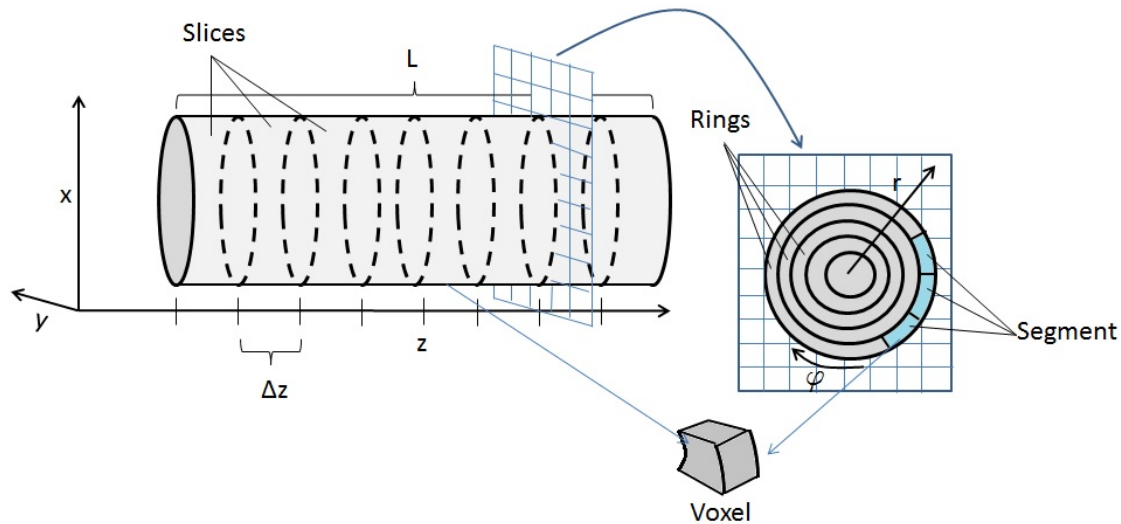


Figure 2.15.: **Geometric principle of voxelisation in SSC.** The given source volume is segmented in longitudinal, radial and azimuthal direction. The smallest entity in three dimensions is called a voxel.

implemented up to the calculation of the differential spectrum of the electrons produced in β -decay and even for the integrated spectrum. For each voxel a distinct response function is calculated. Thus, the computed integrated spectrum consists in a superposition of spectra from the individual voxels.

In the SSC code the source variables, listed above, are modelled through different C++ classes. Density distribution, temperature distribution and velocity distribution are summarised in gas dynamics classes. Here the actual density distribution is calculated using given input values for inlet and outlet pressure and for the temperature distribution. All calculations of density distributions in the different gas dynamics classes²¹ are based on pre-calculated data from the simulation of gas dynamics in the corresponding component. These calculations are discussed in sections 4.2.3, 4.2.6 and 4.2.5. At this point it should be emphasised that the description of gas dynamics in the source and especially the accurate modelling of the column density (actually column density times scattering cross section) is essential for the adequate calculation of the scattering processes. Since scattering is the main energy loss mechanism of β -decay electrons in the source, the accurate modelling of the source spectrum is based on a precise description of gas dynamics.

In table 2.1 a standard set of KATRIN operational parameters can be found. Many of the spectra produced in this thesis refer to this standard set.

2.4.2.2. Calculation of KATRIN β -electron spectra

Two different kinds of spectra need to be disentangled. The first one is the differential spectrum, which represents the kinetic energy of emitted electrons at the point of β -decay. The second one is the integrated spectrum, which is the propagated and energy integrated differential spectrum, according to the set of main spectrometer retarding voltages, that can be measured at the detector.

Differential spectrum

The differential spectrum can be calculated using Fermi's theory of β -decay as discussed in section 1.5.2.4. However, in a realistic experimental environment the pure β -decay

²¹There are different gas dynamic classes for different components (WGTS, first pump port DPS1, ...), compare section 4.2.8.

Table 2.1.: **Reference parameters for the calculation of analytical spectra and toy measurements.** Values are taken from [AAB⁺05].

parameter		setting
column density	ρd	$5 \times 10^{21} \text{ m}^{-2}$
inelastic scattering cross section	σ_{in}	$3.45 \times 10^{-22} \text{ m}^2$
Scattering probabilities	P_0	41.33%
	P_1	29.27%
	P_2	16.73%
	P_3	7.91%
	P_4	3.18%
magnetic flux	Φ	191 T cm^2
magnetic fields	B_s	3.6 T
	B_a	$3 \times 10^{-4} \text{ T}$
	B_{max}	6 T
tritium purity	ϵ_T	0.95
background rate	R_{bg}	0.01 cps
spectral endpoint of tritium β -decay	E_0	18 575 eV
detection efficiency	ϵ_{det}	0.9
analysis interval		$[E_0 - 30 \text{ eV}, E_0 + 5 \text{ eV}]$
measurement time distribution		standard measurement time distribution (3 years)

spectrum from equation (1.66) has to be corrected for the bulk gas and thermal molecular motion as well as for vibrational and rotational excitations of the mother and daughter molecules. The main effects modifying the β -decay spectrum and their particular spectral influence are listed below.

1. Nuclear recoil

Since the daughter nucleus needs to carry away the momentum of the emitted β -electron, the corresponding molecule receives some recoil energy. Close to the spectral endpoint E_0 , this energy, E_{rec} , can be approximated [AAB⁺05] as

$$E_{\text{rec}} = \frac{m_e}{M_{3\text{HeT}^+}} \approx 1.7 \text{ eV}, \quad (2.21)$$

with the electron mass m_e , and $M_{3\text{HeT}^+}$ designating mass of the daughter molecule from β -decay of a T_2 -molecule. For the nuclear recoil correction of other decaying isotopologues present in the WGTS, e.g. DT and HT, the different mass of the daughter molecule needs to be taken into account.

2. Final State distribution

The leptonic phase space from β -decay of the tritiated hydrogen isotopologues is decreased by the rotational, vibrational and electronic excitations of the daughter molecule. These excitations are described by the so called final state distribution (FSD) – it assigns a probability P_f to an excitation energy E_f . Thus, the initial β -decay endpoint E_0 gets shifted to an effective endpoint $E_{0\text{eff}}$:

$$E_{0\text{eff}} = E_0 - E_f \quad \text{with probability } P_f, \quad (2.22)$$

and the β -decay spectrum becomes a superposition of the single final state corrected spectra with endpoint energy $E_{0\text{eff}}$. The different tritiated molecules (T_2 , DT, HT) have different FSDs and thus correspond to different endpoint energies. To include decays of these molecules in the β -decay spectrum, information from Laser Raman

measurements need to be used to weight the contributions from the different isotopologues correctly. The FSDs that are used in SSC are based on calculations published in [DTSJ06, DT08] and [SJF00].

Apart from excitations of the daughter molecule, also the excitations of the mother molecule have to be considered. The decaying molecule can have different angular momentum $J = 0, 1, 2, 3, \dots$. The population of the individual J states is Boltzmann distributed according to the temperature T [DTSJ06], therefore the probability for a molecule to be in state J before β -decay, $P_j(T)$, becomes

$$P_j(T) = \frac{g_s g_j}{A} e^{-\frac{\Delta E_j}{k_B T}}, \quad (2.23)$$

with energy difference to the ground state ΔE_j normalisation constant A , and g_j and g_s accounting for the number of degenerate rotational states J (with $g_j = 2J+1$) and nuclear spin degeneracy, respectively. Here homonuclear molecules, like T_2 and H_2 , need to be treated separately from heteronuclear molecules like HT . Homonuclear molecules have two different states with regard to the two embedded atoms – the ortho-state with parallel nuclear spins and a para-state with anti-parallel nuclear spins. Ortho-states have a spin degeneracy of three, while para-states have a spin degeneracy of one. The ratio of occurrence of both states, which is called ortho-para ratio, depends on the molecular temperature. More information about the ortho-para ratio and the relation to the final state distribution in KATRIN can be found in [Kle14] and [KY14]. In the work presented therein, an ortho-para ratio of 0.75 was found to be appropriate for KATRIN.

3. Doppler effect

The decaying molecule in general is not at rest: there are two different kinds of motion. The first one is translational statistical molecular motion at source temperature (isotropic) and the second one is the bulk motion due to the gas flow (in direction flow). Both cause a broadening of the energy spectrum, $\frac{d^2N}{dtdE}$, of the emitted β -electrons through the Doppler effect. This can be expressed by a convolution $(g \otimes \frac{d^2N}{dtdE})(E_f)$ of the initial spectrum with the broadening function $g(\Delta E)$ corresponding to the Doppler energy shift ΔE :

$$\Delta E = E_f - E_i = \frac{1}{2} m_e (\vec{v}_e + \vec{v}_{T_2})^2 - \frac{1}{2} m_e \vec{v}_e^2. \quad \text{with } \vec{v}_e^2 \gg \vec{v}_{T_2}^2: \quad (2.24)$$

$$\Delta E \approx m_e \vec{v}_e \vec{v}_{T_2}. \quad (2.25)$$

Here \vec{v}_e denotes the electron velocity vector and \vec{v}_{T_2} the gas velocity, which consist of the thermal molecule velocity with most probable velocity $v_{th} = \sqrt{2k_B T/m_{T_2}}$ [WAWJ04], and the bulk gas velocity u . Since the gas flow is almost one-dimensional, see section 4.2.3, the bulk velocity can be approximated by its z component u_z . Both motions are included in the broadening function, which is a Gaussian distribution:

$$g(\Delta E) = \frac{1}{\sqrt{4\pi E_f k_B T m_e / m_{T_2}}} e^{-\frac{1}{2} \left(\frac{\Delta E - u_z \sqrt{2m_e E_f}}{\sqrt{2E_f k_B T m_e / m_{T_2}}} \right)^2} \quad (2.26)$$

For a temperature of 30 K the average energy shift ΔE is about 130 meV [Höt12]. It is of the order of the KATRIN neutrino mass sensitivity which underlines the importance of considering the Doppler effect in the calculation of source spectra.

4. Radiative corrections

This term includes interactions of the β -decay electrons with real and virtual photons in the Coulomb field of the nucleus. The related energy losses are included in SSC by a energy dependent factor $f_{rad}(E)$ from [RW83].

Integrated spectrum

With the current measurement principle, KATRIN is not able to directly observe the differential β -decay spectrum $\frac{d^2N}{dtdE}$ described above. It can only measure the integral rate $\sum_i \frac{dN(qU_i)}{dt}$ for a set of main spectrometer retarding energies qU_i . In the following, referring to the integrated spectrum for a given set of retarding voltages the term $\frac{dN}{dt}(qU)$ will be used. The calculation scheme and functionalities of the two classes of spectra are depicted in figure 2.16. Besides the actual energy integration, which needs to take into account the transmission function of the spectrometer, the energy losses during the propagation of a β -decay electron need to be considered. Thus, the integrated signal rate for a given value of qU can be calculated as:

$$\frac{dN}{dt}(qU) = N_T \epsilon_{\text{det}} \frac{\Omega}{4\pi} \int_{qU}^{E_0} \frac{d^2N}{dtdE} R(E, qU) dE. \quad (2.27)$$

Here ϵ_{det} denotes the detection efficiency and N_T the number of tritium atoms in the source. The response function $R(E, qU)$ was already introduced in section 2.1.2. It includes both, the spectrometer transmission function and the energy loss due to scattering. The solid angle ratio

$$\frac{\Omega}{4\pi} = \frac{1}{2} (1 - \cos \theta_{\text{max}}) \quad (2.28)$$

includes the effect from the reflection of electrons with polar emission angle larger than θ_{max} from equation (2.8) due to the magnetic mirror effect.

Scattering processes

If an electron scatters inelastically off a tritium molecule it loses at least 10 eV of its kinetic energy [AAB⁰⁵]. The probability distribution for electron energy losses due to scattering, ϵ , is described by the energy loss function $f(\epsilon)$ as given in equation (2.14). The values of the total inelastic scattering cross section σ_{in} and differential inelastic cross section $\frac{d\sigma_{\text{in}}}{d\epsilon}$ that enter $f(\epsilon)$ were obtained in previous measurements described in [ABB⁰⁰]. The measured value of the total inelastic cross section, $(3.40 \pm 0.07) \cdot 10^{-18} \text{ cm}^2$, and the determined parametrisation of $f(\epsilon)$ (see [Höt12] and [Zie13] for details) are implemented in SSC. However, both quantities are not known to the 10^{-3} level as required for KATRIN. Thus, they will be determined by dedicated measurements using the rear section electron gun. The energy loss function can be determined measuring the response function for different gas column densities in the source. The data need to be analysed with a deconvolution procedure, as described in [HVWW16]. The measurement of the inelastic scattering cross section is directly related to the column density through the probability for i -fold scattering P_i . The measurement procedure is further described in section 4.5.1. If and how both quantities can be disentangled is discussed in section 4.1.

To reach the KATRIN sensitivity goal of 200 meV (90% C.L.), a proper description of the electron scattering processes in the source is essential. This goes along with an adequate description of gas dynamics (density, column density and velocity distribution) in the whole source section. Even small column density changes on the per-mill level need to be included correctly. Thus, one of the key aspects of this thesis is the extension and improvement of the SSC gas dynamics model.

2.4.3. Spectrum fitting software KaFit

The KAFIT module is the tool for statistical parameter inference in the KATRIN software package KASPER. To gain access to the absolute neutrino mass scale, KATRIN relies on a multi-parameter fit – the neutrino mass is extracted from a spectral shape analysis of

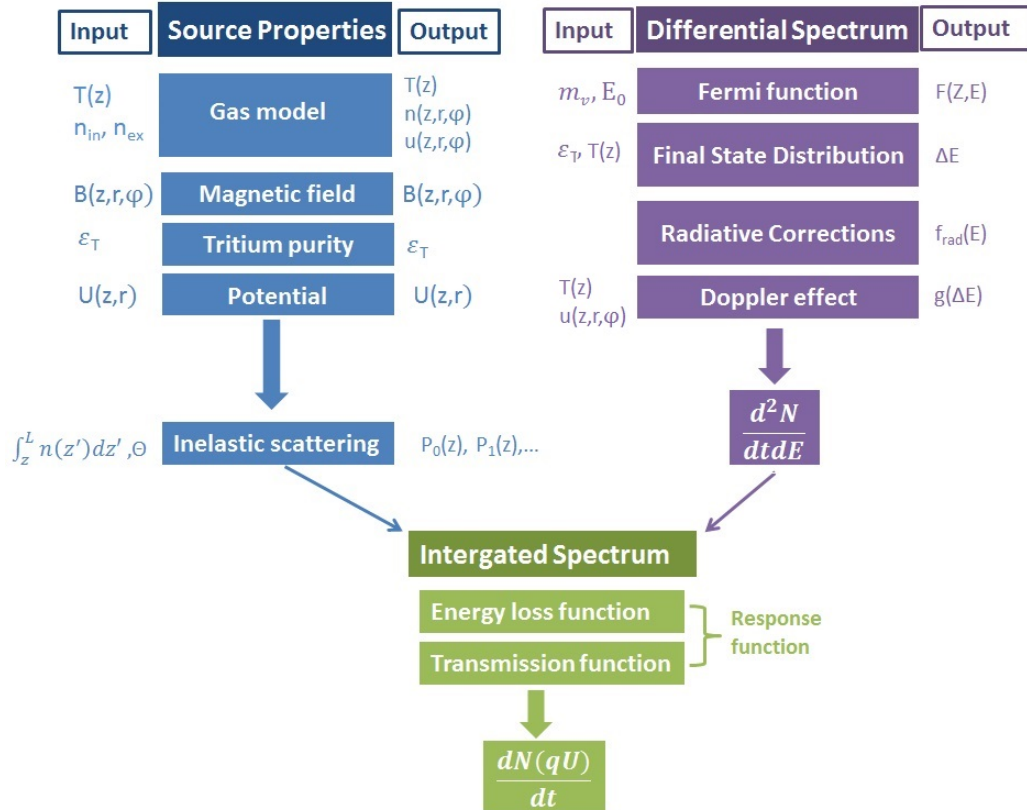


Figure 2.16.: **Schema of the calculation of integrated and differential spectra with SSC.** To model the spectrum $\frac{dN}{dt}(qU)$ measured with KATRIN, the differential electron spectrum, corrected for the above described effects, needs to be integrated over energy for a given spectrometer retarding energy qU . Before integration, it needs to be multiplied by the response function, which includes the energy losses due to scattering and the transmission function of the spectrometer.

the measured electron spectrum. The tools for such an analysis are provided by KAFIT. Based on the work of M. Käfer [Käf12], M. Hötzl [Hö12] and M. Kleesiek [Kle14], it implements a variety of statistical methods to fit free parameters of the analysed model and construct confidence intervals. Moreover, it offers the possibility to investigate systematic effects influencing the electron spectrum measured with KATRIN and thus the neutrino mass sensitivity.

In the following a brief overview of the functionalities of KAFIT and the analysis of KATRIN spectra is given. Detailed information on the probabilistic and parameter estimation methods can be found in [Hö12] and [Kle14].

The neutrino mass analysis and also investigation of systematics of KATRIN data is based on the comparison between measured and modelled electron β -decay spectra. In the calculation of the analytical spectrum, some undetermined parameters are treated in the analysis as free nuisance parameters that are estimated along with m_ν^2 fitting the analytical to the measured spectrum. In general four standard fit parameters are used [AAB⁺05]: the neutrino mass squared, m_ν^2 , the tritium endpoint energy, E_0 , the signal amplitude, A_s , and the background rate, R_{bg} .

For the analysis of systematic effects an analogous procedure as in the actual neutrino mass analysis can be used, only that the experimentally measured data are replaced by simulated toy data generated with the SSC model. In the generation of these toy data, the fit parameters m_ν^2 , E_0 and R_{bg} need to be replaced by user defined values. The amplitude is related to the number density of tritium molecules in the source. The analytical model and the model that generates the toy data differ by the systematic effect that should be investigated.

Generation of KATRIN spectra

The spectral distribution of the measured rates for given retarding voltages are covered by the source simulation software SSC. Thus, specifying a measurement time distribution that fixes a set of retarding voltages and times measured at this points, $\{qU, t_{qU}\}$, and a background rate R_{bg} , an integral count rate spectrum $N_{th0}(qU_i)$ can be calculated:

$$N_{th0}(qU_i) = \left(\frac{dN}{dt} + R_{bg} \right) \cdot t_{qU}. \quad (2.29)$$

To account for the statistical nature of a measurement, the spectrum $N_{th0}(qU_i)$ needs to be treated as the expectation value from a Poisson distribution with statistical uncertainty $\sigma = \sqrt{N_{th0}(qU_i)}$ for each measurement point. Thus, the toy measurement spectrum $N(qU_i)_{th}$ reads:

$$N_{th}(qU_i) = \text{Poisson}(N_{th0}(qU_i)). \quad (2.30)$$

Exemplary toy measurement spectra with and without non-zero neutrino mass for standard KATRIN operation parameters, listed in table 2.1, are shown in figure 2.17. The theoretical spectrum (without statistical randomness) is given for comparison. The generation of KATRIN spectra with KAFIT and SSC is purely analytical. Still, Monte Carlo data from the calculation of the energy loss function can be incorporated in the calculation (see [Gro15] for further information).

Ensemble testing and sensitivity

The parameter estimation for the (at least) four fit parameters m_ν^2 , E_0 , A_s and R_{bg} is performed by a minimisation of the difference between the analytic and the measured spectrum. This can be represented by a maximisation of the likelihood function $L(\Theta|X)$. It equals the probability, $p(X|\Theta)$, that a measurement X will be observed if a set of parameters Θ is realised. For the neutrino mass analysis with KATRIN the measurement

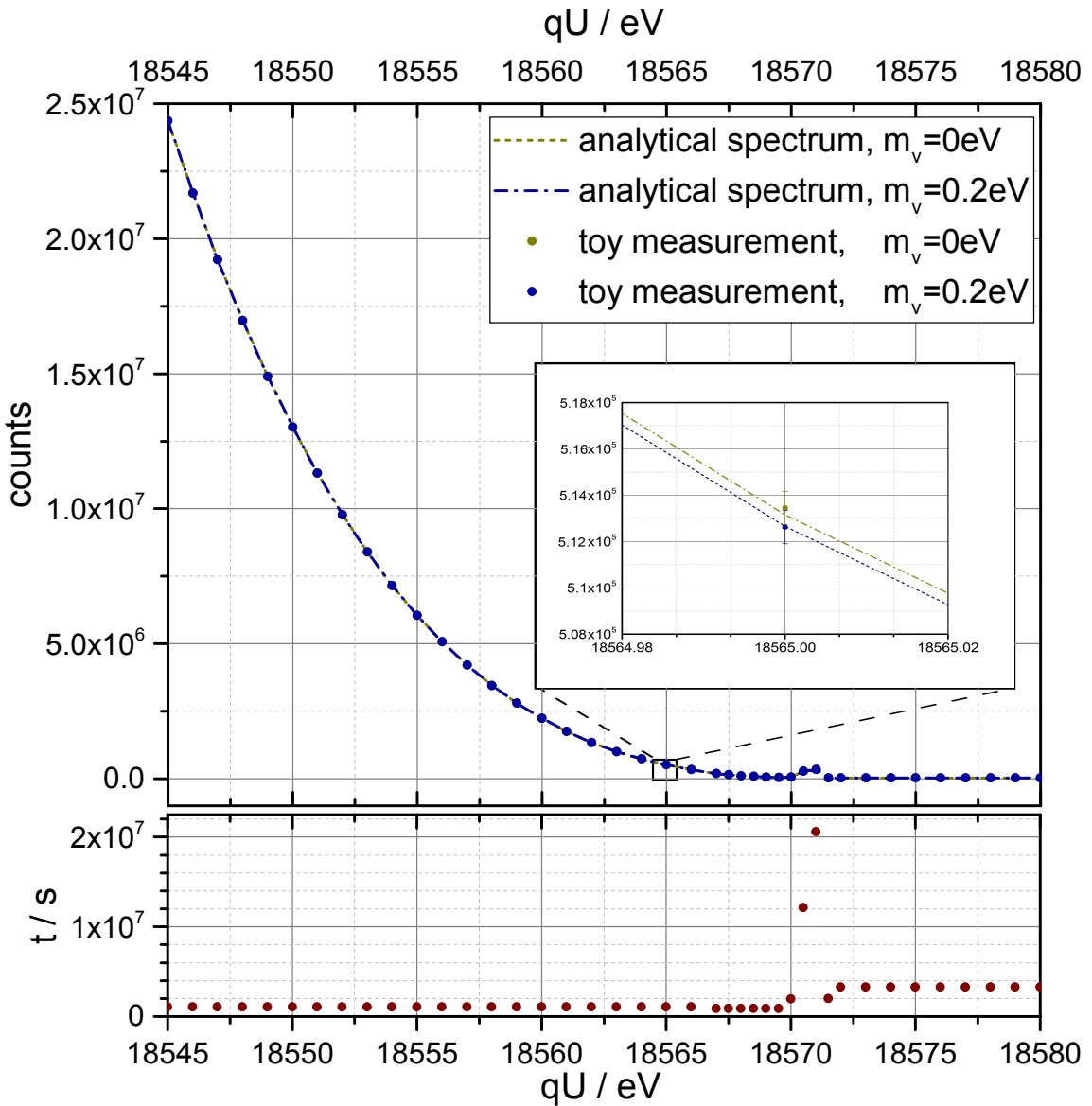


Figure 2.17.: **Toy measurement and analytical spectra for two neutrino masses.**

The toy measurements include the statistical Poisson uncertainty as given in equation (2.30). All spectra are generated for a standard measurement time distribution from [AAB⁺05] which is shown below the spectra. A background rate of 0.01 Hz and a total measurement live time of three years is assumed.

X stands for the measured rate, $N_{\text{exp}}(qU)$, at spectrometer retarding energy qU and the parameter set Θ is given by the free fit parameters which are by default m_ν^2 , E_0 , A_S and R_{bg} . For a given set of measurement points qU_i the likelihood function is:

$$L(m_\nu^2, E_0, A_S, R_{\text{bg}} | N_{\text{exp}}) = \prod_i p(N_{\text{exp}}(qU_i) | N_{\text{th}}(qU_i, m_\nu^2, E_0, A_S, R_{\text{bg}})). \quad (2.31)$$

Instead of maximising the likelihood $L(\Theta | X)$, in practice often the negative log-likelihood, $-\log L(\Theta | X)$, is minimised. The method of least squares is an equivalent approach under the assumption of Gaussian distributed errors of N_{exp} [Kle14]. It is represented by the minimisation of the χ^2 function

$$\chi^2(m_\nu^2, E_0, A_S, R_{\text{bg}} | N_{\text{exp}}) = \sum_i^{n_{\text{ret}}} \sum_j^{n_{\text{pix}}} \left(\frac{N_{\text{exp},j}(qU_i) - N_{\text{th},j}(qU_i, m_\nu^2, E_0, A_S, R_{\text{bg}})}{\sqrt{N_{\text{th},j}(qU_i)}} \right). \quad (2.32)$$

and will be used in the KATRIN analysis. The summation over the index j represents the contributions from the 148 detector pixels, if the segmentation is activated in the spectrum simulation.

The actual χ^2 minimisation can be performed using different algorithms like MINUIT from the ROOT library [ABB⁺09].

The neutrino mass sensitivity study, including the analysis of several systematic effects, can be performed using the method of ensemble testing. Therefore, a large number of KATRIN toy measurements is generated. For each data set the parameter estimation for the at least four fit parameters, which means the minimisation of the χ^2 function from equation (2.32), has to be done. The parameter estimates obtained for the neutrino mass are filled in a histogram. For a large number of entries, this histogram can be fitted by a Gaussian with mean values $\mu(m_\nu^2)$ and variance $\sigma(m_\nu^2)$. By comparison of the mean value $\mu(m_\nu^2)$ and the true value, $m_{\nu0}^2$, that was used for generating the toy measurement, the systematic neutrino mass squared shift, Δm_ν^2 , is obtained as

$$\Delta m_\nu^2 = \mu(m_\nu^2) - m_{\nu0}^2. \quad (2.33)$$

The outcome of an exemplary ensemble test with 10 000 full KATRIN measurements, and corresponding 10 000 best fit values for the neutrino mass, is depicted in figure 2.18. The standard deviation of the Gaussian fit is representative for the statistical measurement uncertainty $\sigma_{\text{stat}}(m_\nu^2)$ [Höt12].

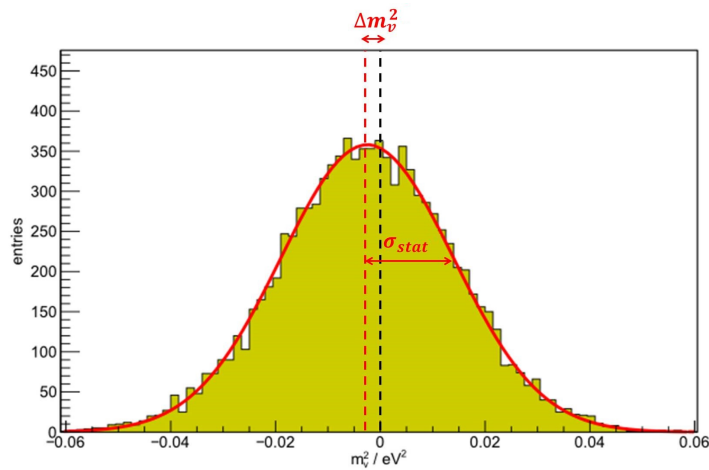


Figure 2.18.: **Systematic neutrino mass shift Δm_ν^2 and statistic uncertainty σ_{stat} from an exemplary ensemble test with 10 000 full Katrin measurements.** The ensemble test is performed implementing a systematic effect from a column density error of 0.2%. Standard parameter and standard measurement time distribution given in table 2.1 and figure 2.17 are used for the calculation of spectra. A background rate of 0.01 mcps is assumed. The resulting systematic neutrino mass shift is equal to the mean $\mu_{m_\nu^2}$ of the Gaussian fitted to the ensemble of estimates, since a vanishing neutrino mass was assumed for the calculation of the analytical spectrum. Here, the result is $\Delta m_\nu^2 = (-2.42 \pm 0.17) \cdot 10^{-3} \text{ eV}^2$. The Gaussian width, which is representative for the statistical uncertainty, is $\sigma_{\text{stat}} = (16.5 \pm 0.12) \cdot 10^{-3} \text{ eV}^2$.

3. Temperature distribution in the first Differential Pumping Section DPS1

Contents

3.1.	The modes of heat transfer	69
3.2.	Cooling concept of the DPS1 pump ports	70
3.3.	Simulation of heat transfer processes in the DPS1	72
3.3.1.	Heat transport in the neon and helium cooling tubes	72
3.3.2.	Calculation of heat transport in the first pump port	76
3.3.3.	Modelling of demonstrator measurement	82
3.3.4.	Calculation of heat transport in the second pump port	85
3.4.	Conclusion	87

The absolute temperature as well as temperature gradients are fundamental operational parameters of the WGTS. The temperature distribution determines the gas dynamical properties pressure and velocity that are essential ingredients for the calculation of the β -electron energy spectrum at the detector. To build an adequate gas model for the source, it is important to know the temperature within the WGTS central beam tube as well as in the adjacent pump ports and beam tubes of the DPS1-F and DPS1-R. A homogeneous and stable WGTS beam tube temperature is crucial to sustain the required per-mill stability in gas density level [Höt12]. The most critical part with regard to temperature stability is the central 10 m beam tube of the WGTS, as about 98% of the total gas density are contained in this part (see section 4.2). The temperature at this part of the beam tube needs to be stable at the per-mill level [AAB⁰⁵]. The cooling system consists of two tubes that are half filled with liquid neon under saturation vapour pressure running along the WGTS tube as depicted in figure 2.8. This allows a stabilised temperature in the range of 27 K to 30 K. An overview of the cooling principle of the WGTS cryostat is given in section 2.3.1.1, an more detailed description can be found in [GBB⁰⁸]. The novel beam tube temperature stabilisation concept was proven to function and to even surpass specifications shown in the demonstrator measurements [GBH¹³]. No experimental data are available on the temperature distribution at the pump ports and beam tubes of the first differential pumping system adjacent to the central WGTS beam tube in front and rear direction, DPS1-F and DPS1-R, yet. Since a large heat load is coming from the turbo-molecular pumps (TMPs), this distribution may deviate significantly from the central WGTS beam tube temperature.

The pump port and beam tube temperature is needed as crucial input for the calculation of gas dynamical properties in these domains and their contribution to the total column density. This way also the gas flow reduction factor of the DPS1-F can be computed. Aside from the calculation of the density and velocity distributions, the pump port temperature is needed to determine the pumping speed of the turbo-molecular pumps (Leybold MAG W2800). It is strongly influenced by the temperature of the gas molecules at the rotor blades [SK05]. This temperature can only be determined knowing the wall temperature of the set-up.

The heat load on WGTS beam tube and pump ports is mainly caused by thermal radiation of the TMPs that operate at temperatures of about 333 K to 393 K. It needs to be tested, if and for which TMP working temperature the WGTS beam tube temperature is influenced significantly. Moreover, the impact of the adjacent domains which operate at room temperature s (DPS2, and Rear Section) needs to be simulated. With regard to the planned UV-irradiation of the rear wall [rswg12], it has to be tested if the reflected radiation can heat up parts of the WGTS central beam tube.

The data available from previous test measurements with the demonstrator [GBH¹³, Höt12, Bod11] cover only the central WGTS beam tube and the first pump ports of DPS1-F and DPS1-R¹. Furthermore, the conditions of this test experiment were different from the actual KATRIN conditions, as will be discussed in section 3.3.3. Therefore heat transfer simulation of the corresponding domains are required to get information about their absolute temperature and temperature distribution.

The present chapter summarises the heat transfer calculations for the two pump ports and beam tubes of the DPS1-F and DPS1-R done in the scope of this work. Section 3.1 starts with a brief introduction to the essential mechanisms of heat transfer used within the simulations in section. The cooling concept of the pumping chambers is outlined in section 3.2. The calculation of the temperature distribution for the DPS1-F and DPS1-R is presented in section 3.3 and the results are compared with data from demonstrator test measurements.

¹The actual temperature distribution at the pump port was not measured

3.1. The modes of heat transfer

In a realistic model of the pump port temperature three different mechanisms of heat transfer need to be considered: conduction, convection, and thermal radiation. Their main characteristics are summarised in the following.

Conduction

Heat energy is transferred between two bodies contacting without the transport of mass. The conductive heat flux q_{cond} between two reservoirs with temperature difference ΔT and conductivity k can be expressed with the differential form of *Fourier's law* [Fou22]:

$$q_{\text{cond}} = -k\nabla T. \quad (3.1)$$

Integrating (3.1) over the surface area A the heat current, $I_{Q_{\text{cond}}}$, is obtained for a transport over length d :

$$I_{Q_{\text{cond}}} = \frac{\Delta T k A}{d}. \quad (3.2)$$

Therefore, the conductive heat load for a given material can be reduced by increasing the length of the system and decreasing its area. For that purpose bellows can be used. In solids, conduction is driven by the lattice vibrations and movement of free electrons (in metals) [Suk05]. In fluids it is caused by collisions of the more mobile molecules.

Convection

Convective heat transport is driven by mass transfer and motion of fluids and gases. The flow type, laminar or turbulent, is of great importance for convection [Sto04, Suk05]. In the following only laminar flow is considered, since for the application in the KATRIN tritium source the flow in the cooling pipes can be supposed laminar. The convective heat flux caused by a temperature difference ΔT over surface A can be expressed with the help of the convective heat transfer coefficient h_c that depends on the fluid itself and on the fluid flow [RK11]:

$$q_{\text{cv}} = h_c \Delta T \quad (3.3)$$

or, in terms of the transferred heat current:

$$I_{Q_{\text{cv}}} = \Delta T \dot{m} c_p. \quad (3.4)$$

Here \dot{m} denotes the mass flow rate, and c_p the heat capacity at constant pressure. Computing convective heat transfer is rather complicated, as non-isothermal flow and velocity distribution of the fluid need to be included.

Radiation

In radiation heat transport energy is transferred by photons in electromagnetic waves. the heat flux q_r emitted by a black body obeys the *Stefan-Boltzmann law* [Ste79]. Including the emissivity ϵ , with $\epsilon \leq 1$, of the emitting surface the heat flux per unit of surface for a grey body can be written as

$$q_r = \epsilon \sigma T^4. \quad (3.5)$$

Here σ denotes the Stefan-Boltzmann constant. The emissivity in general strongly depends on surface parameters like composition, roughness, and temperature [BL95]. For simulating radiative heat transfer in more complicated geometries the so-called view factors need

to be included. They specify the percentage of surface area in line of sight with another radiating surface.

For solids the most important heat transfer mechanism is conduction [RK11]. Convection can be neglected since molecules cannot move freely through the material. Radiation heat transfer through solids needs to be considered only in case of opaque surfaces or if an opaque material (gas, vacuum) is located in between two surfaces. For fluids all three mechanisms need to be respected. In case of gases, unless at very high pressures, conduction can be neglected [RK11]. For vacuum applications the radiation that is transferred through the vacuum needs to be considered.

For the temperature simulation of the pump ports in the DPS1, conductive heat transfer in solids, in the tube walls, as well as conduction and convection in fluids, in the different coolants, and radiative heat transfer processes within the beam tube and pump port need to be modelled.

3.2. Cooling concept of the DPS1 pump ports

The four-fold and two-fold pump ports of the DPS1-F and DPS1-R are connected to four and two TMPs, respectively. The pumps operate at a significantly higher temperature than the WGTS beam tube, as their rotor blades get heated up by eddy currents caused by the surrounding magnetic field from the superconducting magnets [GKRW12]. The temperature of the rotor blades strongly depends on the magnetic field and the magnetic shielding. A temperature below 363 K is recommended by the constructor for long-term operation. The critical short-term operation temperature is about 393 K. Conductive heat transfer is hindered by bellows and cooling tubes at the radiation shield and at the entrance to the pump port. To prevent pump port and beam tube to be heated up by the large radiation heat load coming from the rotor blades of the TMPs, concentric radiation shields are installed. They are blackened by plasma spray coating with a $\text{Al}_2\text{O}_3/\text{TiO}_2$ mixture. Due to the large emissivity of the radiation shields, $\epsilon \geq 0.92$ [Bay03], and their connection to the nitrogen cooling a large amount of radiative heat gets absorbed and transported out of the system. The influence of rotor blade temperature on the temperature of the pump port is tested in section 3.3.2. The cooling concept for the beam tube connecting first and second pump port is equivalent to the WGTS beam tube cooling, with the addition of a separate Ne/Ar condenser. The beam tube connecting first and second pump port of the DPS1 is cooled down to 30 K. At the second beam tube of the DPS1 the cooling liquid is changed to saturated nitrogen with a temperature of 80 K. Additional heat load comes from the flange at the beginning of DPS that has room temperature. Its influence on the beam tube temperature will be tested in section 3.3.4.

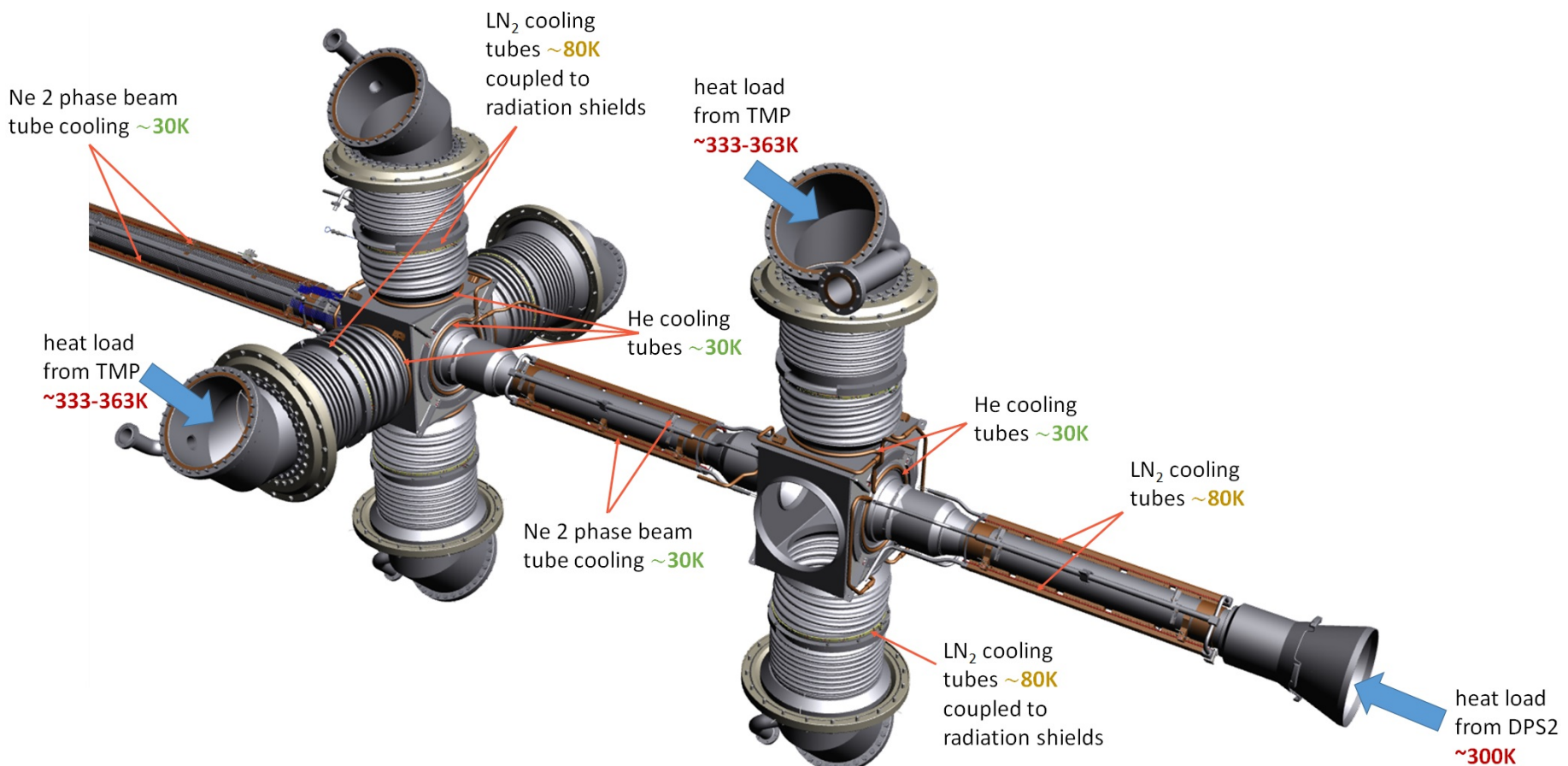


Figure 3.1.: **Cooling system of the DPS1.** The WGTS beam tube itself is stabilised at 30 K with the two phase neon tube lining the beam tube, compare figure 2.8. Radiation enters at the pump port from the TMPs as well as from the DPS2 which operates at room temperature. Blackened copper radiation shields cooled by LN₂ at the connection to the TMPs reduce the radiative heat load from the TMPs. The pump port itself is cooled by gaseous helium at 30 K at the entrances of the different tubes. The beam tube connecting the second pump port with the DPS2 is cooled to 80 K with LN₂.

3.3. Simulation of heat transfer processes in the DPS1

A simulation of the temperature distribution in the DPS1-F and DPS1-R needs to contain all three components of heat transport explained in section 3.1:

- conduction – heat is transferred through the wall material and in the boundary layer between the wall of the cooling tube and coolant as well as in the coolant itself;
- convection – cooling liquids carry away the heat load from the walls through their flow;
- radiation – dominant for domains in line of sight with the warm parts of the model (TMPs, flange to DPS, rear wall), can even reach distant parts by reflection.

Therefore a combination of heat transport in fluids and solids including radiation heat transport is used. All simulations are carried out within the software package COMSOL Multiphysics [COM14c] based on the finite elements method. The main input properties for the materials used in the model are summarized in table 3.1. All other material specific parameters from the equations (3.1), (3.3) and (3.5) are taken from the material library implemented in COMSOL [Mul14b]. Due to the high complexity of the set-up, some simplifications with regard to the heat transport model of the cooling tube including the corresponding cooling liquid are worked out in section 3.3.1. Separating fluid flow and non-isothermal heat transfer from the actual pump port temperature calculation, the simulation of the pump port temperature can then be reduced to a model containing heat transport in solids (conductive heat transfer) and heat transport through radiation. The first and second pump port with parts of the connected beam tubes are calculated separately (sections 3.3.2 and 3.3.4).

3.3.1. Heat transport in the neon and helium cooling tubes

In order to avoid a complicated non-isothermal model coupling, the heat transfer between tube and surrounding cooling tube is calculated separately. This way it is tested, whether the temperature of the cooling liquid changes significantly due to the heat load uptaken. If this is not the case, the temperature at the cooling tube surface can be used as fixed input for the complete set-up. The model contains a test tube of stainless steel (radius = 145 mm, length = 40 cm, width = 2 mm) and the enclosing cooling tube (width = 2 mm) filled with the coolant (liquid nitrogen or gaseous helium). To simulate the heat load coming from the TMP the model contains an additional test surface radiating at high temperature. Due to the geometry of the pump port, this test surface looks different for the nitrogen and helium simulation as can be seen in figure 3.2 a) and b). The temperature of the warm test surface is about 200 K to 320 K for the nitrogen cooling simulation and 80 K to 280 K for the helium simulation.

The velocity and pressure field of the coolant to be simulated needs to be known in order to compute the convective heat transfer correctly (compare equation (3.4)). This calculation, documented in appendix A, is used as an input for the fluid heat transfer calculation². The temperature at the inlet boundary of the cooling tube is fixed at 77 K and 30 K for the nitrogen and helium model, respectively. The heat flux in reverse normal direction $-\vec{n}$ of the flow outlet boundary is set to zero:

$$-\vec{n} \cdot (-k\nabla T) = 0, \quad (3.6)$$

i.e., there is no heat flux entering through this boundary. Using equations (3.1) and (3.3) and the law of conservation of energy, the heat fluxes in the coolant are governed through

$$\rho c_p \vec{v} \cdot \nabla T = \nabla \cdot (k \nabla T) + Q, \quad (3.7)$$

²The first isothermal flow approach is iteratively improved using the temperature distribution obtained from the heat transfer simulation.

Table 3.1.: **Input parameters for temperature simulation in DPS1.** Given are all parameters for the different materials that need to be implemented in the model with ratio of specific heats γ and emissivity ϵ . All other coefficients not given here are taken from the COMSOL material library [Mul14b]. The calculation of the adjusted bellow conductivity, k_0 from [Mul14b], can be found in appendix B.

domain	material	parameter	value
Tubes	steel, polished	ϵ	0.2 ([GN06])
Bellow WGTS beam tube		ϵ	0.2
		k	$k_0 \cdot 0.247$
Bellow 1 st beam tube DPS1-F/ DPS1-R		ϵ	0.2
		k	$k_0 \cdot 0.439$
1st bellow tube to TMP		ϵ	0.2
		k	$k_0 \cdot 0.384$
2nd bellow tube to TMP		ϵ	0.2
		k	$k_0 \cdot 0.4$
Bellow 2 nd beam tube DPS1-F		ϵ	0.2
		k	$k_0 \cdot 0.439$
Bellow 2 nd beam tube DPS1-F		ϵ	0.2
		k	$k_0 \cdot 0.2$
Bellow entrance DPS		ϵ	0.2
		k	$k_0 \cdot 0.162$
Bellow in font of rear wall		ϵ	0.2
		k	$k_0 \cdot 0.23$
TMP rotor	aluminium alloy	ϵ	0.3 [WM02]
Radiation shield	coated copper	ϵ	0.92 [Bay03]
Coolant	nitrogen (liquid)	$c_p(T)$	2.05 kJ kg^{-1} to 2.06 kJ kg^{-1} [Bar99]
		$\mu(T)$	0.141 mPas to 0.158 mPas [Bar99]
		Q_v	199 kg J^{-1} [Eki06]
		$T_b(p)$	79.5 K to 81.8 K ([Hae81])
		γ	1.1 ([Bar99])
Coolant	nitrogen (gas)	γ	1.4 [Bar99]
Coolant	helium (gas)	γ	1.66 [Bar99]

with Q denoting additional heat sources.

Nitrogen cooling

The simulation of the liquid nitrogen cooling contains phase transitions if the nitrogen temperature is above the boiling temperature $T_b(p)$. After the phase transition, which depends on the position along the tube, liquid and gaseous nitrogen are simulated independently. Nitrogen is injected with a temperature of 77 K at a pressure of 1.5 bar. Pressure and velocity distribution of the nitrogen are taken from calculations in appendix A. The resulting temperature distribution of the simulated geometry can be seen in figure 3.2 a). The maximal temperature value of nitrogen when flowing through the cooling tube for the different irradiation temperatures are summarized in table 3.2. The influence of phase change turns out to be negligible, as it only occurs in the last centimetres of the outlet region to a fraction below 10%. The nitrogen cooling works efficiently, as the temperature of the tube surface at the end of the simulated tube is significantly reduced compared to the temperature of the warm test surface. It is close to the nitrogen temperature, as can be seen in table 3.2. Since the nitrogen temperature hardly changes over the length of the cooling tube, using a fixed temperature of 80 K, which is the highest nitrogen temperature obtained in the simulation, seems a valid simplification.

Table 3.2.: **Temperatures from nitrogen coolant simulation.** Given are maximal nitrogen coolant temperature when flowing through the cooling tube T_{\max,N_2} and the maximal temperature of the tube surface at its end T_e for different temperatures T_s of the irradiating test surface.

T_s in K	T_{\max,N_2} in K	T_e in K
200	78.3	78.1
250	78.9	79.7
300	79.5	82.6
320	79.8	84.2

Helium cooling

The helium cooling stage of the pump port uses gaseous helium with an initial temperature of 30 K and an inlet pressure of 5 bar. To test, if the temperature of the helium increase significantly when flowing through the cooling tube, the model used to test the nitrogen cooling is slightly modified – The test surface along the model geometry at one sight is replaced by an extension of the initial tube as can be seen in figure 3.2 b). This tube extension has a fixed temperature between 80 K to 280 K. Pressure and velocity distribution of the helium are taken from calculations in appendix A. The simulated temperature distribution for the modelled geometry for a test surface temperature of 120 K is depicted in figure 3.2. The maximal temperature values of the helium flowing through the cooling tubes are summarized in table 3.3 for different irradiation temperatures of the test surface. For irradiation temperatures below 140 K the helium temperature hardly changes from its inlet value of 30 K. To use a constant, fixed temperature of 30 K along the cooling tube for the actual pump port calculations is again a valid simplification, at least for temperatures below about 140 K. For the demonstrator model described in section 3.3.3, elevated temperatures of the tube adjacent to the helium cooling tube need to be considered since there is no pre-cooling through nitrogen at the radiation shields reducing the heat flux

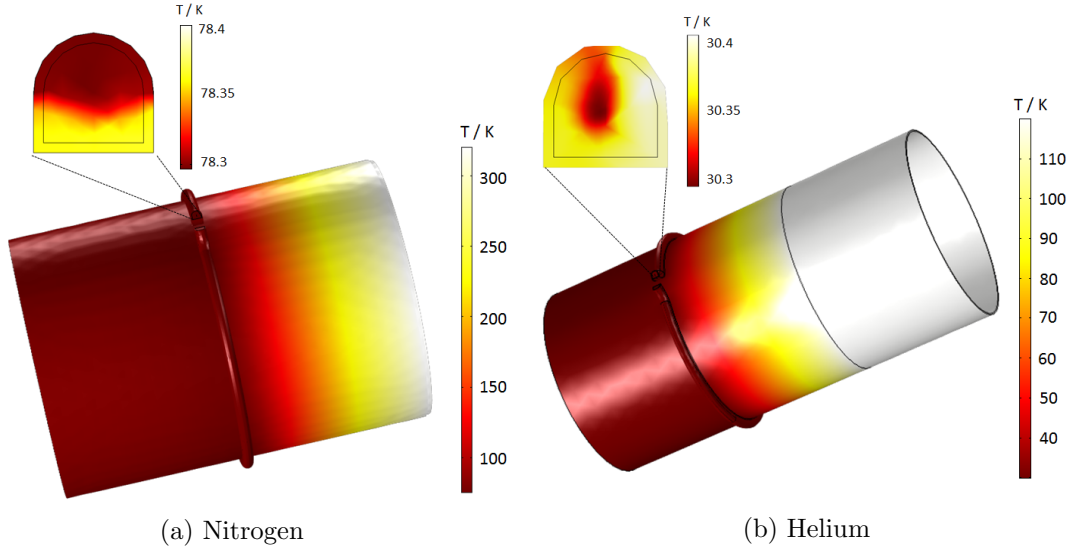


Figure 3.2.: Temperature distribution from N_2 and He coolant simulation The temperature of the irradiating surface is 320 K for N_2 and 80 K for He. Note the different temperature scales for the two simulations.

from the pumps.³ In a pre-simulation the temperature of the tube adjacent to the copper shield turns out to be about 250 K to 280 K. Using such elevated test surface temperatures leads to the helium heating up considerably at some parts. However, the average temperature along the cooling tube remains below 31.5 K as shown in table 3.3. This averaged He-coolant temperature is used for the corresponding demonstrator simulations described in section 3.3.3. The nitrogen and helium coolant simulations reveal that the simulation

Table 3.3.: Temperatures from helium coolant simulation. Given are maximal temperatures for the helium coolant $T_{\max,\text{He}}$ and the wall at the tube end T_e as well as the average temperature \bar{T} along the coolant tube for different temperatures T_s of the irradiating surface.

T_s in K	$T_{\max,\text{He}}$ in K	T_e / K in K	\bar{T}
80	30.3	30.3	30.1
100	30.42	30.5	30.15
120	30.55	30.6	30.2
140	31	30.8	30.22
250	31.9	31.7	30.95
280	32	36.8	31.1

of the actual heat transport processes in the fluid is not necessary within the pump port model. It can be replaced by a fixed and constant surface temperature of the cooling tube. Therefore, in the following just conductive heat transport in the solid pump port material as well as radiative heat transport from all inner surfaces need to be considered.

³This is caused by a malfunction of the former design of the liquid nitrogen supply line [GBSS11]. The radiation shields reached only temperatures of 230 K which means, they are hardly cooled by the nitrogen.

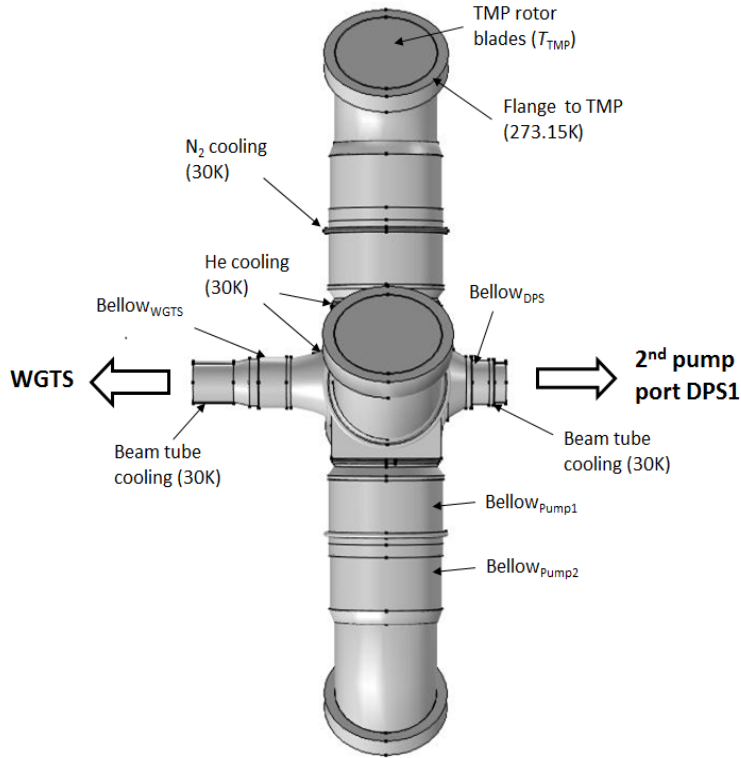


Figure 3.3.: **Set-up of the first pump port model.** Boundaries with fixed temperatures as well as the positions of the different bellows are labelled.

3.3.2. Calculation of heat transport in the first pump port

The pump port model, depicted in figure 3.3, is generated corresponding to the engineering drawings to be found in (appendix...???). It has the same geometry and boundary conditions for front and rear direction (DPS1-F and DPS1-R). The TMP rotor blades that introduce a large heat load into the pump port are represented by flat surfaces with fixed temperature. The position of the TMP is 240 mm withdrawn from the pump connection⁴. The rotor blades are located several centimetres behind the flange to the TMP. While small additional length is not modelled, it should be expected to further reduce the induced heat load due to the lower view factors. The bellows are replaced by simple cylinders with adapted length in order to reduce the number of mesh elements needed to resolve the bellow geometry properly and thereby reduce the required computing resources. The heat transfer coefficients of the bellows are adapted accordingly as calculated in appendix B. The temperature at the surface of the cooling tubes is fixed at 30 K for the gaseous helium and 80 K for liquid nitrogen cooling, as described in section 3.3.1. The end of the WGTS beam tube as well as the onset of the DPS1-F (or DPS1-R respectively) beam tube including the two phase neon cooling tubes at 30 K are included in the model. The temperature of the rotor blades of the TMP, T_{TMP} , determines the main heat load on the pump port. Within the simulations T_{TMP} is varied from 333 K to 393 K. Thus, the effect of rotor temperature on pump port and beam tube end temperature is obtained. A induced temperature difference at these components would influence the gas dynamics of the source significantly and needs to be avoided.

Results for $T_{\text{TMP}} = 333 \text{ K}$

The integrated heat load coming from the rotor blades of the TMP is about 30 W. Due to the kink in direct line of sight of the TMP a large part of the radiation gets reflected

⁴Michael Sturm, personal communication, December 10, 2013

back and forth before it can reach further parts of the pump port. Thus, just one third of the initial radiation load reaches the copper shields. Integrating the adsorbed radiation heat, almost 90% of the initial irradiation is calculated to be absorbed there. This significantly reduces the heat load on the pump port. The conductive heat flux gets reduced by a factor of about three by each of the two bellows (bellow_{pump1} and bellow_{pump2} in figure 3.3). Moreover, the conduction is intercepted by the nitrogen and helium cooling. The temperature on the (rectangular) pump port wall itself does not exceed 31 K and the temperature distribution across the pump port is quite homogeneous, with a maximum deviation smaller than 1 K. Thus, the pump port cooling works efficiently. The temperature distribution at the pump port can be seen in figure 3.4. However, the WGTS beam tube end, about 20 cm before the pump port, gets warmed up to about 33 K, as depicted in figure 3.4a and 3.5 a). This is due to the remaining radiation heat load from the pump port. The WGTS bellow is excluded here. It even gets warmed to a maximal temperature of about 46 K. This effect is further discussed below.

Along the beam tube the temperature depends not only on the longitudinal position, but also on the azimuthal angle ϕ . The maximal temperature difference occurs between 0° (180°), which corresponds to the position of the cooling tubes and 90° (270°). Here, 90° (270°) denotes the maximal azimuthal distance to one of the two cooling tubes. The azimuthal temperature dependence at the main part of the beam tube can be approximated with

$$T(z, \phi) = T(z, 0) + \Delta T_\phi \sin^2(\phi), \quad (3.8)$$

as shown in figure 3.5 b). This approximation is used in section 4.2.3 in order to calculate the gas flow caused by azimuthal temperature differences. The difference ΔT_ϕ is about 0.4 K at the end of the simulated geometry (35 cm before the pump port). It increases to 1.3 K at the end of the beam tube cooling 20 cm before the pump port. However, as the temperature at the beam tube end strongly depends on the bellow geometry and temperature, the actual temperatures is expected to be somewhat lower than the simulation results. As shown in [Höt12], with regard to the Doppler broadening even a unrecognised temperature difference of 2 K along the whole length of the WGTS beam tube would cause a still acceptable systematic neutrino mass shift of 1.6×10^{-3} eV².

Results for $T_{\text{TMP}} = 363$ K

The calculated temperature distribution for a TMP rotor temperature of 363 K is depicted in figure 3.4b. Still 90% of the incoming heat load get absorbed by the radiation shields. Temperatures of the main part of the pump port are comparable to the simulation with lower TMP temperature ($T_{\text{TMP}} = 333$ K) described above. The temperature on the pump port wall still does not exceed 31 K. The warming of the beam tube is slightly enhanced, a maximal temperature, excluding the bellow, of about 34 K is reached. The maximal azimuthal difference at the end of the simulated geometry, 35 cm before the pump port, is 0.45 K, and thus comparable to the $T_{\text{TMP}} = 333$ K simulation described above. This is shown in figure 3.6.

Results for $T_{\text{TMP}} = 393$ K

A rotor blade temperature of 393 K is the limiting temperature for (short time) operation of the TMP. The pump port cooling is still able to absorb the bulk part of the TMP heat load, with the maximal temperature of the pump port reaching 32 K. At the same time, the maximal WGTS central beam tube end temperature is elevated to about 34.5 K, while the WGTS bellow heats up to about 52 K. This effect is further discussed below. The azimuthal difference at the end of the simulated geometry is increased to 0.5 K, as

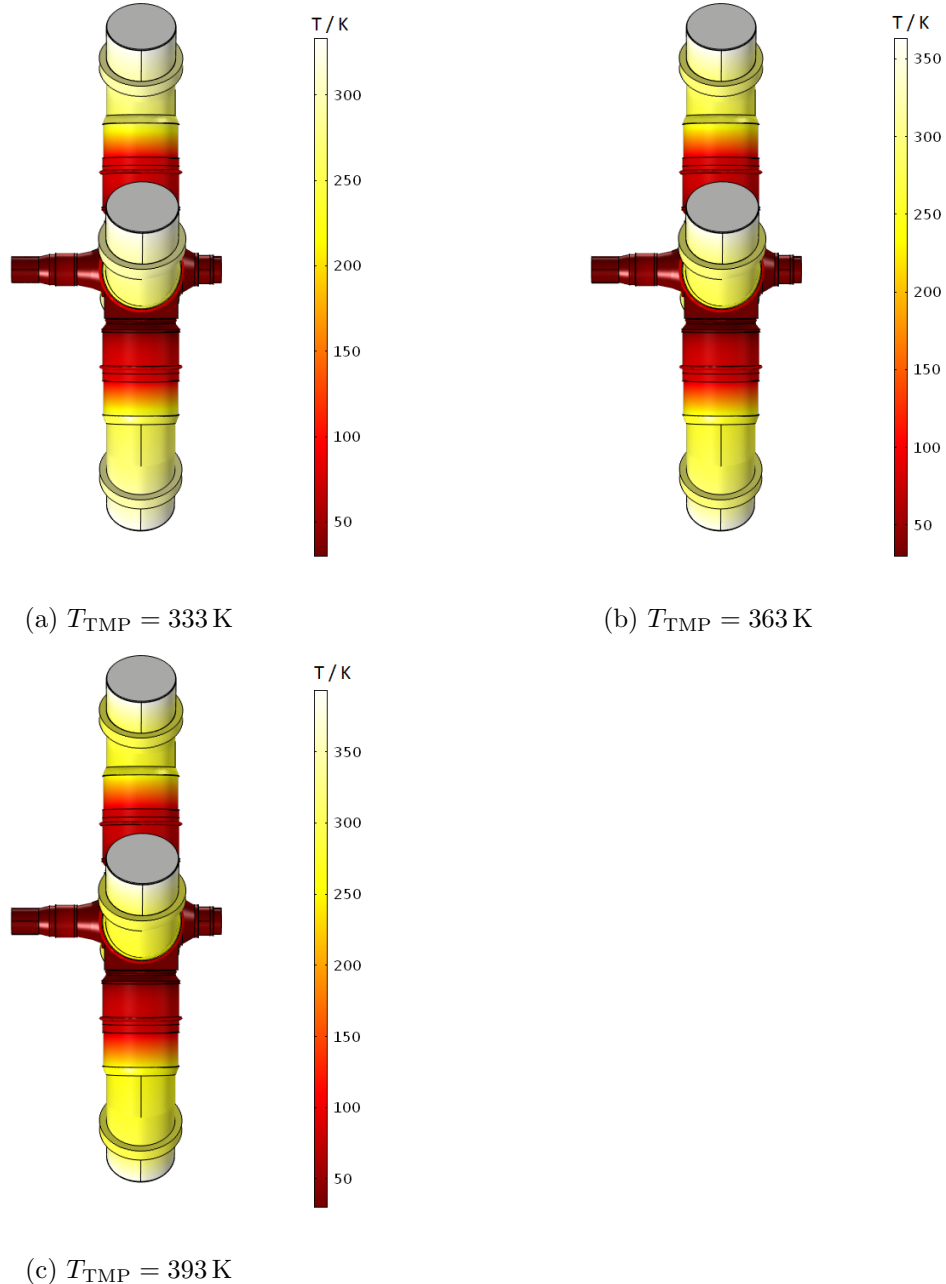


Figure 3.4.: Temperature distribution across the first pump port of DPS1-F and adjacent WGTS beam tube end for different TMP rotor blade temperatures. At the first pump port of DPS1-R the temperature is distributed similarly.

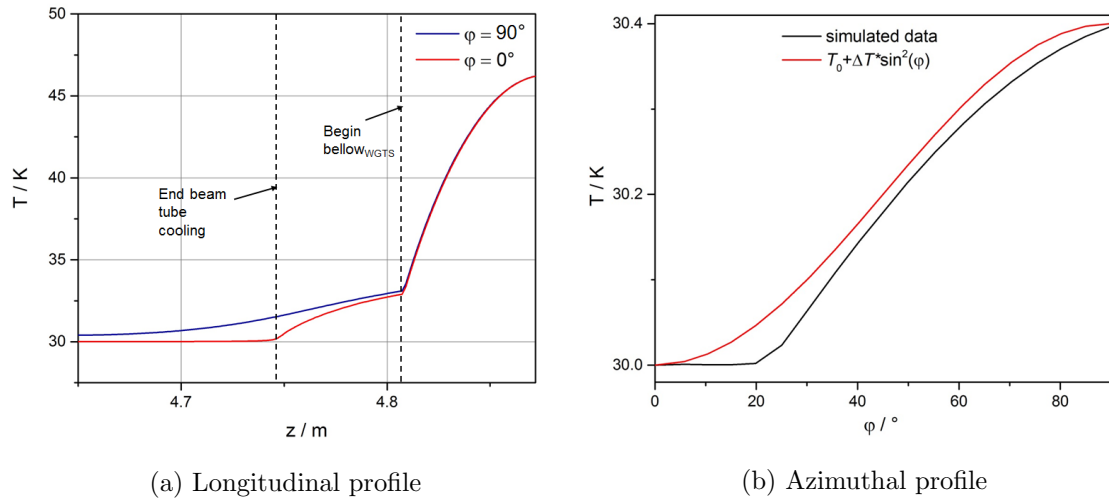


Figure 3.5.: **One-dimensional central WGTS beam tube end temperatures for $T_{\text{TMP}} = 333 \text{ K}$.** In a) the longitudinal temperature dependence is plotted up to the end of the WGTS bellow for different azimuthal positions. b) shows the azimuthal temperature dependence at $z = L_{\text{WGTS}} - 35 \text{ cm}$, which corresponds to the end of the simulated geometry, including the interpolation formula (3.8).

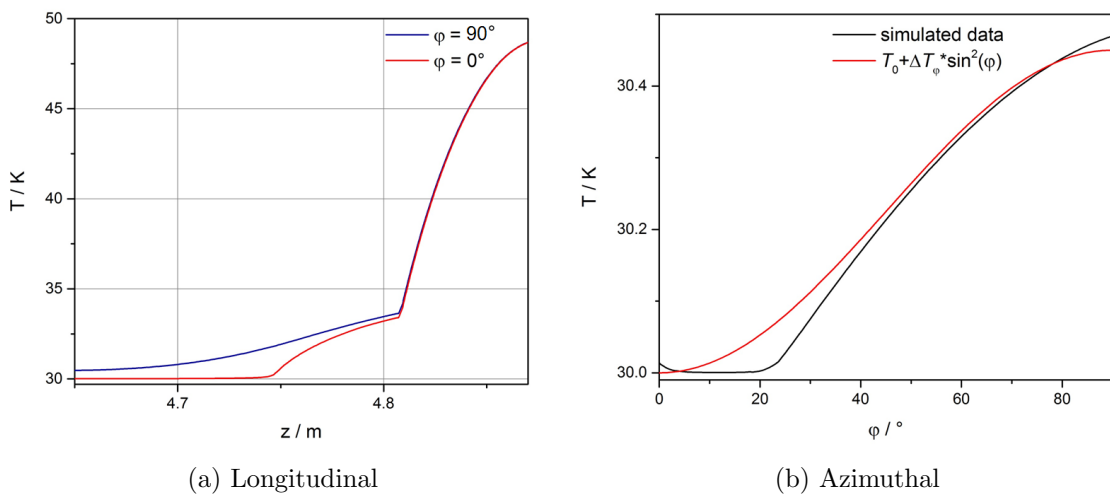


Figure 3.6.: **One-dimensional WGTS central beam tube end temperatures for $T_{\text{TMP}} = 363 \text{ K}$.** In a) the longitudinal temperature dependence is plotted up to the end of the WGTS bellow for different azimuthal positions. b) shows the azimuthal temperature dependence at $z = L_{\text{WGTS}} - 35 \text{ cm}$.

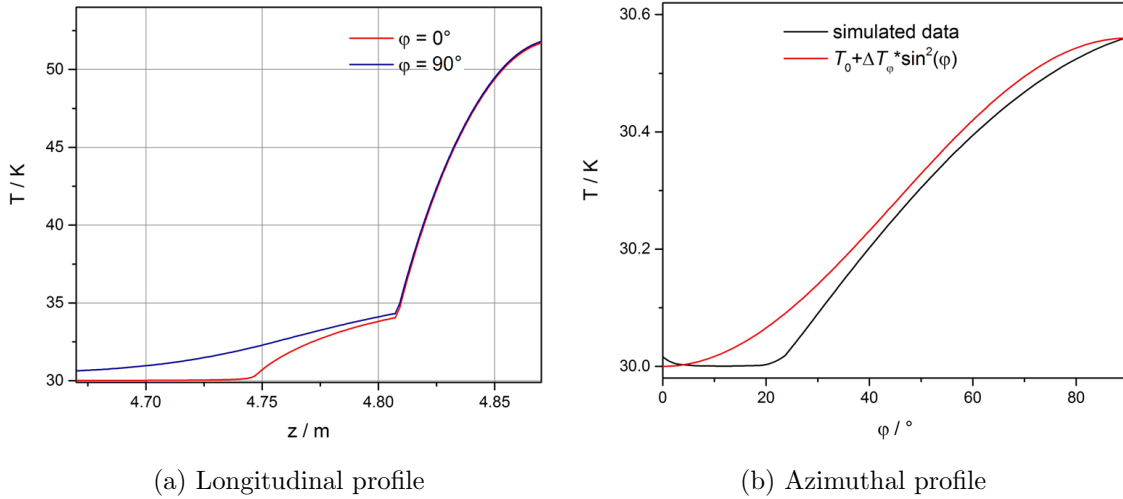


Figure 3.7.: **One-dimensional WGTS central beam tube end temperatures** for $T_{\text{TMP}} = 393 \text{ K}$. In a) the longitudinal temperature dependence is plotted up to the end of the WGTS bellow for different azimuthal positions. b) shows the azimuthal temperature dependence at $z = L_{\text{WGTS}} - 35 \text{ cm}$.

depicted in figure 3.7. The temperature distribution across the whole simulated geometry is depicted in figure 3.4c.

The temperature of the WGTS bellow

The warming of the bellow up to a maximal temperature of 46 K for $T_{\text{TMP}} = 333 \text{ K}$ (48 K for $T_{\text{TMP}} = 363 \text{ K}$ and 52 K for $T_{\text{TMP}} = 393 \text{ K}$) is caused by the radiational head load that reaches the bellow from the TMPs. This is visualised exemplary in figure 3.8b for a rotor blade temperature of 333 K. Four angular regions of maximal irradiation can be identified. These regions of elevated irradiation do form due to the radiation head load from the four molecular pumps. Since the bellows are simplified in the simulation, the heat conductivity is adapted, see table 3.1, to transport the same amount of conductive heat as the component with unsimplified geometry. Therefore, the WGTS bellow conductivity k is reduced by a factor of about four (compare table 2.1). Besides the conductive heat, there is the radiative heat load that is released over the bellow (see figure 3.8b). It cannot be transported out of the bellow that effectively as in the realistic set-up with higher conductivity. The magnitude of this effect is tested simulating the pump port model without adapted WGTS bellow conductivity ($k = k_0$). The temperature of the TMP rotor blades is set to 333 K, 363 K and 393 K as before. The temperature increase of the bellow is significantly reduced, as shown in figure 3.8a for the different rotor blade temperatures⁵. Thus, the temperature uptake of a realistic WGTS bellow is clearly overestimated in the pump port simulation. Since the simulation can provide only an upper limit for the bellow temperature, it needs to be investigated, if an increased bellow temperature has a systematic effect on the neutrino mass measurement.

The temperature of the beam tube and pump port walls influence the temperature of the gas flowing through. This has two effects on the electron spectrum measured with KATRIN. On the one hand it influences the density distribution⁶. On the other hand, an increased

⁵The temperature of the pump port itself hardly changes comparing both WGTS bellow conductivities.

⁶This does hardly cause a systematic effect on the neutrino mass measurement, as the value of the integrated density will be measured. It is thus not based on the gas dynamic simulation that is temperature sensitive, see section 4.5.1.

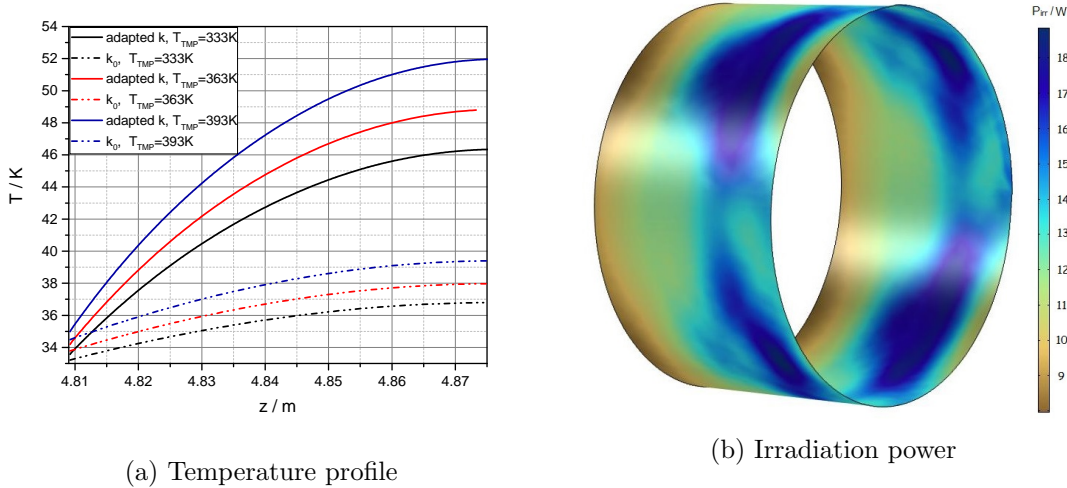


Figure 3.8.: **Temperature and irradiated heat power P_{irr} along the WGTS below.** Simulations are based one a TMP temperature of 333 K. In a) the one-dimensional temperature distribution along the WGTS bellow is shown with adapted (black, $0.25k_0$) and initial heat conductivity (k_0 , red)

gas temperature causes a larger Doppler broadening (the effect is described in 2.4.2.2) of the spectrum of electrons released in this region.

To test the influence of an unrecognised temperature increase along the WGTS bellow on the neutrino mass measurement, KAFIT is used to carry out ensemble simulations (the principle is described in section 2.4.3). The simulated source is segmented into 1000 slices of 1 cm length each. Standard source parameter from table 2.1 are used except for the temperature distribution in the toy measurement – the corresponding source model has an increased WGTS bellow temperature with a maximum of 38 K⁷ and a distribution according to 3.5.

Simulating 4500 KATRIN runs the systematic neutrino mass shift is

$$\Delta m_\nu^2 = (2.6 \pm 2.4) \cdot 10^{-4} \text{ eV}^2 \quad (3.9)$$

which is small compared to other temperature related uncertainties (column density uncertainty from temperature stability, see section 4.7). Thus, limiting the rotor blade temperature below 363 K the increase of WGTS bellow and WGTS beam tube end temperature does not have to be considered further.

In summary, the calculations for the different rotor temperatures show that the pump port temperature does not exceed 32 K. According to the (multiphysics) model, the cooling concept of the pump port is thus validated, even at increased rotor blade temperatures up to the critical operation point of the TMPs. The pump port temperature distribution obtained in the calculations is further used within the gas dynamics calculation for the first pump port in section 4.2.6. The azimuthal temperature difference at the beam tube, induced by the heat load from the pump port and the beam tube cooling, can be approximated with the expression in equation (3.8). At the end of the beam tube cooling, about 20 cm before the pump port, the WGTS beam tube gets warmed slightly by the heat load that is not absorbed by the pump port helium cooling system. Maximal temperatures from 32.5 K to 34 K are reached, depending on the actual rotor blade temperature.

⁷This corresponds to the simulation with $T_{TMP} = 363$ K (see figure 3.8a) which is the limiting temperature for long-term stable TMP operation.

As long as the central WGTS parameter column density, that is closely connected to the temperature, is determined by measurements, the actual temperature distribution affects the neutrino mass analysis only by a changed thermal velocity and gas velocity profile. These velocities influence the β -electron energy through the Doppler effect. In [Höt12] the effect from increased thermal velocity, for a constant temperature shift of 3 K along the WGTS, was tested. The influence on the neutrino mass was found to be small. The temperature shift at the WGTS below from the simulation is larger than the just mentioned 3 K. It was calculated to be about 6 K to 12 K depending on the TMP rotor blade temperature. Though, the impact on the neutrino mass measurement through the larger Doppler broadening was shown to be small for rotor blade temperatures not exceeding 363 K.

3.3.3. Modelling of demonstrator measurement

In order to test the accuracy of the pump port temperature simulation results against actual data, a similar model is built in order to reproduce the conditions of the previous measurements with the demonstrator. A more detailed description of the demonstrator measurements can be found in [GBH⁺13, Höt12, Bod11]. The demonstrator set-up with included WGTS beam tube and first pump port had an overall length of 12 m. It was designed to test the cooling system and the WGTS temperature stability and homogeneity as well as the cool-down procedure prior to magnet manufacturing and full assembly. For this test the pumps had been replaced by blackened blind flanges. The measurements were done with a flange temperature of 300 K. To further emulate the heat load coming from the TMPs, the blind flanges were heated up to 373 K. In the model, the blind flange emissivity is set to 0.8. Due to large impedances on the liquid nitrogen supply tube, the radiation shield was operated at about 230 K instead of the design value of 80 K [GBH⁺13]. This is considered in the model presented here by leaving out the nitrogen cooling. By consequence, the heat load on the helium cooling circuit is significantly increased compared to the previous simulations since there is no pre-cooling through nitrogen. To estimate the temperature of the helium coolant within the cooling tube, a representative temperature for coolant flowing through the test tube in section 3.3.1 has to be defined. In a test simulation with fixed helium tube temperature at 30 K an average value of 220 K is found for the tube surrounding the radiation shield⁸ for a blind flange temperature of 300 K. An elevated blind flange temperature of 373 K results in an average temperature next to the radiation shield of about 280 K. Thus, using the values from table 3.3, the helium temperature of 30 K when entering the cooling tube needs to be increased in the simulation by about 0.95 K to 1.1 K in order to consider the heat load uptaken by the helium coolant. Compared to the simulations in section 3.3.2, the helium coolant tube temperature is increased in the demonstrator model to a value of 31.1 K.

The measured temperatures at the front side of the demonstrator showed a larger deviation from the main beam tube temperature than the rear data. This was probably caused by insufficient heat sinking of the temperature sensor lead [Bod11, GBH⁺13]. On the rear end the additional heat load from the sensors is considerably reduced. Therefore, only data from the demonstrator rear end, that are not biased by a heat load not accounted for in the simulation, are used for comparison.

The resulting temperature distributions at the first pump port for blind flange temperatures T_{flange} of 300 K and 373 K are depicted in figure 3.9. The temperature along the pump port and WGTS beam tube is slightly elevated due to the non-functional liquid nitrogen cooling. The temperature of the radiation shields is increased significantly to about 220 K compared to 80 K with nitrogen cooling. The measured value for the temperature of the radiation shield is about 230 K which is in good agreement with the simulated

⁸This tube corresponds to the test tube in the helium coolant simulation in section 3.3.1.

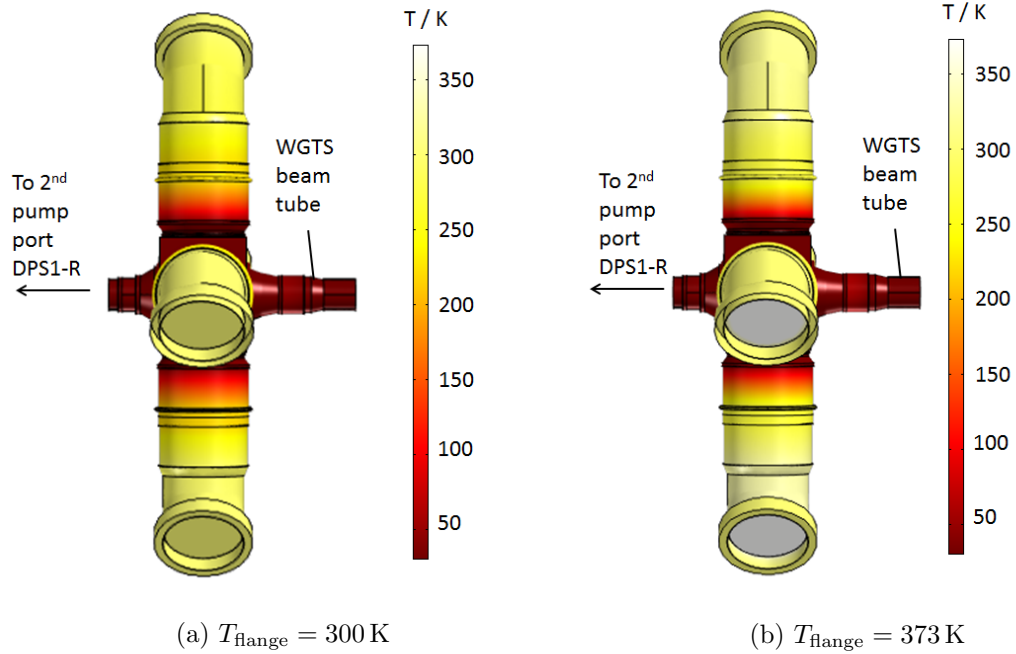


Figure 3.9.: Temperature distribution at the first pump port of DPS1-R for demonstrator model.

value. However, the heat load from the pumps can still be reduced significantly through the gaseous helium cooling. The longitudinal profile at the end of the WGTS beam tube is depicted in figure 3.10 for two azimuthal positions, along and with maximal angular distance to the beam tube cooling. As already seen in the previous simulation results described in section 3.3.2, the WGTS bellow heats up significantly compared to the adjacent tube parts. Table 3.4 compares the simulated temperature at the end of the WGTS beam tube with corresponding measurement data from [GBH⁺13, Höt12]. Since the model ends 35 cm behind the pump port, at $z = -4.6975 \text{ m}$, only data from the last demonstrator sensors, about 25 cm behind the pump port, at $z = 4.76 \text{ m}$, are used for comparison. The simulated values exceed the measured ones significantly for both blind flange temperatures. Looking at the simulated longitudinal temperature profile at the end of the beam tube, the temperature increase at the bellow is again clearly visible. This introduces a further heat load to the connected WGTS tube end and can explain the difference between measured and simulated data. The simulated (232 K) and measured temperature (230 K) of the radiation shield for a blind flange temperature of 300 K agree very well. For the actual pump port temperature, a value of 34 K was measured with elevated flange temperature [GBH⁺13]. The corresponding simulated temperature of about 32.5 K matches again quite well the measured value. The discrepancy of about 5% is mainly caused by the approximated helium flow and helium temperature. Already an increase of 1 K in helium temperature causes the pump port temperature to go up to about 33.4 K. Thus, one can conclude that regarding the uncertainties resulting from the demonstrator measurement set up and especially from the approximations made in the configuration of the simulation, measurement and calculation are in good agreement. Testing just one beam tube position certainly does not allow comprehensive verification of the correctness of the whole simulation. Nevertheless, it indicates that the heat transfer equations in the model are handled correctly and that the simplified geometry parts and the adjusted boundary conditions do not affect the model solution significantly. Hence, the simulated distributions can be used further on as conservative approach within the the gas dynamics model described in

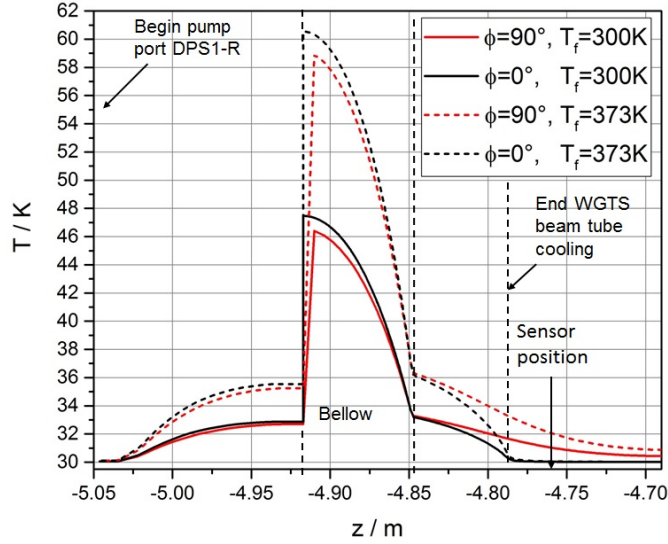


Figure 3.10.: **Temperature distribution at the end of the WGTS beam tube for the demonstrator model.** Results for a flange temperature of 300 K are plotted as solid line, dashed lines correspond to the elevated flange temperature of 373 K. The distribution at an azimuthal angle $\phi = 0^\circ$, where one of the two cooling tube lines the WGTS beam tube, is plotted in black. The temperature distributions for $\phi = 90^\circ$, that corresponds to a maximal distance to the cooling tubes, are plotted in black.

Table 3.4.: **Temperatures from demonstrator measurement compared to simulation.** For various azimuthal ϕ positions of the temperature sensors and TMP flange temperatures T_{flange} , the temperature differences to the mean beam tube temperature of 30 K are given both for the measured data and as obtained from the simulation. The cooling tubes are lining the beam tube at 0° and 180° .

	T_{flange} in K	ϕ in K	$\Delta T(-4.76 \text{ m})$
data	300	90°	0.2
	300	270°	0.1
	373	90°	0.5
	373	270°	0.4
simulation	300	90	1
	373	90	2

section 4.2.

3.3.4. Calculation of heat transport in the second pump port

The temperature of the second pump port of the DPS1 in front and rear direction is needed, on the one hand, as input for the calculation of gas flow through this domain. On the other hand, the calculation of the temperature distribution can be connected to the flow calculation in order to obtain the temperature of the gas at the position of the TMP. Knowing the gas temperature, the pumping speed can be deduced as further described in section 4.2.6. This procedure is not possible for the first pump port of the DPS1 since the gas is not rarefied down to a truly collisionless molecular flow which would enable a full three dimensional gas flow calculation needed for that purpose. Front and rear direction are simulated separately since the geometry and boundary conditions of the adjacent domains (DPS for DPS1-F and rear wall and UV-lamp for DPS1-R, respectively) differ. Notwithstanding, the geometry of the pump port and adjacent beam tubes included in the model are only slightly modified.

Front direction

The model of heat transfer processes in the second pump port in DPS1-F includes the upstream (WGTS direction) and the downstream beam tube that is connected to the DPS. Thus, the effect from radiation coming from the DPS, operating at room temperature, can be included. Since the DPS flange is in direct line of sight, its heat radiation can reach the beam tube further upstream. The effect on the beam tube temperature is tested in the simulation. The beam tube to the DPS is cooled by liquid nitrogen at a temperature of about 80 K. The geometry of the two-fold pump port is similar to the first pump port described above, except that the connections to two pumps are blinded. The TMP rotor blade temperature is fixed at 333 K.

The simulated temperature distribution along pump port and beam tubes is depicted in figure 3.11. The pump port gets warmed to a maximal temperature of 34 K at the blinded outlets. However, due to the reduced heat load with only two TMPs operating instead of four, the warming of the beam tube connected to the pump port is significantly smaller⁹ ($T_{beamtube} < 31$ K) than for the corresponding simulation of the first pump port. Even the maximal temperature of the bellow is below 33 K. Due to the asymmetric irradiation configuration, the form of the azimuthal temperature profile for 0° (beam tube cooling axis) and 90°, shown in figure 3.11, is modified compared to the four-fold pump port model. The warm DPS flange in line of sight with the beam tubes causes a slight temperature increase of about 15 mK at a position 0.5 m behind the pump port (in WGTS direction). At the end of the corresponding beam tube, the temperature rise is limited to about 1 mK. Hence, the heat load from the DPS on the main WGTS beam tube, located at even greater lateral distance, can be neglected.

Rear direction

The model of heat transfer processes in the second pump port of the DPS2-R includes the downstream (WGTS direction) and the upstream beam tube up to the rear wall. Thus, the effect from radiation coming from the warmer rear wall, operated at room temperature, can be included. Compared to the DPS, introducing a heat load on the adjacent DPS1-F, the rear wall has a higher emissivity of about 0.4¹⁰. In the model the influence from UV irradiation of the rear wall is included, since part of the UV light gets reflected at the rear wall and introduces an additional heat load on the system. This way it is tested if the

⁹not considering the bellow temperature

¹⁰Kerstin Schönung, personal communication, November 16th, 2015

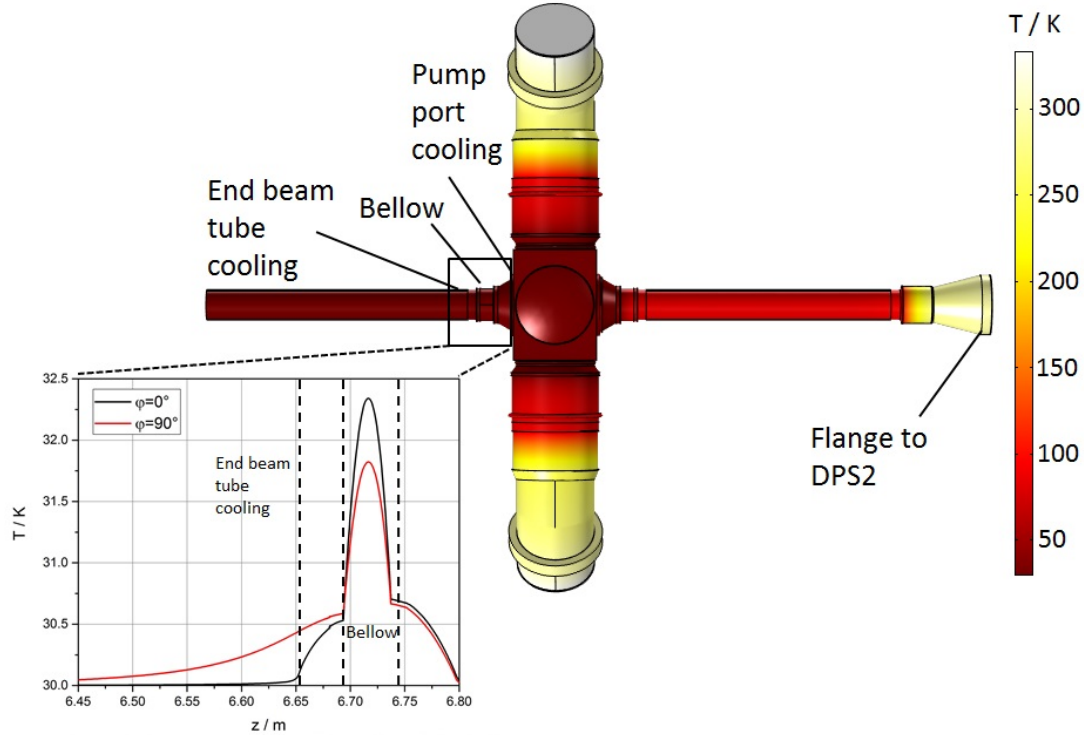


Figure 3.11.: Simulated temperature distribution of the second pump port of DPS1-F.

UV irradiation needs to be limited in power, since the rear wall is in direct line of sight with the WGTS beam tube. Like in the corresponding DPS1-F model, the beam tube connecting second pump port and the subsequent domain, in this case, the rear section, is cooled by liquid nitrogen at a temperature of about 80 K. The geometry of the two-fold pump port itself is similar to the second pump port in the DPS1-F described above. The model is calculated for a TMP rotor blade temperature of 333 K.

The UV lamp produces photons with a wavelength λ around 200 nm [rswg12] with a rate of 1×10^{16} photons/s striking the rear wall¹¹. This corresponds to a radiant power P_λ of

$$P_\lambda = 1 \times 10^{16} \text{ s}^{-1} h \frac{c}{\lambda} \approx 10 \text{ mW} \quad (3.10)$$

arriving at the rear wall. Assuming the UV light impinges on the rear wall with an average angle of 45° , polar and azimuthal angles within the cone are approximated to range from -22.5° to 22.5° . Thus, the solid angle is about 0.46π which corresponds to roughly 20% of the radiated UV power. To have a radiant power of 10 mW at the rear wall surface, the radiation power of the UV surface is set to $\frac{1}{0.2} \cdot 10 \text{ mW}$. The implemented scheme of rear wall and UV irradiation is depicted in figure 3.12.

The simulated temperature along pump port and beam tube is depicted in figure 3.13. It is comparable to the profile of the second pump port in front direction (DPS1-F). The maximal temperature difference between those front and rear results is about 300 mK in the region of the bellow. As in the DPS1-F simulation, the beam tube in WGTS direction does not get warmed by the heat load coming from the rear wall. Already at a distance of 50 cm from the pump port in WGTS direction, the temperature difference to the nominal 30 K beam tube temperature is reduced to 30 mK. Thus, one can conclude that neither the rear wall at room temperature nor the additional heat load from the UV irradiation have a significant influence on the temperature distribution at the WGTS beam tube that is

¹¹Manuel Klein, personal communication, March 14th, 2016

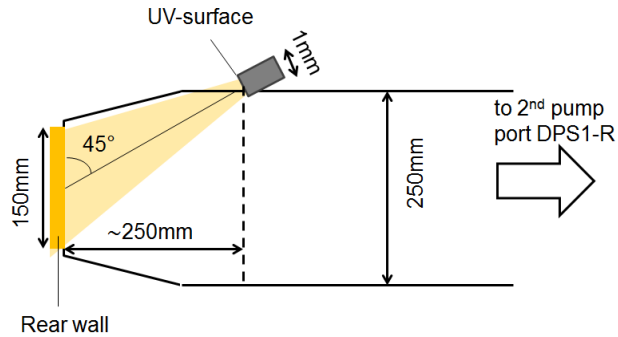


Figure 3.12.: **Schema of rear wall and UV-lamp model.** It is part of the DPS1-R second pump port model.

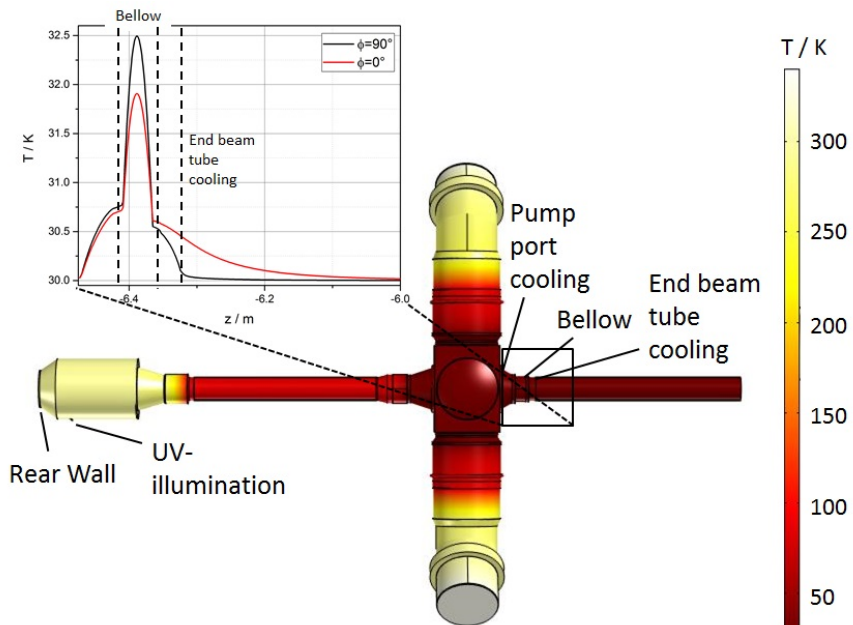


Figure 3.13.: **Temperature distribution second pump port DPS1-R.**

situated in even larger distance than the ports which were investigated by the simulation presented here. The negligible influence of the UV irradiation can be explained by the quite low corresponding heat load. The heat load from the rear wall alone, with reflection effects included, is about 7.7 W. Thus, even an increased irradiation power of 50 mW reaching the rear wall would alter the radiation heat load from the rear wall by less than 1%. Thus, the heat load from the rear section on the main WGTS beam tube does not need to be considered in the WGTS gas model.

3.4. Conclusion

In this chapter, a model of the temperature distribution in the differential pumping sections DPS1-F and DPS1-R adjacent to the tritium source beam tube was presented. The influence of elevated temperatures of the rotor blades of the TMPs, due to the operation in magnetic fields, on pump port and beam tube temperature was investigated. The impact on the pump port temperature itself was shown to be small. The maximum temperature increase was calculated to be about 2 K for the maximum possible rotor blade temperature of 393 K. However, a temperature increase in parts of the WGTS beam tube bellows was

recognised. This is likely to be related to be partially caused by simplifications of parts of the geometry. Referring to the results obtained in section 3.3.2, from a source modelling point of view, the rotor blade temperature should be limited to 363 K in order to reduce the warming of the bellow and WGTS beam tube end region. Since this matches the limiting temperature for long term stable operation given by the manufacturer, in practise, no further restrictions to the rotor blade temperature and shielding of magnetic fields needs to be imposed.

Within the model of the second pump port, the impact of the elevated temperature of the adjacent domains, DPS and rear wall, on the pump port and beam tube temperature was investigated. The effect was found to be negligible with regard to the temperature of the central WGTS beam tube.

The obtained temperature distributions of first and second pump port and adjacent beam tubes are important input values to model the gas dynamics in these domains. This process is described in the following chapter.

To validate the simulation, a model corresponding to the demonstrator set-up was built. Simulated and available measurement data agree quite well with maximal differences of about 5%. This corresponds to a temperature uncertainty of 1.5 K, which does not harm the gas dynamics simulation of the pump port.

4. Characterization of gas dynamics in the Source and Transport Section

Contents

4.1. Column density as a key parameter	90
4.2. Simulation of gas dynamics in the Source and Transport Section	94
4.2.1. Theoretical framework	94
4.2.2. Input parameters for intermolecular and gas surface interaction	100
4.2.3. The gas model framework of the KATRIN source	101
4.2.4. Modelling of end effects in the WGTS beam tube	105
4.2.5. Gas dynamics in the WGTS beam tube – a comparative calculation	106
4.2.6. Modelling of gas flow in the DPS1	110
4.2.6.1. Determination of TMP pumping probability	111
4.2.6.2. First pump port	112
4.2.6.3. Second pump port and adjacent beam tubes	114
4.2.7. Modelling of pump failure in the DPS1	117
4.2.8. The gas model of KATRIN in SSC – current status	118
4.3. Uncertainties of the gas model	120
4.3.1. Model dependent uncertainties	120
4.3.2. Uncertainty related to input parameters	122
4.4. Modelling of column density changes	124
4.4.1. Limits for modelling of column density variation	128
4.5. Experimental determination of the column density	133
4.5.1. Absolute measurements	133
4.5.2. Monitoring measurements	134
4.6. Verifying the gas model – possible test measurements	135
4.7. Gas dynamics and systematic uncertainty of the neutrino mass measurement	137
4.7.1. Neutrino mass uncertainty related to $\Delta(\rho d \cdot \sigma)$	138
4.7.2. Column density versus scattering cross section	138
4.7.3. Effect of density model	139
4.7.4. Combined gas dynamical uncertainty	142
4.8. Summary	143

Inside the source and transport section a large amount of molecular tritium needs to be circulated to provide a high β -decay activity of about $1.7 \times 10^{11} \text{ s}^{-1}$. This requires a large tritium throughput of $1.8 \text{ mbar l s}^{-1}$ and a WGTS injection pressure of about 0.334 Pa . On the other hand, the entering of any tritium into the spectrometer section needs to be prevented. This implies a suppression of tritium flow from the WGTS injection chamber to the pre-spectrometer by 14 orders of magnitude [AAB⁰⁵]. The gas flow and density profile in between needs to be modelled since it can not be determined by measurement. The model allows to calculate the gas reduction factors of the individual components and the amount of tritium entering the CPS. Furthermore, the detailed and accurate description of gas flow and density inside the WGTS is essential to reliably take into account source related effects in the calculation of the electron spectrum for electrons leaving the source. One of these effects is the electron energy loss due to inelastic scattering on gas molecules. The parameter determining this process is the product of two quantities, namely the column density of the gas and the total cross section for electron scattering on molecular tritium. It needs to be known with a trueness of 2×10^{-3} [AAB⁰⁵, Höt12, Ant15]. Thus, a correct modelling of the scattering process requires a precise knowledge of the column density which makes the simulation of the gas flow inside the WGTS indispensable.

The broad range of gas flow regimes, from continuum flow in the injection region in the middle of the WGTS beam tube to molecular flow in the transport section, can only be handled by a comprehensive gas model that simulates the components (beam tubes, pump ports) separately and uses correct boundary conditions to connect the individual calculations. This motivated the extension of the former source gas model, that used the WGTS beam tube calculation only, to a comprehensive, extendible WGTS-DPS gas model within the scope of this thesis.

Emphasis is also placed on the accurate calculation of column density changes. While model and input parameter related uncertainties influencing this calculation are considered thoroughly, it will be shown in this chapter that the gas model can actually be used to update the column density between the monitoring measurements on a sub per-mill level, according to the particular operation conditions, and to decrease the uncertainty estimated in [AAB⁰⁵].

The error budget of the neutrino mass analysis related to the gas dynamical properties of the source is reviewed. Uncertainties from measurements of the absolute column density and from column density variations are considered separately. Furthermore, the actual density and velocity distribution are included in the analysis.

This chapter starts by introducing the key parameter column density and how it is related to the spectrum of β -decay electrons measured at the detector in section 4.1. Next, in section 4.2, the modelling of gas flow from the pressure controlled buffer vessel up to the beginning of the DPS2 as well as the assembly to a full source gas model is described. The uncertainties of the gas model and its components are described in section 4.3. Once the column density is determined, the modelling of column density changes is a crucial point which is further illustrated in section 4.4. How the column density can be accessed experimentally is discussed in section 4.5. Possible test measurements to verify the gas model during the STS commissioning phase are illustrated in section 4.6. In the last part of this chapter, in section 4.7, the impact of uncertainties in the description of gas dynamics and related parameters on the neutrino mass measurement is discussed.

4.1. Column density as a key parameter

The column density is calculated by integrating the gas particle density along the beam tube axis (z -axis). Two different column densities need to be disentangled – the overall gas column density, ρd_{gas} , and the active tritium column density, ρd_{T_2} . The active column density determines the rate of β -decay, while the gas column density determines the

probability for electrons to scatter on gas molecules. The two quantities are related by the tritium purity ϵ_T :

$$\rho d_{T_2} = \epsilon_T \cdot \rho d_{\text{gas}}. \quad (4.1)$$

In the following, the gas column density will be abbreviated with ρd . Neither the gas column density nor the active column density can be determined directly and continuously by an absolute measurement – the column density is always correlated with the total inelastic scattering cross section for electron scattering on tritium molecules as will be discussed below. However, once a reference value is obtained for the column density times scattering cross section, there are different methods to monitor changes in the column densities precisely: beta induced X-ray spectroscopy (BIXS) in the rear section, the forward beam monitor (FBM) in the CPS and the rear section electron gun. They are described briefly in sections 2.3.4 and 4.5.

Increasing the gas column density for constant ϵ_T increases the β -decay rate and decreases the probability P_0 for electrons to leave the source unscattered since the probability $P_i(z)$ of electrons produced at position axial z for i -fold scattering follows a Poisson distribution [ABB⁰⁰]

$$P_i(z) = \frac{(\rho d(z) \cdot \sigma)^i}{i!} e^{-\rho d(z) \cdot \sigma}, \quad (4.2)$$

with total inelastic scattering cross section σ . In equation (4.2) the electron momentum is assumed to be in z -direction. The case of different polar angles is discussed below (see equation (4.6)). The dependence of the scattering process on the gas column density will be exploited to measure the column density, or, better to say, the product of column density and scattering cross section $\rho d \cdot \sigma$. Therefore, monoenergetic electrons will be shot through the source and transport section using an electron gun installed at the rear section. This procedure is described further in section 4.5.1.

The column density does not only influence the spectral shape of the β -decay electrons through the energy loss by scattering, but it also impacts the amplitude of the spectrum through the actual decay rate. To put a limit on fluctuations of the measured rate that cannot be modelled correctly, a stability requirement of 0.2% on the active column density was derived in [AAB⁰⁵] and [Höt12]. Since the (stable) amplitude of the measured β -decay spectrum is used as a fit parameter in the neutrino mass analysis, as described in section 2.4.3, its absolute value does not need to be modelled.

The requirement on the knowledge of the accuracy of the gas column density as well of the product from gas column density and scattering cross section cannot be determined that straight forward and is discussed in the following.

The needed accuracy of $\rho d \cdot \sigma$ is related to the requirement of a precise modelling of energy loss processes due to scattering. The distribution of scattering energy losses ϵ is described by the energy loss function $f(\epsilon) = \frac{1}{\sigma_{\text{in}}} \frac{d\sigma}{d\epsilon}$. The integrated spectrum $\frac{dN}{dt}$, measured at the detector for a given main spectrometer retarding voltage qU , can be calculated by integrating the product of tritium density $n_{T_2}(z)$ and response function $R(E, qUz, \theta)$ over the length L of the gas column¹:

$$\frac{dN}{dt} \propto \int_0^L n_{T_2}(z) \int_0^{E_0} \frac{d^2N}{dtdE} \cdot R(E, qUz, \theta) dEdz. \quad (4.3)$$

With average response function (for an isotropic source)

$$\bar{R}(E, qU) = \frac{1}{\rho d \cdot \epsilon_{T_2} (1 - \cos \theta_{\text{max}})} \int_0^{\theta_{\text{max}}} \int_0^L n(z) R(E, qUz, \theta) \sin \theta d\theta dz \quad (4.4)$$

¹Strictly, the integration would have to be performed over the full length of the transport section. However, since the contributing fraction of the column density after the second pump port of the WGTS is below 5×10^{-4} , only the WGTS length of 16 m needs to be considered.

one obtains

$$\frac{dN}{dt} \propto \rho d_{T_2} \int_0^{E_0} \frac{d^2N}{dt dE} \bar{R}(E, qU) dE. \quad (4.5)$$

The averaged response function $\bar{R}(E, qU)$ does no longer represent electrons produced at a distinct (axial) source position but is an average over all electrons that are produced in the source. Thus, any z dependence in the source parameters (density, temperature,...) gets averaged out. The polar emission angle with respect to the magnetic field lines, θ , enhances the path length due to the electron cyclotron motion around the magnetic field lines (see equation (2.6)) which is considered in the response function. It transforms the column density to an effective quantity:

$$\rho d_{\text{eff}}(\theta) = \frac{1}{\cos(\theta)} \rho d. \quad (4.6)$$

For a normalised, isotropic angular distribution

$$w(\theta) = \frac{1}{(1 - \cos \theta_{\max})} \sin \theta, \quad (4.7)$$

the column density can be averaged:

$$\overline{\rho d}_{\text{eff}} = \frac{1}{1 - \cos(\theta_{\max})} \rho d_{\text{gas}} \int_0^{\theta_{\max}} \frac{\sin(\theta)}{\cos(\theta)} d\theta \approx 1.24 \rho d_{\text{gas}}. \quad (4.8)$$

θ_{\max} denotes the maximal transmitted source emission angle, which is about 51° for electrons starting in a source magnetic field of 3.6 T. The response function, as introduced in section 2.1.2, accounts for the transmission behaviour of the spectrometer, with transmission function $T(E, qU)$, as well as for the energy loss in the source due to scattering. In the following, the finite spectrometer resolution is neglected and the transmission function is simplified by a step like function $T(E, qU) \approx \Theta(qU - E)$. No further dependencies on the polar angle are considered (isotropic source and spectrometer properties). The averaged response function for unscattered electrons can be computed integrating over all possible (scattering) energy losses ϵ .

$$\bar{R}(E, qU) = \int_0^E \Theta((E - \epsilon) - qU) \cdot \bar{P}_0 \cdot \delta(\epsilon) d\epsilon. \quad (4.9)$$

Using the averaged zero scattering probability

$$\bar{P}_0 = \frac{1}{\rho d(1 - \cos \theta_{\max})} \int_0^{\theta_{\max}} \int_0^L n(z) P(z) \sin \theta d\theta dz \quad (4.10)$$

$$= \frac{1}{\rho d(1 - \cos \theta_{\max})} \int_0^{\theta_{\max}} \int_0^{\rho d} P(\rho d_{\text{eff}}) \sin \theta d\theta d\rho d \quad (4.11)$$

$$= \frac{1}{\rho d(1 - \cos \theta_{\max})} \int_0^{\theta_{\max}} \left[e^{-\rho d'_{\text{eff}} \cdot \sigma} \right]_0^{\rho d} \sin \theta d\theta, \quad (4.12)$$

(it is about 0.41 for a standard column density of $5 \times 10^{21} \text{ m}^{-2}$) the averaged response function for unscattered electrons becomes

$$\bar{R}(E, qU) = \Theta(E - qU) \cdot \frac{1}{\rho d \cdot \sigma(1 - \cos \theta_{\max})} \int_0^{\theta_{\max}} \left(1 - e^{-\rho d_{\text{eff}} \cdot \sigma} \right) \sin \theta d\theta. \quad (4.13)$$

This means, the detected rate is dominated by the product of gas column density and total inelastic scattering cross section. The value of the total column density alone as well as the position dependent local column density $\rho d(z)$ is, to first order, not needed in

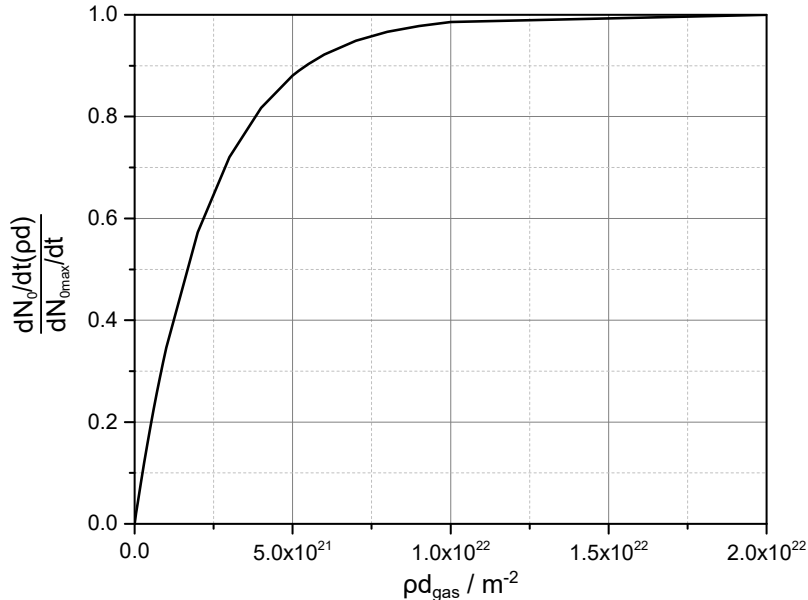


Figure 4.1.: **Rate of unscattered β -decay electrons dN_0/dt in terms of the saturation rate $dN_{0\max}/dt$ as a function of gas column density.** The rate is calculated using the angular average of the effective column density. Here a scattering cross section of $3.4 \times 10^{-22} \text{ m}^2$ from [ABB⁺00] is used.

the analysis of β - decay with KATRIN as the value of the rate amplitude (proportional to the column density) is determined by the fitting procedure. This means, the effect from the density distribution itself only becomes important if local inhomogeneities are present in the source. Such position dependent effects that influence the electron energy are: velocity distribution, temperature distribution, magnetic field inhomogeneities, and electric potential inhomogeneities. To include these second-order effects relevant for a precise description of the β -decay spectrum of the source, the value of the column density alone as well as the density distribution needs to be known. An accuracy requirement was determined for neither of them so far. Previous studies in [AAB⁺05, Höt12, Ant15, Zie13] only consider modifications on either σ or ρd while assuming the other parameter to be known precisely, which is to first order the same as modifying $\sigma \cdot \rho d$. The derived requirement on the accuracy of either column density or total scattering cross section while the other parameter is known precisely is 0.2%. A refined analysis of the influence on the uncertainty of the single parameters while their product is known to the required precision can be found in section 4.7.

The absolute value of the column density can either be obtained from the simulation of gas dynamics or from the measured value of $\rho d \cdot \sigma$ combined with the literature value σ . The gas dynamics simulation as well as the literature value of the total scattering cross section, $\sigma = 3.4 \times 10^{-22} \text{ m}^2$ [ABB⁺00], have relatively large uncertainties compared to the requirement on the product $\rho d \cdot \sigma$ as further specified in section 4.3. How this influences the neutrino mass uncertainty is further investigated in section 4.7 where the dependence on the uncertainty of the density distribution $n(z)$ (or column density distribution $\rho d(z)$) is analysed too.

The rate of unscattered β -decay electrons increases with increasing column density (for constant ϵ_{T_2}). Due to the increasing probability for scattering it saturates for $\rho d_{T_2} \rightarrow \infty$ as to be seen in figure 4.1. This saturation rate of electrons was used to define the column density working point of $5 \times 10^{21} \text{ m}^{-2}$ for the KATRIN neutrino mass measurements. This value corresponds to about 90% of the maximal rate, which is a compromise between high signal rate and reasonable low tritium throughput.

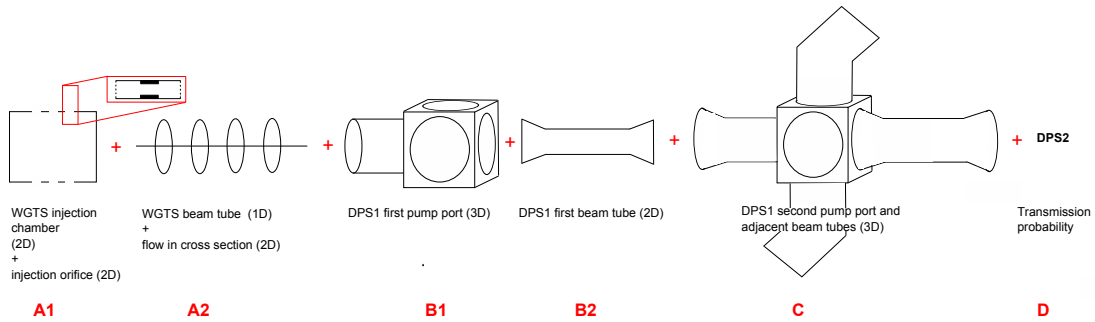


Figure 4.2.: Scheme of simulated WGTS and DPS sections and the corresponding dimensionality of gas dynamic simulation.

4.2. Simulation of gas dynamics in the Source and Transport Section

For an accurate modelling of the spectrum of β -decay electrons leaving the source towards the detector, one of the most important parameters is the product of gas column density and total scattering cross section that determines the probabilities for scattering, as discussed in the previous section. Secondary effects like the velocity distribution and source inhomogeneities of the source magnetic field, plasma potential or temperature can only be included, if the density distribution of the gas is known². Furthermore, changes in column density due to varying operation parameters of the source and transport section, like pressure in the buffer vessel or beam tube temperature, have to be calculated accurately by the gas model. To simulate the gas flow in the whole KATRIN source and transport section that covers the viscous as well as the transitional and the free molecular pressure regime (see figure 4.3), a closed calculation through the whole set-up is not possible. The different pressure regimes as well as the complex geometry of the pump ports require an intricate modelling and numerical approaches to solve the transport equation which is quite demanding in terms of computational resources. Therefore, the calculation is split and some parts are broken down to two- or even one-dimensional sections. The individual parts and their geometric representation are summarised in figure 4.2.

At the outset of this thesis project, the gas model comprised of only one component – the central WGTS beam tube, as summarised in section 4.2.3. To respect all relevant tritium-containing parts, at least those components containing more than 0.05% of the total column density need to be included in the gas model. This means that the density distributions in the DPS1-F and DPS1-R and adjacent beam tubes need to be added. The former structure of the gas model is adapted to be able to include the gas flow through further components and to consider refined calculations of fractions of single components.

4.2.1. Theoretical framework

This section gives a brief introduction into theoretical concepts and central parameters of gas dynamics calculations.

The transport of a gas can be described statistically by the kinetic Boltzmann equation using the distribution function $f(\vec{r}, \vec{v}, t)$ giving the probability to find a particle with velocity \vec{v} at position \vec{r} at time t

$$f(\vec{r}, \vec{v}, t) = \frac{d^6 N}{d^3 \vec{r} d^3 \vec{v}}. \quad (4.14)$$

²The tritium density is obtained weighting the overall gas density with the tritium purity. Separation effects due to different isotope masses can be neglected for the different hydrogen isotopologues and the tritium purity can be assumed to be constant along the length of the WGTS [SK05].

This one particle distribution function is used to describe a large number of gas particles in a macroscopic volume. In the absence of external forces and only considering binary collisions the Boltzmann equation reads [SS98]:

$$\frac{\delta f}{\delta t} + \vec{v} \cdot \frac{\delta f}{\delta \vec{r}} = Q(f, f^*). \quad (4.15)$$

The collisions between two gas particles with distribution functions f and f^* is described by the collision integral $Q(f, f^*)$. It is a complex function of the molecular properties of the colliding particles and their intermolecular potential. Therefore, equation (4.15) can only be solved numerically for some simple cases [SS98]. To solve equation (4.15) analytically, the collision integral needs to be simplified. The methods used in the gas flow calculations presented in this chapter are briefly introduced below.

Depending on the level of rarefaction of a vacuum system, the collision integral may not have to be taken into account at all. The rarefaction is described by the Knudsen number Kn , which is the molecular mean free path l of a gas particle in a volume with characteristic dimension d :

$$Kn = \frac{l}{d}. \quad (4.16)$$

Since it is not appropriate to describe non-equilibrium phenomena in gases with the microscopic quantity l , an equivalent free path λ should be used [Sha16], which is a macroscopic variable:

$$\lambda = \frac{\eta v_m}{p}, \quad (4.17)$$

with gas viscosity η , pressure p and most probable molecular speed v_m . Using this parameter, the gas rarefaction can be characterised by the rarefaction parameter δ :

$$\delta = \frac{d}{\lambda} = \frac{dp}{\eta v_m}. \quad (4.18)$$

The Knudsen number can in general be assumed as the inverse of the rarefaction parameter. Partitioning the gas flow regimes in terms of the rarefaction parameter typically results in three regimes:

- $\delta \gg 1$: hydrodynamic or continuum regime; gas flow can be described by continuum mechanics.
- $\delta \ll 1$: free molecular regime; intermolecular collisions can be neglected
- $\delta \approx 1$: transitional regime; cannot be described by continuum mechanics, intermolecular collisions are not negligible, Boltzmann equation needs to be solved.

The source and transport section of KATRIN covers all three regimes, starting from the gas injection in the hydrodynamic regime over the transition regime around the first pump port in the DPS1 to the free molecular regime at the second pump port of the DPS1, as visualised in figure 4.3.

Which approach is suitable to calculate the gas flow in a certain domain depends on the rarefaction parameter. In the following the methods used in the different gas dynamics calculations that are implemented in the KATRIN gas model are described.

Test Particle Monte Carlo Method (TPMC)

The test particle method can be used to calculate gas flow reduction factors in the free molecular regime. It was introduced by Davis in 1960 [Dav60]. TPMC can be used to calculate molecular flow in a rather complicated geometry with a large number of surface interactions [Bir78]. The interaction between particles can be neglected and single particle

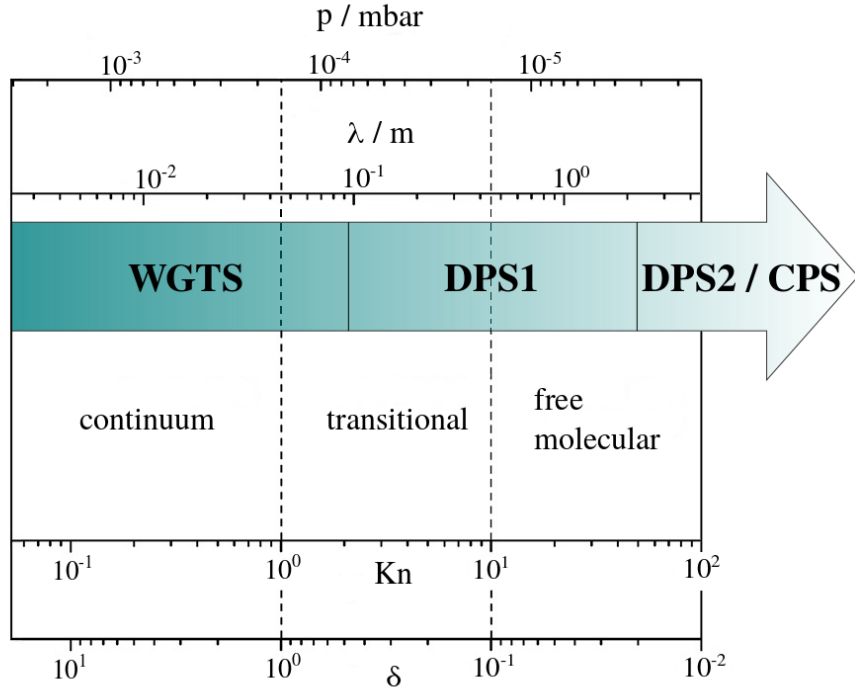


Figure 4.3.: **Range of rarefaction parameter δ and Knudsen number Kn in the source and transport section.** Associated rarefaction regimes, corresponding pressure p and mean free path λ for standard KATRIN measurement conditions are plotted additionally.

tracks can be calculated independently from each other. A particle is tracked until it reaches either an outlet surface or until it is pumped away. Only the wall interaction needs to be considered by a proper interaction term that depends on the adsorption properties (sticking coefficient) of the particular surface material. Particles that have adsorbed at a surface are desorbed again with a pre-defined angular distribution. The incoming particles are generated randomly with a given mean velocity and temperature at the so-called control surface at one side of the geometry. Using a large enough number of test particles and comparing the number of initial particles to particles that pass through the geometry, the reduction factor of the simulated component can be calculated. This method was applied in [Jan15] using the MOLFLOW+ code [AK14] to calculate the reduction factor of the DPS2-F. Results from this computation are used in this work in the modelling of the second pump port of the DPS1-F.

Angular coefficient method

Like the TPMC method, the angular coefficient only considers particle interactions with the walls. Therefore, it can be used to calculate gas flow in the free molecular regime. The model geometry is divided in small subsurfaces. Then the N different subsurfaces are related to each other calculating the angle under which the surfaces see each other. This is shown for two subsurfaces F_1 and F_2 in figure 4.4. For small enough subsurfaces the molecular particle flux, Φ_i reaching surface i from the N different surfaces j in distance r_{ij} can be calculated with [KP09]:

$$\Phi_i = \sum_{j=1}^N \frac{\theta_i \theta_j}{\pi r_{ij}^2} A_i \Phi_j, \quad (4.19)$$

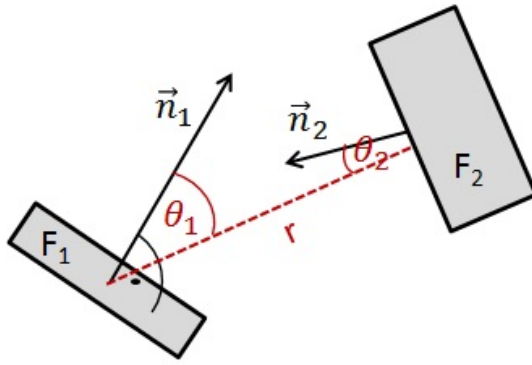


Figure 4.4.: **Scheme of angular coefficient method.** The probability that a particle coming from surface F_1 reaches F_2 is related to the angle between both surface normals in the centre of the surfaces. .

with A_i denoting the surface area of surface i and θ_i (θ_j) the angle between surface normal \vec{n}_i (\vec{n}_j) and the connection line between both surface centres. The different angles and view factor can be summarised in an angular coefficient matrix C_{ij} and the incident flux gets

$$\Phi_i = \sum_{j=1}^N C_{ij} \Phi_j, \quad (4.20)$$

where Φ_j denotes the flux emitted from the surface j . Equation (4.19) is only valid for total particle accommodation at the surfaces (sticking coefficient $s = 1$) – all particles get adsorbed and desorb again diffusely (no absorption, no reflection). In general, equation (4.19) can be modified to account for sticking coefficients different from one.

In the calculation of the gas flow in second pump ports of the DPS1-F and DPS1-R as well as in the adjacent beam tubes in the direction of flow this method is applied, see section 4.2.6. In these simulations only total accommodation can be assumed ($s = 1$).

The angular coefficient method can be used to calculate stationary gas flows in relatively complicated geometries with stationary boundaries. The computing time, $\Delta t_{\text{solution}}$, depends on the number of surface elements: $\Delta t_{\text{solution}} \propto N^2$ [KP09]. It is generally much faster than using the TPMC method [Oss97].

Direct Simulation Monte Carlo (DSMC)

If the mean free path for a particle in a dilute gas comes in the region of the geometry diameter, the particle-particle interactions need to be considered additionally to the wall interactions. This corresponds to gas flow in the transition regime. To simulate flow in this regime the DSMC method can be used. Here the model geometry is divided into a network of cells of relatively small size (the gas flow properties should hardly change through a single cell). A large number of particles is distributed over the model region. Each model particle stands for a certain number of real particles. Then each model particle is moved along a straight line in a time step Δt . The path length is determined according to its initial velocity and flow direction. If its trajectory hits a wall, a surface interaction (like in TPMC) is generated. After the particles have been moved, a representative number of collisions is generated. In DSMC the particle collisions are generated stochastically according to a given distribution function [AG97]. This distribution function $f^M(v)$ is usually a global Maxwellian, with molecular velocity v , which means, ...“No macroscopic motion of one portion of the gas relatively to another” [Sha16]:

$$f^M(v) = n \left(\frac{m}{2\pi k_B T} \right)^{3/2} e^{-\frac{mv^2}{2k_B T}}. \quad (4.21)$$

After the post scattering velocities have been computed, the macroscopic quantities like density, bulk velocity or mass flux can be calculated as they are moments from the distribution function [Son07]. This procedure is repeated up to stationary state. For the calculation of averages of the macroscopic quantities, the simulation needs to be continued [Sha16].

To reduce the statistical scatter of the results, a large number of particles should be generated, as the noise scales inversely with the number of generated particles squared. However, the uncertainty from statistical scatter depends not only on the number of generated particles, but also on physical parameters (pressure drop, temperature...). Therefore, it needs to be evaluated again for each simulated model [Sha16]. For high Mach numbers³, a relatively low number of model particles needs to be generated to reach a low noise level [Sha16, RK09]. The thermal velocity fluctuations that influence the statistical scatter scale with the sound velocity [RK09]. The DSMC method gets inaccurate, as soon as these fluctuations approach range of the bulk velocity, which is the case for low Mach numbers.

The DSMC method is used to calculate the flow in the first pump port of the DPS1-F and DPS1-R, as the gas is in the transition regime in these domains. The modelling is further discussed in section 4.2.6.

Model equations

The so-called model equations simplify the scattering term in the Boltzmann equation (4.15) and make it possible to obtain an approximate solution. First model equations that satisfy the main properties of the Boltzmann equation were proposed in [BGK54] and [Wel54] in 1954. Up to now many different models have been developed. The models used most often [LXSC16] are the BGK model, proposed by Bhatnagar, Gross and Krook [BGK54] and independently by Welander [Wel54], and the S-model, proposed by Sharkov [Sha68].

BGK equation

If the gas molecules that collide with each other are distributed according to a local Maxwellian (f_{loc}^M)⁴, the collision integral $Q(f, f^*)$ from (4.15) can be simplified to [Son07, Sha16]:

$$Q = \nu(f_{\text{loc}}^M - f) \quad \text{with:} \quad f_{\text{loc}}^M(t, \vec{r}, \vec{v}) = \frac{n(\vec{r})}{(\sqrt{\pi}v_m)^3} e^{-\frac{(\vec{v}(\vec{r}) - \vec{u}(\vec{r}))^2}{v_m^2}}, \quad (4.22)$$

with the gas-particle collision frequency ν , most probable molecular speed v_m and bulk velocity u . The BGK model has the shortcoming of not being capable of providing the correct transport coefficients, viscosity η and heat conductivity κ at the same time, see [Sha16, SS98]. Therefore, the BGK model is inappropriate for the description of heat transfer, which needs to be included in the calculation of non-isothermal flow. Depending on the temperature and pressure gradients driving the flow, the results obtained with the BGK model can be off by as much as 30% for the calculation of non-isothermal flow [KBA06]. However, it can be used to model isothermal flow reliably [Sha07].

The BGK equation is used for the calculation of the comparative WGTS beam tube model, presented in section 4.2.5 as well as for parts of the gas flow calculations in the DPS1-F/DPS1-R in section 4.2.6.

³The Mach number is the ratio of bulk gas velocity and speed of sound in the gas.

⁴This does not mean the distribution function of the gas itself, f , is Maxwellian like in equation (4.21) which would mean a global Maxwellian.

S-Model

The S-model forms a variation of the BGK model that gives the correct viscosity and the correct heat conductivity at the same time. The collision integral is given in the following form [SS98]:

$$Q(f, f^*) = \frac{p}{\eta} \left(f_{\text{loc}}^{\text{M}} \left[\frac{2m}{15n(k_B T)^2} \vec{q}(\vec{v} - \vec{u}) \left(\frac{m(\vec{v} - \vec{u})^2}{2k_B T} - \frac{5}{2} \right) \right] - f(\vec{r}, \vec{v}, t) \right). \quad (4.23)$$

Here \vec{q} denotes the heat flux through the gas. The S-model has the disadvantage that the so called H-theorem, an inequality, derived from the entropy balance equation, can neither be proved nor disproved. This can lead to unphysical results [Sha16]. It can however be applied to calculate non-isothermal flows [Sha07].

In the KATRIN gas model this method is used to calculate the non-isothermal flow through the central WGTS beam tube, described in section 4.2.3.

Discrete Velocity method

The discrete velocity method represents the most widely used method to solve the Boltzmann equation and the above presented model equations [Sha16]. The idea is to replace the continuous velocity values by a finite set of nodes. Thus, the velocity distribution function becomes:

$$f(\vec{r}, \vec{v}_i, t) = f_i(\vec{r}, t) \quad (4.24)$$

and the integro-differential kinetic equation is replaced by a set of differential equations for the distribution functions $f_i(\vec{r}, t)$. After choosing some discretisation for the molecular velocity \vec{v} , the moments become quadratures with weights w_i of velocity nodes i . This means, the moments of a function $\Psi(\vec{v})$ with respect to the molecular velocity \vec{v} , e.g. for example the number density or the bulk velocity [Son07], can be approximated with the help of the quadrature

$$\int \Psi(\vec{v}) f(\vec{r}, \vec{v}) d\vec{v} \approx \sum_i \Psi(v_i) f_i(\vec{r}) w_i. \quad (4.25)$$

The number of discrete velocities required to model the gas flow correctly strongly depends on the degree of rarefaction – the more dilute the gas, the higher the required number of velocity nodes [GG15]. For two-dimensional flow, results from different quadratures are compared to the exact solution of the linearised BGK equation in [SBYS11]. Up to a Knudsen number of 1 a quadrature with 36 velocities (D2Q36) gives an error below about 2%. Increasing the Knudsen number to 2, the error increases to about 7 to 8%. The error for a larger quadrature (D2Q64) at this Knudsen number is only about 4 to 5%.

The discrete velocity method is used to solve the kinetic equations obtained with the S-model for the calculation of gas flow in the central WGTS beam tube in section 4.2.3, as well as for the calculation using the BGK equation in the comparative gas flow model of the WGTS beam tube in section 4.2.5.

Linearisation of the Boltzmann equation

If the velocity distribution function is near the equilibrium distribution, small deviations can be expressed in terms of a dimensionless perturbation parameter. Then, the Boltzmann equations, or the model equation, can be linearised with respect to this perturbation parameter.

There are different kinds of linearisations: the linearisation of the global or the local distribution function, or the linearisation of boundary conditions. When the global distribution

function is linearised, it is expressed in terms of a small perturbation ψ with perturbation function $h(\vec{r}, \vec{v}, t)$ and equilibrium distribution function f_0^M [Sha16]:

$$f(\vec{r}, \vec{v}, t) = f_0^M(1 + \psi h((\vec{r}, \vec{v}, t))). \quad (4.26)$$

This linearisation can significantly simplify the problem.

It is applied in the solution of the model equations for the calculation of the gas flow in the WGTS beam tube in section 4.2.3 and section 4.2.5.

Gas surface interaction

A relatively simple, but widely used assumption describing the gas-surface interaction [FY04] is the so-called *cosine-law* derived by Knudsen [Knu09a]. The probability dP for a molecule to leave the wall with a solid angle $d\omega$ at an angle θ to the boundary normal is

$$dP = \frac{d\omega}{\pi} \cos \theta. \quad (4.27)$$

The velocities of the leaving molecules are distributed according to a Maxwellian distribution with the temperature of the wall. This means, the scattered molecule has lost all information on its initial state. The diffuse scattering model was refined by Maxwell [Max90]. He assumed that a fraction α of the impinging molecules leaves the wall according to the cosine law from equation (4.27) and $(1 - \alpha)$ of the molecules are reflected specularly. If the particle is reflected, the absolute value of its velocity is not changed. α is the so-called accommodation coefficient and depends on the surface conditions, the gas species and the gas and surface temperature.

In the case of a thermomolecular pressure difference, where a gas flow is generated by a temperature gradient, the experimental results do not agree with the Maxwell model [SS98, SGM13]. A more complex description of the gas surface interaction was derived by Cercignani and Lampis in [CL71]. In their model the tangential and normal motion with respect to the wall are distinguished and two accommodation coefficients are used: the normal accommodation coefficient α_n and the tangential accommodation coefficient α_t .

The Cercignani-Lampis model is used to describe the gas surface interactions in the WGTS central beam tube and in the first pump port of the DPS1. Total accommodation is assumed for the comparative WGTS beam tube calculation as well as for the flow modelling in the second pump port and adjacent beam tubes in the DPS1.

4.2.2. Input parameters for intermolecular and gas surface interaction

To convert the rarefaction parameter that is used in the dimensionless calculation of gas flow to actual densities or pressures, the inter particle behaviour needs to be included properly. For this purpose, the viscosity can be used. For molecular tritium the viscosity η_{T_2} has not been measured, but it can be inferred from hydrogen or deuterium viscosity using their mass ratio. Below the relation is exemplarily given for deuterium and hydrogen, but can be exchanged with other hydrogen isotopes [AMW87]:

$$\frac{\eta_{D_2}}{\eta_{H_2}} \left(\frac{m_{H_2}}{m_{D_2}} \right)^{1/2} \approx 1. \quad (4.28)$$

This scaling is only valid for temperatures above 300 K [AMW87]; for low temperatures the effect of different spins needs to be considered. For 30 K the discrepancy between measured and calculated D_2 viscosity (using equation (4.28)) at 30 K is about 7% as determined in [AMW86] and [AMW87]. From the measurement of the molecular deuterium viscosity, the tritium viscosity can be inferred using the T_2 - D_2 mass ratio in equation (4.28). This value

still needs to be corrected for the overestimation not considering the spin-effects with a factor of 0.95 to $\eta_{T_2} = 2.425 \times 10^{-6}$ Pa.s. The resulting uncertainty on η_{T_2} is discussed in section 4.3.2.

To include the gas surface interaction discussed in the previous section, the accommodation coefficient α needs to be known. It can be calculated from the viscous slip coefficient $\sigma_p = \sigma_p(\alpha)$ [Sha04b] and the thermal slip coefficient σ_T . It depends on the molecular mass of the gas particles, on the surface roughness of the material (α increases with increasing roughness) [PSBA74, TL74], on surface contamination (a clean surface has a lower α [SS74, Shi75]), as well as on temperature. The temperature dependence is not clear and most experimental studies are done close to room temperature. However, simulations in [CCG05] showed an exponential decay of α with increasing temperature. Measured data of α for most gases are in the range from 0.86 to 0.97 [AP08]. In a recent measurement of α for helium on stainless steel, which constitutes the WGTS and DPS beam tube material, a value of 0.91 was found [HNPM⁺12]. Because of the low temperature and the amount of adsorbed tritium at the cold WGTS beam tube surface, it seems appropriate to assume full accommodation, that is, $\alpha = 1$. The uncertainty on column density caused by not well known accommodation coefficient is further discussed in section 4.3.2.

4.2.3. The gas model framework of the KATRIN source

The gas model of the source and transport section defines the density distribution as well as the temperature and bulk velocity distribution in the tritium containing parts of KATRIN. It is implemented in the framework of the source spectrum calculation software SSC, introduced in section 2.4.2.

The gas model preceding the present dissertation project consisted of calculations of gas flow in one WGTS component only – the central 10 m beam tube. The model included computations for longitudinal and azimuthal temperature inhomogeneities of this element as well. Inlet and outlet density distributions for the injection region and the last 20 cm before the first pump ports in rear and front direction were calculated [PVS11] separately, but not implemented in the KATRIN gas model.

The 10 m beam tube gas model is based on three WGTS operation parameter values:

1. The injection pressure. Actually the pressure averaged over the beam tube cross section with radius R at $z = 0$ m is used:

$$p_{\text{in}} = \frac{1}{2\pi R^2} \int_0^R \int_0^{2\pi} p(z = 0, r, \phi) r dr d\phi. \quad (4.29)$$

Instead of the inlet pressure, the column density measured with the rear section e-gun can be used as input parameter.

2. The beam tube exit pressure. It is similar to the pressure in the first pump port of the DPS1.
3. The temperature distribution on the WGTS beam tube walls.

Below, the procedure used in the model to calculate density and velocity distributions is explained. The principle was worked out by F. Sharipov [Sha03, Sha04a, Sha09, Shr10] and implemented in SSC by W. Käfer [Käf12] and M. Hötzl [Höt12].

One-dimensional WGTS beam tube modelling

The bulk of the total column density (more than 98%) is situated in the central 10 m WGTS beam tube. Therefore, the calculation of the gas flow through this domain needs to be as accurate as possible. Temperature non-uniformity and inlet and outlet effects are considered here more carefully than in the simulation of the other parts of the source

system. Because of the large length-to-radius ratio of about 100 for front and rear part each, an one-dimensional fully developed flow⁵ approach is suitable for the main part of the tube (region A2 in figure 4.2) to reduce complexity. Inlet and outlet regions need to be modelled separately in two and three dimensions (regions A1 and B1 in figure 4.2) as their flow profiles deviate from the fully developed case. For the one-dimensional main beam tube calculation the method described in [Sha97] and [SS98] is used. Dimensionless gradients are defined

$$\text{for pressure: } \xi_p = \frac{r}{p} \frac{dp}{dz}, \quad (4.30)$$

$$\text{and temperature: } \xi_T = \frac{r}{T} \frac{dT}{dz}. \quad (4.31)$$

The mass flow rate \dot{M} , with

$$\dot{M} = \frac{Q\pi r^2 p}{v_m}, \quad (4.32)$$

can be represented in terms of the reduced flow rate Q which, for small gradients, can be written as:

$$Q = G_P(\delta)\xi_p + G_T(\delta)\xi_T. \quad (4.33)$$

Using the dimensionless Poiseuille and thermal creep flow rates $G_P(\delta)$ and $G_T(\delta)$ the mass flow reads:

$$\dot{M} = \frac{\pi R^3}{v_m} \left(-G_P(\delta) \frac{dp}{dz} + G_T(\delta) \frac{p(z)}{T(z)} \frac{dT}{dz} \right). \quad (4.34)$$

Inserting the global Poiseuille coefficient $G = \frac{1}{\delta_{\text{in}} - \delta_{\text{out}}} \int_{\delta_{\text{in}}}^{\delta_{\text{out}}} G_p(\delta) d\delta$ it becomes:

$$\dot{M} = \frac{\pi R^3}{v_m} \left(-G \frac{\delta_{\text{in}} - \delta_{\text{out}}}{L} + G_T(\delta) \frac{p(z)}{T(z)} \frac{dT}{dz} \right). \quad (4.35)$$

The values for $G_P(\delta)$ and $G_T(\delta)$ are taken from literature [SS98, SS94]. They were calculated solving the linearised Boltzmann equation using the simplified S-model scattering kernel, see section 4.2.1. The calculation of the density distribution can be simplified with the help of an interpolation formula

$$G_p = \frac{8}{3\sqrt{\pi}} \cdot (1 + 0.04\delta^{0.7}) \cdot \frac{\ln(\delta)}{1 + 0.78\delta^{0.8}} + \left(\frac{\delta}{4} + \sigma_p \right) \cdot \frac{\delta}{1 + \delta} \quad (4.36)$$

$$G_T = \left(\frac{4}{3\pi} + 2.8\delta + 2\sigma_T\delta^2 \right) \cdot \frac{1}{1 + 6\delta + 6\delta^2 + 2\delta^3}. \quad (4.37)$$

It includes the gas-surface interaction through the viscous slip coefficient $\sigma_p = \left(\frac{2-\alpha}{\alpha} \right) \cdot (1.018 - 0.1211 \cdot (1 - \alpha))$ [Loy68, SS98], and the temperature slip coefficient $\sigma_T = 1.175$ [Sha04b]. To get the pressure distribution $p(z)$ or equally the density distribution $n(z)$, both are connected through $p(z) = n(z)k_B T(z)$ [Sha03], boundary conditions for inlet pressure, outlet pressure and temperature have to be defined. Then, the pressure distribution can be calculated from (4.35) applying a finite difference scheme as used in [Sha96, Sha97, SS98]. If the column density instead of the inlet pressure is given as input value, the described procedure is executed iteratively adapting the inlet pressure until the calculated column density converges to the given one. The density distribution calculated with this gas model for standard KATRIN operation parameters ($p_{\text{in}} = 0.337 \text{ Pa}$, $T = 30 \text{ K}$, $p_{\text{out}} = 0.02p_{\text{in}}$) is shown along with the end effect calculations in figure 4.8.

⁵Fully developed flow is characterised by a parabolic velocity profile in the cross section of a pipe and zero velocity gradient in the direction of flow.

Three-dimensional modelling

The above given one-dimensional profile is only valid in case of a constant temperature in the tube cross sections. Azimuthal temperature gradients cause radial and azimuthal flows and thus change the density profile. The beam tube cooling is achieved via two adjacent cooling pipes (see figure 2.8). Thus, the wall parts that are not touched by the cooling tubes can get heated to a small extent. The largest temperature differences arise at angular positions that are 90° shifted with respect to the cooling tubes. Connecting azimuthal and longitudinal temperature profiles, the WGTS wall temperature profile $T(\phi, z)$ can be approximated with:

$$T(\phi, z) = T(z) + \Delta T(z) \sin^2(\phi), \quad (4.38)$$

see section 3.3. Assuming small pressure and temperature gradients, longitudinal (described above) and azimuthal flow can be calculated separately.

The cross sectional flow computation by F. Sharipov was performed on the basis of the linearised Boltzmann equation using the S-model, according to the method described in [Sha09]. With increasing rarefaction parameter the relative density deviation scaled with the relative temperature deviation increases as shown in figure 4.5b. But then, to get the relative density deviation for the WGTS, the calculations from [Sha09] need to be multiplied by the relative temperature deviation. In the calculations shown in figure 4.5a and 4.5b the temperature distribution determined during the demonstrator measurements [GBH⁺13] is used. It shows a maximal temperature difference of 1 K over the last 0.5 m of the WGTS beam tube. The temperature deviation is minimal in the middle of the WGTS, therefore the slope of the relative density deviation changes as to be seen in figure 4.5b. Calculating the deviations in the total WGTS column density from the one-dimensional model one gets an average of approximately 0.15% for not considering the temperature dependent radial and azimuthal density changes. This would almost deplete the error budget of 0.2%. With regard to the analysis procedure, temperature gradients necessitate a pixel-wise analysis to be able to resolve and model the cross sectional density differences. From a modelling point of view it is possible to correct for any given temperature profile (with reasonable low temperature gradients) using the described precalculated cross sectional distributions for different $\delta = \delta(z)$.

Velocity distribution

The bulk velocity $u_z(\vec{r})$ of the gas can be calculated as a moment from the distribution function f [Son07]:

$$u_z(\vec{r}) = \frac{1}{n(\vec{r})} \int_{-\infty}^{\infty} \int_{-\infty}^{\infty} \int_{-\infty}^{\infty} f(\vec{r}, \vec{v}) v_z d\vec{v}, \quad (4.39)$$

with molecular velocity \vec{v} and particle density n . As the gas is flowing in z -direction, the azimuthal and radial bulk velocity components are small with the exception of the inlet and outlet regions and are not considered here⁶. The velocity distribution function of the 10 m WGTS beam tube was calculated on the basis of the S-model linearised kinetic equation in [Sha09].

In the KATRIN gas model the parabolic shape of the bulk velocity profile in a cross section, which forms the basis for the fully developed flow assumption, is used to describe its radial distribution. Its dependence on the longitudinal position z can be parametrised in terms of two coefficients, $a(\delta)$, and $c(\delta)$, since $\delta(z)$ is known from the one-dimensional density

⁶The cross sectional velocity in the main part of the beam tube due to azimuthal temperature gradients was calculated in [Sha09] to be smaller than 0.33 m s^{-1} even for a large azimuthal temperature difference of 3 K.

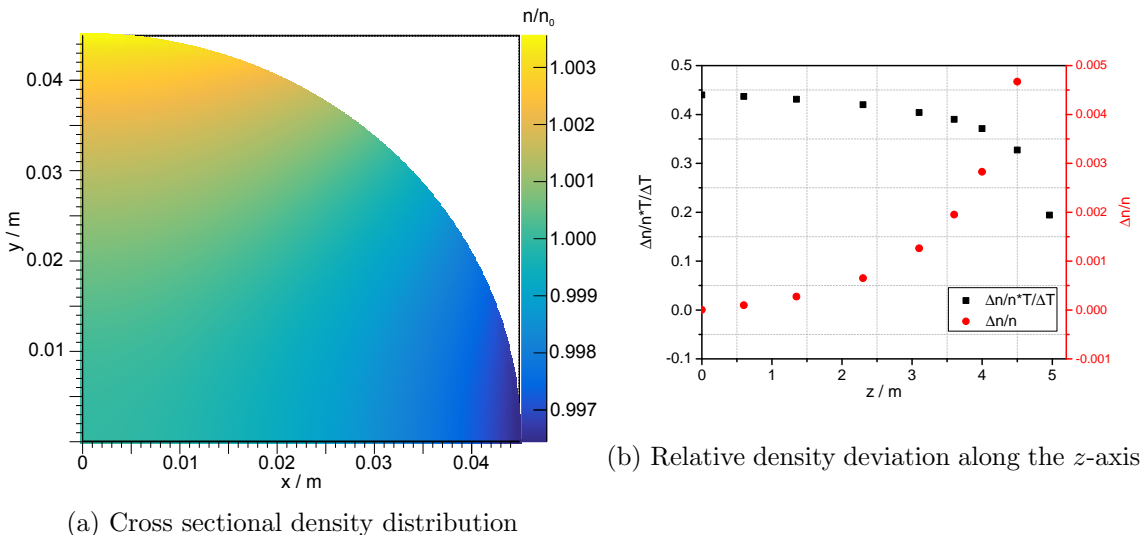


Figure 4.5.: **Density distributions in case of an azimuthal flow and longitudinal and azimuthal temperature gradients.** In the gas flow simulation the temperature distribution from equation (3.8) with $\Delta T = 1\text{ K}$ is used. a) shows the relative density of one quadrant of a WGTS beam tube cross section at $z = 3.6\text{ m}$ compared to density from the one-dimensional calculation. In b) the maximal relative density difference (1D and 3D calculation) for different positions along the z axis are depicted. Red circles without scaling and in black squares with scaling with the relative temperature deviation. Note the different axes for both cases. Data are calculated using the gas model as implemented in SSC.

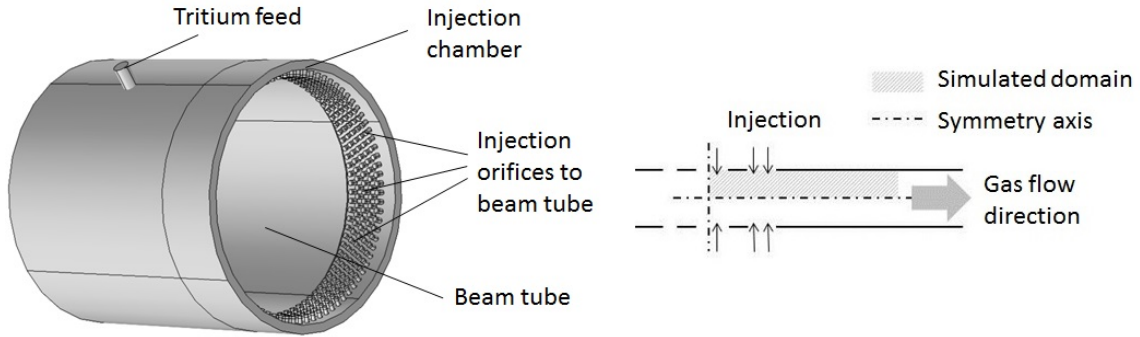


Figure 4.6.: **Injection chamber surrounding the WGTS beam tube in the centre with feed capillary and injection orifices.** The two-dimensional sketch in the right part illustrates the domain for the gas flow simulation.

calculation.

$$u_z(z, r, \phi) = -v_m \frac{R}{p(z)} \frac{dp(z)}{dz} \left(a(\delta) - c(\delta) \left(\frac{r}{R} \right)^2 \right), \quad (4.40)$$

Here v_m denotes the most probable molecular speed, which is about 288 m s^{-1} for a gas temperature of 30 K . The interpolation formulas for $a(\delta)$ and $c(\delta)$ are obtained from the calculated velocity distribution function and can be found in [Höt12] and [Sha09].

At the beginning of this thesis project, the SSC gas model, as described above, consisted of the WGTS central beam tube calculations only. Neither effects from the gas injection into the WGTS and the gas exit to the first pump port nor the density distribution in the adjacent WGTS components were included. Accommodation and viscosity coefficients were fixed in the calculation.

To account for the above mentioned facts the gas model is extended as part of the present work. Results from the simulations that are either required for the model extension or are used to verify its results are presented in the following sections 4.2.4–4.2.7. An overview of the extended SSC gas model is given subsequently in 4.2.8.

4.2.4. Modelling of end effects in the WGTS beam tube

Deviations from the one-dimensional fully developed flow occur in the inlet and outlet regions of the WGTS central beam tube, where the gas flow develops two- and three-dimensional characteristics. Since the influence of these deviations is only local, they can be corrected for still using an one-dimensional model. End corrections for the WGTS central beam tube flow are calculated in [PVS11] using a two dimensional model of 40 cm length for the inlet region (A1 in figure 4.2), and of 20 cm length for the outlet region. The geometry of the injection chamber, shown in the left part of figure 4.6, is far too complicated for a full three-dimensional gas flow modelling. Therefore, the simplified two-dimensional geometry in the right part of figure 4.6 is used in the simulation. The resulting pressure distribution in the inlet region is shown in figure 4.7a. Distributions from the modelling of the outlet region can be found in [PVS11] and [Höt12].

In- and outlet simulations were performed for fixed WGTS input parameters injection pressure p_{in} , and temperature T . For the results to be used in the SSC gas model, the input parameters need to be adjustable. Therefore, an end effect correction has to be implemented in the one-dimensional beam tube model. It is based on a correction ΔL of the tube length L that is replaced by an effective length L_{eff} with $L_{\text{eff}} = L + \Delta L$. This concept works for inlet as well as for outlet effects. Mass flow rate \dot{M} and Poiseuille

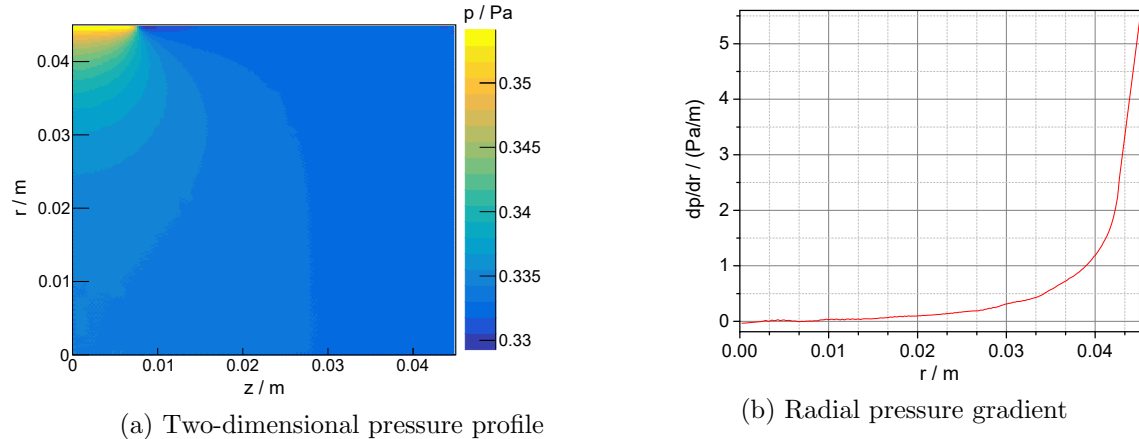


Figure 4.7.: Two dimensional pressure profile and one-dimensional pressure gradient for the WGTS inlet region. The disturbances in the two dimensional pressure distribution in a) are caused by the injection. They are smeared out in radial direction approximately 25 mm after the injection. Here the bulk flow pressure value $p(z)$ is reached. This is verified by the radial pressure gradient at $z = 0$ depicted in b). The derivative approaches zero in a radial distance to the injection of 20 mm.

coefficient G are corrected accordingly:

$$G = \frac{L}{L + \Delta L_{\text{in}} + \Delta L_{\text{out}} \cdot (\delta_{\text{in}} - \delta_{\text{out}})} \int_{\delta_{\text{in}}}^{\delta_{\text{out}}} G_p(\delta) d\delta. \quad (4.41)$$

The method is described in more detail in [SS98, PVS13, PVS14]. The inlet and outlet length corrections for the WGTS are calculated from the two-dimensional flow results in [PVS11]: $\Delta L_{\text{out}} \approx 4.4 \text{ cm}$ for the outlet and $\Delta L_{\text{in}} \approx 8 \text{ cm}$ for the inlet. The method to derive the corrections is given in [PVS13]. The WGTS end corrections reveal an uncertainty of the uncorrected one-dimensional throughput and mass flow value of about 5%. At just about 1%, the corresponding deviation of the one-dimensional column density is somewhat smaller, since inlet and outlet end effect cancel each other in parts, as can be seen in figure 4.8. The WGTS end corrections are implemented in the one-dimensional SSC gas model calculations. By applying these corrections, the column density modelling uncertainty (due to outlet effects) further decreases to 0.4%.

The pressure in the injection chamber surrounding the WGTS beam tube in the injection region was calculated in a separate simulation of the flow through an injection orifice in [Shr10] to be 1.8 times the average beam tube inlet pressure p_{in} .

4.2.5. Gas dynamics in the WGTS beam tube – a comparative calculation

The one-dimensional gas flow calculation in the central WGTS beam tube is crucial to model its gas density distribution, the column density and column density changes correctly. To get a reliable estimate on the model-dependent uncertainty of the calculations described above, a comparative two-dimensional beam tube gas model was set up.

The model is built using the *Rarefied flow* module [COM14a] of the COMSOL Multiphysics software suite [COM14c]. In the following, the newly developed, comparative beam tube model is denoted as the "COMSOL gas model" while the prior beam tube gas model, discussed in section 4.2.3, is called the "Sharipov model".

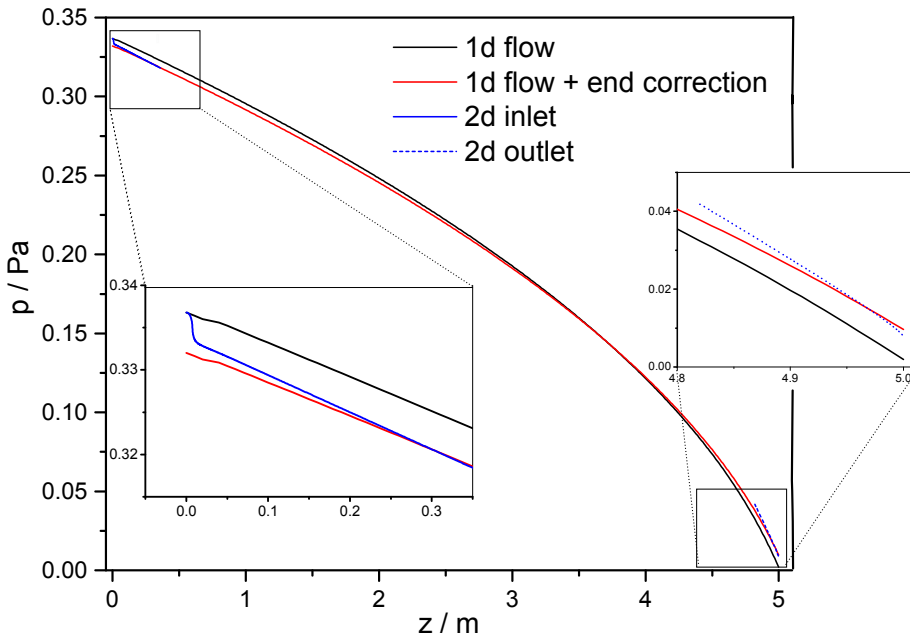


Figure 4.8.: **Pressure distribution on the WGTS beam tube axis with and without considering end effects.** The 1D calculation without considering inlet or outlet effects is plotted in black. The end effect corrected distribution is plotted in red. The cross sectional averaged pressure from the two-dimensional inlet and outlet calculation is shown in blue.

The COMSOL model geometry is depicted in figure 4.9⁷ The length of the simulated model is 10.082 m⁸ and includes the small difference in the length of the front and rear part of the beam tube present in the WGTS geometry. Gas inlets are defined by three injection boundaries in the middle of the beam tube with a width of 3.6 mm each and arranged in a distance of 3.6 mm to each other. An outlet is defined at the rear side at $z = -5.0745$ m and at the front side at $z = 5.0075$ m. .

In the COMSOL model, like in the Sharipov model, the Boltzmann equation is solved with the help of a kinetic equation. This time the BGK equation is used instead of the more complicated S-model. Since the BGK equation is suitable for correct handling of thermomolecular pressure gradients, which means non-isothermal flow, the beam tube temperature is assumed to be constant at $T(z) = 30$ K. The velocity distribution function is calculated using the discrete velocity method. It is discretised in terms of Hermite polynomials by a Gauss-Hermite quadrature. The formalism is based on the method derived in [SYC06]. A two-dimensional quadrature with 36 discrete velocity distribution functions (D2Q36 quadrature) is used. The model geometry is meshed by small triangles with a maximal element size of 8 mm in the main part of the geometry. In the injection region, at $-10 \text{ cm} < z < 10 \text{ cm}$, and in the outlet region, 10 cm before the outlet at front and rear side, smaller mesh elements with a maximal size of 2 mm are used. This results in a total number of 180 000 mesh elements.

In a first simulation, the outlet pressure boundary condition is defined as a total vacuum condition, i.e., the flux emitted from this boundary is zero. This assumption is in general only valid for highly rarefied gas ($Kn > 10$, see [COM14a]). Since the gas at the end of the central beam tube still has a Knudsen number of about 1 to 2 [Sha03], the total vacuum

⁷In the experimental set-up, gas is injected through small orifices that are arranged in five rings (see figure 4.6). In [PVS11] WGTS gas densities were calculated for inlet geometries with one and with three injection boundaries, respectively. The difference in the bulk density distribution as well as in the column density between both inlet configurations was found to be negligible.

⁸This length was taken from the technical drawings of the WGTS beam tube.

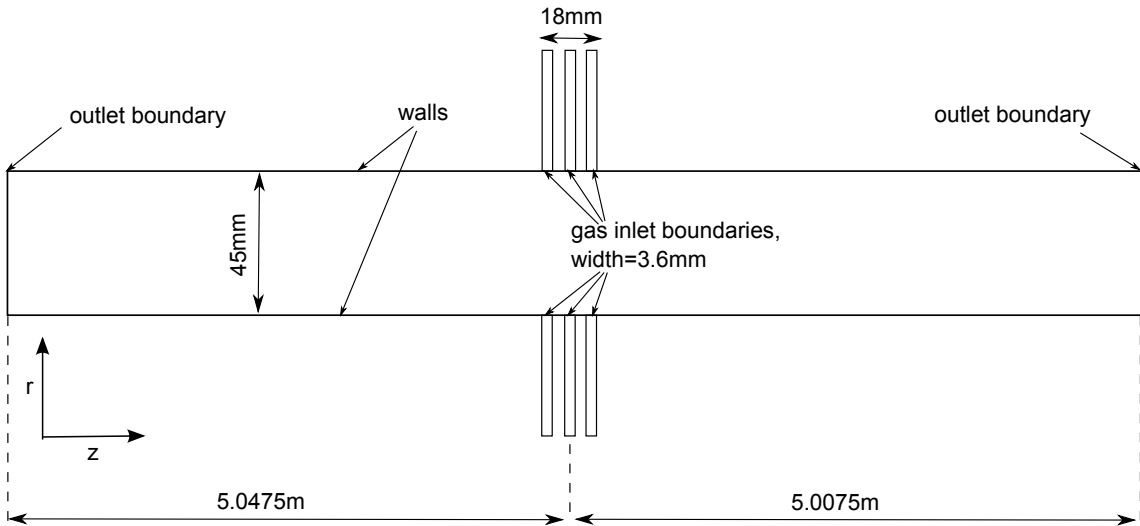


Figure 4.9.: **Schema of the two-dimensional COMSOL beam tube model.** Gas is injected to the inlet boundaries in the centre and leaves the model through the outlet boundaries.

boundary condition is actually not suitable. Thus, the outlet pressure obtained from the initial simulation is used as a pressure outlet boundary condition in a second simulation. The same method was also applied in the Sharipov model [Sha03, SK05, Shr10]. The simulation time for both outlet configurations is about 6 h to 7 h each. The two-dimensional density distribution is depicted in figure 4.10.

The ratio of outlet to inlet pressure obtained from the presented total vacuum simulation is about 0.07 and thus a factor of 1-2 larger than the value obtained in the beam tube simulations by F. Sharipov. To compare both simulations, the same boundary conditions need to be used. Here the difference between the pressure at the injection boundary, used in the presented COMSOL simulation, and the average inlet pressure from equation (4.29), used in the one-dimensional calculations by F. Sharipov, needs to be considered. For a pressure of 0.38 Pa at the inlet boundary an average inlet pressure p_{in} of 0.334 Pa is calculated from the two-dimensional COMSOL model results. To compare the one- and two-dimensional distributions, an average density distribution, $n(z)$, is calculated from the two-dimensional result $n(r, z)$:

$$n(z) = \frac{1}{0.045 \text{ m}} \int_0^R n(r, z) dr. \quad (4.42)$$

Differences in the number density for different radii exceed 0.1% only for the inlet and outlet regions. This verifies the approximation of fully-developed flow adopted in the Sharipov model.

The one-dimensional density distributions along the beam tube axis for both models are depicted in figure 4.11. Excluding the last metre in front of the outlets, the distributions from both models agree within 5%. Since the discrepancy increases with increasing rarefaction it is probably caused by the finite velocity quadrature that shows a similar uncertainty behaviour for increased rarefaction. In spite of the relatively large deviations in the density distributions, the difference in column density is below 1%, since the density difference changes sign along the beam tube. This agrees with the model-dependent column density uncertainty of about 1% stated in [Sha03], which will be further discussed in section 4.3.1.

The influence of the different density distributions on the simulated electron spectrum

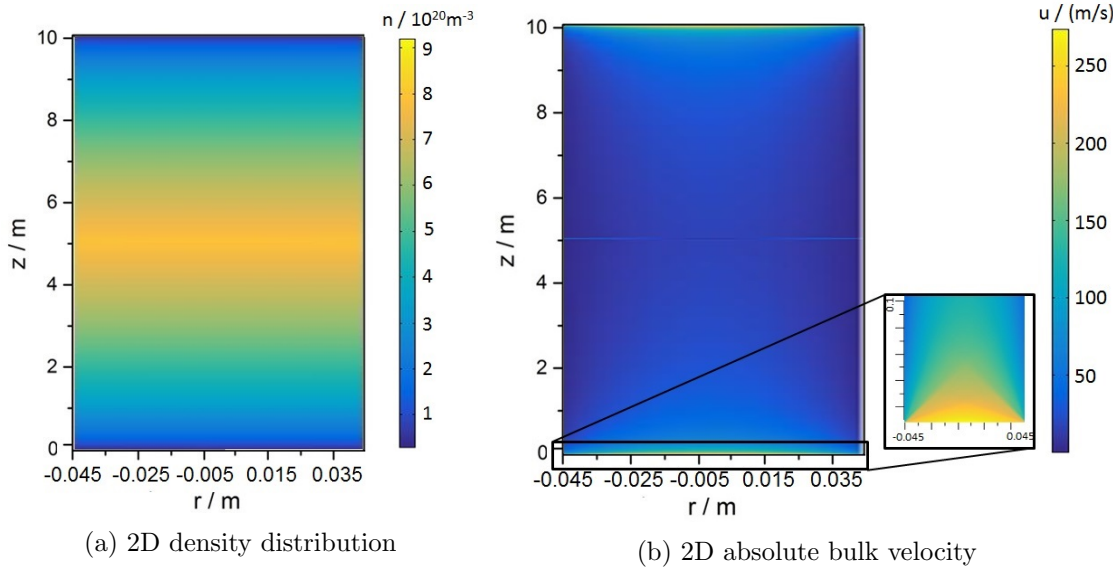


Figure 4.10.: Two-dimensional density and absolute bulk velocity distributions for the COMSOL WGTS beam tube model.

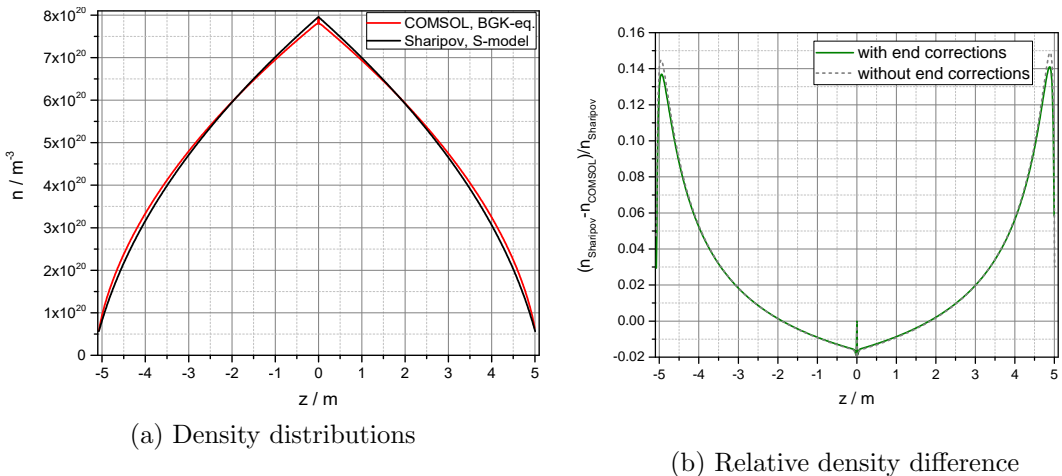


Figure 4.11.: Longitudinal density distributions from the two WGTS beam tube models and their relative differences. The general form of both density distributions, shown in the left figure, is similar. The relative difference between both models is shown in the right figure (grey dashed line – without end corrections in the Sparipov model, green solid line – with end corrections in the Sharipov model). Large differences occur mainly in the outlet region of the WGTS beam tube, where the rarefaction is already large ($\delta \approx 1.5$). In this region, the uncertainty from the discrete velocity method (quadrature D2Q36) used in the COMSOL calculation is already about 8%, see section 4.2.1. The influence from end corrections for the Sharipov model is small (about 1% in the outlet region).

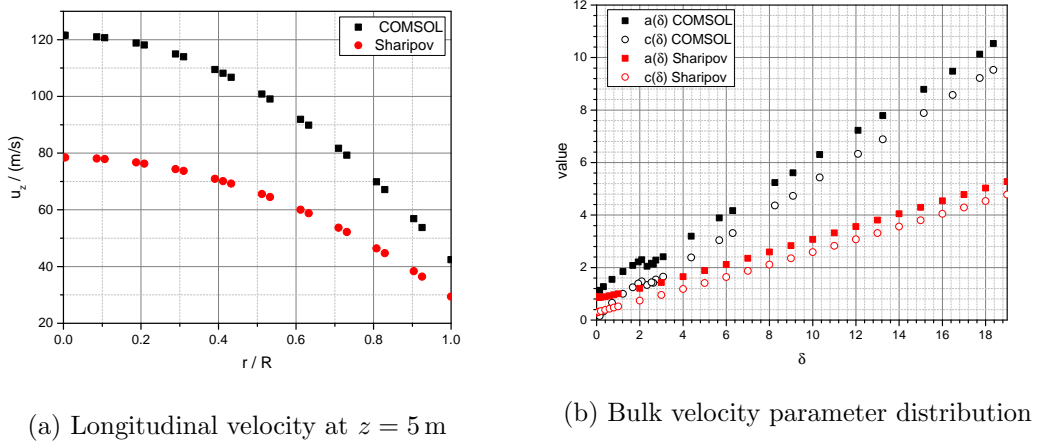


Figure 4.12.: **Radial distribution of longitudinal velocity and values for the velocity parametrisation for the two WGTS beam tube models.** The parametrisation is given in terms of the rarefaction parameter δ . The longitudinal velocity next to the outlet at $z = 5$ m is given relative to the radial coordinate (with beam tube radius $R = 0.045$ m).

and neutrino mass uncertainty are investigated in section 4.7.

The WGTS beam tube velocity distribution calculated with the COMSOL model differs from the Sharipov model solution – this holds especially near the beam tube outlet, where the gas flows quite rapidly. Outlet velocities of the order of 200 m s^{-1} are calculated. The radial distribution of bulk velocities next to the outlet boundary at $z = 5$ m is shown in figure 4.12a for both models. The large discrepancy is mainly caused by the finite velocity method, which is not suitable for high bulk velocities of the order of the thermal molecular velocity. Like the Sharipov model, the longitudinal velocity $u_z(z, r)$ obtained with the COMSOL model can be parametrised with the help of (4.40) quite well. The resulting distribution for the two parameters $a(\delta)$ and $c(\delta)$ is shown in figure 4.12b for both models.

The influence of the velocity model on the resulting modelled β -decay electron spectrum is tested in combination with the corresponding density model in section 4.7. A combination of both models (e.g. COMSOL density model, Sharipov velocity model) should not be used, since in this case the mass flow would not be conserved.

4.2.6. Modelling of gas flow in the DPS1

The column density inside the DPS1 contributes below 2% to the total column density of the source and transport section. However, in order to consider the spatial distribution of the magnetic field and the gas velocity that are both notably inhomogeneous in this domain, the density distribution inside the DPS1 has to be included in the gas model of the source. A gas dynamic simulation of this domain also gives also access to a more accurate value for the adjacent outlet pressure of the 10 m.

Simulating the gas flow in the DPS1 is quite challenging – the gas flow is in the transition regime at the position of the first pump port and develops into the free molecular regime at the second pump port (compare figure 4.3). Furthermore, the relatively complex, non-radial symmetric geometry of the two pump ports requires a three-dimensional modelling and prohibits a reasonably accurate analytical solution. In previous simulations of this component discussed in [MDLS09] a TPMC approach (see section 4.2.1) was used. This method is not suitable due to the regime of rarefaction in the first parts of the DPS1. Regarding the second pump port and the adjacent beam tube connecting DPS1-F and DPS2 in front direction and accordingly DPS1-R and rear section in the opposite direction, the

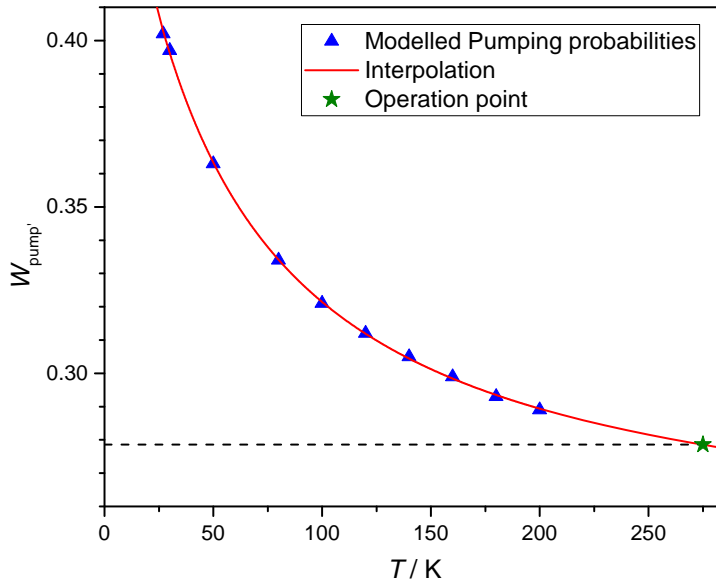


Figure 4.13.: **Pumping probability for gas particles reaching the TMP in the first and second pump port of the DPS1 vs gas temperature.** Data points are taken from [SK05]. In principle, the pumping probabilities differ for first and second pump port since the gas flow and temperature distribution are slightly different. However, this effect is small compared to the uncertainty of the pumping probability which is about 10%.

prior model boundary conditions do not match the current constraints: The temperature distribution at the confining walls was taken to be constant on assumption of the former (now obsolete) DPS2 design. The same holds for the outlet boundary condition at the end of the DPS1-F which used a transition probability different from the current value calculated in [Jan15]. Thus, the simulations of the DPS1 components needed to be updated. The modelling is divided into a three-dimensional simulation of the simplified first pump port geometry, a two-dimensional simulation of the beam tube connecting first and second pump port and a three-dimensional simulation including the second pump port, and the tube to the DPS2. The particular simulation geometries can be seen in figure 4.2.

4.2.6.1. Determination of TMP pumping probability

Knowledge of the probability for gas molecules reaching the rotor blades of the turbo-molecular pumps to be pumped out is essential to determine the boundary conditions for the pumping surfaces. This problem was investigated in [SK05]. There the dependence of transmission probability and pumping speed on the tritium gas temperature was investigated between 27 K and 200 K. The resulting data are given in figure 4.13. Gas temperature and pumping probability are strongly correlated. Thus, the gas temperature entering the TMP needs to be calculated to determine the actual pumping probability. It can be calculated using the temperature distribution at the pump port walls (calculated in the previous chapter) in a non-isothermal gas flow simulation. To avoid such a complicated and time consuming flow simulation, a trick can be used: Upon reaching the TMP, the gas streams in a free molecular flow. For an accommodation coefficient of 1 the molecule temperature is equal to the temperature of the surface were the last wall interaction took place. Combining the view factors of these surfaces with respect to the first

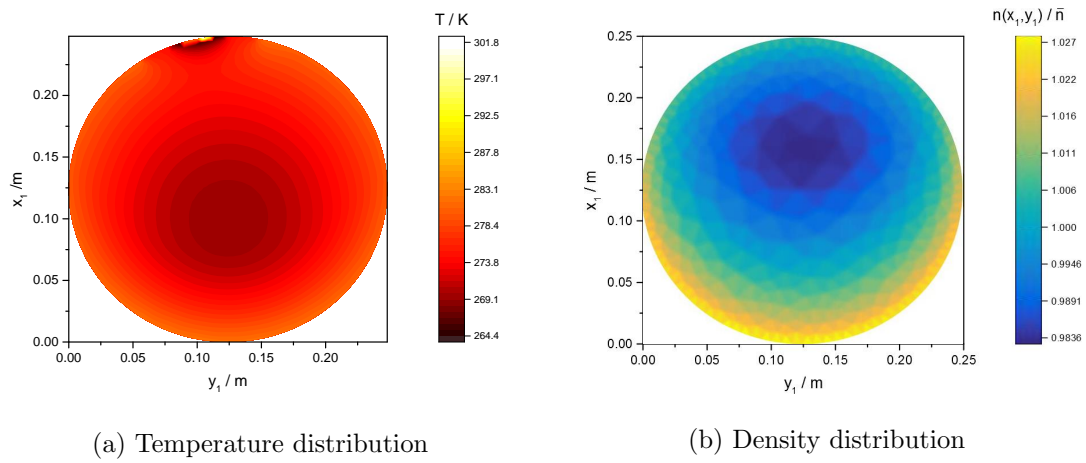


Figure 4.14.: Gas temperature and relative density distribution at the position of the first stage of TMP rotor blades. The rotor blades of the TMP are replaced by a disc with radius of 125 mm that gets heated by irradiation of the pump port walls.

stage of TMP rotor blades with the temperature of these surfaces, the gas temperature at the corresponding position can be approximated (neglecting the influence from density of flow emitted from the desorbing surfaces).

The wall temperature distribution is fixed to the one obtained in section 3.3.2 and section 3.3.4. The modelled TMP surface at fixed temperature of 333 K is replaced by a total absorbing disc ($\epsilon = 1$, no reflection, no thermal conductance) with undefined temperature – The disc temperature is determined purely by radiation from surfaces in direct line of sight.

The simulated temperature distribution at the disc surface is shown in figure 4.14a. To get the mean temperature of gas entering the TMP rotor blades, the disc surface temperature is averaged over the gas density distribution⁹, which is depicted in figure 4.14b.

The resulting average gas temperature at the rotor blade position is about 275 K. Interpolating the data from [SK05], this gas temperature corresponds to a transmission probability of about 0.275, as depicted in figure 4.13. The transmission probability W_{pump} of a TMP is related to the pumping speed S by [SK05]:

$$S = \frac{\sqrt{\pi}}{2} \frac{T}{273.15 \text{ K}} (R_{\text{ex}}^2 - R_{\text{in}}^2) v_{\text{m}} W_{\text{pump}}. \quad (4.43)$$

Using internal and external rotor blade radii of $R_{\text{in}} = 0.06 \text{ m}$ and $R_{\text{ex}} = 0.12 \text{ m}$, the pumping speed of the TMP for molecular tritium for the above calculated gas temperature conditions is about 2300 l s^{-1} . Considering the uncertainty of the approximated gas temperature and from the interpolation of the pre-calculated transmission probabilities an uncertainty of about 10 % can be assigned to the calculated pumping speed.

4.2.6.2. First pump port

According to the pressure reduction factor inside the central beam tube of the WGTS the gas flow is in the transition region ($\delta \approx 1 - 2$) when entering the first pump port of the DPS1. Together with the complicated three dimensional geometry the simulation of gas flow in the first DPS1 pump port requires a distinct Monte Carlo approach (DSMC) [Sha15]. The four tubes connecting the four TMPs with the pumping chamber can be

⁹Here a gas dynamic calculation using an approximated pumping speed of 2000 l s^{-1} is used as described in section 4.2.6.3.

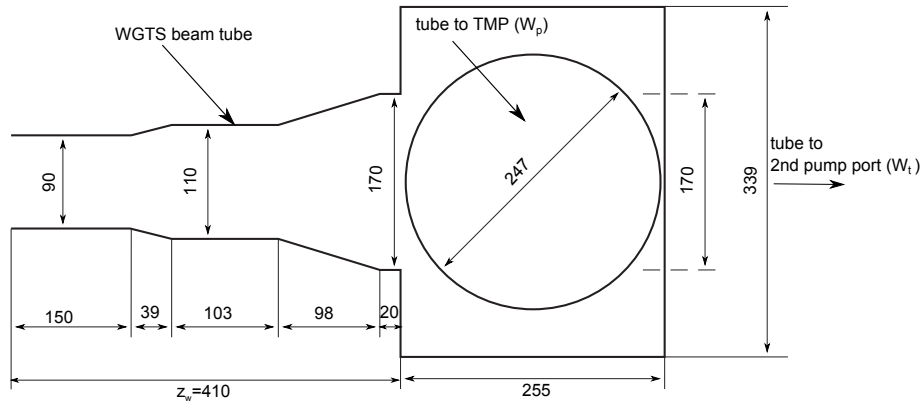


Figure 4.15.: **Model geometry of the first DPS1 pump port and adjacent WGTS central beam tube end.** All lengths are given in millimetres. Pump port model and WGTS beam tube model overlap over the length z_w to match the flow field for both simulations. The tubes connecting the pumping chamber with the TMPs, as well as the tube in the direction of the second pump port are replaced by partially reflecting surfaces with transmission probabilities W_p and W_t .

replaced by surfaces with transmission probability W_p and the pump port geometry can be simplified. In order to obtain a realistic profile for the incoming flow, the pump port model extends by 41 cm into the central WGTS beam tube. This allows to include the change of radius at the end of the 10 m WGTS beam tube, as well as to connect the flow field from the adjacent WGTS beam tube simulation smoothly to the pump port calculation. The simplified pump port model is depicted in figure 4.15.

The temperature along the pump port is essential to build an accurate flow model. As shown in the previous chapter in section 3.3.2 the temperature on the walls of the pumping chamber is almost homogeneous ($\Delta T < 2$ K) and does not exceed 31 K. Thus, the influence of thermomolecular flow is small compared to the uncertainty from statistical scatter of the simulation which is about 1% [Sha15]. Thus, an isothermal approach is considered suitable.

The transmission probability of the tubes leaving the pump port, W_p and W_t , can be approximated depending on their length-to-radius ratio ρ as discussed in [Ber65, LB66]:

$$W_{p,t} = 1 + \frac{\rho^2}{4} - \frac{\rho}{4} (\rho^2 + 4)^{1/2} - \frac{\left((8 - \rho^2) (\rho^2 + 4)^{1/2} + \rho^3 - 16 \right)^2}{72\rho (\rho^2 + 4)^{1/2} - 288 \ln \left(\rho/2 + (\rho^2/4 + 1)^{1/2} \right)}. \quad (4.44)$$

The beam tube connecting pumping chamber and TMP has an average length to radius ratio of about 4 implying a transmission probability of $W_p \approx 0.36$ from equation (4.44). However, parts of the tube are bent and its radius is not constant which causes the actual transmission probability to be lower than approximated above. Thus, gas flow calculations are carried out for transmission probabilities of 0.4 and 0.2. The tube connecting first and second pump port has a length-to-radius ratio of 21. This results in a transmission probability of $W_t = 0.1$. Particles that are not transmitted through the tube get reflected with probability $(1 - W_{t,p})$. The inlet pressure for the pump port simulation at position $z_{inDPS} = LWGTS - z_w$ is taken from the calculation of gas flow through the WGTS beam tube. A WGTS injection pressure p_{in} of 0.332 Pa results in a pressure of 0.0367 Pa at the inlet boundary of the first pump port at $z = z_{inDPS}$. The DSMC calculation was carried out by F. Sharipov. Details on the method of solution can be found in [Sha15].

The resulting two-dimensional density inside the pump port for a transmission probability W_p of 0.2 is depicted in figure 4.16a. The density distribution in the centre (at $r = 0$) along

the pump port and the outlet part of the beam of the WGTS is depicted in figure 4.16b. Here the smooth transition between both calculations can be seen. Depending on the transmission probability W_p , the ratio of pump port outlet to WGTS injection pressure ranges from 0.01 to 0.02. The column density inside the pump port is about 1×10^{-3} times the total column density. Even if the pump port density has an error of 50%, the effect on the total column density is about $1 \times 10^{-3}\%$ (considering pump port ar front and rear side) and, compared to the other contributing errors, insignificant. The flow reduction factor of the first pump port, using $W_p = 0.2$, is about 33. This is, despite the different approach of solution, in agreement with the value of 30 calculated in the above mentioned the TPMC in [MDLS09]. The small difference can be explained by the molecular beaming effect in the TPMC calculation that is artificially enhanced by the neglected intermolecular interactions.

4.2.6.3. Second pump port and adjacent beam tubes

As the gas exits the first pump port of the DPS1, its density is already 40 times smaller than in the centre of the WGTS. This corresponds, depending on the transmission probability of the first pump port, to a rarefaction parameter between 0.2 and 0.4 – the gas flow is still in the transition regime. Therefore, the gas dynamics in the beam tube connecting first and second pump port is simulated on the basis of the BGK equation, similar to the approach used in section 4.2.5. The model represents the beam tube cross section along the beam line and includes a two-dimensional representation of both adjacent pump ports to get a smooth transitions between the calculations and reduce the molecular beaming effect. Since the BGK equation is only valid for isothermal flow, temperature gradients can not be handled correctly.

To evaluate the validity of such an isothermal flow assumption, the fraction of temperature-driven flow can be approximated with the help of equation (4.33). Assuming a maximal temperature difference of 6 K along the beam tube¹⁰ and using representative data for the dimensionless flow rates $G_p(\delta)$ and $G_T(\delta)$ from (4.36) as well as intermediate values for T and p , the order of the dimensionless temperature and pressure gradients, ξ_T and ξ_p , along the tube axis can be approximated

$$\xi_T = \frac{r}{T} \frac{\delta T}{\delta z} \cdot G_T(\delta) \approx \frac{0.045 \text{ m}}{30 \text{ K}} \cdot \frac{2 \text{ K}}{1.1 \text{ m}} \cdot 0.62 \approx 1.7 \times 10^{-3}. \quad (4.45)$$

The tube length L_t is about 1.1 m. To approximate ξ_p , the flow is assumed to be in the molecular regime¹¹. In this case, the already calculated transmission probability $W_t \approx 0.1$ can be used to calculate the pressure difference along the tube $\Delta p = \frac{4q}{W_t v_m \pi r^2}$. The average pressure along the tube \bar{p} can be approximated with half the sum of the pressures at tube entrance and outlet.

$$\xi_p = -\frac{r}{p} \frac{\delta p}{\delta z} \cdot G_p(\delta) \approx \frac{r}{\bar{p}} \cdot \frac{\Delta p}{L_t} \cdot G_p(\delta). \quad (4.46)$$

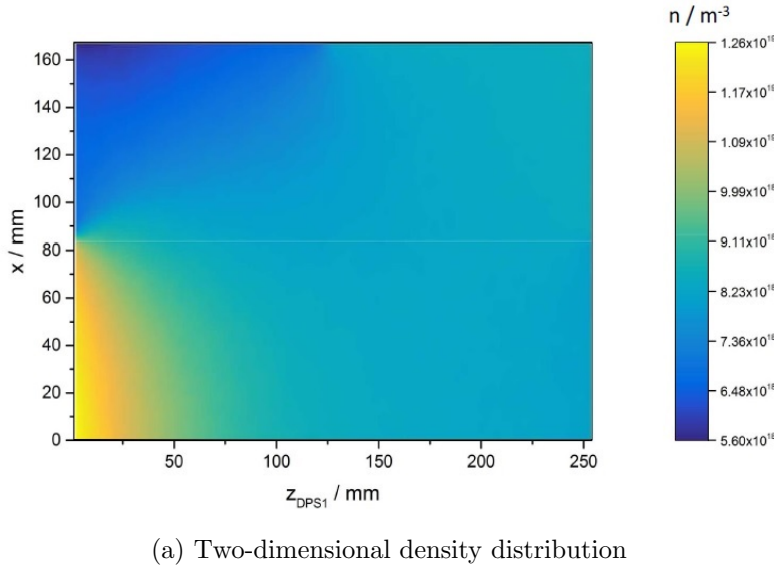
Using the above calculated factors for flow rate reduction in the first pump port and pressure reduction of central beam tube and pump port, the average pressure (for standard WGTS operation parameters) can be calculated. Thus ξ_p gets:

$$\xi_p \approx \frac{0.045 \text{ m}}{5.5 \times 10^{-5} \text{ mbar}} \cdot \frac{6.5 \text{ mbar}}{1.1 \text{ m}} \cdot 1.41 \approx 0.068. \quad (4.47)$$

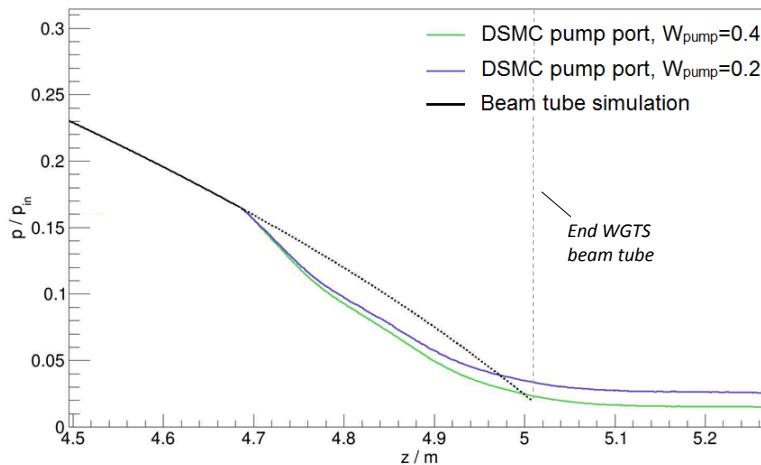
Plugging both gradients into equation (4.33), an dimensionless flow rate uncertainty of about 10% is obtained which induces a column density uncertainty of similar size. This

¹⁰The temperature difference along the corresponding tube is, according to the calculations in section 3.3.4, even below 3 K.

¹¹Since here only the order of ξ_p needs to be approximated, this is a valid assumption.



(a) Two-dimensional density distribution



(b) One-dimensional density distribution

Figure 4.16.: **Density distributions in the first pump port of the DPS1.** In a) the density distribution is plotted in the pump port cross section at $y = 0$ m. In b) the density distribution for first pump port and WGTS beam tube end is projected on the z -axis. Data are plotted for two limiting values assumed for the transmission probability W_p .



Figure 4.17.: Three-dimensional density distribution of the second pump port of the DPS1 and adjacent beam tubes.

uncertainty does not harm the source model and its scattering probabilities since the domain's column density is about 0.27% of the total column density. Therefore, the corresponding total column density uncertainty is smaller than 5.5×10^{-4} (considering contributions from front and rear side). The calculated density distribution for this domain is shown as part of the complete WGTS density distribution in figure 4.18 (dotted blue line).

At the entrance of the second pump port the gas flow is in the free molecular regime, as its rarefaction parameter is between 0.025 and 0.0125. This allows for gas flow simulations through more complex geometries and the second pump port can be simulated in a three-dimensional approach without simplifications of the geometry. To account for the molecular beaming effect, the model contains the just mentioned tube entering the second pump port. The temperature changes significantly from about 30 K at the beginning of the domain to room temperature at the flange to DPS2, as discussed in section 3.3.4. In contrast to the adjacent tube model, temperature gradients need to be included here, since the thermomolecular flow reaches the order of the Poiseuille flow. The molecular flow interface within the COMSOL microfluidics module [COM14a] is used for the calculations. It applies the angular coefficient method discussed in section 4.2.1. The model contains the pumping ducts and the TMPs are replaced by a partially absorbing surface. The gas temperature dependent transmission probability for the TMP $W_{\text{pump}'}$ and corresponding pumping speed $S = 2300 \text{ l s}^{-1}$ have been calculated above. The temperature distribution on the pump port walls is taken from the heat transfer simulations in section 3.3.4. The particle flux emitted from the pumping surface Q_{emis} relative to the incoming particle flux Q_{in} is considered using

$$Q_{\text{emit}} = (1 - W'_{\text{pump}}) Q_{\text{in}}. \quad (4.48)$$

The adjacent DPS2 is represented by a partially absorbing surface with transmission probability 0.2. This value is obtained connecting the particular transmission probabilities of the following DPS2 components (calculated in [Jan15]) according to the principle used in [LDH⁺06] and [MDLS09]¹².

The calculated three-dimensional density profile is shown in figure 4.17. The density reduction factor of the second pump port and adjacent beam tube obtained in the simulation

¹²The pump 0 at the beginning of the DPS2 was not considered in the calculations in [Jan15].

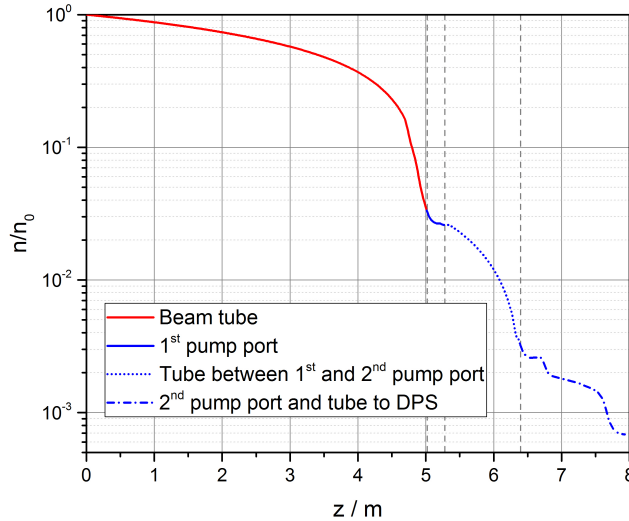


Figure 4.18.: **Density distribution of the WGTS composite gas model up to DPS2.** Relative density distribution for WGTS and DPS1 at the beam tube axis in front direction including beam tubes and pump ports.

is about 4.7, the contribution to the column density amounts to 0.03%. In the TPMC calculations in [MDLS09] an outlet transmission probability of 0.1 was used, according to calculations for the former DPS2 design in [LDH⁺06]. Nevertheless, the calculated flow reduction factor of about 10 is still comparable with the one obtained in this work. Though, the density distributions from both simulations differ, the density reduction factor calculated in [MDLS09] is about a factor two lower. However, since the domain's column density accounts less than 0.04% to the total value, this does not harm the KATRIN sensitivity.

For the composite gas model of the source all separately modelled components need to be connected. As parts of the preceding domains are always included in the subsequent model, a smooth density transition between the neighbouring components is established. This can be seen in figure 4.18. Density and flow reduction factors for all components up to the DPS2 and rear section are summarised in table 4.1. The geometry of the different front and rear sided components is taken to be mirrored. Still, the small asymmetry in the WGTS beam tube geometry leads to slightly different reduction factors in front and rear direction. The total density reduction factor from the injection in the WGTS up to the beginning of the DPS2 is about 2000 and an overall DPS1 flow reduction of about 400 is obtained. Using the results from [Jan15], where a reduction factor of about 4.5×10^5 was obtained for the DPS2, a combined gas flow reduction factor of 1.8×10^8 is obtained for the two differential pumping section DPS1-F and DPS2.

4.2.7. Modelling of pump failure in the DPS1

Different from the calculations and models presented above, the simulation described in this section will not be used in the KATRIN gas model to calculate the source β -decay spectrum. Instead, these calculations will be employed in commissioning measurements, discussed in section 4.6, to verify the gas model predictions.

The model geometry is similar to the three-dimensional model of the first pump port in the DPS1 as described in section 4.2.6, the only difference being the beam tube leaving the pump port in direction of flow is extended by 26 cm. The pumping probability at the beam

Table 4.1.: Reduction factors and column densities for the modelled WGTS components. Density and flow reduction factors, x_n and x_q , are given for each simulated domain. Small differences in front and rear distributions are due to a small WGTS beam tube asymmetry.

Domain	$n_{\text{out}}/n_{\text{in,WGTS}}$	$\rho d/\rho d_0$	x_n	x_q
WGTS beam tube front	0.034	0.492	29.2	-
WGTS beam tube rear	0.033	0.499	30.4	-
DPS1-F 1 st pp	0.026	1.1×10^{-3}	1.3	33
DPS1-R 1 st pp	0.025	1.1×10^{-3}	1.3	33
DPS1-F 1 st bt	2.34×10^{-3}	2.7×10^{-3}	11.1	-
DPS1-R 1 st bt	2.23×10^{-3}	2.6×10^{-3}	11.1	-
DPS1-F 2 nd pp+bt	5×10^{-4}	3.1×10^{-4}	4.7	11.7
DPS1-R 2 nd pp+bt	5.2×10^{-4}	3×10^{-4}	4.7	11.7
Complete front direction	5.2×10^{-4}	0.492	1980	386

tube outlet surface is set to 0.1. The transmission probabilities W_p for the surfaces that represent the connection to the TMPs is set to 0.2 in the initial calculation. In the two successive simulations, the failure of first one and then two TMPs is simulated by setting the corresponding transmission probability to zero. The pressure at the inlet boundary is set to 0.037 Pa. The wall temperature is assumed to be 30 K for the whole model.

The gas flow is calculated by applying the model equations (BGK-model) in the frame of the transitional flow module in COMSOL, as used in section 4.2.6.3. Since the model needs to be three dimensional and the geometry is quite complicated, the discretisation of the geometry is quite coarse to reduce the degrees of freedom in the calculation. 1×10^4 elements are used to mesh the geometry, in the DSMC simulation of the first pump port (section 4.2.6) the number of individual cells was 20 times as large. Still, the solution is memory consuming since the number of degrees of freedom is about 1×10^6 . Due to the coarse mesh, the model has large uncertainties. Their magnitude can be approximated by a comparison with the prior DSMC results of the first pump port – here differences of about 50% in the components column density and its density reduction factor are obtained. However, since the pump port column density does only account by about 0.1% to the total column density, the overall effect is washed out. Only the ratio of column density with all pumps working and with one or two pumps down needs to be compared. One does not need to be sensitive to the absolute column density.

The density distribution along the pump port is significantly affected by the number of working TMPs, as depicted in figure 4.19. The pump port outlet density increases by about 15% if one TMP does not work and by 50% if two TMPs do not work. The pump port column density increases by about 16.8% and 36.2%, respectively. The total column density increase for one and two pumps being switched off can be measured and compared to the predictions from the gas model, as will be discussed further in section 4.6.

4.2.8. The gas model of KATRIN in SSC – current status

The gas flow simulations described in the previous sections need to be implemented in the SSC gas model to be used in the KATRIN analysis. The structure of the SSC gas model did not allow to complete the modelling of the beam tube gas density by including further components. Within the scope of this thesis (together with M. Kleesiek) a composite SSC gas model structure was introduced. It allows to connect the calculations of density and

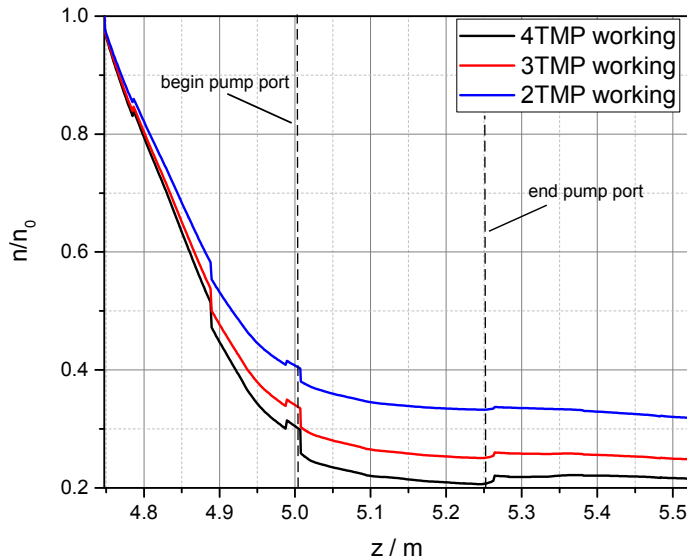


Figure 4.19.: **Density distribution in the first pump port of DPS1 for assumed shut-down of one and two TMPs, respectively.** The density is plotted along the beam tube axis ($r = 0$ m). The ripples at the beginning and at the end of the pump port density distribution are caused by the relatively coarse discretisation of the model geometry.

velocity distribution in different components as well as refined calculations of particular parts of components. The structure is based on the SSC class *SSCGasDynamicsComposite* that connects different supplementary gas models, if specified. The density distribution from a reference gas dynamics model is used to scale the supplementary density models positions where the models overlap. Since most of the implemented supplementary gas models are based on pre-calculated density distributions, the inlet density scaling is only valid in a certain range – the gas flow does not change linearly with the inlet pressure. This problem is further discussed in section 4.3.1. The velocities are smoothly connected between neighbouring models by averaging between both models in a transition region. Different kinds of supplementary gas models are implemented in SSC:

- *SSCGasDynamicsDPS1* – Gas model of the first pump port of DPS1 (front and rear direction). Pre-calculated density and velocity set from the data obtained in section 4.2.6.2. (three-dimensional model).
- *SSCGasDynamicsInlet* – Model of the inlet region from $z = -45$ mm to 45 mm. The modelling is based on the calculations described in section 4.2.4 (two dimensional model depending on r and z coordinates.)
- *SSCGasDynamicsTransport* – Two-dimensional model of beam tube connecting first and second pump port (front and rear direction) depending on r and z coordinates. Based on data obtained in section 4.2.6.3.
 - Three-dimensional model of the second pump port of the DPS1 and the adjacent tube to the DPS2. Based on density and velocity distributions obtained in 4.2.6.3.

After scaling¹³ of the density distributions of the different components, the column density of the full gas model is adjusted to the user-defined input value.

¹³A scaling factor is calculated for each domain (the 10 m WGTS beam tube that has a scaling factor of one). Therefore, the densities in where the domain overlaps with its precursor (in inverse direction of flow) is used. The obtained ratio is used to scale the density of the whole domain in order to get a smooth density transition between both domains.

The gas model for the 10 m beam tube is refined. End effects are implemented in the calculations using the method of an effective length, as introduced in section 4.2.4. Furthermore, it is slightly adapted to work with user-defined values for the macroscopic parameters accommodation coefficient and viscosity.

The comparative WGTS beam tube calculation with COMSOL is implemented in two new density classes *SSCDensityCOMSOL1D* and *SSCDensityCOMSOL2D* for one- and two-dimensional modelling, respectively. These data will be predominantly used to test the influence of the density distribution uncertainty on the neutrino mass squared in section 4.3.1. Since the COMSOL classes are based on pre-calculated data, sheets are calculated for input pressures from 0.315 Pa to 0.348 Pa in steps of 1×10^{-3} Pa to 5×10^{-3} Pa. Thus, for a variable inlet pressure from 0.315 Pa to 0.348 Pa the density can be calculated accurately by interpolating between the pre-calculated data sets. To account for a possible reduction of column density in the WGTS data sheets for 5%, 10%, 20% and 50% of the nominal column density are prepared.

4.3. Uncertainties of the gas model

In this section, the uncertainties of the gas flow calculations that form the gas model of the source and transport section are discussed. Model dependent uncertainties like numerical errors or such, that are induced by simplifying either the domains geometry or the governing flow equations and input parameter-induced uncertainties are considered separately.

4.3.1. Model dependent uncertainties

The bulk of the gas density, about 98-99%, is situated in the 10 m beam tube in the centre of the WGTS. Therefore, the uncertainties related to the gas model for this specific component are investigated separately from those of the remaining (DPS1) components. In the following, only uncertainties that are related to the model description are considered. The contribution of the single components to the uncertainty of the total column density is visualised in figure 4.20.

WGTS beam tube gas model

The model dependent column density uncertainty in the 10 m WGTS beam tube calculations is determined by the uncertainty of relative flow rate coefficients $G_p(\delta)$ and $G_T(\delta)$ that are used to calculate the density distribution inside the WGTS (see equation (4.35)). Calculations in [GPS11] and [SK09] showed a maximal flow rate model discrepancy of less than 2.5% in the transition regime ($\delta \approx 1$) comparing results from the BGK equation, the S-Model and the DSMC method. As parts of the WGTS beam tube are in the hydrodynamic regime that can be calculated more reliably, the throughput and column density uncertainty for the one-dimensional WGTS 10 m beam tube calculation will clearly be below 2%.

Effects from two-dimensional flow in the region of inlet and outlet cause a deviation of 4% for the gas throughput while the influence on column density is below 1%. The latter can be further reduced to 0.4% if the flow rates are corrected with the help of the method of the effective length.

Azimuthal temperature gradients cause non-axial flow contributions, as well. However, if the longitudinal temperature profile is known, the azimuthal flow can be included in the gas model reliably.

A comparative isothermal 10 m beam tube simulation (see section 4.2.5), based on a different model approach, showed local density differences up to 14% in the outlet region. Still, both models agree within 2% in a central region 3 m around the inlet, where about

80% of the total density can be found. Therefore, the column density difference for both models is only about 1% and confirms the value given above.

The remaining uncertainties of the WGTS beam tube density calculation are related to the gas model input parameters and are summarised in section 4.3.2.

DPS1 gas model components

First pump port

The major uncertainty of the DPS1 gas model is related to the transmission probability for the tubes connecting pump port and TMPs. It has a rather large influence on the density distribution in the pump port. Testing transmission probabilities of 0.2 and 0.4, a pump port column density difference of 40% was reported in [Sha15]. The pressure at the end of the pump port is increased by a factor of two for the lower transmission probability. In the SSC composite gas model, the relative density distribution in the pump port¹⁴ is scaled with the density at the connection between beam tube and pump port model at $z = L_{\text{WGTS}} - 41$ cm. Since the gas flow depends non-linearly on the injection pressure (if interactions between gas particles cannot be neglected), the density scaling can only be used for scaling factors similar to 1. This requirement can be relaxed if the rarefaction gets larger. In [Sha15] the gas throughput was varied by 10% ($q(293\text{ K}) = 1.925 \text{ mbar l s}^{-1} \pm 10\%$) to test how accurate the density scaling in the first pump port works. This corresponds to a pressure variation of about 5% at the beginning of the first pump port. The pump port column densities from the model calculation with updated throughput, and from the one obtained from scaling with the pump port inlet pressure ratio, agree within 5%. This discrepancy is small compared to the contributions from other uncertainties discussed above. The statistic scattering of the solution, as introduced in section 4.2.1, contributes about 1% to the total density uncertainty and is thus insignificant.

In total this yields an uncertainty of about 46% for the calculated pump port column density as well as for the 10 m WGTS beam tube exit pressure. This exit pressure uncertainty is important, since it translates to an inlet pressure uncertainty of equal size in the subsequent domain (see figure 4.20).

The pump port density contributes by about 0.1% to the total column density, see table 4.1. Since both pump ports (rear and front side) need to be considered, the related uncertainty of the overall column density ρd_{gas} is about 0.1%.

Beam tube connecting first and second pump port

One of the main contributions to the uncertainty of this gas model was already discussed in section 4.2.6 – the model was solved assuming isothermal flow. Thus, temperature gradients on the beam tube due to radiation heat load from the pump port can not be considered. The related column density uncertainty for a reasonable size of temperature gradients was approximated to be below 5%.

The solution of this model is based on the discrete velocity method with a D2Q36 quadrature. For Knudsen numbers of about 1, which is the order of rarefaction of this component, this quadrature is related to an uncertainty of the order of 10% in the density distribution as discussed in section 4.2.1.

Like in the adjacent pump port component, the density in this domain is scaled according to the density at the transition to the connecting upstream component when used in the *SSC* composite gas model. For inlet pressure variations of 10% this implies a discrepancy of roughly 5% for the scaled column density and the outlet pressure of this component.

Still, the uncertainty from the outlet pressure of the first pump port model, which is the inlet pressure for this component, needs to be considered. It can be estimated to cause another 50% uncertainty for the column density of this component. Since the compo-

¹⁴Calculated for a WGTS injection density $n_{\text{in}} = 8.28 \times 10^{20} \text{ m}^{-3}$ and a throughput of $q = 1.926 \text{ mbar l s}^{-1}$.

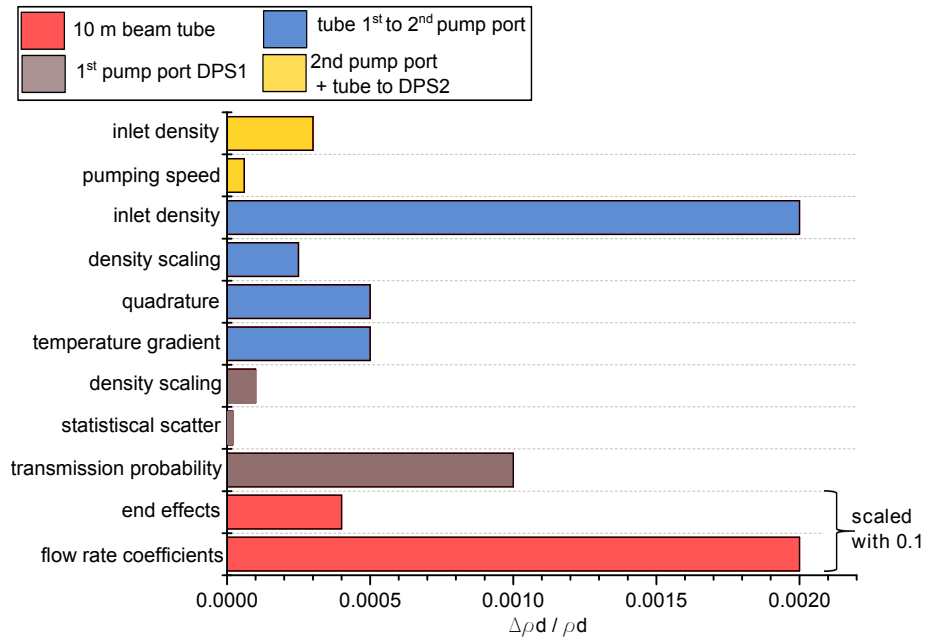


Figure 4.20.: **Contributions of single domains to uncertainty of total column density.** Uncertainties marked by a bar of same colour belong to the same component. The 10m WGTS beam tube model has the largest uncertainty – it is scaled by a factor of 0.1. The second largest contribution comes from the uncertainty of the transmission probability ΔW_p of the tube connecting the TMP with the first pump port. This domain's outlet density has an uncertainty of equal size. This outlet uncertainty propagates through all subsequent domains as an uncertainty in the inlet density of the particular domain. Contributions from components at rear and front side of the WGTS have been considered. The overall column density calculation uncertainty is far above the required 0.2%.

ment contributes about 0.1% to the total column density, another 2.5×10^{-3} total column density uncertainty is induced, . for front and rear side combined.

Second pump port and beam tube to DPS2

The pumping speed, or transmission probability at the pumping surface, influences the density distribution. Varying the pumping probability by about 10% causes density changes between 5 and 8%. The transmission probability for the model outlet surface (connection to the DPS2) does influence the density and gas flow reduction factor of this component, too. It mainly determines the density in the beam tube part of the model. Changing the transmission probability from 0.2 to 0.1 alters the pump port density by less than 5%. However, the density at the outlet is changed by about 30%. The flow rate reduction factor decreases by 32%. The error induced by scaling of the obtained distribution to the actual outlet pressure of the previous component can be neglected, since the gas flow is in the free molecular regime. The contribution to the total column density uncertainty is insignificant, since the modelled domain contributes only a fraction of about 5×10^{-4} to the overall column density.

4.3.2. Uncertainty related to input parameters

As shown in section 4.2.2, the parameters viscosity and accommodation coefficient, η_{T_2} and α , have not been measured for tritium and are thus approximated using H_2 and D_2 data. The tritium viscosity is obtained using the η_{D_2} value at 30 K scaled with the T_2 - D_2

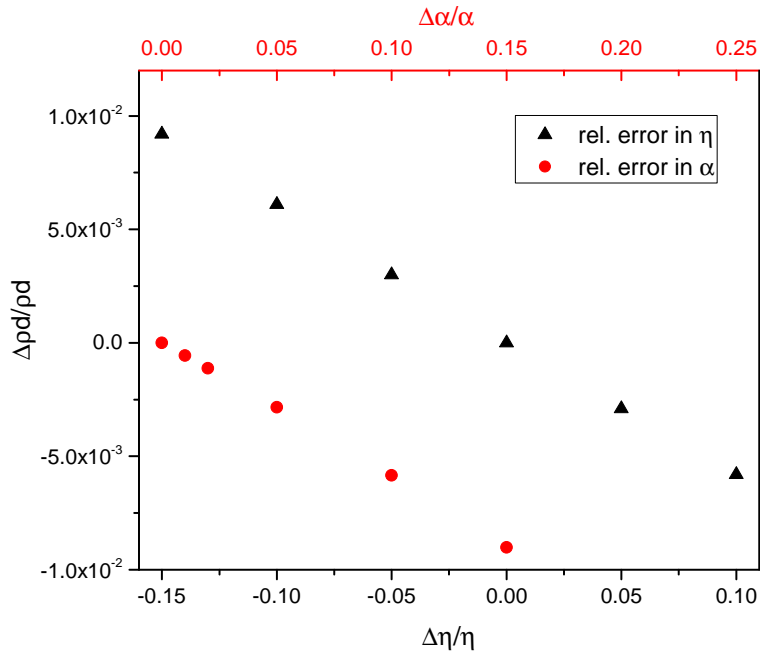


Figure 4.21.: **Influence from uncertainties of viscosity and accommodation coefficient on column density.** The viscosity-related uncertainties are represented by black triangles. Red dots indicate accommodation coefficient-related uncertainties. (Note the different axes for both parameter uncertainties.

mass ratio and a correction factor of 0.95 that is inferred from measured η_{H_2} and η_{D_2} values at 30K. The discrepancy between calculated and measured D_2 viscosity can be used to infer the T_2 viscosity uncertainty – it is smaller than 7%.

Another uncertainty of 2.5% has to be added if the viscosity is not corrected for other hydrogen isotopologues being present in the WGTS gas mixture to about 5%. Though, even for a conservative estimate of $\Delta\eta_{T_2}/\eta_{T_2} = 10\%$ the column density is merely influenced by about 0.7%, as depicted in figure 4.21.

An accommodation coefficient of about 0.91 is inferred from measurements with helium on stainless steel, since no data are available for tritium on steel, see sec. 4.2.2. For the T_2 gas in the WGTS, the accommodation coefficient is assumed to be 1 because of the low WGTS beam tube temperature of 30K and the adsorbed tritium layers at the tube walls. Nevertheless, the uncertainty of the KATRIN accommodation coefficient is assumed to be 10%. This corresponds to a column density uncertainty of about 0.75% as depicted in figure 4.21.

Besides the above discussed model-related and transport parameter-induced uncertainties, the influence of the WGTS gas flow variables inlet pressure, p_{in} , WGTS 10 m beam tube outlet pressure, p_{ex} , and beam tube temperature need to be considered. Since neither p_{in} nor p_{ex} can be measured directly, their values can only be inferred from conductance measurements which induce relatively large uncertainties up to 10% (further discussed in section 4.4). Even without considering their influence, the uncertainty on the calculation of the WGTS column density is about 2.3% which clearly exceeds the KATRIN limit¹⁵ which would cause a neutrino mass squared uncertainty larger than 0.01 eV² [Höt12] which is far to large to be tolerated. Therefore, the determination of the absolute value of the

¹⁵Here it should be noted that in [AAB⁰⁵] the accuracy of the column density determination have only been considered in combination with the measurements of the energy loss function.

column density is not possible with the gas model. It needs to be determined by dedicated measurements further described in section 4.5.1.

The column density uncertainty discussed in this section does only hold for the calculation of the absolute value. Uncertainties from the modelling of column density changes has much lower uncertainties and is discussed in the following section.

4.4. Modelling of column density changes

The determination of the product of column density and scattering cross section by an absolute measurement is inevitable. Still, this measurement can not be performed continuously. Thus, several monitoring methods will be used to check experimentally if the column density variation is below the required 0.2% level on a time scale of minutes.

In this section it will be shown, that the gas model can be used to calculate reliably how the column density changes for small variations of the buffer vessel pressure p_B , for changes of the pressure in the pump port, p_{ex} , and for small temperature drifts. These precisely monitored changes can be used in the calculation of the source electron spectrum which would reduce the uncertainty related to variations of the column density (column density precision). After discussing the relation between the variation of WGTS operational parameters and column variations, the modelling limits of these changes will be derived in 4.4.1.

Once the column density is measured with the electron gun this value, ρd_{exp} , will be implemented in the gas model, to calculate the corresponding gas model inlet pressure $p_{\text{in,th}}^{16}$. The column density is related to a certain set of main parameters: Inlet pressure, p_{in} , temperature distribution, pressure in the first pump port (related to the pumping speed) and tritium purity¹⁷. When either of these parameters drifts, the column density will be affected as well: $\rho d = \rho d(p_{\text{in}}, T(r, z), p_{\text{ex}}, \epsilon_T)$. The temperature distribution and tritium purity can be measured directly and be used to update gas model and column density. The WGTS beam tube inlet and exit pressures can not be determined by measurement. Their relative changes need to be derived from the pressure in the pressure controlled buffer vessel (in the following called buffer vessel for simplicity), p_B , and accordingly from the pressure measured next to the turbo molecular pumps in the first pump port of the DPS1, p_{TMP} .

Before the actual calculation of column density changes is described, the column density uncertainty limits for changing of operational parameters need to be defined (column density precision). Assuming a balance between the (measurement) uncertainty of the absolute column density times inelastic scattering cross section, $\Delta(\rho d)_{\text{abs}}$, and the uncertainty due to variations of operational parameters, $\Delta\rho d_{\text{var}}$, the total column density times scattering cross section uncertainty can be calculated:

$$\frac{\Delta\rho d \cdot \sigma}{\rho d \cdot \sigma} = \sqrt{\left(\frac{\Delta\rho d \cdot \sigma}{\rho d \cdot \sigma}\right)_{\text{abs}}^2 + \left(\frac{\Delta\rho d}{\rho d}\right)_{\text{var}}^2} \approx \sqrt{2} \left(\frac{\Delta\rho d}{\rho d}\right)_{\text{var}}. \quad (4.49)$$

Aiming for combined uncertainty lower than 0.2% for the column density times scattering cross section ($\frac{\Delta\rho d \cdot \sigma}{\rho d \cdot \sigma}$), the uncertainty budget of column density variations yields:

$$\left(\frac{\Delta\rho d}{\rho d}\right)_{\text{var}} \leq 1.4 \times 10^{-3}. \quad (4.50)$$

¹⁶This calculated inlet pressure is not equal to the real inlet pressure according to the uncertainty of the gas model column density calculation. However, when plugged into the gas model it provides the correct column density.

¹⁷For the calculation of the changes in ρd_{gas} only large changes in ϵ_T altering the gas viscosity by more than 1 to 2% need to be considered.

If uncertainties from variation of the three main contributing WGTS operation parameters x each contribute equally this means a maximal column density uncertainty of

$$\left(\frac{\Delta \rho d}{\rho d} \right)_{\text{var},x} \leq 1.4 \times 10^{-3} / \sqrt{3} \approx 8 \times 10^{-4}. \quad (4.51)$$

caused by variations of a single operation parameter. The limit (4.51) represents a conservative approach since it is assumed that all parameters change and the drift is only in one direction. For fluctuations in both directions, the effects would partially cancel.

Variation of the buffer vessel pressure

Neither the pressure in the injection chamber, nor the inlet pressure, p_{in} , as defined through equation (4.29), can be measured directly. The quantity that can be measured is the pressure in the buffer vessel. It is related to the inlet pressure by the conductance C of the tube connecting both positions¹⁸ and through the gas throughput q

$$q = (p_B - p_{\text{in}}) \cdot C. \quad (4.52)$$

A precise quantitative relation between both pressures cannot be derived since the determination of the conductance (experimentally or analytically) has large uncertainties. Still, for reasonable small variations of about 1%, the relative change in buffer vessel pressure can be accurately related to the relative change in inlet pressure. For $p_{\text{in}} \ll p_B$ and constant temperature conditions, equation (4.52) can be transformed

$$\frac{\Delta q}{q} = \underbrace{\left(C + p_B \cdot \frac{\delta C}{\delta p_B} \right) \frac{p_B}{q}}_{\beta_{p_B}} \frac{\Delta p_B}{p_B} \quad , \text{ with: } \frac{1}{C} = \frac{1}{C_{\text{capillary}}} + \frac{1}{C_{\text{loop}}}. \quad (4.53)$$

In equation (4.53) $C_{\text{capillary}}$ denotes the conductance of the capillary inside the WGTS cryostat feeding T_2 in the injection chamber and C_{loop} the conductance of the tube that leaves the buffer vessel and that is connected through the capillary. For a circular tube in the viscous regime the conductance increases with increasing tube diameter d and decreases with increasing tube length l : $C \propto \frac{d^4}{l}$ [WAWJ04]. With a tube diameter of $d_{\text{loop}} = 25 \text{ mm}$ and a length $l_{\text{loop}} = 10 \text{ m}$ the conductance C_{loop} is significantly larger than $C_{\text{capillary}}$, as, $d_{\text{capillary}} = 2.1 \text{ mm}$ and $l_{\text{capillary}} = 5 \text{ m}$. Thus, according to equation (4.53), the large conductance of the loop can be neglected. The feed capillary is thermally coupled to the WGTS beam tube. Therefore, the capillary is assumed to have a constant temperature of about 30 K and temperature gradients that would influence the conductivity can be neglected. The buffer vessel pressure is about 10 mbar and C_{loop} is large which means, the pressure at the entrance to the capillary can be assumed to be about 10 mbar. Thus, the flow at the entrance of the capillary is clearly hydrodynamic. However, if the capillary flow approaches the WGTS injection chamber the gas is in the transition regime¹⁹. The conductance of a tube with gas flow in the hydrodynamic and in the transition regime both can be approximated using the formula derived by Knudsen [Knu09b]. He supposed an average conductance that can be calculated adding the conductance in the free molecular and viscous case, C_{m} and C_{vis} :

$$C = C_{\text{vis}} + ZC_{\text{m}} \quad , \text{ with } Z \text{ going from 0.8 to 1.} \quad (4.54)$$

¹⁸The two lines are a capillary inside the WGTS cryostat feeding the gas into the injection chamber and a tube from the buffer vessel that belongs to the KATRIN loop part

¹⁹Using an injection chamber pressure of about 6×10^{-3} mbar, see section 4.2.4, and $r_{\text{capillary}} = 1.05 \text{ mm}$ the rarefaction parameter is calculated to be 0.9.

The correction term Z is taken to be 1 in the following. Using the equation from Hagen-Poiseuille for the viscous part and the one obtained by Knudsen for the free molecular part, equation (4.54) reads:

$$C = \frac{\pi}{12} \frac{d^3 v_m}{l} \left(\frac{3}{32} \frac{\bar{p}d}{\eta v_m} + 1 \right). \quad (4.55)$$

The average pressure in the capillary, \bar{p} , can be approximated with $p_B/2$, as $p_B \gg p_{in}$. Small changes in buffer vessel pressure are related to a variation of the throughput by the coefficient β_{p_B} introduced in equation (4.53). It can be calculated, plugging equation (4.55) in equation (4.53) and using²⁰ $p_B = 10 \text{ mbar}$ and $q = 1.8 \text{ mbar l s}^{-1} \cdot \frac{30 \text{ K}}{273.15 \text{ K}}$. This means: $\beta_{p_B} \approx 2$.

Since the calculation of the conductance with the help of equation (4.55) is an approximation, it is assumed to be as accurate as 10% which is also the quality that can be reached from a dedicated conductance measurement of the capillary. This translates to an uncertainty of the coefficient β_{p_B} , and thus on the calculation of throughput variation, of 10% as well.

Throughput and column density variation are linked by the coefficient α_q :

$$\frac{\Delta \rho d}{\rho d} = \frac{d \rho d}{d q} \cdot \frac{\Delta q}{\rho d} = \underbrace{\frac{d \rho d}{d q}}_{\alpha_q} \cdot \frac{q}{\rho d} \cdot \frac{\Delta q}{q}. \quad (4.56)$$

For a stable temperature in the buffer vessel and in the WGTS beam tube the throughput variation is related to a change in the injection pressure p_{in}

$$\frac{\Delta \rho d}{\rho d} = \underbrace{\frac{\delta \rho d}{\delta p_{in}}}_{\alpha_{p_{in}}} \cdot \underbrace{\frac{p_{in}}{\rho d}}_{\beta_{p_{in}}} \cdot \left(\underbrace{\frac{\delta q}{\delta p_{in}}}_{\beta_{p_{in}}} \cdot \frac{p_{in}}{q} \right)^{-1} \frac{\Delta q}{q}. \quad (4.57)$$

From equations (4.56) and equation (4.57) it follows that $\alpha_q = \alpha_{p_{in}} (\beta_{p_{in}})^{-1}$. The coefficients $\alpha_{p_{in}}$ and $\beta_{p_{in}}$ are related to relative changes in the WGTS injection pressure:

$$\frac{\Delta \rho d}{\rho d} = \alpha_{p_{in}} \frac{\Delta p_{in}}{p_{in}}, \quad \frac{\Delta q}{q} = \beta_{p_{in}} \frac{\Delta p_{in}}{p_{in}}. \quad (4.58)$$

The values of $\alpha_{p_{in}}$ and $\beta_{p_{in}}$ for standard KATRIN parameters can be determined using the central 10 m beam tube gas model from section 4.2.3 – Column density and throughput changes according to slightly varying inlet pressures need to be calculated. The influence of the gas flow in other components in direction of flow is not included here, since the bulk of the column density resides in the central WGTS beam tube.

The result is depicted in figure 4.22. The coefficients $\alpha_{p_{in}}$ and $\beta_{p_{in}}$ can be read off the slope of the shown distributions

$$\alpha_{p_{in}} \approx 1.06, \quad \beta_{p_{in}} \approx 1.7 \quad \rightarrow \quad \alpha_q \approx 0.62. \quad (4.59)$$

These values match the approximated values in [Sha03] quite well. To verify the calculated coefficients, the inlet pressure influenced column density changes are calculated one more time using the comparative beam tube model from section 4.2.5. Here the coefficient $\alpha_{p_{in, COMSOL}}$ is calculated to be about 1.059 which is in perfect agreement with the other model coefficient.

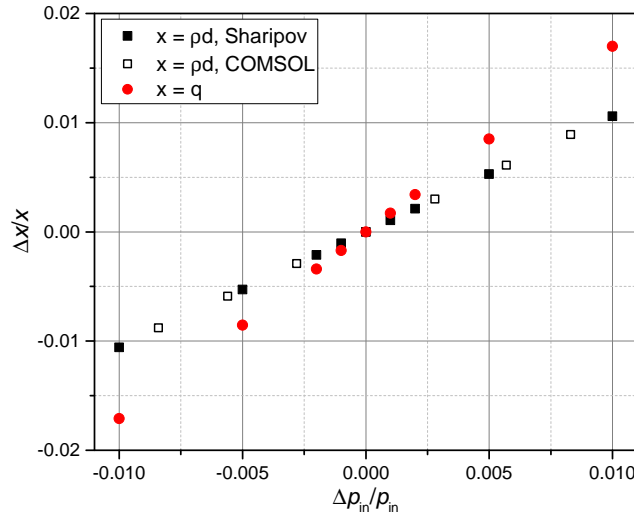


Figure 4.22.: **Dependence of relative throughput and column density changes on the variation of inlet pressure.** For the column density changes, data from the two different beam tube models (Sharipov, COMSOL) are shown. Throughput changes are calculated with the Sharipov model only. From the slope of the distributions, the coefficients $\alpha_{p_{in}}$ (red dots) and $\beta_{p_{in}}$ (black squares) can be deduced: COMSOL model – $\alpha_{p_{in}} \approx 1.059$, Sharipov model – $\alpha_{p_{in}} \approx 1.062$ and $\beta_{p_{in}} \approx 1.7$.

It is important to update all coefficients to the particular measurement conditions (buffer vessel pressure, conductance, throughput, temperature), for the calculation of the given coefficients design values from [AAB⁺05] had been used.

Now it can be deduced, how column density and injection pressure react if the buffer vessel pressure changes:

$$\frac{\Delta \rho d}{\rho d} = \alpha_q \cdot \beta_{p_B} \cdot \frac{\Delta p_B}{p_B} \approx 1.24 \cdot \frac{\Delta p_B}{p_B} \quad (4.60)$$

$$\frac{\Delta p_{in}}{p_{in}} = \beta_{p_{in}}^{-1} \cdot \beta_{p_B} \cdot \frac{\Delta p_B}{p_B} \approx 1.18 \cdot \frac{\Delta p_B}{p_B}. \quad (4.61)$$

This means, that the inlet pressure obtained for an initial buffer vessel pressure can be adjusted to a changed buffer vessel pressure. To this end, the initial inlet pressure needs to be multiplied by the measured buffer vessel pressure change $\Delta p_B/p_B$ and by a factor of 1.18.

If the buffer vessel pressure change is not corrected for in the gas model, it needs to be stable below $8 \times 10^{-4} / (\alpha_q \cdot \beta_{p_B}) \approx 7.6 \times 10^{-4}$, as derived from equation (4.51). This strict requirement can be relaxed by a factor of about 8.5, if the gas model is used to correct for these changes as further discussed in section 4.4.1 below.

Variation of temperature distribution

Changes in the temperature distribution changes can be updated in the gas model without further modifications. If the gas model is not updated an inaccuracy of the calculated

²⁰reference value from [AAB⁺05] and [Sha03]

column density develops, which depends on the magnitude of the variation ($\Delta x/x$) as depicted in figure 4.23. A correlation coefficient α_T with

$$\alpha_T = \frac{\delta \rho d}{\delta T} \cdot \frac{T}{\rho d} \quad (4.62)$$

can be read off the slope of the corresponding graph. The analysed temperature shift ΔT is related to the whole WGTS beam tube temperature ($\text{WGTS} = \text{const} = T_0 + \Delta T$). The calculation of temperature induced column density changes is performed for both WGTS central beam tube gas models.

The temperature coefficients α_T derived from both models (Sharipov model – $\alpha_T = 1.06$, COMSOL model – $\alpha_T = 1.022$) agree within 3.6%. This discrepancy has to be included in the uncertainty analysis in section 4.2.3. With the particular column density requirement from equation (4.51) and $\alpha_T \approx 1.06$ one can infer that the temperature needs to be stable below 7.5×10^{-4} . This requirement can be relaxed by a factor of 20 if the temperature in the gas model is updated regularly, as further discussed in section 4.4.1.

Variation of beam tube outlet pressure

The pressure in the first pump port of the DPS1, here denoted as beam tube outlet pressure, is an input parameter in the calculation of the WGTS gas profile. If it varies while WGTS inlet pressure and temperature remain constant, the column density changes as shown by the red circles in figure 4.23. Column density and outlet pressure are related by the coefficient $\alpha_{p_{\text{ex}}}$:

$$\frac{\Delta \rho d}{\rho d} = \alpha_{p_{\text{ex}}} \frac{\Delta p_{\text{ex}}}{p_{\text{ex}}}. \quad (4.63)$$

From the slope of the corresponding curve in figure 4.23 $\alpha_{p_{\text{ex}}}$ is calculated to be about 0.029. Combined with equation (4.50) this leads to a pump port pressure stability requirement of 2.5%. It can be further relaxed if the gas model is updated for the changed outlet pressure as discussed in section 4.4.1.

Like the WGTS inlet pressure, the pressure in the pump port cannot be measured directly. However, next to the pumps, the pressure is measured. In principle, for changes smaller than 10%, the measured pressure changes next to the TMP, p_{TMP} , can be directly related to the change of pressure in the pumping chamber:

$$\frac{\Delta p_{\text{ex}}}{p_{\text{ex}}} \approx \frac{\Delta p_{\text{TMP}}}{p_{\text{TMP}}}, \quad (4.64)$$

and the gas model can be updated. The validity of equation (4.64) is analysed in appendix E.

4.4.1. Limits for modelling of column density variation

For small amplitudes of long-term drifts and slow variations of the operational parameters, the theoretical gas model can be used to calculate changes in the column density and update the value. The characteristic time scale for parameter changes to be visible in the density distribution is given by the average time, τ , a molecule needs to go through the WGTS which is about 0.5 s. About five times τ after any small parameter change, the gas should be in equilibrium again. This is verified by a time-dependent test model in appendix D. Thus, small parameter changes (not larger several than per cent) that occur at time scales larger than about 5 s can be resolved by the gas model and included in the analysis.

For instance, in a column density measurement the WGTS operation parameters at the moment of the electron gun measurement are plugged into the gas model. The obtained

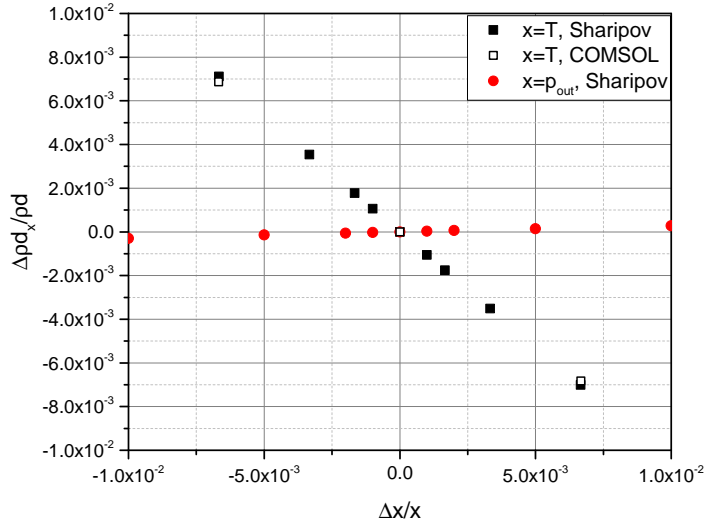


Figure 4.23.: **Column density change induced by absolute beam tube temperature changes (black) and changes in the pump port pressure (red).** The temperature dependency, coefficient α_T , is analysed for both beam tube density models: Sharipov model – $\alpha_T = 1.06$, COMSOL model – $\alpha_T = 1.02$ respectively. The outlet pressure dependency is investigated for the Sharipov mode, the coefficient $\alpha_{p_{ex}}$ is determined as 0.029.

injection pressure corresponds to the measured column density for this configuration. For changes in the buffer vessel pressure, the initial injection pressure is updated according to relation (4.60). The same procedure is applied, for drifts of temperature or outlet pressure. The column density correction reduces the uncertainty from WGTS operation parameter instabilities (see remarks above). This way even eventual (but not expected) parameter changes above the per mill level can be partially be compensated. The limits of such a compensation are derived in the following. Here uncertainties that are related to the gas dynamics model $\left(\frac{\Delta \rho d_x}{\rho d}\right)_m$ need to be disentangled from uncertainties err_x related to the determination of the WGTS parameter change $\frac{\Delta x}{x}$ or to its column density correlation parameter α_x . Both uncertainties add to the total uncertainty $\frac{\Delta \rho d_x}{\rho d}$ related to the change of the particular operational parameter x

$$\frac{\Delta \rho d_x}{\rho d} = \sqrt{\left(\frac{\Delta \rho d_x}{\rho d}\right)_m^2 + \left(\alpha_x \cdot \text{err}_x \frac{\Delta x}{x}\right)^2}. \quad (4.65)$$

The modelled inlet pressure uncertainty, $\Delta p_{in} \approx 2.3\%$, that is related to the gas model uncertainty itself, can be used to get an estimate of the contribution from the gas model $\left(\frac{\Delta \rho d_x}{\rho d}\right)_m$. The way the column density changes induced by variations of operation parameters depend on the absolute value of the inlet pressure needs to be investigated. For two different initial inlet pressures p_{in} and $p_{in} + \Delta p$ the relative difference reads

$$\begin{aligned} \left(\frac{\Delta \rho d_x}{\rho d}\right)_m = & \frac{\rho d(p_{in}, x) - \rho d(p_{in}, x(\frac{\Delta x}{x} + 1)) - \rho d(p_{in} + \Delta p, x)}{\rho d(p_{in}, x)} \\ & - \frac{\rho d(p_{in} + \Delta p, x(\frac{\Delta x}{x} + 1))}{\rho d(p_{in}, x)}. \end{aligned} \quad (4.66)$$

In the following a difference Δp of 5% is assumed which exceeds the gas model inlet pressure uncertainty to arrive at a conservative estimation.

Below, contributions from the three main gas flow related WGTS operation parameters are analysed separately.

Inlet density variation

Due to the poorly known capillary conductance and the related uncertainty of the coefficient β_{p_B} of 10%, the calculation of inlet pressure changes from equation (4.60) for a given initial inlet pressure has a relative uncertainty of about $0.1 \cdot \beta_{p_B} \cdot \frac{\Delta p_B}{p_B}$. The comparison of the coefficients $\alpha_{p_{in}}$ calculated with the two WGTS beam tube models showed a small discrepancy of 2×10^{-3} . It is small compared to the conductance related uncertainty and can be neglected. Adding model and parameter induced term according to equation (4.65) gives the full uncertainty from calculations of column density changes induced by inlet pressure variations

$$\frac{\Delta \rho d_p}{\rho d} = \sqrt{\left(\frac{\Delta \rho d_p}{\rho d}\right)_m^2 + \left(\alpha_{p_{in}} \cdot \beta_{p_B} \cdot 0.1 \cdot \frac{\Delta p_B}{p_B}\right)^2}. \quad (4.67)$$

The uncertainty as a function of the inlet pressure variation is depicted in figure 4.24a – buffer vessel pressure changes up to about 0.65% can be modelled within the required precision of $\Delta \rho d / \rho d \leq 7.6 \times 10^{-4}$. For buffer vessel pressure changes smaller than 2×10^{-3} , which is the precision required from [AAB⁺05]²¹, the related uncertainty in column density can be even reduced to 2.5×10^{-4} .

Temperature variation

For the calculation of the range of validity of the gas model column density correction for temperature changes, the uncertainty from temperature sensor measurement can be neglected due to its high precision ($\leq 0.1\%$) [BBB⁺12, GBSS11]. The uncertainty of the correlation factor α_T of about 3.5% was calculated above comparing results from the two different beam tube gas models. Thus, equation (4.65) reads

$$\frac{\Delta \rho d_T}{\rho d} = \sqrt{\left(\frac{\Delta \rho d_T}{\rho d}\right)_m^2 + \left(\alpha_T \cdot 0.035 \cdot \frac{\Delta T}{T}\right)^2}. \quad (4.68)$$

The column density uncertainty caused by temperature variations including the corrections from the gas model is depicted in figure 4.24b. Relative temperature changes up to 1.3×10^{-2} can be handled by the gas model within the required precision of 7.6×10^{-4} . On the other hand, if the temperature keeps stable on the per mill level, as required in [AAB⁺05]²², the related column density uncertainty can be reduced to 1×10^{-4} .

Pump port pressure variation

The WGTS 10 m beam tube outlet pressure is not measured directly. Still, changes measured at the pressure sensors next to the TMPs can be related to the outlet pressure variation by equation (4.64). The associated uncertainty is approximated using a test simulation that can be found in appendix E. As a result, an uncertainty of 40% for the calculation of the relative changes of pump port pressure, for pressure changes up to 20%, can

²¹In [PSB15] a gas injection stability below 0.1% was demonstrated in the pressure operation range of KATRIN.

²²In test measurements with the WGTS demonstrator from 2010-2012, even a temperature stability of $5 \times 10^{-5} \text{ h}^{-1}$ was measured [GBH⁺13].

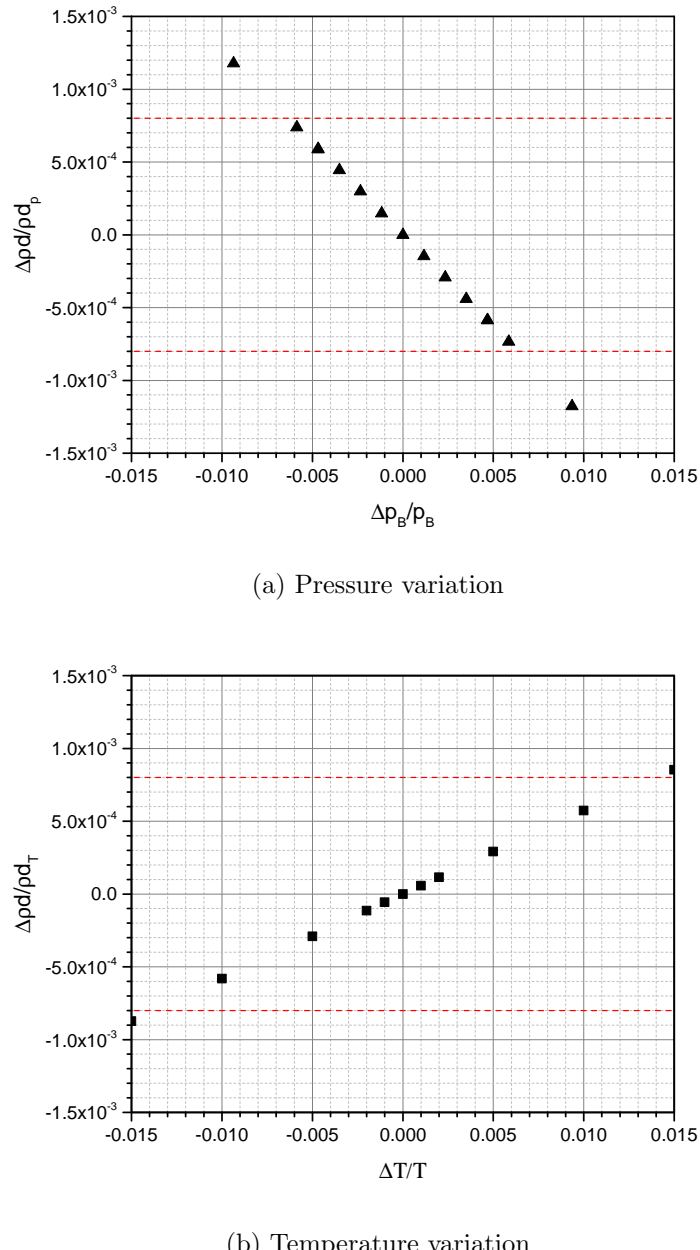


Figure 4.24.: **Uncertainty in the calculation of relative column density changes due to temperature and buffer vessel pressure variations.** The limits for the particular column density uncertainties are visualised by the red dotted lines. For the calculations a standard inlet pressure of 0.337 Pa is assumed. The temperature variation ΔT reflects a assumed simultaneous shift across the whole WGTS beam tube.

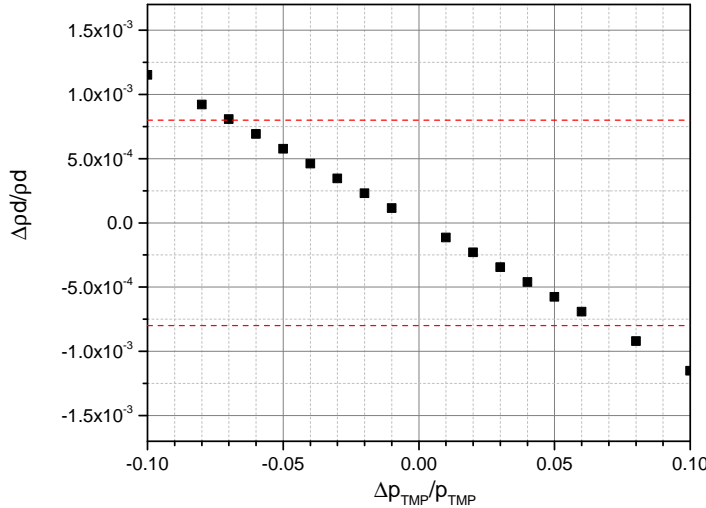


Figure 4.25.: **Uncertainty in the calculation of column density caused by variation of pressure next to the TMPs at the first pump port.** The gas model is used to update the density distribution for changed beam tube exit pressure. The limits for the particular column density uncertainties are visualised by the red dotted lines. For the calculation, a standard inlet pressure of 0.337 Pa is assumed.

be derived. Using the same procedure as for the temperature and buffer vessel pressure, the uncertainty of the column density calculation reads

$$\frac{\Delta \rho d_{p_{\text{ex}}}}{\rho d} = \sqrt{\left(\frac{\Delta \rho d_{p_{\text{ex}}}}{\rho d}\right)_{\text{m}}^2 + \left(\alpha_{p_{\text{ex}}} \cdot 0.4 \cdot \frac{\Delta p_{\text{TMP}}}{p_{\text{TMP}}}\right)^2}. \quad (4.69)$$

The first term in equation (4.69) can be neglected since its influence on the column density, for outlet pressure variations below 10%, is of the order of 1×10^{-5} . The effect of measured pressure variations next to the TMPs on the gas model column density precision is depicted in figure 4.25. Pump port pressure variations up to 7% can be considered correctly by the gas model. On the other hand, if the outlet pressure keeps stable on the per cent level, the related column density error can be reduced to 1×10^{-4} .

The contributions from the particular monitoring parameters p_B , T , and p_{TMP} discussed above need to be added to get the total uncertainty from variations of the gas column density ρd_{gas} . Using the stability requirements from [AAB⁰⁵] for the model parameters T , as well as p_{in} and p_{ex} (which are related to the monitored parameters p_B and p_{TMP}) the column density can be calculated with a precision of

$$\frac{\Delta \rho d}{\rho d}_{\text{var}} = \sqrt{(2.5 \times 10^{-4})^2 + 2 \cdot (1 \times 10^{-4})^2} \lesssim 3 \times 10^{-4}. \quad (4.70)$$

Hence, with the help of the gas model it is possible to reduce the uncertainty of column density changes caused by variations of WGTS operation parameters, p_B , T , p_{TMP} from 2×10^{-3} , as stated in [AAB⁰⁵], to 3×10^{-4} , even if all three WGTS gas operation parameters drift.

Reducing the uncertainty from unresolved column density variation, $\left(\frac{\Delta \rho d}{\rho d}\right)_{\text{var}}$ to 3×10^{-4} ,

the accuracy requirement for the measurement of the absolute column density times scattering cross section, $\left(\frac{\Delta \rho d \cdot \sigma}{\rho d \cdot \sigma}\right)_{\text{abs}}$, from equation (4.49) can be relaxed to 1.9×10^{-3} .

On the other hand, if the $\left(\frac{\Delta \rho d \cdot \sigma}{\rho d \cdot \sigma}\right)_{\text{abs}}$ requirement is not relaxed, the gas model can be used to include parameter drifts larger than 2×10^{-3} .

If the gas model should be used to update the source and spectrum model in between the absolute e-gun measurements (discussed in the following section 4.5) it first needs to be tested and verified experimentally. Suitable test measurements during the commissioning phase of the source and transport section are further discussed in section 4.6.

4.5. Experimental determination of the column density

The absolute value of the column density needs to be determined by a dedicated measurement to reach the required 0.14% accuracy²³ (here the value from equation (4.49) is used derived from the column density trueness requirement of 0.2%). The relative column density changes can also be experimentally monitored on a per mill level to detect fluctuations and support the calculations from the gas model. Absolute and relative instruments are described separately in the following two sections. A more detailed discussion can be found in [BBB¹²].

4.5.1. Absolute measurements

For the measurement of the absolute value of column density times scattering cross section an electron gun (e-gun) is implemented in the rear section. The set-up of this measurement device is specified in [Bab14] and [rswg12]. To deduce the column density ρd , the electron beam is first sent through the beam line with the WGTS evacuated (reference measurement at zero column density) and afterwards through the beam line with a WGTS filled with gas of column density ρd . The comparison of the number of unscattered electrons reaching the detector for filled and empty WGTS gives the zero-scattering probability P_0 (introduced in section 4.1) from equation (4.2) as:

$$P_0(\rho d) = \frac{dN_{\text{egun}}}{dt}(\rho d, U_{\text{MS}} \approx E_{\text{e0}}) / \frac{dN_{\text{egun}}}{dt}(0, U_{\text{MS}} \approx E_{\text{e0}}). \quad (4.71)$$

For the empty WGTS configuration, the scattering on residual gas molecules needs to be negligible (probability for scattering $< 1 \times 10^{-4}$). This corresponds to a column density less than $3 \times 10^{18} \text{ m}^{-2}$ which is a 10^3 reduction in pressure and column density compared to the nominal operating values. To detect only the rate of unscattered electrons, the main spectrometer retarding voltage, U_{MS} , needs to be set between the e-gun electron energy at emission, E_{e0} , and $E_{\text{e0}} - 10 \text{ eV}$ ²⁴. A detailed Monte-Carlo simulation of the e-gun response function and an investigation of the e-gun parameters (e-gun energy, angle, energy spread, rate, etc.) influence on the determination of the inelastic cross section can be found in [Ant15]. In a detailed KASSIOPEIA simulation it was worked out that about 1.4×10^7 e-gun electrons are required to reach a precision of 0.2% for the $\rho d \cdot \sigma$ measurement at a 2σ confidence level. For a reasonable electron emission rate of $\approx 1 \times 10^5 \text{ s}^{-1}$ [rswg12, Bab14] this number implies a measurement time of about 2.5 min. The electron energy spread as well as the angular spread²⁵ of the e-gun beam are included in the simulation.

²³The requirement can be relaxed if the gas model is used to model small parameter changes and thus improve the column density precision. Adapting the coefficients in equation (4.49) results in a relaxed accuracy of 0.19%.

²⁴10 eV is the minimal energy loss for electrons that have scattered once [AAB⁰⁵].

²⁵At an angle of 1.8° between electron motion and magnetic field line in a WGTS magnetic field of 3.6 T, the angular spread is about 0.73° .

The simulations do not include the rate stability of the e-gun. Preliminary test measurements indicate an e-gun stability of about 0.1% over several hours [MP15]. Including the rate stability would cause an uncertainty above the limit of 0.19% for the absolute value of the inelastic scattering cross section times column density. Still, the overall measurement uncertainty can be decreased by a longer measurement time (about 5 min) since the statistical Poisson error for a measurement time of 2.5 min is still twice as large as the uncertainty due to the angular spread, which goes with $\tan \theta \cdot \Delta\theta$. Still, some more detailed calculations are required to determine the upper sensitivity limit that can be reached by the e-gun absolute column density times scattering cross section measurement.

Since column density and scattering cross section occur always combined in the calculation of scattering probabilities (compare equation (4.2)) only the product of both values, $\rho d \cdot \sigma$, can be measured, as discussed in section 4.1. The column density alone is obtained inserting a reference cross section of $3.40(7) \times 10^{-18} \text{ cm}^2$ from literature [ABB⁰⁰]. Thus, the uncertainty of the determination of the absolute value of the column density alone is determined by the accuracy of the measured product and the uncertainty of the total inelastic scattering cross section. Using the value from [ABB⁰⁰], this means an accuracy of 2% for both, column density and total scattering cross section, while the product is known with an accuracy of 2×10^{-3} . What these particular uncertainties imply for the neutrino mass measurement is investigated in section 4.7.

Due to the requirement on e-gun rate stability, the e-gun measurement procedure just described cannot be used to monitor the absolute column density over a time scale of days and longer. Furthermore, it cannot be performed simultaneously with the neutrino mass measurement runs. It can only be performed during intervals at the beginning or at the end of a measurement period and whenever the WGTS can be evacuated.

4.5.2. Monitoring measurements

The above described e-gun measurement can determine the absolute value of the column density times scattering cross section at certain discrete times only. The column density may indeed change in between such measurements due to beam tube temperature, buffer vessel pressure or pumping speed fluctuations or drifts. Relative column density changes are on the one hand described theoretically with the help of the gas dynamics model, as discussed in section 4.4. On the other hand can be monitored directly by continuous activity and regular e-gun measurements to check if the drifts are in the allowed 0.1% region. These activity measurements are:

- Beta Induced X-ray Spectroscopy (BIXS)

The β -decay electrons that are produced in the source are magnetically guided either towards the rear section or towards the detector section. Since almost all electrons that move in detector direction will be reflected by the spectrometer high voltage, almost all source β -decay electrons will be impinging the rear wall and get absorbed there. Upon impact at the rear wall they produce X-rays. These X-rays are monitored continuously by particular silicon drift detectors in the rear wall vessel (see figure 2.13). A variation in the detected rate of X-rays is directly correlated to a changed β -activity in the source. To reach a precision of 0.1% in the measurement of count rate changes, 1×10^6 X-rays need to be detected. This means a sampling time of about 70 s, which was obtained by Monte-Carlo simulations in [Röl15] and sets the time scale for the determination of activity changes in the WGTS with the BIXS system. A detailed description of the design of the KATRIN BIXS system and related test measurements can be found in [Röl15].

- Forward Beam Monitor (FBM)

The FBM is situated at the front end of the source and transport section between the

last two superconducting solenoids in the CPS. Its main components are two silicon PIN diode detectors that are mounted on a detector board [EHH⁺15]. It directly measures the β electrons in the outermost rim of the flux tube in order not to shadow any signal electrons that would be transmitted onto the detector. Activity changes at this monitoring position are taken as being representative for the whole flux tube. Moving the FBM through the flux tube (not during neutrino mass measurements), it can be tested, if the column density profile is as homogeneous over the cross section as expected from the gas model, see section 4.2.3. The dominant uncertainty is the stability of the detector amplification factor (which may be subject to variations, for instance, due to temperature instabilities) [Ell15]. The required precision of the detection of column density changes will be reached after a measurement time of about 30 s [Hau15]. Further information about the FBM design and measurement principle can be found in [EHH⁺15].

- E-gun near-time monitoring

Changing the measurement procedure from the absolute column density determination, it is possible to detect relative changes in the gas column density with an improved precision of 0.1% [rswg12] and without evacuating the WGTS. This can be achieved measuring at two different retarding potentials and using the ratio between the detected rates for the two retarding potentials. The first measurement point can still be set between E_{e0} and $E_{e0} - 10$ eV. For a second measurement point about 50 eV in the spectrum the quotient between the detected rates at both voltages is sensitive to column density changes. For small changes of about 0.2% this dependency is even linear and can be used to check for gas column density changes [Bab15]. Still, data obtained during this measurement cannot be used for the neutrino mass analysis. The required measurement time to reach a precision of 0.1% is about 5 min and thus quite large compared to the other activity monitoring measurements. Frequently using this method would cause a significant loss of measurement time. However, it is quite useful for test and commissioning measurements (see section 4.6) since it can be used with an inactive gas in the source.

To monitor the gas column density, the changes of the active column density ρd_{T_2} measured with BIXS and with the FBM need to be connected to the monitoring of the tritium purity to get the changes of gas column density ρd_{gas} .

4.6. Verifying the gas model – possible test measurements

The SSC gas model provides the powerful tool of a nearly continuously updated column density. This would enlarge the stability range of WGTS operational parameters and at the same time relax the requirement on the measurement of absolute column density times scattering cross section as discussed in detail in section 4.4.1 and 4.4. To be used in the source modelling for the neutrino mass analysis, its predictions still need to be verified experimentally. This can be done during the STS inactive (without tritium) commissioning measurements in the so-called commissioning phase IIIa [?] using deuterium gas. Proposals for the test measurements overviewed below can be found in [col16].

Test column density calculation for small buffer vessel pressure changes

For a small change of pressure in the pressure controlled buffer vessel, the corresponding relative WGTS inlet pressure change was calculated to be $\frac{\Delta p_{\text{in}}}{p_{\text{in}}} \approx 1.18 \cdot \frac{\Delta p_B}{p_B}$, as shown in section 4.4. The column density can be updated, correcting the inlet pressure obtained from the initial column density. This model relation can be verified in the following way:

1. Set the pressure in the pressure controlled buffer vessel (about 10 mbar) to achieve the nominal column density (about $5 \times 10^{21} \text{ m}^{-2}$).

2. Measure the product of column density and scattering cross section $\rho d \cdot \sigma$ with the rear section e-gun according to the prescription in section 4.5.1. It is crucial to have stable temperature and pressure conditions (deviation below 5×10^{-4}) during the e-gun measurement.
3. Normalise measured $\rho d \cdot \sigma$ to expected (literature) cross section value. Calculate the inlet pressure p_{in0} with the SSC gas model for the obtained column density.
4. Start relative e-gun measurement, see section 4.5.2 – measure the rate quotient for initial buffer vessel pressure set at main spectrometer voltages U_{MS} and U'_{MS} with: $U_{MS} = (E_{e0} - [0 - 10 \text{ eV}])/e$ and $U'_{MS} = (E_{e0} - 50 \text{ eV})/e$. The WGTS operation parameters need to be stable below 5×10^{-4} .
5. Modify buffer vessel pressure. Recommended sequence (for example): $\pm 5\%$, $\pm 2\%$, $\pm 1\%$, $\pm 0.5\%$, $\pm 0.2\%$ and $\pm 0.1\%$. Determine for each pressure configuration the column density change with a relative e-gun measurement.
6. Calculate inlet pressure change $\Delta p_{in}/p_{in}$ for each buffer vessel pressure change according to equation (4.60) and modify initial inlet pressure $p_{in} = \Delta p_{in0}/p_{in0} \cdot p_{in0}$. Use the gas model to calculate column density for each pressure configuration.
7. Compare measured and calculated column density change.

To approximate the duration of this procedure, at least 5 minutes for each relative e-gun measurement have to be considered. The time to establish stable conditions in the puffer vessel as well as in the WGTS for each pressure step has to be considered too. This gives an estimate of about 2 h to 3 h for the total measurement duration (assuming the WGTS is evacuated at the beginning of the measurement). According to the gas model results shown in figure 4.24a a column density precision of 0.13% can be reached in the modelling of buffer vessel pressure variations up to 1%. Thus, calculation and measurement should agree in the determined column density within the 0.1% e-gun measurement precision at least up to the 0.8% buffer vessel pressure changes. One should keep in mind that the change in detected rate quotients for the two main spectrometer potentials can only be converted one-to-one to a change in column density if the column density variation is limited to 2% and thus also only for buffer vessel pressure changes in the equivalent range. The same method can in principle be used changing the beam tube temperature in small steps instead of the buffer vessel pressure.

Test gas model by closing TMP valves

This test measurement provides a more general test of the gas model and its predictions for the fraction of residing in the components beam tube and of the impact of a failure of a TMP. The procedure is summarised as follows:

1. According to 1.) from the above described buffer vessel variation measurement.
2. According to 2.) from the above described measurement.
3. According to 3.) from the above described measurement, but include data for the first pump port of DPS1 from the calculations in section 4.2.7.
4. According to 4.) from the above described measurement.
5. Close the valve to a) one and to b) two TMP(s) in the first pump port of the DPS1-F and/or DPS1-R. An e-gun measurement needs to be performed for each TMP to determine the relative column density change.
6. Calculate the relative column density change. Use the pump port density data corresponding to the particular pump configuration from section 4.2.7 for gas dynamics model of the the first pump port in SSC.

Table 4.2.: Relative deviation of overall column density for different TMP working configurations. The column density shift caused by the failure of two pumps or closure of the valves at the pumps should be measurable with an e-gun resolution of 1×10^{-3} .

	1 valve closed	2 valves closed
DPS1-F or DPS1-R	6.5×10^{-4}	1.9×10^{-3}
DPS1-F and DPS1-R	1.3×10^{-3}	3.8×10^{-3}

7. Compare measured and calculated column density changes.

If one (two) TMP is not operational, the column density in the pump port increases by 16.8% (36.8%). Since the pump port outlet density follows with a 15% rise, the column density in the adjacent components also increases by 15% (assuming a linear density scaling). Using the results from table 4.1, the expected shift in column density can be calculated; these are summarised for several configurations in table 4.2.

The closing of one TMP valve will hardly be visible in the e-gun measurement since the e-gun measurement sensitivity for relative column density changes is only about 1×10^{-3} . However, the effect from two or more closed valves should be measurable.

4.7. Gas dynamics and systematic uncertainty of the neutrino mass measurement

Any unaccounted effect that influences the electron energy spectrum has a direct impact on the neutrino mass squared determined with KATRIN (see section 5.5). Processes affecting the potential energy, set by the difference between electrostatic source potential at the location of β -decay process and the potential in the analysing plane in the spectrometer, and processes affecting the kinetic energy of the electron itself need to be disentangled. With regard to the electron kinetic energy change, scattering is one of the most important source-related effects. The scattering probability strongly depends on the gas dynamical properties of the source – the larger the column density, the higher the probability for an electron to undergo scattering with gas molecules (see equation (4.2)).

Up to now, concerning the description of gas dynamical properties of the source, only uncertainties related to the average scattering probabilities have been considered. As shown exemplarily for the zero scattering probability in equation (4.13), the average scattering probabilities depend only on the full column density times inelastic scattering cross section, not on the actual density distribution. Since only these averaged probabilities have been considered so far, the effect of either the column density [Höt12], or the inelastic scattering cross section [Ant15] have been analysed. Considering only first order effects, which means: no inhomogeneities from temperature, velocity, magnetic field or potential in the source, it is actually equivalent to modify either the column density or the value of the total inelastic scattering cross section, since only the product from both quantities needs to be known (compare section 4.1).

If any effect from source inhomogeneities needs to be considered, the degeneracy between scattering cross section and column density is broken. Still, the sole quantity that can be determined precisely is the product of both parameters. Even starting from this accurately determined product, the values of column density and scattering cross section alone have relatively large uncertainties of about 2% each. Consequences of the easing of the $pd \cdot \sigma$ ambiguity combined with gas model uncertainties have not been analysed so far. At this point not only the column density but also the density distribution needs to be known. The modelling of the density distribution has even larger uncertainties, as

discussed in section 4.3.1. Therefore, implications from an inaccurate density distribution are also analysed in this section.

It is important to use an appropriate velocity distribution²⁶ along with each density model, since the gas velocity distribution influences the electron spectrum through the Doppler effect [Höt12].

The principle of the sensitivity analysis used in the following sections was introduced in section 2.4.3. Each of the analyses below uses a standard analysis interval from $E_0 - 30$ eV to $E_0 + 5$ eV with a standard measurement time distribution as depicted in figure 2.17 and a nominal background rate of 10 mHz. The toy measurement data are generated using the assumption of zero neutrino mass. Ensemble of typically 3000 to 5000 full KATRIN measurements are simulated for each analysis.

4.7.1. Neutrino mass uncertainty related to $\Delta(\rho d \cdot \sigma)$

As discussed in section 4.5.1, even the absolute value of total scattering cross section times column density can only be determined with an accuracy of about 1.4×10^{-3} to 2×10^{-3} with the e-gun measurement. Besides this relatively large absolute measurement uncertainty, which consumes bulk of the entire column density related error budget, there is the uncertainty from monitoring and modelling of column density changes. If all the WGTS operation parameters pressure in the buffer vessel, pump port pressure and temperature are stabilised on the per-mill level (see section 4.4) the related uncertainty on the column density monitoring is 3×10^{-4} (only, if the gas model is used to update ρd). To give a impression of the order of the product $\rho d \cdot \sigma$ reference values from [AAB⁰⁵] for both parameters can be used which results in

$$\rho \cdot \sigma = 5 \times 10^{21} \text{ m}^{-2} \cdot 3.45 \times 10^{-22} \text{ m}^2 \approx 1.725. \quad (4.72)$$

Depending on the e-gun measurement accuracy, the total uncertainty of the value of $\rho d \cdot \sigma$ is between 0.15% and 0.2%. For the neutrino mass analysis this equals a systematic shift between

$$\Delta m_\nu^2 = (-1.87 \pm 0.25) \cdot 10^{-3} \text{ eV}^2 \text{ and } \Delta m_\nu^2 = (-2.62 \pm 0.25) \cdot 10^{-3} \text{ eV}^2,$$

which is in good agreement with values from [AAB⁰⁵] and [Höt12].

4.7.2. Column density versus scattering cross section

Column density as well as total inelastic scattering cross section can only be determined with an accuracy of 2%, as illustrated in section 4.5. Since to first order only the product from column density and scattering cross section is needed to model the scattering processes in the source while there is accurate information on this product, the situation is different from the one considered in [Höt12] and [Ant15]. To include second order effects, which means spatial inhomogeneities, in the calculation of the source spectrum, it is important to use a fine enough discretisation of the WGTS to resolve such inhomogeneities. For the analysis described in this section, the WGTS is thus divided into 500 equidistant slices of 2 cm width each.

To consider shifted values of ρd and σ individually while keeping their product fixed at 1.7 (see equation 4.72) both quantities are deflected by a similar magnitude but in the opposite direction. For example, if the column density is changed by 5%, the scattering cross section σ_0 needs to be shifted²⁷ to $1/1.05\sigma_0$. This way, column density uncertainties of

²⁶For the artificial models used in this section (constant and triangular density) the velocity distribution is obtained from the conservation of mass flow $\rightarrow p \cdot v = \text{const.}$

²⁷The shift of the cross section is almost similar (5%) to the shift of the column density.

Table 4.3.: **Neutrino mass squared shift from uncertainty of column density and scattering cross section.** The product of both quantities is identical in toy measurement data and analytical spectrum and fixed to a value of 1.725.

$\frac{\Delta \rho d}{\rho d}, \frac{\Delta \sigma}{\sigma}$	$\Delta m_\nu^2 / 10^{-3} \text{ eV}^2$
10%	-1.36 ± 0.29
5%	-0.35 ± 0.29
2%	-0.261 ± 0.25

10%, 5%, 2% are analysed. All spectra are calculated using the standard one-dimensional WGTS 10 m beam tube gas model from section 4.2.3. The neutrino mass squared shift is determined from ensembles of 3000 to 4500 KATRIN measurements. The results are summarised in table 4.3.

For a realistic column density and inelastic cross section uncertainty of 2%, the induced neutrino mass squared shift is about $-2.6 \times 10^{-4} \text{ eV}^2$ and almost one order of magnitude smaller than the uncertainty related to the absolute measurement of $\rho d \cdot \sigma$. This means, that a better knowledge on the total inelastic scattering cross section, which at the same time reduces the uncertainty of the column density, hardly improves the modelling of the electron-T₂ gas scattering processes in the WGTS. A 2% uncertainty on the knowledge of the total inelastic scattering cross section is, in terms of modelling of scattering processes in the WGTS, consistent with the related Δm_ν^2 limits from [AAB⁰⁵]. This is different from statements in [Ant15, Zie13, AAB⁰⁵], where a cross section accuracy of 0.2% was demanded.

4.7.3. Effect of density model

The description of the density distribution $n(z)$ inside the WGTS, required to model spatial source parameter inhomogeneities correctly, is based on the gas model of the source. The column density from the gas model is adjusted to the column density derived from the e-gun measurement for a pre-defined inelastic scattering cross section. Still, there are large uncertainties regarding the density and velocity distribution, as discussed in section 4.3.1. To get information on the related neutrino mass squared uncertainty, different density models are compared in the neutrino mass analysis:

- Sharipov model,
- COMSOL model,
- triangular profile,
- constant density.

Since one of the most important source inhomogeneities is the velocity distribution, it is important to include the velocity distribution that belongs to any particular given density distribution. The column density is fixed to $5 \times 10^{21} \text{ m}^{-2}$ for all density distributions. All models are compared to the Sharipov model, which is assumed to be the most reliable one. Thus, the Sharipov model is used to simulate the toy measurement data, according to the procedure described in section 2.4.3. A different density distribution is used to build the analytic source model which is fitted to the toy measurement data. The temperature is assumed to be 30 K for the whole WGTS beam tube. Only the density distribution inside the WGTS is used for analysis, since the bulk of the tritium molecules are situated there. For the calculation of the spectrum, the 10 m long WGTS beam tube is segmented into 1000 equidistant slices. A radial or azimuthal division is not applied, since density variations in a WGTS beam tube cross section are small due the constant beam tube wall temperature. Inlet and outlet effects can be neglected for this analysis.

Sharipov model vs constant density

In this simulation a constant WGTS density of $5 \times 10^{20} \text{ m}^{-3}$ is used for the analytical model. The velocity profile according to this distribution is set to a constant value of 30 m s^{-1} , which is approximately the average velocity for the given column density in the Sharipov model.

After the simulation of an ensemble of 3000 full KATRIN measurements, a systematic shift of

$$\Delta m_\nu^2 = (-6.1 \pm 0.36) \cdot 10^{-3} \text{ eV}^2$$

is derived from the ensemble of best-fit m_ν^2 values.

This relatively large neutrino mass shift almost reaches the limit of $7.5 \times 10^{-3} \text{ eV}^2$ from [AAB⁰⁵] for a single experimental parameter. The large uncertainty is mainly caused by the velocity profile connected to the different density profiles.

The constant density model will not be used for the analysis of KATRIN data. It is indeed far to simplistic and does not use the information on the gas flow that is available from gas dynamical calculations. Still, it demonstrates that the KATRIN density and velocity models need to be as accurate as possible.

Sharipov model vs triangular density

Like the realistic density distribution obtained from gas dynamics simulation, the triangular density model has its maximum in the middle of the 10 m WGTS beam tube and decays towards the front and rear ends, assuming a pump port to inlet density ratio of 0.02. The velocity distribution is calculated using the continuity equation for the particle flow:

$$\nabla(n\vec{v}) = 0. \quad (4.73)$$

Using a constant beam tube temperature and neglecting end effects the flow profile can assumed to be one-dimensional. Thus, density and velocity are connected through $n(z) \cdot v(z) = \text{constant}$. Setting the outlet velocity to 100 m s^{-1} , the velocity profile can be calculated:

$$v(z) = \pm \frac{100 \text{ m s}^{-1} \cdot 0.02 \cdot n_{\text{in}}}{n(z)}. \quad (4.74)$$

The triangular velocity and density distribution for a column density of $5 \times 10^{21} \text{ m}^{-2}$, as used to model the analytical source spectrum, are depicted in figure 4.26.

The influence on the neutrino mass measurement is determined by the simulation of 4500 full KATRIN measurements. The resulting neutrino mass shift is

$$\Delta m_\nu^2 = (-5.1 \pm 2.5) \cdot 10^{-4} \text{ eV}^2.$$

Compared to the prior density model, the shift is significantly reduced, since density and velocity distribution are comparable and source inhomogeneities can be mapped by both models to a similar extent.

Sharipov model vs COMSOL model

In a last step, the impact on the neutrino mass measurement from the density distributions that are most similar to each other are compared: the nominal beam tube density calculation with the Sharipov model, and the comparative beam tube calculation which is the COMSOL model (see section 4.2.5). Density and velocity distributions along the beam tube axis at $r = 0 \text{ m}$ are depicted in figure 4.27 for both models. Compared to the density models tested before, the deviations in the densities along the beam tube are small. However, as discussed in section 4.2.5, the velocity distributions show large differences up to 100% – the bulk velocity is significantly increased in the COMSOL model. It almost

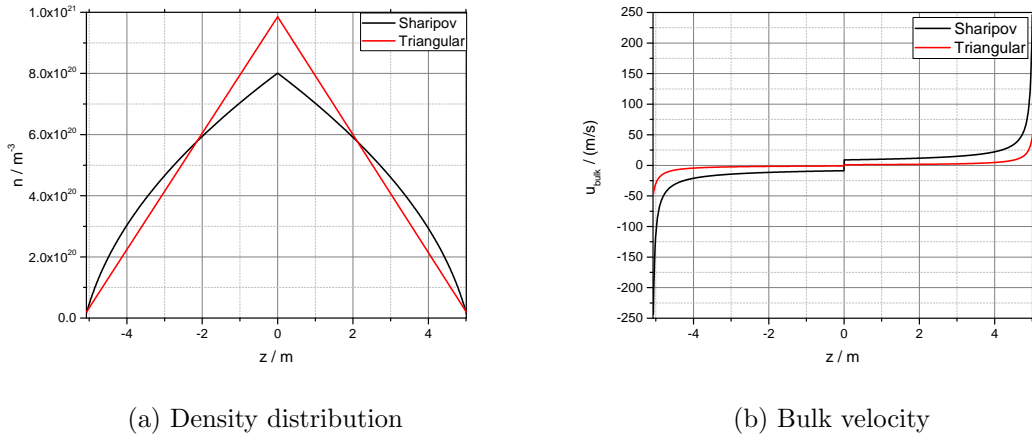


Figure 4.26.: **Density and velocity distribution for the triangular density model.**

The nominal Sharipov model is shown for comparison. Both density distributions produce the same column density of $5 \times 10^{21} \text{ m}^{-2}$.

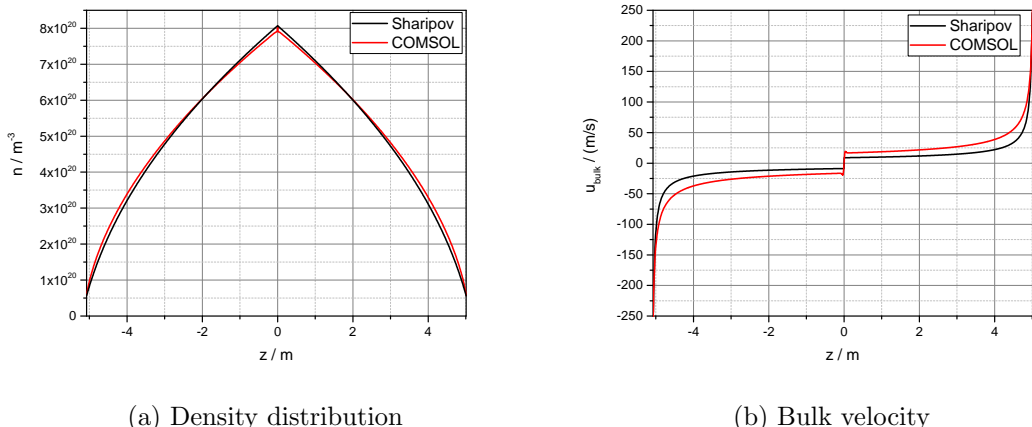


Figure 4.27.: **Density and velocity distribution for the COMSOL model.** The nominal Sharipov model is shown for comparison. Both density distributions produce the same column density of $5 \times 10^{21} \text{ m}^{-2}$.

reaches the thermal molecular velocity of 288 m s^{-1} in the outlet regions.

The influence on the neutrino mass measurement is determined simulating 4500 full KA-TRIN measurements

$$\Delta m_\nu^2 = (-7.5 \pm 2.4) \cdot 10^{-4} \text{ eV}^2. \quad (4.75)$$

Despite the similar density distribution of both models, the neutrino mass squared shift is larger than for the triangular density model (the mass squared shifts still agree within the statistical uncertainty limit originating in the ensemble test method). This difference can only be caused by secondary effects – mainly the significantly diverging bulk velocities and the corresponding electron energy modification by the Doppler effect. This assumption is tested by interchanging the COMSOL velocity model in the calculation of the analytical spectrum with the triangular velocity model, as shown in figure 4.27, that produces significantly lower velocities ($\leq 100 \text{ m s}^{-1}$)²⁸. In that case, the shift in m_ν^2 is pushed below 1×10^{-4} , which underlines again the importance of a proper bulk velocity model.

To analyse the impact of the gas model and its uncertainties for a fixed column density the

²⁸Both models should actually not be combined to calculate realistic source spectra.

Table 4.4.: **Gas model configuration for ensemble simulations with full gas dynamics uncertainty.**

	Gas dynamics model	$\rho d / \text{m}^{-2}$	σ / m^2	$\rho d \cdot \sigma$
toy measurement	Sharipov	5.11×10^{21}	3.388×10^{-22}	1.7313
analytical model	COMSOL	5×10^{21}	3.456×10^{-22}	1.728

uncertainty from the density model needs to be considered combined with the uncertainty from the velocity model. Uncertainties from both distributions cannot be disentangled in the electron spectrum and need to be analysed together. Comparing two realistic models, which mainly differ in their velocity distributions, a neutrino mass squared shift of $\Delta m_\nu^2 = (-7.5 \pm 2.4) \cdot 10^{-4} \text{ eV}^2$ is derived. This represents a quite conservative approach, since one of the velocity distributions shows partially unrealistically large bulk velocities. Still, the actual uncertainty of the velocity model cannot be determined differently then by comparison of both density models. Thus, the calculated mass shift is representative for the neutrino mass uncertainty caused by the gas model density and velocity distributions.

4.7.4. Combined gas dynamical uncertainty

To investigate the full gas dynamics related uncertainty, the particular contributions described above can not simply be added. All of them are correlated. Thus, to obtain a characteristic value, the properties and parameters of the one-dimensional gas models for the generation of the toy measurement are modified with respects to each other in the following properties and parameters:

- Both beam tube gas models (Sharipov and COMSOL) are used.
- The implemented $\rho d \cdot \sigma$ values have a difference of 0.2%.
- A individual ρd and σ difference of 2% is induced.

The corresponding model configurations for generation of the toy measurement data and the analytical model are summarised in table 4.4.

The neutrino mass squared shift obtained from the ensemble test with 5000 full KATRIN measurements is

$$\Delta m_\nu^2 = (2.62 \pm 0.25) \cdot 10^{-3} \text{ eV}^2. \quad (4.76)$$

The bulk of the uncertainty is related to the determination of the product of column density and scattering cross section if source spatial inhomogeneities are reasonably small and if the velocity can be assumed to be described by a proper model. It should be noted that this number only holds if the gas model is used to calculate the effect of operational parameter changes. Otherwise it has to be checked if the combined monitoring uncertainty and absolute e-gun measurement uncertainty is still within the required 2×10^{-3} column density trueness.

All inhomogeneities in the source need to be included in the gas model testing to obtain a realistic approximation of the second order effects in the response function. Thus, a realistic model for the source potential profile (it was not considered in the calculations presented above) needs to be considered. Such potential profiles can be obtained in plasma simulations of the source that are discussed in the following chapter. The profile used here to introduce the potential inhomogeneity is depicted in figure 5.34b (it is used in the calculation of toy measurement data and in the analytical spectrum both). The calculated neutrino mass shift of

$$\Delta m_\nu^2 = (3.06 \pm 0.24) \cdot 10^{-3} \text{ eV}^2 \quad (4.77)$$

is slightly increased compared to the one given in equation (4.76) which demonstrates the impact of second order effects – for large inhomogeneities like present in the source potential distribution they cannot be neglected and contribute to the error budget. The neutrino mass squared shift given in includes the main source variable inhomogeneities (distributions of temperature, magnetic, velocity and potential) through realistic models and can thus be seen as representative for the total systematic uncertainty related to the description of gas dynamical processes.

4.8. Summary

In this chapter, the extension of the former KATRIN single-component beam tube gas model to a full WGTS gas model including all beam tube and pump port components from the WGTS injection up to the rear section in rear direction and up to the DPS2 in forward direction was described. Total density and gas flow reduction factors of about 2000 and 400 were calculated in the simulation of the components of the WGTS, respectively (see table 4.1). Different model assumptions have been used to calculate the gas flow in the components separately.

To implement the individual components in the calculation of the source spectrum, the former gas dynamics structure in SSC had to be overhauled. By adjusting the in- and outlet densities of the adjacent components and scaling the whole model to the column density, determined independently by measurement, the gas model provides an accurate description of density and velocity distribution through the whole 16 m length of the WGTS. Uncertainties related to the density distribution and the total column density of the models of the particular components have now been analysed thoroughly.

Special emphasis was put on the time-resolved determination of the column density. Here the absolute column density determination by an e-gun measurement and the gas model based calculation of relative changes were disentangled. Both parts need to be included separately in the total uncertainty budget for the value of column density times cross section. To reach the required trueness of 2×10^{-3} on $\rho d \cdot \sigma$, the e-gun measurement of $\rho d \cdot \sigma$ needs to be performed with an accuracy between 1.4×10^{-3} and 1.9×10^{-3} , depending on the actual stability of the WGTS operation parameters and whether or not the gas model is used to model the induced column density changes. Up to now, only the feasibility of an e-gun absolute measurement accuracy of 2×10^{-3} was considered using a realistic e-gun energy and angular spread, but disregarding the e-gun rate stability. It remains to be tested up to which level this accuracy can be improved. Otherwise, the trueness requirement of column density times scattering cross section needs to be modified. With regard to the uncertainty induced by the calculation of relative column density changes, in previous considerations [AAB⁺05, BBB⁺12, Höt12] named as monitoring uncertainty, it was demonstrated that it can be reduced to 3×10^{-4} if temperature, beam tube inlet and outlet pressure keep stable on the per mill level as required in [AAB⁺05] (the outlet pressure only needs to be stabilised on the per cent level). At that point the fact that neither the beam tube injection pressure nor the exit pressure (i.e., the pressure in the first pump port) can be measured directly, but need to be derived from pressure sensors at different positions was included.

To apply the gas model for the neutrino mass analysis, it needs to be verified experimentally: – Two test measurements to verify the gas model have been proposed that are recommended to be performed during the commissioning phase of the source and transport section.

For the determination of the systematic neutrino mass uncertainty related to the description of gas dynamics, the interrelation of column density and total inelastic scattering cross section for the description of the scattering probabilities has been analysed. It was shown

that, if spatial source inhomogeneities like those of velocity, magnetic field, temperature and electric potential are included in the source modelling, the actual density distribution needs to be known. The need for a proper modelling of the velocity distribution was underlined.

Systematic effects induced by the density and velocity distribution in the gas model, by the uncertainty of the measured product of column density and inelastic scattering cross section and its monitoring, as well as by the uncertainty of the individual values of scattering cross section and column density had at first been analysed separately. It was shown here that the actual column density and scattering cross section do not need to be known at an accuracy level significantly better than 2%, as long as their product can be determined precisely – the related neutrino mass squared shift for 2% uncertainty of the particular values of ρd and σ is one order of magnitude smaller than the shift due to 0.2% uncertainty of the product, $\rho d \cdot \sigma$. A combined ensemble simulation including all these effects revealed a neutrino mass uncertainty of $\Delta m_\nu^2 = (3.06 \pm 0.24) \cdot 10^{-3} \text{ eV}^2$ related to the overall description of gas dynamical processes in the WGTS.

5. Investigation of Plasma Phenomena in the WGTS

Contents

5.1. Theoretical considerations	148
5.1.1. Potential, work function and plasma sheath	148
5.1.2. Charged particle transport and fluid approach	153
5.2. General remarks on the WGTS plasma conditions	159
5.3. Modelling of the WGTS plasma	165
5.3.1. Previous WGTS plasma models	166
5.3.2. Development of a realistic two-dimensional WGTS plasma model	167
5.3.2.1. Electron diffusion model	169
5.3.2.2. Three-particle fluid model including space charge influence	171
5.3.3. Influence of plasma conditions and parameters on the WGTS potential	190
5.3.3.1. Column density	191
5.3.3.2. Electron energy and electron energy distribution	194
5.3.3.3. Geometry length	198
5.3.3.4. WGTS magnetic field	201
5.3.4. Impact of boundary bias and work function on WGTS potential	205
5.3.4.1. Rear wall bias at constant surface potential	205
5.3.4.2. Work function differences of tube and rear wall	208
5.3.5. Effect of electron emission at rear wall	223
5.4. Experimental access to WGTS plasma potential	228
5.4.1. The ^{83m}Kr mode of the Windowless Gaseous Tritium Source . .	229
5.4.1.1. Plasma simulation results for ^{83m}Kr mode conditions .	229
5.4.1.2. Converting results from ^{83m}Kr mode to 30 K mode . .	230
5.4.2. Experimental optimisation of rear wall bias voltage	231
5.5. Implications of plasma potential for neutrino mass uncertainty 236	
5.5.1. Gaussian potential fluctuations in the WGTS	237
5.5.2. Potential distribution from plasma simulation	239
5.5.2.1. Rear wall and beam tube at equipotential	240
5.5.2.2. Differences in rear wall - beam tube surface potential .	241

5.5.2.3. Plasma potential and systematic neutrino mass uncertainty – an approximation	242
5.6. Summary	243

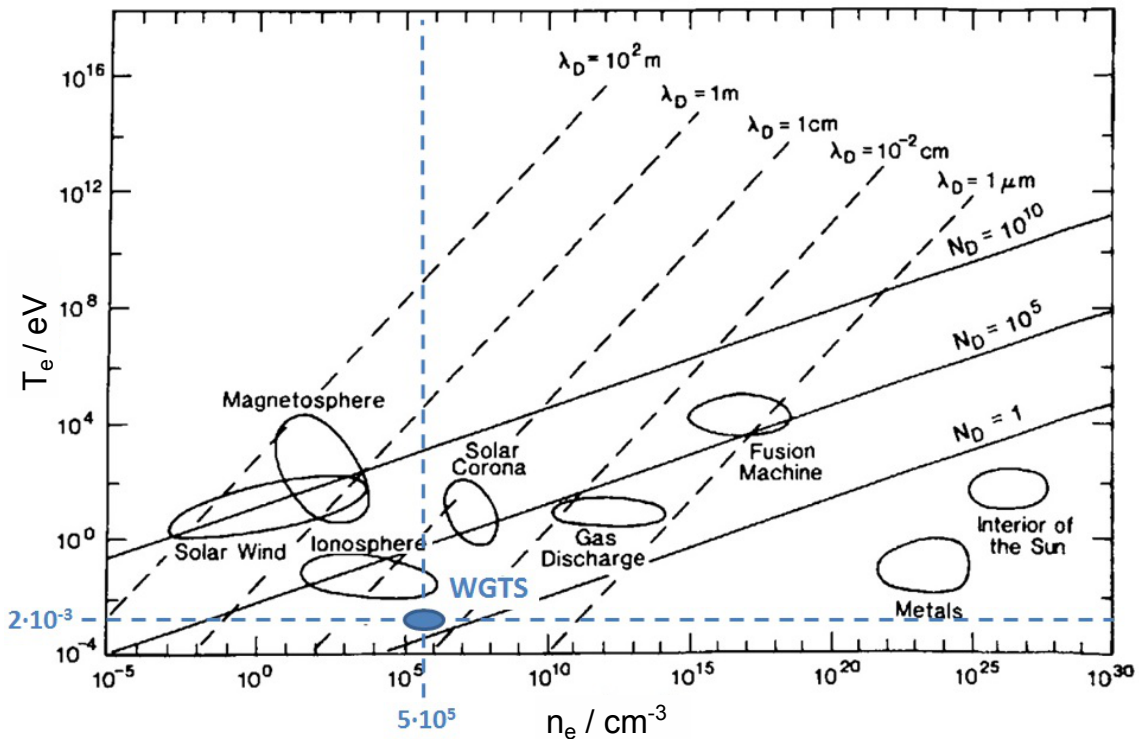


Figure 5.1.: Electron temperature T_e and density n_e for various types of plasma.

Debye length λ_D and plasma parameter N_D are included by dashed and solid lines. Due to its low electron temperature and comparably low electron density, the region marked “WGTS plasma” is set apart from the remaining types. Image adapted from [Gal12].

Electrons and tritium ions form a quasi-neutral plasma inside the WGTS. This plasma is quite different to plasmas in other applications:

- It is extremely cold, even for a low temperature plasma¹ ($T_{\text{gas}} = T_{\text{ion}} = 30 \text{ K}$).
- The number density of charged particles is low (about $1 \times 10^{11} \text{ m}^{-3}$ to $1 \times 10^{12} \text{ m}^{-3}$ [WGT04])².
- The generation of charged particles is not due to discharges caused by a large external electric field or by high temperatures, but due to internal β -decay and secondary ionisation of gas molecules by fast β -decay electrons.
- The length-to-radius ratio of the plasma containing WGTS is large.

The exceptional properties of WGTS plasma compared to other plasmas can be seen in figure 5.1. An estimation of its characteristic variables, such as electron and ion densities and potential, is therefore impossible without dedicated simulations. Even building an adequate numerical model is quite challenging.

Since the local potential inside the WGTS directly translates into energy of β -decay electrons emerging at this point, it is crucial to achieve an almost homogeneous and stable potential. Therefore a limit of 10 meV for the maximal variation in source potential across

¹A classical low temperature plasma has temperatures of about $1 \times 10^4 \text{ K}$ for a thermal one and about 300 K for a non-thermal one [DKMS05].

²Comparable densities can be found in space plasmas (see figure 5.1.)

the plasma volume is indicated in [AAB⁰⁵]. In general the effect from potential variations within the source on the deduced neutrino mass can be compared to fluctuations in the main spectrometers retarding potential [Bab14]. The strong magnetic field inside the rear section and source and transport section, within the range of 0.2 T to 5.6 T [AAB⁰⁵], confines the electrons along the magnetic field lines, which means that their transversal conductivity can be neglected. Therefore, in [AAB⁰⁵] and [rswg12], the first conducting surface crossing the field lines (i.e. which is the rear wall) is assumed to determine the potential inside the plasma. However, this statement has not been tested and with regard to the complexity of the WGTS plasma its validity seems questionable. Within this work the influence of the rear wall and beam tube walls on the potential distribution in the WGTS is analysed with respect to a realistic WGTS plasma. A plasma model is set up including the neutral gas flow, creation and recombination reactions as well as variable potentials at confining rear and tube walls.

This chapter starts with an overview of some theoretical concepts that are needed to characterise and simulate the WGTS plasma. Section 5.2 defines the basic plasma conditions and parameter values in the WGTS. The actual process of WGTS plasma modelling is described in section 5.3 starting with simple electrostatic assumptions that evolve into a full multi-particle plasma model. A measurement procedure that will be used to determine characteristic properties of the WGTS plasma potential experimentally, the Krypton mode, is introduced in section 5.4. Finally, the influence of different potential distributions and of Krypton-measurement results on the neutrino mass uncertainty are reviewed in section 5.5.

5.1. Theoretical considerations

In general a plasma is an ensemble of charged particles that is usually electrically neutral and is characterised by its “collective behaviour” [vK14, DKMS05, BHL10]. It is classified according to its charged particle density and the electron temperature³. The typical length scale, so-called Debye-length λ_D is given by

$$\lambda_D = \left(\frac{\epsilon_0 k_B T_e}{n_e e^2} \right)^{1/2} \quad (5.1)$$

for a thermal plasma, with Boltzmann constant k_B and vacuum permittivity ϵ_0 . For length scales smaller than λ_D the quasi-neutrality is not valid, since Coulomb and diffusive forces do not compensate any more [vK14] as shown schematically in figure 5.2. The condition for the collective particle behaviour, characteristic for a plasma, can be written with the help of the Debye-length:

$$n_e^{1/3} \gg \frac{1}{\lambda_D}, \quad (5.2)$$

or in terms of the plasma parameter N_D :

$$N_D = \frac{4}{3} \pi n_e \lambda_D^3, \quad N_D \gg 1. \quad (5.3)$$

For the charged particles in the WGTS this condition is fulfilled, as can be seen from figure 5.1. Hence, this case can be treated as a low density plasma.

5.1.1. Potential, work function and plasma sheath

In general the absolute potential of an electron in front of a metallic surface depends on the metal properties such as work function and applied voltage. The work function Φ of a

³In general the ion temperature T_i is equal to the gas temperature T but not to the electron temperature T_e , except for so-called thermal plasmas, where $T_e = T_i$.

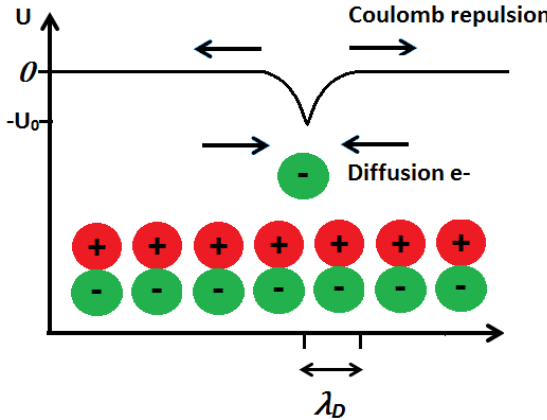


Figure 5.2.: **Concept of Debye-length.** If an additional charge is added to the quasi-neutral plasma, all charge carriers arrange to compensate this additional charge due to repulsive Coulomb and attractive diffusion forces. For microscopic scales $< \lambda_D$ a potential difference U_0 arises.

metal can be defined as the energy difference "...between a lattice with an equal number of ions and electrons, and the lattice with the same number of ions, but with one electron removed" [WB35]. In other words, Φ corresponds to the energy needed to extract one electron from the metal (at 0 K) to infinity. If an electron is removed from the surface or if an electron comes near to the surface the electrostatic potential across the metal surface rises due to the forming of a double layer [WB35, Bar36, Fre28]. Thus, the work function can be calculated using this rise in potential $\Delta\phi$ and the energy at the Fermi level E_F [LK71]:

$$\Phi = \Delta\phi - E_F. \quad (5.4)$$

The potential energy $U(x)$ of an electron removed from the metal to distance x can be calculated using the concept of an image charge created in the metal at position $-x$. Considering the corresponding Coulomb force with electric permittivity ϵ_0 , the potential energy, at least for distances greater than the lattice parameter of the metal [Bro14], reads:

$$U(x) = E_F + \Phi - \int_x^\infty \frac{-e^2}{4\pi\epsilon_0 z^2} dz = E_F + \Phi - \frac{-e^2}{16\pi\epsilon_0 x}. \quad (5.5)$$

The electron potential is depicted in figure 5.3. Already after 5 nm the Coulomb repulsion drops below 0.1 eV and becomes negligible compared to the work function, which is of the order of several electronvolts [LK71]. Thus, the vacuum potential U_∞ in front of the surface can be calculated with

$$U_\infty = \phi + E_F. \quad (5.6)$$

When a potential ΔU is applied at the metal, the Fermi level is shifted according to this potential. The work function does not change, therefore the vacuum energy changes:

$$U_\infty = \phi + E_F + \Delta U. \quad (5.7)$$

If metals with different work functions (and therefore also different Fermi levels) are in contact with each other, the Fermi levels adapt and a difference in vacuum energy develops in front of these surfaces. Aiming for a uniform vacuum potential, it is important to provide surfaces with homogeneous work function. The difference in vacuum potential between metal surfaces in electric contact with each other is useful to measure the work function of a given metal surface using the Kelvin Probe method, developed by W. T. Kelvin [Kel98]. This method has also been used to determine the work functions for the

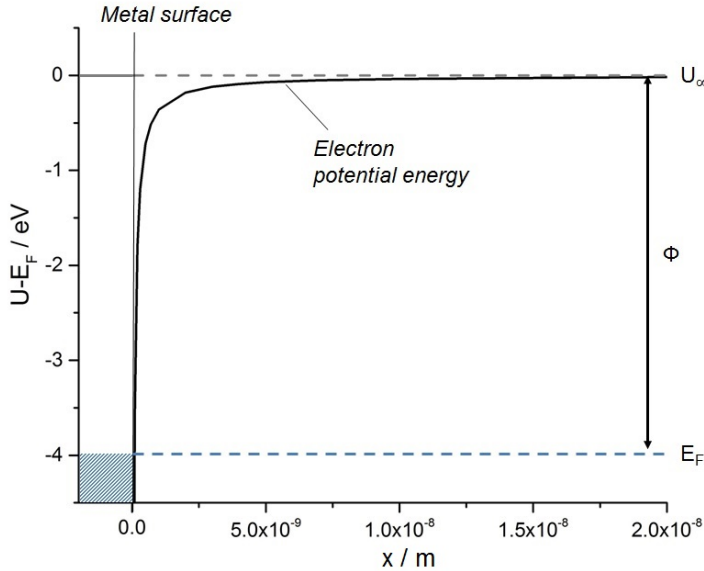


Figure 5.3.: **Energies in front of a metal surface.** A representative work function of 4 eV is used. Already after few nanometres the electron potential energy $U(x)$ is equal to the potential at infinite distance.

KATRIN rear wall candidates which is further described in [Sch16].

For a plasma the potential distribution in front of a wall, $U(x)$, slightly changes compared to the vacuum case. In the following it is derived for a planar plasma in front of a non-conducting, so-called floating, surface⁴, where the flux densities $\Gamma_{i,e}$ of (positive) ions i and electrons e are equal: $\Gamma_e = \Gamma_i$. The potential distribution next to the wall can be derived with the help of the law of conservation of energy:

$$\frac{1}{2}Mv_i^2(x) + eU(x) = \frac{1}{2}Mv_0^2, \quad (5.8)$$

with index 0 denoting values in the bulk of the plasma, M the ion mass, and v_i the velocity of ions. Furthermore, one needs the continuity equation:

$$\Gamma_i = \Gamma_e = n_i v_i = n_0 v_0 = n_e v_e, \quad (5.9)$$

as well as the electron energy distribution. The electrons are assumed to be in equilibrium with the ions and thus their energy distribution can be described by a Boltzmann distribution[Div01]. In this case, the electron density distribution can be approximated with [vK14]

$$n_e(x) = n_0 e^{eU(x)/k_B T_e}. \quad (5.10)$$

The plasma bulk potential $x \ll \lambda_D$, is assumed to be at zero potential. Plugging equations 5.9, 5.8 and 5.10 into the Poisson equation for the electrical potential

$$\frac{d^2U(x)}{dx^2} = \frac{n_e(x) - n_i(x)}{\epsilon_0} \quad (5.11)$$

$$\text{one obtains: } \frac{d^2U(x)}{dx^2} = \frac{en_0}{\epsilon_0} \left(e^{eU(x)/k_B T_e} - \left(1 - \frac{eU(x)}{E_0} \right)^{-1/2} \right). \quad (5.12)$$

⁴In case of a conducting wall not the electron and ion flux densities at each point of the wall, but integrated over the wall surface need to be equal each other, as balancing currents flow through the wall material. In case of more than one conducting wall in contact with each other and with the plasma, only the sums of electron and ion fluxes through all walls need to be equal.

This is the non-linear equation for the form of the plasma potential across the so-called plasma sheath next to the wall. The general concept of plasma sheaths and potential distributions in the sheaths has been worked out by Langmuir and Tonks [TL29]. From this equation one can derive the Bohm criterion [Div01]. The required steps can be found in [vK14]. The Bohm criterion states that ions must have a large velocity at the beginning of the sheath at $x = 0$. This velocity must be larger than the so called Bohm-velocity, v_B , in order for the electron and ion fluxes to be equal [Div01]:

$$v_i(0) > v_B = \sqrt{\frac{k_B T_e}{M}}. \quad (5.13)$$

To estimate the resulting potential at the surface, U_w , the ion velocity can be taken to be equal to the Bohm-velocity. The electron velocity $v_{e,th}$ can be assumed to be thermal⁵[vK14]. Therefore, the electron flux becomes: $\frac{1}{4}n_0v_{e,th}e^{\frac{eU_w}{k_B T_e}}$. Using relations (5.9) and (5.13), one obtains:

$$U_w = -\frac{k_B T_e}{e} \ln \left(\frac{M}{2\pi m_e} \right)^{1/2}, \quad (5.14)$$

where m_e is the electron mass. The ions need to be accelerated in a pre-sheath before entering the sheath region with Bohm-velocity by a potential difference $U_w - U_p$, where U_p is the potential in the bulk of the plasma. The ion velocity is assumed to be small⁶ before reaching the plasma sheath $v_i = 0$. Thus using

$$(U_p - U_w)e = \frac{Mv_B^2}{2}, \quad (5.15)$$

the plasma potential with respect to the floating potential, U_w , can be calculated:

$$U_p - U_w = \frac{k_B T_e}{2e}. \quad (5.16)$$

The corresponding potential distribution is depicted in figure 5.4. In the considerations above, the work function of the surface is neglected. For the simple case of a planar plasma and homogeneous density distribution along the surface, the work function and an applied voltage, ΔU , can in a simple approximation be added to the plasma potential (compare equation (5.7)):

$$U_p - U_w = \frac{k_B T_e}{2e} + \phi + E_F + \Delta U. \quad (5.17)$$

In other words, the potential in the bulk of the plasma is equal to the vacuum potential plus the potential drop that occurs in the sheath due to the difference in electron and ion fluxes.

Effect from electron emission at the wall

If additional electrons are emitted from a surface in contact with a plasma (for example by secondary electron emission or photo-electric emission) the plasma-boundary interactions described above can change depending on the ratio γ of emitted to initial electron flux. In the following still a cold, planar plasma in front of a floating wall is assumed. Thus, the currents of electrons and ions that leave the plasma through the wall, $I_j = q \int_{\text{wall}} \Gamma_j dA$, with charge q , still need to be equal:

$$I_i = I_e + I_k. \quad (5.18)$$

⁵The velocity component induced by the electric field arising in the sheath region is assumed to be small compared to the thermal velocity of the electrons, which is in general the case.

⁶This assumption holds especially, if there is no electric field in the bulk of the plasma, and the plasma has low temperature.

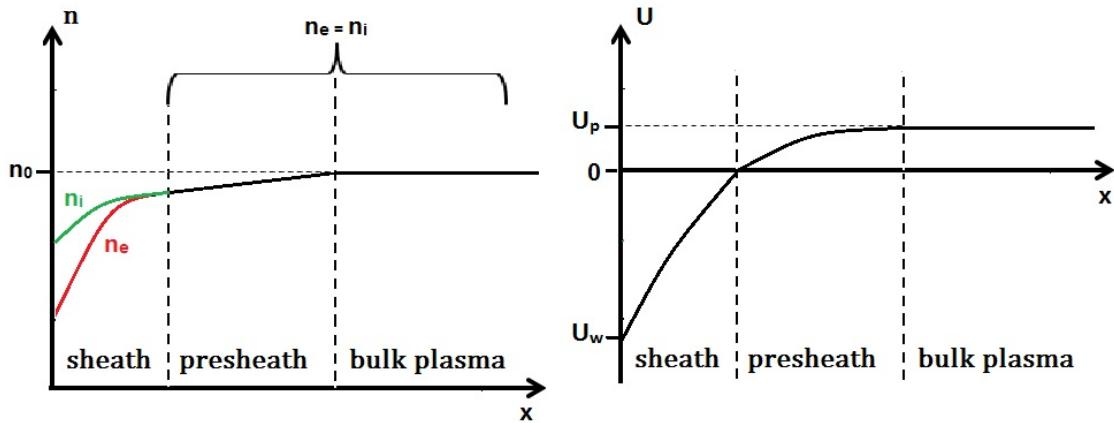


Figure 5.4.: **Potential and density distribution in plasma sheaths.** Due to their higher mobility, the electrons can reach the wall faster than the ions. Thus, in the sheath a positive space charge is formed. The potential drop in the sheath accelerates the ions and thus adjusts the electron and ion fluxes. The space charge in the sheath region causes the bulk potential U_p to be larger than zero.

Here I_e denotes the initial electron current and I_k the electron current emitted from the surface. However, the compensation of the additional electron current by forming of a negative plasma sheath, as described for a plasma-wall interaction without additional electron emission, just works up to a critical emission ratio $\gamma_k < 1$. When the flux exceeds this critical value, there are two possibilities for the sheath and the potential:

1. Space charge limited sheath – a potential dip U_s with $U_s < U_w$ forms next to the wall. This dip reflects the additional electron current back to the wall, thus dropping γ below γ_k . More information can be found in [HW67, TLC04, Sch93].
2. Formation of a positive (inverse) sheath (negative plasma potential). In [Cam13, Tac14] it was stated, that the formation of a positive sheath could also balance the additional electron flux. This solution is obtained if one allows for zero ion fluxes (relax the Bohm criterion). In this case, a negative layer forms in the sheath region and the potential rises monotonically to the wall with a potential difference $|U_{p2}|$ being significantly smaller than in the negative sheath case ($|U_{p1}|$). The width of the sheath is reduced [Cam13]. In this case, the ion flux would be zero everywhere.

Density and potential distributions for both cases are depicted in figure 5.5. The actual plasma-wall interaction depends on the electron emission as well as electron and ion temperatures [TLC04, Tac14, Cam13]. In case of conducting walls the results can in general be adapted from the floating wall solution, since the overall fluxes still need to compensate each other.

The description of the influence of plasma-wall interactions on the bulk plasma potential by basic theoretical considerations is limited to simplified, one-dimensional approaches. To get a better insight on their impacts on a more complicated, two-dimensional plasma configuration they are included in the WGTS plasma simulations described in section 5.3. Here the influence of different wall potentials as well as electron emission at the wall is tested.

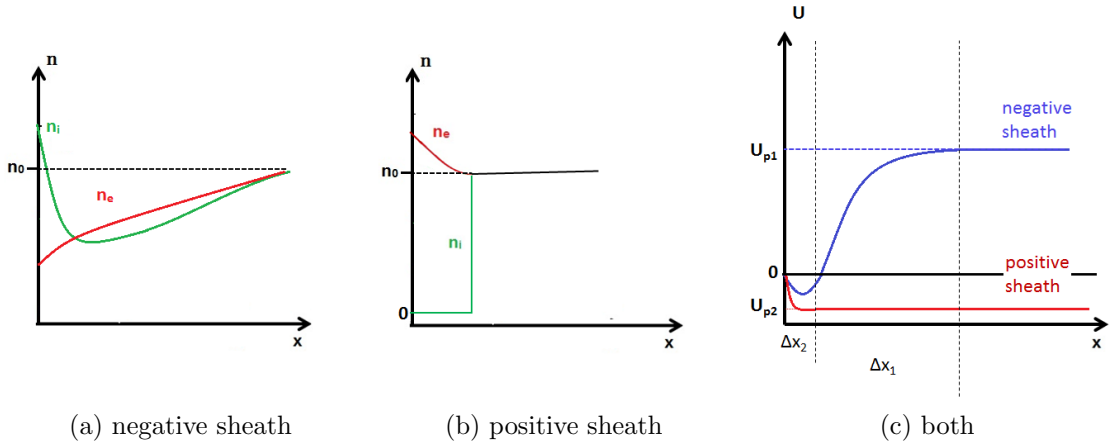


Figure 5.5.: **Sheath potential and density distributions at an emissive wall.** In case of a positive sheath the wall potential is positive and its distribution monotonic. The density distribution for the positive sheath is dominated by an electron layer next to the wall. The negative sheath forms a double layer with a small potential dip next the wall. The width of the sheath is much smaller for the positive sheath (Δx_2) than for the negative sheath (Δx_1). Distributions according to [TLC04, Cam13].

5.1.2. Charged particle transport and fluid approach

In general the motion of charged particles in electromagnetic fields is defined by the Maxwell equations. It can be computed with the Lorentz equation:

$$\frac{\delta \vec{v}}{\delta t} = \vec{F}_L = q \left(\vec{E} + \vec{v} \times \vec{B} \right). \quad (5.19)$$

To be able to describe a large amount of particles, a single particle approach based on (5.19) is not suitable. Therefore, a bulk approach can be used, that introduces “...the concept of an electrically conducting fluid” [GR95]. Electrodynamics and fluid motion are coupled by the Lorentz force \vec{F}_L that is plugged into the Boltzmann equation (5.20), which describes the fluid transport statistically [RT01], to act as the exterior force \vec{F}_{out} :

$$\frac{\delta f}{\delta t} + \vec{v} \nabla f + \frac{1}{m} \vec{F}_{\text{out}} \cdot \nabla_v f = \left(\frac{\delta f}{\delta t} \right)_{\text{col}}. \quad (5.20)$$

Here f denotes the particle energy distribution function. Commonly a fluid model that uses a bulk approach for each species is employed, in order to be able to solve the resulting set of partial differential equations (PDEs) for a large number of particles [SVG94, SVG⁺95, CR04]. In such models, important macroscopic variables arising from the integration of the distribution function are density, flux, average velocity, species temperature, pressure and heat flux. In this field a widely used method is the drift-diffusion approximation [Ho01, CR04]. In the drift-diffusion approximation, the number of PDEs that need to be solved is reduced by introducing algebraic equations for the particle flux densities Γ_j . The species transport is governed by terms of the density gradients ∇n_j , the electric field E and the corresponding potential U :

$$\begin{aligned} \frac{\delta n_j}{\delta t} + \nabla \vec{\Gamma}_j &= R_j \\ \vec{\Gamma}_j &= \pm \mu_j n_j \vec{E} - \nabla (D_j n_j) = \pm \mu_j n_j \nabla U - \nabla (D_j n_j). \end{aligned} \quad (5.21)$$

Here the parameters μ_j and D_j are the mobility and diffusivity tensor, respectively, including effects of the magnetic field, if present, and interactions with the neutral gas.

Furthermore, the mass conservation equation from the 0th term of the Boltzmann equation (5.20) is used [vK14]:

$$\frac{\delta n_j}{\delta t} + \nabla (n_j \vec{v}_j) = R_j \quad \text{in stationary state:} \quad \frac{\delta n_j}{\delta t} = 0, \\ \nabla (n_j \vec{v}_j) = R_j. \quad (5.22)$$

Taking equations (5.21) and (5.22) and the Poisson equation (5.11) for the computation of the electric field and predefining the transport parameters diffusion coefficient D_j and mobility μ_j as well as rate constants or cross sections for the reaction rate R_j , one can solve the plasma transport problem. The drift diffusion method can only be applied if the density is large enough, such that the coulomb fields of the individual particles effect each other [Div01]. The thermal velocity of the ions has to be much larger than the convective velocity – which is generally not the case for low gas densities. However, results can often be adapted to higher gas flow velocities [LL05, BHL10]. Furthermore, the plasma volume has to be much larger than the mean free path of the charged particles.

To derive an expression for the mobility, charged particle motion in a magnetic field \vec{B} pointing in z-direction with cyclotron frequency $\omega_c = eB/m$ and mean charged particle-neutral collision time τ is assumed. Taking the collision frequency $1/\tau$ to be independent of neutral particle velocity, which excludes again very low density plasmas, one arrives at the mobility tensor [Sha08]:

$$\mu_{e,i} = \begin{pmatrix} \frac{\mu_0}{1+(\omega\tau)^2} & s \frac{\omega\tau\mu_0}{1+(\omega\tau)^2} & 0 \\ (-s) \frac{\omega\tau\mu_0}{1+(\omega\tau)^2} & \frac{\mu_0}{1+(\omega\tau)^2} & 0 \\ 0 & 0 & \mu_0 \end{pmatrix}. \quad (5.23)$$

Here, s denotes the sign of the particles' charge. The mobility in z-direction is the zero-field mobility μ_0 . The xx and yy components of μ represent the radial mobility, whereas the off-diagonal components represent the mobility in azimuthal direction. For large $\omega_c\tau$ the radial mobility can be approximated with $\approx 1/(B^2\mu_0)$ and the azimuthal component becomes $\approx 1/(B\mu_0)$. Mobility and diffusivity are related by the Einstein equation

$$D = \frac{\mu k_B T}{|q|}, \quad (5.24)$$

where q denotes the particles charge. Knowing the mobility, one can also compute the conductivity tensor:

$$\sigma_j = n_j e \mu_j. \quad (5.25)$$

Thus, one obtains the drift current density due to an electric field which can be defined using Ohm's law:

$$\vec{j}_{i,e \text{ (el)}} = \sigma_{i,e} \vec{E}. \quad (5.26)$$

The diffusive current density due to concentration gradients is

$$\vec{j}_{i,e \text{ (diff)}} = -e \nabla n_{i,e} D_{i,e}. \quad (5.27)$$

Diffusive and migrative current densities are included in the drift-diffusion approximation, with $j_j = e\Gamma_j$ (5.21). If there exists a neutral gas flow with velocities, v_g , of the order of the charged-particle drift and diffusion velocities, the convective current density becomes important and one has to add a convective term:

$$\vec{j}_{i,e \text{ (conv)}} = e v_g n_{i,e}. \quad (5.28)$$

Ambipolar Diffusion

The drift diffusion approximation (5.21) holds for ions as well as electrons separately. They are coupled through the electric field, that can, in absence of external forces, be computed solely by the Poisson equation (5.11). However, in general the distributions of both particles can be simplified using the concept of ambipolar diffusion: Electrons diffuse faster than ions due to their higher mobilities. Therefore, an intrinsic electric field builds up, that slows down the electrons and accelerates the ions. However, the particle and flux densities of both species are assumed to be equal through the bulk plasma: $\Gamma = \Gamma_e = \Gamma_i$, $n = n_e = n_i$ [RT01, GZS80, LL05, BHL10]. Thus, the intrinsic electric field can be written in terms of the species mobilities, and the motion of particles can be combined using the ambipolar diffusion coefficient D_a :

$$E = \frac{D_i - D_e}{\mu_i + \mu_e} \cdot \frac{\nabla n}{n} \quad (5.29)$$

$$\Gamma = -\frac{\mu_i D_i + \mu_e D_e}{\mu_i + \mu_e} \cdot \frac{\nabla n}{n} \quad (5.30)$$

$$D_a = -\frac{\mu_i D_i + \mu_e D_e}{\mu_i + \mu_e} \stackrel{\mu_e \gg \mu_i}{\approx} D_i \left(1 + \frac{T_e}{T_i} \right). \quad (5.31)$$

Since the electric field is related to the ambipolar diffusion coefficient, it can be inferred that E is characterized by the ratio T_e/T_i . The drift velocity is determined by the slower ion drift. If a strong magnetic field is present, the mobilities get tensor properties. For the diffusion along the field lines (5.31) holds. Across the field lines, the diffusion is governed by the much slower electron diffusion [RT01, Div01, GZS80]:

$$D_{a\parallel} \approx \left(1 + \frac{T_e}{T_i} \right) D_{i\parallel}, \quad D_{a\perp} \approx \left(1 + \frac{T_i}{T_e} \right) D_{e\perp}. \quad (5.32)$$

However, depending on the actual conditions, the diffusion in one distinct direction does not need to be ambipolar, just the sum of the fluxes in all directions needs to be equal for electrons and ions. In case of a strong magnetic field in a plasma chamber confined by conductive walls, the so-called short-circuiting-effect could appear. It denotes the flow of balancing currents through the walls short-circuiting the ambipolar field. [GR95, GZS80, RT01]

Diffusion in a cylinder

The case of a bounded, weakly ionised plasma in a strong magnetic field was already investigated in [RT01, SG11, FMA05, ZT80]. As this case is at least comparable to the WGTS conditions, results for this special kind of plasma are given in short here. However, to be able to derive an analytic solution for the transport equations by the separation of radial and azimuthal terms, no charged particle production or recombination terms are included. This situation corresponds to a decaying plasma. Some general conclusions with regard to boundary and plasma potential can be adopted for the WGTS plasma which helps to evaluate the results from section 5.3 and 5.3.3. For deriving the general form of the potential distribution in a cylindrical geometry with length L and radius R in a magnetic field parallel to the axis, the ideas described in [RT01] and [ZT80] are followed here. In order to get the transport process and the corresponding transported species, four different diffusion time scales $\tau_{j\alpha}$ for electrons and ions in radial \perp and parallel \parallel direction with corresponding diffusion constants $D_{j\alpha}$, with $\psi = 2.405$, are distinguished here⁷. This time scales are needed to determine the dominating diffusion terms and thus

⁷Radial distributions of electrons and ions can be approximated by zero-order Bessel functions [DKMS05].

The term $\psi = 2.405$ corresponds to the first zero in this function and is used to obtain the zero-density boundary condition.

the dominating boundary potentials:

$$\tau_{e\parallel} = L^2 / (\pi^2 D_{e\parallel}), \quad \tau_{e\perp} = R^2 / (\psi^2 D_{e\perp}); \quad (5.33)$$

$$\tau_{i\parallel} = L^2 / (\pi^2 D_{i\parallel}), \quad \tau_{i\perp} = R^2 / (\psi^2 D_{i\perp}). \quad (5.34)$$

In general, due to the magnetic confinement and the high electron parallel mobility: $\tau_{i\perp} \ll \tau_{e\perp}$ and $\tau_{e\parallel} \ll \tau_{i\parallel}$. Depending on the shortest of the two short diffusion times, $\tau_{i\perp}$ and $\tau_{e\parallel}$, one can identify the characteristic time scale of changes in the plasma as well as characteristic fluxes that determine the plasma potential. For KATRIN the electron and ion diffusion times are calculated to be:

$$\tau_{e\parallel} \approx 0.065 \text{ s} \quad \tau_{i\perp} \approx 30 \text{ s}. \quad (5.35)$$

Thus, the characteristic time scale is given by the longitudinal diffusion of electrons. For the approximation of diffusion times (5.35) averaged zero field mobilities μ_0 of $6 \times 10^4 \text{ m}^2/(\text{Vs})$ for electrons and $17 \text{ m}^2/(\text{Vs})$ for ions are used. Another important condition to derive the plasma potential distribution is the biasing potential of the end and side walls, U_{rear} and U_{wall} , or, more specifically, the difference between both: $\Delta = U_{\text{rear}} - U_{\text{wall}}$. For a collision dominated plasma, where the mean free path of the charged particles is significantly shorter than the tube length and the electrons can be assumed to cool down to gas temperature, the two-dimensional density distribution can be separated into two one-dimensional distributions [SG11, FMA05, GZS80]:

$$n_j(r, z) = g(r)f(z)n_{j0}. \quad (5.36)$$

Here $g(r)$ and $f(z)$ are the radial and axial density distribution functions and n_{j0} is the central charged particle density. The spatial distribution in the direction of the closest boundary, which is determined by the diffusion times $\tau_{j\alpha}$ described above, can be described by the corresponding one-dimensional distribution [GZS80]. Thus, assuming the electrons to be distributed according to the Boltzmann law [RT01]

$$n_e(U) = n_e(0)e^{\frac{eU}{T_e}}, \quad (5.37)$$

and considering the random thermal motion of electrons with temperature T_e , the electron flux density $\Gamma_{e\parallel}$ through the end wall in axial direction is

$$\Gamma_{e\parallel} = n_e \sqrt{\frac{T_e}{2\pi m_e}} e^{\frac{e\Delta U}{T_e}}, \quad (5.38)$$

where ΔU is the potential drop in the sheath next to the wall. In general ΔU is the difference between the potential at position (r, z) at time t and the bulk value of the plasma. In the absence of sources and sinks the parallel electron flux stays constant through the whole tube, as $\Gamma_{e\perp}$ can be neglected for a short tube. So the plasma potential can be written as

$$\Delta U(r, z, t) = -\frac{T_e}{e} \ln \frac{\sqrt{2\pi/2} \frac{\delta N}{\delta t}}{n \sqrt{T_e/m_e}}. \quad (5.39)$$

The change of the particle number integrated along the beam axis $\frac{\delta N}{\delta t}$ is equal to twice the outgoing electron flux through one wall $\Gamma_{e\parallel}(z = 0)$, as electrons can leave in front (at $z = L$) and rear direction (at $z = 0$)⁸, as long as their motion stays one-dimensional, and therefore:

$$\Delta U(r, z, t) = -\frac{T_e}{e} \ln \frac{\sqrt{\pi/2} \frac{\delta N}{\delta t}}{n \sqrt{T_e/m_e}}. \quad (5.40)$$

⁸This holds for a completely bounded cylinder. In case of the WGTS, the electrons can only leave the model at the rear wall, which means a factor two reduction in the potential difference $\Delta U(r, z, t)$.

This holds only, if the plasma potential is determined by the longitudinal electron diffusion. Plugging this potential into the drift diffusion equation (5.21) leads to a second-order partial differential equation that is solved by the Bessel function of first kind J_0 . Thus, the particular solution [GZS80, RT01, ZT80] reads:

$$n(r, z, t) = C J_0(\psi r/R) f(z) \exp\left(-\frac{t}{\tau_{i\perp}}\right). \quad (5.41)$$

Here $f(z)$ contains the density dependence on the longitudinal coordinate, compare equation (5.36), and C is a factor that depends on the actual boundary conditions. When plugging $n(r, z, t)$ from equation (5.41) and

$$\frac{\delta N}{\delta t} = \frac{\delta}{\delta t} \left(\int_0^L n(r, z, t) dz \right) = -\frac{n(r, z, t)}{\tau_{i\perp} f(z) \int_0^L f(z) dz} \quad (5.42)$$

into equation (5.40) the radial dependence of the potential cancels. Hence, $U(r, z) = U(z)$ except for a small region next to the side walls. This means that outside the small edges there is no radial electric field penetrating the tube. Changing the tube wall potential therefore only affects the potential in this small sheath next to the tube wall. However, in case of a negatively biased end wall with respect to the side walls the situation is different [RT01, ZT80]. The width of the region in which equation (5.41) is not valid increases, with $\Delta = U_{\text{rear}} - U_{\text{wall}}$ becoming more negative. The drop of the potential between plasma and tube wall, which happens in case of positive Δ in the sheath next to the side wall, vanishes for the tube walls becoming positive at least at a critical value of the difference between the boundary potentials, Δ_C . If Δ is decreased further, the transverse motion of ions is blocked, a radial electric field builds up, and the side wall potential can penetrate into the plasma. The critical potential difference Δ_C can be approximated calculating the potential drop between wall and tube centre in axial direction by plugging (5.41) into equation (5.40):

$$e\Delta_C \approx T_e \ln \frac{\tau_{i\perp} T_e^{1/2}}{L (2\pi m_e)^{1/2}}. \quad (5.43)$$

Since any source terms are neglected in the derivation of the plasma density distribution presented above, relation (5.41) does not hold for the WGTS plasma conditions. However, as long as equation (5.39) holds, which is given for $\Delta_C \lesssim \Delta$, the radial dependences of $\Gamma_{e,\parallel}$ and n_e cancel and the assumption of vanishing radial electric fields holds for the WGTS plasma case too. Also the general effect of blocking of the transverse ion motion causing a radial electric field for a positive tube wall ($\Delta \lesssim \Delta_C$) can be adopted to the WGTS plasma.

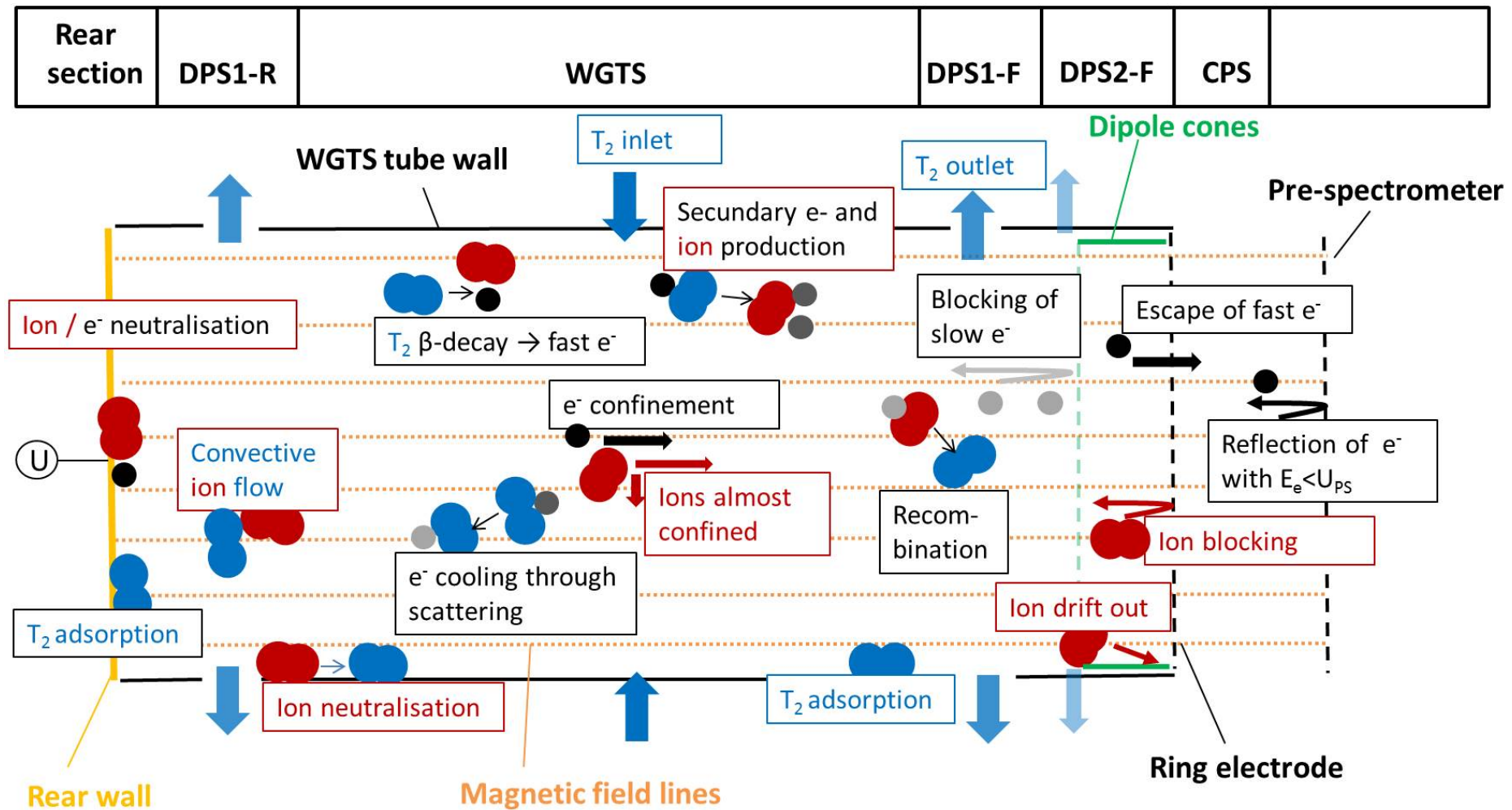


Figure 5.6.: Schema of charged particle creation and loss processes in the WGTS plasma. The boundaries for the longitudinal movement of ions and thermalised electrons are plotted in addition. The corresponding plasma-containing components from rear section to the CPS (and pre-spectrometer, where only fast electrons are left) are marked above.

5.2. General remarks on the WGTS plasma conditions

Basically the WGTS contains a large amount of neutral tritium molecules. Primary charged particles, electrons and HeT^+ ions, are created through the β -decay of T_2 molecules. The bulk of charge carriers is created in secondary processes – through ionisation of tritium molecules by the fast β -decay electrons. Most of the created ions form clusters containing three, five or even more tritium atoms. For a roughly estimated electron density of $1 \times 10^{11} \text{ m}^{-3}$ to $1 \times 10^{12} \text{ m}^{-3}$ [WGT04] and electrons assumed to be in thermal equilibrium with the neutral gas ($T_e = 30 \text{ K}$), a Debye length of $1 \times 10^{-3} \text{ m}$ to $3 \times 10^{-4} \text{ m}$ results for the plasma in the source. The corresponding plasma parameter has values of about 420 to 115 and fulfils the requirement presented in equation (5.3). Thus, a treatment of the charged-particle processes within a plasma model is still legitimate.

The neutral gas and the electrons and ions are surrounded by the WGTS tube wall in radial direction as well as by the rear wall in one longitudinal direction. Besides the scattering and cooling of electrons, the neutral gas influences the plasma inducing convective ion currents proportional to gas flow velocity. Especially in the beam tube end regions this velocity is not negligible compared to the thermal ion velocity as $v_g \approx 100 \text{ m s}^{-1}$ and $v_{th} \approx 280 \text{ m s}^{-1}$ (compare chapter 4). Furthermore, the density distribution of the tritium molecules is quite important since electrons and ions are produced according to this distribution.

The charged particles are confined by a strong magnetic field. However, the ions can, to a small extend, move in directions transversal to the field line which may have an effect due to the large length to radius ratio of the WGTS as in general described in section 5.1.2. Up to the dipole electrode in the DPS2-F⁹ there is no barrier for the electrons. Most of them, moving in this direction, besides the high energetic β -electrons, get reflected back to the WGTS. In rear direction they get absorbed at the rear wall to about 60% [Bab14]. The ions get also absorbed or neutralised at the rear wall. In front direction, when reaching the DPS2-F, they get reflected by a ring electrode and drifted out by electric dipoles [Win11, Rei09]. They can not be reflected to the WGTS since they are hindered by the gas flow in opposite direction.

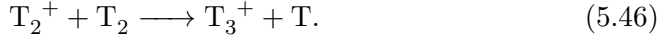
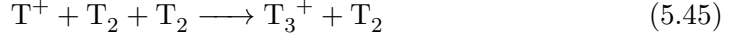
Although the WGTS beam tube is grounded, its boundary potential cannot be assumed to be constant. Work function differences have the same effect as an applied wall potential difference, as described in section 5.1. The other confining wall, the rear wall, is designed to have a rather smooth work function with differences below 20 meV [Sch16, rswg12]. Here an additional voltage of about $\pm 10 \text{ V}$ can be applied to influence the impinging electron current. The boundary conditions with respect to the work functions of the stainless steel tube and the rear wall are further discussed below. A scheme of the most important processes in the WGTS plasma is depicted in figure 5.6.

Charged particle creation in the WGTS

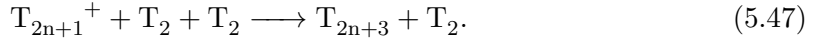
Assuming a nominal column density of $5 \times 10^{21} \text{ m}^{-2}$ a β -decay activity of $1 \times 10^{11} \text{ s}^{-1}$ is reached. If β -electrons would not ionise the gas molecules, the WGTS would charge up rapidly. Only about 59% of the highly energetic β -electrons with energies near the endpoint ($E_e \approx 16.5 \text{ keV}$) scatter on tritium molecules before they leave the source [AAB⁰⁵]. But the scattering cross section goes up for lower energies as $\propto 1/\sqrt{E_e}$ (Born approximation) [TINY90]. Thus, the β -decay electrons produce a large amount of low energy secondary ions and electrons. Simulations by F.Glück showed that one β -decay electron produces on average 15 secondary electrons and ions [WGT04]. While the primary tritium decay and

⁹The dipole electrode will create a negative potential (the voltage of one of the electrodes is set to about -100 V [Win11]) in order to remove positive ions through the induced drift. Most of the low-energy electrons can not cross this potential barrier, while the highly energetic β -electrons are hardly affected.

collision ionisation processes due to β -electrons produce mainly¹⁰ T^+ , ${}^3He^+$, $({}^3HeT)^+$ and T_2^+ , the equilibrium state is dominated by clustered tritium ions, basically T_3^+ and T_5^+ [WGT04, Glü10, Win11]. They are in essence produced through the following reactions [Glü10]:



Larger ion clusters form through



The clustered ions recombine mainly via dissociative recombination processes [Win11]:



The rate \dot{N}_j of a particular creation or recombination reaction j is given by the species densities of the participating particles, here only electrons and ions, n_e and n_{ion} , as well as from the reaction rate coefficient k_j :

$$\dot{N}_j = k_j \cdot n_e n_i. \quad (5.49)$$

The rate coefficient is energy dependent and can be calculated by averaging the reaction cross section $\sigma_j(E)$ over the actual electron energy distribution $f(E)$ [CO12]:

$$k_j(E) = \int_0^{\infty} \sqrt{\frac{2\epsilon}{m_e}} \sigma_j(\epsilon) f(\epsilon) d\epsilon. \quad (5.50)$$

In thermal equilibrium, the electron energy distribution $f(E)$ can be assumed to follow a Maxwell-Boltzmann distribution. In measurements performed to determine rate constants, this thermal equilibrium is generally assumed [HYSM88, BB49]. The rate coefficients for tritium cluster recombination are large [Glü10]. For T_3^+ -ions the measured rate coefficient ranges from $1 \times 10^{-8} \text{ cm}^3 \text{ s}^{-1}$ to $1 \times 10^{-7} \text{ cm}^3 \text{ s}^{-1}$ and coefficients for T_5^+ ions are of the order of $1 \times 10^{-5} \text{ cm}^3 \text{ s}^{-1}$ [GNP⁺03, BM90, FMM06]. Thus, the recombination process needs to be included in the plasma simulations. The effective WGTS recombination coefficient k_{eff} with respect to the different ion species (mainly T_3^+ and T_5^+) can be approximated with the help of the species density ratio x_i as used in [GNP⁺03]:

$$k_{\text{eff}} = \left(k_{T_3^+} + x_i k_{T_5^+} \right) \frac{1}{1 + x_i}. \quad (5.51)$$

With $x_i \approx 0.5$ the WGTS effective recombination rate constant is about $4 \times 10^{-12} \text{ m}^3 \text{ s}^{-1} \approx 2.4 \times 10^{12} \text{ m}^3 \text{ s}^{-1} \text{ mol}^{-1}$.

The energy distribution and mean energy of the charged particles, especially electrons, is quite important for the particle reactions, since the reaction coefficients in general are energy dependent [BM90, FMM06]. Ions typically undergo a large number of collisions with the gas molecules in the WGTS¹¹. Therefore, their temperature can be assumed to be equal to the gas temperature of 30 K. The energy distribution of electrons in plasmas is rather complex. In the following it is discussed for the WGTS plasma conditions.

¹⁰In addition T^- -ions can be produced through dissociative electron capture; compared to the other reactions, the rate should be small [Win11].

¹¹If one assumes the fluxes to be convection dominated, the mean free path λ of the molecules should be equal to the gas mean free path which is of the order of millimetres (compare chapter 4).

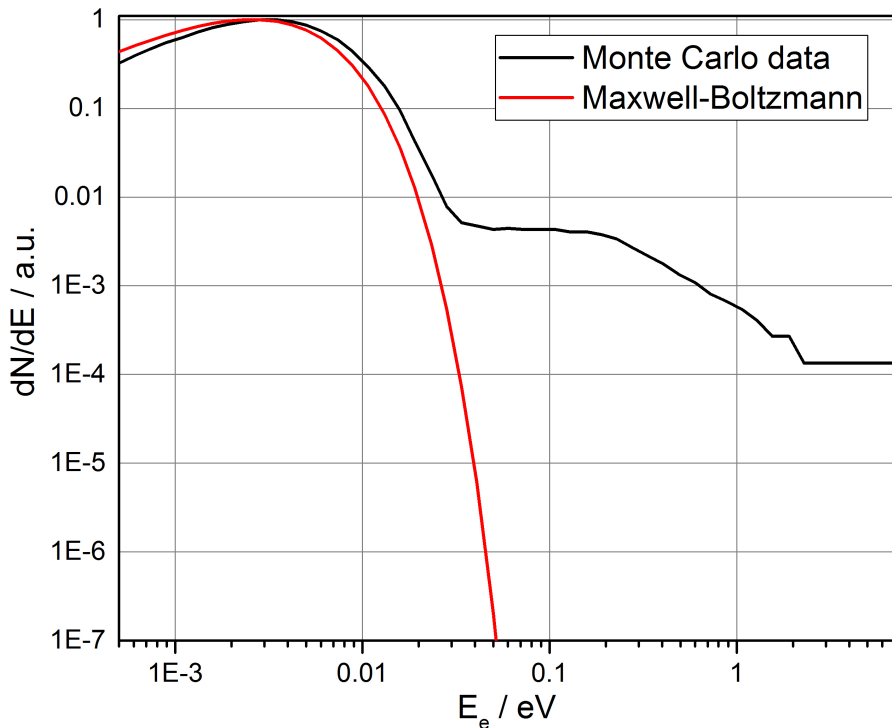


Figure 5.7.: **Electron energy distribution of secondary electrons.** The corresponding gas temperature is 30 K. The data obtained from Monte-Carlo simulation are in good agreement with a Maxwell-Boltzmann distribution for electrons in equilibrium with gas and ions, except for the high-energy tail observed in the simulation data. The primary β -decay electrons are not included as their mean energy is far above the secondary electron spectrum.

Energy distribution of electrons

The mean energy of the electrons in the WGTS plasma was studied in a detailed Monte Carlo simulation by F. Glück including a wide range of energy loss mechanisms. The resulting distribution¹² is given in figure 5.7. The average energy of the secondary electrons produced by fast β -electrons is about 10 eV [Glü02], electrons with larger energies will lose energy quite fast through electronic excitation and ionisation of the molecules as collision partners (review of corresponding cross sections in [TRC83] and [BB02]). From there on the ro-vibrational energy losses dominate the decrease in energy. It starts at electron energies of about 2 eV to 5 eV and runs down to about 100 meV [TRC83, TINY90]. Below 100 meV only the elastic collisions are left. Despite the small energy loss per collision, they are able to cool down the electrons further, since the cross section for this reaction is large (about $1 \times 10^{-15} \text{ cm}^2$ [TRC83, TINY90]). Thus, the electrons can cool down to the 30 K gas temperature because of the large length of the WGTS. This is confirmed by the Monte Carlo simulations. The corresponding typical energy of electrons is about 3 meV. However, their energy distribution is not exactly equal to a typical equilibrium Maxwellian since there is a high-energy tail left, see figure 5.7. The effects of this feature are tested in section 5.3. In addition to the low energetic secondary electrons there are still the high energetic β -decay electrons. Their initial energy profile is modified by the scattering off tritium molecules. However, their mean energy is still of the order of keV and far above the secondary electron energy. For higher gas temperatures of about 110 K (Krypton-mode conditions) the electron cool down still works efficiently (Ferenc Glück, personal communication, March 27, 2015). This implies an electron energy of about 14 meV for the Krypton mode. The effects of larger electron energy on the WGTS plasma are also investigated in section 5.3.

Charged particle transport parameters

To define the full equation of transport, the drift-diffusion approximation (5.21) needs to be extended by a convection term. To get the drift-diffusion current, the mobility values need to be specified. The diffusivity can be computed using the Einstein equation (5.24). The zero-field mobility μ_0 of T_3^+ ions and electrons for a central gas density of $1 \times 10^{21} \text{ m}^{-3}$ at 30 K are $\mu_{0,\text{T}_3^+} \approx 17 \text{ m}^2 \text{ V}^{-1} \text{ s}$ with an uncertainty of about 10% [MMMM68] and $\mu_{0,e} \approx 6 \times 10^4 \text{ m}^2 \text{ V}^{-1} \text{ s}$ with an uncertainty of about 5%, respectively [RF91]. The mobility is gas density dependent as the collisions with gas molecules need to be considered. One can approximate the change in mobility due to the decreasing WGTS density towards the ends using $\mu(n) \approx \frac{n_0}{n} \mu_0$. These approximated mobilities deviate only within about 2% from the measured values $\mu(n)$ [RF91]. Plugging the zero-field mobilities given above and a WGTS magnetic field of 3.6 T into equation (5.23), the ratio of radial to longitudinal mobility is about 3×10^{-4} for ions and only 2×10^{-11} for electrons. Using equation (5.25) the same holds for the corresponding radial and transversal ion and electron conductivities. This means that, despite the magnetic confinement, there exist non-negligible ion currents in radial direction caused by collisions with T_2 . They need to be compensated by the longitudinal electron currents in order to keep the plasma neutral, as described by the concept of ambipolar diffusion in section 5.1.

Gas velocities, needed to compute the convective transport, increase towards the ends of the WGTS as can be seen in chapter 4. At the first pump port this velocity is about 100 m s^{-1} , which means that it needs to be considered for the ion current but can be neglected for the electron current as the electron thermal velocity is much higher than the gas velocity. Realistic profiles of gas velocity as well as of the neutral number density need

¹²This simulation was carried out for homogeneous potential. It does not contain energy losses/gains by potential electric fields in the real WGTS plasma.

to be included in the plasma model in section 5.3.

Surface conditions

The work function of a surface influences the plasma potential as shown in section 5.1.1. Especially differences in the work function due to intrinsic material properties or due to adsorption at the materials surface are important. The materials of interest with regard to the WGTS simulations in section 5.3 are stainless steel (beam tube material) and gold (gold coated substrate¹³, rear wall material). Since the endpoint of the β -decay electron spectrum does not need to be known, as it is determined separately during neutrino mass analysis [Höt12], only the stability and homogeneity of the plasma potential and thus of the work function difference of the two materials is required. The average work function difference of both materials of about 100 meV [Bab14] can be compensated by applying a balancing voltage at the rear wall.

Intrinsic effects that can change the work function – such as impurities, shear strains or cracks – are summarised with regard to the WGTS beam tube in [Wer15]. Here as well as in [Ott13] shifts up to 1 eV are supposed to be possible. These intrinsic work function variations can assumed to be randomly distributed over the material. Since the WGTS is operated at 30 K a large amount of tritium will adsorb at the steel walls [Chr88, Züt03]. In general the amount of adsorbed substance depends on the gas density to which the material is exposed. Therefore, the coverage of the WGTS and shifts in work function due to tritium coverage are not randomly distributed but are related to the tritium density profile. The actual tritium coverage of the WGTS¹⁴ is investigated in appendix F. The surface coverage θ is calculated to be about 1.01 to 1.15 monolayers, which means, a difference of 0.14 mono-layers within the WGTS beam tube is found. The coverage profile follows the tritium gas density profile as expected. Differences between both slopes are due to desorption effects that depend on the actual coverage. One should keep in mind that this profile has large uncertainties regarding the binding energies for the layers above the first monolayer. Thus, an almost constant accommodation of one monolayer along the tube is also possible and the assumption of 14% difference represents a conservative approach.

The change in work function depending on the surface coverage can be calculated as follows [PF83]:

$$\Delta\Phi = 9 \times 10^9 \cdot 4\pi n_s \theta \mu(\theta). \quad (5.52)$$

Here n_s denotes the number of adsorption surface sides of the substrate material and μ the dipole moment of the adsorbate-adsorbent bond. The dipole moment is induced due to the polarisation of the covalent bound between adsorbate and adsorbent. Thus, a change in the charge distribution is created which changes the work function. The sign of the work function shift changes for atomic compared to molecular adsorption [Sch02, PF83] due to the different polarities of the adsorbed species (H_2^+ , 2H^- [RF80]). Thus, for adsorption of atomic hydrogen the work function shift is negative.

Since the WGTS is operated at 30 K only atomic adsorption of tritium is relevant directly on the steel surface. The thermal energy of the tritium molecules is still large enough to desorb quickly after molecular adsorption. Instead of desorbing, the molecularly adsorbed tritium can also dissociate and adsorb atomically (see appendix F). In [BR54] a work function shift of -190 meV was recorded for a mono-layer coverage of hydrogen on steel at room temperature. Differently orientated single Fe-crystals (111, 100, 110) were measured in [BEGW77]. Here work function differences of -310 meV to 95 meV were

¹³Investigations of different substrate materials can be found in [Sch16].

¹⁴The coverage is given in terms of monolayers. One mono-layer coverage corresponds to single occupancy of all free adsorption sites of the adsorbing material.

found. The discrepancy for individual orientations is due to the amount of depolarisation of adsorbed atoms as the distance between adsorbed atoms is different. In case of multilayer adsorption, only at temperatures below the critical temperature, the additional hydrogen molecules adsorbing on the mono-layer are physisorbed with a significantly reduced binding energy as stated in appendix F. Thus, the tritium molecules physisorbed on the tritium are less polarised resulting in a lower change of work function with respect to the already adsorbed mono-layer induced change. Such a saturation behaviour was recorded in [PF83, DNN08, BEGW77, Mad73]. The saturation coverage for hydrogen on steel and tungsten is stated to be reached at $\theta = 2$ [Mad73, BEGW77]. Actually the dependence of work function on coverage is dependent on the substrate, as depicted in figure 5.8. For some materials the dependence is not linear due to the induced change in dipole moment[BEGW77, PF83]. The discrepancy is large for very low coverages [Chr88]. Moreover, experiments and theory differ [JC03]. Thus, no closed description of the work

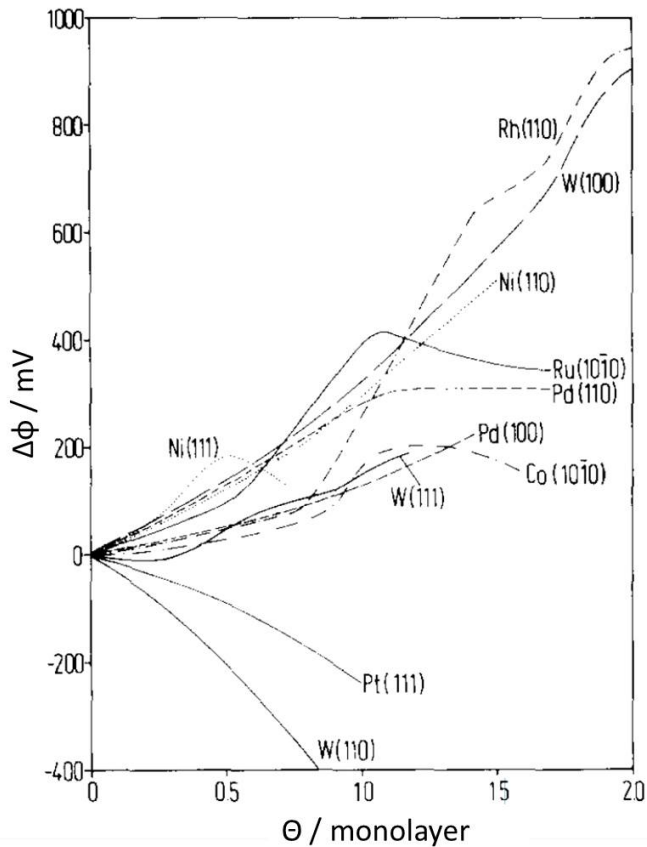


Figure 5.8.: **Work function dependence on surface coverage θ for H_2 adsorption on different metals.** The dependency $\Delta\Phi(\theta)$ varies for different metal substrates. Even for the same substrate, the slope changes for different coverage ranges. Image adapted from [Chr88].

function shift for different coverages seems possible at this point. In the modelling of the WGTS adsorption behaviour and induced work function shifts in section 5.3, the work function profile is assumed to be linearly increasing from injection to both ends connected to the almost linear decrease in coverage calculated in appendix F. The difference $\Delta\Phi_{\text{WGTS}}$ between injection and tube end is estimated from the shift between mono-layer covered and uncovered steel, which is about -190 meV. Using the linear dependence on coverage, a work function shift of $\Delta\theta(\Phi_{\text{max}} - \Phi_0) = 0.14 \cdot 190$ meV ≈ 27 meV is expected between WGTS injection and outlet region.

The rear wall material gold was chosen because of its low tritium adsorption probability

and its well defined work function [rswg12]. Since the rear wall will be operated at room temperature, no molecular adsorption of hydrogen can occur [Bab14, Sch13b, rswg12]. The chemisorption of dissociated H₂ (as well as T₂) is suppressed as an activation barrier [Chr88] exists for this process. The corresponding required activation energy was measured in [SD92, SD94] to be quite large (36 kJ mol⁻¹) compared to the thermal energy of about 2.5 kJ mol⁻¹. The corresponding rear wall equilibrium coverage was calculated in [Bab14] to be about $\theta = 7 \times 10^{-5}$. However, this result was obtained under ideal assumption with regard to surface homogeneity and cleanliness as well as number of adsorption sites. Measurements of tritium adsorption on gold-coated beryllium within the TRIADE experiment are described in [Röl15]. Here a surface coverage $\theta \approx 0.07$ and $\theta \approx 0.18$ for differently orientated crystal surface was derived from experimental results. However, measurements were carried out at a pressure of 1×10^{-3} mbar. The pressure in the rear wall chamber is equal to the pressure at the end of DPS1R which was calculated in section 4.2 to be about 1.5×10^{-5} mbar. Thus, the amount of adsorbed tritium at the rear wall will be clearly lower than the value measured in the test experiment. The actual rear wall coverage can not be calculated precisely since in [Röl15] idealised assumptions regarding surface flatness, location of adsorption sites and distribution of adsorption probability were made. In [LSD87] work function shifts due to the adsorption of hydrogen on gold at 78 K of about 2 meV were found at a surface coverage was about 4×10^{-3} . Using equation (5.52) and assuming a constant dipole moment for both coverages, the upper bound of WGTS work function shift due to adsorbed tritium corresponding to a coverage of $\theta = 0.07$ is

$$\Delta\Phi(0.07) \approx \Delta\Phi(4 \times 10^{-3}) \cdot \frac{0.07}{4 \times 10^{-3}} = 35 \text{ meV.} \quad (5.53)$$

The rear wall material itself was found to have a very homogeneous work function. Measurements in [Sch16] showed an overall surface homogeneity of 9.4 meV rms as well as an homogeneity of 10 meV over a surface that can be dissolved by a single detector pixel. The distribution of the work function was found to be smooth and not random.

Within the plasma simulation, described in the following section, effects from randomly distributed work function shifts as well as from shifts following particular distributions (density related, radial, asymmetric) at the rear wall as well as at the beam tube walls are investigated.

5.3. Modelling of the WGTS plasma

The distribution of the potential in the WGTS needs to be known precisely in order to deduce an accurately averaged β -electron spectrum. Furthermore, the influences of the confining walls, particle temperatures and densities as well as influence of additional electron emission on the plasma density and potential need to be tested in order to optimise the source boundary conditions for a preferably homogeneous plasma potential. Thus a complete model of the WGTS needs to include

- Creation and recombination reactions for electrons and ions.
- Inflow and outflow, as well as neutralisation processes of electrons and ions at the walls.
- Interactions of charged particles with the neutral gas.
- Density and velocity distribution of the neutral gas.
- Adjustable potential and potential distribution on confining walls.

- Adjustable particle temperatures.
- Electron emitting rear wall.

The variety of those processes can not be represented by an analytic model. Previous approaches, presented in the following section, are limited with regard to space charge influences and dimensionality. They need to be step-wise extended to a two-dimensional, axisymmetric three-particle fluid plasma model within section 5.3.2. This representative WGTS plasma model is used to study effects from WGTS surface potential conditions in section 5.3.4. In section 5.3.5 it is used to investigate how the emission of additional electrons at the rear wall influences the space charge and potential distribution.

5.3.1. Previous WGTS plasma models

Conductivity based model

A previous two-dimensional WGTS plasma model presented in [Bab14, Ott13] used an electrostatic approach within the finite element software FEMM [Mee14]. Longitudinal and transversal conductivities were used that represent the dominant particle currents in the respective direction: $\sigma_{\parallel} = \sigma_{e\parallel}$ (longitudinal, electron dominated), $\sigma_{\perp} = \sigma_{i\perp}$ (transversal, ion dominated). Using equation (5.25) they were calculated from the corresponding entry in the mobility tensor (5.23) and from a approximated charged-particle density. Electrostatic potentials were defined at the confining walls. Due to the large ratio of longitudinal to transversal conductivity and the large length to radius ratio numerical problems occurred and geometry and conductivities were adjusted using a scaling law derived in [Ott13]. Within this model the plasma potential was found to be dominated by the rear wall with only small penetration depth of the tube wall potential. The Debye length, which was calculated to be of the order of 0.3 mm. Rear wall patch potentials with extensions much larger than the Debye length were found to penetrate into the plasma. Considering the real particle densities and corresponding saturation currents, longitudinal (electron) currents needed to balance the transversal (ion) currents were found to be too large to be driven by the electrons. Thus, it was concluded that the radial tube wall potentials may dominate the WGTS plasma as radial electric fields penetrate into the plasma. Even a break down of the plasma condition was supposed since quasineutrality does not hold anymore. However in fixing the conductivity it is assumed that the electron and ion density distribution is a priori in a stationary state as well as that it is neutral through the whole geometry. The impact on the particle densities from actual currents and from developing, intrinsic, electric fields is neglected. Thus, the results are questionable with regard to a realistic WGTS plasma.

Quasineutral one-dimensional plasma model

An earlier WGTS plasma model described in [NM04] is a self consistent three-particle, one-dimensional, model including electrons, T_3^+ ions and T_2 gas. Charged particles are generated by β -decay and secondary ionisation with an average ionisation yield of five secondary electron-ion pairs per β -electron. The model includes recombination effects for different recombination coefficients from $1 \times 10^{-8} \text{ cm}^3 \text{ s}^{-1}$ to $1 \times 10^{-5} \text{ cm}^3 \text{ s}^{-1}$. The drift diffusion equations for the particle fluxes are solved using an iterative method. The flow of the neutral gas from the inlet in the centre towards the exits on both ends was included. This leads to the following equation for the density distribution:

$$\frac{d}{dz} \left(D_a \frac{dn}{dz} \right) - \frac{d}{dz} (nv_g) + (N_i + 1) q_\beta n_{T_2} - k_{\text{eff}} n^2. \quad (5.54)$$

Here q_β denotes the β -decay rate per volume and D_a the ambipolar diffusion coefficient. In this approach quasineutrality is assumed, i.e., ion and electron densities are set equal:

$n_e = n_i = n$. Therefore, the solution is only valid for small values of $\frac{n_e - n_i}{n_e}$. The Poisson equation is not included directly. It can be used to calculate charge densities iteratively by plugging in the electric field obtained from the quasineutral solution. Symmetric conditions are assumed for the rear and front part of the tube. The walls are assumed to be floating. The resulting density and potential distributions along the tube axis for different recombination coefficients, here denoted with α , are shown in figure 5.9. Expanding this model to two dimensions, the problem can no longer be compressed into one relatively simple equation like (5.54) as the set of equations for the different fluxes increases. Furthermore, especially when a magnetic field is included, the fluxes for electrons and ions in a specific direction differ and the concept of ambipolar diffusion and floating walls can no longer be used. Particularly next to boundaries the assumption of electron and ion densities to be equal can no longer be maintained, since the density gradients, causing diffusive fluxes, disagree considerably here. Moreover, if quasineutrality is assumed, no effect of potential ion and electron saturation currents, possibly leading to the charging of the plasma, can be seen.

Nevertheless, it is quite remarkable that the solution keeps stable even when the recombination coefficients, and thus also the plasma density, are varied on a large scale. The form of the electron density distribution as well as the scale and distribution of the potential are still comparable, see figure 5.9. The stability of its solution demonstrates the strength of the fluid approach. Crucial plasma parameters can be varied achieving still comparable results. This will be shown in the scope of the following sections.

5.3.2. Development of a realistic two-dimensional WGTS plasma model

A realistic WGTS plasma model needs to include all aspects listed in the beginning of this section. The previous models presented above were not able to cover the full range of these effects. However, the fluid approach used in the quasineutral, one-dimensional model is quite promising. To be able to detect charging of the WGTS, it needs to be extended and the Poisson equation needs to be included directly in the set of equations. Furthermore, a second dimension needs to be added to investigate the effect of radial and longitudinal fluxes which was found to be large in the conductivity based model. Thus, the new plasma model developed within the scope of this thesis is a two-dimensional, cylindrical, three-particle model that contains actual electron and ion densities as well as the flow of neutral background gas.

For the solution of the model a time-dependent approach is chosen. A stationary approach causes numerical problems since the initial guess to start from in the solution process needs to be close to the steady state solution for the complex fluid model. A time dependent solution does not need to be in steady state at any time. It allows to slowly approach the stationary solution, if present, by iteratively increasing time steps and solving the system of partially differential equations defined by the model for each time step. More information on this subject is summarised in [COM14d]. Still, the initial conditions¹⁵ need to be chosen properly for the numerical solution to converge. A proper set of initial conditions is achieved by a stepwise extension of the plasma model using the result of the particular previous model for each step.

To simplify the WGTS plasma problem, the electron energy distribution is fixed to a Maxwellian distribution as discussed in section 5.2. The mean electron energy is also fixed and set to gas temperature for all simulations presented in this section¹⁶.

The new, realistic WGTS plasma model is developed starting from an electron diffusion model described in section 5.3.2.1. This gives a first approximation of the electron density

¹⁵In the time dependent solution this is equal to the initial guess of the solution at $t = 0$.

¹⁶The electric fields in the plasma are not considered in the calculation of the electron energy distribution. However, they can be assumed to be small for quasineutral conditions. Thus, their impact on electron energy can be neglected as long as quasineutrality holds and the mean electron energy can be fixed.

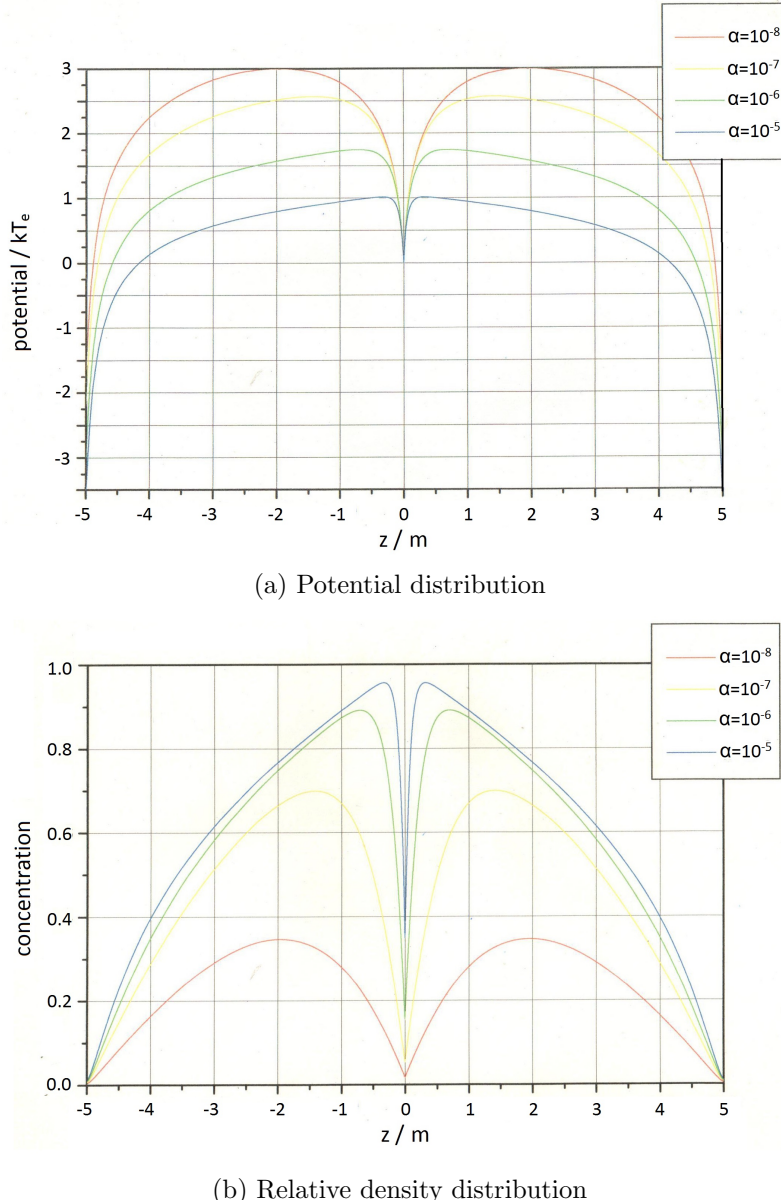


Figure 5.9.: **Potential and relative electron density distribution along the WGTS beam tube axis for the self-consistent quasineutral plasma model.** The one-dimensional model is symmetric in geometry and boundary conditions. The coordinate origin is defined at the gas injection. Adapted from [NM04].

distribution¹⁷. In a next step ions and an intrinsic electric field calculation are implemented in the model in section 5.3.2.2 using the Poisson equation (5.11). This three-particle fluid model is first calculated in an one-dimensional approach. Here, the electron density and potential distribution obtained in the model solved before is used as initial condition. Effects of the gas flow and of the recombination process are tested in separate simulations. The obtained longitudinal potential and density distributions are then used as initial conditions for a two-dimensional, planar plasma model with the same, large aspect ratio of longitudinal and transverse dimensions as that of the axisymmetric WGTS geometry. It allows to investigate the effect from transversal ion flow and boundary potential differences. Finally, again using the result of the prior model as starting point for electron density and potential distribution, an axial symmetric model is built that includes the correct form of the gradient in transversal direction and represents the WGTS cylindrical geometry. The topologically similar but simpler planar model is frequently chosen in COMSOL calculations since it converges more readily than the corresponding axial symmetric model. In section 5.3.3 the stability of the plasma model is tested. Here the impact of different model input parameters that have large uncertainties such as electron energy or rate coefficients and of parameters that can be changed during operation such as gas density and magnetic field is investigated. All simulations described in the following sections are done using the plasma module within the COMSOL Multiphysics simulation suite [COM14b].

5.3.2.1. Electron diffusion model

To arrive at appropriate initial conditions for the three particle fluid plasma model, the electron density distribution needs to be approximated. This is done with the help of a single-fluid electron transport model using the *Drift-Diffusion* module in COMSOL [COM14b]. It includes the drift and diffusive electron current densities from (5.26) and (5.27). Since in a first attempt all boundaries are taken to be grounded, and full neutrality is assumed through the whole plasma, no electric fields can arise and the drift term is zero. Therefore, the potential distribution does not need to be calculated before and can be taken to be zero through the whole plasma. The model is built in one dimension, as the transversal electron currents are small and can be neglected. The axis runs along the beam tube axis¹⁸. Electrons can leave the 10 m long model geometry by reaching the rear wall at $z = 0$ m. The front boundary, at $z = 10$ m, reflects the electrons. To compensate the loss of electrons, an electron source term is applied for the whole geometry. The production rate R_e taken to be constant, is computed from nominal column density, β -decay half life $T_{1/2}$ and secondary electron yield $y_e = 15$:

$$R_e = \frac{\ln 2}{T_{1/2}} \cdot \frac{2\rho d}{10 \text{ m}} y_e \pi r^2 \approx 2.7 \times 10^{13} (\text{s}^{-1} \text{m}^{-3}). \quad (5.55)$$

The average electron energy is set to be 2 meV and the energy distribution is taken to be Maxwellian. This energy information is used to compute the diffusivity, D_e , as well as thermal fluxes through the wall and the resulting recombination at the rear wall, the only outlet in the model. To see if the electron drift-diffusion approach can give a realistic approximation for the electron density distribution, the outgoing integrated fluxes through the k different boundaries need to be added and compared to the production rate of electrons in the WGTS:

$$\sum_k j_{\text{out},k} = R_e z_{\text{max}} \approx 2.7 \times 10^{14} (\text{s}^{-1} \text{m}^{-2}). \quad (5.56)$$

¹⁷Since the fluid model starts to solve assuming a neutral state, the ion density does not need to be computed beforehand.

¹⁸Here $z = 0$ m corresponds to the rear end of the central WGTS beam tube.

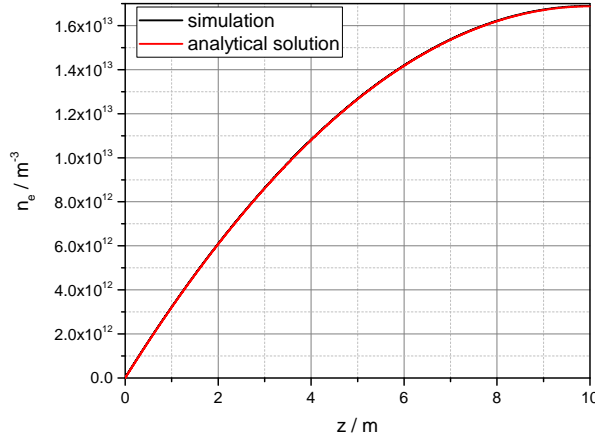


Figure 5.10.: **Electron density distribution for electron diffusion.** The simulated electron fluid model (black) and analytic solution (red) are in excellent agreement.

Solving the model, the outgoing diffusive electron flux through rear boundary of about $2.698 \times 10^{14} \text{ s}^{-1} \text{ m}^{-2}$ is similar to the produced electron rate. The electron density profile is shown in figure 5.10. It is determined by the electron reflection and outflow process. The density increases monotonously in front direction due to the reflective boundary at $z = 10 \text{ m}$ and decreases next to the rear wall due to the electron outflow at $z = 0 \text{ m}$.

Besides the described numerical solution, it is also possible to derive the solution analytically. Therefore the stationary transport and source terms which can be combined to the stationary diffusion equation need to be solved for:

$$j_e = -D \frac{dn_e}{dx} \quad (5.57)$$

$$\frac{dj_e}{dx} = R_e. \quad (5.58)$$

For constant electron production rate R_e and electrons that can only leave at $x = 0$, this means: $j_e(L) = 0$ and $j_e(0) = -R_e L$. Thus, equation (5.57) is solved by

$$j_e(x) = R_e x - R_e L. \quad (5.59)$$

At $x = 0$ the electrons get absorbed which means their density is vanishing. Plugging equation (5.59) into equation (5.58) and using the electron density boundary condition at $x = 0$, the electron density distribution is determined as

$$n_e(x) = -\frac{R_e}{2D} (x^2 - 2Lx). \quad (5.60)$$

The solution is plotted in figure 5.10 using the same input data as for the numerical model. Both solutions agree very well. Keep in mind that a constant electron creation rate was used to derive equation (5.60). This assumption will be used further on. The longitudinal diffusive currents, the only ones occurring in this model, are shown to play an important role. They are able to drive out produced electrons without a significant accumulation of electrons – the average electron density is about $1.1 \times 10^{13} \text{ m}^{-3}$, as to be seen in figure 5.10. Using the simulation data, this means an average diffusion time of

$$\frac{1}{10 \text{ m}} \int_0^{10 \text{ m}} n_e(z) dz / R_e \approx 0.417 \text{ s}, \quad (5.61)$$

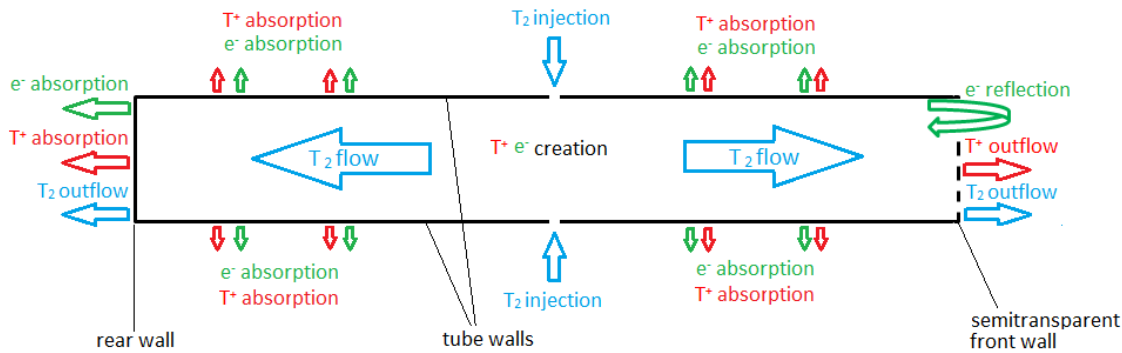
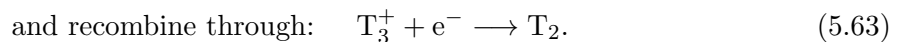


Figure 5.11.: Sketch of charged and neutral particle sources and sinks in the fluid model.

which is in good agreement with the analytical result of 0.412 s. This time agrees with the time a T_2 molecule needs to diffuse from the injection point to the end of the WGTS according to section 4.2 about 0.4 s). The effect from transversal diffusive currents has to be tested in addition. Since they were calculated to be large in the conductivity-based model, this may significantly change the value of the other contributing currents. This is investigated further in the three-particle fluid model described in the following section.

5.3.2.2. Three-particle fluid model including space charge influence

In the simulations described in the prior section neither the diffusion of ions nor the effect from space charges and induced electric fields are included. These internal electric fields are crucial to determine processes in a plasma, since the particles influence each others motion significantly through their Coulomb fields, as explained within the concept of ambipolar diffusion in section 5.1. Therefore, in this section the electron drift-diffusion model is extended by the particle-particle coupling through the Poisson equation as well as electron-ion creation and annihilation processes and separate ion diffusion. Ions¹⁹ and electrons are created directly from T_2 by an artificial reaction:



These creation and recombination equations (5.62) and (5.63) violate the mass conservation. Actually T_3^+ ions and electrons are produced in secondary reactions through more complex processes as shown in section 5.2. Since the implemented creation rate coefficient, specified in section 5.2, is related to the beta decay rate of T_2 molecules²⁰, the production rate of charged particles, $\dot{N}_{i,e}$, can be represented by (5.62) and is implemented in the model related to the tritium density: $\dot{N}_{i,e} = k \cdot n_{T_2}$. The rate coefficient k used in the following simulations is $7 \times 10^{-8} \text{ s}^{-1}$. The influence of the high energetic β -decay electrons, they leave the WGTS nearly unhindered, can be included by adding an additional ion creation term with rate coefficient equal to the rate of β -decay:



Since the T_2 gas flow is fixed and computed separately its density distribution, $n_{T_2}(r, z)$, is not influenced by relations (5.62), (5.62) and (5.64). The same argument holds for the recombination process: the recombination rate coefficient is given in terms of T_3^+ density

¹⁹only T_3^+ ions are implemented as representative species, since it is the most abundant one [Glü05].

²⁰The rate coefficient is computed from the beta decay rate times the number of secondary electrons produced per primary β -electron (15).

and the gas profile is not influenced by equation (5.63). Since the ionisation degree of the plasma is of the order of 1×10^{-8} , the charged particle reactions hardly influence the overall tritium density and the stationary gas density profile is a valid assumption. This assumption also allows to simplify the actual process of adsorption and desorption of tritium ions at the walls – Ions hitting the wall get neutralised, which is for fixed gas profile equivalent to them being absorbed. Desorption does not need to be considered. As mentioned in section 5.2, the rear wall is taken to be totally absorbing for electrons, the front boundary reflects them. An ion outlet boundary condition regarding the flux density is specified at front boundary and rear wall:

$$\Gamma_{i,\text{diff}} = 0, \quad (5.65)$$

therefore their charge is transported out of the model. All relevant sources and sinks of the three different species are summarised in figure 5.11.

At the front end ($z = 10 \text{ m}$) there is a vanishing electric field boundary condition in normal direction, since a condition related to the potential needs to be specified for each boundary. This means, the electric field is zero outside of the geometry.

At first, an one-dimensional model is built to test the influences of recombination processes as well as of gas flow since both where not included in the results of cylindrical plasmas discussed in section 5.1. Furthermore, an approximate description of the electron density and potential distribution is needed as starting parameters for the more complex two-dimensional simulations. The final step of an axial symmetric plasma model is discussed in the last part of section 5.3.2.2. All three-particle fluid models are computed using the *DC Discharge* module in COMSOL [COM14b]²¹. The solution process for all models starts with a simulation using a coarse discretisation of the geometry and initial electron density and potential values from the prior model²². The result of the coarse discretisation is used as initial condition for the next simulation with a finer mesh size. This procedure is repeated with ever finer mesh sizes until the solution is not influenced by the mesh size anymore. ion

One-dimensional model

The three-particle fluid model needs to be solved in an one-dimensional geometry first to obtain improved initial conditions for the following more complex two-dimensional simulation. Moreover, the model is used to check if the partial differential equations (5.22) and (5.21) are fulfilled by the solutions obtained using numerical differentiation. The effect of recombination and convection is investigated in different simulations.

The model consists of a 10 m long line, representing the central WGTS tube axis. The potential is fixed to be 0 V at the rear end of the geometry. The T_2 background gas density is approximated using a triangle function with a maximum of $8 \times 10^{20} \text{ m}^{-3}$ at the inlet at $z = 5 \text{ m}$ and an outlet value of $n_{T_2,\text{out}} = 0.02n_{\text{in}}$ at both ends corresponding to the WGTS outlet values obtained in section 4.2. The one-dimensional neutral gas flow itself needs to be conserved through the model as it is used as convective force for the ion flow in the in the simulation including the gas. The T_2 velocity profile, $v_{T_2}(z)$, is approximated with the help of the outlet velocity, $v_{T_2,\text{out}} \approx 120 \text{ m s}^{-1}$, from section 4.2:

$$j_{T_2} = n_{T_2}(z)v_{T_2}(z) = \text{const.}; \quad v_{T_2}(z) = \frac{n_{T_2,\text{out}}v_{T_2,\text{out}}}{n_{T_2}(z)}. \quad (5.66)$$

Density and velocity profiles, as used in the simulation, are depicted in figure 5.12. Due

²¹It couples drift diffusion equations for different particles with convective gas flow and intrinsic electric fields (Poisson equation).

²²The electron drift-diffusion solution is used for the first one-dimensional calculation of the three-particle fluid model. The solution for this model is used as initial condition for the first step of the two-dimensional three-particle fluid model and this solution is used as input for the cylinder-symmetric model.

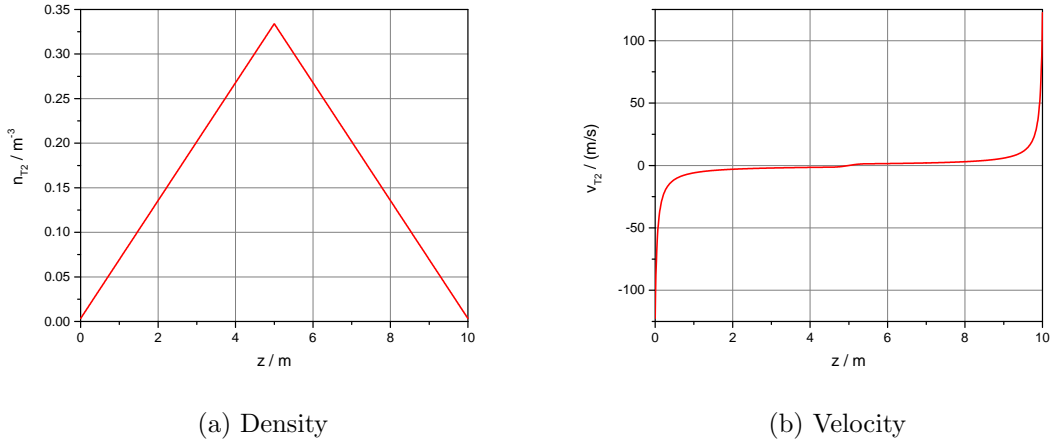


Figure 5.12.: **T₂ density and velocity model for 1D plasma.** The velocity distribution is calculated to achieve constant T₂ flux according to equation (5.66).

to the degree of dimensionality and the two directions of flow, rear and front direction, a singularity develops in the injection region in the middle of the geometry – the velocity needs to cross the origin in order to obtain a smooth transition between both flow regions. The solution is obtained by iteratively improving the mesh size, as described above. The final mesh for all one-dimensional simulations has a maximum width of 1×10^{-3} m in the main part and in a region 0.03 m around the rear edge a maximum of 1×10^{-6} m to be able to dissolve the edge effects. The results hardly change when refining the edge resolution from 1×10^{-5} m to 1×10^{-6} m²³. Thus, a minimal mesh element distance of 1×10^{-5} m in regions adjacent to the geometry edges can be used further on. This is important for the two-dimensional models, where a significantly larger number of mesh elements is needed to resolve the geometry.

Simulation without recombination and convection

To build a fluid model as simple as possible, the process of recombination as well as the convective transport term are not included. Charged particles are still created according to equation (5.62), but can only be lost through the walls. The transport of ions is only due to drift (equation 5.26) and diffusion (equation 5.27). The stationary state ($\frac{\delta n_e}{\delta t} = 0$) is approached after a simulated time of about 350 s which is quite high compared to the other simulations where the stationary state is reached within the order of of seconds for similar initial conditions²⁴. This can be explained when looking at the ion diffusion time from (5.34), which is of the order of 200 s. Since longitudinal motion is the only way for ions to leave the source, the longitudinal diffusion time defines the stationary state. The resulting charged particle density distribution is plotted in figure 5.13. The central steady state electron density is about 1.3×10^{15} m⁻³ which is much higher than expected from the previous models and theoretical calculations (about 1×10^{11} m⁻³ to 1×10^{13} m⁻³). It is caused by the large time to reach the stationary state.

This simulation underlines the importance of the recombination process which prevents this accumulation of charges. Thus, the recombination process is included in all following simulations.

Simulation with recombination and without convection

This model equals the previous model, except for the recombination process (5.63) that is included here. Since the electron density is unrealistically high in the simulation results

²³The difference for the electron density and potential distribution from the corresponding solutions is smaller than 1%.

²⁴Initial values taken from the solution of the electron diffusion model

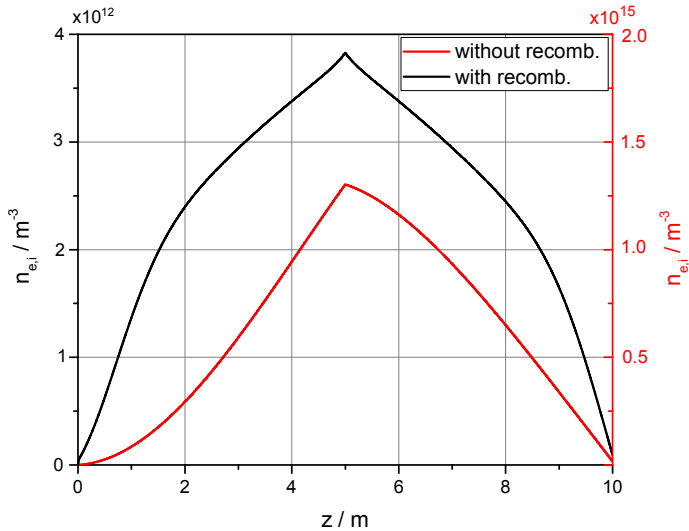


Figure 5.13.: **Ion and electron density distribution for 1D discharge plasma with and without recombination process.** The electron and ion density without recombination is about 200 times larger than with recombination. Mind the different scales for the two simulations (red: without recombination, black: with recombination). The form of the density profile is related to the underlying tritium density from figure 5.12.

without convection, initial conditions are again taken from the solution of the electron drift-diffusion plasma model.

The electron (and ion) density calculated including the recombination process is shown in figure 5.13. Its central value is about $3.7 \times 10^{12} \text{ m}^{-3}$ and the density decays to both ends. The net rate R_{net} of produced electron/ion pairs over the model length is

$$R_{\text{net}} = \int_{-L/2}^{L/2} (R_{e,i} - R_{\text{rec}}) dz \approx 4.55 \times 10^{12} / (\text{m}^2 \text{s}) \hat{=} 7.29 \times 10^{-7} \text{ A m}^{-2}. \quad (5.67)$$

This corresponds to a production rate of about $4.6 \times 10^{-9} \text{ A}$ within the WGTS volume. In steady state, this amount of particles also has to leave the WGTS volume. The outgoing electron flux at the rear wall, $j_{e,\text{out}}$, equals the produced electron rate as well as the sum of the outgoing ion fluxes at rear and front side²⁵, as depicted in figure 5.14b. Only a small part of about 0.1% of the ions are flowing out through the front boundary. The maximum potential builds up in the middle of the geometry at $z = 5 \text{ m}$, as can be seen in figure 5.14a. The absolute potential value is determined by the difference in electron and ion densities at the rear edge ($z = 0 \text{ m}$), where electrons leave the geometry faster than the ions, as described in section 5.1. The solution is tested to check whether the drift diffusion equation as well as the continuity equation is fulfilled despite the low charged particle densities. Thus, the obtained distributions of densities, density gradients and electric field are plugged into equation (5.21). With regard to current conservation, as shown in figure 5.14b, the electron and ion currents are equal over the whole length of the model as expected from section 5.1. Still, one has to note, the fluxes are non-constant despite of the motion being one-dimensional. This is due to the not constant charged particle net production rate, resulting from the density profile and the recombination process. Using numerical differentiation to plug the solution in the drift diffusion differential equations one obtains an agreement within 1×10^{-8} , i.e. in order of the numerical error. Thus, the obtained solution can be considered as valid.

²⁵respecting the different signs from outlet normal direction and particles charge

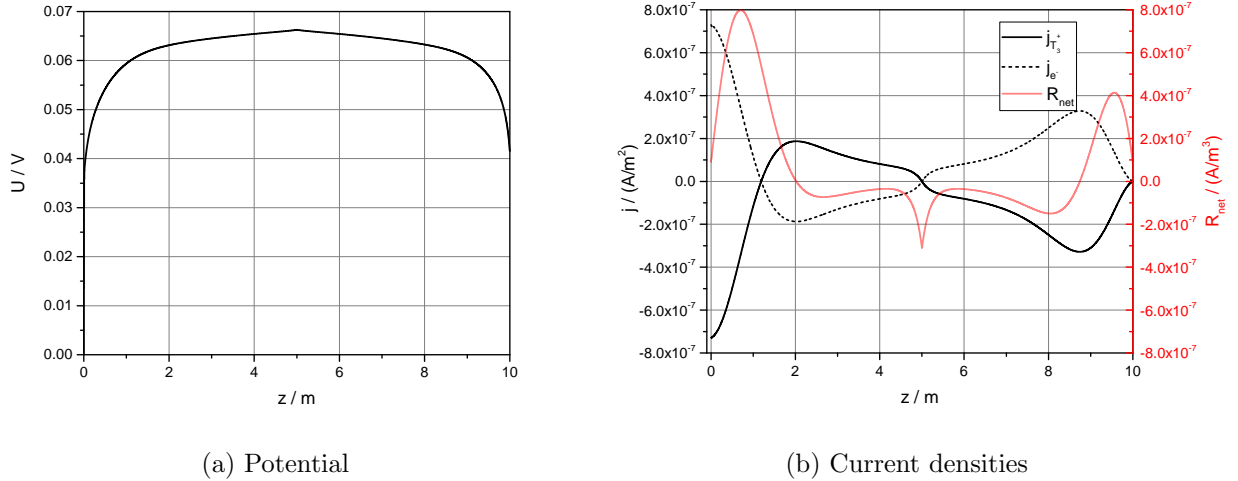


Figure 5.14.: **Potential distribution and current densities for 1D Discharge Plasma without convection.** The electron and ion (in b)) current densities are plotted along with the net production rate R_{net} . Mark the different unit dimensions since the net electron production rate still needs to be integrated along the z -axis to get the created electron current density.

Simulation with recombination and with convection

In this model, the convective gas flow is implemented to test the order of magnitude of convective ion fluxes compared to the other ion fluxes. In general, for the fluid approach to be valid, the convective flux should not dominate the ion motion as discussed in section 5.1.2. The gas velocity (depicted in figure 5.12) is taken from equation (5.66) in order not to violate the continuity equation for the background gas flow.

However, the solution from this simulation does not fulfill the continuity equation (5.22) for the ions anymore. The sum of outgoing ion fluxes $\sum j_{\text{out},i} \approx 3.52 \times 10^{-6} \text{ A m}^{-2}$ does not match the produced rate $R \approx 2.32 \times 10^{-6} \text{ A m}^{-2}$. Due to the singularity in the velocity and convective flow distribution at $z = 5 \text{ m}$, an effective T_3^+ inlet arises inducing non physical ion fluxes. The problem including convection can only be solved in two dimensions, as in one dimension it is not possible to have a smooth and constant neutral gas flow through the WGTS. The actual ratio of convective to total ion fluxes can therefore not be derived here. Nevertheless, the convective flow seems to have a considerable magnitude and needs to be considered further on. In the previous quasineutral one-dimensional model the singularity problem was handled by specific boundary conditions and by adding an initial flux density term $\Gamma_0 \delta(z)$ to the expression in equation (5.9).

The presented one-dimensional calculations show that is possible to solve the drift-diffusion equations coupled to the Poisson equation for the WGTS plasma conditions using a three-particle fluid model. Quasineutrality is not assumed a priori like in the model described in section 5.3.1. The importance of the recombination process is underlined. However, due to a singularity in the one-dimensional background gas flow, it is not possible to include convective effects properly within the used approach. This reduces the outflow of ions and the space charge potential that builds up in the WGTS is significantly larger than the mean electron kinetic energy, as calculated in section 5.3.1. The forms of the density and potential profiles are different from figure 5.9, they do not show the characteristic dips in the centre, which can likewise be explained by the missing gas flow. The gas flow singularity problem can be solved using a model of higher dimensions, as described in the following section. The electron density and potential distribution from the convection free

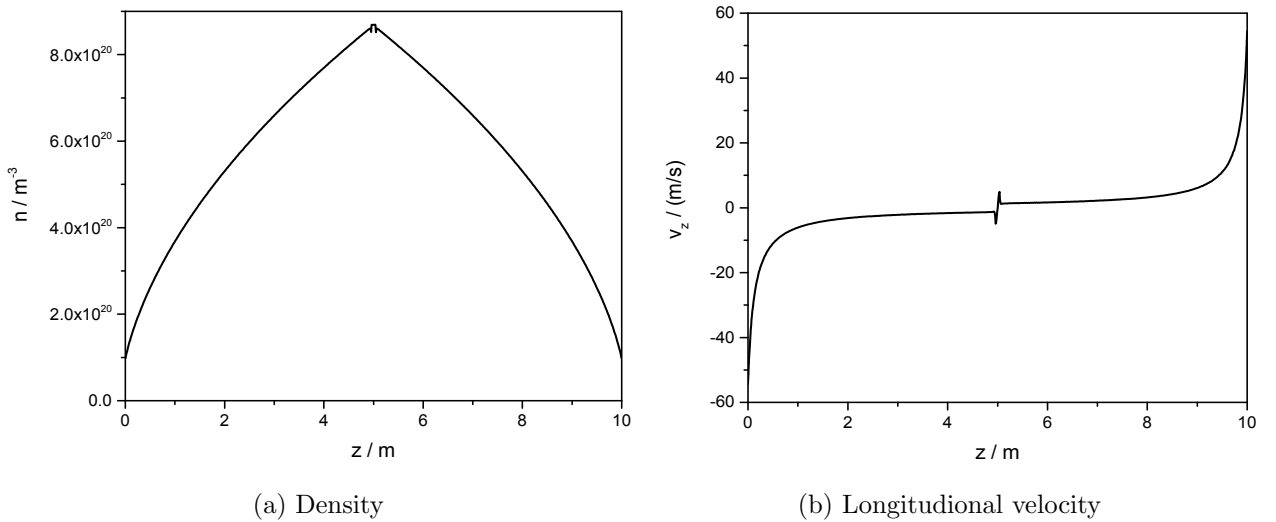


Figure 5.15.: **Density and axial velocity distribution for the T_2 background gas at the beam tube axis ($x = r = 0 \text{ m}$) as used in the two-dimensional plasma models.**

model are used as initial parameters.

Two-dimensional models

The singularity at the origin in the one-dimensional model vanishes in the two-dimensional extension, since a second velocity direction as well as an inflow boundary can be added. However, the continuity equation still needs to be checked to see if any further virtual fluxes or singularities arise. Adding a further dimension to the simulation makes the model far more complicated to solve. For comparable mesh element edge length, the number of mesh elements increases from about 1.5×10^4 for the one-dimensional model to 3×10^5 for the two-dimensional model and the number of degrees of freedom increases from 6×10^4 to 1×10^6 , respectively. Furthermore, the results are less intuitive to rank. The plasma is no longer confined by a wall in only one direction but there are particle motion and confining walls in r (cylinder-symmetric model) or x (planar model) and z direction. Since it is still a two-dimensional simulation, the gradients pointing in the third dimension (perpendicular to the plane geometry for the planar model and in azimuthal direction for the axisymmetric model) are set to zero. This is a reasonable approach for a component with isotropic conditions like the WGTS. Due to the magnetic confinement the ion fluxes to the tube walls are much higher than the electron fluxes in this direction. A similar situation is described theoretically in section 5.1.2. An auxiliary ion inlet boundary condition is defined at the gas inlet ($z = 4.995 \text{ m}$ to 5.005 m , $x = r = \pm 0.045 \text{ m}$) to overcome the problems from the one-dimensional simulation and to guarantee ion flux conservation by setting the flux gradient at the boundary to zero. Since the transversal motion of charged particles is blocked, only neutral T_2 gas can enter and there is no additional source term. To get the two-dimensional T_2 gas density and velocity profile, needed for the charged particle production rates and realistic ion convection terms, a coarse gas dynamic simulation is carried out first. The resulting T_2 density and velocity distribution along the beam tube axis are depicted in figure 5.15. The transversal gas velocity, that has sizeable values only in the gas inlet and outlet regions, is also implemented in the plasma model. Each of the two-dimensional models is solved in 6 to 8 steps, iteratively improving the mesh size. The final mesh consists of layers with a minimal width next to the wall of $1 \times 10^{-5} \text{ m}$ on each of the boundaries confining the model geometry, as defined in the above described one-dimensional model. Apart from these regions, the triangular mesh has an edge length

of about 2 mm to 6 mm.

Two different types of two-dimensional plasma flow models are presented in the following. The first model is a planar plasma, corresponding to a plasma between two conducting plates. It is built in Cartesian coordinates. The plates have a length of 10 m in z -direction and a distance 0.09 m in x direction. In the third dimension (y -direction) they are extended infinitely. The second model is an axisymmetric model and corresponds to a cylindrical, isotropic plasma. It is built using cylinder coordinates. The model needs to be handled differently. The vector differential operator changes with respect to the transversal direction. For a vector field \vec{A} , with components (A_x, A_y, A_z) and (A_r, A_ϕ, A_z) respectively, this means:

- Planar plasma (Cartesian coordinates)

$$\begin{aligned} \text{Divergence: } \nabla \cdot \vec{A} &= \frac{\delta}{\delta x} A_x + \frac{\delta}{\delta y} A_y + \frac{\delta}{\delta z} A_z \\ \text{Gradient: } \nabla \vec{A} &= \begin{pmatrix} \frac{\delta}{\delta x} \\ \frac{\delta}{\delta y} \\ \frac{\delta}{\delta z} \end{pmatrix} \vec{A} \end{aligned} \quad (5.68)$$

- Axial-symmetric plasma (cylinder coordinates)

$$\begin{aligned} \text{Divergence: } \nabla \cdot \vec{A} &= \frac{1}{r} \frac{\delta (r A_r)}{\delta r} + \frac{1}{r} \frac{\delta}{\delta \phi} A_\phi + \frac{\delta}{\delta z} A_z \\ \text{Gradient: } \nabla \vec{A} &= \begin{pmatrix} \frac{\delta}{\delta r} \\ \frac{1}{r} \frac{\delta}{\delta \phi} \\ \frac{\delta}{\delta z} \end{pmatrix} \vec{A}. \end{aligned} \quad (5.69)$$

For both models a zero boundary condition is assumed for gradients in the out of plane- y - respectively ϕ -direction, as the particle flows and fields in the plasma are assumed to be two-dimensional:

$$\frac{\delta A_y}{\delta y} = 0, \quad \frac{1}{r} \frac{\delta A_\phi}{\delta \phi} = 0. \quad (5.70)$$

The simpler form of the differential operator and the zero-gradient boundary conditions makes the planar plasma easier to solve²⁶. Therefore, a planar plasma model is built and solved first. The results are used as initial values for the axisymmetric model. The differences between both plasma geometries become important mainly in transversal direction (x - and r -direction) which influences the motion of ions. In z -direction (axial) the solutions for planar and cylindrical plasma should be qualitatively similar, as shown in [Pfe66]. Therefore, the planar plasma can be used to check, whether the two-dimensional drift-diffusion approach is suitable to solve the WGTS plasma as done for the one-dimensional case. It is also used to test if the continuity equation is fulfilled. Furthermore, the general influence of boundary potential polarity, as discussed in section 5.1.2 theoretically, is investigated by applying different (constant) potentials at rear and lateral tube walls. The planar plasma model results are afterwards used to build the final axisymmetric plasma model.

Planar plasma

In the following the results for the two-dimensional planar plasma calculations are presented. At first, it is tested if the shortfalls that occurred in the one-dimensional calculations can be remedied by the two-dimensional approach – the validity of the continuity

²⁶In general less iterations are needed and the calculation time is about 50% faster, depending on the initial conditions.

Table 5.1.: **Outgoing plasma currents in the two-dimensional planar model.** Integrated ion and electron currents at the specified boundaries in boundary normal direction with grounded walls and $E_e = 2.1 \text{ meV}$. The tube wall losses need to be considered two times. The surface integral of the effective electron/ion creation rate that needs to compensate these losses is about $2.24 \times 10^{-6} \text{ A m}^{-1}$.

species	boundary	I_{drift} / A m^{-1}	I_{conv} / A m^{-1}	I_{diff} / A m^{-1}
ion	rear wall ($z = 0 \text{ m}$)	7×10^{-7}	1.5×10^{-7}	1×10^{-7}
	front ($z = 10 \text{ m}$)	6×10^{-8}	9.5×10^{-7}	5.5×10^{-8}
	lateral walls ($x = \pm 0.045 \text{ m}$)	2×10^{-7}	$< 1 \times 10^{-9}$	2×10^{-8}
electron	rear wall	-2.65×10^{-4}	$< 1 \times 10^{-10}$	2.67×10^{-4}

equation for electrons and ions is checked. Furthermore, the resulting density, density gradients and electric field profiles are plugged in the drift-diffusion partial equations (5.21), like done for the one-dimensional solution. Lateral tube wall and rear wall are taken to be grounded. At first, the electron and ion fluxes from the solution of the planar model are analysed. Outgoing ion and electron currents integrated over the corresponding boundaries are summarised in table 5.1. Since the boundaries are one-dimensional in a two-dimensional simulation, all given currents are in A m^{-1} which can be converted into a corresponding current through a cylindrical cross section for the axial fluxes, or through a cylindrical half surface for the transversal fluxes, by multiplying with $\pi \cdot r$. A discrepancy of 6.7% is found between ion production (production rate about $2.24 \times 10^{-6} \text{ A m}^{-1}$) and outflow of ions by summation of all outgoing ion currents (about $2.47 \times 10^{-6} \text{ A m}^{-1}$). It is mainly caused by discretisation effects when integrating the fluxes at the boundaries. Electrons can only leave the model at the rear wall. Because of the positive plasma potential relative to the walls, an electron repelling electric field builds up which causes a large electron drift in positive z -direction. It is overcompensated by a large diffusion current in the opposite direction. Thus, an electron current of about $2.4 \times 10^{-6} \text{ A m}^{-1}$ leaves the model at the rear wall. The discrepancy of about -8% compared to the electron creation rate is again caused by boundary discretisation effects. An improvement of these results can be achieved by using a time consuming modelling with an even finer mesh. However, it was checked, the results for potential and particle densities do not change significantly with a finer mesh size at the edges anymore. From table 5.1 it can be seen that the bulk of the ions leave the model in longitudinal z -direction. Compared to the total outflow, the outflow in transversal direction consumes about 20%. The dominating ion outflow component is convection. Although the gas velocities are similar, the convective flow through the front boundary is significantly larger than through the rear wall, as the ion density is six times higher at the front boundary (see figure 5.17). A quite large ion drift occurs at the rear wall in order to compensate there the diffusive electron loss. It is driven by the sheath potential in front of the rear wall. However, about half of the total amount of leaving ion fluxes are driven by convection in the case of small, only space charge-induced electric fields. Therefrom the importance of a proper description of the background gas flow can be deduced. Finally, the obtained solution is tested by plugging it into equation (5.21) via numerical differentiation. The error is, like in the one-dimensional case, below 1×10^{-8} for the given discretisation.

Summary of results from planar simulations

In the following the results for potential and density distribution as well as dominating

fluxes for different surface boundary potential configurations are summarised. What is important for the potential and electron density distribution is the difference between rear wall and tube wall as explained in section 5.1. For the sake of simplicity (and without loss of generality), therefore, the tube wall is taken to be grounded²⁷ and the rear wall boundary is set to varying potentials. Thus, it is tested if the conclusions drawn for a decaying plasma also hold for the WGTS plasma.

Grounded Tube and rear wall

For this case the different components of the electron and ion currents have already been discussed above. The resulting potential distribution for the grounded lateral walls is in general in good agreement with the expectation of plasma potential and density behaviour in contact with a wall as described in section 5.1. The longitudinal and transversal potential profiles are plotted in figure 5.16. Sheath potentials up to about 6 meV, that match the order of magnitude given by equation (5.14), occur at the walls as well as potential variations of similar size within the bulk plasma. The latter indicate residual space charges and are necessary to properly balance the charge transport by drift currents.

The magnitude of the space charge potential is compatible to the potential from the one-dimensional, quasineutral simulation in [NM04]. Especially the potential and density profiles match quite well when the influence from electron reflection and transversal ion currents, not considered in [NM04], are neglected. The potential dip in the centre occurs since the T_2 gas is supposed to be injected there perpendicularly to the magnetic field and hence depleted from any charged particles, since the latter cannot cross the magnetic field lines but are deflected towards the walls of the many narrow inlet nozzles. Within the WGTS, the gas starts creating electrons and ions by beta decay and ionisation which accumulate during their longitudinal transport towards the exits. Then electrons diffuse into the depleted zone up to the point at which their space charge generates compensating drift currents. In the former one-dimensional quasineutral calculations in [NM04] this feature did show up, too. The longitudinal and radial density distributions for electrons and ions are depicted in figure 5.17. Quasineutrality holds quite well except for the sheaths next to the walls. In front of the rear wall, the densities are distributed as expected from the classical wall sheath description: the electron density decreases to almost zero, while a positive space charge builds up due to the net electron loss to the wall. This space charge region is expected to have a width of several times the Debye length [vK14]. For an average sheath electron density of $4 \times 10^{11} \text{ m}^{-3}$ the Debye length is about $5.4 \times 10^{-4} \text{ m}$. Thus, the simulated sheath width of about 3 mm matches the expectation quite well. The same holds for sheaths at the lateral walls. Their width is about 2 mm to 5 mm depending on the actual electron density. Different from the classical plasma-wall interaction, the WGTS electrons can not leave through the transversal wall²⁸ as their transversal mobility is almost zero due to the magnetic confinement. However, the ions that still can diffuse towards the lateral walls to some extent cause an increased longitudinal electron flow in the region next to the wall by ambipolar diffusion (see section 5.1.2). As a result an ion sheath forms next to the transversal tube walls comparable to the sheath at the rear wall. The sheaths at rear and front wall are depicted in figure 5.16c. The radial distribution of axial electron fluxes is also responsible for the decrease in potential towards the radial centre depicted in figure 5.16b.

For the simulation assuming a simplified two-dimensional, planar plasma with a homogeneous potential distribution at the boundaries the potential differences that build up in the plasma are well within the KATRIN requirements. The effect from different boundary potential configurations is investigated below.

²⁷This corresponds to the actual KATRIN WGTS operation.

²⁸Only a small thermal flux of electrons is able to leave transversally.

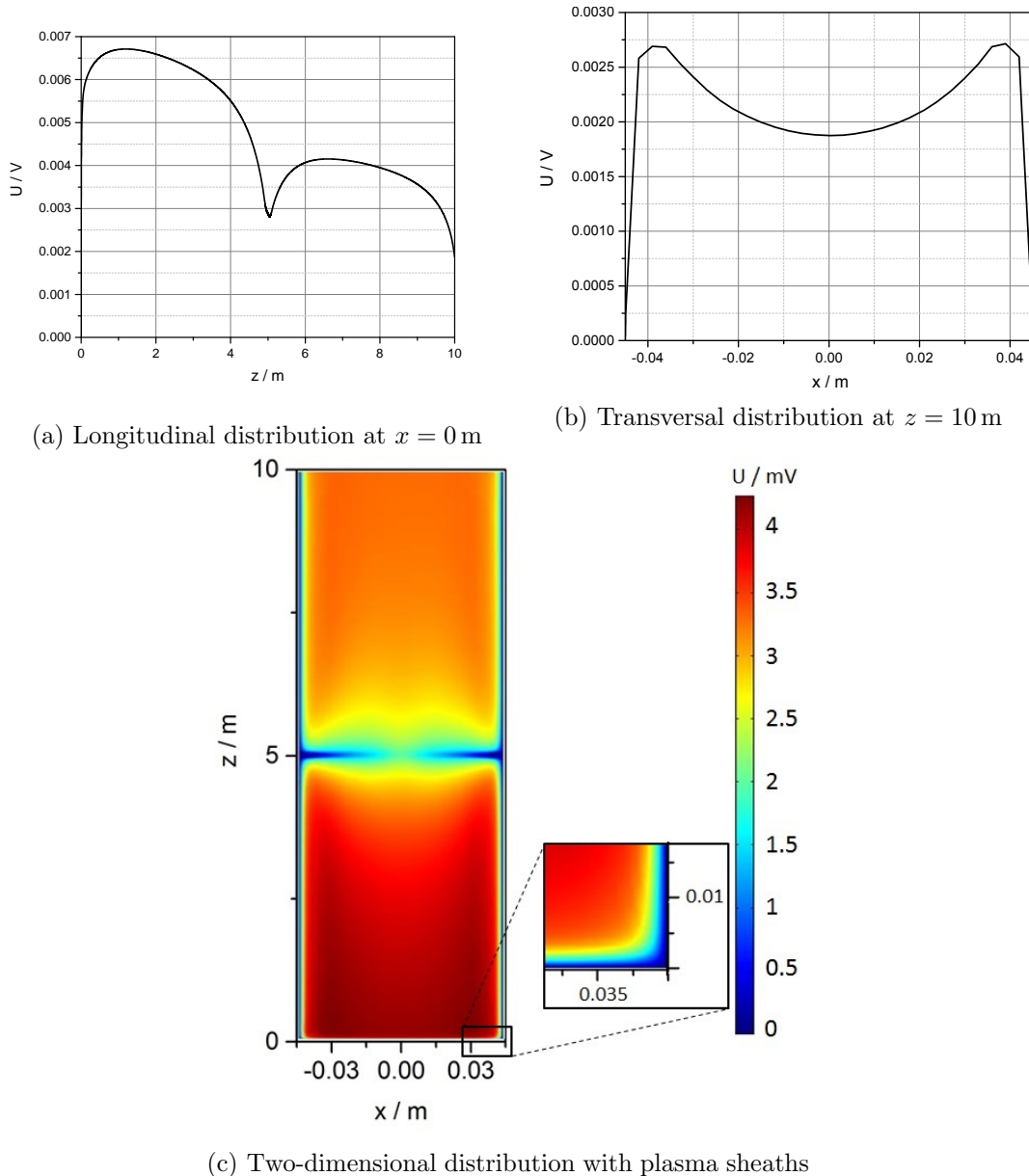


Figure 5.16.: **Potential distributions for the planar three-particle drift-diffusion model with tube and rear wall grounded.** (a) Longitudinal and (b) transversal potential profiles. Plasma sheaths form next to the rear wall as well as next to the tube walls as shown in the two-dimensional distribution in c). In these regions the drop from plasma to wall potential occurs.

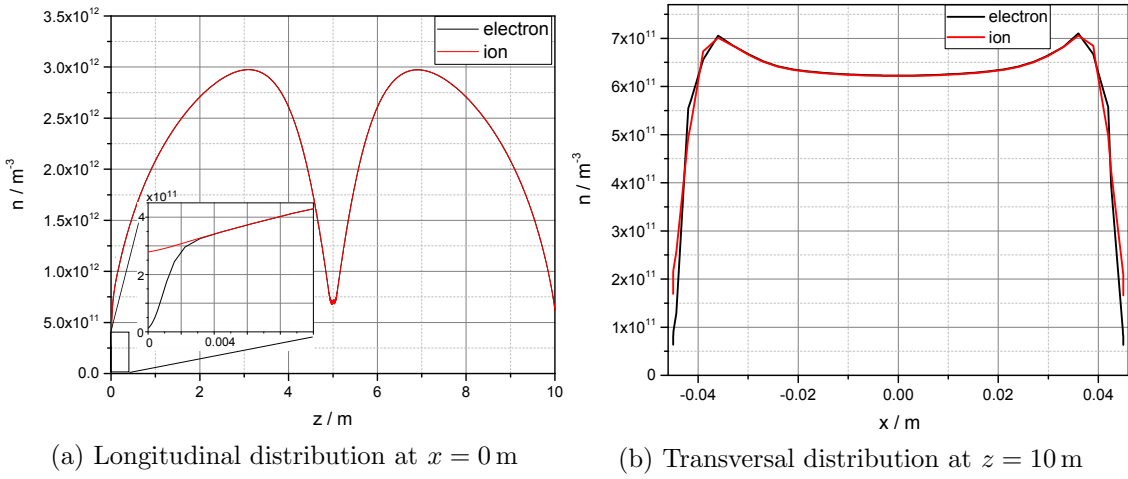


Figure 5.17.: **One-dimensional density distributions for the three-particle, planar drift-diffusion model with tube and rear wall grounded.**

Rear wall biased negatively

To test the effect of a rear wall at more negative potential than the tube wall, the rear wall voltage U_{rear} is set to 0 V and the tube wall potential is set to $U_{\text{wall}} = 1$ V. The voltage difference of -1 V between both boundaries is clearly below the critical value Δ_C from equation (5.43) which is about -20 mV for the WGTS operated at 30 K and a mean electron energy of 2 meV. For this boundary configuration, the electron drift to the rear wall is blocked.

Looking at the results, the plasma potential is bound to the tube wall, as can be seen in figure 5.18. There is only a small region of about 4 cm that is influenced directly by the rear wall potential. This is expected from theoretical considerations for $\Delta < \Delta_C$, see section 5.1.2. The bulk potential value is about 0.1 V to 0.2 V below the plasma potential determining lateral wall surface potential. This means that negative space charges are created, which is different from the general plasma-wall interaction potential described in section 5.1 and from the slightly positive plasma potential described for the grounded model above.

Electron and ion source and sinks need to mutually compensate in steady state. Since not enough electrons can leave the plasma through the rear wall, the electron density and thus the recombination rate goes up which reduces the effective number of created electrons/ions to about $1 \times 10^{-6} \text{ A m}^{-1}$. To compensate the high migrative electron currents from the electron repelling electric field at the rear wall into the plasma, high diffusive currents build up that still cause a net electron outflow. Ions moving in transversal direction are repelled by a positive electric field next to the walls. Thus, the transversal ion outflow is negligible. Ions are lost mainly through the front boundary and partially through the rear wall. The hindered electron flux towards the rear wall results in an overall negative space charge, different from the positive space charge for the typical plasma confined by walls as described in section 5.1.1. The resulting electron and ion density distributions are shown in figure 5.19. The axial density distribution, see figure 5.19a is comparable to the grounded boundary case discussed above. However, next to the rear wall an electron-depleted region arises since the electrons are repelled by the large negative potential at the wall. For the transversal distribution an atypical rise in charged particle density can be seen in the sheath region next to the tube walls (figure 5.19b). Since the transversal particle motion is determined by ions as the transversally more mobile particle species, the transversal density distribution is likewise determined by the ion motion. Ions are repelled by the positive potential at the tube walls and accumulate there. This can not be compensated by transversal electron motion, as the latter is blocked by the magnetic

confinement. Only the radial distribution of the longitudinal electron flux can be changed – it is reduced next to the lateral walls compared to the centre at $x = 0\text{ m}$. This has the effect of increasing the electron density next to the lateral walls and the charge of the ions, accumulated there, can be compensated. The plasma potential increases from the end of the plasma sheath next to the rear wall to the front boundary by about 150 mV as depicted in figure 5.18a.

The discussed planar plasma with a rear wall biased at large negative potential causes large potential inhomogeneities in longitudinal direction. These inhomogeneities are far beyond the KATRIN requirements. Thus, a large negative rear wall potential²⁹ needs to be avoided.

Rear wall biased positively

From the theoretical considerations in section 5.1.2, a positive voltage at the rear wall with respect to the lateral walls should determine the plasma potential. This is tested by using a rear wall voltage of 1 V and a lateral wall voltage of 0 V. Again, the potential difference $\Delta = 1\text{ V}$ is large compared to the thermal energy of the electrons and thus determines the charged particle outflows.

The resulting potential distribution is depicted in figure 5.20. This time the rear wall determines the value of the plasma potential inside the tube, as expected. The penetration depth of the lateral wall potential is less than 1 cm as depicted in figure 5.20b. The increased transversal outflow of ions causes a large longitudinal inhomogeneity of the plasma potential, see figure 5.20a. The potential shifts by about 0.3 V within the length of the model. Although the electrons can leave the source at the rear wall unhindered, as there is no blocking electric field, they are not able to compensate the large transversal ion current. This results in an overall negative space charge inside the WGTS. Considering the different surface areas of the outflow boundaries, A_{rear} and A_{tube} , the electron and ion saturation currents, $I_{\text{e,sat}}$ and $I_{\text{i,sat}}$, read [Pie10]:

$$I_{\text{e,sat}} = -\frac{1}{4}A_{\text{rear}}v_{\text{e,th}}n_{\text{e},0}e = -\frac{1}{4}A_{\text{rear}}n_{\text{e},0}e\sqrt{\frac{8k_{\text{B}}T_{\text{e}}}{\pi m_{\text{e}}}} \quad (5.71)$$

$$I_{\text{i,sat}} = -0.61A_{\text{tube}}v_{\text{B}}n_{\text{i},0}e = -0.61A_{\text{tube}}n_{\text{i},0}e\sqrt{\frac{k_{\text{B}}T_{\text{i}}}{m_{\text{i}}}}. \quad (5.72)$$

Assuming the ion density close to the tube wall $n_{\text{i},0}$ to be equal³⁰ to the electron density next to the rear wall $n_{\text{e},0}$, the ratio of electron to ion saturation current in the two-dimensional configuration is about 0.4. As the bias difference between tube and rear wall is large compared to the thermal energy of the charged particles, the electron and ion currents flowing through the corresponding boundary reach their saturation value – more ions than electrons can leave the model. Thus, large negative space charges arise and the plasma potential settles below the rear wall potential. The space charge is, like in the configurations described above, distributed in longitudinal direction. Ions leave the model through the whole WGTS length and cause the integral space charge, $\int_0^z \int_{-R}^R (n_{\text{i}} - n_{\text{e}}) \text{d}r \text{d}z$, to decrease with z . Thus, the plasma potential along any axis parallel to the z -axis also decreases, about 300 mV, from rear wall to front boundary. Plasma sheaths occur only at the transversal walls. Here the region where electron and ion density differ is large (about 2 cm), see figure 5.21, which causes the large width of the sheath. In contrast to the two models discussed above, electron and ion density are almost equal next to the rear wall,

²⁹“Large” in this context means negative potentials with absolute value far above the mean electron energy compared to the lateral wall potential.

³⁰The average electron and ion density next to the sheath at the tube walls is larger than the average electron and ion density next to the rear wall, thus even increasing the ion-electron saturation current ratio.

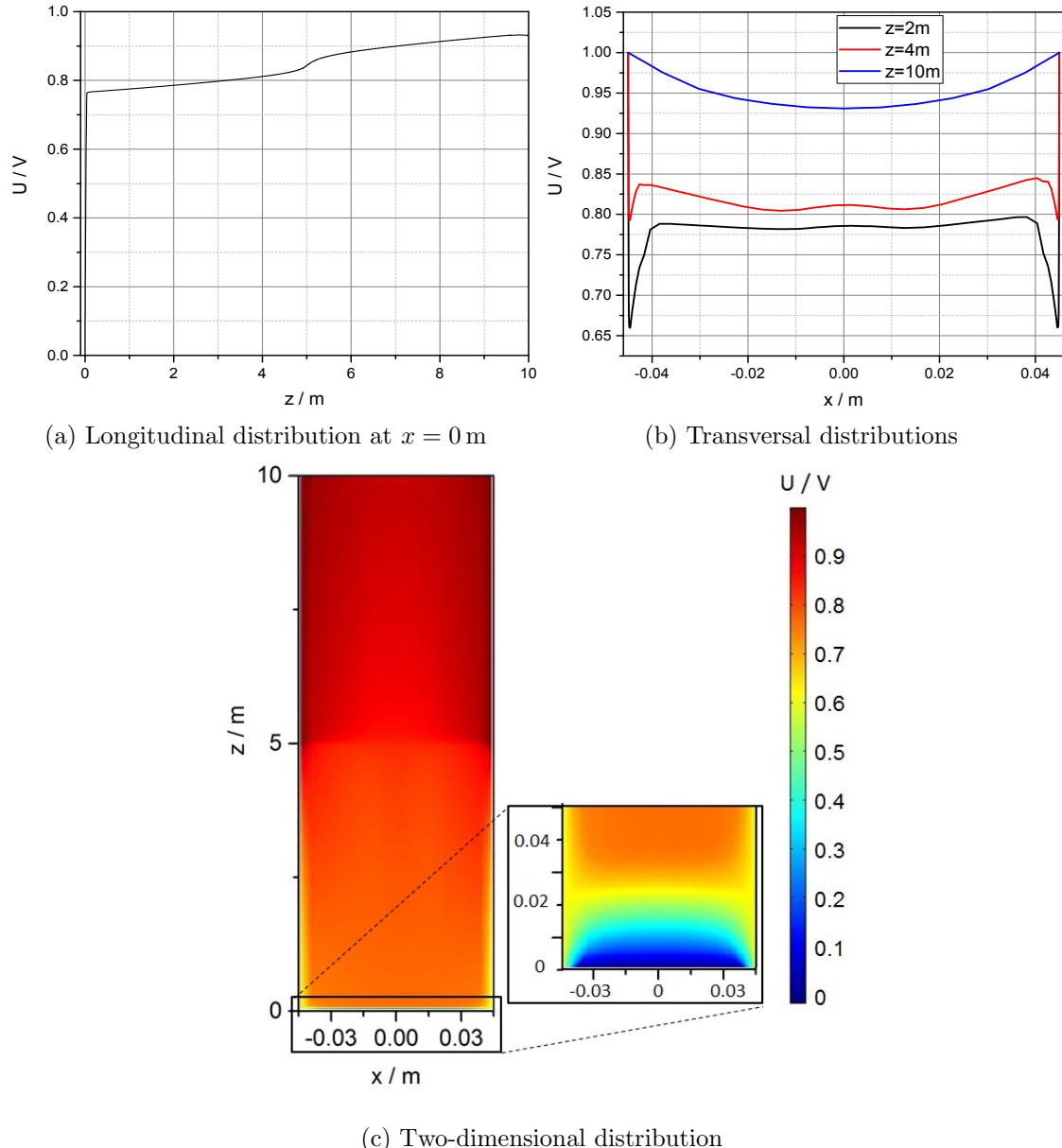


Figure 5.18.: **Potential distributions for the three-particle drift-diffusion model with $U_{\text{rear}} = 0 \text{ V}$, $U_{\text{wall}} = 1 \text{ V}$.** The plasma sheath that forms next to the rear wall is shown within the two-dimensional distribution in c).

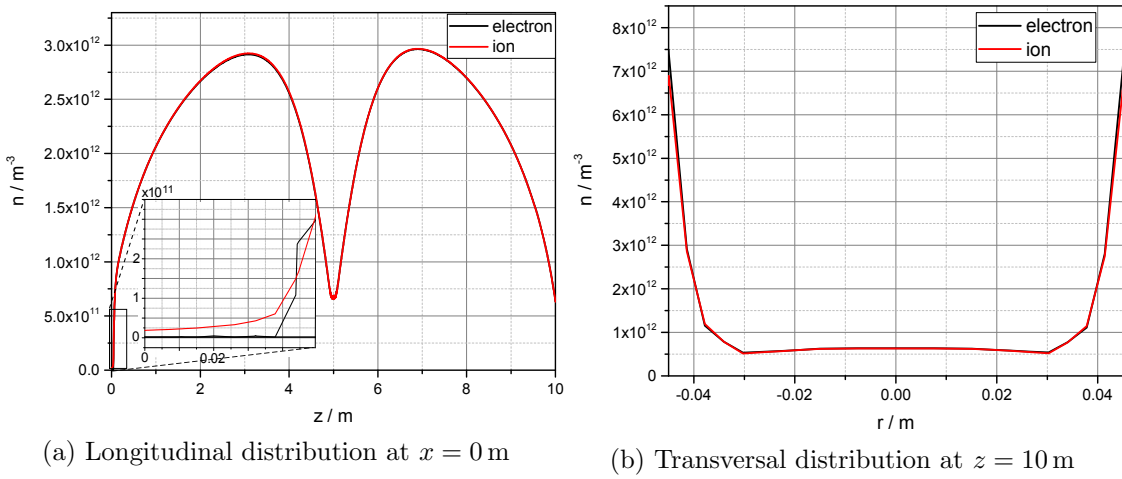


Figure 5.19.: **One-dimensional density distributions for three-two particle drift-diffusion model with $U_{\text{rear}} = 0 \text{ V}$, $U_{\text{wall}} = 1 \text{ V}$.**

as depicted in figure 5.21a. Therefore no sheath can form there.

Reducing the applied voltage difference between tube and rear wall to 0.1 V, the large transversal outflow of ions can be reduced as the current is below its saturation value. The tube plasma potential is still set by the rear wall voltage, but the maximal longitudinal potential difference is reduced to less than 20 mV as can be seen in figure 5.22. The transversal sheath width and thus the penetration depth of the wall potential is reduced to about 6.5 mm.

For all boundary potential configurations described above the plasma potential is not homogeneous in longitudinal direction. The size of the potential differences is determined by the distribution of space charges which means, by electron and ion fluxes through the boundaries. In case of a positively biased rear wall, the absolute value of the plasma potential is determined by the rear wall potential. If it is biased clearly negatively, $\Delta \ll \Delta_C$, the tube wall potential penetrates deep into the plasma or even settles its absolute potential value. This is also expected from the theoretical considerations in section 5.1.2. If the potential difference is larger than the critical difference, $\Delta > \Delta_C$, but too small to cause the ion and electron currents at tube and rear wall to saturate, $\leq 0.1 \text{ V}$, the total space charge is positive and determined by the loss of electrons. If it is clearly larger than 0.1 V, the charged particle currents saturate and the total space charge is negative and determined by the loss of ions.

Cylinder symmetric plasma model

The above presented two-dimensional planar model underrates the loss of ions at the tube walls. The ratio of electron to ion saturation current decreases by a factor of two to 0.19 because of the different geometric configuration of corresponding outlet boundaries:

$$\frac{I_{e,\text{sat}}(\text{planar})}{I_{i,\text{sat}}(\text{planar})} \cdot \frac{I_{i,\text{sat}}(\text{cylinder})}{I_{e,\text{sat}}(\text{cylinder})} \quad n(\text{planar}) = n(\text{cylinder}) \quad R \cdot \frac{2\pi RL}{\pi R^2} = 2. \quad (5.73)$$

This influences the space charge distribution and thus the potential distribution. Furthermore, the planar model simplifies the differential operator in radial direction, see (5.68). This influences not only the radial (ion) flow, as ion and electron flow are linked through ambipolar diffusion. To include the right amount of particle loss, the two-dimensional model is extended into an axisymmetric model, representing a bounded cylinder. Aside

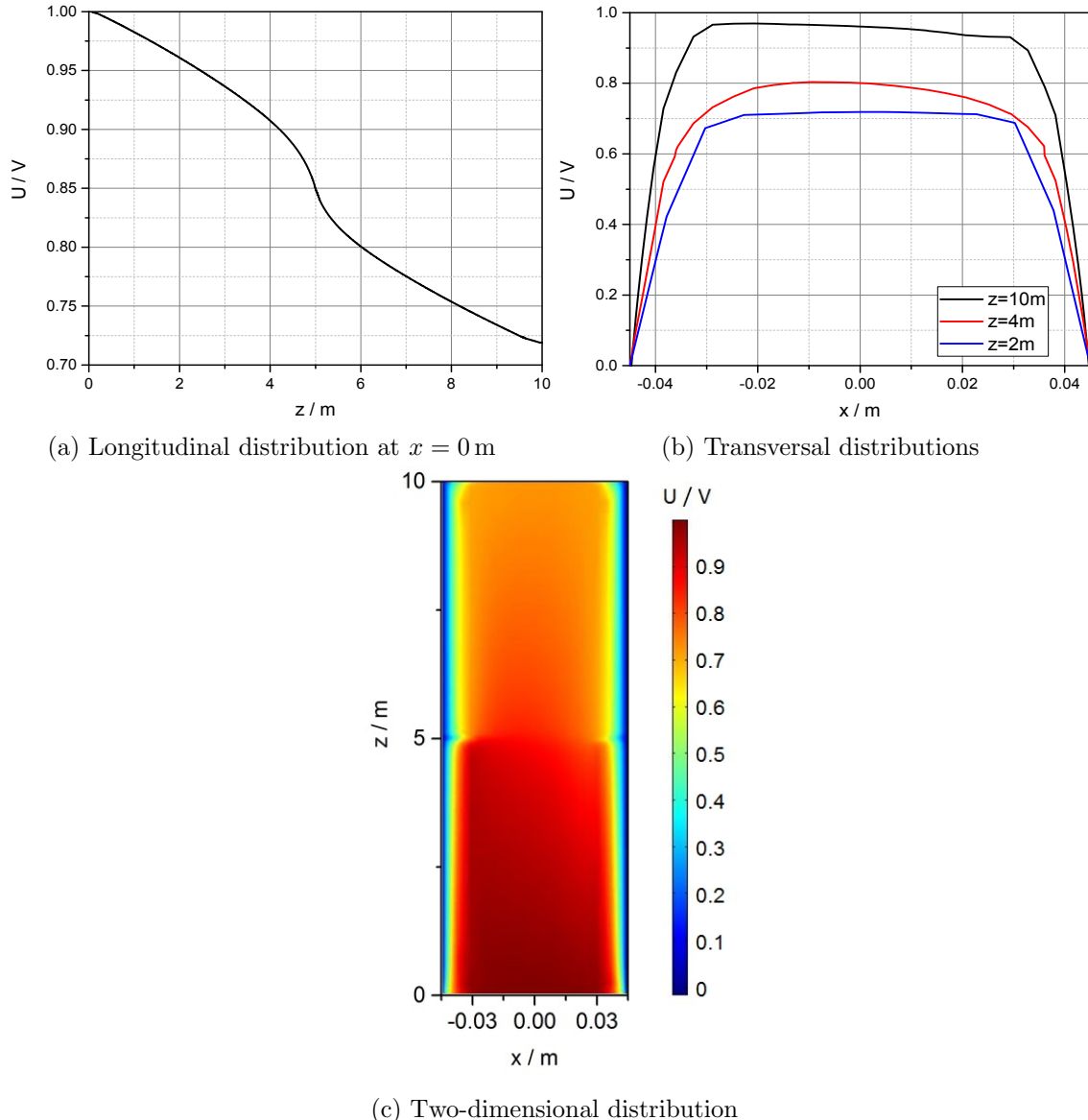


Figure 5.20.: Potential distributions for the three-particle drift-diffusion model with $U_{\text{rear}} = 1 \text{ V}$, $U_{\text{wall}} = 0 \text{ V}$.

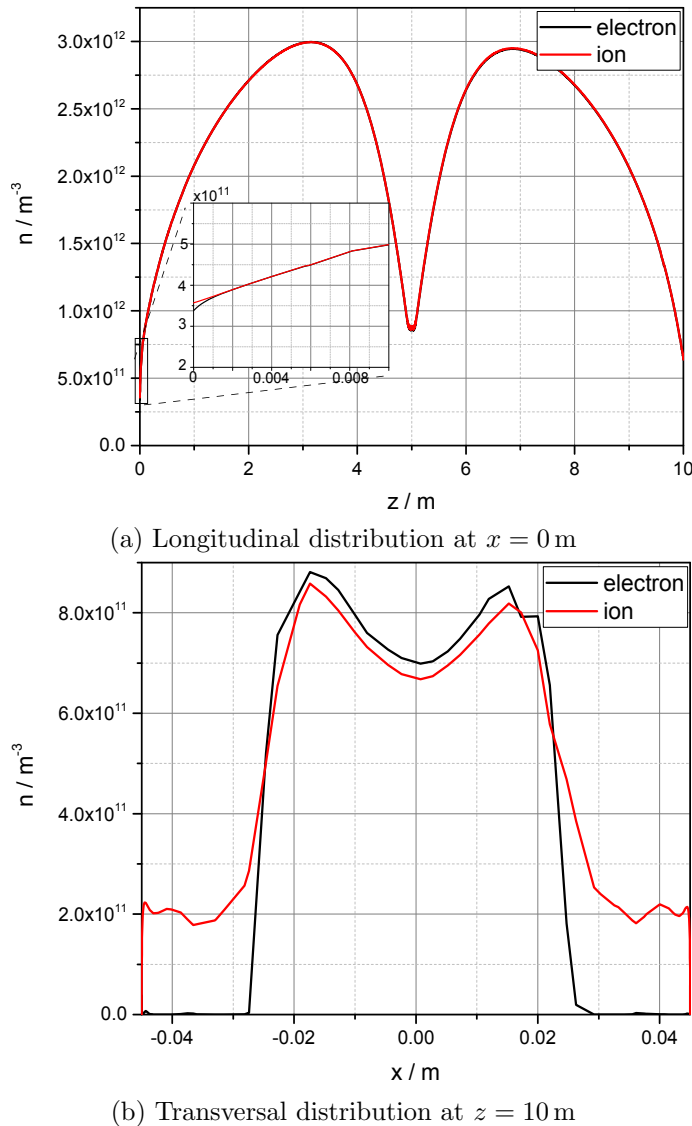


Figure 5.21.: **One-dimensional density distributions for the three-particle drift-diffusion model with $U_{\text{rear}} = 1$ V, $U_{\text{wall}} = 0$ V.**

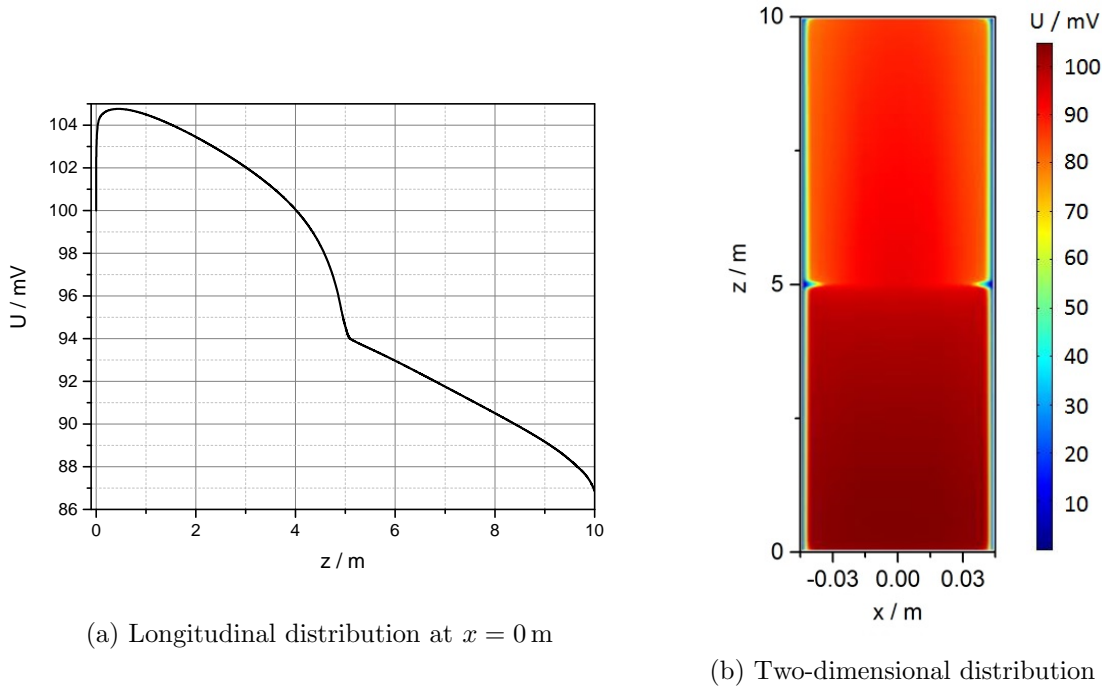


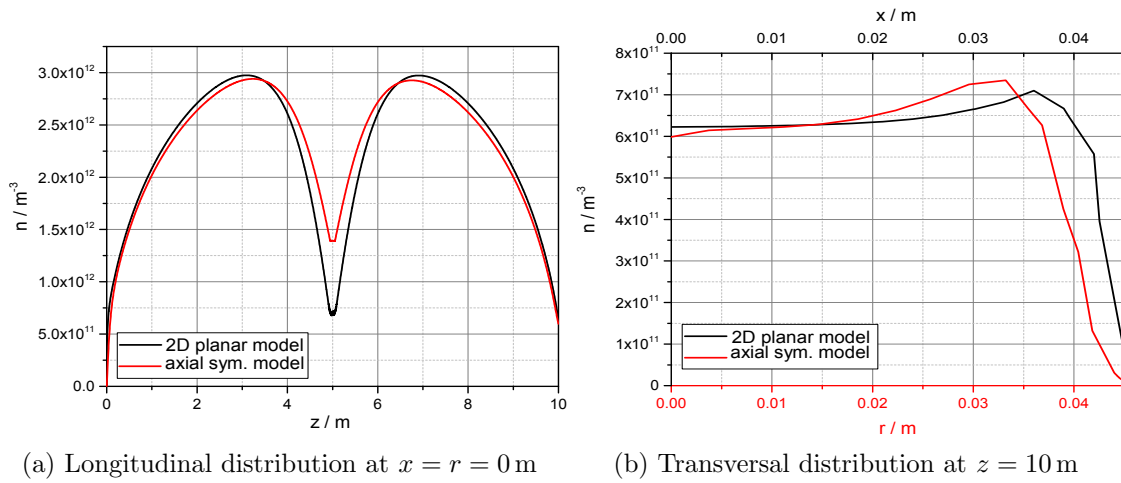
Figure 5.22.: Potential distributions for the three-particle drift-diffusion model with $U_{\text{rear}} = 0.1$ V, $U_{\text{wall}} = 0$ V.

from the modified form of the differential operator and the zero gradient boundary condition in azimuthal direction, boundary conditions are identical to the two-dimensional model as shown in figure 5.11. The background gas density and velocity distribution is the same as for the planar model with $x = r$. Thus, the initial creation rate of charged particles, not considering the recombination, is also unchanged. Initial values for electron density and potential distribution are taken from the planar plasma solution with grounded walls.

In the following results from both two-dimensional models are compared. This is done for the grounded WGTS as well as for a slightly positively biased rear wall ($\Delta = 0.1$ V), where the influence of increased transversal ion fluxes is larger.

Comparison cylinder symmetric and planar model

At first, results for the configuration with all boundaries grounded are compared. In solution of the axisymmetric model, the effective rate of charged particle creation is 2.26×10^{-6} A m⁻¹, and thus almost the same as for the planar model since the production rate is the same and the recombination rate does not change significantly. Therefore, also the charged particle density distribution hardly changes. Only the radial sheath width slightly increases as depicted in figure 5.23b. This is connected to the increased outflow of transversal ion fluxes that can be seen in figure 5.24. The integrated ion current leaving the plasma through the radial tube walls is about 4×10^{-7} A m⁻¹ and thus almost twice the value of the corresponding planar simulation. On the other hand, the longitudinal ion fluxes leaving the plasma are comparable to the planar model. Thus, the ratio of total longitudinal to transversal ion fluxes leaving the model decreases from 4.6 to 2.3 and the influence of transversal ion flows increases. The space charge potential that builds up next to the rear wall is comparable for both simulations. It is decreased by about 1 mV due to the increased overall ion outflow. Also the slope of the longitudinal potential distribution in the radial centre of the tube, that is plotted in figure 5.25, is comparable for both simulations. The radial inhomogeneity is increased compared to the planar model because of the larger transversal ion flows. The potential increases throughout almost the whole



(a) Longitudinal distribution at $x = r = 0$ m (b) Transversal distribution at $z = 10$ m

Figure 5.23.: **Electron density distributions for the axisymmetric model with all boundaries grounded.** Results from the axisymmetric model are plotted in red, the corresponding two-dimensional planar model results are given for comparison (black).

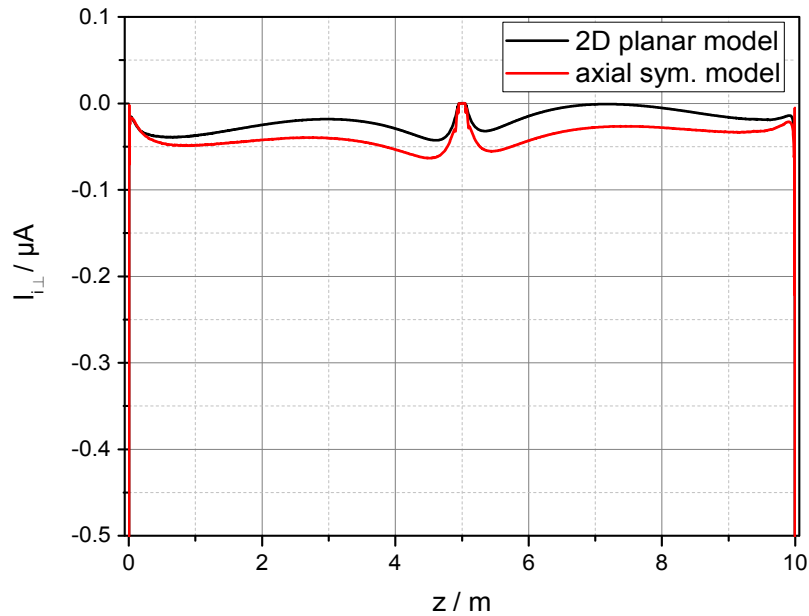


Figure 5.24.: **Transversal ion currents $I_{i\perp}$ of axisymmetric and two-dimensional planar model with all boundaries grounded.** The normal direction is pointing to smaller radii, therefore outgoing fluxes are negative.

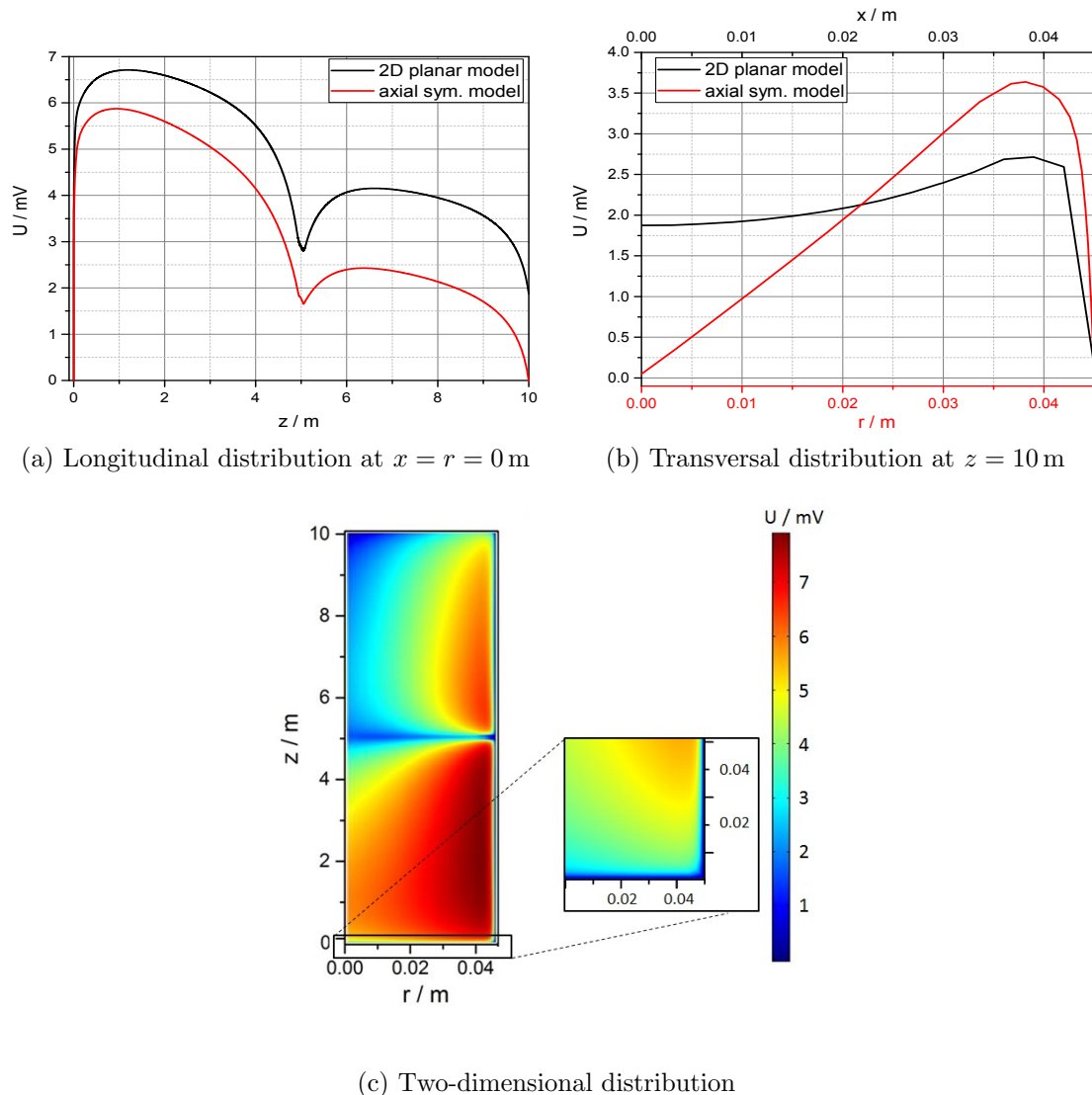


Figure 5.25.: **Plasma potential distributions for the axisymmetric model with all boundaries grounded and the results from the corresponding planar model.** For the transversal two-dimensional distributions only positive radii are plotted because of the symmetry axis at $r = 0$ m.

radial cross section, besides the small sheath region, where the plasma potential drops to tube potential. This prevents the radial outflow of ions from increasing.

With rear and tube walls at equipotential the impact of transversal ion currents turns out to be quite low compared to configurations with potential differences between rear and lateral wall. In the cylinder-symmetric model the longitudinal ion flow is still dominating. Therefore, results for a second rear wall voltage with $\Delta = 0.1$ V are tested. Here the effect from increased transversal ion flow is considerably larger.

The simulation result for the transversal ion current density leaving through the lateral wall boundary in comparison to the corresponding two-dimensional planar model current density can be seen in figure 5.26a. The current calculated with the cylinder-symmetric model is again larger than the two-dimensional planar model solution. This increased outflow of ions is connected to a decrease in charged particle density, see figure 5.26b. The charged particle density is reduced to about 85% of the two-dimensional planar model density. The plasma potential, as depicted in figure 5.28 is clearly influenced by the changed distribution of flows. Compared to the planar model, it even changes the sign of the slope

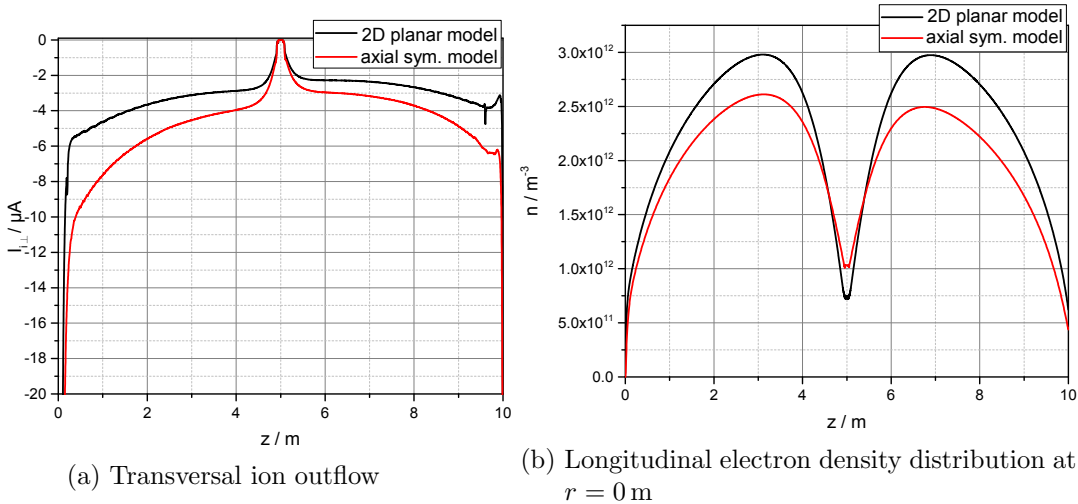


Figure 5.26.: Transversal ion outflow and longitudinal electron density distribution for cylindrical and two-dimensional planar plasma with $\Delta = 0.1$ V.

in longitudinal projection, see figure 5.28a. The transversal potential inhomogeneity increases with z , as can be seen in figure 5.28c. The potential drop in the transversal plasma sheath, with a width of about 5 mm, is comparable to the two-dimensional planar model case. Yet, the transversal potential in the bulk of the plasma is not homogeneous. The potential drop of about 8.5 mV through bulk up to the sheath is even larger than the drop in the sheath, as depicted in figure 5.28b. This transversal distribution is caused by the non-vanishing transversal electric field, compare figure 5.27.

For low biasing voltages ($|\Delta| < 0.03$ V) axisymmetric and two-dimensional planar model show similar distributions of plasma potential and electron density as well as of fluxes and space charges. When transversal flows get larger (larger boundary potential differences), the results for the potential distribution from both models become different because of the difference in saturation currents. Thus, for low bias voltages, where both model currents are not saturated, general conclusions drawn from the planar model can be assumed to be valid for the cylindrical plasma as well. Therefore, the planar plasma model can be used to investigate the influence of different plasma parameters like magnetic field, recombination coefficient and gas column density. This is discussed in the following section. In the region, where saturation starts in the axisymmetric model, the potential differences will be larger than for the two-dimensional planar model, where currents are still unsaturated. Due to differences in the distribution of fluxes, the form of the radial potential distribution changes between both models. To evaluate the influence of the potential distribution on the spectrum of β -electrons it is important to know the absolute values of inhomogeneities of the potential. Therefore, in section 5.3.4 the cylinder-symmetric model is used to calculate an optimised rear wall bias to minimise these inhomogeneities. In this context the influence from distributions of surface potentials on the plasma potential is tested.

5.3.3. Influence of plasma conditions and parameters on the WGTS potential

The WGTS plasma model has relatively large uncertainties with regard to recombination coefficients, electron energy and electron energy distribution. Conditions like magnetic field or column density can deviate from the nominal values used in the model above in special operation phases. Furthermore, in the plasma model the plasma is only contained in the central 10 m beam tube. The impact of the mentioned effects on the potential

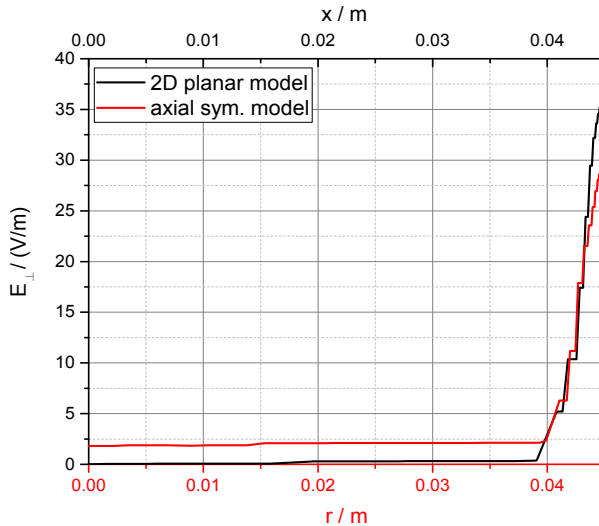


Figure 5.27.: **Transversal Electric field for cylinder-symmetric model with $\Delta = 0.1$ V.** The results for the corresponding two-dimensional planar simulation are given for comparison.

distribution and on the stability of the results of the steady state solution is investigated in this section. Since the solutions for cylinder-symmetric and planar model are comparable, at least for low biasing voltage differences, the planar model is used to investigate the above mentioned effects. It converges faster than the axisymmetric model, with a lower number of iterations due to the simplified transversal gradients. It still allows to deduce the order of shifts in the potential distribution and the qualitative plasma behaviour.

5.3.3.1. Column density

Within the first measurements with tritium inside the WGTS the actual amount of tritium will be significantly lower than the standard tritium column density. To see how a different column density influences the plasma density and potential distribution, a configuration using a fraction x_T of the standard column density is calculated³¹. Here one needs to disentangle two configurations:

1. Standard gas column density $\rho d_{\text{gas},0} = 5 \times 10^{21} \text{ m}^{-2}$, reduced tritium column density $\rho d_{T_2} = x_T \rho d_{\text{gas},0} < \rho d_{\text{gas},0}$
2. Standard tritium purity, reduced gas column density $\rho d_{\text{gas}} = \rho d_{T_2} = x_T \rho d_{\text{gas},0}$.

For a reduced tritium column density the plasma density will be even lower than the already low density in standard mode, compare section 5.2. Thus, at some point of charged particle reduction, the fluid model is not applicable anymore. Then the distance between charged particles is too large to be significantly influenced by the Coulomb fields of the other particles. Thus, the tritium reduction factor x_T is set to 50%, which produces a still large enough charged particle density. Hence, a tritium column density of $\rho d_{T_2} \approx 2.5 \times 10^{21} \text{ m}^{-2}$ is implemented in configuration 1) and 2) which means, the initial electron creation rate is equal for both configurations. The background gas density and velocity distribution for the reduced column density compared to the standard column density are depicted in figure 5.29. While the gas density is reduced to about 50% compared to the standard column density (figure 5.29a) the velocity distribution is similar for both cases (figure 5.29b). The longitudinal velocity is only slightly reduced for the reduced density case. The reduced density profile from figure 5.29a is used for configuration 1) and

³¹Actually not the column density but the injection pressure is reduced which is roughly the same.

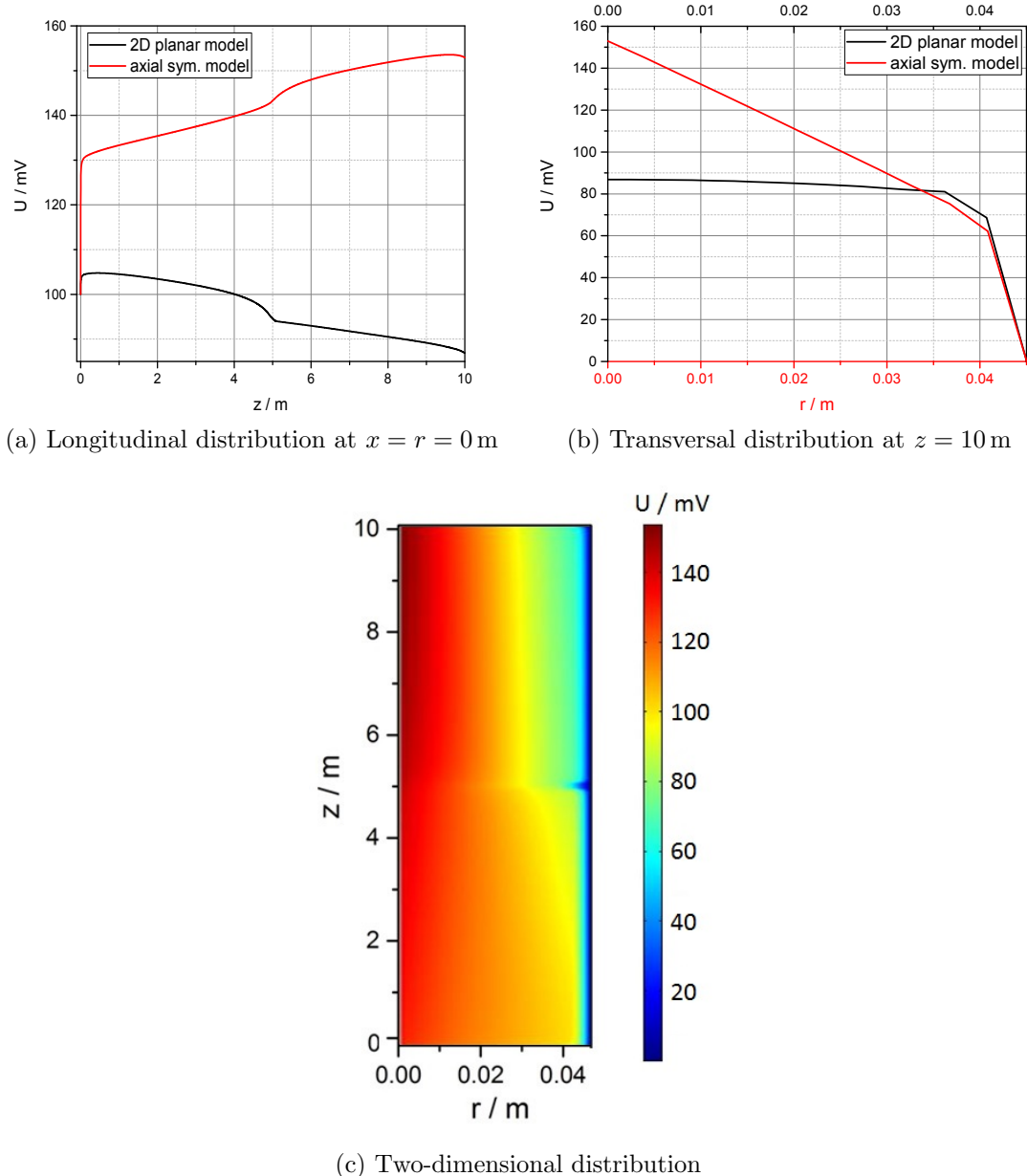


Figure 5.28.: Plasma potential distributions for the axisymmetric model for boundaries at $\Delta = 0.1$ V and the results from the corresponding two-dimensional planar model.

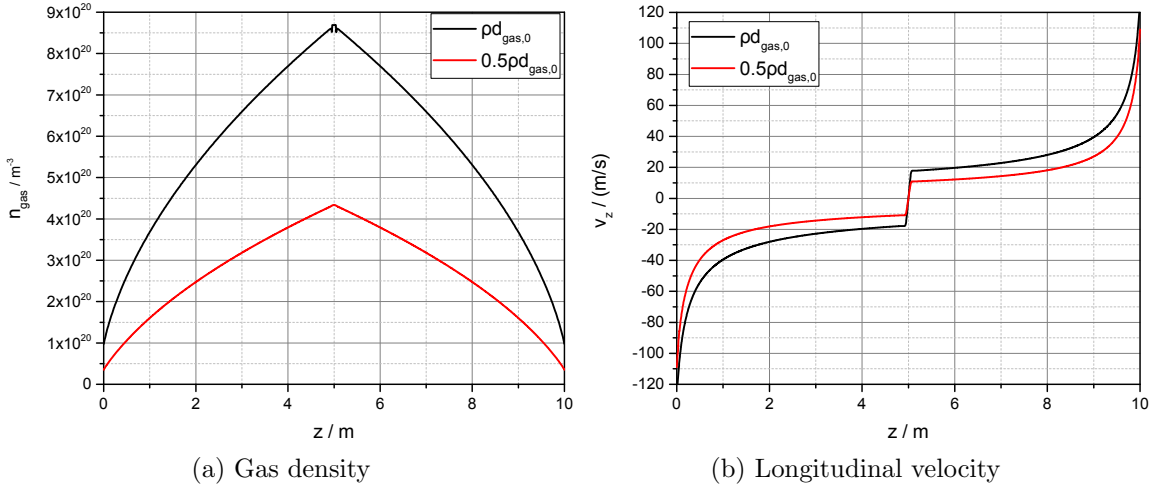


Figure 5.29.: **Background gas profiles for standard, $\rho d_{\text{gas},0}$, and reduced column density $0.5 \rho d_{\text{gas},0}$.** Axial distributions at $x = 0 \text{ m}$.

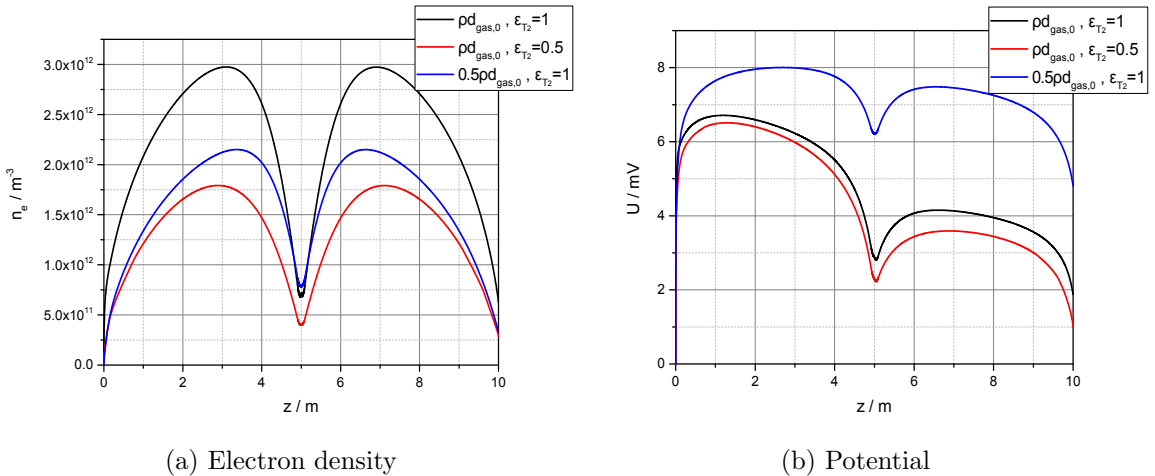


Figure 5.30.: **Longitudinal electron density and plasma potential profiles for changed column density and tritium purity, ϵ_{T_2} , compared to the standard background gas properties with $\rho d_{\text{gas},0}$ and $\epsilon_{T_2} = 1$.** Axial distributions at $x = 0 \text{ m}$.

2) for the charged particle production. For the specification of the mobilities as well as for the convective ion velocity, standard column density values, $\rho d_{\text{gas},0}$, are used in 1). In 2) the reduced column density gas properties, $x_T \rho d_{\text{gas},0}$, are used.

The computed longitudinal electron distribution as well as the potential distributions for configuration 1) and 2) are depicted in figure 5.30. Although the tritium density is reduced to half its initial value, the electron density reduction is only about 30% for the standard mobility and velocity, case 1), and about 40% for the adapted mobility, case 2). This is caused by the reduced recombination rate. The density difference between case 1) and 2) is due to the changed mobility. With regard to the potential distribution, the configurations with the same mobilities, case 1) and the standard configuration, show similar potential distributions as can be seen in figure 5.30b and figure 5.31. The absolute space charge potential is increased to about 8 mV for the high mobility case 2). However, the potential distribution is more homogeneous as becomes apparent in the two-dimensional distributions in figure 5.31. While the longitudinal zero field mobility is increasing, the radial mobility decreases. This reduces the transversal ion fluxes, which improves the plasma

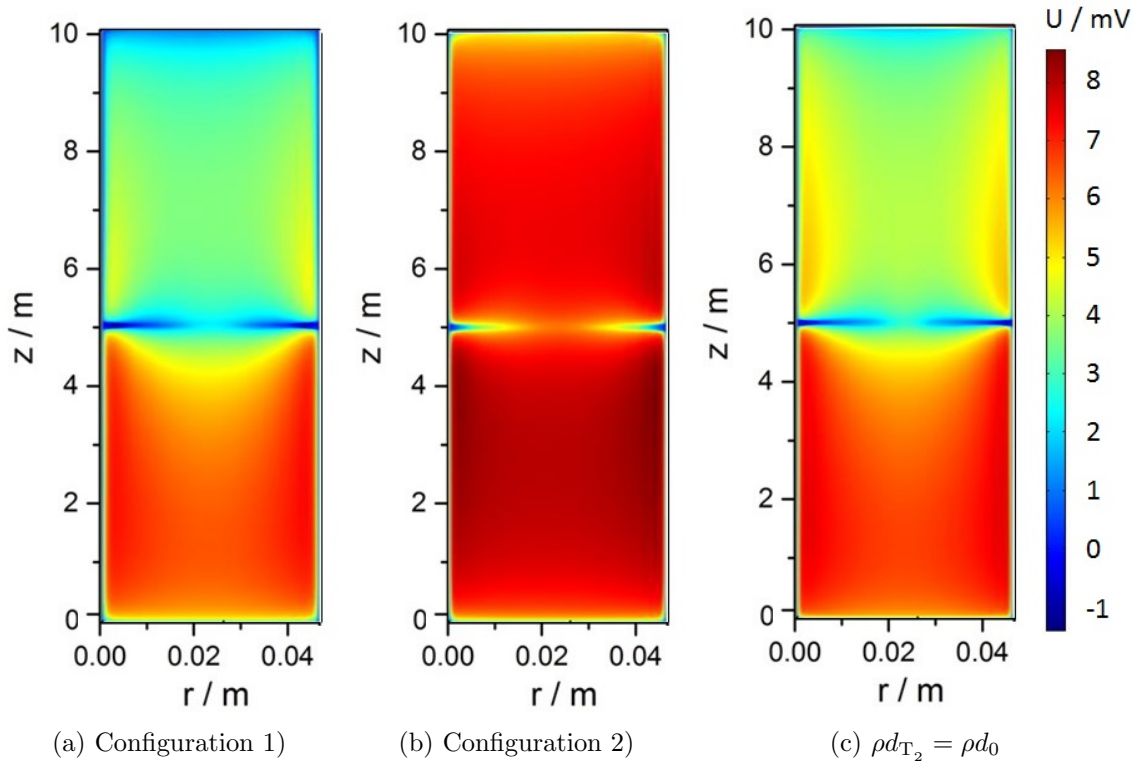


Figure 5.31.: Two-dimensional plasma potential distribution for reduced gas column density and tritium purity, ϵ_{T_2} , configuration 1) and 2), as well as standard properties with ρd_0 and $\epsilon_{T_2} = 1$.

homogeneity.

5.3.3.2. Electron energy and electron energy distribution

The electron energy has a large impact on the plasma behaviour as it influences the electron flux, see (5.38). Moreover, it determines the cross sections of the different reactions in the plasma, described in section 5.2. Thus, it has a direct impact on the density and potential distribution. Four electron energy related parts can be distinguished:

Change in	Influence on
mean electron energy	electron outflow recombination rate coefficient
energy distribution (not Maxwellian)	recombination rate coefficient electron outflow rate

In the following, effects from changes in mean electron energy and energy distribution are discussed separately.

Mean electron energy

The average electron energy cannot be assumed to be known precisely, since the Monte-Carlo simulation for the calculation of the electron energy spectrum in the WGTS plasma does not include actual plasma effects like intrinsic electric fields and energy dependent outflows. Thus, the mean electron energy and temperature can slightly differ from the calculated fully thermalised value of 30 K. In case of measurements with a lowered gas density, the temperature of the electrons may also change, since they are, depending on the actual density reduction, no longer able to thermalise to gas temperature by electron-molecule collisions. Furthermore, the measurements at an elevated gas temperature of

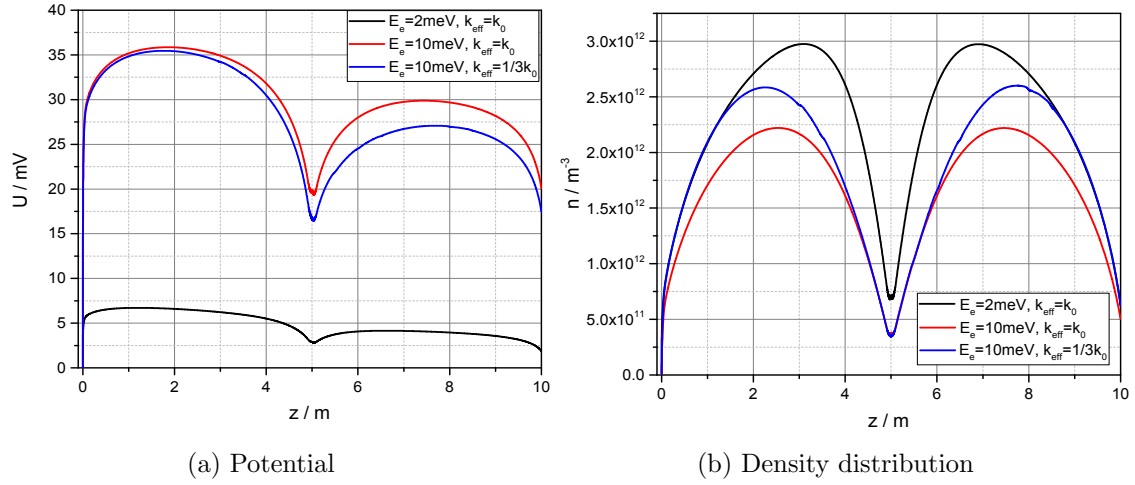


Figure 5.32.: **Energy dependence of electron density and potential distribution.**

Axial distributions at $x = 0$ m. Compared are solutions for electron energies of 2 meV and 10 meV with and without adapted recombination rate coefficient.

110 K with krypton cause the electron energy to change to about 14 meV, if they are still able to thermalise. Therefore, it needs to be tested how the mean electron energy influences the plasma conditions. To do so, a mean electron energy of 10 meV is implemented in the plasma model. Results are compared to the 2 meV configuration described before. The electron energy distribution is still assumed to be Maxwellian. Thus, just the dependence of the recombination process on a change in mean electron energy needs to be considered. For the recombination of electrons with T_3^+ ions this dependence was calculated to be³² in [MNF⁺84]: $k_{\text{rec},T_3^+} \propto \left(\frac{300\text{ K}}{T_e}\right)^{0.8}$. In case of T_5^+ ions the energy dependence can be approximated with: $k_{\text{rec},T_5^+} \propto \left(\frac{300\text{ K}}{T_e}\right)^{0.69}$ [MBJ84]. Thereby, for the effective recombination coefficient from equation (5.51) a value of about $1.3 \times 10^{-12} \text{ m}^3 \text{ s}^{-1}$ results for an electron energy of 10 meV. This is about one third of the recombination coefficient at 2 meV, which would lead to an increase in electron density. On the other hand, a higher electron energy causes a higher electron flux through the rear wall. This decreases the electron density, while the ion flux stays comparable. Therefore, a higher space charge potential is expected.

The result of these two opposing effects can be seen in figure 5.32b, where the density distributions for electron energies with and without adapted recombination coefficient are plotted. The effect of an increased electron flux is larger than that of the reduced recombination rate coefficient – the particle density for the elevated electron energy decreases. The plasma potential is lifted, as expected, by a factor of five to 35 mV and corresponds roughly to the floating potential of equation (5.14). The change in potential along the beam tube z -axis increases to 19 mV, see figure 5.32a. However, this value is less affected by the increase in electron energy than the absolute value of the potential, as the transversal ion flow, responsible for the change in longitudinal potential, is not influenced directly³³. For the elevated electron energy with adapted recombination coefficient the outflow of electrons is about $3.9 \times 10^{-6} \text{ A m}^{-1}$. This means an increase of about 60% compared to the outflow for 2 meV electrons. The penetration depth of the transversal wall potential, which corresponds to the transversal sheath width, is also slightly raised to 7 mm.

³²The recombination process of deuterium and hydrogen ions is assumed to be comparable to the recombination process of tritium ions due to the similar atomic structure.

³³The absolute potential value is only affected by the electron flux through ambipolar diffusion.

Electron energy distribution

Rate coefficients

Besides the dependence on mean electron energy, also the actual energy distribution needs to be considered. A changed distribution function influences the electron current as well as the recombination rate, see (5.50). Both effects are considered separately. The electron energy distribution function obtained by Monte Carlo simulation, as described in section 5.2, is not an exact equilibrium Maxwell distribution. There is a tail of electrons at high energies, see figure 5.7. However, in the rate coefficient measurements used within the plasma model the electrons are assumed to follow a Maxwell-Boltzmann distribution. To test an energy distribution different from Maxwellian, energy dependent cross sections for all reactions involved in the recombination process would need to be used. However, for the actual plasma calculations only the rate constant for the mean electron energy E_e , $k_{\text{eff}}(E_e)$ from (5.50), can be used. It is a parameter already averaged over the electron energy distribution. To include the energy distribution directly in a plasma model, one would need to simulate either single particles or introduce new electron species with different mean energies. This can not be combined with the bulk approach and a fixed electron energy distribution function used in the presented three-particle fluid model. The effect of a changed recombination rate coefficient on the WGTS plasma can be tested indeed. The mentioned electron energy distribution with a high energy tail (figure 5.7) would cause a lower rate constant, as the recombination cross section decreases with higher electron energy. Therefore, in the following different rate coefficients with $k_{\text{rec},1} = 0.5k_0$ and $k_{\text{rec},2} = 0.1k_0$, are implemented in the model for mean electron energies of 2 meV. Here k_0 denotes the recombination rate for Maxwell distributed electrons corresponding to a mean energy of 2 meV as used in the simulations above. Additionally a test simulation assuming a higher rate constant of $k_{\text{rec},3} = 10k_0$ is calculated, as the absolute value of the rate constant has quite large uncertainties and may be underestimated [Glü05, NM04]. For $k_{\text{rec},1}$ the effective production rate of electrons is $2.88 \times 10^{-6} \text{ A m}^{-1}$ which is about 30% higher than the production rate for k_0 . For $k_{\text{rec},2}$ the effective electron production rate further increase to $4.5 \times 10^{-6} \text{ A m}^{-1}$, which is more than twice the production rate for k_0 . For the elevated recombination coefficient $k_{\text{rec},3}$ the production rate decreases to about $9.1 \times 10^{-7} \text{ A m}^{-1}$, which is about 40% of the initial value. The electron and ion density increases with decreasing recombination rate coefficient. The dependency is not linear as the particle outflow is affected by the changed densities, too. The absolute recombination rate decreases despite the increased charged particle density. Longitudinal density distributions for the different rate coefficients are depicted in figure 5.33b. The appropriate plasma potential distributions are shown in figure 5.33a. The offset of the plasma potential next to the wall (space charge potential) is hardly changed. This only depends on the relative number of electrons compared to the amount of ions leaving the plasma through the wall. This number stays almost at the same value as both densities are changed. The slope of the potential distribution decreases with decreasing recombination coefficient. Thus, the longitudinal plasma potential difference increases to 6.5 mV for $k_{\text{rec},2}$. It is minimised for largest recombination coefficient $k_{\text{rec},3}$.

Electron outflow

The other quantity that is influenced by the distribution of electron energies is the electron flux going out at the rear wall. For a fluid model with a single electron species, though, it is determined using the averaged electron velocity \bar{v}_e [GR95]:

$$\Gamma_e = n_e \int v_e \frac{f(v_e)}{n_e} dv_e = n_e \bar{v}_e. \quad (5.74)$$

Therefore, the electron flux leaving the plasma is the same for different distribution functions with the same average electron energy. As the presented plasma model uses a single-

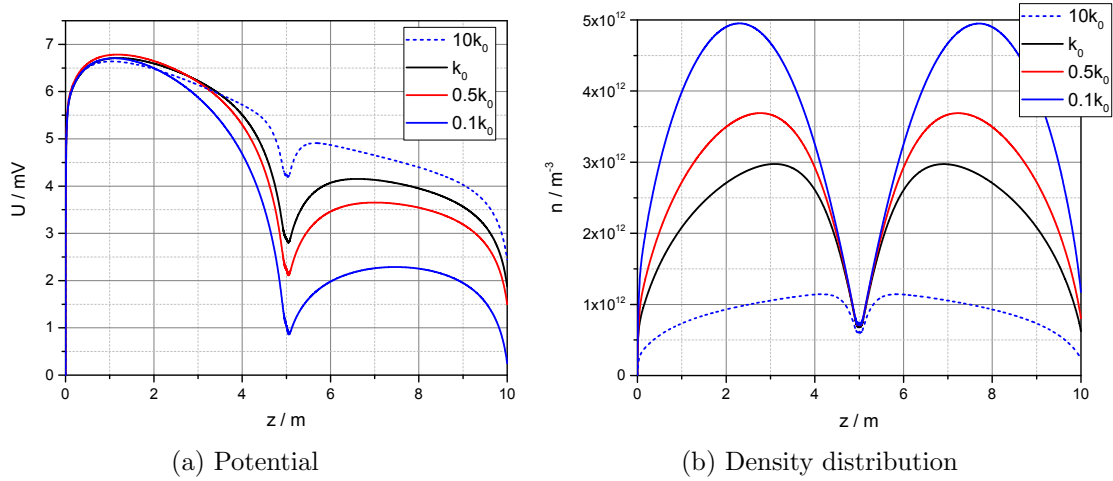


Figure 5.33.: **Effect of recombination rate coefficient on electron density and potential distribution.** Axial distributions at $x = 0$ m. Compared are the solutions for different recombination rate coefficients with respect to the rate coefficient k_0 for Maxwell distributed 2 meV electrons.

electron fluid approach, it is not affected by the actual energy distribution. When dropping the assumption of a single-electron fluid model and introducing an additional high energy electron species, additional fluxes of high energy electrons can be tested. This high energy electron contribution was investigated in [IB90] assuming a Maxwellian plasma with additional high energy mono-energetic electrons. In [GMS95] the high electron energy influence starting from a bi-Maxwellian plasma with a low and a high electron temperature was examined. The electron energy distribution influences the plasma properties mainly in the region of the sheaths [GGBK06, DDJK05]. High energy electrons within the spectrum cause higher space charge potentials. The actual deviation from the ideal one-temperature Maxwellian case depends on the number of high energy electrons compared to the number of low energy, or thermal electrons. The ion flow as well as the plasma potential in the bulk is still determined by the thermalised, low temperature electrons [DDJK05, GMS95], at least for reasonable low high energy electron densities [DDJK06]. As the electron current through the wall, especially at a negative biased wall, is governed by the high temperature electrons, the floating potential at the wall is also determined by these hot electrons [DDJK05, GMS95]. An additional drop of the near wall potential $\Delta\Phi$ further accelerates the ions to compensate the loss of fast electrons. For a floating wall this extra potential drop can be calculated with the high energy electron current, I_{e^*} , compared to the ion current [DDJK05, DDJK06]:

$$|\Delta\Phi| = T_e \ln \left(\frac{I_i}{I_i - I_{e^*}} \right). \quad (5.75)$$

Here T_e denotes the thermal, Maxwellian electron temperature. Using the distribution function showed in figure 5.7, the fraction of secondary electrons in the WGTS plasma with energies above the thermal distribution is clearly below 1%, the influence of the high energetic primary β -electrons is discussed below. The ion flux to the rear wall is assumed to be undisturbed by the high energy electrons. Thus, it can be taken from table 5.1 to be about $1 \times 10^{-6} \text{ A m}^{-1}$. To calculate the flux of the high energy secondary electrons, only the initial electron production rate needs to be considered, as the process of recombination can be neglected for such high energies. An initial electron production rate, without recombination, of about $6 \times 10^{-6} \text{ A m}^{-1}$ causes a high energy electron production rate smaller than $0.01 \cdot 6 \times 10^{-6} \text{ A m}^{-1} = 6 \times 10^{-8} \text{ A m}^{-1}$. This rate corresponds to the

high energy electron flux at the rear wall. Plugging these values into equation (5.75), an additional potential shift of $0.06T_e$ induced by fast secondary electrons is obtained. This shift is smaller than 1 meV and would therefore be negligible. However, when the ion flux to the rear wall decreases, while the high energy electron flux remains, the shift in potential increases. This can be caused by a higher recombination rate that can not be excluded, since the recombination rate coefficient has large uncertainties. For a ten times higher recombination rate coefficient, corresponding fluxes are calculated above, $\Delta\Phi$ becomes $0.16T_e$ which is still below 1 meV. For changed boundary potentials, the ion flux through the rear wall can also decrease. This could lead to potential shifts of several times the electron temperature. Quite large space charge potentials forming at the wall in the case of I_{e*} becoming comparable or even larger than I_i are also stated in [DDJK04]. This is most likely not the case for KATRIN, unless the recombination rate is orders of magnitude higher than assumed, which would drastically reduce the ion density. Furthermore, as described in [DDJK06], the electron energy distribution may become non-local, which could further increase the potential drop in the sheath. In the region next to the rear wall such inhomogeneities may arise, since electrons produced there are not able to thermalise before they reach the rear wall. Though they are unlikely, the formation of space charge potentials of the order of several times the electron energy can not be excluded for the WGTS plasma. To be able to compensate for the eventually large positive space charge building up in the WGTS, additional electrons can be emitted at the rear wall. This is further discussed in section 5.3.5.

Primary β -electrons

The influence of the β -electrons that can leave the WGTS fast is tested, by adding an additional ion source term from equation (5.64). Thus, just the positive net charge of about 6% that is created by these fast electrons is included in the simulation. The actual fast electrons do not need to be modelled, since they flow out of the WGTS nearly undisturbed by the plasma.

The simulated electron and ion density distributions are depicted in figure 5.34a. Quasineutrality holds through the bulk of the plasma. The overall space charge is increased by about 8%. This difference is reflected by the potential distribution to be seen in figure 5.34b. As expected from the considerations above, the influence of the high energy β -electrons on the potential distribution is small³⁴. The longitudinal homogeneity is hardly affected. Since the effect of net space charge production by high energy β -electrons is small, it is neglected in the following calculations.

5.3.3.3. Geometry length

The geometry of the described plasma model only reflects the main WGTS beam tube. The longitudinal distance between the rear wall and the dipoles in the DPS2-F in the KATRIN set-up, corresponding to the plasma model end boundaries, is roughly 20 m. Limiting the model length to 10 m reduces the number of mesh elements needed to resolve the geometry and thus the degrees of freedom. This simplifies the solution process significantly. Already at the end of the WGTS the gas density is reduced by a factor of 50. Going into the DPS1-F/R, the density is reduced even further, about a factor of 2000 at the entrance to the DPS2-F, as discussed in section 4.2. This means a significant increase in mobility while the charged particle density drops further. The reduced gas density also influences the mean free path λ_e of the electrons. Assuming only elastic collisions, which have the largest cross section of about $1 \times 10^{-19} \text{ m}^{-2}$ in the meV electron energy region as discussed in section 5.2, and a central gas density of $8 \times 10^{20} \text{ m}^{-3}$, the mean free path

³⁴Using (5.75) a potential difference of the order of $0.3T_e$ is expected which matches the simulated differences quite well.

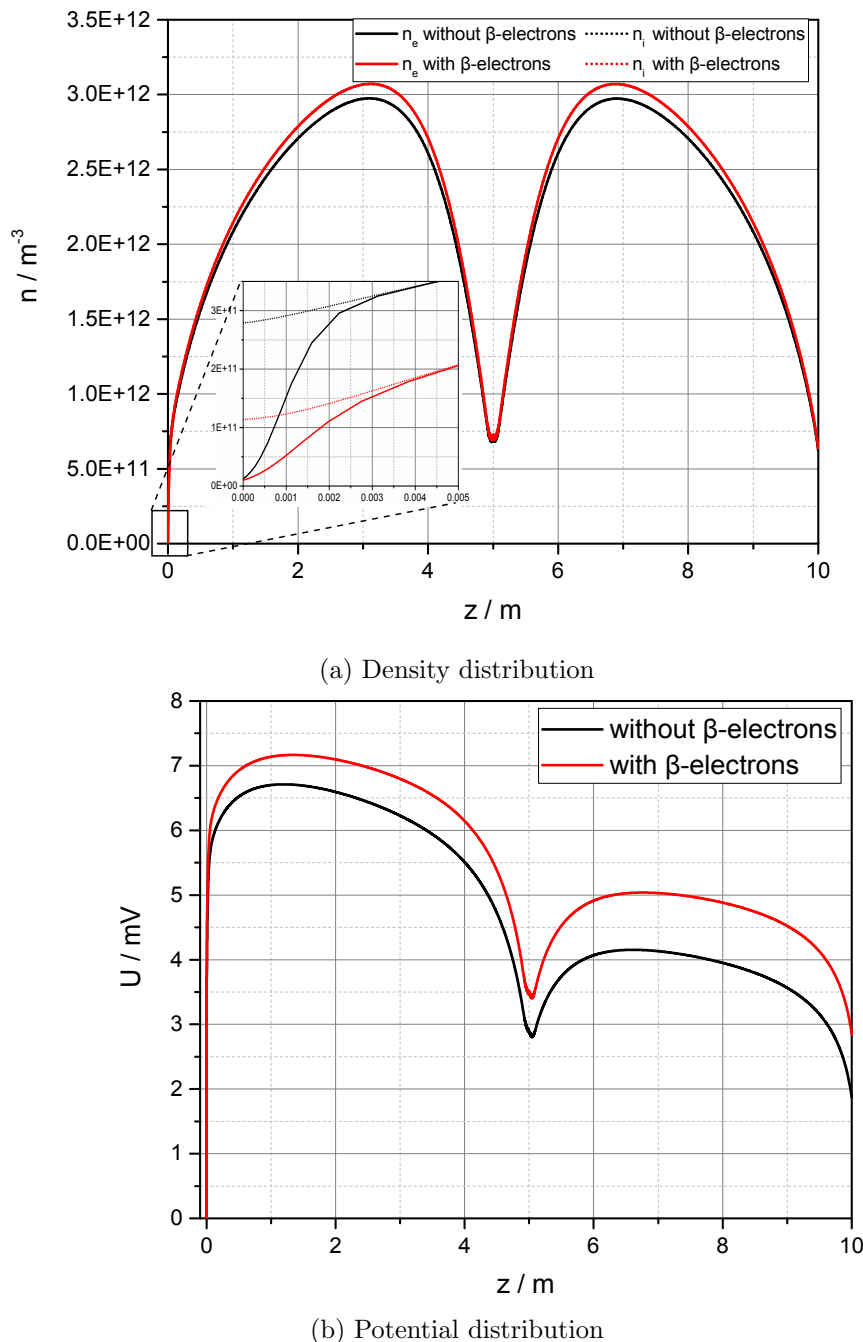


Figure 5.34.: **Effect of β -electron induced space charge.** Longitudinal distributions at $x = 0$ m. Compared are the solutions with (red) and without (black) positive net space charge from primary β -electrons.

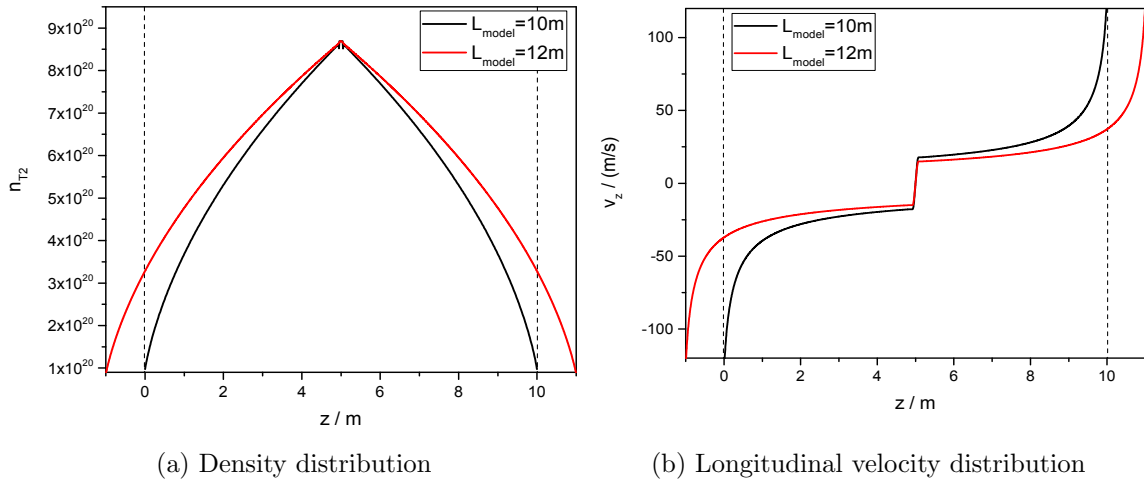


Figure 5.35.: **Longitudinal background gas profiles for $L_{\text{WGTS}} = 12\text{ m}$ and $L_{\text{WGTS}} = 10\text{ m}$.** The values within the central 10 m differ which has to be considered when comparing the results for the corresponding plasma models.

in terms of the density reduction factor $x_d = n_{T_2}(z)/n_{T_2}(0)$ becomes

$$\lambda(z) \approx \left(n_{T_2}(z) \sigma_{\text{el}} \right)^{-1} \propto 1\text{ cm}/x_d. \quad (5.76)$$

At the end of the WGTS the mean free path of the electrons is already about 0.5 m. For the ions the mean free path is lower³⁵. However, at the end of the WGTS beam tube it is enhanced to several centimetres and linearly increases with density reduction, see chapter 4. Furthermore the charged particle densities get lower, as the production rate goes down with the gas density. This reduces the effect of recombination. As the neutral-charged particle interaction as well as the ion-electron recombination is significantly reduced, particles can be expected to stream nearly undisturbed, apart from the intrinsic Coulomb coupling, and the flux reaching the end boundaries should be of the same order as the flux at the ends of the central WGTS beam tube at $z = 0\text{ m}$ and $z = 10\text{ m}$ ³⁶. Therefore, the fluxes are assumed to be comparable for the 10 m model geometry and the central part of the 20 m KATRIN set-up. Since the fluxes leaving the plasma through the different boundaries determine the potential and density distribution also the plasma potentials for both configurations are assumed to be similar. To verify this, the model geometry is increased to 12 m with the injection region at $z = 6\text{ m}$. A background gas model adapted to the increased length is calculated first. The resulting T_2 density and longitudinal velocity distributions are depicted in figure 5.35. The calculated electron density distribution for the 12 m-model at ground potential is depicted in figure 5.36. As expected, the form of the distribution remains unchanged by the modified length. The increased maximal electron density is mainly due to the difference in T_2 column density in both models, see figure 5.35. In the transversal density distribution at the end of the particular model, both models have again a similar slope. The higher electron density at the wall is again caused by the T_2 density. The potential distribution remains similar for both model lengths as can be seen in figure 5.37. The space charge potential offset is almost unchanged by the

³⁵It corresponds to the mean free path of the neutral gas molecules.

³⁶Electrons that are produced at low gas density have significantly higher energies as there are almost no gas molecules for them to thermalise on. The fraction of these electrons is assumed to be low compared to the flux of low energy electrons from the high density parts of the model. The number of primary β electrons is reduced to 1 – 2% of the electrons produced in the main WGTS beam tube as about 98% of the total column density are situated in the central WGTS. Furthermore, the low gas density causes the number of ionising collisions to be significantly reduced.

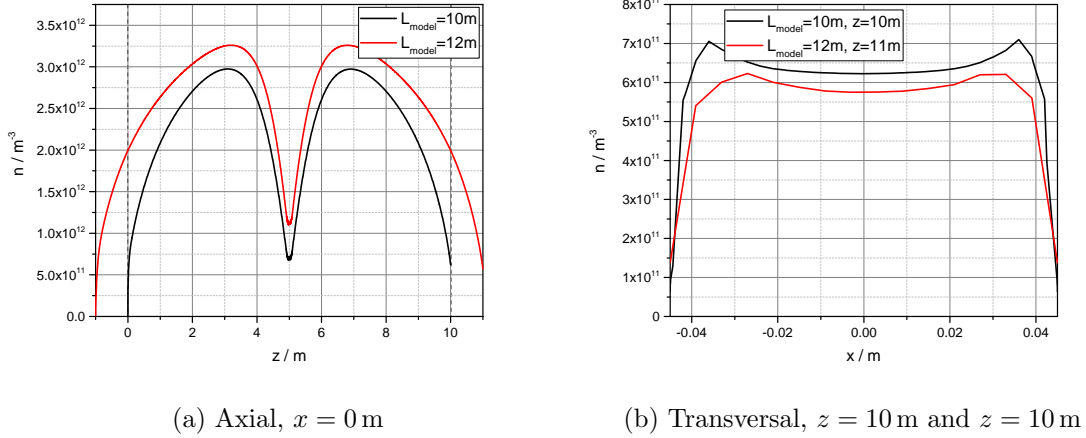


Figure 5.36.: **Electron density distributions for $L_{\text{WGTS}} = 12$ m and $L_{\text{WGTS}} = 10$ m with rear wall at ground potential.** Data for the transversal density distributions are taken from the end of the particular model, at $z = 10$ m and $z = 11$ m (the 12 m model starts at $z = -1$ m), respectively.

length adaptation.

To see if the transversal outflow of ions, that increases significantly for a positive rear wall voltage as discussed above, causes a model length dependent potential difference, a rear wall voltage of 0.1 V is used in the calculation. The resulting longitudinal potential distribution is depicted in figure 5.38. The maximal longitudinal potential differences increases from 18 mV for the 10 m-model to 20 mV for the 12 m-model. To prevent the WGTS from charging up, the boundary voltage differences of Δ should be significantly lower than 0.1 V. This is further discussed in section 5.3.4. For relatively small rear wall - tube wall potential differences of the order of 10 mV, the length of the model does not affect the general conclusions for potential and density distribution drawn from the reduced length model and it can be used to describe and examine the WGTS plasma. For larger boundary potential differences, where the longitudinal to transversal ion outflow gets of the order of one and lower, the effect of model length needs to be considered to estimate the longitudinal potential difference. This length effect is even increased for the cylinder-symmetric case.

5.3.3.4. WGTS magnetic field

If the WGTS is operated at a reduced magnetic field of 3 T, the magnetic confinement of the charged particles is affected. Thus, according to equation (5.23), the transversal relative to the longitudinal mobility increases by about 20%. For electrons the transversal motion is still negligible. For ions, however, the increased outgoing radial flux needs to be considered. The transversal ion motion is blocked in the case of positive tube wall potential, $\Delta \ll -\frac{3}{2}k_B T_e$. Here, the solutions will be comparable for both magnetic field values. Thus, only the grounded WGTS case and configurations with positive boundary potential difference Δ need to be considered.

In the case of the WGTS being grounded, there is almost no change in density and potential distribution for the lowered magnetic field compared to the standard value. The differences are smaller than 2%. Only the transversal outgoing ion flux increases from $4.4 \times 10^{-7} \text{ A m}^{-1}$ to $6.6 \times 10^{-7} \text{ A m}^{-1}$. However, the influence is small, as the longitudinal fluxes are still dominant, compare table 5.1.

For the configuration with $\Delta = 1$ V $\gg \frac{3}{2}k_B T_e$ the transversal ion flux is already saturated and cannot increase anymore. Therefore, the solution is not affected by a lowered mag-

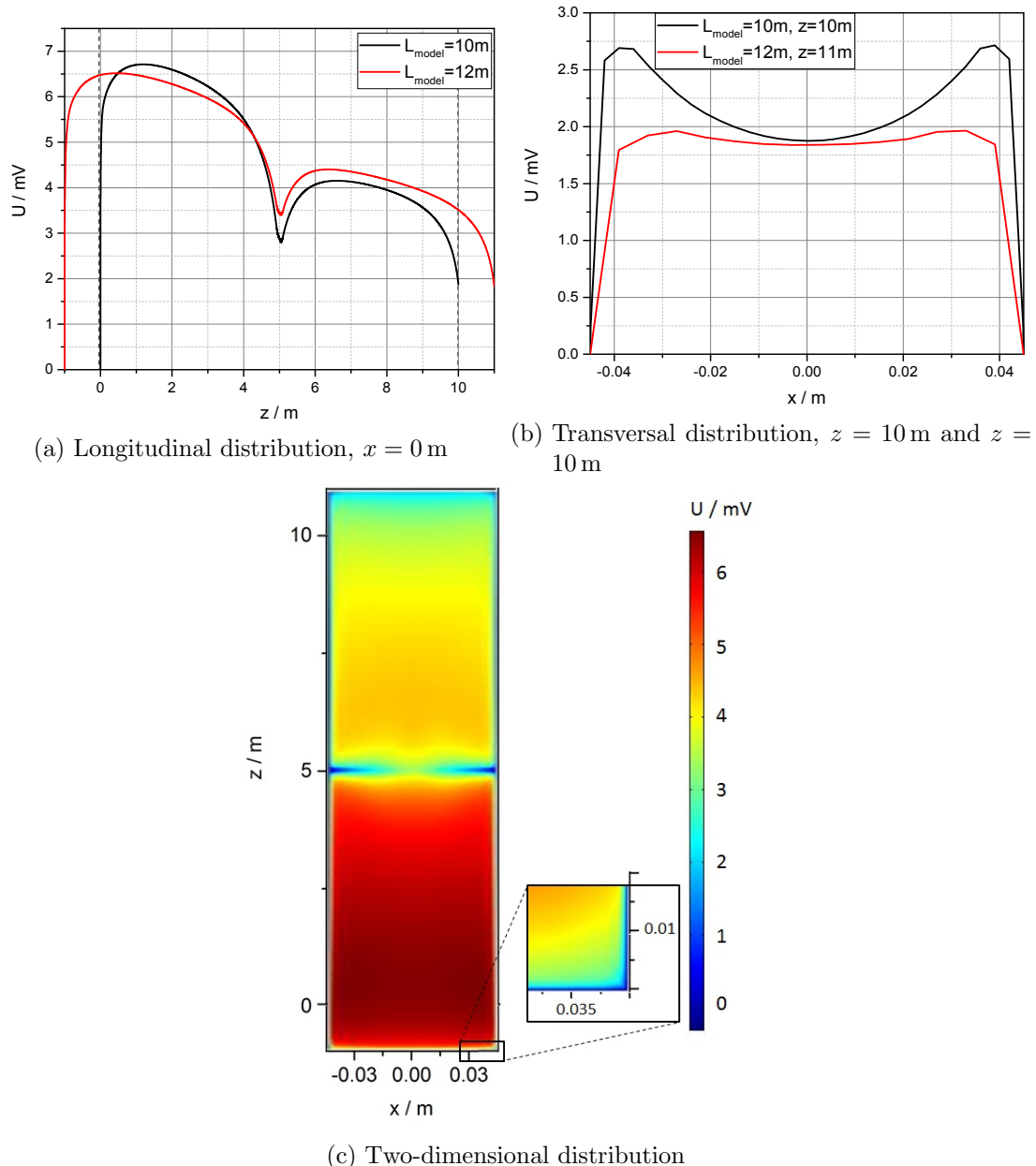


Figure 5.37.: **Potential distributions for $L_{\text{WGTS}} = 12\text{ m}$ and $L_{\text{WGTS}} = 10\text{ m}$ with rear wall at ground potential.** Data for the transversal potential distributions are taken from the end of the particular model, at $z = 10\text{ m}$ and $z = 11\text{ m}$, respectively.

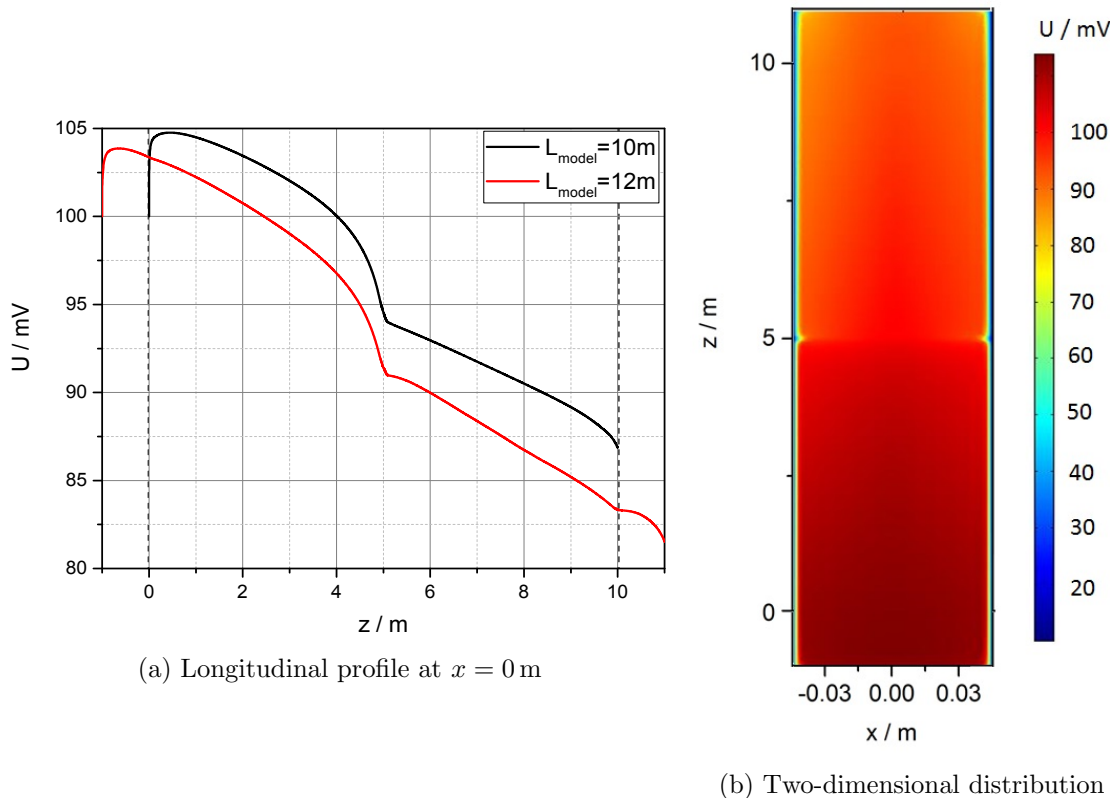


Figure 5.38.: **Plasma potential distributions for $L_{\text{WGTS}} = 12 \text{ m}$ and $L_{\text{WGTS}} = 10 \text{ m}$ with $\Delta = 0.1 \text{ V}$.**

netic field and the potential and density distributions do again not change significantly. Compared with the standard magnetic field, the differences are about 1%.

If $\Delta = 0.1 \text{ V}$, the outgoing fluxes are not saturated³⁷ as already discussed in a prior model configuration. In this case, the changed transverse ion mobility has a visible effect on the plasma potential, see figure 5.39a. As depicted in figure 5.39b the outgoing ion flux at the transversal wall at $x = -0.045 \text{ m}$, or equivalently at $x = 0.045 \text{ m}$, increases by 26% for the decreased magnetic field. The longitudinal potential difference decreases by 6% to 17 mV as the overall space charge is reduced from $6.68 \times 10^{-9} \text{ C m}^{-1}$ to $6.1 \times 10^{-9} \text{ C m}^{-1}$ due to the larger transversal ion current. However, in case of an overall negative space charge (Δ is negative or above ion saturation voltage) the potential difference will increase.

If the WGTS magnetic field is reduced to 3 T, the influence on the contained plasma is small for reasonably low values of $|\Delta|$ below or equal 0.1 V. Potential and density distribution change by less than 10%. In case of an overall positive space charge the magnetic field reduction even has the positive effect of slightly reducing the longitudinal potential inhomogeneity.

Summary of tested effects

The large ratio of longitudinal electron mobility to transversal ion mobility combined with the large length to radius ratio of the WGTS can cause numerical instabilities while solving the drift-diffusion equations as seen in [Glü02]. However, the solution of the WGTS plasma problem obtained with the presented three-particle fluid model is quite robust. It is stable under the variation of the plasma determining parameters and boundary conditions. This stability makes it possible to test the impact which different conditions have on the

³⁷This holds at least for the two-dimensional planar model. For the cylindrical model, this value will be reached earlier, see equation (5.73), at about 0.05 V.

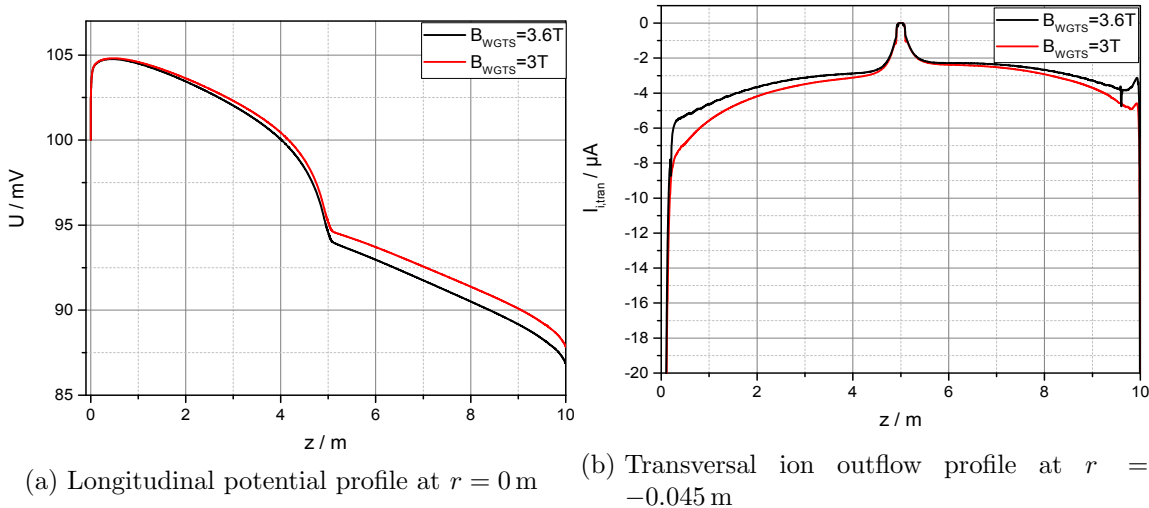


Figure 5.39.: Distribution of longitudinal potential and transversally outgoing ion flux, $I_{i,\text{tran}}(z)$ with nominal and reduced magnetic field for a rear wall bias off 0.1 V.

Table 5.2.: Summary of the tested plasma parameters and conditions and their impact on the potential distribution in the WGTS compared to the two-dimensional plasma model using standard operation parameters. Here \uparrow denotes an increase, \downarrow a decrease, \nearrow a weak increase and \approx comparable values.

Tested parameter	U_{abs}	$ \Delta U $	Implications for KATRIN	Remarks
Column density ($\rho d_{T_2} = 0.5\rho d_0$) $\rho d_{\text{gas}} = 2\rho d_{T_2}$ $\rho d_{\text{gas}} = \rho d_{T_2}$	\approx \uparrow	\approx \downarrow	Plasma in first tritium measurements	Model unsuitable for even lower densities $n_e \approx 0.7n_e(\rho d_0)$ $n_e \approx 0.6n_e(\rho d_0)$
Electron energy Absolute value (\uparrow)	\uparrow	\nearrow	Higher E_e : krypton mode, non-thermalised electrons	Plasma potential of the order of floating potential (for low values of Δ)
Distribution (high energy tail)	\uparrow	\uparrow	High energy tail in $f(E_e)$	Fluid model unsuitable.
Recombination coef. (\uparrow)	\approx	\downarrow	Influenced by E_e and $f(E_e)$	$n_e \approx 1/\sqrt{k_{\text{rec}}}$, large uncertainty on k_{rec}
Tube length (\uparrow)			Length of plasma column longer than 10 m	
Grounded case	\approx	\approx		Effect low as $j_{i,\perp}$ low
Positive U_{rear}	\approx	\nearrow		$j_{i,\perp}$ large
B-Field (3 T)	\approx	\approx		Tested for $\Delta = 0.1\text{ V}$, effect from grounded tube even smaller
Cylinder-symmetry Grounded case	\downarrow	\nearrow	More realistic model	$j_{i,\perp}/j_{i,\parallel}$ and radial inhomogeneity increase
Positive U_{rear}	\uparrow	\uparrow		$j_{i,\perp}$ low $j_{i,\perp}$ large, 21% increase in integral radial ion outflow

plasma and its potential distribution as presented in the course of this section. The influences on plasma homogeneity and overall space charge potential are summarised in table 5.2. Most tested variables have a small influence on the WGTS plasma behaviour. Connected uncertainties in WGTS plasma potential homogeneity are of the order of the electron temperature, excluding the effect from electron energy distribution. The electron energy has the largest impact of the tested parameters. It influences mobilities, cross sections and fluxes. Large uncertainties are connected to the electron energy distribution function since in the presented fluid model only Maxwell distributed electrons can be used. An analytic estimation of the influence of the high energy tail in the energy spectrum produces only small shifts in the overall potential distribution. This estimation has large uncertainties with regard to the ratio of ion flux and low electron energy flux to high energy electron flux. However, for the plasma potential to be increased by more than the electron temperature, the flux of high energy electrons needs to be comparable to the ion flux. This is most unlikely to occur in KATRIN, since this would mean a recombination rate coefficient orders of magnitude higher than assumed or unreasonably large longitudinal plasma inhomogeneities.

5.3.4. Impact of boundary bias and work function on WGTS potential

In this section an optimised rear wall potential is examined, aiming for a homogeneous plasma potential. Furthermore, the impact of work function differences and their distributions at the confining walls on the plasma potential homogeneity is tested.

The maximal longitudinal difference of the optimised plasma potential distribution has to be below the KATRIN limit of 10 meV [AAB⁰⁵]. In radial direction, requirements can be relaxed, since radial differences can be monitored by the focal plane detector as long as they are on length scales larger than the corresponding detector pixel size. As the magnetic field is different at detector, rear wall and WGTS while the magnetic flux³⁸ is conserved, the mapped pixel sizes vary for the different components. For the WGTS with a magnetic field of 3.6 T the total mapped cross-sectional area is about 53 cm². With 148 detector pixels equal in area, a WGTS cross section of about 36 mm² can be resolved by one detector pixel. Averaging for convenience over the twelve concentric rings gives an average radial distance of about 2.9 mm that can be resolved by the detector³⁹. The “bulls-eye” area in the middle of the detector wafer with a projected radius of about 6.8 mm in the WGTS needs to be considered separately. Thus, the radial plasma potential difference within the resolution limit of 2.9 mm has to be below 10 mV. Within the outer 4 mm of the WGTS cross section even this requirement can be relaxed since this region is outside of the mapped inner flux tube. Besides the potential homogeneity, the surface potential of the tube wall has to be prevented from penetrating into the plasma. The corresponding WGTS steel surface has large work function inhomogeneities that can be significantly larger than 10 mV, as described in section 5.2. Thus, the WGTS plasma would not meet the KATRIN requirements if the plasma potential is determined by the tube wall surface potential and wall potential differences can penetrate into the plasma.

5.3.4.1. Rear wall bias at constant surface potential

As seen in the simulation results above, the WGTS plasma potential distribution is dominated by space charges that cause an additional offset of the plasma potential compared to the general potential determining wall surface potential. The formation of large space charges has to be avoided since they can lead to large inhomogeneities in the potential distribution. Negative space charges are worse than positive ones since the former cannot be compensated by electron injection. Negative space charges can either be caused by

³⁸transported magnetic flux $\Phi = 191 \text{ T cm}^2$

³⁹Here the four pixels in the centre of the detector are not considered.

Table 5.3.: Differences in potential for different rear wall voltages assuming constant surface potentials. Given are the maximal longitudinal difference ΔU_z , the maximal total radial difference ΔU_r , the maximal radial pixel difference outside of the last 4 mm ΔU_r^* and the maximal radial difference in the last 4 mm $\Delta U_{r,s}^*$. The potential distributions are calculated for two electron energies E_e .

E_e / meV	U_{rear} / mV	ΔU_z / mV	ΔU_r mV	ΔU_r^* mV	$\Delta U_{r,s}^*$ mV
2	-10	9.2	15	2.5	3
	-5	7.2	9	1.5	4
	-2	5.4	5.7	0.6	5.7
	0	5.2	7.3	0.5	7.3
	2	4.9	8.9	0.5	8.9
	5	5.5	11.7	0.8	11.7
	10	6.2	16.7	1.2	17.3
3.9	-10	9.3	15.6	2.5	10.7
	-6	7.2	12.2	1.7	12.2
	-3	7.6	13.8	1.1	13.8
	0	7.7	15.7	0.9	15.5
	3	8.1	17.5	1	17.5
	10	9	24.5	1.5	23

large axial ion outflow at negative rear wall voltage, with $\Delta < \Delta_c$, where the tube wall penetrates into the plasma potential. Or, a positive rear wall voltage, larger than about 0.05 V to 0.07 V, causes saturation currents and a corresponding net loss of ions. This generates large differences in the longitudinal potential distribution and can even lead to the break down of quasineutrality as shown for the two-dimensional planar plasma with $\Delta = 1$ V. For the grounded cylindrical model, a small positive space charge potential builds up with a maximal longitudinal difference of about 5.2 mV. The maximal radial potential difference is about 7.3 mV in the sheath region within the outer 4 mm. Outside of the sheath region, the maximal radial pixel difference is reduced to about 0.5 mV. This plasma potential does already match the KATRIN requirements. However, the average energy of electrons thermalised at 30 K is about 3.9 meV and therefore a bit higher than the electron temperature the model is calculated for (2 meV). As shown above, this elevated electron temperature causes an increased space charge potential of 12.6 mV at $r = 0$ m. The longitudinal potential inhomogeneity increases to 7.7 mV at maximum. Hence, it is tested, if a small voltage bias, above the critical voltage difference Δ_c , can further reduce space charges and longitudinal potential differences. Considering the critical potential Δ_c , see equation (5.43), of about -20 meV and -39 mV, for an average electron energy of 2 meV and 3.9 meV, rear wall bias voltages of between -10 mV to 10 mV are tested. The resulting two-dimensional potential distributions for a realistic average electron energy of 3.9 meV are plotted in figure 5.40. It is clearly visible that, as expected, with increasing rear wall voltage the influence of the radial tube wall potential diminishes. On the other hand, the space charge induced voltage offset increases. The maximal longitudinal and radial potential differences are summarised in table 5.3. All tested rear wall bias voltages meet the KATRIN requirement on potential homogeneity. A potential difference of the order of the electron kinetic energy can even minimise the longitudinal potential difference. Indeed, the work function difference between the steel tube and the gold coated rear wall is not known with a precision of 10 mV. Thus, the actual optimised rear wall voltage needs to be tested experimentally. This can be done using the krypton mode further described in section 5.4.

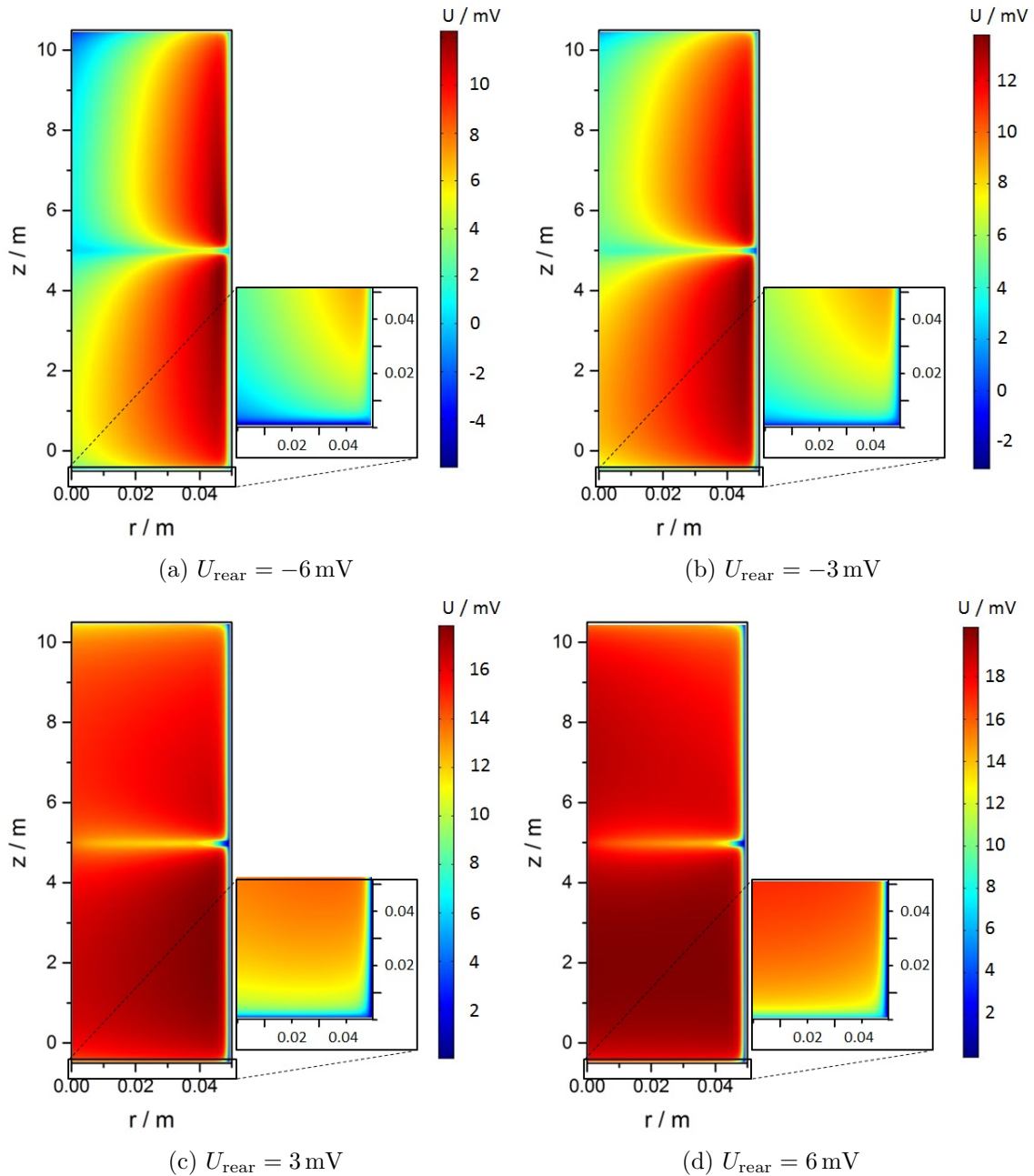


Figure 5.40.: Two-dimensional plasma potential distributions for the axisymmetric model from different rear wall voltages and an average electron energy of 3.9 meV.

5.3.4.2. Work function differences of tube and rear wall

Up to now, all surface potentials were assumed to be constant. In a realistic scenario, though, one has to take into account large work function differences between individual patches as discussed in section 5.2. Therefore, the impact of such surface inhomogeneities on the plasma potential needs to be investigated. Rear wall and tube wall potential differences are analysed separately.

Rear wall inhomogeneities

The tube wall is assumed to be grounded for the following tests of rear wall inhomogeneities. At first spatially large rear wall surface potential differences are investigated to see, if they can penetrate into the plasma. Then smaller surface patches at different potentials are implemented.

Bisected rear wall surface potential

Half of the rear wall is assumed to have a different surface potential. The absolute value of the non-zero surface potential of 50 mV is chosen above the absolute value of the critical potential $|\Delta_C|$ of about 20 mV, but below the limiting value of 100 mV where the currents start to saturate as described above. As the model is axisymmetric, there are two possibilities to arrange the potential differences. Testing for negative and positive shifts, the following configurations are implemented:

- i) $|r| \leq 0.0225 \text{ m} \rightarrow U_{\text{rear}}(r) = 0 \text{ V}$
 $|r| > 0.0225 \text{ m} \rightarrow U_{\text{rear}}(r) = 0.05 \text{ V}$
- ii) $|r| \leq 0.0225 \text{ m} \rightarrow U_{\text{rear}}(r) = 0.05 \text{ V}$
 $|r| > 0.0225 \text{ m} \rightarrow U_{\text{rear}}(r) = 0 \text{ V}$
- iii) $|r| \leq 0.0225 \text{ m} \rightarrow U_{\text{rear}}(r) = 0 \text{ V}$
 $|r| > 0.0225 \text{ m} \rightarrow U_{\text{rear}}(r) = -0.05 \text{ V}$
- iv) $|r| \leq 0.0225 \text{ m} \rightarrow U_{\text{rear}}(r) = -0.05 \text{ V}$
 $|r| > 0.0225 \text{ m} \rightarrow U_{\text{rear}}(r) = 0 \text{ V}.$

The resulting longitudinal potential distribution at different radial positions for the positive rear wall offset are plotted in figure 5.41. For the negative rear wall offset results are shown in figure 5.42. It is clearly visible that the plasma potential depends not only on the rear wall voltage differences but also on their relative arrangement, especially when looking at the two-dimensional distributions shown in figures 5.43 and 5.44. Only in the configuration with a positive rear wall difference and a rear wall potential equal to the tube wall potential in the region next to the tube (configuration ii) the rear wall potential is “transported” through the tube. This can be seen in figure 5.41b and figure 5.43b. When the surface potential arrangement is changed, the plasma potential distribution also changes although the averaged rear wall surface potential remains at the same value. In this case (configuration i) the plasma distribution is comparable to the case of a homogeneous rear wall at 0.05 V. This is depicted in figure 5.41a and figure 5.43a.

For negative potential differences of -0.05 V the plasma behaviour changes. For both configurations (iii and iv) the more positive part of the rear wall determines the potential (for a beam tube wall that is at a potential of 0 V).

The variation of the plasma potential properties linked to the actual rear wall surface

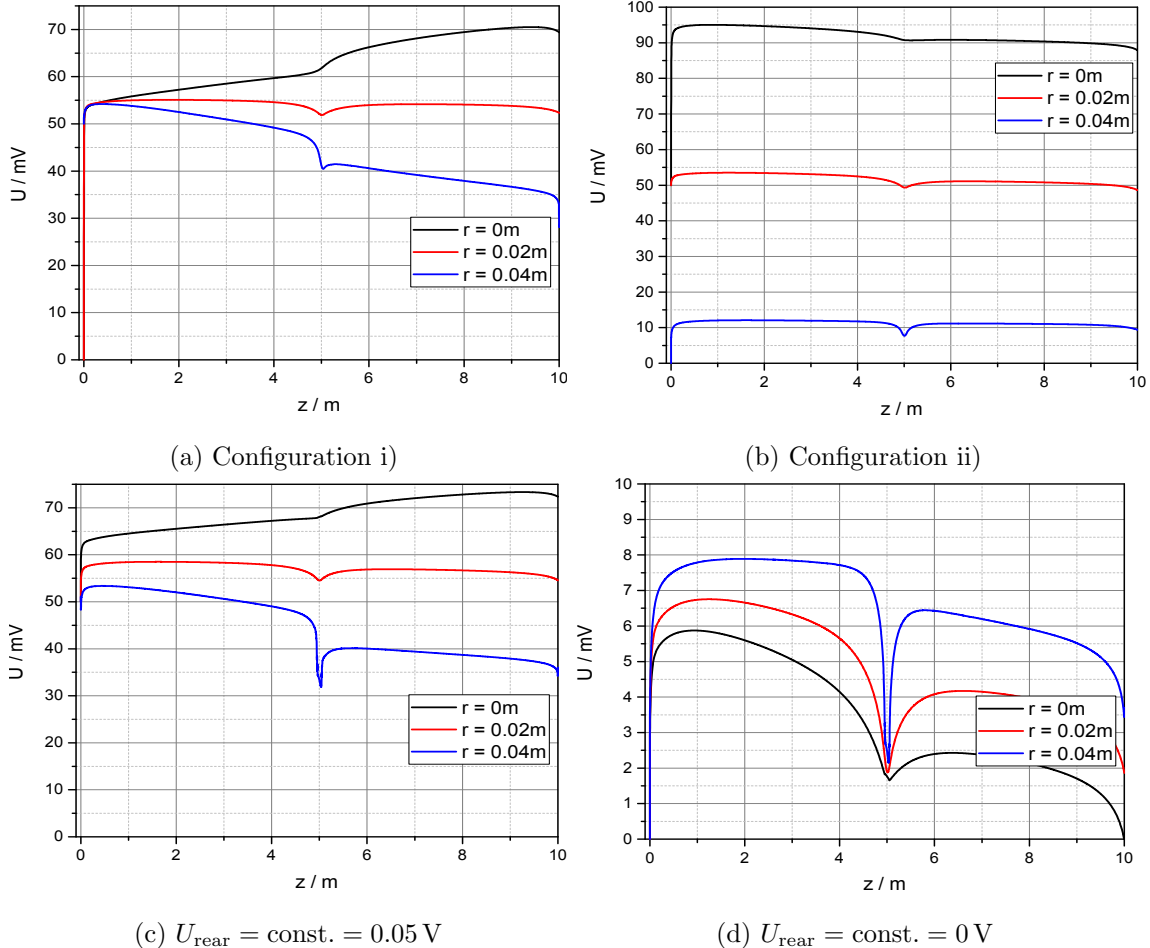


Figure 5.41.: Longitudinal plasma potentials for configuration i) and ii) (see text), plotted at $r = 0 \text{ m}$, $r = 0.02 \text{ m}$ and $r = 0.04 \text{ m}$. Corresponding distributions for homogeneous rear wall surface potential at 0 V and 0.05 V are given for comparison.

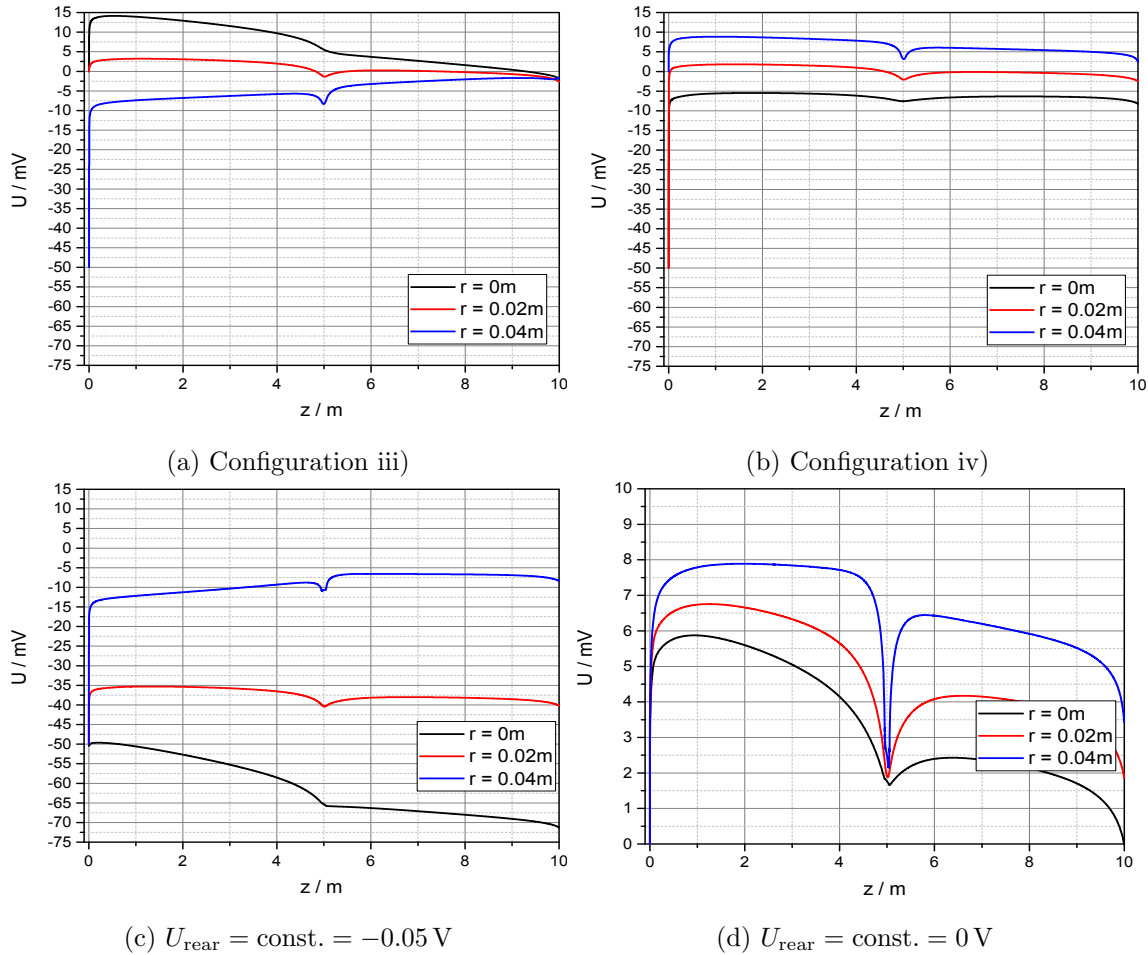


Figure 5.42.: **Longitudinal plasma potential distributions for the bisected rear wall with $U_{\text{rear,iii}} = -0.05 \text{ V}$ and $U_{\text{rear,iv}} = 0 \text{ V}$ at $r = 0 \text{ m}$, $r = 0.02 \text{ m}$ and $r = 0.04 \text{ m}$.** Corresponding distributions for homogeneous rear wall surface potential at 0 V and -0.05 V are given for comparison.

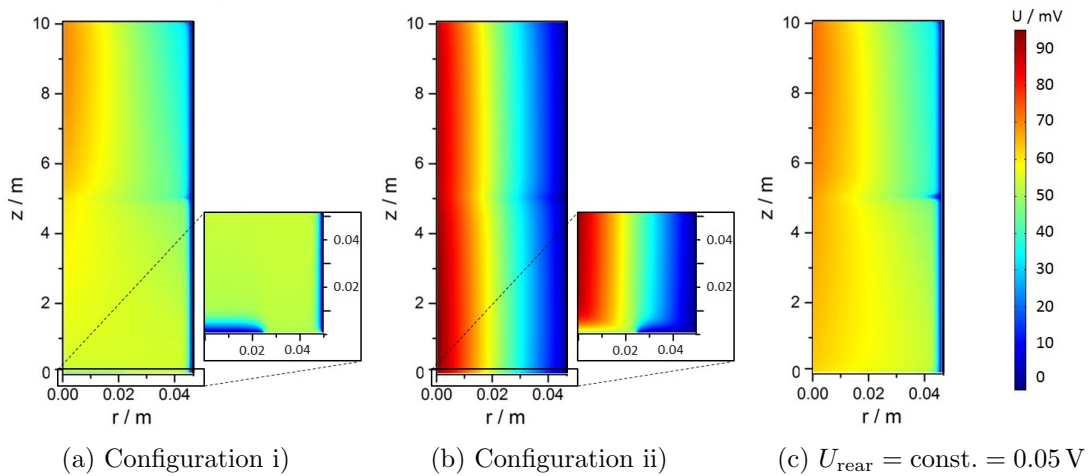


Figure 5.43.: **Two dimensional plasma potential distributions for the bisected rear wall with $U_{\text{rear,i}} = 0.05 \text{ V}$ and $U_{\text{rear,ii}} = 0 \text{ V}$.** Corresponding distributions for homogeneous rear wall surface potential at 0.05 V is given for comparison.

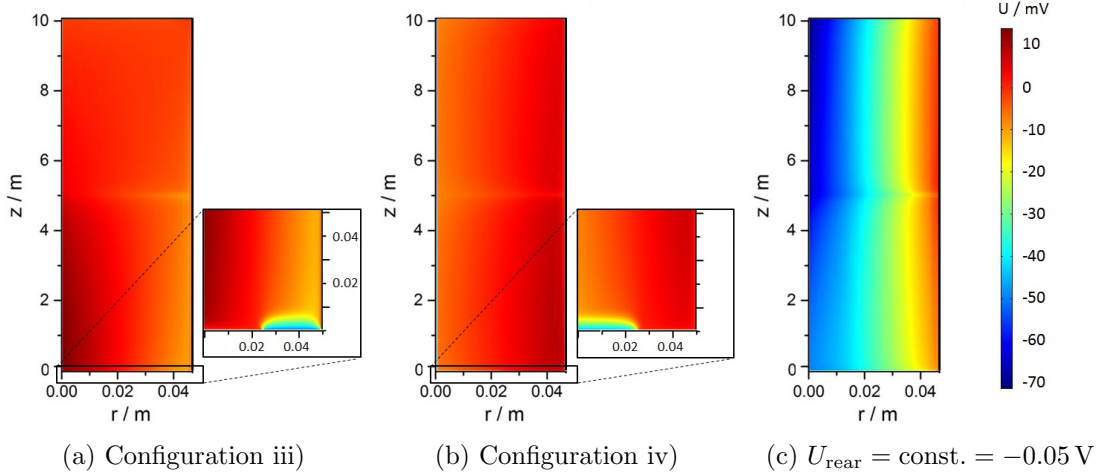


Figure 5.44.: **Two dimensional plasma potential distributions for the bisected rear wall with $U_{\text{rear,iii}} = -0.05 \text{ V}$ and $U_{\text{rear,iv}} = 0 \text{ V}$.** Corresponding distributions for homogeneous rear wall surface potential at -0.05 V is given for comparison.

potential configuration can be explained by looking at the radial ion currents. Their longitudinal distribution at $r = 0.025 \text{ m}$, where the rear wall surface potential changes, are depicted in figure 5.45a for positive rear wall surface potential differences and in figure 5.45b for negative surface potential differences. For a positive potential difference (configuration i and ii) as well as for the rear wall at constant positive potential, the ion current densities at $r = 0.025 \text{ m}$ are positive – the ions move in the direction of the tube wall. The similarity in plasma potential for the configuration i) and the constant rear wall potential of 0.05 V is also reflected by the similar radial ion current densities – they are smaller than the current densities in longitudinal direction at the rear wall. Thus, they do not significantly influence the radial distribution of electron fluxes. For configuration ii) the radial ion current from the radial centre to the tube wall is large since the ions are accelerated by a radial electric field throughout the whole length of the WGTS. The boundary potential difference is negative and thus does not block the ion motion. Therefore large space charge potentials can only form in the centre, around $r = 0 \text{ m}$ where the radial ion current component is zero due to the symmetry. For a negative rear wall difference (configuration iii and iv), the potential differences are not able to penetrate into the plasma independent of the actual arrangement. The potential profiles of these two configurations are almost mirror images of each other with axis of reflection at $r = 0.025 \text{ m}$. The ion current density distribution in radial direction at $r = 0.025 \text{ m}$, depicted in figure 5.45b, reflects the mirrored plasma properties. Although the surface distribution does not penetrate into the bulk of the plasma, the plasma radial electric field and the actual potential distribution do depend on the actual rear wall surface potential. For constant negative rear wall potential the radial ion current in wall direction is blocked by the relative positive wall potential. The flux into the radial centre increases significantly compared to the prior configurations. This reflects the relatively large negative electric field that causes large difference in the radial plasma potential which deviates from the prior bisected rear wall configurations.

What can be learned from the presented examples is that the rear wall voltage does in general not determine the plasma along the axis with the corresponding radius, except for configurations like in ii). Dependent on the actual configuration, an averaged potential can build up in the bulk that shows only space charge induced radial differences along the beam tube axis.

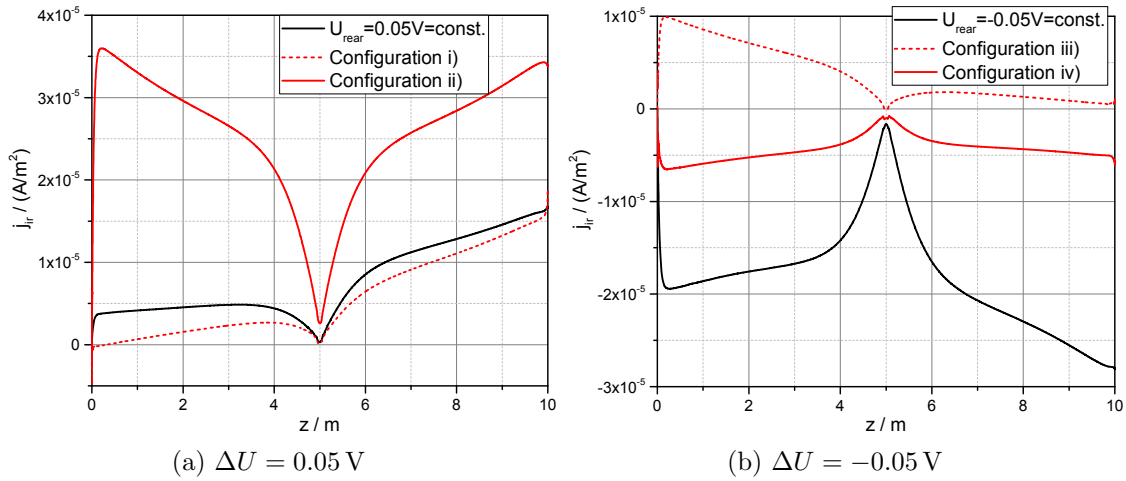


Figure 5.45.: **Longitudinal distribution of radial ion current densities for bisected rear wall at surface potential transition ($r = 0.025$ m).** Besides the configurations i)-iv) given above, current densities for homogeneous rear wall surface potential at 0.05 V and -0.05 V are given for comparison.

Patch potentials at the rear wall

In the following it is investigated how smaller patches influence the plasma potential. At first, a still large overall patch area of one third of the rear wall surface is tested (single patch width of the order of two times the averaged imaged detector pixel size of 2.9 mm). In a second step, the number of patches and patch area is reduced.

The first three 5 mm patches⁴⁰, arranged with a distance of 5 mm, are tested with different potentials and a maximal difference to the rear wall voltage of 40 mV, as deduced for the mainly adsorption induced maximal work function difference in section 5.2. Also patch potentials of 0.02 V, 0.01 V, -0.01, -0.02 V and -0.04 V are analysed.

The calculated potential distributions are depicted in figure 5.46 and figure 5.47. Obviously, the potential patches do not penetrate into the bulk plasma. They get washed out already after about 1 cm, as already seen for most of the configurations of the bisected rear wall surface. For the negative patch potentials the whole potential distribution in longitudinal direction hardly depends on the actual value of the patch potential (compare table 5.4). The same holds for the radial distribution to be seen in figure 5.47. Besides the sheath region next to the rear wall it is almost homogeneous with maximal potential differences of about 6 mV.

In case of positive patch potentials, the absolute potential increases significantly with increased patch voltage. The plasma potential distribution in axial direction is still homogeneous since the maximal longitudinal potential difference is about 7.5 mV for a patch potential of 40 mV (see table 5.4). However, looking at the radial behaviour, the distribution becomes inhomogeneous, as depicted in figure 5.46 and 5.47. This is caused by the increased radial electric field in large parts of the tube. Although the actual patch structures are washed out, the plasma potential for positive patch potentials can not be compared to the result of a constant, averaged rear wall potential – the potential that builds up in the bulk is significantly larger than the space charge potential that builds up assuming a constant rear wall voltage $U_{\text{rear}} \leq U_{\text{patch}}$. Furthermore, the profile of the electron fluxes leaving the plasma through the rear wall is changed. The potential in the tube is influenced more by those surface parts, where the electron flux leaving the plasma is larger, equation compare (5.39). This aspect is further investigated by using smaller patches. This time a single patch is tested. Radial patch widths of 3.5 mm and 1 mm are

⁴⁰Since the model is cylinder-symmetric, the patches are rings with radial width of 5 mm.

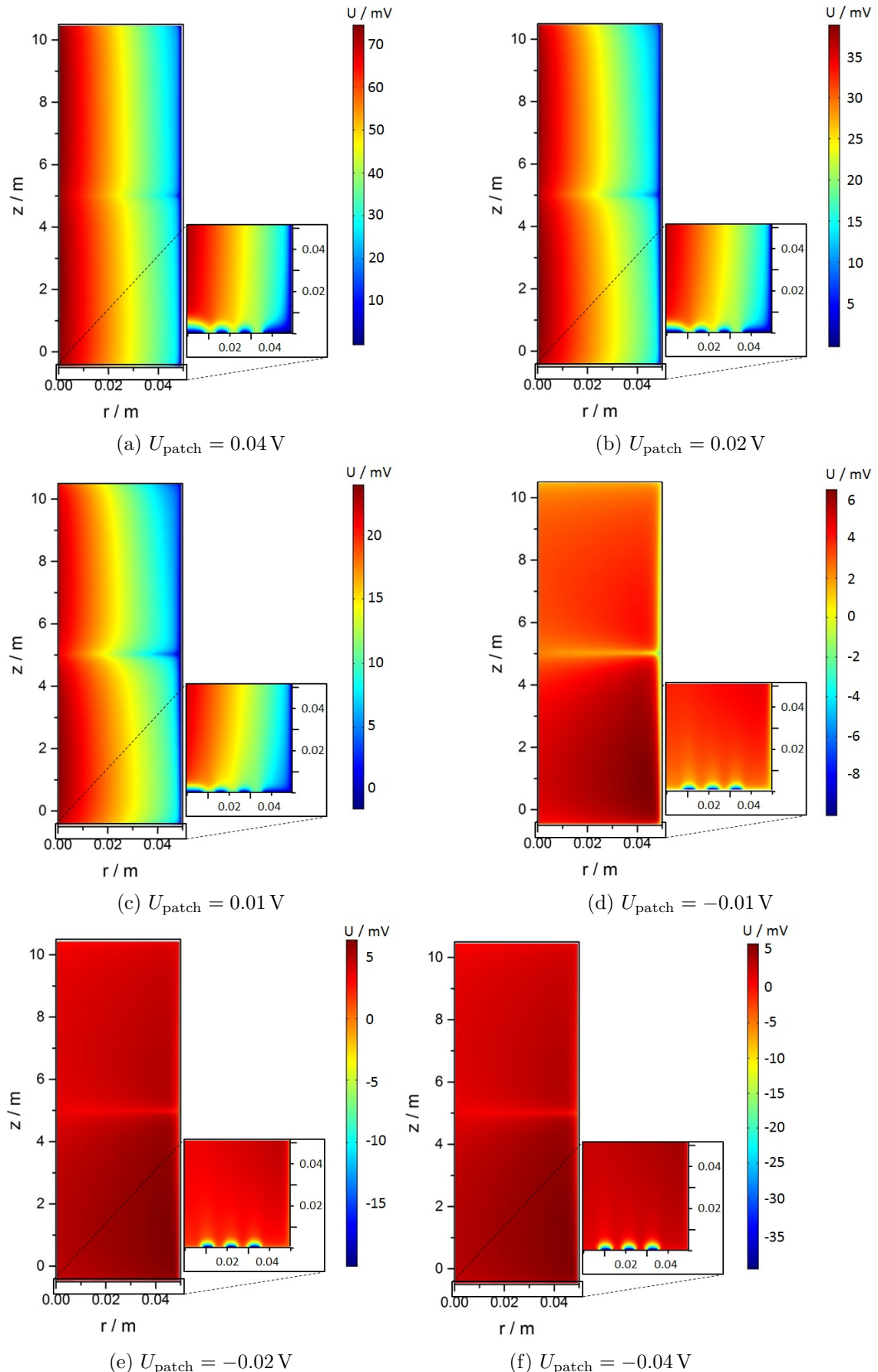


Figure 5.46.: **Two-dimensional plasma potential for $3 \times 5 \text{ mm}$ rear wall patches at different patch voltages.** The main rear wall voltage is set to 0 V in all configurations.

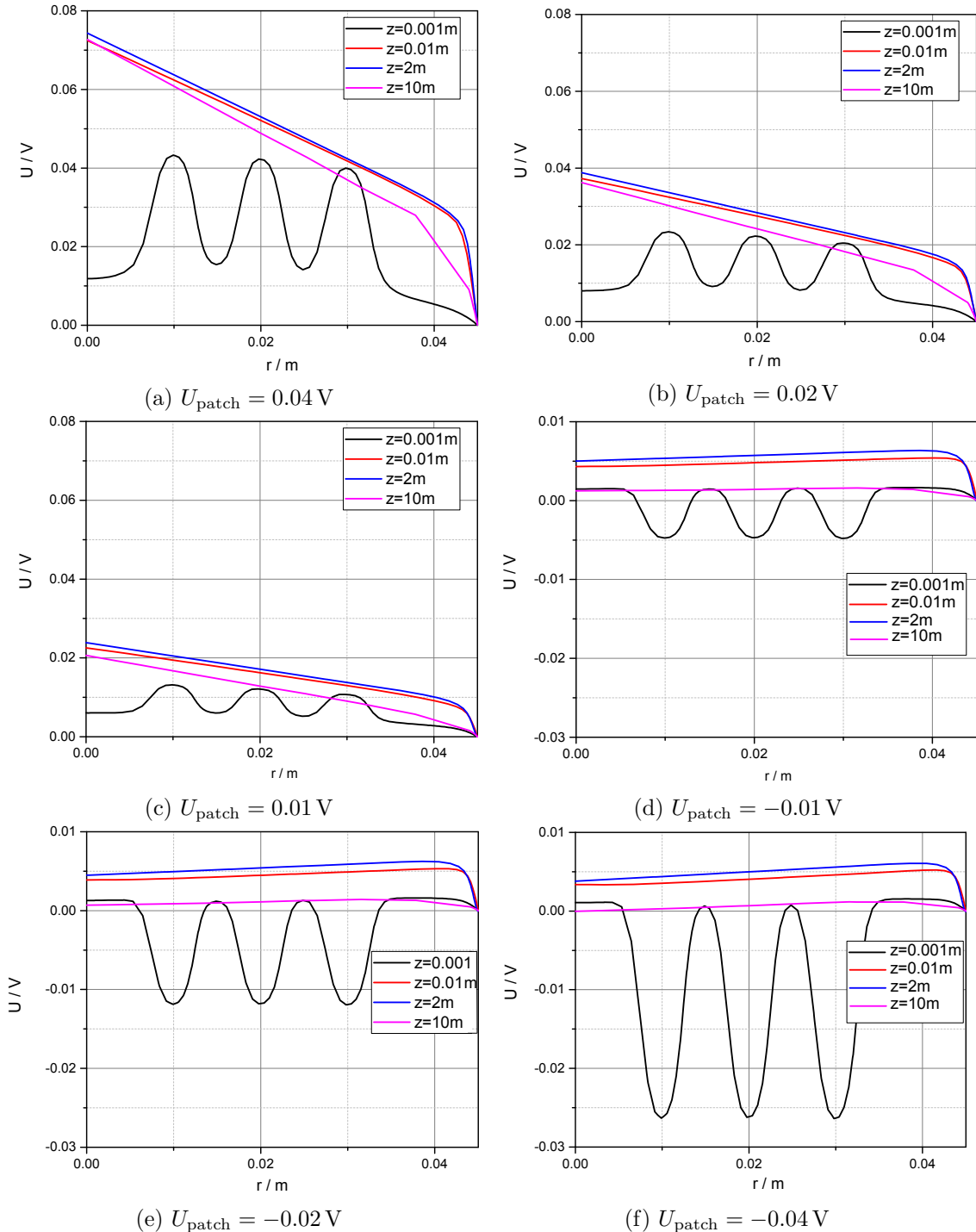


Figure 5.47.: **Radial distribution of plasma potential at different longitudinal positions for 5 mm rear wall patches at different patch voltages.** The main rear wall voltage is set to 0 V in all configurations. Note the changed scales for positive and negative rear wall patches.

Table 5.4.: **Absolute space charge potential value U_{abs} (at $r = 0\text{ m}$) and maximal longitudinal potential differences ΔU_z for different patch potentials.**
 The given maximal potential differences do not include the potential drop in the sheath region. The width of each of the three patches is 5 mm.

$U_{\text{patch}} / \text{mV}$	$U_{\text{abs}} / \text{mV}$	$\Delta U_z / \text{mV}$
-40	4	5.5
-20	4.6	5.5
-10	5.1	5.5
10	24	6
20	39	7
40	74.5	7.5

Table 5.5.: **Absolute space charge potential value U_{abs} (at $r = 0\text{ m}$) and maximal longitudinal potential differences ΔU_z for one rear wall patch of 3.5 mm and 1 mm with different patch potentials.** Averaged plasma potentials U_{abs}^* calculated from (5.77) and averaged rear wall surface potential \bar{U}_{rear} are given for comparison.

Patch width / mm	$U_{\text{patch}} / \text{mV}$	$U_{\text{abs}} / \text{mV}$	$\Delta U_z / \text{mV}$	$U_{\text{abs}}^* / \text{mV}$	$\bar{U}_{\text{rear}} / \text{mV}$
3.5	-10	6.5	5.5	-2	-0.7
3.5	10	16	5	4	0.7
3.5	20	29	6	12.5	1.6
3.5	50	67	7	39	3.9
3.5	100	95	9	82	8.5
1	-20	7	5.5	-2	-0.2
1	-10	7	5.5	-2	-0.1
1	10	7.5	5.7	0	0.1
1	20	11	6.7	4.7	0.2
1	50	18.8	8.5	18.5	0.6

used⁴¹. The results are summarised in table 5.5. The corresponding central longitudinal potential distributions (at $r = 0\text{ m}$) are plotted in figure 5.48a.

Like in the previous case, the rear wall surface potential profile does not penetrate into the bulk plasma. It is washed out already after several centimetres. However, for positive patch potential, the bulk potential that builds up in the plasma is again not determined by the rear wall surface potential averaged over the radius, see table 5.5. Since the patch surface fraction is small, the patch potential hardly influences the average rear wall potential. What is important with regard to the plasma potential is not the potential mean over the rear wall surface area but the average with the electron flux density leaving the plasma at the rear wall, see (5.39). The electron flux density is strongly influenced by the patch potentials as can be seen in figure 5.49a where the increased outflow in the patch region is clearly visible even in the logarithmic plot. Thus, the electron flux density at the rear

⁴¹This is about 7% of the cross sectional WGTS area. A fraction of 7% of the surface area corresponds to the maximal area that will be covered by adsorbed tritium, as discussed in section 5.2.

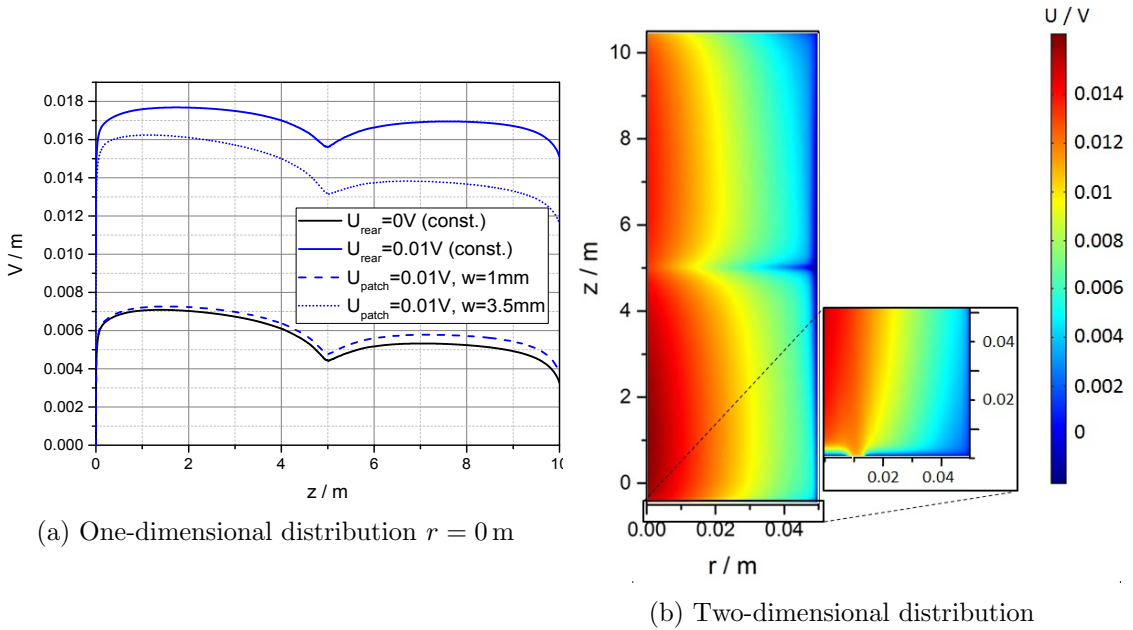


Figure 5.48.: **One- and two-dimensional potential distribution for one rear wall patch.** In the one-dimensional distribution, results for radial patch widths of 3.5 mm and 1 mm are shown. Here potential distributions for constant rear wall potential are included for comparison. The two-dimensional distribution is plotted for a patch width of 3.5 mm. The patch potential is 0.01 V. The rear wall potential U_{rear} is zero.

wall needs to be included into the calculation of the averaged tube potential:

$$U_{\text{abs}}^* \approx \frac{\int_0^R (U_{\text{rear}}(r) - \Delta U_s(r)) \Gamma_{\text{e}\parallel}(r) dr}{\int_0^R \Gamma_{\text{e}\parallel}(r) dr}, \quad (5.77)$$

where ΔU_s denotes the potential drop in the sheath next to the wall. Using the longitudinal electron flux densities at $z = 0 \text{ m}$ and calculating ΔU_s with equation (5.39), the expected absolute potential values U_{abs}^* are given in table 5.5 according to equation (5.77). The flux averaged values are significantly higher than the average rear wall potential. This is comparable to the actual solution of the model. Thus, it becomes clear why the plasma potential is shifted despite the small patch size – even through the patch area is small, a large fraction of the total electron current leaves the plasma. However, this approximation is derived using equation (5.39), where a homogeneous, negative surface potential⁴² of a one-dimensional plasma is assumed. For an inhomogeneous surface like the modelled one, a correct handling of the problem requires the two-dimensional approach. The different longitudinal electron fluxes can influence each other through radial ion currents (ambipolar diffusion). The longitudinal ion currents are hardly influenced by the patch potential, while the radial ion current increases significantly, as can be seen in figure 5.49b. This two-dimensional effect explains the discrepancy between the calculated, flux averaged plasma potential and the modelled space charge potential.

To test whether a rear wall bias can change the patch influence, rear wall voltages of 0.01 V and -0.01 V are implemented in the model. The patch potentials are shifted relative to the rear wall voltage. As depicted in figure 5.50 for a rear wall - patch difference of 0.02 V,

⁴²with respect to the plasma potential

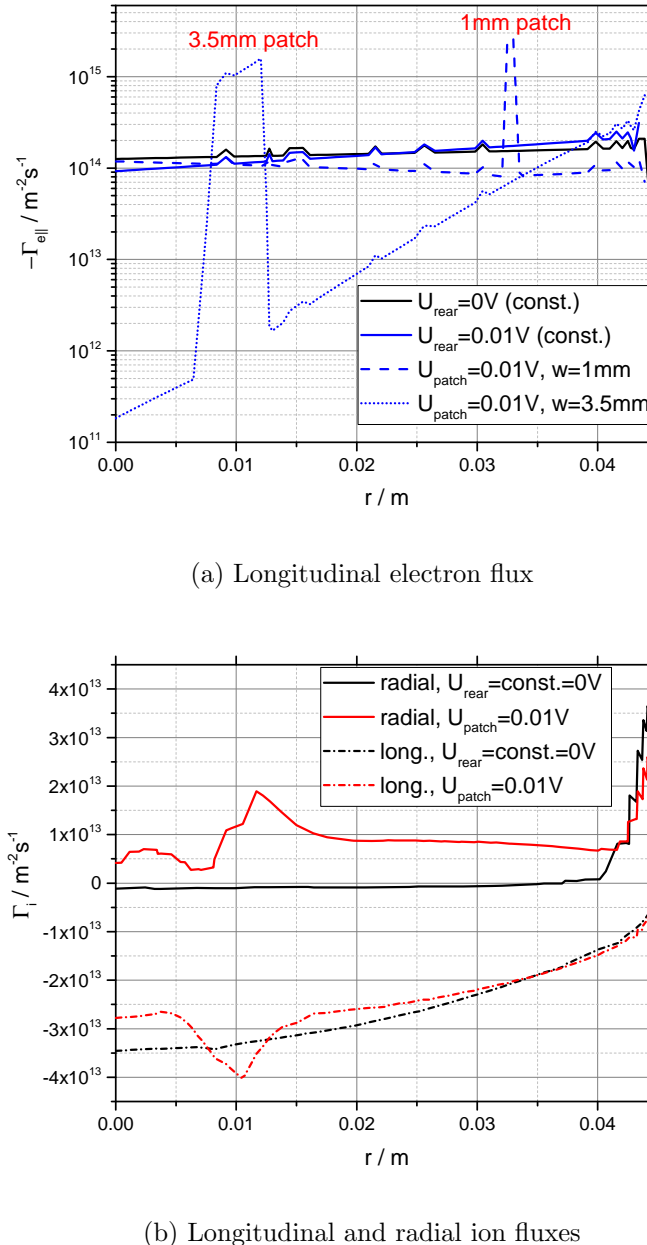


Figure 5.49.: **Electron and ion flux density distributions for one rear wall patch of 3.5 mm and 1 mm at 0.01 V.** For the patch simulation, the actual rear wall potential is zero. Distributions for homogeneous rear wall potentials of 0 V and 0.01 V are shown for comparison. The electron fluxes are shown at $z = 0$ m, while the longitudinal and radial ion fluxes are plotted for $z = 0.01$ m. The longitudinal ion flux is hardly changed, while the radial ion flux as well as the longitudinal electron flux are influenced by the presence of the patch potential.

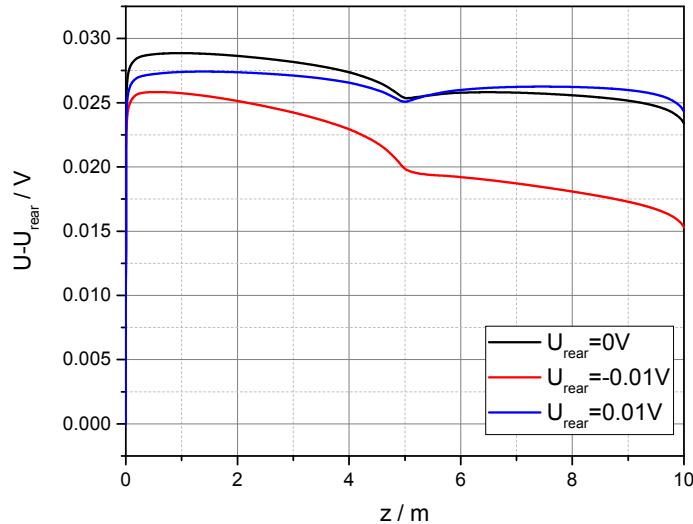


Figure 5.50.: **Influence of rear wall bias voltage U_{rear} on plasma potential profile.**

Here one patch with radial width of 3 mm and a surface potential of $U_{\text{patch}} = 0.02 \text{ V} + U_{\text{rear}}$ is assumed. The plasma potential U is shown with respect to the actual rear wall bias.

the general patch influence on the plasma potential is not changed by a voltage bias. The bias only influences the longitudinal potential homogeneity. A slightly positive rear wall potential reduces ΔU_z while a negative voltage increases the inhomogeneity.

It can be concluded, that patch potentials of considerable size (of the order of 3 mm), do have a strong influence on the plasma space charge potential but not on the longitudinal plasma homogeneity. The smaller the patches are, the lower their influence on the absolute potential. For 1 mm patch width, only large patch potentials $\leq 0.02 \text{ V}$ can effect the plasma potential. For large patch potentials, the electron flux through the patch gets saturated and can not be increased anymore. As the largest expected work function variations are of the order of 30 mV (adsorption induced) and 10 mV (surface induced, [Sch16]), this aspect is not further investigated. Negative patches do not influence the plasma potential, neither the absolute value nor the homogeneity. Biasing the rear wall at reasonable small voltages, below about 10 mV, does not change the patch influence. It only slightly modifies the longitudinal plasma homogeneity. Optimising the rear wall voltage would mean, to use a positive voltage of the order of several times the electron temperature. This differs from the slightly negative value of the optimised rear wall voltage found for the homogeneous rear wall surface above.

WGTS tube wall inhomogeneities

The large steel wall beam tube surface can be expected to have a much less homogeneous work function than the rear wall, as discussed in appendix 5.2. Large surface potential differences in patches as well as a large area that is influenced by the adsorption of tritium have to be considered. As both work function changing effects have different distributions, continuously for the adsorption shift and randomly for the surface inhomogeneity shift, as well as different scales of work function changes, both effects are investigated separately.

Adsorption induced work function change at the tube wall surface

Operating at 30 K a large amount of tritium is expected to adsorb at the WGTS beam tube surface. As discussed in section 5.2, this will lead to a position dependent shift in the work function of the steel surface. The profile of adsorbed monolayers of tritium at the tube surface is calculated in appendix F. Plugging this profile into (5.52), one obtains a

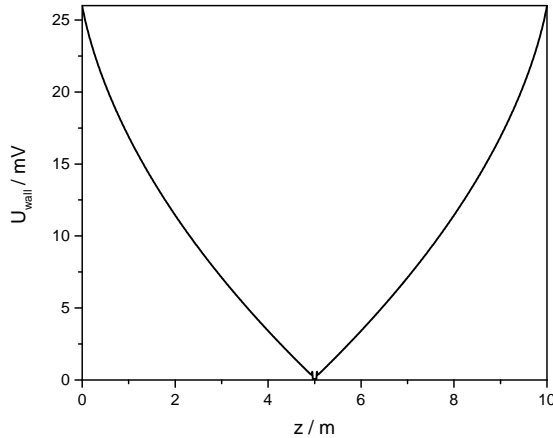


Figure 5.51.: **Adsorption induced surface potential profile on the beam tube surface.** The profile has an offset of 26 meV compared to the actual calculated work function shift.

distribution for the work function changes due to the adsorption of tritium. The induced maximal difference of the steel tube work function is about 26 mV between the injection and the end region. In the plasma simulation, the implemented tube surface potential profile, that is depicted in figure 5.51, is shifted to 0 V at the origin⁴³. Thus, the mean voltage at the tube wall surface is 0.01 V. The potential distribution is simulated for rear wall voltages of 0 V, 0.01 V and 0.02 V.

Looking at the calculated potential distributions depicted in figure 5.52 and 5.53 it becomes clear that the tube surface potential is not able to penetrate directly into the bulk plasma. This is expected from the theoretical considerations regarding the plasma in a conducting cylinder in section 5.1.2. The difference Δ between rear wall potential, with $U_{\text{rear}} = 0$ V and tube surface potential averaged over the length of the tube, $\int_0^L U_{\text{wall}}(z) dz / L \approx 10$ mV, is about -10 mV. This value is above the critical value Δ_C of -20 mV from equation (5.43), where the tube wall potential becomes dominant. Therefore, the calculated potential distributions for the different rear wall voltages can be compared to distributions obtained from calculation with zero wall potential and shifted rear wall potential. The effective tube wall boundary potential for the adsorption model and the corresponding difference to the rear wall potential is calculated from the tube wall surface potential averaged over the inward ion flux⁴⁴ ($j_{\text{ir}} < 0$). This is compatible with the effective rear wall potential calculation in the rear wall patch simulation described above. As can be seen from figure 5.52a and 5.52b, the potential distributions obtained for the zero wall potential and the adapted rear wall potential matches the adsorption induced profile quite well. The longitudinal potential profiles for both models deviate only about 1 mV. Solely in the radial sheath, in about 3 mm distance to the tube wall, the differences due to the modified surface potential distribution can be seen. Optimising the rear wall potential for this tube wall adsorption model, the optimised values $U_{\text{rear, opt}}$ can be approximated with the optimised rear wall potential for grounded tube wall plus the effective tube wall boundary potential: $U_{\text{rear, opt}} \approx -0.002$ V + 0.025 V = 0.023 V.

For the general case of adsorption induced tube wall work function shifts one would need to calculate the effective tube wall surface potential. This can only be done when knowing the

⁴³This is the same as applying a negative voltage of 26 mV at the rear wall, as only the relative potential difference between both surfaces influences the plasma behaviour.

⁴⁴The wall potential has the largest influence for blocked radial ion flux, see section 5.1.2.

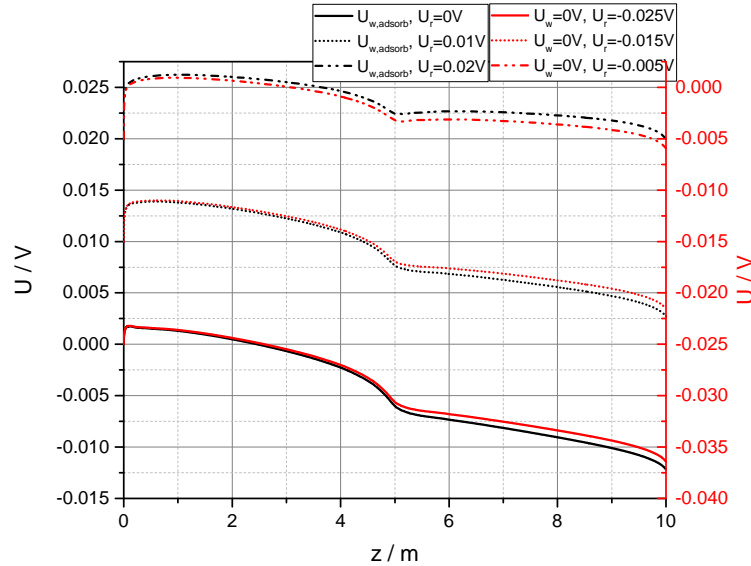
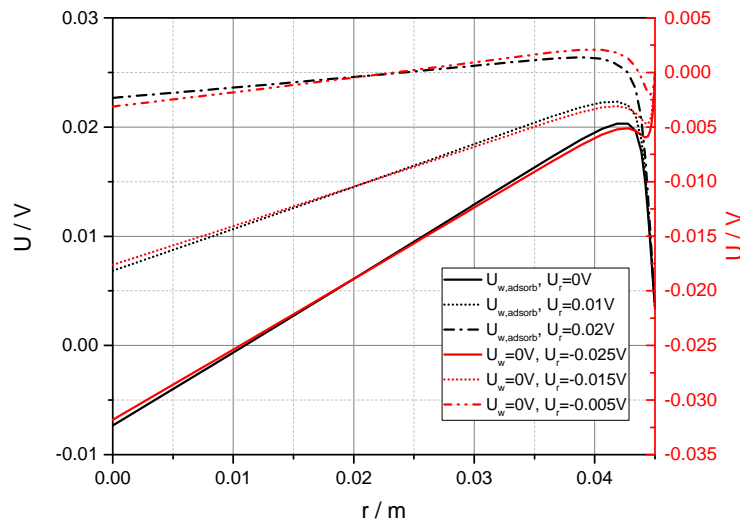
(a) Longitudinal distribution at $r = 0$ m(b) Radial distribution at $z = 6$ m

Figure 5.52.: **Longitudinal and radial potential distribution for adsorption induced tube surface potential profile.** Results for the adsorption induced surface potential profile $U_{\text{wall}}(z) = U_{w,\text{adsorb}}$ from figure 5.51 for different rear wall potentials are plotted in black. They are compared to distributions for zero wall potential $U_{\text{wall}} = U_w = 0$ V and different rear wall voltages plotted in red. The scales of both distributions are shifted by 0.025 V.

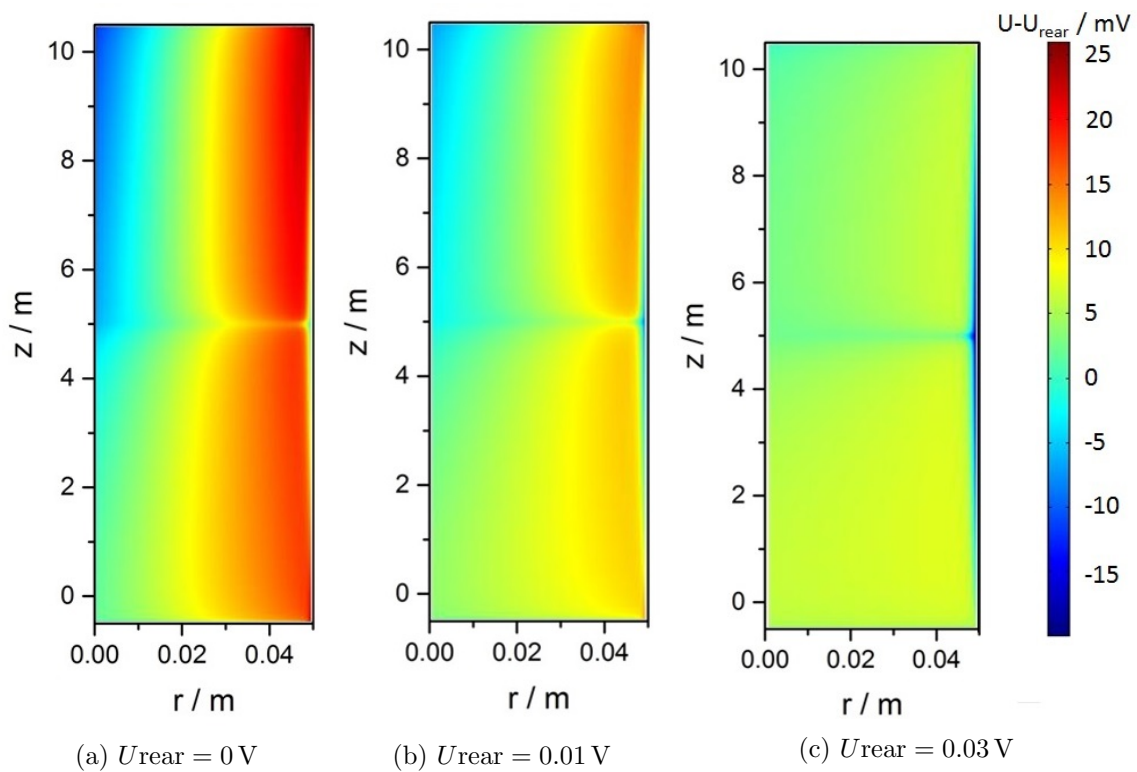


Figure 5.53.: **Two-dimensional potential distribution for adsorption induced tube surface potential profile.** Results for the adsorption induced surface potential profile $U_{\text{wall}}(z) = U_{w,\text{adsorb}}$ from figure 5.51 for different rear wall potentials are given relative dependent on the actual rear wall voltage for comparison. The applied rear wall voltage mainly influences the radial distribution.

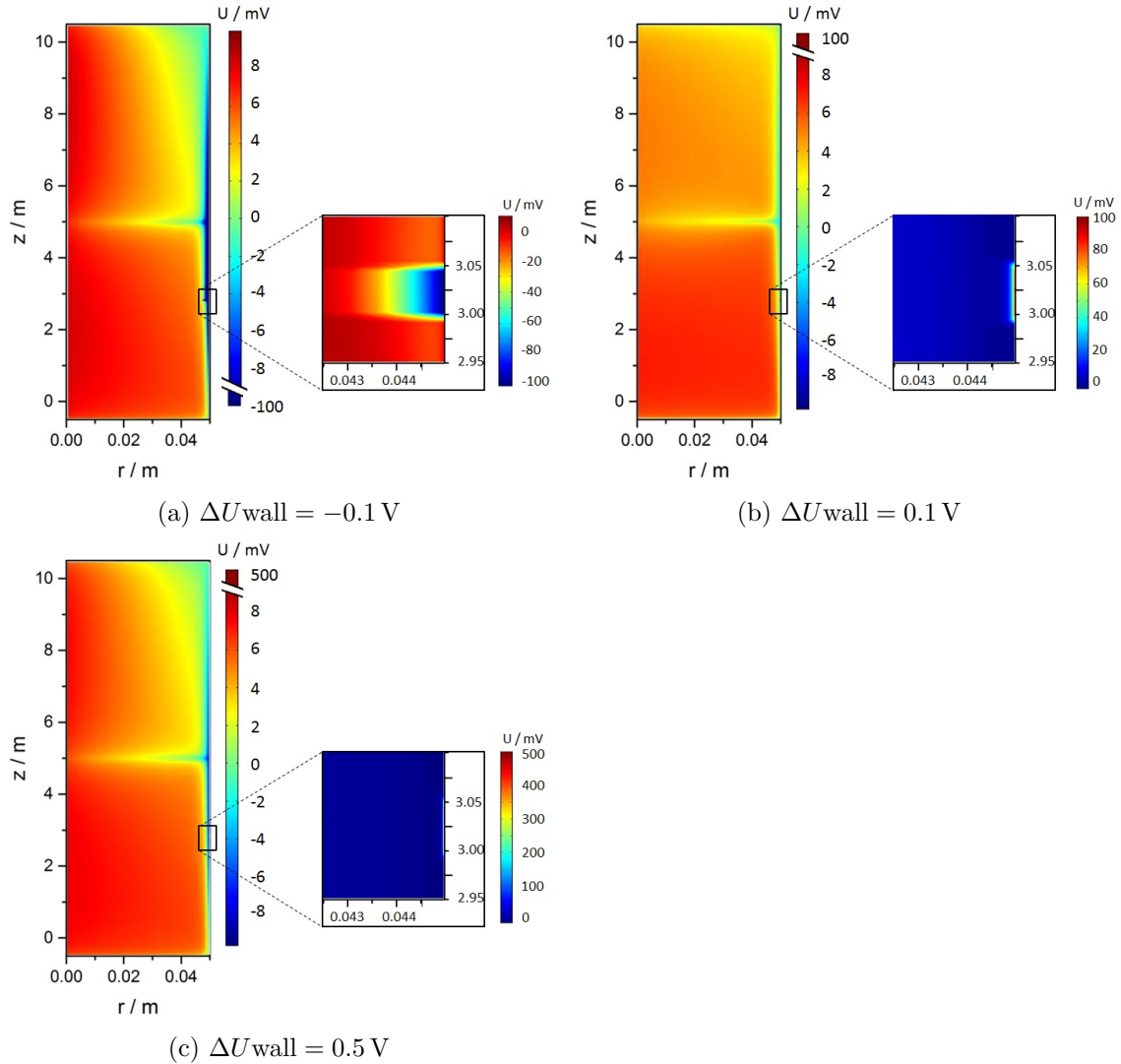


Figure 5.54.: **Two-dimensional potential distribution for 5 cm surface inhomogeneity with work function shift ΔU_{wall} .** Mind the different scales of the zoomed in regions.

transversal ion fluxes, thus already requiring a plasma simulation. Therefore, the effective surface potential can be approximated estimated with the maximal adsorption induced work function shift $\Delta\Phi_{\text{max}}$. The optimised rear wall potential can than be calculated⁴⁵ to be: $U_{\text{rear, opt}} \approx -\Delta\Phi_{\text{max}} - T_{\text{e}}$.

Surface inhomogeneities at the tube wall

The beam tube has a relatively large steel surface. Therefore, work function differences due to surface inhomogeneities, like cracks or impurities will be present (compare section 5.2). These can be of considerable magnitude. The effect of a beam tube surface inhomogeneity on the plasma potential is investigated in the following. The length (in z -direction) of this inhomogeneity is set to 5 cm. Due to the cylinder-symmetry of the model, it is surrounding the plasma at $z = 3$ m. The work function shift of the inhomogeneity is varied between -0.1 V to 0.5 V in different simulations. All other surface parts are set to zero potential. The calculated potential distributions are depicted in figure 5.54 and 5.55. As shown in figure 5.55a, the patch potential does not penetrate into the bulk plasma. It is washed

⁴⁵Here the work function of rear wall and uncovered tube wall are assumed to be equal.

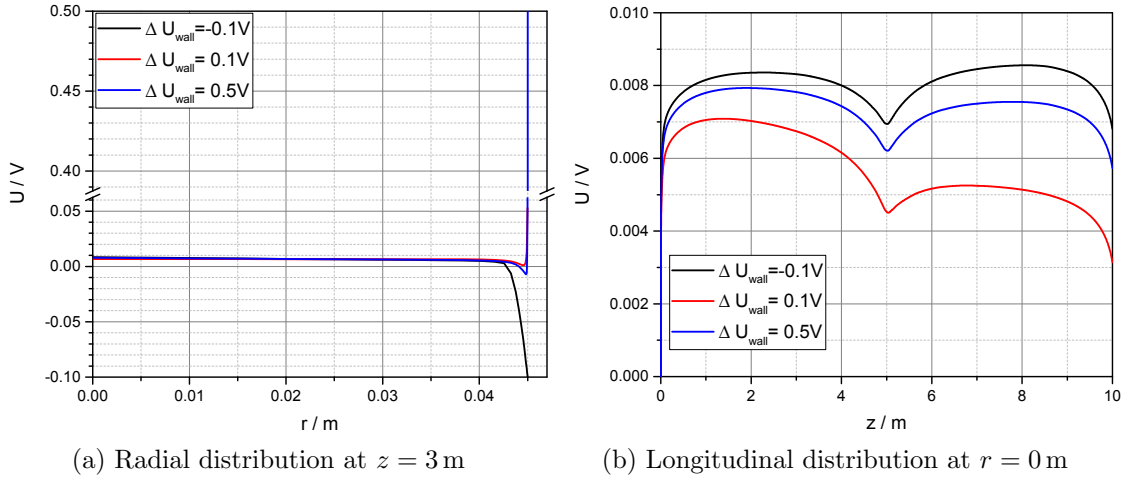


Figure 5.55.: **One-dimensional potential distribution for 5 cm surface inhomogeneity with work function shift ΔU_{wall} .** The penetration depth of the patch potential is smaller than 5 mm.

out after several millimetres. The formed bulk potential is comparable for the different patch potential magnitudes, as can be seen in figure 5.55b and 5.54. This holds for the absolute value as well as for the longitudinal homogeneity. In general, the bulk potential (at $r = 0 \text{ m}$) decreases slightly with decreasing work function difference. However, for a negative patch potential ($\Delta U_{\text{wall}} = 0.1 \text{ V}$), the bulk potential (at $r = 0 \text{ m}$) is maximal, while the radial inhomogeneity is maximal, too. This is connected to the increased radial ion fluxes.

Since the radial penetration depth of beam tube work function differences is small, inhomogeneities will not significantly influence the longitudinal plasma homogeneity – the maximal longitudinal potential difference is smaller than 7 mV which is still below the KATRIN homogeneity limit. The beam tube work function differences have a small impact on the value of the bulk potential since the flux profiles of electrons and ions get affected.

5.3.5. Effect of electron emission at rear wall

For electrons with a Maxwellian energy distribution and mean energies up to 10 meV, the effect from net electron outflow on the plasma potential is of the order of 4 to 5 times the electron temperature. This holds for small potential differences Δ as shown in section 5.3.2.2. For electrons that show a high energy tail in their distribution function, the space charge effect will be larger due to the increased electron flux through the wall. For the standard KATRIN operation mode at 30 K, with nominal column density and high tritium purity, and neglecting non-local effects in the electron energy distribution, the additional potential difference caused by the high energy tail was estimated to be below 1 meV in section 5.3.3. However, considering uncertainties on rate coefficients, surface potentials and local electron energy distribution, the formation of a space charge potential of several times the electron temperature can not be excluded. This space charge potential induces large transversal ion currents, that can lead to longitudinal potential differences above the KATRIN potential homogeneity limit of 10 mV.

To be able to eliminate the positive space charges, the rear wall can be illuminated by an UV light source. Electrons are released from the rear wall surface through the photo electric effect. With a wavelength λ of about 200 nm and a rear wall work function Φ_{rear} of about 4.2 eV [Sch16], an average energy $E_{\text{e,ph}}$ of

$$E_{\text{e,ph}} = \frac{hc}{\lambda} - \Phi_{\text{rear}} \approx 2 \text{ eV} \quad (5.78)$$

Table 5.6.: **Characteristic plasma potential values for electron emitting rear wall and mean electron energy of 2 meV.** Absolute space charge potential value U_{abs} (at $r = 0\text{m}$), maximal longitudinal potential differences ΔU_z and integrated space charge densities, $\int \rho_s \text{d}V$, for different rear wall electron emission rates $R_{\text{e,w}}$.

$R_{\text{e,w}} / 1 \times 10^{12} \text{s}^{-1}$	$U_{\text{abs}} / \text{mV}$	$\Delta U_z / \text{mV}$	$\pi \int_0^r \int_{-L/2}^{L/2} \rho_s r' \text{d}r' \text{d}z / 1 \times 10^8$
0	5.75	5.2	1.75
0.01	5.75	5.2	1.73
0.05	5.7	5.2	1.7
0.1	5.65	5.2	1.67
0.5	5.2	5.4	1.41
1	4.9	5.7	1.19
2	4.4	6	0.87
10	2.8	7.3	-0.12
50	0.7	8.5	-1.49

results for the photo electrons. They cool down to gas temperature like the secondary electrons, that are produced by fast β -electrons.

The standard effective WGTS electron production rate calculated in the cylinder-symmetric model is about $2.26 \times 10^{-6} \text{ A m}^{-1}$. This corresponds to $2.26 \times 10^{-6} \text{ A m}^{-1} \frac{\pi r}{2e} \approx 1 \times 10^{12} \text{ s}^{-1}$ electrons that are produced in the WGTS. This value has an uncertainty of about 50% due to the large uncertainty of the reaction rate coefficients of about $\pm 50\%$ as discussed in section 5.3.3. To evaluate the quantitative influence of an electron emitting rear wall on the space charge potential, the plasma model is slightly modified. The overall electron flux through the rear wall gets:

$$\Gamma_e(z=0)' = \Gamma_e(z=0) - \frac{R_{\text{e,w}}}{\pi(0.045 \text{ m})^2}, \quad (5.79)$$

with $\Gamma_e(z=0)$ denoting the electron flux density from the plasma and $R_{\text{e,w}}$, which is the rear wall electron emission rate. Emission rates of $5 \times 10^{10} \text{ s}^{-1}$, $1 \times 10^{11} \text{ s}^{-1}$, $5 \times 10^{11} \text{ s}^{-1}$, $1 \times 10^{12} \text{ s}^{-1}$, $2 \times 10^{12} \text{ s}^{-1}$, $1 \times 10^{13} \text{ s}^{-1}$ and $5 \times 10^{13} \text{ s}^{-1}$ are implemented in the plasma model. The magnitude of the actual resulting shift in space charge potential is investigated.

The simulated longitudinal (at $r = 0\text{m}$) and radial (at $z = 10\text{m}$) potential distributions for different emission rates and an electron energy of 2 meV are depicted in figure 5.56a and 5.56b. The values for the absolute plasma potential at $r = 0\text{m}$, U_{abs} , as well as the maximal longitudinal potential difference and the space charge density integrated over the simulated surface are given in table 5.6.

The emission of additional electrons starts to create a visible effect at a rear wall emission rate of about $5 \times 10^{10} \text{ s}^{-1}$. For very large emission rates, about $5 \times 10^{13} \text{ s}^{-1}$, a potential dip forms next to the rear wall that reflects electrons emitted at the rear wall back. This result matches the expectation from the theoretical considerations in section 5.1.1 where the formation of a potential dip above a critical emission rate is predicted. The integrated space charge density as well as the absolute potential decrease with increasing emission electron rate. Up to emission rates of $2 \times 10^{12} \text{ s}^{-1}$ the influence on the longitudinal potential difference is smaller than 1 mV. The form of the potential distribution is hardly influenced by the electron emission, at least for emission rates lower than about $5 \times 10^{12} \text{ s}^{-1}$. For electron emission rates larger than $5 \times 10^{12} \text{ s}^{-1}$ all positive space charges can be compensated, compare table 5.6. If the emission rate gets too large, about $1 \times 10^{13} \text{ s}^{-1}$, the WGTS charges up negatively and the absolute value of produced space charge and potential in-

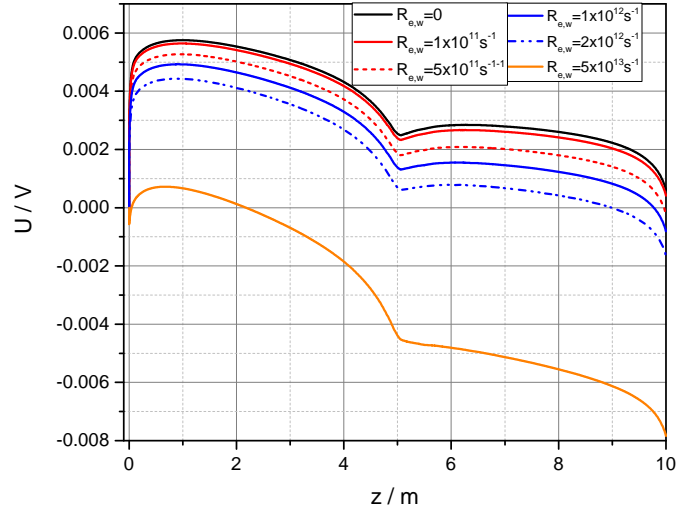
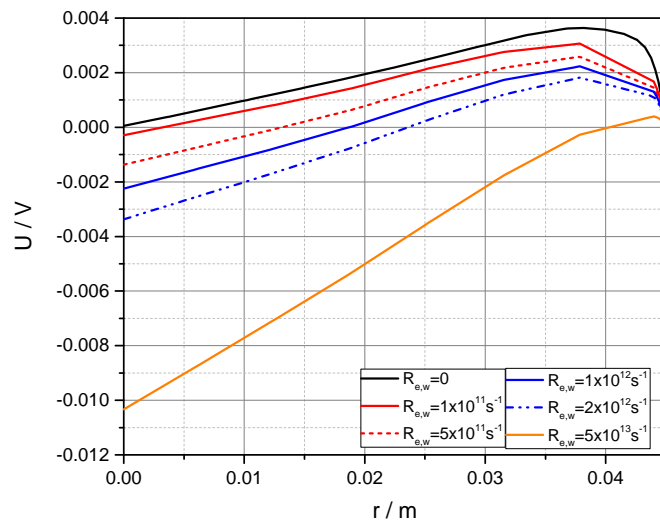
(a) Longitudinal profile at $r = 0$ m(b) Radial profile at $z = 10$ m

Figure 5.56.: **Potential distributions for mean electron energy of 2 meV with electron emission at the rear wall.** The results are obtained from an axisymmetric two-dimensional plasma simulation.

homogeneity gets worse than without electron injection.

From the simulation results no beneficial effect from rear wall electron emission can be deduced. However, due to the limitations mentioned above, the simulation should only be used to approximate the impact on space charge potential shifts. In the following potential rear wall emission effects for high-energy plasma electrons and electron distributions deviating from the Maxwellian case are given. Since the sum of all electron and ion currents needs to be equal (see equation (5.18)) the electron current from the plasma I_e needs to compensate the additional electron current I_k . For I_e to increase, the space charge potential needs to decrease. This decrease can be approximated with

$$\frac{I'_e}{I_e} = 1 - \frac{I_k}{I_e}. \quad (5.80)$$

For Maxwell distributed electrons (5.38) can be used to calculate the potential shift due to electron emission:

$$\Delta U' - \Delta U = T_e \ln \left(1 - \frac{I_k}{I_e} \right). \quad (5.81)$$

For an emission rate that equals the initial electron flux this means a shift in space charge potential of $\Delta U' - \Delta U = T_e \ln(2)$. For an electron energy of 2 meV this corresponds to about 0.9 meV. This matches the simulated value of 0.7 meV. For a slightly different electron energy, the flux I_e changes according to equation (5.38). Assuming the electron density at the beginning of the sheath does not depend on energy, compare figure 5.32b for constant recombination coefficient, the flux scales with $\sqrt{T_e}$. Here a constant ratio between space charge potential and electron temperature is assumed⁴⁶ The dependence of the recombination rate coefficient on the mean electron temperature is not included. Thus, in terms of the electron flux at electron temperature $T_{e,0}$, the potential difference due to electron emission, equation (5.81), gets:

$$\Delta U' - \Delta U \approx T_e \ln \left(1 - \sqrt{\frac{T_{e,0}}{T_e}} \frac{I_k}{I_{e,0}} \right). \quad (5.82)$$

When the electron temperature is increased, the space charge potential ΔU increases. At the same time, the potential shift for a given electron emission rate increases too. This is depicted in figure 5.57. The approximation formula (5.82) matches the order of the emission induced space charge potential shift quite well, even though it was calculated for a floating wall. Deviations are mainly due to the non-linear dependence of space charge potential on electron temperature. Thus, the effects from the transversal fluxes on the order of the space charge shift can be neglected.

Increasing the emission rate decreases the space charge potential and the induced shift in space charge potential can be calculated using (5.81). However, if the plasma electron current reaches its saturation current, it can not increase further and can not compensate the electron emission at the wall anymore. Thus, the outflow of ions needs to be decreased and the potential decreases further. Now the plasma starts to be charged negatively. The WGTS saturation current for electrons can be calculated with equation (5.71) to be about 1.3×10^{13} electrons/s for an electron mean energy of 2 meV. Here an electron sheath density of $3.5 \times 10^{12} \text{ m}^{-3}$ from figure 5.17 is used. The calculated saturation current matches the simulated emission rate at which the WGTS charges up negatively, compare table 5.1. To get access to the question whether the electron emission at the rear wall can help to compensate space charges in the case of high-energy, non-Maxwellian, electron fluxes going out at the rear wall, two simplified approaches can be used:

⁴⁶This holds only for small temperature differences as the dependence between maximal space charge potential and temperature is generally not linear.

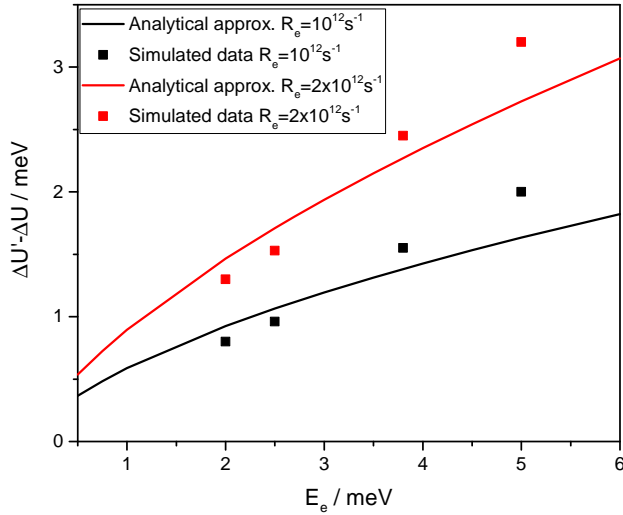


Figure 5.57.: **Electron emission induced shift in space charge potential over electron temperatures for different rear wall emission rates, calculated values from equation (5.82) vs. simulated values.** Data points from simulation are taken at the centre at $r = 0 \text{ m}$. The electron emission rate at the rear wall is assumed to be $1 \times 10^{12} \text{ s}^{-1}$ (black) or $2 \times 10^{12} \text{ s}^{-1}$ (red). Deviations between equation (5.82) and simulated values are mainly caused by the space charge to electron temperature ratio that is actually non-linear in electron temperature.

1. Increase the mean electron energy of Maxwell distributed electrons. The corresponding space charge potential that can be compensated is depicted in figure 5.57. It is approximately 0.5 times the electron temperature.
2. Divide the electron current density to the wall in a Maxwellian part according to equation (5.38) and a high energy part j^* [DDJK06]. The corresponding potential energy shift in the sheath ΔU can be approximated with: $\Delta U = -U_0 + \Delta U^*$, where U_0 is the space charge potential for Maxwell distributed electrons with temperature T_e and ΔU^* is the additional potential shift due to the high-energy electron flux. When additional electrons are emitted at the wall, the corresponding current density j_k needs to be compensated by the low temperature electron current $j'_{e,M}$. The high-energy current can be assumed to be undisturbed by the plasma potential since the energy of these electrons is significantly larger than the plasma potential. Furthermore, the number density of high energy electrons is assumed to be small compared to the density of the low-energy electrons. Assuming the rear wall emission current to be equal to the undisturbed Maxwellian current density $j_{e0,M}$ ⁴⁷, with sheath potential difference $\Delta U_{0,M} = -U_0$, one gets:

$$j'_{e,M} - j_{e,M} = j_k \\ e^{-\frac{U_0+U^*+\Delta U_k}{T_e}} - e^{-\frac{U_0+U^*}{T_e}} \approx e^{-\frac{U_0}{T_e}} \quad (5.83)$$

$$\Delta U_k \approx -T_e \ln \left(1 + e^{\frac{U^*}{T_e}} \right). \quad (5.84)$$

⁴⁷As given above, this corresponds to a plasma electron flux of $1 \times 10^{12} \text{ s}^{-1}$ flowing out at the rear wall, assuming 2 meV electrons and about $1.4 \times 10^{12} \text{ s}^{-1}$ for 3.8 meV electrons (thermalised at 30 K).

This holds for emission currents significantly smaller than the electron saturation current. Thus, especially for $U^* \geq 2T_e$, the potential shift for $j_k = j_{e0,M}$ is of the order of the shift induced by the high energy electron current.

The emission of electrons at the rear wall was shown to be a tool to reduce the formation of positive space charges in the WGTS. For Maxwell distributed electron energies the effect can be calculated with the help of the introduced plasma model. For emission rates of the order of two times the WGTS effective electron production rate of $1 \times 10^{12} \text{ s}^{-1}$, space charge compensation shifts of the order of the electron temperature can be reached. Here the effect of the actual energy distribution of the emitted electrons is neglected. Transversal ion currents are shown to have a minor effect since the simulated data, obtained in a two-dimensional simulation, are reproduced rather well by a one-dimensional analytic derivation. However, in this case the electron emission at the rear wall needs to be carefully adjusted. If the emission rate reaches a critical limit, which is roughly the saturation current of the thermalised plasma electrons, the plasma charges negatively and the homogeneity gets worse than without electron emission.

The compensation was shown to be more effective in the case of larger space charges, originating from non-thermalised high energy electrons, using a simplified analytic approach. For rear wall emission rates of the order of thermalised electron currents leaving the WGTS, the potential shift induced by high energy electrons can be compensated. Here the density distribution at the beginning of the edge is assumed to be only weakly affected by the change in potential. Furthermore, effects from transversal fluxes are assumed to be small.

The influence on the longitudinal plasma homogeneity can not be investigated completely. For thermalised electrons, the homogeneity is slightly increased by the emission of electrons. Since the homogeneity can be assumed to depend on the absolute space charge potential, it will probably be considerably improved by the electron emission for the case of a large number of high-energy electrons.

5.4. Experimental access to WGTS plasma potential

The homogeneity of the plasma potential inside the WGTS is a crucial parameter for the neutrino mass measurement since neutrino mass and potential are directly correlated in the measured β -electron spectrum – The actual retarding potential is determined by the voltage difference between the point of β -decay in the source and the analysing plane in the main spectrometer. Therefore, for KATRIN operation the potential variations need to be constrained to below 10 mV [AAB⁺⁰⁵]. In the plasma simulations presented in section 5.3, WGTS potential distributions falling below as well as exceeding this goal were found by adopting a range of realistic operation scenarios. Although the actual form of the potential distribution was shown to be comparable for different input parameters chosen in the model, the value of the space charge potential as well as the potential inhomogeneity are found to strongly vary with these parameters. The most important ones are central value and form of the electron energy distribution, surface potentials and work function inhomogeneities. These values have large uncertainties, which translates into a large uncertainty of the plasma potential in the source. Thus, the potential distribution inside the WGTS needs to be accessed by measurement to evaluate its effect on neutrino mass uncertainty correctly. For this purpose it is planned to use mono-energetic conversion electrons from ^{83m}Kr mixed into the WGTS gas [AAB⁺⁰⁵]. The following section gives a short overview on the corresponding KATRIN krypton mode. A plasma simulation for the conditions of the ^{83m}Kr mode is discussed in section 5.4.1.1 since operation conditions are different from the standard neutrino mass mode and the plasma distribution may look different. In the last part of this section it is discussed, which is the optimal rear

wall potential setting with regard to plasma homogeneity and how it can be determined experimentally.

5.4.1. The ^{83m}Kr mode of the Windowless Gaseous Tritium Source

To investigate effects that influence the difference between the potential at the point of β -decay in the WGTS and the potential in the analysing plane in the spectrometer, small admixtures of a radioactive isotope producing mono-energetic electrons should be circulated together with the tritium gas [RBSJ⁺91, AAB⁺05, BGZ⁺08]. The position of the measured electron line is linked to the potential difference between source and analysing plane. Additional smearing of the line can be caused by inhomogeneities in the potential difference between source and spectrometer. Knowing the potential distribution in the analysing plane, the width and absolute value of the potential distribution in the WGTS can in principle be deduced.

The isotope ^{83m}Kr is an optimal candidate for this investigation since it produces a set of conversion electron lines with a small width, it is gaseous at slightly modified KATRIN operation conditions and it has a half life of $T_{1/2} = 1.83\text{ h}$ [McC15] which is low enough not to influence the routine neutrino mass measurements. The main electron conversion lines of ^{83m}Kr are positioned around 18 keV and 32 keV [PBB⁺92]. The krypton itself is produced using its parent nucleus ^{83}Rb , the generation process is further described in [VSD⁺14]. Since ^{83m}Kr freezes out at temperatures lower than about 90 K to 100 K at the given typical pressure conditions [BGZ⁺08], the beam tube temperature needs to be increased compared to the neutrino mass measurements at 30 K. The actual operation temperature still needs to be determined in the range between 87 K and 120 K. In the following, a representative operation temperature of 110 K is assumed. To maintain the same amount of tritium in the source as in the 30 K mode the injection pressure needs to be increased to about 12.6×10^{-3} mbar. Still, the gas density profiles are comparable for both operation temperatures [Sha03], the relative deviation is below 10% and thus not of concern.

The analysis of the data from the KATRIN krypton mode regarding the potential distribution inside the WGTS was investigated in [Hua10] and recently in [Mac16]. The latter work revealed that up to four parameters describing the potential distribution inside the source can be obtained from the analysis of the measured conversion line⁴⁸. From the expected form of the plasma profile, as presented in sections 5.3.2.2 and 5.4.1.1, it is recommended to use either a linear profile or a profile with constant potential in the rear part, U_0^r , and the front part, U_0^f , each

$$U(z) = U_0^r(-(z - 5\text{ m})) + U_0^f((z - 5\text{ m})), \quad (5.85)$$

to fit the plasma potential distribution. Using a two-parameter analysis, sensitivities on these parameters of up to 10 meV can be reached within a 17 h measurement (assuming a ^{83m}Kr activity of 1×10^4 Bq) [Mac16]. The given measurement time is related to an analysis of the rate of all 148 detector pixels. It thus averages the distribution over the flux tube cross section. Radial differences can only be investigated in a ring-wise analysis which would mean a measurement time increase by a factor of about 10.

5.4.1.1. Plasma simulation results for ^{83m}Kr mode conditions

Due to the increased gas temperature required for the krypton mode, the charged particle recombination rates and viscosities need to be adjusted in the plasma model. The column density is similar to the standard 30 K mode. The secondary electrons are still assumed to cool down to gas temperature. Based on experimental data given in [RF91], the electron mobility is taken to be about $3 \times 10^4 \text{ m}^2/(\text{Vs})$ which means a reduction by a factor of two

⁴⁸If it is not specified otherwise, the L₃ line at 30.477 keV is used for analysis.

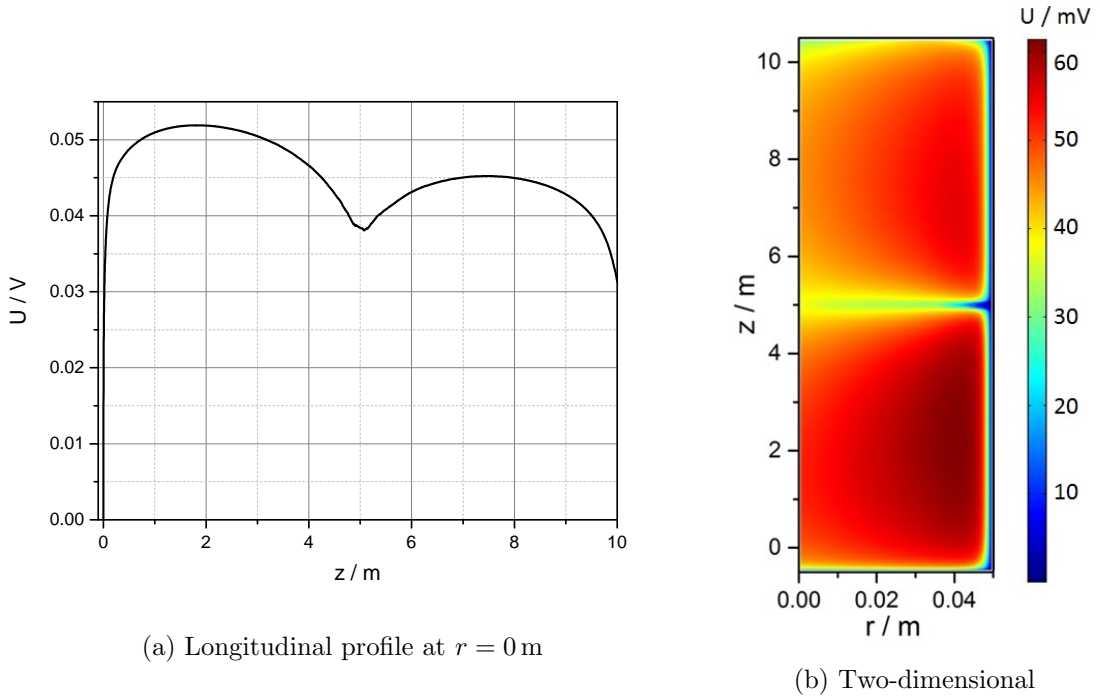


Figure 5.58.: **Potential distribution for operation in $^{83\text{m}}\text{Kr}$ mode.**

compared to the prior simulations at 30 K. The ion mobility is assumed to be slightly increased to $18 \text{ m}^2/(\text{Vs})$ [MMMM68]. The recombination rate coefficient is taken to be inversely linear dependent on electron and ion temperature [BB49] and are thus assumed to be reduced by a factor of four to $1 \times 10^{-12} \text{ m}^3 \text{ s}^{-1}$.

With the conditions in the plasma model presented in section 5.3.2.2 adapted and the above mentioned parameters replaced, the plasma potential distribution for the krypton mode can be simulated. This results in the potential distribution depicted in figure 5.58. As expected, the characteristic values of the potential distribution (absolute value and maximal longitudinal difference) differ from the 30 K results while its general form stays comparable. Due to the elevated electron temperature the space charge potential next to the rear wall rises to about 50 – 60 mV, depending on the radial position. The longitudinal inhomogeneity also increases to 20 mV on axis and to 45 mV for the outer radial coordinates at about $r = 40 \text{ mm}$. Such an increased space charge potential and large longitudinal potential inhomogeneity match the expectations from section 5.3.3 due to the decrease in recombination coefficient and longitudinal mobility and due to the increased mean electron energy.

5.4.1.2. Converting results from $^{83\text{m}}\text{Kr}$ mode to 30 K mode

The krypton mode reveals general properties of the plasma potential distribution. At least two parameters are accessible which are related to the mean potential inside the WGTS and the potential homogeneity (standard deviation), respectively. However, the results of the studies at 110 K need to be extrapolated to the model of the potential distribution at 30 K. To investigate the evolution with temperature, plasma simulations with different temperatures of the WGTS background gas are calculated. The gas and tritium column density are fixed for all models as this is assumed to be valid for the limiting conditions of 110 K and 30 K. Thus, the gas temperature only influences the charged particle mobilities, the recombination rates as well as the mean charged particle energies. Ions and electrons are assumed to fully thermalise. The rate of charged particle creation is taken to be similar for the different gas temperatures.

In figure 5.59 the results are given for the mean and the standard deviation of the longitudinal potential at a fixed radial position. Since the potential is inhomogeneous in radial direction, their values as a function of the gas temperature are given at the centre of the tube ($r = 0$ m) and at the edge of the flux tube⁴⁹ ($r = 0.041$ m). The longitudinal mean of the plasma potential shows a linear increase with increasing gas temperature. Thus, measuring with krypton at two different temperatures (for example at 110 K and 150 K) one can extrapolate the mean potential at 30 K. The lateral beam tube work function change due to the increased adsorption at lower temperatures is assumed to be compensated by the applied rear wall voltage for this computation. The standard deviation of the plasma potential (in longitudinal direction) also increases with temperature since the plasma inhomogeneity increases. However, the data points do scatter and no distinct relation between gas temperature and standard deviation can be derived. Furthermore, one needs to keep in mind the large uncertainties of rate coefficients and mobilities (see section 5.2) that influence the plasma potential distribution and thus its standard deviation. Still, the measured potential standard deviation obtained for 110 K can be used as an upper limit for the 30 K case, assuming the surface potential difference between beam tube wall and rear wall to be the same for both temperatures.

5.4.2. Experimental optimisation of rear wall bias voltage

To minimise the inhomogeneity of the WGTS plasma potential, it is important to have rear wall and beam tube walls on approximately the same surface potential, as discussed in section 5.3.4. Surface potential differences of about 100 mV between rear wall and lateral beam tube surface can already lead to longitudinal potential differences of the order of 30 mV, as shown in section 5.3. This significantly exceeds the source electric potential homogeneity requirement of 10 mV.

The rear wall bias voltage $U_{\text{rear, opt}}$ minimising the source plasma potential inhomogeneity can be calculated using the mean electron energy \bar{E}_e and the work function difference between the WGTS beam tube material and the rear wall material, $\Delta\Phi$, as shown in section 5.3.4.1:

$$U_{\text{rear, opt}} \approx \Delta\Phi - \bar{E}_e. \quad (5.86)$$

Since the mean electron energy is relatively small (about 14 meV for 110 K and 3.9 meV for 30 K) the optimised rear wall voltage needs to minimise predominately the work function difference of rear wall and beam tube surface which can be of the order of 1 V. It is important to note that $\Delta\Phi$ changes if the WGTS is operated at 110 K and at 30 K due to the temperature dependence of gas adsorption at the beam tube surfaces, as discussed in section 5.2. This adsorption induced work function shift between 110 K and 30 K, $\Delta\Phi_{\text{ad}}$, can be of the order of 200 mV and the optimised rear wall bias voltage changes as

$$U_{\text{rear, opt}}(30 \text{ K}) \approx U_{\text{rear, opt}}(110 \text{ K}) + (\bar{E}_e(110 \text{ K}) - \bar{E}_e(30 \text{ K})) + \Delta\Phi_{\text{ad}}. \quad (5.87)$$

Since $\Delta\Phi_{\text{ad}}$ is not known precisely enough, the optimisation needs to be separately done for the 110 K krypton mode and for the 30 K mode. The different procedures are described in the following.

$T = 110 \text{ K}$

The results from the plasma potential characterisation described in section 5.4.1 can be used to minimise the longitudinal plasma potential inhomogeneity. When the linear plasma model is used to fit the krypton data (see section 5.4.1) this corresponds to a minimisation of the absolute value of the potential slope. Using the rectangular model, also described

⁴⁹For larger radii the potential inhomogeneity is generally larger than in the centre, at least for small surface potential differences between beam tube wall and rear wall.

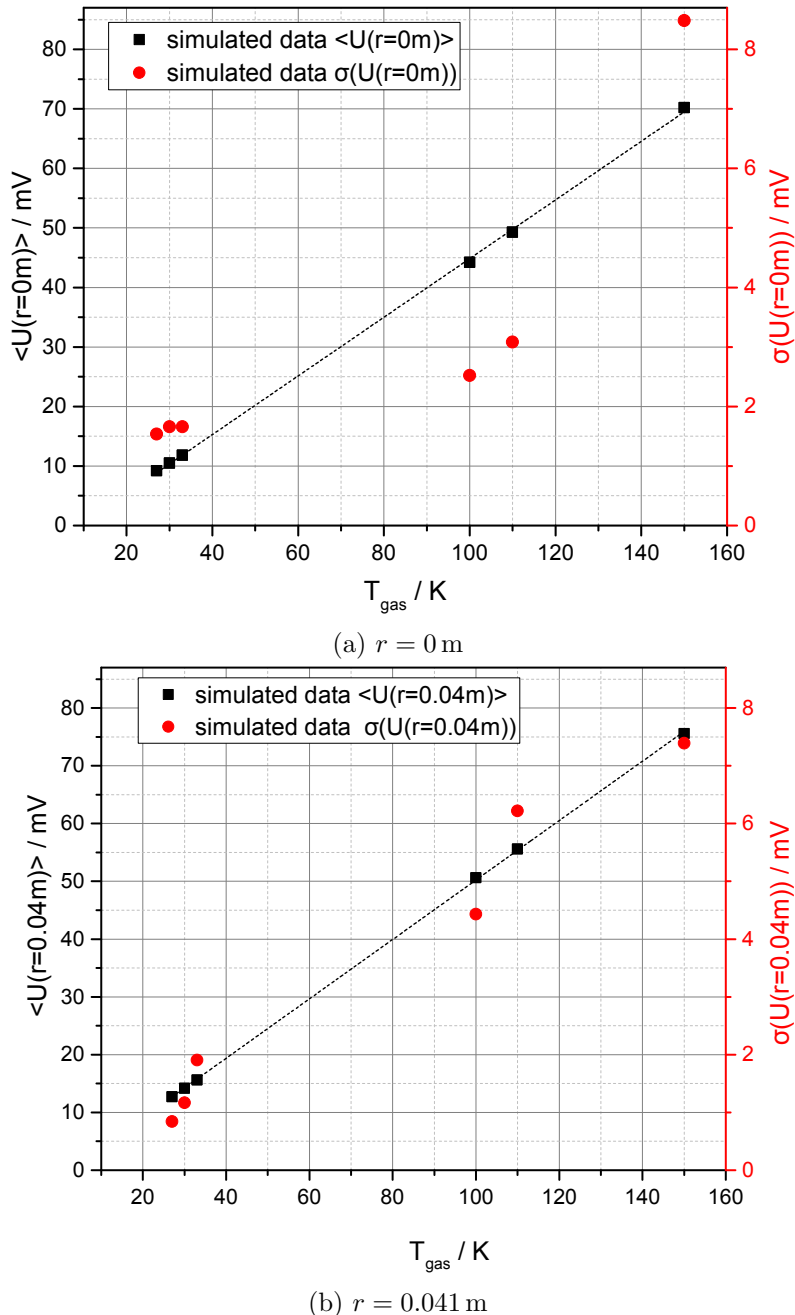


Figure 5.59.: **Simulation results of mean potential and standard deviation of the plasma potential in the source for different gas temperatures.** The longitudinal potential distribution is averaged along the z -axis. Results are given for the radial centre in a) and for the outer flux tube edge in b). The mean potential (black squares) is displayed on the left axis, the standard deviation (red circles) on the right axis. Knowing their dependence on gas temperature, the results from $^{83\text{m}}\text{Kr}$ mode can be used to deduce the corresponding values for the 30 K mode.

in section 5.4.1, the difference $|U_0^r - U_0^f|$ needs to be minimised. The plasma potential analysis with krypton needs to be done for different values of the rear wall voltage bias. The optimisation should start with relatively large voltage steps between the compared rear wall voltages of about 100 mV to 500 mV. If potential distributions with such large rear wall voltage differences are compared, the sensitivity requirement on the obtained plasma parameters is of the order of 50 mV. This sensitivity can be achieved within 1 min up to 1 h, depending on the amount of krypton activity achieved in the WGTS [Mac16]. The steps for the tested rear wall voltages should be reduced (the sensitivity requirements need to be raised accordingly) iteratively down to 10 mV or less.

$T = 30\text{ K}$

At a WGTS beam tube operation temperature of 30 K krypton cannot be used, as it freezes out at the beam tube walls [BGZ⁺08].

The work function shift that is induced at the beam tube walls due to the increased adsorption at 30 K can be sizeable, up to 200 meV, as shown in section 5.2. The optimal rear wall voltage can be determined either based on experimental data or based on the simulation of adsorption at the beam tube surface combined with literature data.

Experimental determination of $U_{\text{rear},\text{opt}}(30\text{K})$

Since only the tritium β -decay spectrum can be used for the direct analysis of the characteristics of the source electric potential one is no longer sensitive to the actual potential distribution or inhomogeneity. Still, one parameter can in principle be accessed by a measurement with tritium – the average space charge potential. In general the following consideration holds: the lower the absolute value of the space charge potential, the more homogeneous the plasma potential distribution becomes (compare tables 5.4, 5.5 and 5.6).

Four possible methods to optimise the rear wall potential bias at 30 K in terms of space charge minimisation are detailed below:

1.
 - Determine the column density ρd_0 for the WGTS working at a temperature of 110 K with the rear section e-gun. Measure the β -decay rate at the detector for applying the optimized voltage for krypton conditions $U_{\text{rear}0} = U_{\text{rear},\text{opt}}(110\text{ K})$ at the rear wall and use a main spectrometer potential of $U_{\text{MS}0}$.
 - Cool the WGTS beam tube down to 30 K, measure the column density ρd_1 with the e-gun.
 - Measure the β -decay rate (at 30 K) for the rear wall biased at potential $U_{\text{rear},\text{opt}}(110\text{ K})$ and the main spectrometer at potential $U_{\text{MS}0}$ with the focal plane detector.
 - Repeat this measurement at 30 K for different rear wall voltages $U_{\text{rear}} = U_{\text{rear},\text{opt}}(110\text{ K} + \Delta U)$. The main spectrometer voltage needs to be adapted, such that the potential difference between rear wall and spectrometer keeps constant ($U_{\text{MS}} = U_{\text{MS}0} + \Delta U$). This way, the measurement is sensitive to the space charge potential in the source.
 - Monitor column density changes (with FBM, BIXS, gas-model) during the whole measurement procedure and correct the measured rate for the column density fluctuations.

The column density-corrected absolute difference, S_{measure} , between the detector rate measured at 110 K and the rate measured at 30 K needs to be minimised by the

variation of the voltage difference ΔU (at 30 K):

$$S_{\text{measure}} = |\rho d_0 \int_0^{\Delta t} \frac{dN(U_{\text{rear}0})}{dt} (110 \text{ K}) dt - \rho d_2 \int_0^{\Delta t} \frac{dN(U_{\text{rear},0} + \Delta U)}{dt} (30 \text{ K}) dt|. \quad (5.88)$$

By the minimisation of S_{measure} the space charge potential U_{abs} can be minimised for the 30 K mode.

To derive the sensitivity of the measured signal S_{measure} to changes in the space charge potential, the column densities are not considered. Thus equation (5.88) becomes

$$S'_{\text{measure}} \approx \left| \frac{d^2 N(U_{\text{rear}0})}{dt dU} \Delta t \Delta U \right|. \quad (5.89)$$

The lowest WGTS plasma potential difference that can be distinguished by this measurement can be calculated looking at the signal-to-background ratio SB . For a background rate N_{bg} the signal-to-background ratio is:

$$SB = \frac{S'_{\text{measure}}}{N_{\text{bg}}} \approx \frac{\frac{d^2 N(U_{\text{rear}0})}{dt dU} \Delta t \Delta U}{2 \left(\sqrt{\frac{dN}{dt} \Delta t} + dn \frac{dN}{dt} \Delta t \right)}. \quad (5.90)$$

In the calculation of the background rate, statistical rate fluctuations as well as relative instabilities, dn , due to temperature or inlet pressure instabilities that cannot be resolved by the column density monitoring are considered. From equation (5.90) the required measurement times Δt for different main spectrometer potentials settings and analysed voltage differences can be calculated.

Aiming for a signal to noise ratio of 3 and assuming a standard KATRIN rate stability (or monitoring precision) of 1×10^{-3} between the measurement points only voltage differences of about 100 mV can be detected in a measurement time of about 8 d in an analysis that considers the rate at the different detector rings separately. A ring dependent analysis is required due to the large radial inhomogeneities in the plasma potential that changes with modified rear wall voltage.

Even if an improved rate stability of 1×10^{-4} is assumed, the required measurement time to resolve space charge potential differences of 50 mV in a ring-wise analysis is still about 2 d as indicated in figure 5.60.

The sensitivity of the discussed method of space charge minimisation is quite low (see figure 5.60) and strongly depends on the rate stability. Therefore, this measurement is only suitable for a qualitative test of the rear wall influence on the plasma potential. Here the rates at different rear wall voltages need to be compared to the rate changes expected from the β -decay spectrum. This way, it can be tested whether the plasma potential indeed follows the rear wall voltage. No information from the krypton mode is required.

2. Measure the endpoint of the electron spectrum from tritium β -decay for 30 K and 110 K. From the difference of both values one obtains information on the space charge potential. To optimise the rear wall potential with a sensitivity of about 60 mV, which is required for a longitudinal potential inhomogeneity below 20 mV, an average space charge potential difference between the rear wall potential bias configurations of 20 mV needs to be resolved. The measurement time for an endpoint sensitivity of 20 mV is roughly 10 d for a total count rate analysis. The required ring-wise endpoint determination would already need about 100 d of measurement time. The endpoint measurement needs to be done at least twice (for 110 K and for 30 K) not considering the actual rear wall voltage optimisation that requires endpoint measurements at different rear wall voltages.

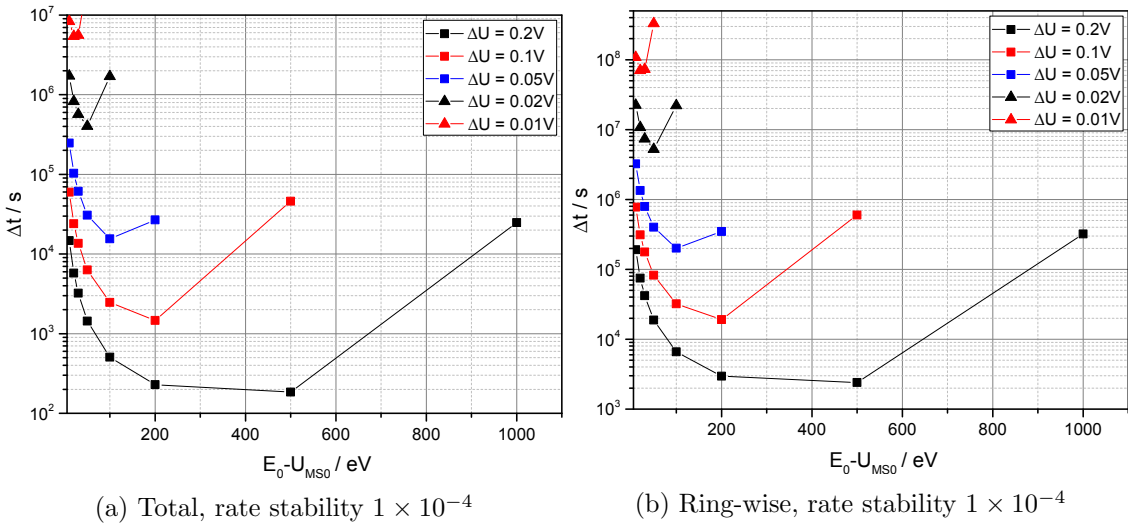


Figure 5.60.: **Measurement time Δt and main spectrometer potential U_{MS0} as a function of retarding potential differences ΔU for the optimisation of U_{rear} .** The difference in retarding potential is equal to the change in (mean) space charge potential. Values are given for various space charge potential differences ΔU that need to be resolved looking at the rate difference measured at the detector. The results are plotted for rate stabilities of 1×10^{-4} for a total (left) and ring-wise (right) count rate analysis. The working point of the main spectrometer voltage determines the amplitude of the measured β -decay rate and needs to be adapted for the analysed potential difference ΔU .

3. Measure the adsorption of tritium on steel at 110 K and 30 K in a dedicated side experiment. Knowing the change in tritium coverage, the corresponding change in work function can be approximated using equation (5.52). The optimised rear wall voltage bias can then be calculated by plugging the value obtained with krypton mode, $U_{rear, opt}(110\text{ K})$, and the calculated work function change into equation (5.87).
4. Measure the adsorption induced work function change of steel at 110 K compared to 30 K in a dedicated side experiment. The measurement can be done with hydrogen instead of tritium, supposing both isotopes behave similarly with regard to adsorption. The atmosphere to which the measured steel probe should be comparable to that of the central beam tube under real KATRIN measurement conditions. The sample needs to be cooled down to 110 K and 30 K, respectively and the work function needs to be measured. Plugging the measured work function change and $U_{rear, opt}(110\text{ K})$ in equation (5.87) $U_{rear, opt}(30\text{ K})$ can be determined.

Since the space charge potential cannot be minimised using the β -decay electron spectrum in a reasonable amount of time without input from the plasma model, only the last two options are feasible. Both need to be done in a separate test experiment. Here the direct measurement of the work function change should be preferred, since in this case the rear wall voltage optimisation is purely based on experimental data. The adsorption measurement has the disadvantage that the change in work functions still needs to be calculated using (5.52) or it needs to be extrapolated from literature data.

Simulation based determination of $U_{rear, opt}(30\text{ K})$

If the adsorption induced work function change is not measured, it can be roughly estimated from the modelling of adsorption at the WGTS beam tube surface described in appendix F. Here differences of about 0.7 monolayers are calculated for the beam tube

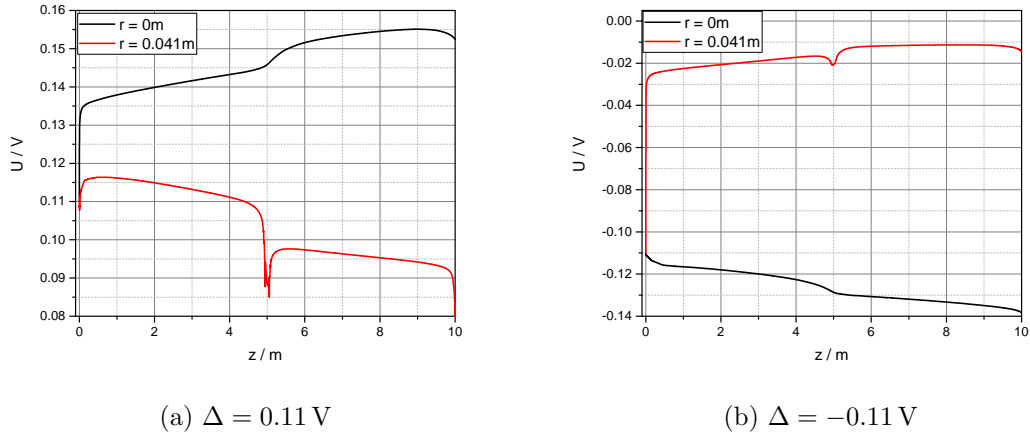


Figure 5.61.: **Longitudinal source potential distribution assuming a rear wall-beam tube voltage difference Δ of ± 110 mV.** If the rear wall potential is not optimised experimentally and neither tritium coverage nor work function shift at 30 K are measured, the surface potential difference Δ can only be estimated with an uncertainty of about 110 mV.

coverage at 30 K compared to 110 K.

Using equation (5.52) and assuming a work function shift of 190 mV in case of adsorption of a full monolayer, the work function shift between 30 K and 110 K mode can be approximated to be -130 mV. Here the dipole moment of the beam tube surface material is simplified to be constant and independent of coverage, see section 5.2.

It is important to note that the adsorption model as well as the approximation of the work function change both are subject to large uncertainties – the resulting uncertainty of the work function change is of the order of 100 mV. Considering the sensitivity of the rear wall voltage optimisation in krypton mode, the maximal sensitivity for the optimised rear wall potential at 30 K without further experimental data is approximately 110 mV. Using a surface voltage difference of 110 mV in the plasma model, a maximal longitudinal potential inhomogeneity of 29 mV is obtained as depicted in figure 5.61.

The systematic uncertainties with regard to the determination of the neutrino mass caused by surface potential differences between rear wall and beam tube surface and related source potential inhomogeneities are explored in more depth in the following section.

5.5. Implications of plasma potential for neutrino mass uncertainty

To be able to measure the neutrino mass at the sensitivity targeted with KATRIN, the retarding energy E_{ret} , which corresponds to the difference of the potential at the point of β -decay in the WGTS and the potential in the analysing plane, needs to be known precisely. Necessarily this calls for an accurate model of the WGTS plasma potential.

If the retarding energy gets smeared out by a Gaussian with variance σ^2 , the shift in neutrino mass squared can be approximated with [RK88]

$$\Delta m_\nu^2 = -2\sigma^2. \quad (5.91)$$

Such a smearing can be caused by fluctuations of the high voltage at the main spectrometer, as well as by local or temporal instabilities in the WGTS plasma potential. In [AAB⁺05] a limit of 5×10^{-3} eV² is set on the neutrino mass uncertainty induced by retarding voltage fluctuations. The main part to this uncertainty budget was assumed to be related to

the stability of the high voltage. Contributions from plasma inhomogeneity were assumed to be a factor of five smaller. Therefore, requirement on high voltage stability was set to 60 mV, which corresponds to a long-term relative precision of 3×10^{-6} at 18.6 kV [Thü07]. In contrast, the inhomogeneity of the plasma potential in the source was estimated to be small. Calculations in [NM04], discussed in section 5.3.1, showed a WGTS plasma inhomogeneity of the order of several times the electron kinetic energy and thus below 10 meV (compare figure 5.9). The respective uncertainty on m_ν^2 was deduced from equation (5.91) to be below 2×10^{-4} eV². The inhomogeneity of the plasma potential in longitudinal direction was assumed to be distributed according to a Gaussian. No information on the actual longitudinal or radial potential distribution was available for this estimate.

The simplified picture given in [AAB⁺05] for the plasma potential distribution as well as for the impact of the source potential distribution on the neutrino mass measurement needs to be revisited. Information from the newly developed, two-dimensional plasma model, which was presented in section 5.3, needs to be included. The impact of a realistic potential distribution on the retarding energy and the measured β -electron spectrum cannot simply be approximated by a Gaussian smearing. Thus, it is important to use a proper description of the potential distribution in the WGTS.

A realistic model of the WGTS potential is implemented in the source spectrum calculation package SSC. Thus, the influence of other source properties like density profile and scattering probabilities can be included in the analysis. The limited features of the SSC version preceding the present dissertation project did not allow to include any potential profile in the calculation of the β -decay spectrum. Classes for the different potential models have been implemented in SSC as a part of the present work. In the following sections, the neutrino mass uncertainty induced by the WGTS potential distribution is derived with the help of these models. To this end, the method of ensemble testing is used, as introduced in section 2.4.3. Toy data are generated based on different (non-vanishing) potential distributions inside the WGTS. To deduce the m_ν^2 an analytical spectrum is calculated and compared to the toy measurement. This analytical spectrum uses the zero potential assumption. This way, the impact of the source potential distribution on the calculated neutrino mass squared can be deduced.

5.5.1. Gaussian potential fluctuations in the WGTS

At first random potential fluctuations through the whole WGTS volume are studied. Then, surface potential fluctuations at the rear wall, that are transported through the WGTS by the magnetic flux tube, are analysed.

Potential fluctuations in the WGTS volume

This potential model corresponds to the potential configuration assumed in [AAB⁺05]. Implementing this potential profile in the calculation of the source spectrum allows to consider actual source properties such as temperature, tritium density distribution, and gas velocity. The potential needs to be defined for each of the WGTS voxels⁵⁰. For the implementation of Gaussian type potential fluctuations in the WGTS volume, the potential for voxel i is picked randomly⁵¹ from a Gaussian distribution with mean value \bar{U} , standard deviation ΔU and probability density function $f(U_i)$:

$$f(U_i) = \frac{1}{\Delta U \sqrt{2\pi}} e^{-\frac{(U_i - \bar{U})^2}{2\Delta U^2}}. \quad (5.92)$$

⁵⁰It is constant over each voxel, since this is the smallest analysing unit available in SSC.

⁵¹Here a Mersenne-Twister pseudo-random number generator [MN98] that is already implemented in the KATRIN simulation software package is used.

In this approach, for practical reasons the retarding energy $E_{\text{ret},i}$ for voxel i is modified compared to the zero potential case:

$$E'_{\text{ret},i} = E_{\text{ret},i} - eU_i. \quad (5.93)$$

This holds for any configuration of the potential of the different voxels.

For the ensemble test the WGTS is segmented into 1000 parts (slices) in longitudinal direction with a length of 1 cm each. It is not divided in radial or azimuthal direction. For the generation of toy measurement data the potential of each voxel is set according to equation (5.92) and standard background rate of 10 mcps is assumed. One-dimensional gas density and velocity distributions for a column density of $5 \times 10^{21} \text{ m}^{-2}$ are used.

For the analytical model which is fit to the toy measurement data the source properties are identical except for the potential distribution – zero potential is used for all voxels.

The analysis is done for a measurement interval of $[E_0 - 30 \text{ eV}, E_0 + 5 \text{ eV}]$ and using the standard measurement time distribution from [AAB⁺05] for three effective years of data taking.

Different standard deviations ΔU ranging from 10 mV to 200 mV are tested. Each ensemble test consists of 3000 KATRIN toy measurements. The results are visualised in figure 5.62.

The neutrino mass uncertainty induced by Gaussian potential fluctuations in the WGTS volume fits the expectation from equation (5.91) quite well. Thus, random inhomogeneities of the plasma potential inside the WGTS can be approximated by equation (5.91) without further consideration of the actual source properties.

Surface potential fluctuations at the rear wall

In a more realistic scenario, only the surface potential at the rear wall is randomly distributed. For a rear wall determining the potential along the flux tube, the potential of any given point inside the WGTS beam tube can be computed considering the magnetic field configuration at the rear wall as well as in the source. At first, the rear wall is divided into N segments. The surface potential at each segment is fixed using equation (5.92). For the potential of voxel i , that is centred at position (r, ϕ, z) inside the WGTS, the radial position r_r of the corresponding rear wall segment is calculated using the conservation of the magnetic flux:

$$r_r = \sqrt{r^2 \frac{B(r, \phi, z)}{B_r}} \quad \text{for } r \geq 0 \quad (5.94)$$

$$r_r = -\sqrt{r^2 \frac{B(r, \phi, z)}{B_r}} \quad \text{for } r < 0. \quad (5.95)$$

Here B_r denotes the magnetic field at the rear wall and $B(r, \phi, z)$ the magnetic field inside the WGTS at position (r, ϕ, z) . The angular variable ϕ is assumed to be conserved which is suitable for this simplified potential model. The potential of the WGTS voxel i is set to the potential of the rear wall segment with radial and azimuthal coordinates (r_r, ϕ) .

To test the effect of this potential distribution on the neutrino mass squared, the WGTS is divided into small concentric rings of 1 mm width. Each ring is divided into 50 angular segments. Apart from the potential model for the generation of the toy measurement data, the same procedure as described for the previous potential model is used. Standard deviations of the rear wall potential from 10 mV to 200 mV are analysed. Results are depicted in figure 5.62.

The deduced uncertainty in neutrino mass squared for given rear wall potential fluctuation ΔU is comparable to the results for the previous volume fluctuation model. It matches

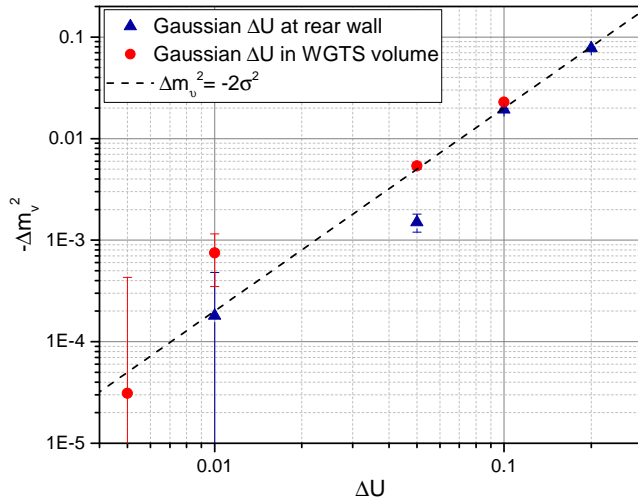


Figure 5.62.: **Neutrino mass uncertainty from Gaussian WGTS potential fluctuations.** Results are given for Gaussian fluctuations over the whole WGTS volume (red circles) and for fluctuations at the rear wall surface, that penetrate into the WGTS (blue triangles). The theoretical expectation of the uncertainty in neutrino mass squared for a potential standard deviation of ΔU from equation (5.91) is plotted for comparison.

the theoretically derived value from equation (5.91) as well. Thus, the effect of Gaussian fluctuations is, as expected, not amplified by the source properties neither for radial and azimuthal nor for radial, azimuthal and longitudinal fluctuations.

5.5.2. Potential distribution from plasma simulation

The randomly varying potential distribution is in fact not a good approximation for the WGTS plasma potential. The plasma simulations in section 5.3.2.2 show a source potential distribution that is to first order monotonous (apart from the central region around the gas injection orifices) along the z -axis. Merely implementing the mean value and the standard deviation of this distribution in equation (5.25) cannot reflect the position dependent effect on the measured electron spectrum, as already expressed in [Mac16]. To get a better model for the probability distribution $P(U)$ for electrons that reach the detector to be born in a potential U , the potential distribution needs to be combined with the electron density and the zero-scattering probability⁵² $P_0(z)$ at the corresponding source position. Therefore, a histogram is filled including the potential at source position z weighted with $P_0(z) \cdot n(z)$. The resulting probability distribution for a realistic source potential is illustrated in figure 5.63. Here the probability distribution from a potential from plasma simulation (see small graph in the upper right corner) with $\bar{E}_e = 3.9$ meV and grounded walls is compared to a Gaussian probability distribution of same potential mean and standard deviation.

The probability distributions differ significantly. The potential probability distribution from plasma simulation is peaked twice with sharp upper edges. The two-fold peaked structure is caused by the decline in the plasma potential in the beam tube centre (around

⁵²Depending on the analysis interval in principle also electrons that have scattered one or two times need to be considered. For scattered electrons things get more complicated as the scattering energy loss needs to be taken into account. However, using unscattered electrons shows the general effect of a realistic potential distribution.

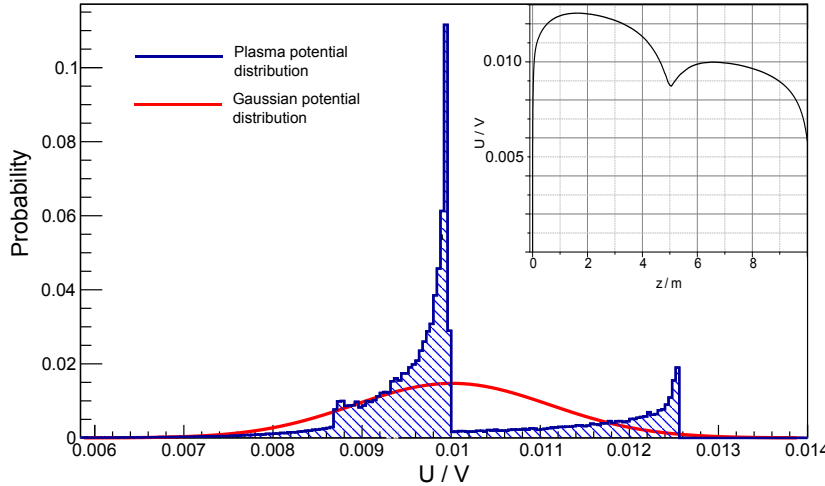


Figure 5.63.: **Probability distribution of electrons reaching the detector unscattered to be created at source potential U .** The probability distribution for the potential profile obtained by plasma simulation (with $\bar{E}_e = 3.9$ meV, grounded boundaries) is represented by the blue shaded area. The corresponding longitudinal potential profile is shown in the embedded figure in the upper right. The mean potential (0.01 V) and corresponding standard deviation (0.0011 V) of this distribution are plugged into equation (5.92) to compare simulation data to the corresponding Gaussian probability distribution (red line).

$z = 0$). The high amplitude of the main potential is related to the high electron density in the centre of the source.

Given that the probability distribution obtained from the potential model differs markedly from a simple Gaussian, equation (5.91) is not applicable for calculating the effect on neutrino mass from the plasma potential distribution as also stated [Mac16]. Instead, the plasma potential simulation data need to be used to build an appropriate potential model to analyse the induced neutrino mass uncertainty. Such an appropriate model is used in the following sections. Since the boundary potential difference was shown to be important for the plasma homogeneity, distributions with boundaries at different potentials are tested.

5.5.2.1. Rear wall and beam tube at equipotential

The plasma potential distribution which was simulated in section 5.3.4.1 for 3.9 mV mean plasma electron energy and rear wall and beam tube at the same surface potential represents the WGTS potential distribution with lowest achievable inhomogeneity. Here, a maximal longitudinal potential difference of 7.7 mV and a maximal radial potential difference (inside the analysed flux tube) of 4 mV were obtained. The maximal longitudinal standard deviation of this spatial potential distribution is about 3 mV.

The SSC WGTS model is divided into 500 slices in longitudinal direction, with a length of 2 cm each. To resolve the radial potential inhomogeneity it is further segmented into rings of 3.5 mm width. The generated toy measurement data include the potential profile from the plasma simulation. The theoretical model that is fitted to the generated data uses the null potential hypothesis. Nominal operation values given in table 2.1 are used. 4000 KATRIN measurements with reference measurement time distribution from [AAB⁺05] and an analysis interval $[E_0 - 30 \text{ eV}, E_0 + 5 \text{ eV}]$ are simulated.

The resulting difference in neutrino mass squared is

$$\Delta m_\nu^2 = (-5.8 \pm 2.8) 10^{-4} \text{ eV}^2.$$

Using the approximation (5.91) for Gaussian differences and a standard deviation of 3 mV one would expect only a tiny shift of $-1.8 \times 10^{-5} \text{ eV}^2$. This means an increase by a factor of 30 for the realistic distribution. Therefore, even without considering a work function induced surface potential difference between rear wall and beam tube wall, the limit of $2 \times 10^{-4} \text{ eV}^2$ from [AAB⁺05] cannot be met.

5.5.2.2. Differences in rear wall - beam tube surface potential

The work functions of rear wall and beam tube material are generally different, which induces a potential difference between both surfaces. In the krypton mode at 110 K, this difference can be accessed by measurements with pure krypton, a krypton-deuterium gas mixture, and a krypton-tritium gas mixture. If the difference is measured, it can be compensated by a rear wall voltage bias. However, the shift in work function due to the different amount of adsorbed gas at 110 K and 30 K is not known and the voltage compensating this difference needs to be optimised experimentally as discussed in section 5.4.2. This optimisation is only possible to a certain degree. Not compensating the surface potential difference causes a larger inhomogeneity in the potential distribution. In the following, plasma potentials induced by various surface voltage differences are tested. A full analysis, including the radial potential differences, is done exemplarily for two cases:

- i) An experimentally optimised rear wall voltage ($\Delta = 60 \text{ mV}$)
- ii) A rear wall voltage setting, which is solely based on the calculation of the adsorption induced work function shift between 30 K and 110 K ($\Delta = 110 \text{ mV}$).

i) Experimentally optimised rear wall voltage

The configuration with all surfaces on equipotential cannot be assumed to be realisable, as discussed above. Still, the large surface potential differences between gold and steel surface can be reduced in terms of an improved rear wall bias setting (methods described in section 5.4.2 have a sensitivity on the parameters describing the potential distribution of about 20 mV⁵³). For this configuration, denoted here as “experimentally optimised”, an absolute space charge potential difference of about 20 mV has to be assumed compared to the grounded boundary configuration. A plasma distribution with a space charge difference of 16 mV (compared to the grounded tube configuration) can be calculated using the WGTS plasma model for various boundary potential differences Δ . A rear wall potential of about 60 mV with the lateral wall set to 0 V induces such a space charge potential. Thus, it is tested how a plasma potential configuration with $\Delta = 60 \text{ mV}$ compared to the zero potential hypothesis influences the neutrino mass determination. The longitudinal distribution of the tested plasma potential is shown in figure 5.64 at two radial coordinates. The maximal longitudinal potential inhomogeneity is about 20 mV. Large differences are also present in radial direction.

Other than this specific source potential configuration, all analysis settings are described in the previous section. 4000 full KATRIN toy measurements (three years of data taking, full source strength) are simulated. Therefrom the neutrino mass squared uncertainty is calculated to be

$$\Delta m_\nu^2 = (-1.14 \pm 0.26) \cdot 10^{-3} \text{ eV}^2,$$

which is, due to the larger inhomogeneities in the potential profile, almost twice as large as the above derived uncertainty from the potential distribution for boundary surfaces on equipotential and a factor of five to six larger than the systematic neutrino mass shift assumed in [AAB⁺05].

⁵³Higher sensitivities are also possible, but will increase the duration of the pre-measurements significantly.

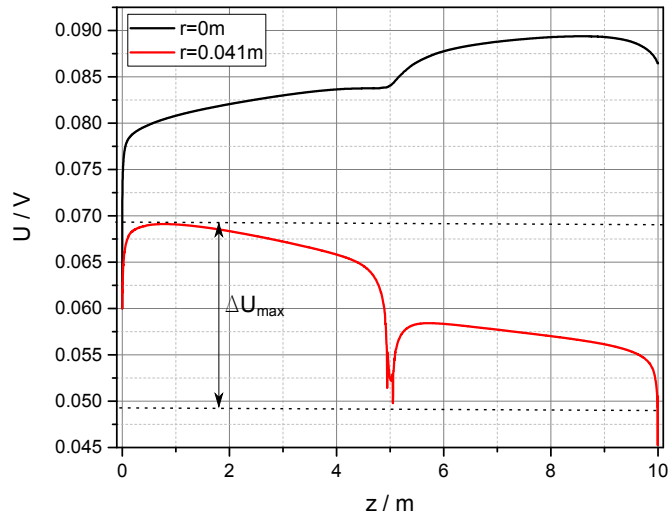


Figure 5.64.: **Plasma profile for experimentally optimised rear wall voltage.** The optimisation is assumed to be limited by a space charge potential of 20 mV compared to the grounded boundary configuration. This corresponds approximately to a voltage difference of 60 mV between rear wall and beam tube wall. Shown are the longitudinal potential distributions at $r = 0$ m and at about 0.041 m. ΔU_{\max} denotes the maximal longitudinal potential difference in this distribution.

ii) Non-optimised rear wall voltage

If it turns out that it will not be feasible to reduce the surface potential difference between rear wall and beam tube surface either directly, by analysis of the β -spectrum, or indirectly, by measuring adsorption properties at different temperatures, the surface rear wall and beam tube potentials can differ up to 110 mV, see section 5.4.2. This would cause a maximal longitudinal potential inhomogeneity of 29 mV and also large radial differences, as depicted in figure 5.61. The toy measurement data are generated ion *SSC* using the potential distribution shown in figure 5.61a. The WGTS is divided into 500 slices and 13 rings to incorporate the radial inhomogeneity. Measurement time distribution and interval are identical to the previous simulations. In the ensemble test, 5000 KATRIN measurements are simulated. As a result, a systematic neutrino mass shift of

$$\Delta m_{\nu}^2 = (-1.5 \pm 0.25) \cdot 10^{-3} \text{ eV}^2$$

can be derived. It is a factor of seven larger than the limit of $2 \times 10^{-4} \text{ eV}^2$ from [AAB⁺05]. The systematic neutrino mass uncertainty induced by a realistic plasma potential is larger than initially estimated – the potential probability distribution is different than assumed and its longitudinal profile is less homogeneous than expected due to the influence of the previously disregarded boundary potential differences. This means, the uncertainty budget needs to be adapted with regard to the potential distribution – a limit for Δm_{ν}^2 of about $-1.5 \times 10^{-3} \text{ eV}^2$ constitutes a reasonable and conservative approach.

5.5.2.3. Plasma potential and systematic neutrino mass uncertainty – an approximation

If the influence of radial potential inhomogeneity is small, the plasma potential can be approximated by a linear distribution as shown in [Mac16]. This can be used to derive a general relation between longitudinal potential inhomogeneity and induced neutrino mass shift.

To obtain this relation the plasma distributions from the two-dimensional plasma potential simulations $U(r, z)$ are simplified to one-dimensional distributions $U(r = 0, z)$. The radial average of the standard deviation of the longitudinal potential distributions is smaller than the corresponding standard deviation at $r = 0$ m for all values of Δ tested in the corresponding plasma simulations⁵⁴. Thus, the discussed one-dimensional approach can serve as an upper limit on $|\Delta m_\nu^2|$, since the absolute value of the deduced neutrino mass shift is slightly overestimated.

Still, it should be noted: To derive the sign of the neutrino mass shift the radial potential distribution needs to be considered. The slope of the longitudinal potential distribution can vary with the radial coordinate, as depicted in figure 5.61a, which has an influence on the sign of the induced shift.

Using several one-dimensional linear plasma profiles, the general influence of a given longitudinal potential inhomogeneity ΔU_z on the derived value of the neutrino mass squared is investigated. The results are depicted in figure 5.65.

The derived linear relation can be used to estimate the systematic neutrino mass squared shift that is induced by a given plasma distribution with maximal longitudinal potential inhomogeneity ΔU_z :

$$\Delta m_\nu^2 = (4.5 \pm 6.3 + (6.4 \pm 0.3) \cdot \Delta U / \text{mV}^{-1}) \cdot 10^{-5} \text{ eV}^2. \quad (5.96)$$

Thus, the sign of the systematic shift changes if the slope of the potential distribution changes sign (negative ΔU_z). This is completely different from what is expected from Gaussian potential distributions (see equation (5.91)) that cause in any case a negative neutrino mass squared shift.

This change in the polarity of the shift can be explained by looking at the potential probability distribution, introduced in section 5.5.2, for a longitudinal linear potential profile with positive and negative slope each. Both distributions are depicted in figure 5.66a. They are not symmetric with regard to their mean value. In the parameter estimation used in KATRIN a change in mean potential is compensated by a shift of the fit parameter E_0 , the endpoint energy. A changed slope of the potential distribution cannot be compensated that way. For negative slope of the longitudinal potential distribution there is a tail in the direction of lower potentials in the probability distribution, while for positive slope the tail is in the direction of larger potentials. The corresponding influence on the integrated spectrum is shown in figure 5.66b – The positive slope causes a rate increase near the endpoint energy while the negative slope causes a rate decrease. This corresponds to the positive and a negative neutrino mass squared shift, respectively, that was seen in the neutrino mass squared parameter estimation.

5.6. Summary

The knowledge of the retarding energy, which is the potential difference between the point of β -decay in the WGTS and the crossing point of the analysing plane in the spectrometer, is crucial for an accurate modelling of the electron spectrum measured at the detector. The potential in the WGTS is determined by plasma processes. The plasma inside the WGTS mainly consists of secondary electrons and ions, created by ionisation of tritium molecules by fast β -decay electrons. A dedicated modelling of the plasma formation in the WGTS and of its properties is required to calculate the potential distribution in the source.

In the scope of this chapter, a comprehensive WGTS plasma model was derived. Starting from the one-dimensional electron diffusion equation, it evolved by adding a second charged particle component, tritium ions, as well as a neutral gas species that determines

⁵⁴The standard deviation is calculated based purely geometric grounds, i.e., no density distributions or scattering probability distributions are included here.

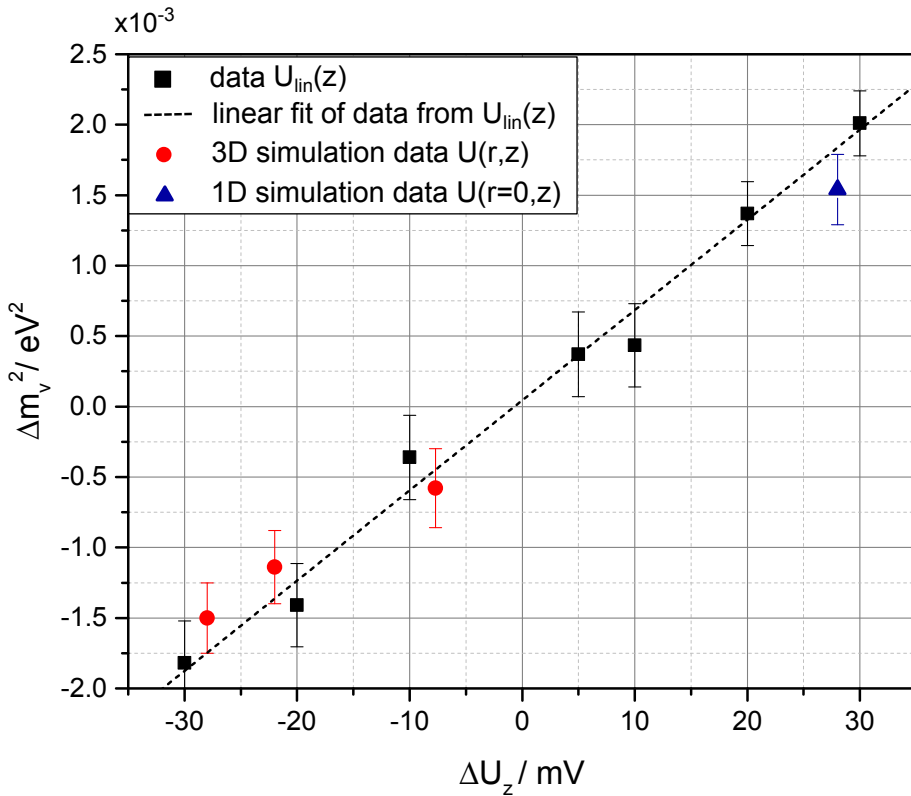


Figure 5.65.: **Systematic neutrino mass squared shifts Δm_ν^2 induced by different plasma profiles as function of the longitudinal plasma inhomogeneity ΔU_z .** Neutrino mass squared shifts are calculated for linear potential profiles $U_{\text{lin}}(z)$ (black squares) as well as for potential profiles (three-dimensional (red circles) and one-dimensional (blue triangles)) from plasma simulation. For all distributions ΔU_z corresponds to the maximal longitudinal potential inhomogeneity. The mass square shifts induced by the linear profile can be linked to ΔU_z using a linear fit to the data points: $\Delta m_\nu^2 = (4.5 + 6.4 \text{ mV}^{-1} \Delta U) \cdot 10^{-5} \text{ eV}^2$ ($\chi^2 = 1.79$, #d.o.f.=9). Mass shifts related to the potential profiles from plasma simulation are well within the range approximated with the linear approach.

For the linear, one-dimensional approximation to be applicable, the radial potential differences of the investigated potential distribution needs to be smaller than ΔU_z in the main part of the inner flux tube.

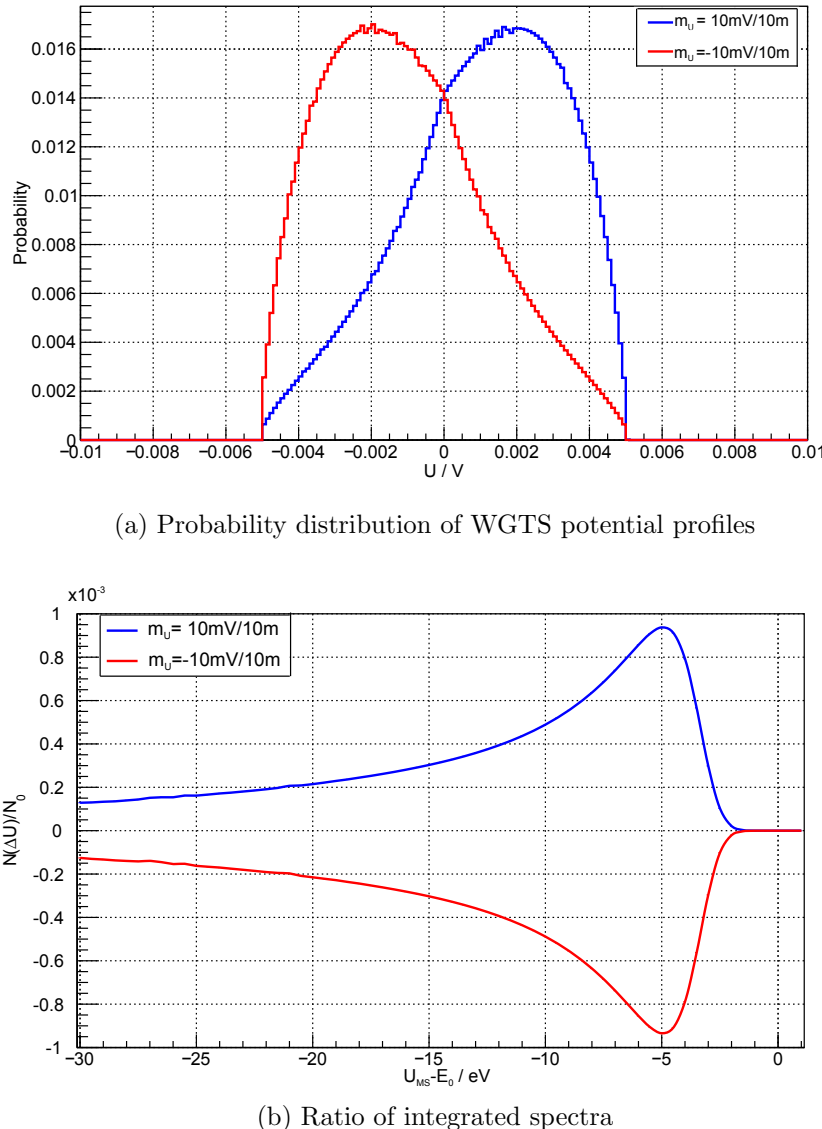


Figure 5.66.: **Probability distribution function and relative rate differences of integral electron spectra for linear potential profiles with different sign of slope.** The linear potential profiles related to the distributions shown have slopes of $m_U = \pm 10 \text{ mV}/10 \text{ m}$ and an offset of 0 V. The rates of the integrated spectra $\dot{N}(\Delta U)$ are plotted relative to rate for zero potential \dot{N}_0 as a function of the main spectrometer retarding potential. A nominal background rate of 10 mcps is considered. Probability and relative rate are given as a function of the difference between endpoint energy E_0 and retarding voltage U_{MS} .

the rate of particle creation as well as the charged particle mobilities. By including the Poisson equation the generation of space charges and related plasma potentials could be investigated.

In a next step, a two-dimensional model was built using the results from the previous model as initial conditions. The flow of neutral gas was included as convective component. The final step constitutes an axisymmetric plasma model. It is representative for the conditions present in the WGTS.

Since the model is sensitive to uncertainties of important parameters such as mobilities or rate coefficients, the influence of a variety of parameters on the actual potential and charged particle density distribution was tested. The general form of the solution was shown to be stable for the different configurations. Numerical instabilities, that occurred in previous analyses, were not encountered here.

Different boundary potential bias configurations as well as local and global work function inhomogeneities due to surface defects and adsorption were tested.

The results are summarised in the following:

- The potential difference between rear wall and lateral beam tube walls, Δ , is determining the plasma potential with regard to the rear wall. It also determines the homogeneity of the longitudinal potential distribution inside the WGTS.
- In general it can be noted that, the smaller $|\Delta|$, the more homogeneous is the potential distribution inside the plasma. An optimised longitudinal potential homogeneity can be reached if Δ is about $-T_e$.
- If Δ is below a critical value Δ_C , which is about -40 mV for standard KATRIN conditions and electrons thermalised at 30 K, the surface potential of the lateral beam tube walls penetrates into the bulk WGTS plasma. Otherwise, the rear wall potential mainly dominates the absolute value of the plasma. The difference between wall and plasma potential generally drops within a narrow plasma sheath, which is of the order of millimetre for the WGTS plasma.
- The potential inside the WGTS beam tube is related to the potential at the boundary walls, but its actual value deviates in either direction from the plasma potential determining wall surface potential due to the formation of space charge potentials. For $\Delta < \Delta_C$ the space charge potential becomes negative, as the electron outflow at the rear wall is hindered while ions can leave the plasma through front and rear direction. Negative space charges do also form when the electron flux gets saturated, since the ion flux through the lateral walls has a larger saturation value due to the larger beam tube surface. This happens for relatively large positive values of $\Delta \gtrsim 0.05$ V. These effects can, notwithstanding the somewhat different experimental conditions of the set-up, explain the negative space charge potential that was unexpectedly found in the WGTS plasma of the Troitsk Neutrino-Mass Experiment [BGZ⁰⁸].
- Surface inhomogeneities at the rear wall were shown in general not to penetrate through the whole plasma column but to be washed out already after several centimetres.

It was shown that the potential distribution that forms inside the WGTS depends on the actual geometric pattern of the inhomogeneities, at least for inhomogeneities of about 1 cm and larger. The longitudinal electron fluxes and their radial distribution as well as ion fluxes in radial and longitudinal direction need to be considered. For relatively large inhomogeneities these fluxes do depend on the geometric composition, i.e. their value and position with respect to the beam tube wall.

Depending on the actual width and surface potential shift of the surface inhomogeneity, it can even determine the whole plasma potential. The surface potential

needs to be averaged with the fluxes leaving the source to get an estimate of the potential that forms in the plasma. Such a flux averaged surface potential only weakly affects the longitudinal potential homogeneity – As long as the standard deviation of the surface potential is small, the plasma potential inhomogeneities remain small, as well.

- Lateral wall inhomogeneities do, like rear wall inhomogeneities, hardly penetrate into the plasma. This was tested for lateral wall surface potential differences up to 500 mV.

To estimate the effective wall potential that determines the absolute value of the plasma potential, the surface potential distribution needs to be weighted with the ion flux leaving the model at the corresponding position.

The adsorption induced surface potential profile likewise will not penetrate into the plasma as long as the average value of the rear wall-beam tube surface potential difference Δ is above a critical value Δ_C .

The influence of the adsorption profile on the bulk potential can be reduced by adapting the rear wall potential.

- If the boundary surfaces are on almost equal surface potential ($\Delta \leq 10$ mV) the KATRIN design potential homogeneity requirement of $\Delta U_z \leq 10$ mV can be reached. The same holds for reasonable patch potential configurations, that mainly influence the space charge potential and to a lesser extent the longitudinal homogeneity. Rear wall patch sizes up to 5 mm with patch potential differences up to 40 mV as well as lateral beam tube wall patches with sizes of 5 cm and patch potential differences from -100 mV to 500 mV were investigated.
- The krypton mode, that will be used to investigate the WGTS plasma potential distribution experimentally, was treated in dedicated simulations since the experimental conditions are different from the tritium measurement conditions (increased gas temperature of about 110 K). The gas temperature mainly determines the electron temperature, since the electrons are presumed to thermalise. The electron energy determines the outflow of electrons and thus the space charge potential. It was shown that for similar surface potential differences, the results of the WGTS potential inhomogeneity obtained with the krypton measurements at temperatures from 100 K to 150 K, can to a good approximation be scaled down to 30 K.
- The most critical prerequisite for achieving a homogeneous plasma potential is the compensation of the work function difference between rear wall and beam tube wall by the rear wall potential bias. In the krypton mode this optimised compensation can be achieved through analysis of the krypton lines. The resulting potential distribution can be assumed to have longitudinal potential differences smaller than 10 mV. Due to changes in the adsorption behaviour of tritium on the stainless steel wall between 110 K and 30 K the beam tube work function may shift by up to 130 mV. The rear wall potential bias needs to be changed from krypton to nominal tritium mode in order to compensate for this work function change.
- A number of general measurement procedures have been proposed to obtain the work function shift or to directly reduce the plasma inhomogeneity for the nominal 30 K tritium conditions.

The realistic source potential distributions created with the plasma model were used to investigate the systematic neutrino mass uncertainty caused by a non-constant potential profile. Large differences to the assumptions in [AAB⁺05] and [BGZ⁺08] were found. The relevance of the plasma potential for the neutrino mass determination with KATRIN is summarised in the following.

- It was shown that potential inhomogeneity σ and neutrino mass squared shift are not, as assumed in [AAB⁺05] and [BGZ⁺08], related to each other by $\Delta m_\nu^2 = -2\sigma^2$, given that the potential probability distribution in fact cannot be approximated by a Gaussian. To visualise the potential probability distribution, the number of electrons born at each potential value was calculated. Therefore, the potential distribution was connected to the product of electron density distribution and zero-scattering probability distribution. The obtained potential probability distribution was shown to be markedly different from a Gaussian distribution, which explains the increased neutrino mass squared shifts that were calculated.
- The minimal achievable neutrino mass squared shift is given by the WGTS configuration with all surfaces on equal potential. For the related plasma potential configuration, the purely space charge dominated neutrino mass squared shift is $\Delta m_\nu^2 = (-5.8 \pm 2.8) \cdot 10^{-4} \text{ eV}^2$.
- A reasonable sensitivity on the value of the absolute plasma potential that can be reached through the reduction of the surface potential difference using dedicated measurements is 60 mV. This is related to a longitudinal plasma inhomogeneity of about 22 mV which causes a neutrino mass squared shift of $\Delta m_\nu^2 = (-1.14 \pm 0.26) \cdot 10^{-3} \text{ eV}^2$.
- If adsorption induced work function shifts at the beam tube surface for a temperature change from 110 K to 30 K cannot be accessed by measurement, the work function change can be calculated based on modelling of adsorption processes. Considering the related uncertainties, the lowest surface potential difference that can be guaranteed to be adjusted is 110 mV. The related plasma potential with a maximal longitudinal inhomogeneity of 29 mV causes a neutrino mass squared shift of $(-1.5 \pm 0.25) \cdot 10^{-3} \text{ eV}^2$.
- The plasma potential distributions at constant radius can be approximated by linear distributions. Several potential distributions had been analysed. The derived linear relation between neutrino mass squared shift and longitudinal plasma inhomogeneity can be used to approximate the effect of any realistic WGTS plasma potential distribution.

The realistic model of the WGTS plasma processes and its boundary conditions reveal larger plasma potential differences and different contributions to the electron spectrum than expected at the outset of this thesis project. Thus, the systematic uncertainty budget related to the WGTS potential distribution needs to be adapted. In a conservative approach, the systematic neutrino mass squared uncertainty related to the plasma potential distribution should be quoted with $1.5 \times 10^{-3} \text{ eV}^2$. Still, the actual potential inhomogeneity and related neutrino mass effect strongly depend on the knowledge of the configuration of surface potential differences between rear wall and beam tube wall.

6. Conclusions and Outlook

The KATRIN experiment will mark a major milestone in the field of neutrino physics as it will enter the sub-electronvolt scale of absolute neutrino masses with an unequalled sensitivity of 200 meV (90% C.L.) in a direct, kinematic measurement. Thereby, it constitutes a new generation of neutrino mass experiments. The measurement with KATRIN is based on the kinematic approach of high precision spectroscopy of single β -decay of tritium using the well established MAC-E filter principle. Predecessor experiments that applied this method were able to set the current best model-independent direct neutrino mass limit of 2.0 eV (95% C.L.). To be sensitive to a mass scale one order of magnitude below the current limit, the KATRIN experiment needs to combine a tritium source providing a large signal rate (β -decay rate $>10^{11} \text{ s}^{-1}$) with a spectrometer featuring an excellent energy resolution (below 1 eV at 18.6 keV).

The ambitious sensitivity goal sets high requirements regarding the understanding and control of systematic effects influencing the shape of the measured β -decay spectrum. The proper modelling of the physical processes in the tritium source is of major importance to be able to either take these effects into account in the neutrino mass analysis, or to rate their impact on the outcome of this analysis reliably.

In the thesis at hand the characteristics of a variety of processes related to the rarefied gas flow and plasma properties of the source have been evaluated constructing comprehensive models. This simulation results have been implemented in the calculation of source spectra and have been used to quantify the impact each of the analysed processes and their respective modelling uncertainties have on the neutrino mass analysis with KATRIN.

Gas dynamics properties of the source

One of the main systematic uncertainties of the KATRIN experiment is related to the description of the scattering of signal β -decay electrons on gas molecules in the source. To be able to reliably model these scattering processes which influence the shape of the electron spectrum measured with KATRIN the product of column density and scattering cross section needs to be known with an uncertainty below 0.2%.

In order to calculate the column density accurately, the previous KATRIN gas model, which consisted solely of the 10 m WGTS beam tube, needed to be extended with gas flow calculations of the pump ports and beam tubes of the DPS1 since a non-vanishing fraction of the gas remains in these domains.

Due to the complexity of the modelling of rarefied gas flow as well as large differences in geometry and gas flow characteristics of the components mentioned above, each of them

had to be simulated in a separate model. To be able to combine these calculations to a gas model covering the whole source section, the already existing beam tube gas model had to be overhauled.

As a result, all but about 1% of the total column density was shown to be present in the central 10 m beam tube part of the source. This demonstrates the necessity for the gas density in the simulated components to be included in the source modelling to match 0.2% accuracy requirement on integrated density. On the other hand, it relaxes the accuracy demands on the gas flow modelling in the pumping section. A gas flow reduction factor of 400 was calculated for the combination of both pump ports in the DPS1 while the gas density was shown to be reduced by a factor of 2000 when entering the DPS2.

The accuracy of the column density calculated with the implemented gas model was shown to be determined by the uncertainty of the gas flow modelling in the 10 m beam tube. To get a reliable estimate on the uncertainty related to the model assumptions, a second simulation that used a different approach for the calculation of the transport equations was set up. Column density results of both models were shown to agree within 1% while their density distributions showed discrepancies up to 15% in the outlet regions (the differences in calculated velocities are even larger).

Considering the limited knowledge of the transport parameters as well as of the input values for inlet and outlet pressure, the overall model column density uncertainty exceeds the 0.2% accuracy requirement by far – a direct determination of the product from column density and scattering cross section using the electron gun in the rear section is thus indispensable. Such a measurement was shown not only to reach a column density times scattering cross section accuracy of 0.2%. It can also be used to relax the requirement on the knowledge of the value of the total scattering cross section, for which literature currently provides an accuracy of only 2%.

The column density may be subject to changes in between the absolute e-gun measurements due to fluctuations of source operation parameters. Different activity measurements will be used to monitor if the column density stability exceeds 0.2% during KATRIN operation. In this thesis work it was demonstrated that the gas model can be used to account for these changes in the calculation of the β -decay spectrum of the source. Its relatively low accuracy in the description of the absolute column density notwithstanding, the model can be used to compute column density changes for variations of operational parameters up to the per cent level precisely. Dedicated investigations including all model dependent uncertainties as well as those related to the input parameters verified the applicability of the gas model to calculate small relative column density changes. Assuming a design per mill stability of operation parameters, the uncertainty related to the monitoring of the column density can be pushed down from the initially proposed 2×10^{-3} to 3×10^{-4} . This allows to relax the requirement on the e-gun measurement determining the absolute value of the column density from 1.4×10^{-3} to 1.9×10^{-3} .

In addition to the modelling of the integrated quantity, column density, the influence of the actual distribution of the gas density through the source section was investigated in the scope of this thesis work – the accurate description of the gas distribution in the source section forms the basis to include the distribution of all other source variables: temperature, magnetic field, velocity and electric potential correctly in the calculation of the source spectrum. To get a handle on the required density accuracy level, various models of the density and velocity distributions were compared in ensemble simulations. The largest impact was shown to be related to the velocity distribution – comparing realistic distributions from the two beam tube model simulations, a non-vanishing neutrino mass shift of $(-7.5 \pm 2.4) \cdot 10^{-4} \text{ eV}^2$ was calculated underlining the importance of the use of accurate models for the distributions of density and velocity.

Since only the product of column density and scattering cross section can be determined

by an absolute measurement, it was tested whether a column density and scattering cross section accuracy of 2% is sufficient as long as the product is known to an accuracy of 0.2%. This question was shown to be related to the above mentioned source inhomogeneities – in case of a homogeneous source the individual values of the parameters in the product of column density and scattering cross section cannot be distinguished. Using a realistic source model it was shown that the particular uncertainties of both parameters can influence the neutrino mass analysis – but only if they are larger than about 5%. The effect from an uncertainty of 2% was shown to be almost indistinguishable from zero.

Combining all mentioned uncertainties related to the gas dynamical properties of the source with a model containing realistic distributions of temperature, magnetic field and potential in a dedicated ensemble test revealed a neutrino mass squared shift of $(3.06 \pm 0.24) \cdot 10^{-3} \text{ eV}^2$. Despite being larger than the limiting value, the uncertainty related to the gas dynamical description of the source can be regarded to be well under control since the given number includes several uncertainties that have not been considered in the design report (the single uncertainty related to the gas dynamical properties of the source that was respected in the investigations in the design report was the monitoring uncertainty of the column density).

Different test measurements to be performed during the commissioning of the KATRIN beam line are proposed that will allow to verify the predictions of the gas model.

Plasma phenomena in the source

The emission of β -decay electrons leads to the formation of a cold, low density plasma in the source by a large number of secondary ionisation processes. The electric fields present in the plasma determine the potential distribution inside the WGTS. This distribution is of large importance since it determines the starting potential energy of the electrons produced in the β -decay of tritium in the source.

In this thesis work an extensive plasma model was constructed. Starting from an one-dimensional approach considering the electron transport driven by diffusion and external electric fields, it evolved to a two-dimensional axial-symmetric three-fluid plasma description including the internal electric field produced by the formation of space charges.

Different from previous approaches, the model solutions do not exhibit numerical instabilities and were shown to be stable under the variation of various plasma parameters.

The source plasma is confined by the beam tube steel surface in radial direction and by the gold surface of the rear wall in longitudinal direction (rear direction). Being a conductive surface hit by the magnetic flux tube and the confined plasma particles, the rear wall was designed to determine the plasma potential. How the work function difference of about 1 eV between the steel surface and the gold plated rear wall influences the plasma potential distribution was unknown.

By virtue of extension in radial direction, it was possible to investigate the influence of these boundary surface potential differences with the newly developed plasma model. A difference of 1 eV between beam tube and rear wall surface was found to produce a large plasma potential inhomogeneity of about 250 meV along the beam tube axis. A boundary potential difference of about 100 mV still causes a plasma potential inhomogeneity of about 25 meV, already more than twice as large as the limit for differences in the plasma potential distribution stated in the KATRIN design report. In contrast to what has been expected, large voltage differences between the plasma confining surfaces cause the plasma to charge negatively – depending on the sign of the difference, either the outflow of electrons is blocked by a negative electric field in the direction of flow while the ions are still able to leave the domain, or the electron flux saturates while the ion flux can still increase due to the larger surface of the beam tube (only ions can reach the beam tube walls due to the magnetic confinement of the much less massive electrons).

The optimised boundary configuration that produces the highest possible potential homogeneity was shown to be present in case of a rear wall surface potential slightly more negative than the beam tube surface (the difference is of the order of the electron temperature e.g., about 3.9 mV for 30K). Setting all boundaries to equal potential produces similar results – for the equipotential case, the maximal inhomogeneity along the beam tube axis was found to be about 6-7 meV.

Since the surfaces can not be assumed to exhibit a homogeneous work function, the influence of variously distributed inner surface potentials with differences of diverse sizes on the plasma and its potential distribution was also investigated. Looking at the rear wall, the material-specific inhomogeneities are small (not larger than 10 meV). Still, due to tritium adsorbing at its surface larger shifts of the order of 30 mV may occur.

A detailed analysis of various rear wall surface potential differences revealed that, different than previously assumed, the rear wall surface potential distribution does not penetrate through the whole length of the flux tube – its structures are washed out on a scale of centimetres or even millimetres in longitudinal direction. This means that the radial inhomogeneity of the plasma does not increase in case of a large number of rear wall patches. The absolute value of the space charge potential is, however, strongly influenced even by small scale potential differences.

The work function of the beam tube material has significantly larger inhomogeneities (up to 1 eV). In addition, tritium has a high probability to adsorb on the beam tube surface. An approximation of the relevant adsorption processes showed a position dependent adsorption profile which is connected to the pressure profile along the tube. The induced work function differences of 26 meV were however shown to hardly penetrate into the plasma volume, they are washed out after several millimetres. The same holds for small scale surface inhomogeneities, patches of magnitudes from -0.1 V to 0.5 V were investigated but had only minor influences on the plasma homogeneity (at least if the rear wall was biased accordingly).

It can be concluded: differences (of reasonable magnitude) across a single plasma facing surface are not harmful for KATRIN, whereas discrepancies between different surfaces can have a large impact.

Biassing the rear wall at a certain voltage can in principle balance the work function difference of beam tube and rear wall. Measurements with monoenergetic electrons from $^{83\text{m}}\text{Kr}$ circled in the source were shown to give access to that difference which is not known a priori. Still, due to the different beam tube temperature required for the krypton measurements (about 110K), the behaviour of tritium adsorption along the tube wall is expected to change.

Different methods are proposed to investigate the boundary potential differences for nominal tritium operation conditions – the lowest surface potential differences that can be verified to be established is 60 mV involving a plasma potential inhomogeneity of 20 mV.

The probability distribution function of the potential profile that builds up in the source was shown not to be Gaussian, in contrast to what has been assumed before. Therefore, the effect on the derived neutrino mass is larger than expected – the smallest achievable neutrino mass squared shift, related to a configuration with all boundary surfaces at equipotential and a plasma potential inhomogeneity smaller than 6 mV, was derived to be $(-5.8 \pm 2.8) \cdot 10^{-4}\text{ eV}^2$.

The equipotential case is probably not attainable for realistic experimental conditions. To give a conservative approximation, a reasonable boundary potential difference of 110 meV was assumed for which a neutrino mass squared shift of $(-1.5 \pm 0.25) \cdot 10^{-3}\text{ eV}^2$ was derived. The latter should be quoted as representative value of a systematic neutrino mass squared uncertainty related to plasma processes in the source.

Outlook

Commissioning of the components of the source section and of the full KATRIN beam line has started and is proceeding at the time of completion of this thesis.

This inactive commissioning phases offers the unique chance to test and verify the gas model experimentally. A number of measurements have been proposed that have to be executed in these phases, before the apparatus is first loaded with tritium. It needs to be tested whether the outcome of these measurements matches the predictions of the gas model. In case of discrepancies, the model needs to be reviewed. Otherwise, it can be applied in the neutrino mass analysis.

An open issue with regard to the gas model is the connection to a large number of sensors, supplying among others temperature and pressure information, whose data are needed for real-time source modelling. Large efforts have already been made providing the relevant tools.

The plasma model needs to be investigated once there is a reasonable amount of tritium in the source, which will only be after completion of the inactive phases. The general approach with recommendations for essential test measurements was presented in this thesis. Detailed measurement plans need to be worked out.

Validating the predictions of the constructed models is the last step in understanding and rating the plasma and gas dynamical processes of the source. Verifying that the induced systematic uncertainties are under control is an important step to reach the 200 meV neutrino mass sensitivity with KATRIN.

Appendix

A. Calculation of flow in the cooling tubes

To model the convective heat transfer in the cooling fluids of the pump port cooling system, simulated in section 3.3.1, a coupling between heat transfer and fluid flow simulation is required. For the pump port modelling, this is achieved using an iterative procedure.

The flow of the coolants liquid nitrogen and helium through the cooling tubes is simulated in order to obtain the pressure and velocity distribution for the calculation of the convective heat transfer in section 3.3.1. The model is build in COMSOL Multiphysics, using the fluid flow module [COM14a]. The geometry of the cooling pipe, adapted to the test model in section 3.3.1, is depicted in figure A.1. Laminar flow is assumed for both modelled coolants (nitrogen and helium) and their pressure and velocity distributions are calculated based on the Navier-Stokes equations.

The starting point is an isothermal flow simulation with fixed fluid and wall temperatures. Fixed pressures are used for inlet (N₂: 5 bar, He: 1.5 bar) and outlet (N₂: 4 bar, He: 1.3 bar) boundary conditions. The simulated velocity and pressure distribution of the fluid is used as input for the calculation of the temperature distribution along the boundaries of the cooling pipe as described in section 3.3.1.

In a second step, the wall temperature distribution is implemented as boundary condition to model the non-isothermal flow through the cooling pipe. The calculated pressure and velocity distributions are implemented in the test model in section 3.3.1 providing a more accurate calculation of the convective heat transfer. In principle, this procedure can be continued further.

The described procedure is executed for different amounts of incoming heat from the radiating test surface in section 3.3.1, since its temperature affects the temperatures of the cooling pipe surfaces. The velocity and pressure distributions hardly change for the different tested temperatures of the radiating surface since also the temperature of the coolant hardly changes. The velocity distributions at the outlet boundary of the modelled cooling tube are plotted for both coolants in figure A.2.

B. Calculation of bellow heat transfer coefficients

In order to simplify the model and reduce the number of mesh elements needed to resolve the pump port geometry, all bellows in the model are replaced by cylindrical tubes. The validity of such an approach with respect to transported radiation heat was shown in [Jan15] within an uncertainty below 10%. The geometry of such a bellow is depicted in figure B.3. The length off the tube l is the same as the effective length of the bellow, its width is the width w of the bellow. The tube inner radius r is calculated from outer and inner radius, r_{\min} and r_{\max} of the bellow:

$$r = \frac{r_{\max} + r_{\min}}{2} - \frac{w}{2}. \quad (6.1)$$

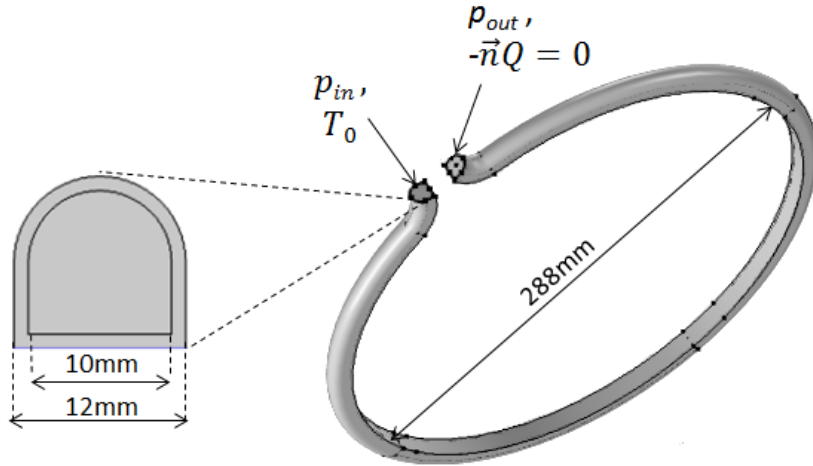


Figure A.1.: Geometry of tube model for coolant flow simulation.

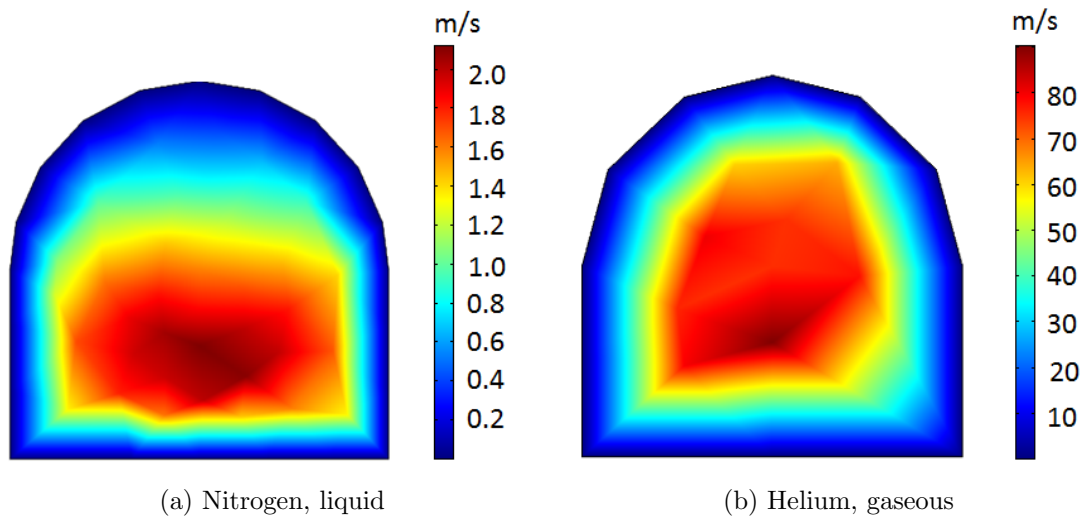


Figure A.2.: **Outlet velocity distributions of nitrogen and helium coolant.** The temperature of the corresponding radiating surface is 120 K for the shown nitrogen results and 80 K for given helium results.

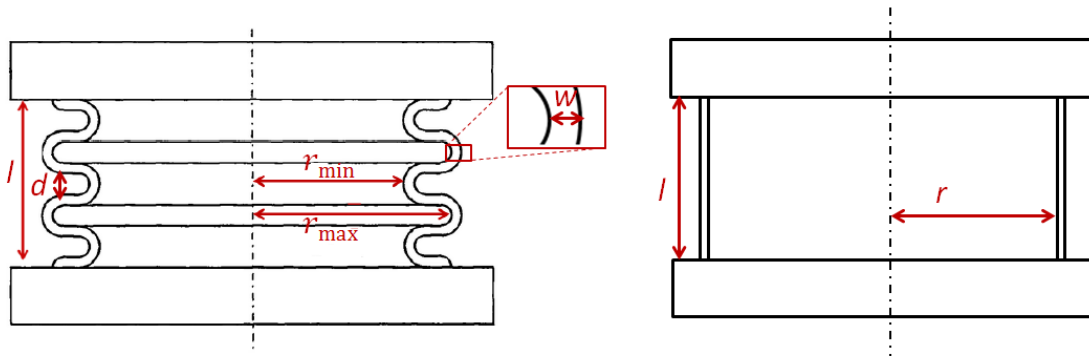


Figure B.3.: Bellow and adjusted cylinder geometry.

In order to transport the same amount of conductive heat, the conductivity of the bellow needs to be adjusted. Using equation (3.2) one gets:

$$k \frac{A}{l} \Delta T = k_0 \Delta T \frac{A_0}{l_0}. \quad (6.2)$$

The length of the unfolded bellow l_0 can be calculated with:

$$l_0 = 16(r_{\max} - r_{\min} - d) + (n + 0.5)\pi d, \quad (6.3)$$

here n denotes the number of slats and d is the slat diameter with:

$$d = \frac{l - w}{2n + 1} - w. \quad (6.4)$$

Thus, the bellows average area A_0 can be calculated using:

$$A_0 = \frac{\pi \left(\left((r_{\min} + w)^2 - r_{\min}^2 \right) + \left(- (r_{\max} - w)^2 + r_{\max}^2 \right) \right)}{2}. \quad (6.5)$$

Plugging this in equation (6.2,) the conductivity of the cylinder gets:

$$k = k_0 \frac{A_0 l}{A l_0}. \quad (6.6)$$

The geometries of the different bellows and corresponding adjusted conductivities for the cylinders used in the simulations in chapter 3 are summarised in table B.1.

Table B.1.: Geometry data and adjusted conductivities for bellows used in the heat transfer models of the DPS1 pump ports. The conductivity k of the corresponding cylinders is given in terms of the initial material conductivity k_0 .

domain	r_{\max} in mm	r_{\min} in mm	l in mm	w in mm	n	k/k_0
Bellow WGTS beam tube	68.5	52	68	0.4	7	0.25
Bellow DPS1F beam tube	118.5	57	43	0.3	4	0.44
1st bellow tube to TMP	157.5	140	125	0.4	7	0.38
2nd bellow tube to TMP	155.5	140	125	0.4	7	0.4
Bellow before DPS2	71.1	49	95	0.3	11	0.162
Bellow after DPS1R	68.5	52	92	0.4	10	0.23

C. Technical data MAG W 2800

Technische Daten

Produkt: TURBOVAC MAG W 2800
 Katalog-Nr.: 400006V0071

Anschlussflansch Saugseite:	DN 250 CF	
Anschlussflansch Druckseite:	DN 40 ISO-KF	
Saugvermögen		
N ₂ - Stickstoff:	2400 l/s	
Ar - Argon:	2450 l/s	
He - Helium:	2650 l/s	
H ₂ - Wasserstoff:	2100 l/s	
Gasdurchsatz		
N ₂ - Stickstoff:	- - -	
Ar - Argon:	- - -	
He - Helium:	- - -	
H ₂ - Wasserstoff:	- - -	
Kompressionsverhältnis		
N ₂ - Stickstoff:	1,0 x 10 ⁹	
Ar - Argon:	- - -	
He - Helium:	- - -	
H ₂ - Wasserstoff:	- - -	
Enddruck:	< 1,0 x 10 ⁻¹⁰ mbar	< 7,5 x 10 ⁻¹¹ Torr
Max. Vorpakuumdruck für N ₂ :	3,0 mbar	2,3 Torr
Nenndrehzahl:	28800 min ⁻¹	28800 rpm
Hochlaufzeit:	≈ 10 min	
Max. Leistungsaufnahme:	1100 W	
Leistungsaufnahme bei Enddruck:	100 W	
Schutzart:	IP 20	
Zulässige Umgebungstemperatur:	5 - 40°C	41 - 104°F
Kühlung standard:	Wasser	
Kühlung optional:	- - -	
Kühlwasseranschluss:	1/4" Rohr	
Kühlwasserverbrauch:	120 - 350 l/h	
Zulässiger Kühlwasserdruk:	2 - 7 bar	
Zulässige Kühlwassertemperatur:	10 - 30°C	50 - 86°F
Abmessungen:	siehe Maßblatt	
Gewicht:	≈ 75,0 kg	≈ 165,6 lbs

Technische Änderungen vorbehalten

Copyright © Oerlikon Leybold Vacuum GmbH

Figure C.4.: Technical data sheet for the Leybold Turbovac MAG W 2800 from [Oer16].

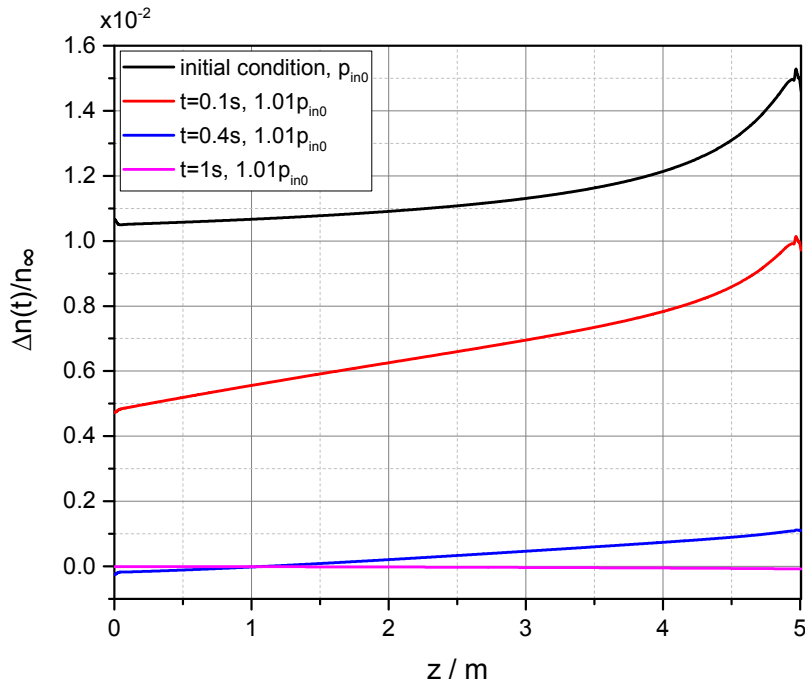


Figure D.5.: **Relative difference in density distribution at different times after a small inlet pressure disturbance.** The initial inlet pressure, $p_{0\text{in}}$, is ramped up within 0.1 s to $1.01p_{0\text{in}}$. The density distribution at time t is given relative to the equilibrium density after the disturbance ($n(t \rightarrow \infty) = n_\infty$). The initial condition for $p_{0\text{in}}$ is shown in black. Equilibrium is reached again after about 1 s, shown in magenta.

D. Simulation of characteristic time scale for pressure changes

To get an estimate for the time scale τ at which a change in the set of operational WGTS parameters can be properly reflected by the gas model, the time the gas flow needs to reach equilibrium conditions after a small temporal disturbance of flow needs to be known. Therefore, a disturbance of 1% is introduced in the WGTS beam tube model that was presented in section 4.2.5. The stationary solution of the beam tube model is used as initial condition. Then, the inlet pressure is ramped up within 0.1 s to $1.01 \cdot p_{0\text{in}}$.

The principle of solution for the time dependent problem works similar to the stationary problem. The variable time is used as parameter and the problem is solved separately for the conditions present at each time with small steps in between the analysed times.

For the elevated inlet pressure, the equilibrium condition ($n(t > \tau) = n(t \rightarrow \infty) = n_\infty$), with equilibrium density n_∞ , is reached about 1 s after the gas flow disturbance induced by the increased pressure. In figure D.5 the longitudinal distribution of the relative ratio of time dependent density with respect to the equilibrium density ($(n(t) - n_\infty)/n_{infty} = \Delta n(t)/n_{infty}$) is shown. Already after about 0.4 s, which is about twice the time a gas molecule needs to pass the beam tube from the injection to the outlet in front or rear direction¹, the disturbance is almost washed out.

E. Modelling of pump port pressure changes

To obtain a relation between pump port inlet pressure, which equals the exit pressure in the gas dynamic calculation inside the 10 m WGTS beam tube in section 4.2.3, a two-dimensional model of the pump port is build as depicted in figure E.6. Different from

¹Due to the elevated bulk gas velocity computed in this model, the time scale is shorter than in the Sharipov density model.

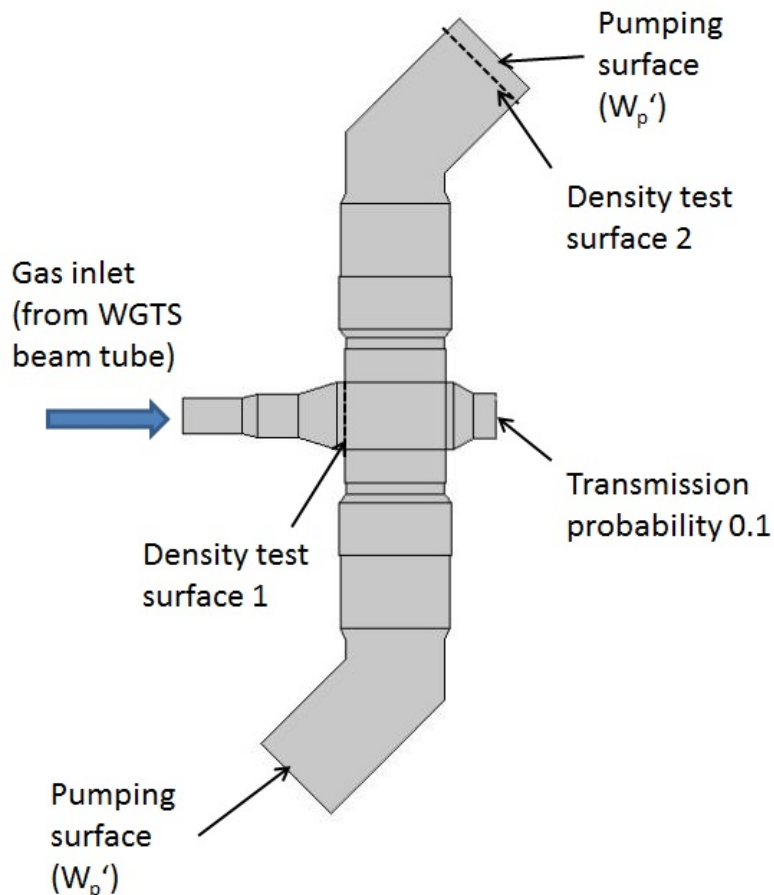


Figure E.6.: **Scheme of the two-dimensional first pump port model in the DPS1.**

The inlet density profile is taken from the WGTS beam tube density simulation described in section 4.2.5. The pumping probability is varied by $\pm 50\%$. Then the relative density change at test surfaces 1 (beam tube outlet) and 2 (next to the pump) are compared.

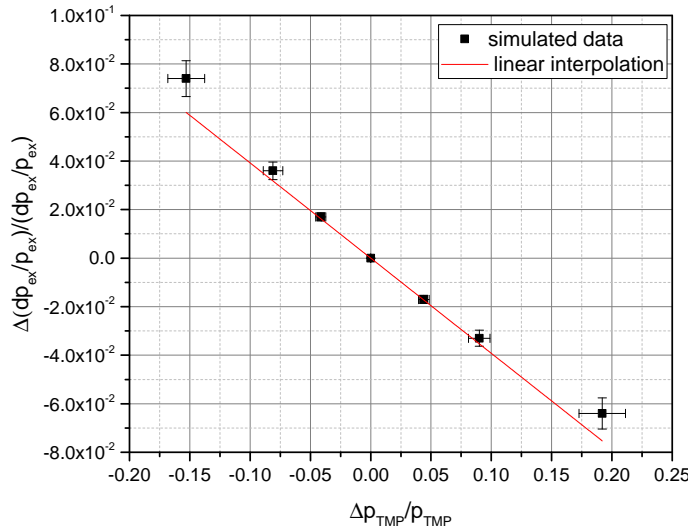


Figure E.7.: **Uncertainty of relative relative WGTS beam tube outlet pressure change $\Delta(dp_{\text{ex}}/p_{\text{ex}})/(dp_{\text{ex}}/p_{\text{ex}})$. It is given as a function of the pressure changes measured by the pressure sensor next to the TMPs at the first pump port of the DPS1 $\Delta p_{\text{TMP}}/p_{\text{TMP}}$.**

the model in section 4.2.6, it includes the ducts to the TMPs and thus also the position where pressure sensors are situated² The model inlet pressure equals the pressure at the corresponding position in the beam tube calculation described in section 4.2.5 for a WGTS beam tube injection pressure of 0.34 Pa. The outlet in the longitudinal direction is represented by a pumping surface with transmission probability 0.1. The position of the first rotor blades of the TMP is also represented by a pumping surface. The initial transmission probability at the TMP surface is set to 0.275 and varied by 50%.

From the resulting pressure distribution, the change in averaged pressure values from surface 1 (WGTS beam tube outlet pressure p_{ex} as used in the density calculation for the central 10 m WGTS beam tube) and surface 2 (pressure at the position of the pressure sensor, p_{TMP}) are compared. The calculation is performed using the *transitional flow* module within the COMSOL software package, as already described in section 4.2.5. Since the pump port cannot be assumed to be accurately represented by a two-dimensional geometry, an uncertainty of 10% is adopted for each evaluated density change. The resulting relation between relative uncertainty in the calculation of the pressure change $\frac{\Delta p_{\text{ex}}}{p_{\text{ex}}}$ and the pressure change that can be measured by the pressure sensors next to the TMPs $\frac{\Delta p_{\text{TMP}}}{p_{\text{TMP}}}$ is depicted in figure E.7. Both changes are approximately connected³ by a factor of 0.4

$$\frac{\Delta (dp_{\text{ex}}/p_{\text{ex}})}{(dp_{\text{ex}}/p_{\text{ex}})} \approx 0.4 \cdot \frac{\Delta p_{\text{TMP}}}{p_{\text{TMP}}}. \quad (6.7)$$

Thus, taking the pressure changes measured by the sensor next to the TMP for the pressure change of the beam tube exit pressure, an uncertainty of 40% for needs to be considered for $\Delta(dp_{\text{ex}}/p_{\text{ex}})/(dp_{\text{ex}}/p_{\text{ex}})$ in the gas model in section 4.4.

²The pump port model described in section 4.2.6 is three-dimensional and cannot include the full pump port up to the TMPs due to the complex Monte Carlo flow calculation.

³ for variations of p_{TMP} below 20%

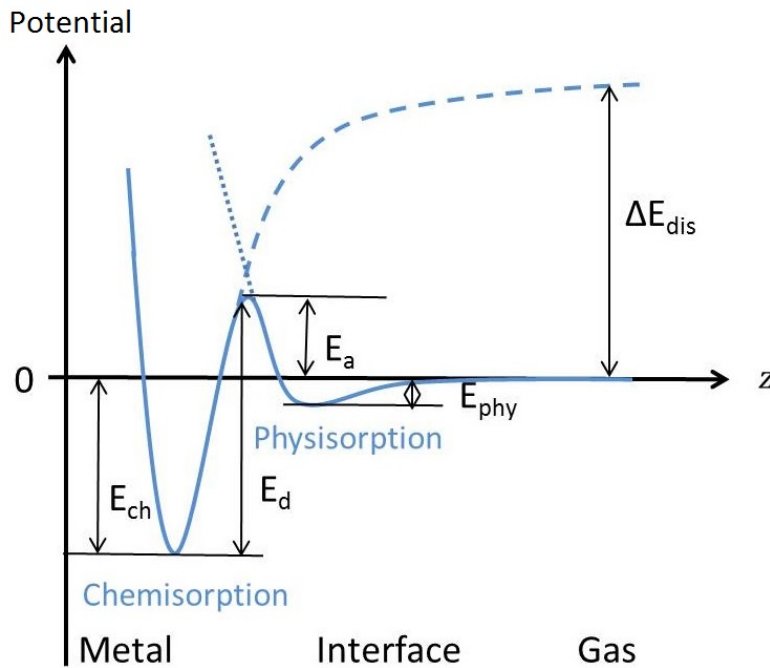


Figure F.8.: **Types and energies of adsorption depending on the distance to the surface.** The zero energy state corresponds to the ground state of a molecule in the gas phase. E_{phy} denotes the binding energy for physisorption, E_{ch} the adsorption energy for chemisorption. Depending on the crossing point of chemisorption and physisorption curves (corresponding energy E_a), the chemisorption process is activated or spontaneous. ΔE_{dis} denotes the dissociation energy from molecular state in two atoms.

F. Modelling of tritium adsorption at the WGTS tube walls

It is important to have an estimate for the work function shift due to the adsorption of tritium at the WGTS beam tube walls. Therefore, the actual amount of adsorbed tritium and its profile needs to be known. The equilibrium coverage θ is determined by adsorption, surface diffusion, desorption and permeation processes. The process of gas adsorption depends on the structure of the solid and the gas molecule. In general there are two kinds of adsorption: chemisorption and physisorption. They have large differences in their adsorption strength. Gas particles can be adsorbed in molecular state through van der Waals forces – This process is called physisorption. The binding is quite weak, as it is formed through fluctuations in the electronic shell [Str11]. A stronger binding with a covalent character can be achieved through chemisorption. Here, the molecule is usually first dissociated and the two atoms are bound separately [Chr88]. The energies involved in the different processes of adsorption (and desorption) are summarised in figure F.8. Depending on the crossing point of the physisorption and chemisorption potential energy curve, E_a , the dissociative chemisorption process can have an activation barrier (if $E_a > 0$). This barrier influences the kinetics of adsorption as it modifies the sticking probability s which then reads $s' = s \cdot e^{-\frac{E_a}{kT}}$. For non-activated adsorption the barrier vanishes, $E_a = 0$. On most metal surfaces, the dissociative adsorption of Hydrogen (and its isotopes) is non-activated [BMP08] like for hydrogen adsorbing on iron surfaces [PS85]. Therefore, the adsorption of tritium at the stainless steel walls of the WGTS beam tube is assumed to be non-activated.

The sticking probability s is approximately equal to 1 for cold molecular hydrogen isotopes that adsorb on a pre-adsorbed hydrogen isotope layer (multilayer adsorption). For

adsorption on a cold steel surface (in the first layer), the sticking probability is reduced. The actual value strongly depends on the surface properties as well as surface and gas temperatures [Sou86]. A sticking probability of 0.5 for hydrogen molecules on stainless steel was stated in [Bas80, Bas81]. The sticking probability of tritium should be comparable [Sou86], therefore a value of 0.5 is used in the following for the modelling of tritium adsorbing on the WGTS beam tube walls in the first layer.

The binding energy of physisorption for molecular hydrogen is low. It is in the range of -1 kJ mol^{-1} to -10 kJ mol^{-1} [Züt03, DS99]. For gas temperatures lower than the critical temperature (for hydrogen this is about 33 K [LMM76]) the formation of multilayers of adsorbed molecules is possible [Dab01]. In this case, the adsorption energy of the second and following layers is often stated to be equal to the energy of condensation ΔQ_{con} [Str11, Züt03, BET38] of the adsorbed substance. For hydrogen the energy of condensation is about -0.9 kJ mol^{-1} [Chr88] and for tritium at 30 K roughly -1.5 kJ mol^{-1} [Sou86].

Depending on the actual smoothness of the surface, a second monolayer can be necessary to saturate the surface for which the interaction of the adsorbed particle with the initial surface can be neglected [MJS01, Wan15]. Therefore, in the following calculations, the binding energy of the second layer is assumed to be equal to the energy of physisorption E_{phy} , which is higher than the energy of condensation. In [MJS01] the desorption characteristics of molecular hydrogen physisorbed on stainless steel (The energy of desorption for physisorbed molecules is equal to the inverse energy of adsorption, see figure F.8.) were measured. In this measurement two desorption peaks appear at 1.6 kJ mol^{-1} and at 6.03 kJ mol^{-1} , with a suppressed desorption intensity of the second peak. In a conservative approximation (leading to an increased adsorption probability in the second layer), the binding energy of hydrogen physisorbed on stainless steel is taken to be the average of both measured values and thus $-3.82 \text{ kJ mol}^{-1}$ ⁴. In [GS12] the isotopic effect on the energy of adsorption for different hydrogen isotopes is stated to be small. For physisorption of hydrogen and deuterium on graphite, the difference in adsorption potentials was found to be about 4 to 8% [OR62, KSJE72]. Since no data for the energy of physisorption for T_2 on stainless steel are available, the binding energy found for hydrogen is increased by 10% which yields a physisorption energy of -4.2 kJ mol^{-1} that is used in the following calculations.

The binding energy for the dissociatively adsorbed hydrogen atoms that are directly bound on the steel surface, E_{ch} , is about -87 kJ mol^{-1} [BBC⁺03].

For the process of desorption of the different adsorption layers two cases have to be distinguished, depending on the actual type of adsorption: dissociative desorption and desorption of physisorbed molecules.

In order to desorb at temperatures below the binding energy, chemisorbed atoms need to recombine with each other. In the recombination process a large enough amount of energy ΔE_{dis} is released and the molecule is able to leave the strongly bound chemisorption state (see figure F.8). Thus, the rate of dissociative desorption is determined by the surface recombination rate. Atoms adsorbed at the surface can only recombine if another atom is near enough and thus, the recombination rate is determined by surface diffusion processes.

The kinetics of adsorption is often described using the model proposed by Langmuir [Lan18]:

$$R_{\text{ad}} = \frac{s}{n_{\text{max}}} f(\theta) \frac{p}{\sqrt{2\pi k_B T m}} \quad (6.8)$$

$$\text{with: } f(\theta) = \begin{cases} 1 - \theta & \text{for molecular adsorption} \\ (1 - \theta)^2 & \text{for dissociative adsorption,} \end{cases} \quad (6.9)$$

⁴It should be noted, that the adsorption energy strongly depends on the surface cleanliness and smoothness as well as on adsorbed oxide or water layers. Generally, the desorption energy for hydrogen molecules physisorbed on metals is below 5 kJ mol^{-1} [GS12].

Here m denotes the mass of the adsorbed species, θ the number of occupied adsorption sites compared to the total number of adsorption sites (θ is also called coverage), n_{\max} the material dependent number of surface sites for adsorption ($\theta = 1$ for filled monolayer), and p the pressure of the gas in front of the surface. For the WGTS stainless steel tube the number of surface sites is estimated to be about $2 \times 10^{19} \text{ m}^{-25}$ [BEGW77].

Using equation (6.8) the adsorption rate R_{ad} for adsorption below the monolayer coverage depends on the number of free surface sites ($1 - \theta$). The Brunauer-Emmett-Teller description [BET38] of adsorption extends the Langmuir model to the adsorption of multilayers. It is assumed, that once a particle is adsorbed, it can either desorb or a second particle adsorbs directly at the first particle which causes the maximal number of adsorption sites within a single layer n_{\max} to be equal for each layer and the total number of adsorbed particles can be written: $n_{\text{a}} = n_{\max} \cdot \theta$. Thus, the adsorption rate for the first layer and following multilayers reads:

$$R_{\text{ad},1} = \frac{s_1}{n_{\max}} (1 - \theta)^2 \frac{p}{\sqrt{2\pi k_{\text{B}} T m}} \quad \theta \leq 1 \quad (6.10)$$

$$R_{\text{ad}} = \frac{s}{n_{\max}} \frac{p}{\sqrt{2\pi k_{\text{B}} T m}} \quad 1 < \theta, \text{ for zeroth order adsorption.} \quad (6.11)$$

s_1 denotes the sticking probability for adsorption at the metal surface (adsorption in the first layer) and s the sticking probability for adsorption at the already adsorbed hydrogen layer(s).

Only the particles in the particular uppermost layer can be desorbed. For the first layer, which is assumed to be chemisorbed, the desorption is determined by molecular recombination of the adsorbed atoms and thus by the diffusion process, as the atoms need to diffuse over the surface in order to find a partner to recombine. The recombination rate is thus assumed to be equal to the desorption rate from the first layer which can be written:

$$R_{\text{des},1} = -2k_{\text{rec}} \exp\left(-\frac{E_{\text{dif}}(1 - \theta)}{N_{\text{A}} k_{\text{B}} T}\right) \theta^2 c_1^2 \quad \theta \leq 1 \quad (6.12)$$

with coefficient k_{rec} , activation energy for diffusion, E_{dif} , and species surface concentration c_1 . Since it is a second order process, the rate depends on θ^2 . The activation energy for diffusion of deuterium on a stainless steel surface is about 13.6 kJ mol^{-1} and the corresponding rate coefficient $k_{\text{rec}} \approx 8.4 \times 10^{-26} \text{ m}^2 \text{ s}^{-1}$ [BEWW80]. The activation energies of the different hydrogen isotopes for the diffusion in stainless steel were found to be comparable. Thus, the deuterium data are used for the description of tritium surface diffusion. The desorption of the physisorbed molecules (for $\theta > 1$) is a first order process [MJS01]. However, in [Wan15] the desorption process of higher layers (larger than one) is stated to be zeroth order and does thus not depend on the coverage. As given above, the desorption energy E_{d} for the second layer is assumed to be -4.2 kJ mol^{-1} . For the third layer the interaction with the initial metal surface is negligible, thus $E_{\text{d}} = -\Delta Q \approx 1.5 \text{ kJ mol}^{-1}$. Thus, the desorption rates from the second layer ($R_{\text{des},2}$) and from layer i , with $i > 2$, ($R_{\text{des},i}$) can be calculated

$$R_{\text{des},2} = -\nu \exp\left(-\frac{E_{\text{d}}}{N_{\text{A}} k_{\text{B}} T}\right) (\theta - 1) n_{\max} \quad \theta = 2, \quad (6.13)$$

$$R_{\text{des},i} = -\nu \exp\left(-\frac{\Delta Q}{N_{\text{A}} k_{\text{B}} T}\right) n_{\max} \quad 2 < \theta \leq i. \quad (6.14)$$

The frequency factor $\nu \approx 1 \times 10^{12} \text{ s}^{-1}$ represents the surface vibration frequency of weakly adsorbed molecules [Laf98, VRM⁺05].

Atoms adsorbed at the surface can also diffuse through the bulk and leave the material

⁵The value was measured for a Fe(110) surface.

at the opposite surface. This process is called permeation. For steady state conditions, which means a vanishing concentration gradient in the bulk material, the permeation rate R_{per} can be written in terms of the pressure difference $p - p'$ between both surface sides using *Richardson's law* [LKNH11]:

$$R_{\text{per}} = -KD \frac{p^{0.5} - p'^{0.5}}{d}. \quad (6.15)$$

Here d denotes the thickness of the material, K the solubility and D the bulk diffusivity. The pressure in the WGTS cryostat outside of the beam tube is low compared to the pressure in the beam tube. In this case p' can be set to zero in equation (6.15).

For tritium in stainless steel the literature values for the solubility and diffusivity are: $K = 0.194 \text{ mol}/(\text{m}^3 \text{Pa}^{0.5}) e^{-\frac{10.2 \text{ kJ}}{N_A k_B T}}$ [SFOI84], and $D = 5.9 \times 10^{-7} \text{ m}^2 \text{ s}^{-1} e^{-\frac{51.9 \text{ kJ mol}^{-1}}{N_A k_B T}}$ [RFG93].

To approximate the coverage profile of the tritium adsorbed at the WGTS stainless steel walls, the *Surface Reactions* module of COMSOL is used [Mul14a]. An one-dimensional model of the beam tube surface starting from the injection ($z = 5 \text{ m}$) to the end of the central WGTS beam tube ($z = 10 \text{ m}$) is build. The density of the gas molecules impinging on the beam tube surface is taken from the gas dynamics calculation in section 4.2. The equations (6.10) to (6.14) as well as relation 6.15 are used to calculate the adsorption and desorption rates for the different layers:

$$\frac{\delta c_i(z)}{\delta t} = -\frac{\delta \phi_m}{\delta z} + R_{\text{ad},i} + R_{\text{des},i} + R_{\text{per}}, \quad (6.16)$$

with c_i denoting the adsorbed tritium surface concentration in the i^{th} layer and ϕ_m the molecular surface diffusion flux. The surface diffusion term, with surface diffusivity $D_{\text{surf}} = 1.8 \times 10^{-5} e^{\frac{14.8 \text{ kJ mol}^{-1}}{k_B T N_A}}$ [BEWW80], is included for the atoms adsorbed within the first layer, as the ad- and desorption rates within the first two layers depend on the local coverage:

$$\phi_m = -D_{\text{surf}} \nabla c_i, \quad (6.17)$$

The resulting tritium coverage is depicted in figure F.9. The first monolayer is saturated over the whole beam tube surface due to the relatively large activation energy for surface diffusion which causes a low recombination rate in this layer. The second layer is partially filled with a difference of 0.14 momolayers between injection and beam tube end region. The tritium gas density profile is additionally plotted in figure F.9 to compare the slope of both profiles. The slope discrepancy is mainly caused by the second layer desorption process, that is coverage dependent and thus changes the linear dependency of adsorbed gas and free gas density. The strong dependence of the coverage profile on the desorption energy E_d of the second layer should be noted here – If E_d is only slightly reduced from 4.2 kJ mol^{-1} to 4 kJ mol^{-1} the coverage profile changes to almost constant monolayer coverage with only 3% difference, as the rate of desorption is strong and reduces the number of molecules adsorbed in the second layer almost completely. Thus, the 14% difference in longitudinal coverage constitutes, with respect to the induced work function change (larger work function shift for larger amount of adsorbed tritium), a conservative approximation. One should keep in mind that the beam tube surface is not perfectly smooth. There are defects or impurities that can trap the gas molecules as the adsorption energy is increased at this positions [MJS01]. This would cause small scale structures in the coverage distribution. Still, if these defects are of reasonable small size they should not disturb the form of the coverage profile.

Results for $T = 110 \text{ K}$

Compared to 30 K , the adsorption properties at 110 K are different since the above mentioned processes contributing to the kinetics of adsorption and desorption are strongly

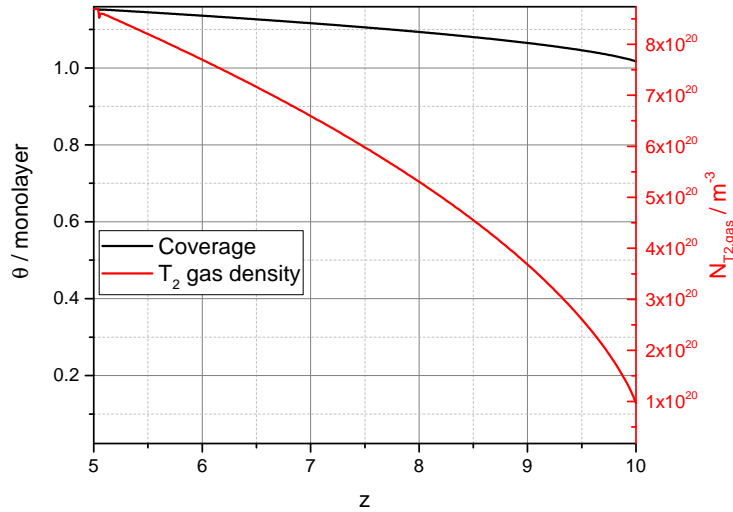


Figure F.9.: **Simulated tritium monolayer coverage along WGTS tube at 30 K.**

The underlying tritium gas profile (red line) in front of the inner tube surface is depicted in addition. Mind the corresponding different axes and scales.

temperature dependent. To be able to use data from the krypton measurements (performed at 110 K) for the optimisation of the rear wall bias voltage (section 5.4.2) the adsorption induced work function shift between both temperature conditions needs to be known. This can be approximated, when the difference in T_2 coverage between both temperatures is known. Therefore, the adsorption model presented above is used to calculate the number of adsorbed monolayers at 110 K. Here the gas density profile from the calculations at 30 K is used. The inlet pressure is adapted for the 110 K measurement in order to reach the same column density for both temperatures.

The calculated beam tube tritium coverage for 110 K is depicted in figure F.10. The average coverage is about 0.34 and the difference in average coverage between 30 K and 110 K is about 0.75 monolayer.

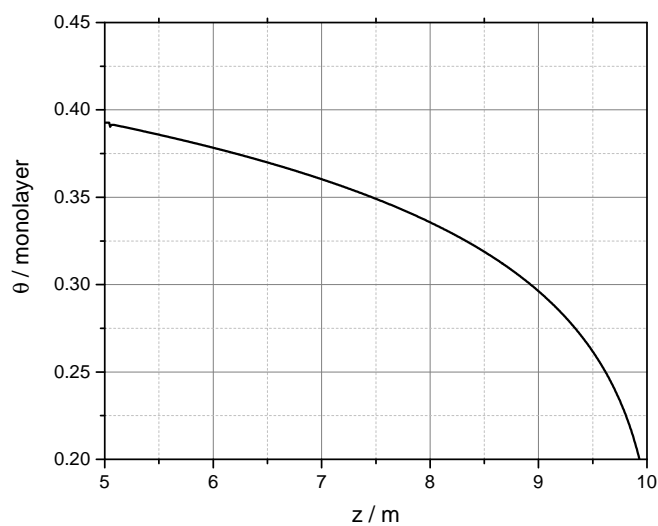


Figure F.10.: Simulated tritium coverage along WGTS tube for 110 K.

Bibliography

[AAA⁺01] Q. Ahmad, R. Allen, T. Andersen, J. Anglin, G. Bühler, J. Barton, E. Beier, M. Bercovitch, J. Bigu, S. Biller, et al. Measurement of the Rate of $\nu_e + d \rightarrow p + p + e^-$ Interactions Produced by B₈ Solar Neutrinos at the Sudbury Neutrino Observatory. *Physical Review Letters*, 87(7):071301, 2001. doi: 10.1103/PhysRevLett.87.071301.

[AAA⁺02] Q. Ahmad, R. Allen, T. Andersen, J. Anglin, J. Barton, E.W. Beier, M. Bercovitch, J. Bigu, S. Biller, R. Black, et al. Direct evidence for neutrino flavor transformation from neutral-current interactions in the Sudbury Neutrino Observatory. *Physical Review Letters*, 89(1):011301, 2002. doi: 10.1103/PhysRevLett.89.011301.

[AAA⁺13a] M. Agostini, M. Allardt, E. Andreotti, A. Bakalyarov, M. Balata, I. Barabanov, M. Barnabé Heider, N. Barros, L. Baudis, C. Bauer, et al. Results on Neutrinoless Double- β Decay of Ge 76 from Phase I of the GERDA Experiment. *Physical Review Letters*, 111(12):122503, 2013. <https://doi.org/10.1103/PhysRevLett.111.122503>.

[AAA⁺13b] B. Aharmim, S. Ahmed, A. Anthony, N. Barros, E. Beier, A. Bellerive, B. Beltran, M. Bergevin, S. Biller, K. Boudjemline, et al. Combined analysis of all three phases of solar neutrino data from the Sudbury Neutrino Observatory. *Physical Review C*, 88(2):025501, 2013. <https://doi.org/10.1103/PhysRevC.88.025501>.

[AAA⁺14] R. Adam, P. Ade, N. Aghanim, Y. Akrami, M. Alves, M. Arnaud, F. Arroja, J. Aumont, C. Baccigalupi, M. Ballardini, et al. Planck 2015 results. I. Overview of products and scientific results. *Astronomy & Astrophysics*, 571:A1, 2014. <http://dx.doi.org/10.1051/0004-6361/201527101>.

[AAA⁺15] K. Abe, J. Adam, H. Aihara, T. Akiri, C. Andreopoulos, S. Aoki, A. Ariga, S. Assylbekov, D. Autiero, M. Barbi, et al. Neutrino oscillation physics potential of the T2K experiment. *Progress of Theoretical and Experimental Physics*, 2015(4):043C01, 2015. doi: 10.1093/ptep/ptv031.

[AAA⁺16] K. Abe, C. Andreopoulos, M. Antonova, S. Aoki, A. Ariga, S. Assylbekov, D. Autiero, M. Barbi, G.J. Barker, G. Barr, et al. Measurement of muon antineutrino oscillations with an accelerator-produced off-axis beam. *Physical review letters*, 116(18):181801, 2016. <https://doi.org/10.1103/PhysRevLett.116.181801>.

[AAB⁺05] J. Angrik, T. Armbrust, A. Beglarian, U. Besserer, J. Blümmer, J. Bonn, R. Carr, B. Bornschein, L. Bornschein, T. Burritt, et al. KATRIN design report 2004. *Wissenschaftliche Berichte FZKA*, 7090, 2005. Available at: <http://bibliothek.fzk.de/zb/berichte/FZKA7090.pdf>.

[AAB¹³] F. An, Q. An, J. Bai, A. Balantekin, H. Band, W. Beriguete, M. Bishai, S. Blyth, R. Brown, G. Cao, et al. Improved measurement of electron antineutrino disappearance at Daya Bay. *Chinese Physics C*, 37(1):011001, 2013. doi: 10.1088/1674-1137/37/1/011001.

[AAB¹⁶] M. Agostini, M. Allardt, A. Bakalyarov, M. Balata, I. Barabanov, L. Baudis, C. Bauer, N. Becerici-Schmidt, E. Bellotti, S. Belogurov, et al. Search of Neutrinoless Double Beta Decay with the GERDA Experiment. *Nuclear and Particle Physics Proceedings*, 273:1876–1882, 2016. <http://dx.doi.org/10.1016/j.nuclphysbps.2015.09.303>.

[ABB⁰⁰] V. Aseev, A. Belesev, A. Berlev, E. Geraskin, O. Kazachenko, Y. E. Kuznetsov, V. Lobashev, R. Ostroumov, N. Titov, S. Zadorozhny, et al. Energy loss of 18 keV electrons in gaseous T and quench condensed D films. *The European Physical Journal D-Atomic, Molecular, Optical and Plasma Physics*, 10(1):39–52, 2000. doi: 10.1007/s100530050525.

[ABB⁰³] M. Apollonio, A. Baldini, C. Bemporad, E. Caffau, F. Cei, Y. Declais, H. De Kerret, B. Dieterle, A. Etenko, L. Foresti, et al. Search for neutrino oscillations on a long base-line at the CHOOZ nuclear power station. *The European Physical Journal C-Particles and Fields*, 27(3):331–374, 2003. doi: 10.1140/epjc/s2002-01127-9.

[ABB⁰⁵] M. Altmann, M. Balata, P. Belli, E. Bellotti, R. Bernabei, E. Burkert, C. Cattadori, R. Cerulli, M. Chiarini, M. Cribier, et al. Complete results for five years of GNO solar neutrino observations. *Physics Letters B*, 616(3):174–190, 2005.

[ABB⁰⁹] I. Antcheva, M. Ballintijn, B. Bellenot, M. Biskup, R. Brun, N. Buncic, P. Canal, D. Casadei, O. Couet, V. Fine, et al. Root – A C++ framework for petabyte data storage, statistical analysis and visualization. *Computer Physics Communications*, 180(12):2499–2512, 2009. doi:10.1016/j.cpc.2009.08.005.

[ABB¹¹] V. Aseev, A. Belesev, A. Berlev, E. Geraskin, A. Golubev, N. Likhovid, V. Lobashev, A. Nozik, V. Pantuev, V. Parfenov, et al. Upper limit on the electron antineutrino mass from the Troitsk experiment. *Physical Review D*, 84(11):112003, 2011. doi: 10.1103/PhysRevD.84.112003.

[ABB¹²] F. An, J. Bai, A. Balantekin, H. Band, D. Beavis, W. Beriguete, M. Bishai, S. Blyth, K. Boddy, R. Brown, et al. Observation of electron-antineutrino disappearance at Daya Bay. *Physical Review Letters*, 108(17):171803, 2012. <https://doi.org/10.1103/PhysRevLett.108.171803>.

[ABB¹⁵] F. An, A. Balantekin, H. Band, M. Bishai, S. Blyth, I. Butorov, G. Cao, J. Cao, W. Cen, Y. Chan, et al. New measurement of antineutrino oscillation with the full detector configuration at Daya Bay. *Physical Review Letters*, 115(11):111802, 2015. <https://doi.org/10.1103/PhysRevLett.115.111802>.

[ABB¹⁶] M. Arenz, M. Babutzka, M. Bahr, J. Barrett, S. Bauer, M. Beck, A. Beglarian, J. Behrens, T. Bergmann, U. Besserer, et al. Commissioning of the vacuum system of the KATRIN Main Spectrometer. *Journal of Instrumentation*, 11(04):P04011, 2016. Available at:<http://stacks.iop.org/1748-0221/11/i=04/a=P04011>.

[ABdV¹⁵] D. M. Asner, R. Bradley, L. de Viveiros, P. J. Doe, J. L. Fernandes, M. Fertl, E. C. Finn, J. Formaggio, D. Furse, A. M. Jones, et al. Single-electron detection and spectroscopy via relativistic cyclotron radiation. *Physical review letters*, 114(16):162501, 2015. <https://doi.org/10.1103/PhysRevLett.114.162501>.

[ACC⁺11] K. Abazajian, E. Calabrese, A. Cooray, F. De Bernardis, S. Dodelson, A. Friedland, G. Fuller, S. Hannestad, B. Keating, E. Linder, et al. Cosmological and astrophysical neutrino mass measurements. *Astroparticle Physics*, 35(4):177–184, 2011. <http://dx.doi.org/10.1016/j.astropartphys.2011.07.002>.

[ACC⁺12] J. K. Ahn, S. Chebotaryov, J. Choi, S. Choi, W. Choi, Y. Choi, H. Jang, J. Jang, E. Jeon, I. Jeong, et al. Observation of reactor electron antineutrinos disappearance in the RENO experiment. *Physical Review Letters*, 108(19):191802, 2012. <https://doi.org/10.1103/PhysRevLett.108.191802>.

[AFG⁺11] S. Abe, K. Furuno, A. Gando, Y. Gando, K. Ichimura, H. Ikeda, K. Inoue, Y. Kibe, W. Kimura, Y. Kishimoto, et al. Measurement of the 8 B solar neutrino flux with the KamLAND liquid scintillator detector. *Physical Review C*, 84(3):035804, 2011. doi: 10.1103/PhysRevC.84.035804.

[AG97] F. J. Alexander and A. L. Garcia. The direct simulation Monte Carlo method. *Computers in Physics*, 11(6):588, 1997. <http://www.algarcia.org/Pubs/DSMC97.pdf>.

[AK14] M. Ady and .R Kersevan. Introduction to the latest version of the test-particle monte carlo code molflow+. Technical report, CERN, 2014. Available at: <http://test-molflow.web.cern.ch/>.

[AMW86] M. Assael, S. Mixafendi, and W. A. Wakeham. The viscosity and thermal conductivity of normal hydrogen in the limit of zero density. *Journal of physical and chemical reference data*, 15(4):1315–1322, 1986. doi: 10.1063/1.555764.

[AMW87] M. Assael, S. Mixafendi, and W. A. Wakeham. The viscosity of normal deuterium in the limit of zero density. *Journal of physical and chemical reference data*, 16(2):189–192, 1987. <http://dx.doi.org/10.1063/1.555778>.

[Ant15] J. Antoni. Monte Carlo Simulations of Systematic Effects due to Inelastic Scattering in the KATRIN Tritium Source, 2015. diploma thesis, Karlsruhe Institute of Technology.

[AP08] A. Agrawal and S. Prabhu. Survey on measurement of tangential momentum accommodation coefficient. *Journal of Vacuum Science & Technology A*, 26(4):634–645, 2008. Available at: <http://dx.doi.org/10.1116/1.2943641>.

[AVV⁺02] J. Abdurashitov, E. Veretenkin, V. Vermul, V. Gavrin, S. Girin, V. Gorbachev, P. Gurkina, G. Zatsepina, T. Ibragimova, A. Kalikhov, et al. Solar neutrino flux measurements by the Soviet–American gallium experiment (SAGE) for half the 22-year solar cycle. *Journal of Experimental and Theoretical Physics*, 95(2):181–193, 2002. doi:10.1134/1.1506424.

[B⁺11] M. Babutzka et al. The Comprehensive Guide to Kasper, 2011. KATRIN internal document, Available at: <https://nuserv.uni-muenster.de/doc/Kasper/develop/KasperGuide.pdf>.

[Bab14] M. Babutzka. *Design and development for the Rearsection of the KATRIN experiment*. PhD thesis, Karlsruhe Institute of Technology, 2014.

[Bab15] M. Babutzka. Column density measurement by the e-gun, 2015. KATRIN internal talk at STS meeting 11th May 2015.

[Bar36] J. Bardeen. Theory of the work function. II. The surface double layer. *Physical Review*, 49(9):653, 1936. <https://doi.org/10.1103/PhysRev.49.653>.

[Bar99] R. F. Barron. *Cryogenic heat transfer*. CRC Press, 1999.

[Bas80] M. Baskes. A calculation of the surface recombination rate constant for hydrogen isotopes on metals. *Journal of nuclear Materials*, 92(2):318–324, 1980. doi: 10.1016/0022-3115(80)90117-8.

[Bas81] M. Baskes. Hydrogen recycling from stainless steel. *Journal of Nuclear Materials*, 99(2):337–339, 1981. doi: 10.1016/0022-3115(81)90205-1.

[Bay03] ZAE Bayern. Bestimmung des Emissionsgrades von 5 beschichteten Strahlungsproben. report, Forschungszentrums Karlsruhe Institut für Technische Physik, 2003. Report ZAE 2-0903-12.

[BB49] M. A. Biondi and S. C. Brown. Measurement of electron-ion recombination. *Physical Review*, 76(11):1697, 1949. <https://doi.org/10.1103/PhysRev.76.1697>.

[BB02] M. J. Brunger and S. J. Buckman. Electron–molecule scattering cross-sections. I. Experimental techniques and data for diatomic molecules. *Physics reports*, 357(3):215–458, 2002. [http://dx.doi.org/10.1016/S0370-1573\(01\)00032-1](http://dx.doi.org/10.1016/S0370-1573(01)00032-1).

[BBB⁺12] M. Babutzka, M. Bahr, J. Bonn, B. Bornschein, A. Dieter, G. Drexlin, K. Eitel, S. Fischer, F. Glück, S. Grohmann, et al. Monitoring of the operating parameters of the KATRIN Windowless Gaseous Tritium Source. *New Journal of Physics*, 14(10):103046, 2012. doi: 10.1088/1367-2630/14/10/103046.

[BBC⁺03] J. Bacher, C. Benvenuti, P. Chiggiato, M. Reinert, S. Sgobba, and A. Brass. Thermal desorption study of selected austenitic stainless steels. *Journal of Vacuum Science & Technology A*, 21(1):167–174, 2003. doi: 10.1116/1.1527953.

[BCDJR85] J. Bahcall, B. Cleveland, R. Davis Jr., and J. Rowley. Chlorine and gallium solar neutrino experiments. *The Astrophysical Journal*, 292:L79–L82, 1985. doi: 10.1086/184477.

[BDJ76] J. N. Bahcall and R. Davis Jr. Solar neutrinos: a scientific puzzle. *Science*, 191:264–267, 1976. <https://www.bnl.gov/bnlweb/raydavis/Science-01-23-76.pdf>.

[BEGW77] F. Bozso, G. Ertl, M. Grunze, and M. Weiss. Chemisorption of hydrogen on iron surfaces. *Applications of Surface Science*, 1(1):103–119, 1977. doi: 10.1016/0378-5963(77)90009-5.

[Bel16] G. Bellini. The impact of Borexino on the solar and neutrino physics. *Nuclear Physics B*, 908:178–198, 2016. <http://dx.doi.org/10.1016/j.nuclphysb.2016.04.011>.

[Ber65] A. Berman. Free molecule transmission probabilities. *Journal of Applied Physics*, 36(10):3356–3356, 1965. <http://dx.doi.org/10.1063/1.1702984>.

[BES80] J. R. Bond, G. Efstathiou, and J. Silk. Massive neutrinos and the large-scale structure of the universe. *Physical Review Letters*, 45(24), 1980. <http://journals.aps.org/prl/pdf/10.1103/PhysRevLett.45.1980>.

[BET38] S. Brunauer, P. H. Emmett, and E. Teller. Adsorption of gases in multimolecular layers. *Journal of the American chemical society*, 60(2):309–319, 1938. doi: 10.1021/ja01269a023.

[BEWW80] M. Braun, B. Emmoth, F. Waelbroeck, and P. Wienhold. Determination of deuterium surface recombination rates on stainless steel. *Journal of Nuclear Materials*, 93:861–865, 1980. doi: 10.1016/0022-3115(80)90219-6.

[BGK54] P. L. Bhatnagar, E. P. Gross, and M. Krook. A model for collision processes in gases. I. small amplitude processes in charged and neutral one-component systems. *Physical review*, 94(3):511, 1954. <http://journals.aps.org/pr/pdf/10.1103/PhysRev.94.511>.

[BGZ⁺08] A. Belesev, E. Geraskin, B. Zhiukov, S. Zadorozhny, O. Kazachenko, V. Kohanuk, N. Lihovid, V. Lobashev, A. Nozik, V. Parfenov, et al. Investigation of space-charge effects in gaseous tritium as a source of distortions of the beta spectrum observed in the Troitsk neutrino-mass experiment. *Physics of atomic nuclei*, 71(3):427–436, 2008. doi: 10.1134/S1063778808030046.

[BHL10] M. Bonitz, N. Horing, and P. Ludwig, editors. *Introduction to Complex Plasmas*. Springer, 2010.

[Bil10] S. Bilenky. *Introduction to physics of massive and mixed neutrinos*. Springer, 2010.

[Bir78] G. Bird. Monte Carlo simulation of gas flows. *Annual Review of Fluid Mechanics*, 10(1):11–31, 1978. <http://www.annualreviews.org/doi/pdf/10.1146/annurev.fl.10.010178.000303>.

[BL95] F. Becker and Z.-L. Li. Surface temperature and emissivity at various scales: Definition, measurement and related problems. *Remote Sensing Reviews*, 12(3-4):225–253, 1995. doi: 10.1080/02757259509532286.

[BM90] J. Brian and A. Mitchell. The dissociative recombination of molecular ions. *Physics reports*, 186(5):215–248, 1990. doi: 10.1016/0370-1573(90)90159-Y.

[BMP08] C. Borchers, T. Michler, and A. Pundt. Effect of hydrogen on the mechanical properties of stainless steels. *Advanced Engineering Materials*, 10(1-2):11–23, 2008. doi: 10.1002/adem.200700252.

[Bod11] T. Bode. Experimentelle Untersuchung der thermischen Eigenschaften der KATRIN-Tritiumquelle am WGTS-Demonstrator. Master’s thesis, Karlsruhe Institute of Technology, 2011.

[BP34] H. Bethe and R. Peierls. The neutrino. *Nature*, 133(3362):532, 1934.

[BP77] S. M. Bilenky and B. Pontecorvo. Lepton mixing and the solar neutrino puzzle. *Comments on Nuclear and Particle Physics*, 7(5):149–152, 1977.

[BPT80] G. Beamson, H. Porter, and D. Turner. The collimating and magnifying properties of a superconducting field photoelectron spectrometer. *Journal of Physics E: Scientific Instruments*, 13(1):64, 1980. <http://iopscience.iop.org/0022-3735/13/1/018>.

[BR54] M. McD Baker and E. K. Rideal. Chemisorption on metals. *Nature*, 174:1185–1186, 1954. doi: 10.1038/1741185a0.

[Bro14] M. Brongsgeest. *Physics of Schottky electron sources: theory and optimum operation*. CRC Press, 2014.

[BSB05] J. N. Bahcall, A. M. Serenelli, and S. Basu. New solar opacities, abundances, helioseismology, and neutrino fluxes. *The Astrophysical Journal Letters*, 621(1):L85, 2005. <http://iopscience.iop.org/article/10.1086/428929/pdf>.

[c⁺14] EXO-200 collaboration et al. Search for Majorana neutrinos with the first two years of EXO-200 data. *Nature*, 510(7504):229–234, 2014. doi: 10.1038/nature13432.

[CAC48] S. Curran, J. Angus, and A. Cockcroft. Beta spectrum of tritium. *Nature*, 162(4112):302–302, 1948. doi: 10.1038/162302a0.

[CAC49] S. Curran, J. Angus, and A. Cockcroft. The beta-spectrum of tritium. *Physical Review*, 76(6):853, 1949. <https://doi.org/10.1103/PhysRev.76.853>.

[Cam13] M. Campanell. Negative plasma potential relative to electron-emitting surfaces. *Physical Review E*, 88(3):033103, 2013. <https://doi.org/10.1103/PhysRevE.88.033103>.

[CCG05] B.-Y. Cao, M. Chen, and Z.-Y. Guo. Temperature dependence of the tangential momentum accommodation coefficient for gases. *Applied Physics Letters*, 86(9):091905, 2005. <http://dx.doi.org/10.1063/1.1871363>.

[CDDJ⁺98] B. T. Cleveland, T. Daily, R. Davis Jr., J. R. Distel, K. Lande, C. Lee, P. S. Widenhain, and J. Ullman. Measurement of the solar electron neutrino flux with the Homestake chlorine detector. *The Astrophysical Journal*, 496(1):505, 1998. <http://stacks.iop.org/0004-637X/496/i=1/a=505>.

[CEIN00] J. Casas, J. R. Espinosa, A. Ibarra, and I. Navarro. Nearly degenerate neutrinos, supersymmetry and radiative corrections. *Nuclear Physics B*, 569(1):82–106, 2000. [http://dx.doi.org/10.1016/S0550-3213\(99\)00605-7](http://dx.doi.org/10.1016/S0550-3213(99)00605-7).

[Cha32] J. Chadwick. Possible existence of a neutron. *Nature*, 129(3252):312, 1932. <http://www.nature.com/physics/looking-back/chadwick/chadwick.pdf>.

[Cho16] S. Choubey. Atmospheric neutrinos: Status and prospects. *Nuclear Physics B*, 908:235–249, 2016. <http://dx.doi.org/10.1016/j.nuclphysb.2016.03.026>.

[Chr88] K. Christmann. Interaction of hydrogen with solid surfaces. *Surface Science Reports*, 9(1):1–163, 1988. doi: 10.1016/0167-5729(88)90009-X.

[CL71] C. Cercignani and M. Lampis. Kinetic models for gas-surface interactions. *Transport Theory and Statistical Physics*, 1(2):101–114, 1971. <http://dx.doi.org/10.1080/00411457108231440>.

[CO12] L. G. Christophorou and J. K. Olthoff. *Fundamental electron interactions with plasma processing gases*. Springer Science & Business Media, 2012.

[col] NuMECS collaboration. NuMECS Positioning Paper. <https://p25ext.lanl.gov/~kunde/NuMECS/>.

[col16] KATRIN collaboration. KATRIN STS Operational Readiness Phase III, 2016. KATRIN internal document, collection of measurement proposals for the inactive commissioning phase IIIa.

[COM14a] COMSOL. *COMSOL 5.0, Molecular Flow Module User's Guide*, 2014.

[COM14b] COMSOL. *COMSOL 5.0, Plasma Module User's Guide*, 2014.

[COM14c] COMSOL. COMSOL Multiphysics Reference Manual, October 2014. version 5.0, Available at <http://www.comsol.com>.

[COM14d] COMSOL. COMSOL Multiphysics Users Guide, October 2014. version 5.0, Available at: <http://www.comsol.com>.

[Cor14] T. Corona. *Methodology and application of high performance electrostatic field simulation in the KATRIN experiment*. PhD thesis, University of North Carolina at Chapel Hill, 2014. Available at: <https://cdr.lib.unc.edu/record/uuid:6f44a9c2-f053-404a-b726-b960d5772619>.

[CR04] G. Chen and L.L. Raja. Fluid modeling of electron heating in low-pressure, high-frequency capacitively coupled plasma discharges. *Journal of applied physics*, 96.11:6073–6081, 2004. <http://dx.doi.org/10.1063/1.1818354>.

[CRH⁺56] C. L. Cowan, F. Reines, F. B. Harrison, H. W. Kruse, and A. D. McGuire. Detection of the Free Neutrino: a Confirmation. *Science*, 124:103–104, 1956. doi: 10.1126/science.124.3212.103.

[Dab01] A. Dabrowski. Adsorption, from theory to practice. *Advances in colloid and interface science*, 93(1):135–224, 2001. [http://dx.doi.org/10.1016/S0001-8686\(00\)00082-8](http://dx.doi.org/10.1016/S0001-8686(00)00082-8).

[Dav60] D. Davis. Monte Carlo calculation of molecular flow rates through a cylindrical elbow and pipes of other shapes. *Journal of Applied Physics*, 31(7):1169–1176, 1960. <http://dx.doi.org/10.1063/1.1735797>.

[DDJK04] V. Demidov, C. DeJoseph Jr., and A. Kudryavtsev. Effect of metastable atoms on near-wall voltage drop in the afterglow of a noble-gas radio-frequency inductive coupled plasma. *Physics of Plasmas (1994-present)*, 11(11):5350–5353, 2004. <http://dx.doi.org/10.1063/1.1795844>.

[DDJK05] V. Demidov, C. DeJoseph Jr., and A. Kudryavtsev. Anomalously high near-wall sheath potential drop in a plasma with nonlocal fast electrons. *Physical review letters*, 95(21):215002, 2005. <https://doi.org/10.1103/PhysRevLett.95.215002>.

[DDJK06] V. Demidov, C. DeJoseph Jr., and A. Kudryavtsev. Nonlocal effects in a bounded afterglow plasma with fast electrons. *Plasma Science, IEEE Transactions on*, 34(3):825–833, 2006. doi: 10.1109/TPS.2006.872338.

[DDL⁺90] D. Decamp, B. Deschizeaux, J.-P. Lees, M.-N. Minard, J. Crespo, M. Delfino, E. Fernandez, M. Martinez, R. Miquel, L. M. Mir, et al. A precise determination of the number of families with light neutrinos and of the Z boson partial widths. *Physics Letters B*, 235(3):399–411, 1990. doi: 10.1016/0370-2693(90)91984-J.

[DES] Deutsches Elektronen-Synchrotron DESY. COBRA Hompage. website COBRA experiment, accessed at 22.09.2016, http://www.cobra-experiment.org/sites/site_cobra-experiment/content/e97947/e99330/Massparabola.JPG.

[DGG⁺62] G. Danby, J. Gaillard, K. Goulian, L. Lederman, N. Mistry, M. Schwartz, and J. Steinberger. Observation of high-energy neutrino reactions and the existence of two kinds of neutrinos. *Physical Review Letters*, 9(1):36, 1962. <https://doi.org/10.1103/PhysRevLett.9.36>.

[DHMW13] G. Drexlin, V. Hannen, S. Mertens, and C. Weinheimer. Current direct neutrino mass experiments. *Advances in High Energy Physics*, 2013, 2013. <http://dx.doi.org/10.1155/2013/293986>.

[Div01] D. A. Diver. *A plasma formulary for physics, technology, and astrophysics*. WILEY-VCH, 2001.

[DKMS05] A. Dinklage, T. Klinger, G. Marx, and L. Schweikhard, editors. *Plasma Physics. Confinement, Transport and Collective Effects*. Springer, Berlin Heidelberg, 2005.

[DM08] S. Dawson and R. N. Mohapatra, editors. *Colliders and Neutrinos: The Window Into Physics Beyond the Standard Model*, volume 1. World Scientific, 2008.

[DNN08] R. Dus, E. Nowicka, and R. Nowakowski. The response of Work Function of Thin Metal Films to Interaction with Hydrogen. *Acta Physica Polonica-Series A General Physics*, 114:S29, 2008. <http://przyrbwn.icm.edu.pl/APP/PDF/114/a114zS03.pdf>.

[DS99] J. De Segovia. Physics of outgassing. Technical report, Cern, 1999. Available at: <http://www.chem.elte.hu/departments/altkem/vakuumtechnika/CERN09.pdf>.

[DT08] N. Doss and J. Tennyson. Excitations to the electronic continuum of $^3\text{He}^+$ in investigations of T^2 β -decay experiments. *Journal of Physics B: Atomic, Molecular and Optical Physics*, 41(12):125701, 2008. doi: 10.1088/0953-4075/41/12/125701.

[DTSJ06] N. Doss, J. Tennyson, A. Saenz, and S. Jonsell. Molecular effects in investigations of tritium molecule β decay endpoint experiments. *Physical Review C*, 73(2):025502, 2006. <https://doi.org/10.1103/PhysRevC.73.025502>.

[DVGG⁺16] E. Di Valentino, S. Gariazzo, M. Gerbino, E. Giusarma, and O. Mena. Dark radiation and inflationary freedom after Planck 2015. *Physical Review D*, 93(8):083523, 2016. <https://doi.org/10.1103/PhysRevD.93.083523>.

[EBB⁺08] F. Eichelhardt, B. Bornschein, L. Bornschein, O. Kazachenko, N. Kernert, and M. Sturm. First tritium results of the KATRIN test experiment TRAP. *Fusion Science and Technology*, 54(2):615–618, 2008. <http://epubs.ans.org/?a=1890>.

[EBB⁺14] M. Erhard, S. Bauer, A. Beglarian, T. Bergmann, J. Bonn, G. Drexlin, J. Goulhon, S. Groh, F. Glück, M. Kleesiek, et al. High-voltage monitoring with a solenoid retarding spectrometer at the KATRIN experiment. *Journal of Instrumentation*, 9(06):P06022, 2014. <http://iopscience.iop.org/1748-0221/9/06/P06022>.

[EBB⁺15] S. Eliseev, K. Blaum, M. Block, S. Chenmarev, H. Dorrer, Ch. E. Düllmann, C. Enss, P. Filianin, L. Gastaldo, M. Goncharov, et al. Direct Measurement of the Mass Difference of Ho 163 and Dy 163 Solves the Q-Value Puzzle for the Neutrino Mass Determination. *Physical review letters*, 115(6):062501, 2015. doi: 10.1103/PhysRevLett.115.062501.

[EGC⁺06] The SLD Electroweak, Heavy Flavour Groups, ALEPH Collaboration, DELPHI Collaboration, L3 Collaboration, OPAL Collaboration, SLD Collaboration, LEP Electroweak Working Group, et al. Precision electroweak measurements on the Z resonance. *Physics Reports*, 427(5):257–454, 2006.

[EHH⁺15] E. Ellinger, N. Haußmann, K. Helbing, S. Hickford, and U. Naumann. The KATRIN Forward Beam Monitor conceptual design document, 2015. KATRIN internal document, Available at: https://fuzzy.fzk.de/bscw/bscw.cgi/963962?op=preview&back_url=959833.

[EHM87] S. Elliott, A. Hahn, and M. Moe. Direct evidence for two-neutrino double-beta decay in Se 82. *Physical Review Letters*, 59(18):2020, 1987. <https://doi.org/10.1103/PhysRevLett.59.2020>.

[Eki06] J. Ekin. *Experimental Techniques for Low-Temperature Measurements: Cryostat Design, Material Properties and Superconductor Critical-Current Testing: Cryostat Design, Material Properties and Superconductor Critical-Current Testing*. Oxford University Press, 2006.

[Ell15] E. Ellinger. The Detector of the FBM Latest Results of Stability Measurements, 2015. Talk at 29th KATRIN Collaboration Meeting, Available at: https://fuzzy.fzk.de/bscw/bscw.cgi/973370?op=preview&back_url=973211.

[Ell16] E. Ellinger. Stability of the FBM detector, 2016. Talk at 30th KATRIN Collaboration Meeting, Available at: https://fuzzy.fzk.de/bscw/bscw.cgi/1008087?op=preview&back_url=21079.

[Erh16] M. Erhard. *Influence of the magnetic field on the transmission characteristics and neutrino mass systematics of the KATRIN experiment*. PhD thesis, 2016. Karlsruhe Institute of Technology.

[F⁺11] S. Fischer et al. Monitoring of tritium purity during long-term circulation in the KATRIN test experiment LOOPINO using laser Raman spectroscopy. *Fusion Science and Technology*, 60(3):925–930, 2011. <http://epubs.ans.org/?a=12567>.

[FAB⁺16] M. Faverzani, B. Alpert, D. Backer, D. Bennet, M. Biasotti, C. Brofferio, V. Ceriale, G. Ceruti, D. Corsini, P. Day, et al. The HOLMES Experiment. *Journal of Low Temperature Physics*, pages 1–8, 2016. doi: 10.1007/s10909-016-1540-x.

[Fer34] E. Fermi. Versuch einer Theorie der β -Strahlen. I. *Zeitschrift für Physik*, 88(3-4):161–177, 1934. doi: 10.1007/BF01351864.

[FHI⁺98] Y. Fukuda, T. Hayakawa, E. Ichihara, K. Inoue, K. Ishihara, H. Ishino, Y. Itow, T. Kajita, J. Kameda, S. Kasuga, et al. Evidence for oscillation of atmospheric neutrinos. *Physical Review Letters*, 81(8):1562, 1998. <https://doi.org/10.1103/PhysRevLett.81.1562>.

[FHK13] G. Feldman, J. Hartnell, and T. Kobayashi. Long–baseline neutrino oscillation experiments. *Advances in High Energy Physics*, 2013, 2013. <http://dx.doi.org/10.1155/2013/475749>.

[Fis14] S. Fischer. *Commissioning of the KATRIN Raman system and durability studies of optical coatings in glove box and tritium atmospheres*. PhD thesis, 2014. Karlsruhe Institute of Technology, available at: <https://publikationen.bibliothek.kit.edu/1000043697>.

[FMA05] A. Fruchtman, G. Makrinich, and J. Ashkenazy. Two-dimensional equilibrium of a low temperature magnetized plasma. *Plasma Sources Science and Technology*, 14(1):152, 2005. <http://iopscience.iop.org/0963-0252/14/1/017>.

[FMM06] A. Florescu-Mitchell and J. Mitchell. Dissociative recombination. *Physics Reports*, 430(5):277–374, 2006. <http://dx.doi.org/10.1016/j.physrep.2006.04.002>.

[Fou22] J. Fourier. *Theorie analytique de la chaleur, par M. Fourier*. Chez Firmin Didot, père et fils, 1822.

[Frä10] F. Fränkle. *Background Investigations of the KATRIN Pre-Spectrometer*. PhD thesis, 2010. Karlsruhe Institute of Technology, available at: <https://publikationen.bibliothek.kit.edu/1000019392>.

[Frä16] F. Fränkle. Status of the KATRIN experiment, 2016. Talk at the DPG Spring meeting, Hamburg 2016, Available at: https://fuzzy.fzk.de/bscw/bscw.cgi/1008749?op=preview&back_url=15294.

[Fre28] J. Frenkel. Über die elektrische Oberflächenschicht der Metalle. *Zeitschrift für Physik*, 51(3-4):232–238, 1928. doi: 10.1007/BF01343198.

[FS03] Y. Farzan and A. Y. Smirnov. On the effective mass of the electron neutrino in beta decay. *Physics Letters B*, 557(3):224–232, 2003. [http://dx.doi.org/10.1016/S0370-2693\(03\)00207-7](http://dx.doi.org/10.1016/S0370-2693(03)00207-7).

[Fur15] D. Furse. *Techniques for direct neutrino mass measurement utilizing tritium beta decay*. PhD thesis, 2015. Massachusetts Institute of Technology, Available at: <https://dspace.mit.edu/handle/1721.1/99313>.

[FY04] R. Feres and G. Yablonsky. Knudsen’s cosine law and random billiards. *Chemical engineering science*, 59(7):1541–1556, 2004. <http://dx.doi.org/10.1016/j.ces.2004.01.016>.

[G14a] S. Görhard. *Background Reduction Methods and Vacuum Technology at the KATRIN Spectrometers*. PhD thesis, Karlsruhe Institute of Technology, 2014.

[G⁺14b] Particle Data Group et al. Review of particle physics Particle Data Group. *Chinese physics. C, High energy physics and nuclear physics*, 38(9):090001, 2014. <http://iopscience.iop.org/1674-1137/38/9/090001>.

[Gal12] P. Gallagher. Introduction to plasma physics, 2012. lecture slides, lectures 1-2, Available at: https://www.tcd.ie/Physics/people/Peter.Gallagher/lectures/PlasmaPhysics/Lecture1n2_basic_properties.pdf.

[GBB⁺08] S. Grohmann, J. Bonn, B. Bornschein, R. Gehring, W. Gil, O. Kazachenko, H. Neumann, M. Noe, and C. Weiss. Cryogenic design of the KATRIN source cryostat. In *Advances in cryogenic engineering*, volume 985, pages 1277–1284, 2008. <http://dx.doi.org/10.1063/1.2908483>.

[GBD⁺14] L. Gastaldo, K. Blaum, A. Dörr, C. E. Düllmann, K. Eberhardt, S. Eliseev, C. Enss, A. Faessler, A. Fleischmann, S. Kempf, et al. The Electron Capture 163 ho experiment ECHo. *Journal of low temperature physics*, 176(5-6):876–884, 2014. doi: 10.1007/s10909-014-1187-4.

[GBH⁺13] S. Grohmann, T. Bode, M. Hötzl, H. Schön, M. Süßer, and T. Wahl. The thermal behaviour of the tritium source in KATRIN. *Cryogenics*, 55:5–11, 2013.

[GBSS11] S. Grohmann, T. Bode, H. Schön, and M. Süßer. Precise temperature measurement at 30K in the KATRIN source cryostat. *Cryogenics*, 51(8):438–445, 2011. <http://www.sciencedirect.com/science/article/pii/S0011227511001135>.

[GDL⁺13] F. Glück, G. Drexlin, B. Leiber, S. Mertens, A. Osipowicz, J. Reich, and N. Wandkowsky. Electromagnetic design of the large-volume air coil system of the KATRIN experiment. *New Journal of Physics*, 15(8):083025, 2013. <http://iopscience.iop.org/1367-2630/15/8/083025>.

[GG15] G. Ghioldi and L. Gibelli. A finite-difference lattice Boltzmann approach for gas microflows. *Communications in Computational Physics*, 17(04):1007–1018, 2015. doi: <https://doi.org/10.4208/cicp.2014.m424>.

[GGBK06] V. T. Gurovich, J. Gleizer, Y. Bliokh, and Y. E. Krasik. Potential distribution in an ion sheath of non-Maxwellian plasma. *Physics of Plasmas (1994-present)*, 13(7):073506, 2006. <http://dx.doi.org/10.1063/1.2226982>.

[GGH⁺13] A. Gando, Y. Gando, H. Hanakago, H. Ikeda, K. Inoue, K. Ishidoshiro, R. Kato, M. Koga, S. Matsuda, T. Mitsui, et al. Limit on Neutrinoless $\beta\beta$ Decay of Xe 136 from the First Phase of KamLAND-Zen and Comparison with the Positive Claim in Ge 76. *Physical Review Letters*, 110(6):062502, 2013. <https://doi.org/10.1103/PhysRevLett.110.062502>.

[GGM61] S. L. Glashow and M. Gell-Mann. Gauge theories of vector particles. *Annals of Physics*, 15(3):437–460, 1961. doi:10.1016/0003-4916(61)90193-2.

[GGMS16] M. Gonzalez-Garcia, M. Maltoni, and T. Schwetz. Global analyses of neutrino oscillation experiments. *Nuclear Physics B*, 908:199–217, 2016. <http://dx.doi.org/10.1016/j.nuclphysb.2016.02.033>.

[GGS58] M. Goldhaber, L. Grodzins, and A. Sunyar. Helicity of neutrinos. *Physical Review*, 109(3):1015, 1958. <https://doi.org/10.1103/PhysRev.109.1015>.

[GKRW12] R. Größle, N. Kernert, S. Riegel, and J. Wolf. Model of the rotor temperature of turbo-molecular pumps in magnetic fields. *Vacuum*, 86(7):985–989, 2012. <http://dx.doi.org/10.1016/j.vacuum.2011.09.009>.

[Glü02] F. Glück. Electric field in WGTS tubes I., 2002. KATRIN internal report, Available at: https://fuzzy.fzk.de/bscw/bscw.cgi/36074?op=preview&back_url=1005311.

[Glü05] F. Glück. Tritium ion concentrations in wgts and transport system, 2005. Internal talk at STS meeting, Available at: <http://fuzzy.fzk.de/bscw/bscw.cgi/d157274/3-Ferenc-Glueck.pdf>.

[Glü10] F. Glück. Ions in the WGTS, 2010. KATRIN internal talk at STS meeting, August 10th 2010.

[GMS95] V. A. Godyak, V. P. Meyliss, and H. R. Strauss. Tonks-Langmuir problem for a bi-Maxwellian plasma. *Plasma Science, IEEE Transactions on*, 23(4):728–734, 1995. <http://ieeexplore.ieee.org/stamp/stamp.jsp?arnumber=467995>.

[GN06] L. Gardner and K. Ng. Temperature development in structural stainless steel sections exposed to fire. *Fire Safety Journal*, 41(3):185–203, 2006. <http://dx.doi.org/10.1016/j.firesaf.2005.11.009>.

[GNP⁺03] J. Glosik, O. Novotný, A. Pysanenko, P. Zakouril, R. Plašil, P. Kudrna, and V. Poterya. The recombination of H3+ and H5+ ions with electrons in hydrogen plasma: dependence on temperature and on pressure of H2. *Plasma Sources Science and Technology*, 12(4):S117, 2003. <http://iopscience.iop.org/0963-0252/12/4/027>.

[GPS11] I. Graur, A. Ph. Polikarpov, and F. Sharipov. Numerical modeling of rarefied gas flow through a slit into vacuum based on the kinetic equation. *Computers & Fluids*, 49(1):87–92, 2011. <http://dx.doi.org/10.1016/j.compfluid.2011.05.001>.

[GR95] R. J. Goldston and P. H. Rutherford. *Introduction to plasma physics*. CRC Press, 1995.

[Gro09] S. Grohmann. Stability analyses of the beam tube cooling system in the KATRIN source cryostat. *Cryogenics*, 49(8):413–420, 2009. <http://dx.doi.org/10.1016/j.cryogenics.2009.06.001>.

[Gro15] S. Groh. *Modeling of the response function and measurement of transmission properties of the KATRIN experiment*. PhD thesis, Karlsruhe Institute of Technology, 2015. Available at: <https://publikationen.bibliothek.kit.edu/1000046546>.

[GS12] R. P. Gangloff and B. P. Somerday. *Gaseous Hydrogen Embrittlement of Materials in Energy Technologies: Mechanisms, Modelling and Future Developments*, volume 2. Elsevier, 2012.

[GZS80] V. E. Golant, A. P. Zhilinsky, and I. E. Sakharov. *Fundamentals of plasma physics*. John Wiley & Sons, 1980.

[Hae81] R. A. Haefer. *Kryo-vakuumtechnik*. Springer, 1981.

[Han10] S. Hannestad. Neutrino physics from precision cosmology. *Progress in Particle and Nuclear Physics*, 65(2):185–208, 2010. <http://dx.doi.org/10.1016/j.ppnp.2010.07.001>.

[Har12] F. Harms. Assembly and First Results of the KATRIN Focal-Plane Detector System at KIT, 2012. diploma thesis, Karlsruhe Institute of Technology.

[Har15] F. Harms. *Characterization and Minimization of Background Processes in the KATRIN Main Spectrometer*. PhD thesis, Karlsruhe Institute of Technology, 2015.

[Har16] F. Harms. Radon – induced backgrounds in the KATRIN Main Spectrometer, 2016. Talk at the DPG Spring meeting, Hamburg 2016.

[Hau15] N. Haubmann. FBM requirements, 2015. KATRIN internal talk at STS Meeting Dec. 7th 2015, Available at: https://neutrino.ikp.kit.edu/katrin/images/b/b4/151207_FBM_req_NHaubmann.pdf.

[HBG⁺16] C Hassel, K Blaum, T Day Goodacre, H Dorrer, Ch E Düllmann, K Eberhardt, S Eliseev, C Enss, P Filianin, A Fäßler, et al. Recent results for the ECHo experiment. *Journal of Low Temperature Physics*, pages 1–12, 2016. doi: 10.1007/s10909-016-1541-9.

[Hen16] R. Henning. Current status of neutrinoless double-beta decay searches. *Reviews in Physics*, 1:29–35, 2016. <http://dx.doi.org/10.1016/j.revip.2016.03.001>.

[HHH⁺99] W. Hampel, J. Handt, G. Heusser, J. Kiko, T. Kirsten, M. Laubenstein, E. Pernicka, W. Rau, M. Wojcik, Y. Zakharov, et al. GALLEX solar neutrino observations: Results for GALLEX IV. *Physics Letters B*, 447(1):127–133, 1999. [http://dx.doi.org/10.1016/S0370-2693\(98\)01579-2](http://dx.doi.org/10.1016/S0370-2693(98)01579-2).

[HHW14] S. Hannestad, J. Hamann, and Y. YY. Wong. Current and future constraints on neutrino physics from cosmology. In *Journal of Physics: Conference Series*, volume 485, page 012008. IOP Publishing, 2014. Available at: <http://iopscience.iop.org/1742-6596/485/1/012008>.

[Hig64] P. W. Higgs. Broken symmetries and the masses of gauge bosons. *Physical Review Letters*, 13(16):508, 1964. <https://doi.org/10.1103/PhysRevLett.13.508>.

[HII⁺91] K. Hirata, K. Inoue, T. Ishida, T. Kajita, K. Kihara, M. Nakahata, K. Nakamura, S. Ohara, N. Sato, Y. Suzuki, et al. Real-time, directional measurement of B 8 solar neutrinos in the Kamiokande II detector. *Physical Review D*, 44(8):2241, 1991. <https://doi.org/10.1103/PhysRevD.44.2241>.

[HKK⁺88] K. Hirata, T. Kajita, M. Koshiba, M. Nakahata, S. Ohara, Y. Oyama, N. Sato, A. Suzuki, M. Takita, Y. Totsuka, et al. Experimental study of the atmospheric neutrino flux. *Physics Letters B*, 205(2-3):416–420, 1988. doi:10.1016/0370-2693(88)91690-5.

[HNPM⁺12] M. Hadj-Nacer, P. Perrier, J. Méolans, I. Graur, and M. Wüest. Experimental study of the gas flows through channels with circular cross sections. In *Journal of Physics: Conference Series*, volume 362, page 012025. IOP Publishing, 2012.

[Ho01] D. Herrebout and others. One-dimensional fluid model for an rf methane plasma of interest in deposition of diamond-like carbon layers. *Journal of Applied Physics*, 90(2):570–579, 2001. <http://dx.doi.org/10.1063/1.1378059>.

[Höt12] M. Hötzels. *Simulation and analysis of source-related effects for KATRIN*. PhD thesis, Karlsruhe Institute of Technology, 2012. Available at: <https://publikationen.bibliothek.kit.edu/1000031259>.

[Hua10] J. Hua. Simulation des Kryptonmodus der Tritiumquelle WGTS im KATRIN Experiment, 2010. diploma thesis, Karlsruhe Institute of Technology.

[HVWW16] V. Hennen, K. Valerius, C. Weinheimer, and I. Wolff. Deconvolution of the energy loss function of the KATRIN, experiment. 2016. to be published.

[HW67] G. Hobbs and J. Wesson. Heat flow through a langmuir sheath in the presence of electron emission. *Plasma Physics*, 9(1):85, 1967. <http://iopscience.iop.org/0032-1028/9/1/410>.

[HYSM88] H. Hus, F. Youssif, A. Sen, and J. Mitchell. Merged-beam studies of the dissociative recombination of H3+ ions with low internal energy. *Physical Review A*, 38(2):658, 1988. <http://journals.aps.org/pra/pdf/10.1103/PhysRevA.38.658>.

[IB90] S. Ingram and N. StJ Braithwaite. The plasma-sheath boundary with fast monoenergetic electrons. *Journal of Physics D: Applied Physics*, 23(12):1648, 1990. <http://iopscience.iop.org/0022-3727/23/12/024>.

[Jan15] A. Jansen. *The Cryogenic Pumping Section of the KATRIN Experiment*. PhD thesis, Karlsruhe Institute of Technology, 2015. Avialable at:<https://publikationen.bibliothek.kit.edu/1000047146>.

[JC03] D. Jiang and E. A. Carter. Adsorption and diffusion energetics of hydrogen atoms on fe (110) from first principles. *Surface science*, 547(1):85–98, 2003. <http://dx.doi.org/10.1016/j.susc.2003.10.007>.

[Käf12] W. Käfer. *Investigation of the KATRIN sensitivity*. PhD thesis, Karlsruhe Institute of Technology, 2012. Available at:<https://publikationen.bibliothek.kit.edu/1000026021>.

[Kan16] M. Kaneda. Results from the Double Chooz experiment. In *EPJ Web of Conferences*, volume 126, page 04023. EDP Sciences, 2016. http://www.epj-conferences.org/articles/epjconf/abs/2016/21/epjconf_icnfp2016_04023/epjconf_icnfp2016_04023.html.

[KBA06] G. E. Karniadakis, A. Beskok, and N. Aluru. *Microflows and nanoflows: fundamentals and simulation*, volume 29. Springer Science & Business Media, 2006.

[KBB⁺05] Ch. Kraus, B. Bornschein, L. Bornschein, J. Bonn, B. Flatt, A. Kovalik, B. Ostrick, E. Otten, J. Schall, T. Thümmler, et al. Final results from phase ii of the Mainz neutrino mass searchin tritium β decay. *The European Physical Journal C-Particles and Fields*, 40(4):447–468, 2005. doi: 10.1140/epjc/s2005-02139-7.

[Kel98] Lord Kelvin. V. Contact electricity of metals. *The London, Edinburgh, and Dublin Philosophical Magazine and Journal of Science*, 46(278):82–120, 1898. <http://dx.doi.org/10.1080/14786449808621172>.

[Kib67] T. W. B. Kibble. Symmetry breaking in non-Abelian gauge theories. *Physical Review*, 155(5):1554, 1967. <https://doi.org/10.1103/PhysRev.155.1554>.

[KKDHK01] H. Klapdor-Kleingrothaus, A. Dietz, H. Harney, and I. Krivosheina. Evidence for neutrinoless double beta decay. *Modern Physics Letters A*, 16(37):2409–2420, 2001. <http://dx.doi.org/10.1142/S0217732301005825>.

[Kle14] M. Kleesiek. *A Data-Analysis and Sensitivity-Optimization Framework for the KATRIN Experiment*. PhD thesis, Karlsruhe Institute of Technology, 2014. Available at: <https://publikationen.bibliothek.kit.edu/1000043301>.

[Kle16] M. Klein. Tritium ions in the Source and Transport Section of KATRIN, 2016. Talk at DPG spring meeting Hamburg 2016.

[Knu09a] M. Knudsen. Die Gesetze der Molekularströmung und der inneren Reibungsströmung der Gase durch Röhren. *Annalen der Physik*, 333(1):75–130, 1909. doi: 10.1002/andp.19093330106.

[Knu09b] M. Knudsen. Die Molekularströmung der gase durch Offnungen und die Effusion. *Annalen der Physik*, 333(5):999–1016, 1909. doi: 10.1002/andp.19093330505.

[KP09] R. Kersevan and J.-L. Pons. Introduction to MOLFLOW+: New graphical processing unit-based monte carlo code for simulating molecular flows and for calculating angular coefficients in the compute unified device architecture environment. *Journal of Vacuum Science & Technology A*, 27(4):1017–1023, 2009. <http://dx.doi.org/10.1116/1.3153280>.

[Kra92] L. M. Krauss. Supernova neutrinos and the signal from the next galactic supernova. *Nuclear Physics B-Proceedings Supplements*, 28(1):106–115, 1992. doi:10.1016/0920-5632(92)90153-J.

[KSJE72] U. S. Kim, R. Schmidt, M. S. Jhon, and H. Eyring. Physical adsorption of the quantum gas. *Proceedings of the National Academy of Sciences*, 69(7):1690–1692, 1972. url<http://www.pnas.org/content/69/7/1690.full.pdf>.

[KUA⁺01] K. Kodama, N. Ushida, C. Andreopoulos, N. Saoulidou, G. Tzanakos, P. Yager, B. Baller, D. Boehnlein, W. Freeman, B. Lundberg, et al. Observation of tau neutrino interactions. *Physics Letters B*, 504(3):218–224, 2001. [http://dx.doi.org/10.1016/S0370-2693\(01\)00307-0](http://dx.doi.org/10.1016/S0370-2693(01)00307-0).

[KY14] P. A. Krochin Yepez. Investigations on the influence of the ortho para tritium ratio on the neutrino mass sensitivity of KATRIN, 2014. Bachelor thesis, Karlsruhe Institute of Technology.

[Laf98] J. Lafferty. *Foundations of vacuum science and technology*. John Wiley & Sons, 1998.

[Lan18] I. Langmuir. The adsorption of gases on plane surfaces of glass, mica and platinum. *Journal of the American Chemical society*, 40(9):1361–1403, 1918. doi: 10.1021/ja02242a004.

[LB66] L. Lund and A. Berman. Flow and self-diffusion of gases in capillaries. part i. *Journal of applied Physics*, 37(6):2489–2495, 1966. <http://dx.doi.org/10.1063/1.1708841>.

[LBDW07] X. Luo, L. Bornschein, C. Day, and J. Wolf. KATRIN NEG pumping concept investigation. *Vacuum*, 81(6):777–781, 2007. <http://dx.doi.org/10.1016/j.vacuum.2005.11.053>.

[LDH⁺06] X. Luo, C. Day, V. Hauer, O. Malyshev, R. Reid, and F. Sharipov. Monte carlo simulation of gas flow through the katrin dps2-f differential pumping system. *Vacuum*, 80(8):864–869, 2006. <http://dx.doi.org/10.1016/j.vacuum.2005.11.044>.

[Lei14] B. Leiber. *Investigations of background due to secondary electron emission in the KATRIN-experiment*. PhD thesis, Karsruhe Institute of Technology, 2014. Available at: <https://publikationen.bibliothek.kit.edu/1000042415>.

[LK71] N. Lang and W. Kohn. Theory of metal surfaces: work function. *Physical Review B*, 3(4):1215, 1971. <https://doi.org/10.1103/PhysRevB.3.1215>.

[LKNH11] S. Lee, H. Kim, S. Noh, and J. Han. Hydrogen Permeability, Diffusivity, and Solubility of SUS 316L Stainless Steel in the Temperature Range 400 to 800 degrees C for Fusion Reactor Applications. *Journal of the Korean Physical Society*, 59(5):3019–3023, 2011.

[LL02] T. J. Loredo and D. Q. Lamb. Bayesian analysis of neutrinos observed from supernova SN 1987A. *Physical Review D*, 65(6):063002, 2002. <http://journals.aps.org/prd/pdf/10.1103/PhysRevD.65.063002>.

[LL05] M. A. Lieberman and A. J. Lichtenberg. *Principles of plasma discharges and materials processing*. John Wiley & Sons, 2005.

[LMM76] W. Leung, N. March, and H. Motz. Primitive phase diagram for hydrogen. *Physics Letters A*, 56(6):425–426, 1976. doi:10.1016/0375-9601(76)90713-1.

[Lob85] P. Lobashev, V. and Spivak. A method for measuring the electron antineutrino rest mass. *Nuclear Instruments and Methods in Physics Research Section A: Accelerators, Spectrometers, Detectors and Associated Equipment*, 240(2):305–310, 1985. doi:10.1016/0168-9002(85)90640-0.

[Loy68] S. Loyalka. Momentum and temperature-slip coefficients with arbitrary accommodation at the surface. *The Journal of Chemical Physics*, 48(12):5432–5436, 1968. <http://dx.doi.org/10.1063/1.1668235>.

[LP14] J. Lesgourgues and S. Pastor. Neutrino cosmology and Planck. *New Journal of Physics*, 16(6):065002, 2014. <http://iopscience.iop.org/1367-2630/16/6/065002>.

[LSD87] E. Lisowski, L. Stobiński, and R. Duś. On the influence of the way of thin gold films preparation on the character of hydrogen adsorption. *Surface Science*, 188(3):L735–L741, 1987. doi:10.1016/S0039-6028(87)80188-7.

[LU00] L. L. Lucas and M. P. Unterweger. Comprehensive review and critical evaluation of the half-life of Tritium. *Journal of research-National institute of standards and technology*, 105(4):541–550, 2000. doi: 10.6028/jres.105.043.

[LXSC16] C. Liu, K. Xu, Q. Sun, and Q. Cai. A Unified Gas-kinetic Scheme for Continuum and Rarefied Flows IV: full Boltzmann and Model Equations. *Journal of Computational Physics*, 314:305–340, 2016. <http://www.math.ust.hk/~makxu/PAPER/UGKS-Boltzmann.pdf>.

[MAB⁺07] R. N. Mohapatra, S. Antusch, K. Babu, G. Barenboim, M.-C . Chen, et al. Theory of neutrinos: a white paper. *Reports on Progress in Physics*, 70(11):1757, 2007. <http://iopscience.iop.org/0034-4885/70/11/R02>.

[Mac16] M. Machatschek. Simulation of the 83mkr Mode of the Tritium Source of the KATRIN Experiment. Master’s thesis, Karlsruhe Institute of Technology, 2016.

[Mad73] T. E. Madey. Chemisorption of H 2 on W (100): Absolute sticking probability, coverage, and electron stimulated desorption. *Surface Science*, 36(1):281–294, 1973. doi:10.1016/0039-6028(73)90262-8.

[Maj37] E. Majorana. Teoria simmetrica dell elettrone e del positrone. *Il Nuovo Cimento (1924-1942)*, 14(4):171–184, 1937. doi: 10.1007/BF02961314.

[Max90] J. C. Maxwell. Scientific papers, vol. 1, 1890.

[MBJ84] J. A. Macdonald, M. A. Biondi, and R. Johnsen. Recombination of electrons with H 3+ and H 5+ ions. *Planetary and Space Science*, 32(5):651–654, 1984. doi:10.1016/0032-0633(84)90117-X.

[McC15] E. McCutchan. Nuclear data sheets for a= 83. *Nuclear Data Sheets*, 125:201–394, 2015. doi:10.1016/j.nds.2015.02.002.

[MDLS09] O. Malyshev, Chr. Day, X. Luo, and F. Sharipov. Tritium gas flow dynamics through the source and transport system of the Karlsruhe tritium neutrino experiment. *Journal of Vacuum Science & Technology A*, 27(1):73–81, 2009.

[Mee14] D. Meeker. Finite Element Method Magnetics, 2014. <http://www.femm.info/wiki/HomePage>.

[Mer12] S. Mertens. *Study of Background Processes in the Electrostatic Spectrometers of the KATRIN experiment*. PhD thesis, Karlsruhe Institute of Technology, 2012. Available at: <https://publikationen.bibliothek.kit.edu/1000027058>.

[MF09] B. Monreal and J. A. Formaggio. Relativistic cyclotron radiation detection of tritium decay electrons as a new technique for measuring the neutrino mass. *Physical Review D*, 80(5):051301, 2009. <https://doi.org/10.1103/PhysRevD.80.051301>.

[MJS01] G. Moulard, B. Jenninger, and Y. Saito. Industrial surfaces behaviour related to the adsorption and desorption of hydrogen at cryogenic temperature. *Vacuum*, 60(1):43–50, 2001. [http://dx.doi.org/10.1016/S0042-207X\(00\)00244-X](http://dx.doi.org/10.1016/S0042-207X(00)00244-X).

[MMMM68] T. Miller, J. Moseley, D. Martin, and E. McDaniel. Reactions of h+ in H2 and D+ in D2; Mobilities of Hydrogen and Alkali Ions in H2 and D2 Gases. *Physical Review*, 173(1):115, 1968. <http://journals.aps.org/pr/pdf/10.1103/PhysRev.173.115>.

[MN98] M. Matsumoto and T. Nishimura. Mersenne twister: a 623-dimensionally equidistributed uniform pseudo-random number generator. *ACM Transactions on Modeling and Computer Simulation (TOMACS)*, 8(1):3–30, 1998.

[MNF⁺84] J. Mitchell, C. Ng, L. Forand, R. Janssen, and J. W. McGowan. Total cross sections for the dissociative recombination of H3+, HD2+ and D3+. *Journal of Physics B: Atomic and Molecular Physics*, 17(24):L909, 1984. <http://iopscience.iop.org/0022-3700/17/24/013>.

[MNS62] Z. Maki, M. Nakagawa, and S. Sakata. Remarks on the unified model of elementary particles. *Progress of Theoretical Physics*, 28(5):870–880, 1962. doi: 10.1143/PTP.28.870.

[MP15] B. Monreal and F. Priester. Rear section status update, 2015. Talk at 28th KATRIN Collaboration meeting, https://fuzzy.fzk.de/bscw/bscw.cgi/950718?op=preview&back_url=950709.

[MPS15] J. Maneira, S. Peeters, and J. Sinclair. Optical calibration of SNO+. In *Journal of Physics: Conference Series*, volume 598, page 012030. IOP Publishing, 2015. <http://iopscience.iop.org/1742-6596/598/1/012030>.

[MS86] S. Mikheyev and A. Y. Smirnov. Resonant amplification of ν oscillations in matter and solar-neutrino spectroscopy. *Il Nuovo Cimento C*, 9(1):17–26, 1986. doi: 10.1007/BF02508049.

[Mul14a] COMSOL Multiphysics. COMSOL 5.0, Surface Reations Module User’s Guide. *Resource Information*, 2014.

[Mul14b] COMSOL Multiphysics. Material library. *Resource Information*, 2014.

[NEB⁺14] D. Nesterenko, S. Eliseev, K. Blaum, M. Block, S. Chenmarev, A. Dörr, C. Droese, P. Filianin, M. Goncharov, E. M. Ramirez, et al. Direct determination of the atomic mass difference of Re 187 and Os 187 for neutrino physics and cosmochronology. *Physical Review C*, 90(4):042501, 2014. <https://doi.org/10.1103/PhysRevC.90.042501>.

[NFB⁺06] S. Nagy, T. Fritioff, M. Björkhage, I. Bergström, and R. Schuch. On the Q-value of the tritium β -decay. *EPL (Europhysics Letters)*, 74(3):404, 2006. <http://iopscience.iop.org/0295-5075/74/3/404>.

[NM04] A. F. Nastoyashchii and I. N. Morozov. One-dimensional self-consistent model of wgt plasma, 2004.

[Oer16] Oerlikon Leybold Vacuum GmbH. *Technische Daten TURBOVAC MAG W 2800*, 6 2016. Available at: https://leyboldproducts.oerlikon.com/pics/FileResources/Orig/TD_TechnischeDaten/TD_400006V0071_DE.pdf.

[OR62] J. Olivier and S. Ross. On Physical Adsorption. XVI. The Physical Interaction of H₂, D₂, CH₄, and CD₄ with Graphite. In *Proceedings of the Royal Society of London A: Mathematical, Physical and Engineering Sciences*, volume 265, pages 447–454, 1962. doi: 10.1098/rspa.1962.0034.

[Oss97] P. Ossipov. The angular coefficient method for calculating the stationary molecular gas flow for arbitrary reflection law. *Vacuum*, 48(5):409–412, 1997. doi: 10.1016/S0042-207X(97)00006-7.

[Ott13] E. Otten. Penetration of patch potentials on rear plate ane WGTS-tube on T2-plasmapotential, 2013. Talk KATRIN collaboration meeting, March 2013.

[OW08] E. Otten and C. Weinheimer. Neutrino mass limit from tritium β decay. *Reports on Progress in Physics*, 71(8):086201, 2008. <http://iopscience.iop.org/0034-4885/71/8/086201>.

[Pal15] M. Pallavicini. Solar neutrinos: experimental review and prospectives. In *Journal of Physics: Conference Series*, volume 598, page 012007. IOP Publishing, 2015. <http://iopscience.iop.org/1742-6596/598/1/012007>.

[Par08] S. J. Parke. CP violation in the Neutrino Sector. *arXiv preprint arXiv:0807.3311*, 2008. Available at: <https://arxiv.org/pdf/0807.3311.pdf>.

[Pat12] R. Patterson. The NOvA experiment: status and outlook. *arXiv preprint arXiv:1209.0716*, 2012.

[Pau30] W. Pauli. Letter to Gauvereinstagung in Tübingen: Sehr geehrte radioaktive Damen und Herren, 1930. published in R. Kronig and V. Weisskopf (Eds.), Wolfgang Pauli, Collected scientivic Papers, Vol.2.

[PBB⁺92] A. Picard, H. Backe, H. Barth, J. Bonn, B. Degen, T. Edling, R. Haid, A. Hermanni, P. Leiderer, T. Loeken, et al. A solenoid retarding spectrometer with high resolution and transmission for kev electrons. *Nuclear Instruments and Methods in Physics Research Section B: Beam Interactions with Materials and Atoms*, 63(3):345–358, 1992. doi: 10.1016/0168-583X(92)95119-C.

[PF83] R. Pasco and P. Ficalora. A work function-chemisorption study of hydrogen on iron: Kinetics and strain effects. *Acta Metallurgica*, 31(4):541–558, 1983. doi: 10.1016/0001-6160(83)90044-5.

[Pfe66] B. Pfeiffer. Skin Effect in Anisotropic Plasmas and Resonance Excitation of Electron-Cyclotron Waves. I. Theory. *Journal of Applied Physics*, 37(4):1624–1627, 1966. <http://dx.doi.org/10.1063/1.1708577>.

[Pie10] A. Piel. *Plasma Boundaries*. Springer, 2010.

[Pon58a] B. Pontecorvo. inverse beta processes and nonconservation of lepton charge. *Zhur. Eksptl. i Teoret. Fiz.*, 34, 1958.

[Pon58b] B. Pontecorvo. Mesonium and antimesonium. *Soviet Phys. JETP*, 6, 1958. http://www.jetp.ac.ru/cgi-bin/dn/e_006_02_0429.pdf.

[Pon12] B. Pontecorvo. Neutrino Experiments and the Question of Leptonic–Charge Conservation. In *Old and New Problems in Elementary Particles*, page 251. Elsevier, 2012.

[Pra11] M. Prall. The katrin experiment and the pre-spectrometer at reduced retarding potential. *Progress in Particle and Nuclear Physics*, 66(2):418–423, 2011. <http://dx.doi.org/10.1016/j.ppnp.2011.01.044>.

[Pri13] F. Priester. *Tritiumtechnologie fÄ4r die fensterlose Quelle WGTS von KATRIN*. PhD thesis, Karlsruhe Institute of Technology, 2013. Available at: <https://publikationen.bibliothek.kit.edu/1000035699>.

[PS85] M. Pick and K. Sonnenberg. A model for atomic hydrogen metal interactions application to recycling recombination and permeation. *Journal of Nuclear Materials*, 131(2):208–220, 1985. doi: 10.1016/0022-3115(85)90459-3.

[PSB15] F. Priester, M. Sturm, and B. Bornschein. Commissioning and detailed results of KATRIN inner loop tritium processing system at Tritium Laboratory Karlsruhe. *Vacuum*, 116:42–47, 2015. <http://dx.doi.org/10.1016/j.vacuum.2015.02.030>.

[PSBA74] B. Porodnov, P. Suetin, S. Borisov, and V. Akinshin. Experimental investigation of rarefied gas flow in different channels. *Journal of fluid mechanics*, 64(03):417–438, 1974. <http://dx.doi.org/10.1017/S0022112074002485>.

[PVS11] S. P. Pantazis, D. Valougeorgis, and F. Sharipov. Numerical simulation of end effects in the WGTS unit, 2011. KATRIN internal report, Available at: https://fuzzy.fzk.de/bscw/bscw.cgi/932831?op=preview&back_url=825925.

[PVS13] S. Pantazis, D. Valougeorgis, and F. Sharipov. End corrections for rarefied gas flows through capillaries of finite length. *Vacuum*, 97:26–29, 2013. <http://dx.doi.org/10.1016/j.vacuum.2013.03.014>.

[PVS14] S. Pantazis, D. Valougeorgis, and F. Sharipov. End corrections for rarefied gas flows through circular tubes of finite length. *Vacuum*, 101:306–312, 2014. <http://dx.doi.org/10.1016/j.vacuum.2013.09.015>.

[QV15] X. Qian and P. Vogel. Neutrino mass hierarchy. *Progress in Particle and Nuclear Physics*, 83:1–30, 2015.

[RBSJ⁺91] R. Robertson, T. Bowles, G. Stephenson Jr, D. Wark, J. F. Wilkerson, and D. Knapp. Limit on ν_e mass from observation of the β decay of molecular tritium. *Physical review letters*, 67(8):957, 1991. doi: 10.1103/PhysRevLett.67.957

[RC56] F. Reines and C. L. Cowan. The neutrino. *Nature*, 178(4531):446–449, 1956.

[Rei09] S. Reimer. Ein elektrostatisches Dipolsystem zur Eliminierung von Ionen in der DPS2-F des KATRIN Experimentes, 2009. diploma thesis, Karlsruhe Institute of Technology.

[RF80] C. M. Ransom and P. Ficalora. An adsorption study of hydrogen on iron and its relation to hydrogen embrittlement. *Metallurgical Transactions A*, 11(5):801–807, 1980. doi: 10.1007/BF02661209.

[RF91] G. Ramanan and G. Freeman. Electron mobilities in low density hydrogen and carbon monoxide gases: Momentum transfer cross sections at very low energies. *The Journal of chemical physics*, 95(6):4195–4200, 1991. <http://dx.doi.org/10.1063/1.460775>.

[RFG93] F. Reiter, K. Forcey, and G. Gervasini. *A compilation of tritium-material interaction parameters in fusion reactor materials*. Commission of the European Communities, 1993.

[RK88] RGH Robertson and D. Knapp. Direct measurements of neutrino mass. *Annual Review of Nuclear and Particle Science*, 38:185–215, 1988. doi: 10.1146/annurev.ns.38.120188.001153.

[RK09] S. Ramanathan and D. L. Koch. An efficient direct simulation Monte Carlo method for low Mach number noncontinuum gas flows based on the bhatnagar–gross–krook model. *Physics of Fluids (1994–present)*, 21(3):033103, 2009. <http://dx.doi.org/10.1063/1.3081562>.

[RK11] M. M. Rathore and R. Kapuno. *Engineering heat transfer*. Jones & Bartlett Publishers, 2 edition, 2011.

[Rod11] W. Rodejohann. Neutrino-less double beta decay and particle physics. *International Journal of Modern Physics E*, 20(09):1833–1930, 2011. <http://dx.doi.org/10.1142/S0218301311020186>.

[Röl15] M. Röllig. *Tritium analytics by beta induced X-ray spectrometry*. PhD thesis, Karlsruhe Institute of Technology, 2015.

[rswg12] KATRIN rear section working group. KATRIN Rear Section Technical Design Report 2012, 2012. KATRIN internal report https://fuzzy.fzk.de/bscw/bscw.cgi/738227?op=preview&back_url=1005311.

[RT01] V. A. Rozhansky and L. D. Tsentrin. *Transport phenomena in partially ionized plasma*. CRC Press, 2001.

[Rup10] S.. Rupp. *Development of a highly sensitive hollow waveguide based Raman system for the compositional analysis of the KATRIN tritium source gas*. PhD thesis, Karlsruhe Institute of Technology, 2010.

[RW83] W W Repko and C Wu. Radiative corrections to the end point of the tritium β decay spectrum. *Physical Review C*, 28(6):2433, 1983. <https://doi.org/10.1103/PhysRevC.28.2433>.

[SAB⁺04] M. Sisti, C. Arnaboldi, C. Brofferio, G. Ceruti, O. Cremonesi, E. Fiorini, A. Giuliani, B. Margesin, L. Martensson, A. Nucciotti, et al. New limits from the milano neutrino mass experiment with thermal microcalorimeters. *Nuclear Instruments and Methods in Physics Research Section A: Accelerators, Spectrometers, Detectors and Associated Equipment*, 520(1):125–131, 2004. <http://dx.doi.org/10.1016/j.nima.2003.11.273>.

[SBYS11] Y. Shi, P. L. Brookes, Y. Wan Yap, and J. E. Sader. Accuracy of the lattice Boltzmann method for low-speed noncontinuum flows. *Physical Review E*, 83(4):045701, 2011. doi: 10.1103/PhysRevE.83.045701.

[Sch93] L. Schwager. Effects of secondary and thermionic electron emission on the collector and source sheaths of a finite ion temperature plasma using kinetic theory and numerical simulation. *Physics of Fluids B: Plasma Physics (1989-1993)*, 5(2):631–645, 1993. <http://dx.doi.org/10.1063/1.860495>.

[Sch02] P. K. Schmidt. *Wechselwirkung von Wasserstoff mit einer Pd (210)-und einer Ni (210)-Oberfläche*. PhD thesis, Freie Universität Berlin, 2002.

[Sch12] K. Scholberg. Supernova neutrino detection. In *Journal of Physics: Conference Series*, volume 375, page 042036. IOP Publishing, 2012. <http://iopscience.iop.org/1742-6596/375/4/042036>.

[Sch13a] M. Schlösser. *Accurate calibration of the Raman system for the Karlsruhe Tritium Neutrino Experiment*. PhD thesis, Karlsruhe Institute of Technology, 2013.

[Sch13b] F. Schneck. Design and setup of the Tritium Adsorption Desorption Experiment (TRIADE), 2013. diploma thesis, Karlsruhe Institute of Technology.

[Sch14] J. Schwarz. *The Detector System of the KATRIN Experiment - Implementation and First Measurements with the Spectrometer*. PhD thesis, Karlsruhe Institute of Technology, 2014. Available at: <https://publikationen.bibliothek.kit.edu/1000042772>.

[Sch16] K. Schönung. *Development of a Rear Wall for the KATRIN Rear Section and investigation of tritium compatibility of Rear Section components*. PhD thesis, Karlsruhe Institute of Technology, 2016.

[SD92] L. Stobiński and R. Duś. Atomic hydrogen adsorption on thin gold films. *Surface science*, 269:383–388, 1992. doi: 10.1016/0039-6028(92)91279-K.

[SD94] L. Stobiński and R. Duś. Model of atomic hydrogen adsorption on thin gold film surface. *Vacuum*, 45(2):299–301, 1994. doi: 10.1016/0042-207X(94)90194-5.

[SFOI84] M. Sugisaki, H. Furuya, K. Ono, and K. Idemitsu. Tritium solubility in SUS 316 stainless steel. *Journal of Nuclear Materials*, 120(1):36–40, 1984. doi: 10.1016/0022-3115(84)90168-5.

[SG11] N. Sternberg and V. Godyak. Two-dimensional cylindrical plasma for intermediate gas pressures. *Plasma Sources Science and Technology*, 20(1):015018, 2011. <http://iopscience.iop.org/0963-0252/20/1/015018>.

[SGM13] .F Sharipov, I. Graur, and O. Malyshev. Vacuum Gas Dynamics: Theory Experiments and Applications, 2013. Short Course at IVC-19th international vacuum congress 2013.

[Sha68] E. Shakhov. Generalization of the Krook kinetic relaxation equation. *Fluid Dynamics*, 3(5):95–96, 1968. doi: 10.1007/BF01029546.

[Sha96] F. Sharipov. Rarefied gas flow through a long tube at any temperature ratio. *Journal of Vacuum Science & Technology A*, 14(4):2627–2635, 1996. <http://dx.doi.org/10.1116/1.579991>.

[Sha97] F. Sharipov. Rarefied-gas flow-through a long tube at arbitrary pressure and temperature drops. *Journal of Vacuum Science & Technology A*, 15(4):2434–2436, 1997. <http://dx.doi.org/10.1116/1.580904>.

[Sha03] F. Sharipov. Numerical Calculation of the Tritium Flow through the KATRIN Beam Line, 2003. KATRIN internal report, Available at: https://fuzzy.fzk.de/bscw/bscw.cgi/92818?op=preview&back_url=825925.

[Sha04a] F. Sharipov. Calculations of Tritium Flow between the Buffer Vessel up to the first Vacuum System, 2004. KATRIN internal report, Available at: https://fuzzy.fzk.de/bscw/bscw.cgi/100305?op=preview&back_url=825925.

[Sha04b] F. Sharipov. Data on the velocity slip and temperature jump coefficients [gas mass, heat and momentum transfer]. In *Proceedings of the 5th International Conference on Thermal and Mechanical Simulation and Experiments in Microelectronics and Microsystems*, pages 243–249. IEEE, 2004. doi: 10.1109/ES-IME.2004.1304046.

[Sha07] F. Sharipov. Rarefied gas dynamics and its applications to vacuum technology, 2007. CERN Accelerator School, vacuum in accelerators, Available at: <https://cds.cern.ch/record/1046845>.

[Sha08] V. D. Shafranov. *Reviews of Plasma Physics*, volume 24. Springer, 2008.

[Sha09] F. Sharipov. Gas circulation due an azimuthal temperature distribution over a micro-tube wall. In *ASME 2009 7th International Conference on Nanochannels, Microchannels, and Minichannels*, pages 373–381. American Society of Mechanical Engineers, 2009. <http://fisica.ufpr.br/sharipov/ICNMM2009-82028.pdf>.

[Sha15] F. Sharipov. Three-dimensional numerical simulation of tritium flow in the source outlet and adjacent pumping chamber, 2015. KATRIN internal report, Available at: https://fuzzy.fzk.de/bscw/bscw.cgi/932322?op=preview&back_url=825925.

[Sha16] F. Sharipov. *Rarefied gas dynamics: fundamentals for research and practice*. John Wiley & Sons, 2016.

[Shi75] F. D. Shields. An acoustical method for determining the thermal and momentum accommodation of gases on solids. *The Journal of Chemical Physics*, 62(4):1248–1252, 1975. <http://dx.doi.org/10.1063/1.430639>.

[Shr10] F. Shripov. Tritium flow through a non-symmetrical source. Simulation of gas flow through an injection hole, 2010. KATRIN internal report, Available at: https://fuzzy.fzk.de/bscw/bscw.cgi/932768?op=preview&back_url=825925.

[SJF00] A. Saenz, S. Jonsell, and P. Froelich. Improved molecular final-state distribution of HeT+ for the β -decay process of T2. *Physical review letters*, 84(2):242, 2000. <https://doi.org/10.1103/PhysRevLett.84.242>.

[SK05] F. Sharipov and D. Kalempa. Separation phenomena in the tritium source and numerical simulations of turbo-molecular pumps, 2005. KATRIN internal report, Available at: https://fuzzy.fzk.de/bscw/bscw.cgi/968578?op=preview&back_url=825925.

[SK09] F. Sharipov and D. V. Kozak. Rarefied gas flow through a thin slit into vacuum simulated by the Monte Carlo method over the whole range of the Knudsen number. *Journal of Vacuum Science & Technology A*, 27(3):479–484, 2009. <http://dx.doi.org/10.1116/1.3106623>.

[Smi03] A. Y. Smirnov. The MSW effect and solar neutrinos. In *Neutrino telescopes. Proceedings, 10th International Workshop, Venice*, pages 23–43, 2003. <https://arxiv.org/pdf/hep-ph/0305106.pdf>.

[Son07] Y. Sone. *Molecular gas dynamics: theory, techniques, and applications*. Springer Science & Business Media, 2007.

[Sou86] P. C. Sours. *Hydrogen Properties for Fusion Energies*. University of California Press, 1986.

[SRS⁺13] M. Schlösser, S. Rupp, H. Seitz, S. Fischer, B. Bornschein, T. James, and H. Telle. Accurate calibration of the laser Raman system for the Karlsruhe Tritium Neutrino Experiment. *Journal of Molecular Structure*, 1044:61–66, 2013. <http://dx.doi.org/10.1016/j.molstruc.2012.11.022>.

[SS74] M. Seidl and E. Steinheil. Measurement of momentum accommodation coefficients on surfaces characterized by Auger spectroscopy, Sims and LEED. *Rarefied gas dynamics*, 1974.

[SS94] F. Sharipov and V. Seleznev. Rarefied gas flow through a long tube at any pressure ratio. *Journal of Vacuum Science & Technology A*, 12(5):2933–2935, 1994. <http://dx.doi.org/10.1116/1.578969>.

[SS98] F. Sharipov and V. Seleznev. Data on internal rarefied gas flows. *Journal of Physical and Chemical Reference Data*, 27(3):657–706, 1998. <http://dx.doi.org/10.1063/1.556019>.

[Ste79] J. Stefan. Über die Beziehung zwischen der Wärmestrahlung und der Temperatur. *Sitzungsberichte der mathematisch-naturwissenschaftlichen Classe der kaiserlichen Akademie der Wissenschaften*, 79(1):391, 1879.

[Sto04] S. Stolpa. Turbulent heat transfer, 2004. research report from South Bend, University of Notre Dame.

[Str11] B. Streppel. *Hydrogen Adsorption on Metal-Organic Frameworks*. PhD thesis, Universität Stuttgart, 2011.

[Stu10] M. Sturm. *Aufbau und Test des Inner-Loop Systems der Tritiumquelle von KATRIN*. PhD thesis, Karlsruhe Institute of Technology, 2010. <https://publikationen.bibliothek.kit.edu/1000019355>.

[Suk05] S. P. Sukhatme. *A textbook on heat transfer*. Universities Press, 4 edition, 2005.

[SV82] J. Schechter and J. W. Valle. Neutrinoless double- β decay in $SU(2) \times U(1)$ theories. *Physical Review D*, 25(11):2951, 1982. <https://doi.org/10.1103/PhysRevD.25.2951>.

[SVG94] R. Stewart, P. Vitello, and D. Graves. Two-dimensional fluid model of high density inductively coupled plasma sources. *Journal of Vacuum Science & Technology B*, 12(1):478–485, 1994. <http://dx.doi.org/10.1116/1.587102>.

[SVG⁺95] R. Stewart, P. Vitello, D. Graves, E. Jaeger, and L. Berry. Plasma uniformity in high-density inductively coupled plasma tools. *Plasma Sources Science and Technology*, 4(1):36, 1995. <http://iopscience.iop.org/0963-0252/4/1/005>.

[SW64] A. Salam and J. C. Ward. Electromagnetic and weak interactions. *Physics Letters*, 13(2):168–171, 1964. doi: 10.1016/0031-9163(64)90711-5.

[SYC06] X. Shan, X-F Yuan, and H. Chen. Kinetic theory representation of hydrodynamics: a way beyond the Navier-Stokes equation. *Journal of Fluid Mechanics*, 550(1):413–441, 2006. doi: 10.1017/S0022112005008153.

[Tac14] F. Taccogna. Non-classical plasma sheaths: space-charge-limited and inverse regimes under strong emission from surfaces. *The European Physical Journal D*, 68(7):1–8, 2014.

[Thü07] T. Thümmler. *Präzisionsüberwachung und Kalibration der Hochspannung für das KATRIN Experiment*. PhD thesis, Universität Münster, 2007. Available at: http://repository.uni-muenster.de/document/miami/0e96c5e3-6f06-489e-a73f-5859fbe9cae7/diss_thuemmler.pdf.

[TINY90] H. Tawara, Y. Itikawa, H. Nishimura, and M. Yoshino. Cross sections and related data for electron collisions with hydrogen molecules and molecular ions. *Journal of Physical and Chemical Reference Data*, 19(3):617–636, 1990. <http://dx.doi.org/10.1063/1.555856>.

[TL29] L. Tonks and I. Langmuir. A general theory of the plasma of an arc. *Physical review*, 34(6):876, 1929. <http://journals.aps.org/pr/pdf/10.1103/PhysRev.34.876>.

[TL74] L. B. Thomas and R. Lord. Comparative measurements of tangential momentum and thermal accommodations on polished and on roughened steel spheres. *Rarefied gas dynamics*, 8:405–412, 1974.

[TLC04] F. Taccogna, S. Longo, and M. Capitelli. Plasma-surface interaction model with secondary electron emission effects. *Physics of Plasmas (1994-present)*, 11(3):1220–1228, 2004. <http://dx.doi.org/10.1063/1.1647567>.

[TRC83] S. Trajmar, D. F. Register, and A. Chutjian. Electron scattering by molecules II. Experimental methods and data. *Physics Reports*, 97(5):219–356, 1983. doi: 10.1016/0370-1573(83)90071-6.

[UD11] M. Ubieto Diaz. *Off-line commissioning of a non-destructive FT-ICR detection system for monitoring the ion concentration in the KATRIN beamline*. PhD thesis, MPIK Heidelberg, 2011. Available at: <http://archiv.ub.uni-heidelberg.de/volltextserver/12942/>.

[Val10] K. Valerius. The wire electrode system for the KATRIN main spectrometer. *Progress in Particle and Nuclear Physics*, 64(2):291–293, 2010. <http://dx.doi.org/10.1016/j.ppnp.2009.12.032>.

[Val16] K. Valerius. Direct probes of neutrino mass, 2016. Talk at the NEUTRINO conference London 2016, Available at: https://fuzzy.fzk.de/bscw/bscw.cgi/1018800?op=preview&back_url=1017099.

[vK14] A. von Keudell. Einührung in die Plasmaphysik, 2014. lecture notes summer semester 2014, Ruhr-Universität Bochum, Available at: <http://reaktiveplasmen.rub.de/files/skripten/skriptPP.pdf>.

[VR15] J. W. F. Valle and J. Romao. *Neutrinos in high energy and astroparticle physics*. John Wiley & Sons, 2015.

[VRM⁺05] G. Vidali, J. Roser, G. Manicó, V. Pirronello, H. B. Perets, and O. Biham. Formation of molecular hydrogen on analogues of interstellar dust grains: experiments and modelling. In *Journal of Physics: Conference Series*, volume 6,

page 36. IOP Publishing, 2005. <http://iopscience.iop.org/1742-6596/6/1/003>.

[VSD⁺14] D. Vénos, M. Slezák, O. Dragoun, A. Inoyatov, O. Lebeda, Z. Pulec, J. Senterrestiová, and A. Špalek. Gaseous source of 83mKr conversion electrons for the neutrino experiment KATRIN. *Journal of Instrumentation*, 9(12):P12010, 2014. <http://iopscience.iop.org/1748-0221/9/12/P12010>.

[Wan13] N. Wandkowsky. *Study of background and transmission properties of the KATRIN spectrometers*. PhD thesis, Karlsruhe Institute of Technology, 2013. Available at: <https://publikationen.bibliothek.kit.edu/1000036631>.

[Wan15] K. Wandelt, editor. *Surface and Interface Science, Solid-Gas Interfaces*. Wiley VCH, 2015.

[WAWJ04] M. Wutz, H. Adam, W. Walcher, and K. Jousten. Handbuch Vakuumtechnik. *Vieweg & Sohn Verlag*, 2004.

[WB35] E. Wigner and J. Bardeen. Theory of the work functions of monovalent metals. *Physical Review*, 48(1):84, 1935. <https://doi.org/10.1103/PhysRev.48.84>.

[Wei35] C. v. Weizsäcker. Zur theorie der kernmassen. *Zeitschrift für Physik A Hadrons and Nuclei*, 96(7):431–458, 1935. doi: 10.1007/BF01337700.

[Wei67] S. Weinberg. A model of leptons. *Physical review letters*, 19(21):1264, 1967. <https://doi.org/10.1103/PhysRevLett.19.1264>.

[Wel54] P. Welander. On the temperature jump in a rarefied gas. *Arkiv fysik*, 7, 1954.

[Wer15] N. Werling. Einflüsse von Variationen der Austrittsarbeit innerhalb des WGTS Strahlrohres auf die Neutrinomassan-Sensitivität des KATRIN-Experiments, 2015. Bachelor thesis, Karlsruhe Institute of Technology.

[WGT04] WGTS charging, 2004. KATRIN internal document, Available at: https://fuzzy.fzk.de/bscw/bscw.cgi/78568?op=preview&back_url=1005311%3fclient_size%3d1463x979.

[Win11] A. Windberger. Berechnungen und Simulationen zum Verhalten von Ionen in der differenziellen Pumpstrecke des KATRIN-Experiments, 2011. diploma thesis, Karlsruhe Institute of Technology, Available at: <https://www.katrin.kit.edu/publikationen/dth-windberger.pdf>.

[WM02] C.-D. Wen and I. Mudawar. Experimental investigation of emissivity of aluminum alloys and temperature determination using multispectral radiation thermometry (MRT) algorithms. *Journal of materials engineering and performance*, 11(5):551–562, 2002. <http://dx.doi.org/10.1016/j.applthermaleng.2011.04.005>.

[Wol78] L. Wolfenstein. Neutrino oscillations in matter. *Physical Review D*, 17(9):2369, 1978. <https://doi.org/10.1103/PhysRevD.17.2369>.

[Wol09] J. Wolf. Size matters: the vacuum system of the KATRIN neutrino experiment. *Journal of the Vacuum Society of Japan*, 52(5):278–284, 2009. <http://doi.org/10.3131/jvsj2.52.278>.

[WS12] L. Winslow and R. Simpson. Characterizing quantum-dot-doped liquid scintillator for applications to neutrino detectors. *Journal of Instrumentation*, 7(07):P07010, 2012. <http://iopscience.iop.org/1748-0221/7/07/P07010>.

[WZ13] C. Weinheimer and K. Zuber. Neutrino masses. *Annalen der Physik*, 525(8-9):565–575, 2013. doi: 10.1002/andp.201300063.

- [Y.16] Zeyuan Y. Recent Results from the Daya Bay Experiment, 2016. Talk at NEUTRINO 2016, London, Available at: https://www.iopconferences.org/IOP/media/uploaded/EV1OP/event_948/09.20___2_.pdf.
- [Zie13] S. Ziegler. Die Extraktion der Energieverlustfunktion beim KATRIN Experiment, 2013. diploma thesis, Karlsruhe Institute of Technology.
- [ZT80] A. Zhilinskii and L. D. Tsendin. Collisional diffusion of a partially-ionized plasma in a magnetic field. *Soviet Physics Uspekhi*, 23(7):331, 1980. <http://iopscience.iop.org/0038-5670/23/7/R02>.
- [Zub12] K. Zuber. *Neutrino physics*. CRC press, 2 edition, 2012.
- [Züt03] A. Züttel. Materials for hydrogen storage. *Materials today*, 6(9):24–33, 2003. [http://dx.doi.org/10.1016/S1369-7021\(03\)00922-2](http://dx.doi.org/10.1016/S1369-7021(03)00922-2).

Acknowledgement / Danksagung

An dieser Stelle möchte ich die Gelegenheit nutzen, mich bei allen zu bedanken, die mich im Verlauf meiner Doktorarbeit unterstützt haben. Besonders möchte ich dabei danken: Prof. Dr. Guido Drexlin, der mir die Möglichkeit gegeben hat, meine Doktorarbeit im Rahmen des KATRIN Experimentes durchzuführen.

Prof. Dr. Christian Weinheimer, der sich trotz seines vollen Terminkalenders kurzfristig dazu bereit erklärt hat, als Zweitgutachter meiner Doktorarbeit zu fungieren.

Prof. Dr. Ernst Otten, für die große Hilfe und Unterstützung bei der Charakterisierung des Quellplasmas, sowie die detaillierten Korrekturvorschläge und die vielen aufschlussreichen Diskussionen.

Dr. Kathrin Valerius für die fachliche Betreuung und auch sonstige Unterstützung, die mir meine Arbeit sehr erleichtert hat, sowie die Mühe und Zeit, die sie in die Korrektur meiner Dissertation gesteckt hat.

Für das Korrekturlesen meiner Arbeit möchte ich mich weiterhin bei Manuel Klein, Florian Heizmann, Hendrik Seitz-Moskaliuk, Marco Kleesiek sowie Moritz Erhard bedanken.

Ein großes Dankeschön auch an alle Kollegen die immer für eine angenehme Arbeitsatmosphäre gesorgt haben und für den ein oder anderen Witz zu haben waren, insbesondere Alexander Jansen, Florian Heizmann, Manuel Klein, Hendrik Seitz-Moskaliuk, Martin Babutzka und Kathrin Valerius – ohne euch hätte das Arbeiten oft weit weniger Spaß gemacht.

Der größte Dank geht an dieser Stelle jedoch an meine Familie: meine Eltern, meine Schwester Katja und meinen Ehemann Thomas, die mich immer unterstützt und motiviert haben und die dafür gesorgt haben, dass ich nie dauerhaft den Kopf hängen lies. Ohne euch hätte ich diese Arbeit nicht schreiben können.

